

## RESEARCH PAPERS

- 021001 Heat Transfer Measurements and Predictions for a Modern, High-Pressure, Transonic Turbine, Including Endwalls**  
James A. Tallman, Charles W. Haldeman, Michael G. Dunn, Anil K. Tolpadi, and Robert F. Bergholz
- 021002 Mass/Heat Transfer in Rotating, Smooth, High-Aspect Ratio (4:1) Coolant Channels With Curved Walls**  
Eashwar Sethuraman, Sumanta Acharya, and Dimitris E. Nikitopoulos
- 021003 Experimental Investigation of the Clocking Effect in a 1.5-Stage Axial Turbine—Part I: Time-Averaged Results**  
Sven König, Bernd Stoffel, and M. Taher Schobeiri
- 021004 Experimental Investigation of the Clocking Effect in a 1.5-Stage Axial Turbine—Part II: Unsteady Results and Boundary Layer Behavior**  
Sven König, Bernd Stoffel, and M. Taher Schobeiri
- 021005 A Method for Estimating the Influence of Time-Dependent Vane and Blade Pressure Fields on Turbine Rim Seal Ingestion**  
Bruce V. Johnson, Ralf Jakoby, Dieter E. Bohn, and Didier Cunat
- 021006 On the Response of a Strongly Diffusing Flow to Propagating Wakes**  
J. P. Gostelow, R. L. Thomas, and D. S. Adebayo
- 021007 Film Cooling From a Row of Holes Supplemented With Antivortex Holes**  
Alok Dhungel, Yiping Lu, Wynn Phillips, Srinath V. Ekkad, and James Heidmann
- 021008 Effects of Combustor Exit Profiles on Vane Aerodynamic Loading and Heat Transfer in a High Pressure Turbine**  
M. D. Barringer, K. A. Thole, and M. D. Polanka
- 021009 An Experimental Study of Combustor Exit Profile Shapes on Endwall Heat Transfer in High Pressure Turbine Vanes**  
M. D. Barringer, K. A. Thole, and M. D. Polanka
- 021010 Migration of Combustor Exit Profiles Through High Pressure Turbine Vanes**  
M. D. Barringer, K. A. Thole, M. D. Polanka, J. P. Clark, and P. J. Koch
- 021011 Analysis of Turbulent Flow in 180 deg Turning Ducts With and Without Guide Vanes**  
Jiang Luo and Eli H. Razinsky
- 021012 Forced Convection Heat Transfer in Channels With Rib Turbulators Inclined at 45 deg**  
Giovanni Tanda and Roberto Abram
- 021013 Unsteady Simulation of an Axial Compressor Stage With Casing and Blade Passive Treatments**  
Nicolas Gourdain and Francis Leboeuf
- 021014 On the Coupling of Inverse Design and Optimization Techniques for the Multiobjective, Multipoint Design of Turbomachinery Blades**  
Duccio Bonaiuti and Mehrdad Zangeneh
- 021015 Experiments on the Physical Mechanism of Heat Transfer Augmentation by Freestream Turbulence at a Cylinder Stagnation Point**  
A. C. Nix and T. E. Diller

(Contents continued on inside back cover)

This journal is printed on acid-free paper, which exceeds the ANSI Z39.48-1992 specification for permanence of paper and library materials. ©™  
♻️ 85% recycled content, including 10% post-consumer fibers.

Editor, **DAVID C. WISLER** (2013)  
Assistant to the Editor: **ELIZABETH WISLER**  
Associate Editors  
Gas Turbine (Review Chairs)  
**K. BRUN** (2009)  
**T. SATTELMAYER** (2009)  
Aeromechanics  
**M. MONTGOMERY** (2009)  
**A. SINHA** (2009)  
Boundary Layers and Turbulence  
**G. WALKER** (2009)  
Compressor Aero  
**ZOLTAN S. SPAKOVSKY** (2011)  
Computational Fluid Dynamics  
**J. ADAMCZYK** (2009)  
**M. CASEY** (2009)  
Experimental Methods  
**W.-F. NG** (2009)  
Heat Transfer  
**R. BUNKER** (2009)  
**J.-C. HAN** (2009)  
Radial Turbomachinery  
**R. VAN DEN BRAEMBUSSCHE** (2009)  
Turbomachinery Aero  
**S. GALLIMORE** (2009)  
**D. PRASAD** (2009)  
**A. R. WADIA** (2009)

**PUBLICATIONS COMMITTEE**  
Chair, **BAHRAM RAVANI**

**OFFICERS OF THE ASME**  
President, **THOMAS M. BARLOW**  
Executive Director, **THOMAS G. LOUGHLIN**  
Treasurer, **T. PESTORIUS**

**PUBLISHING STAFF**  
Managing Director, Publishing  
**PHILIP DI VIETRO**  
Manager, Journals  
**COLIN MCATEER**  
Production Coordinator  
**JUDITH SIERANT**

Transactions of the ASME, Journal of Turbomachinery (ISSN 0889-504X) is published quarterly (Jan., Apr., July, Oct.) by The American Society of Mechanical Engineers, Three Park Avenue, New York, NY 10016. Periodicals postage paid at New York, NY and additional mailing offices.

POSTMASTER: Send address changes to Transactions of the ASME, Journal of Turbomachinery, c/o THE AMERICAN SOCIETY OF MECHANICAL ENGINEERS, 22 Law Drive, Box 2300, Fairfield, NJ 07007-2300.

CHANGES OF ADDRESS must be received at Society headquarters seven weeks before they are to be effective. Please send old label and new address.

**STATEMENT from By-Laws.** The Society shall not be responsible for statements or opinions advanced in papers or ... printed in its publications (B7.1, Par. 3).

**COPYRIGHT © 2009** by the American Society of Mechanical Engineers. For authorization to photocopy material for internal or personal use under those circumstances not falling within the fair use provisions of the Copyright Act, contact the Copyright Clearance Center (CCC), 222 Rosewood Drive, Danvers, MA 01923, tel: 978-750-8400, www.copyright.com. Request for special permission or bulk copying should be addressed to Reprints/Permission Department. Canadian Goods & Services Tax Registration #126148048

- 021016 **A Conceptual Flutter Analysis of a Packet of Vanes Using a Mass-Spring Model**  
Roque Corral, Juan Manuel Gallardo, and Carlos Martel
- 021017 **Effect of Upstream Wake With Vortex on Turbine Blade Platform Film Cooling With Simulated Stator-Rotor Purge Flow**  
Lesley M. Wright, Sarah A. Blake, Dong-Ho Rhee, and Je-Chin Han
- 021018 **Numerical Investigation of Tandem Airfoils for Subsonic Axial-Flow Compressor Blades**  
Jonathan McGlumphy, Wing-Fai Ng, Steven R. Wellborn, and Severin Kempf
- 021019 **Synchronizing Separation Flow Control With Unsteady Wakes in a Low-Pressure Turbine Cascade**  
M. Bloxham, D. Reimann, K. Crapo, J. Pluim, and J. P. Bons
- 021020 **Reduced Rough-Surface Parametrization for Use With the Discrete-Element Model**  
Stephen T. McClain and Jason M. Brown
- 021021 **Effects of Large Scale High Freestream Turbulence and Exit Reynolds Number on Turbine Vane Heat Transfer in a Transonic Cascade**  
Shakeel Nasir, Jeffrey S. Carullo, Wing-Fai Ng, Karen A. Thole, Hong Wu, Luzeng J. Zhang, and Hee Koo Moon

The ASME Journal of Turbomachinery is abstracted and indexed in the following:

*Aluminum Industry Abstracts, Aquatic Science and Fisheries Abstracts, Ceramics Abstracts, Chemical Abstracts, Civil Engineering Abstracts, Compendex (The electronic equivalent of Engineering Index), Corrosion Abstracts, Current Contents, Ei EncompassLit, Electronics & Communications Abstracts, Energy Information Abstracts, Engineered Materials Abstracts, Engineering Index, Environmental Science and Pollution Management, Excerpta Medica, Fluidex, Fuel and Energy Abstracts, INSPEC, Index to Scientific Reviews, Materials Science Citation Index, Mechanical & Transportation Engineering Abstracts, Mechanical Engineering Abstracts, METADEX (The electronic equivalent of Metals Abstracts and Alloys Index), Metals Abstracts, Oceanic Abstracts, Pollution Abstracts, Referativnyi Zhurnal, Shock & Vibration Digest, Steels Alert*

# Heat Transfer Measurements and Predictions for a Modern, High-Pressure, Transonic Turbine, Including Endwalls

**James A. Tallman**  
General Electric Global Research Center,  
Niskayuna, NY 12309

**Charles W. Haldeman**

**Michael G. Dunn**

Gas Turbine Laboratory,  
The Ohio State University,  
Columbus, OH 43220

**Anil K. Tolpadi**  
General Electric Global Research Center,  
Niskayuna, NY 12309

**Robert F. Bergholz**  
General Electric Transportation,  
Cincinnati, OH 45215

*This paper presents both measurements and predictions of the hot-gas-side heat transfer to a modern,  $1\frac{1}{2}$  stage high-pressure, transonic turbine. Comparisons of the predicted and measured heat transfer are presented for each airfoil at three locations, as well as on the various endwalls and rotor tip. The measurements were performed using the Ohio State University Gas Turbine Laboratory Test Facility (TTF). The research program utilized an uncooled turbine stage at a range of operating conditions representative of the engine: in terms of corrected speed, flow function, stage pressure ratio, and gas-to-metal temperature ratio. All three airfoils were heavily instrumented for both pressure and heat transfer measurements at multiple locations. A 3D, compressible, Reynolds-averaged Navier-Stokes computational fluid dynamics (CFD) solver with  $k-\omega$  turbulence modeling was used for the CFD predictions. The entire  $1\frac{1}{2}$  stage turbine was solved using a single computation, at two different Reynolds numbers. The CFD solutions were steady, with tangentially mass-averaged inlet/exit boundary condition profiles exchanged between adjacent airfoil-rows. Overall, the CFD heat transfer predictions compared very favorably with both the global operation of the turbine and with the local measurements of heat transfer. A discussion of the features of the turbine heat transfer distributions, and their association with the corresponding flow-physics, has been included.*

[DOI: 10.1115/1.2985072]

## Introduction

Modern gas turbine engines are continually being pushed toward increased operating temperatures to improve performance. This trend is limited by the ability of the turbine components to withstand the increasingly harsh thermal environment for an economically profitable length of time. Balancing turbine performance with turbine life is perhaps the biggest key design trade-off facing gas turbine engine manufacturers today. Particularly susceptible to this design trade-off are the high-pressure turbine airfoils and endwalls, which are directly exposed to the highest-temperature gas. Understanding, and ultimately predicting, the hot-gas-side heat transfer in the high-pressure turbine stages is key to creating improved turbine designs that operate with higher temperatures, reduced cooling flow penalties, improved performance, and increased component life.

The two primary objectives of this research effort were (1) to develop a better understanding of hot-gas-side heat transfer in high-pressure turbine stages and (2) to demonstrate improved turbine heat transfer prediction capabilities, which can facilitate improved turbine thermal designs. These two objectives were pursued in parallel as follows: first, the hot-gas-side heat transfer was measured across the airfoils and endwalls of a modern, transonic, high-pressure,  $1\frac{1}{2}$  stage turbine over a range of engine-realistic operating conditions (corrected-speed, flow function, pressure ratio, etc.). Second, computational fluid dynamics (CFD) was applied to the configuration of interest, and predictions of the hot-gas-side heat transfer were obtained that agreed well with the measurements. The agreement between measurements and predic-

tions served toward the accomplishment of Objective 2, while a detailed interrogation of the validated predictions served toward the accomplishment of Objective 1.

The findings presented in this paper are in continuation of those presented in two previous papers dealing with the same experimental turbine. Haldeman et al. [1] presented time-averaged heat transfer measurements of the turbine, as well as both time-averaged and time-resolved static pressure measurements. Tallman [2] applied CFD to the turbine case and compared the steady-state predictions of pressure and heat transfer with the time-resolved measurements. In both references, the reported results were limited to the midspan locations of the turbine airfoils. The present paper reports the entire time-averaged data set: including airfoil locations away from the midspan, endwalls, and tips, as well as comparisons between the data and the CFD. In addition, the CFD solutions presented in Ref. [2] have been recomputed as multistage solutions of the entire  $1\frac{1}{2}$ -stage turbine. The new computations presented here show that the novel techniques used by Tallman [2] to predict the heat transfer at midspan work at other locations within the turbine as well.

Dunn [3] reviewed the state-of-the-art regarding turbine external heat transfer in 2001. Dunn concluded that turbine external heat transfer predictions using CFD show promise, but that considerable effort remains before the use of CFD for heat transfer predictions is as commonplace as that for aerodynamic predictions. Since the review by Dunn, further CFD studies have been directed at this effort, primarily focusing on single-airfoil-row calculations of stationary experimental cases: for example, Giel et al. [4] and Yang et al. [5]. Most endwall and tip predictions to date have been focused specifically on that region and not as part of the overall turbine. This has allowed the predictive tools to focus on the local conditions to obtain better predictions. Some recent examples of this type of work occurring after Ref. [3] include Refs. [6–9].

Comparatively, the novelties of the present study are as follows:

Contributed by the International Gas Turbine Institute of ASME for publication in the JOURNAL OF TURBOMACHINERY. Manuscript received July 14, 2006; final manuscript received August 18, 2008; published online January 22, 2009. Review conducted by David Wisler. Paper presented at the ASME Turbo Expo 2006: Land, Sea and Air (GT2006), Barcelona, Spain, May 8–11, 2006.

(a) the experimental turbine case was of considerable realism and provided validation data in areas of the turbine where previously existing data were scarce (i.e., rotating endwalls), (b) the predictions came from CFD computations of the entire  $1\frac{1}{2}$  stage turbine, thus including the influence of the multiple-stage aerodynamics on the hot-gas-side heat transfer, (c) the turbine heat transfer predictions showed a generally good agreement with the measurements at all geometric locations (airfoils, endwalls, and tip), when compared with the levels of agreement observed in the previously referenced works, and (d) the prediction methodology, built around a simple two-equation turbulence model [2], was not “tuned” to match the turbine measurements in any particular area: via turbulence modeling constants or additional turbulence quantity equations.

The inherent complexity of the high-pressure turbine flow field makes understanding and predicting hot-gas-side heat transfer very difficult. To simplify the effort, the addition of cooling or purge flows to the turbine passage was excluded from the scope of this work, although that is currently being pursued. Additionally, the current investigations did not include the influence of surface roughness, which is typically present in real engines and acts to augment hot-gas-side heat transfer. Even without these influences, the turbine heat transfer measurements and predictions stand as a foundation upon which these important factors can be investigated in the future.

### High-Pressure Turbine Case

The turbine case used in this study was a modern, 1.5 stage high-pressure turbine investigated experimentally at the Ohio State University Gas Turbine Laboratory Turbine Test Facility (TTF). The investigated turbine was actual engine hardware at its correct scale, and measurements were taken over a range of real-engine operating points. A very short description of the TTF facility, the turbine case, and the measurement process is included below (due to space limitations), but readers are encouraged to look at the previous publications using this stage as a research tool [1,10,11,2] for more complete facility and measurement descriptions.

**TTF Facility Description.** The TTF consists of a large short-duration shock tunnel, which discharges high temperature/high-pressure air past a fast acting valve, through a rotating turbine, and into an initially evacuated dump tank via one of two different modes: blowdown or shock tube. In blowdown mode, the initially pressurized tunnel simply discharges into the turbine, controlled by the fast-acting valve. This mode does not produce hot gas and as such is used primarily for aerodynamic work. In shock-tube mode, a reflected shock wave is established in the tunnel, with the fast-acting valve timed to open as the shock wave arrives at the turbine. The blowdown mode is used for obtaining measurements over an extended time window (approximately 100 ms), while shock-tube mode allows for higher inlet temperatures to the turbine over a shorter time period ( $\sim 40$  ms), which better facilitates heat transfer measurements.

The inlet total pressure and temperature to the turbine are controlled via the initial conditions in the shock tunnel and are verified by measurement rakes upstream of the turbine. The mass flow rate and pressure ratio across the turbine are controlled using an adjustable exit choke plate sufficiently far downstream of the turbine airfoils. The turbine rotor angular acceleration can be measured and is used to determine the rotor torque and power output.

The turbine can be instrumented with both Kulite pressure sensors and thin platinum film Pyrex gauges for transient pressure and temperature measurements, respectively. The transient temperature signal from the Pyrex gauges can then be used, along with a one-dimensional conduction analysis, to deduce the heat flux to the surface. All measurements from the stage are passed to a data acquisition system (via a slip ring for the rotor), where the time-dependent signals are acquired. All data are acquired at

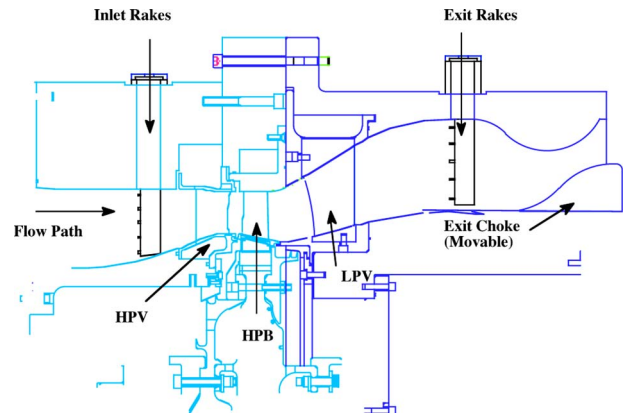


Fig. 1 Rig schematic drawing (stretched image)

100 kHz using a set of anti-aliasing filters set at 45 kHz. This ensures that proper resolution of the time-resolved data is obtained.

**Turbine Case Description.** The specific turbine geometry investigated is the same modern three-dimensional geometry and blade row configuration found in a current, state-of-the-art, commercial gas turbine engine, minus the geometry and flows associated with cooling, as well as without surface roughness. The turbine is a stage and one-half machine (high-pressure vane (HPV), high-pressure blade (HPB), and low-pressure vane (LPV)), with modern airfoils of very strong three-dimensional shape and an operating total pressure ratio in excess of 5. The airfoil numbers for the turbine are 38, 72, and 38 for the HPV, HPB, and HPV, respectively.

A sketch of the main turbine stage is shown in Fig. 1, showing the relative location of the airfoil-rows. The region of the investigated flow path is defined by the location of the inlet and exit rakes. At each rake location, there are two total temperature rakes and two total pressure rakes, with five sensors per rake spaced to cover equal portions of the turbine throughflow annulus area.

The turbine was instrumented with 485 sensors, strategically distributed throughout the turbine’s three airfoil-rows. Each airfoil-row was equipped with both heat-flux gauges and pressure transducers distributed at three span locations: 15%, 50%, and 90% span for the HPV and HPB, and 10%, 50%, and 90% span for the LPV. Additionally, heat-flux gauges and pressure transducers were mounted on the HPV inner and outer endwalls, the HPB platform, and on various HPB tip geometries. Pressure transducers were also mounted in the area between the HPB and LPV on the inner and outer endwalls.

### Experiments Performed

Table 1 outlines the matrix of experiments performed as part of this study and shows the measured turbine operating conditions for the various experiments. A more detailed explanation of these sets of experiments and their intended objectives is reported in Refs. [1,10].

Three groups of experiments are shown in Table 1. The first group obtained static pressure measurements from the facility operating in blowdown mode, while the second and third groups obtained heat transfer measurements from the facility operating in shock-tube mode. The major difference between the second and third group of experiments is the change in turbine inlet total pressure, which corresponds to a Reynolds number variation. The average Reynolds number per meter length ( $Re/L$ ), shown in Table 1, is used to classify these three sets of runs throughout this paper. For all three experimental groups in Table 1, the true non-dimensional inlet Reynolds number (based on chord length) exceeded  $3.5 \times 10^5$  for the HPV, and  $4.5 \times 10^5$  for both the HPB and



**Table 1 Matrix of Experiments**

Exp. data Set No.	Mass flow / vane inlet area (kg/(s m <sup>2</sup> ))	Corrected rotor speed (rpm/K <sup>1/2</sup> )	Total pressure ratio (% target)	Inlet P <sub>o</sub> (kPa)	Inlet T <sub>o</sub> (K)	rpm	Re/L (1/m)
Re/L=6.1 × 10 <sup>6</sup> Pressure measurement data set group—Blowdown mode experimental Group 1 ([10], Table 1)							
26	134.0	360.9	99.96	420.6	388.0	7108.1	5.92 × 10 <sup>6</sup>
27	131.5	360.3	100.04	416.4	390.1	7116.5	5.74 × 10 <sup>6</sup>
31	139.7	360.2	100.32	444.0	395.3	7161.2	6.16 × 10 <sup>6</sup>
32	138.0	359.0	100.32	433.8	397.2	7155.2	6.06 × 10 <sup>6</sup>
Re/L=3.1 × 10 <sup>6</sup> Heat transfer data set group—Shock-tube mode experimental Group 3 ([10], Table 1)							
5	96.6	355.3	99.60	388.0	636.9	8967.1	3.08 × 10 <sup>6</sup>
6	98.0	357.3	99.95	390.4	631.7	8976.4	3.14 × 10 <sup>6</sup>
7	100.9	361.6	98.93	397.7	614.6	8960.6	3.29 × 10 <sup>6</sup>
9	95.9	356.2	100.27	384.7	635.6	8979.8	3.06 × 10 <sup>6</sup>
10	94.9	356.2	100.95	380.6	634.8	8974.4	3.03 × 10 <sup>6</sup>
11	96.7	363.0	100.31	379.6	609.5	8961.7	3.17 × 10 <sup>6</sup>
Mean	97.2	358.3	100.00	386.8	627.1	8970.0	3.13 × 10 <sup>6</sup>
Re/L=4.6 × 10 <sup>6</sup> Heat transfer data set group—Shock-tube mode experimental Group 5 ([10], Table 1)							
16	140.0	360.3	99.17	553.5	617.6	8951.9	4.56 × 10 <sup>6</sup>
17	140.8	358.3	100.20	564.1	635.5	9031.7	4.50 × 10 <sup>6</sup>
18	141.7	360.5	99.99	562.4	622.4	8994.3	4.59 × 10 <sup>6</sup>
19	144.6	361.8	100.38	572.6	619.8	9005.8	4.69 × 10 <sup>6</sup>
20	140.7	361.5	100.26	557.8	621.4	9007.1	4.56 × 10 <sup>6</sup>
Mean	141.6	360.5	100.00	562.1	623.4	8998.2	4.58 × 10 <sup>6</sup>

LPV. Similarly, exit Reynolds numbers exceeded  $1.5 \times 10^6$  for the HPV and  $5 \times 10^5$  for the HPB and LPV, again for all three Table 1 groups. Such Reynolds number values tend to indicate that the airfoils' boundary layers are primarily turbulent, and the agreement of the turbulent CFD heat transfer predictions with rig measurements verifies this.

### Data Reduction and Uncertainty Analysis

The time-averaged pressure data were obtained from the time-resolved measurements by averaging the pressure transducer signal over one rotor revolution. This result was normalized by the average total inlet pressure for the given run, yielding a normalized pressure (PR) between 0 and 1.

The time-averaged heat-flux data were extracted from the time-dependent temperature history of the heat-flux gauges using a semi-infinite solid approximation and a Cook–Felderman algorithm [12]. Heat transfer results are presented as a nondimensional Stanton (St) number defined below:

$$St = \frac{\dot{q}_{\text{wall}}}{\dot{m}/A_{\text{inlet}}[(C_p T_o)_{\text{inlet}} - (C_p T)_{\text{wall}}]} \quad (1)$$

In this definition, the subscript “inlet” refers to the HPV inlet for all locations and not to a local airfoil-row inlet.

A detailed discussion about the uncertainty in the acquisition of time-averaged pressure and heat transfer data in the short-duration facility is presented in Haldeman's dissertation [10]. The instrumentation uncertainty in the measurements of PR varies between  $\pm 0.06\%$  and  $\pm 0.27\%$ . For the St measurements, a more approximate estimate of the instrumentation uncertainty is  $\pm 5\%$ . Since the various experiments were good replicas of each other, and the measurements have been appropriately nondimensionalized, the run-to-run measurement variation range is a good indicator of the

uncertainty. Variations between runs that exceed the expected instrumentation uncertainty indicated a reason for further investigation of the sensors. For all presentations of experimental results in this paper, all available measurements from all appropriate runs are shown, and the spread in the data, along with the estimates given above, can be used to judge the accuracy of the measurements.

**CFD Predictions.** The General Electric Company CFD flow solver turbine and compressor aero (TACOMA) [13] was used to predict the  $Re/L=3.1 \times 10^6$  and  $Re/L=4.6 \times 10^6$  cases shown in Table 1. TACOMA is a fully 3D, compressible, Reynolds-averaged Navier–Stokes flow solver. The solver uses a Runge–Kutta time marching approach, based on the cell-centered finite volume methods of Jameson [14]. A wall-integration approach to modeling the boundary layers was developed, based around the  $k-\omega$  turbulence model of Wilcox [15], the details of which are reported in Ref. [2]. The turbulence production source term treatment of Launder and Kato [16] was also used in the solutions. This helps to avoid spurious turbulence production in flowfield regions of high normal strain rates, such as at a stagnation point. Besides Ref. [2], further turbine heat transfer predictions for validation of the numerical procedure can be found in Tolpadi et al. [17].

**Multistage Turbine Computations.** For inlet boundary conditions, the TACOMA computational methodology requires absolute total temperature, absolute total pressure, two flow angles, and the two turbulence quantities:  $k$  and  $\omega$ . For exit boundary conditions, only the static pressure must be specified. For the computations presented in this paper, all three-blade rows of the turbine (HPV, HPB, and LPV) were computed together in a single, steady, multistage computation. HPV inlet boundary conditions were speci-

fied directly from measurements:  $T_o$  and  $P_o$  as the mean values from Table 1 and flow angles were aligned with the rig flow path (zero swirl). Based on experience with this rig, the HPV inlet turbulence intensity and length scale were set to 5% and 5% of the HPV leading-edge span, respectively. The integrated radial equilibrium equation was used for the LPV exit boundary conditions (Ref. [18], p. 263). The static pressure on the outer casing of the turbine was measured at the exit rake location shown in Fig. 1. This value was used to reference the radial equilibrium equation integration.

With the steady-state multistage solution, all other inlet/exit boundary conditions were handled through solution information exchanges between adjacent airfoil-rows. The information exchanged was in the form of a one-dimensional, tangentially mass-averaged, boundary condition profile. Inlet static pressure solutions were sent to upstream-adjacent airfoil-rows for exit boundary conditions, while the exit ( $T_o$ ,  $P_o$ , angles,  $k$ ,  $\omega$ ) solutions were sent to downstream-adjacent airfoil-rows for inlet boundary conditions.

**Turbine Computational Grids.** The TACOMA CFD flow solver uses structured multiblock computational grids to perform CFD predictions. For the current study, a quarter-O grid blocking topology was used for all three airfoils. The total sizes of the airfoil grids were  $2.0 \times 10^6$ ,  $2.5 \times 10^6$ , and  $1.6 \times 10^6$  grid points for the HPV, HPB, and LPV, respectively. The inlet and exit of the total computational domain were placed at the inlet and exit rake locations shown in Fig. 1. Between the airfoil-rows, the inlet/exit interface planes were nonoverlapping in the axial direction. End-wall wheelspace cavities between the air-foil rows were present in the real turbine geometry but not included in the CFD grids. Cavity purge flows were not present in the experiments, however. The HPB tip geometry was flat and set at a uniform clearance height of 2.1% of the HPB leading-edge span. This clearance height was chosen as a best estimate at the operating clearance height in the TTF facility, based on assembled static tip clearance measurements and calculated growth for operational speed. Near-wall grid cell clustering was employed on all wall boundaries, including the tip, to ensure proper resolution of all boundary layers through the viscous sublayer.

**Turbine Solution Procedure.** The multistage turbine computations were performed in parallel using 32 processors of a modern LINUX cluster. Converged solutions were obtained in about 8 h from a uniform-flow initialization. A multigrid approach to time stepping was employed. Start-up time steps were performed on coarse-grid levels to hasten the early solution convergence. Convergence of the solution was determined by monitoring the error in the velocity solution (local, average, and maximum), the net mass flow rate through the turbine, and the exit mass-average total pressure and temperature. Additionally, changes in the airfoil heat transfer solution were also used as an indicator of convergence. In both of the converged multistage solutions, the inlet and exit mass flow rates for each air-foil row were within 0.3% of the average measured mass flow rate in Table 1.

## Results and Discussion

In this section, detailed comparisons between the measurements and the CFD predictions are made and conclusions about the turbine heat transfer field (and its relation to the aerodynamics) are drawn. Results from both the  $Re/L=3.1 \times 10^6$  and  $Re/L=4.6 \times 10^6$  cases shown in Table 1 are presented. The discussion is divided into subsections dealing with the turbine aerodynamics (static pressure field): HPV heat transfer, HPB heat transfer, and LPV heat transfer. In general, the comparisons of measurements and predictions were found to be in very solid agreement with one another throughout the turbine and for both Reynolds numbers.

**Turbine Static Pressure.** Figure 2 shows the measured and predicted normalized static pressure (PR) distributions on the

HPV, HPB, and LPV airfoils. Because the convective heat transfer to the turbine is a direct consequence of the complex turbine aerodynamics, it is imperative that the predicted aerodynamics be in reasonable agreement with the measurements before conclusions about the heat transfer predictions can be drawn. In Fig. 2, PR comparisons are made at 15%, 50%, and 90% span, with the exception of the LPV, where 10% span is reported instead of 15%. It was reported in Haldeman [1] that the nondimensional pressure loading on the airfoils is very much independent of the Reynolds number. Therefore, both the  $Re/L=3.1 \times 10^6$  and  $Re/L=4.6 \times 10^6$  predictions are shown on the same plot, along with the measurements taken at  $Re/L=6.1 \times 10^6$ . For all three airfoils and at all three spanwise locations, the two prediction curves are nearly identical.

The measured and predicted pressure distributions for the HPV are shown in Fig. 2(a). At all three spanwise locations, agreement between the measurement and prediction is excellent on the pressure-side of the airfoil and around the leading edge. The pressure drop across the turbine gives rise to a choked flow through the HPV. The throat of the nozzle occurs from the pressure-side trailing edge to the suction surface at about  $S=0.4$ . Downstream of the throat on the suction-side, the time-averaged pressure measurement is influenced by unsteady effects from the downstream rotor, while the steady-state predictions are not. The suction-side predictions downstream of the throat show a very good agreement with the measurements, indicating that the unsteady influence is small. This includes the location at 90% span between  $S=0.3$  and 0.5, where the pressure increases noticeably in the flow direction. The largest discrepancy between prediction and measurement occurs at 15% span,  $S=0.75$ , where the prediction is high by 8% of the inlet total pressure. The contours of predicted PR at the bottom of Fig. 2(a) are fairly uniform in the radial direction, particularly on the pressure-side and up to the throat on the suction-side.

Figure 2(b) shows the measured and predicted pressure distributions for the HPB. Overall, the agreement between the distributions is very good, and all of the major trends observed in the measurements are reproduced with the prediction. On the pressure-side of the airfoil, the agreement is very strong at both 15% and 50% span. At 90% span,  $S=-0.8$ , data sets 26 and 27 indicate a different flow acceleration (pressure decrease) than that observed in data sets 31 and 32. The predicted pressure distributions in that region fall in-between, with values greater than those found in data sets 26 and 27 but less than those found in data sets 31 and 32. The complex acceleration of the flow around the suction surface ( $0.0 < S < 0.5$ ) is well predicted, although between  $S=0.1$  and 0.3, the predictions fall slightly below the measurements at both 15% and 90% span. The minimum airfoil values (PR  $\sim 0.1$ ) and locations ( $S \sim 0.5$ ) are in good agreement at both 15% and 50% span. For the same location at 90% span, the predictions once again fall slightly above data sets 26 and 27 and slightly below data sets 31 and 32, but overall do a fine job of matching the entire set of measurement points.

At 50% span and  $S=0.7$ , the impingement of the trailing-edge shock on the suction surface of the blade is observed in the data, and this feature appears to be well predicted by the solutions. The same pressure increase is also seen in the predictions at 15% span, but measurements downstream of the shock are lacking; thus, similar conclusions about the prediction accuracy cannot be drawn. At 90% span, a similarly abrupt pressure rise cannot be observed. At this location, the pressure measurements will be influenced by not only the shock but also the leakage vortex. The accuracy of the pressure predictions in this region provides evidence that the combined influence is accurately reproduced, thus lending credibility to the heat transfer predictions in the vicinity of these flows.

Figure 2(c) shows the measured and predicted pressure distributions for the LPV. The LPV geometry exhibits only a small amount of total turning (less than 30 deg); hence the distributions are much flatter than for the HPV or HPB. Across the airfoil span,

Part A: HPV

Part B: HPB

Part C: LPV

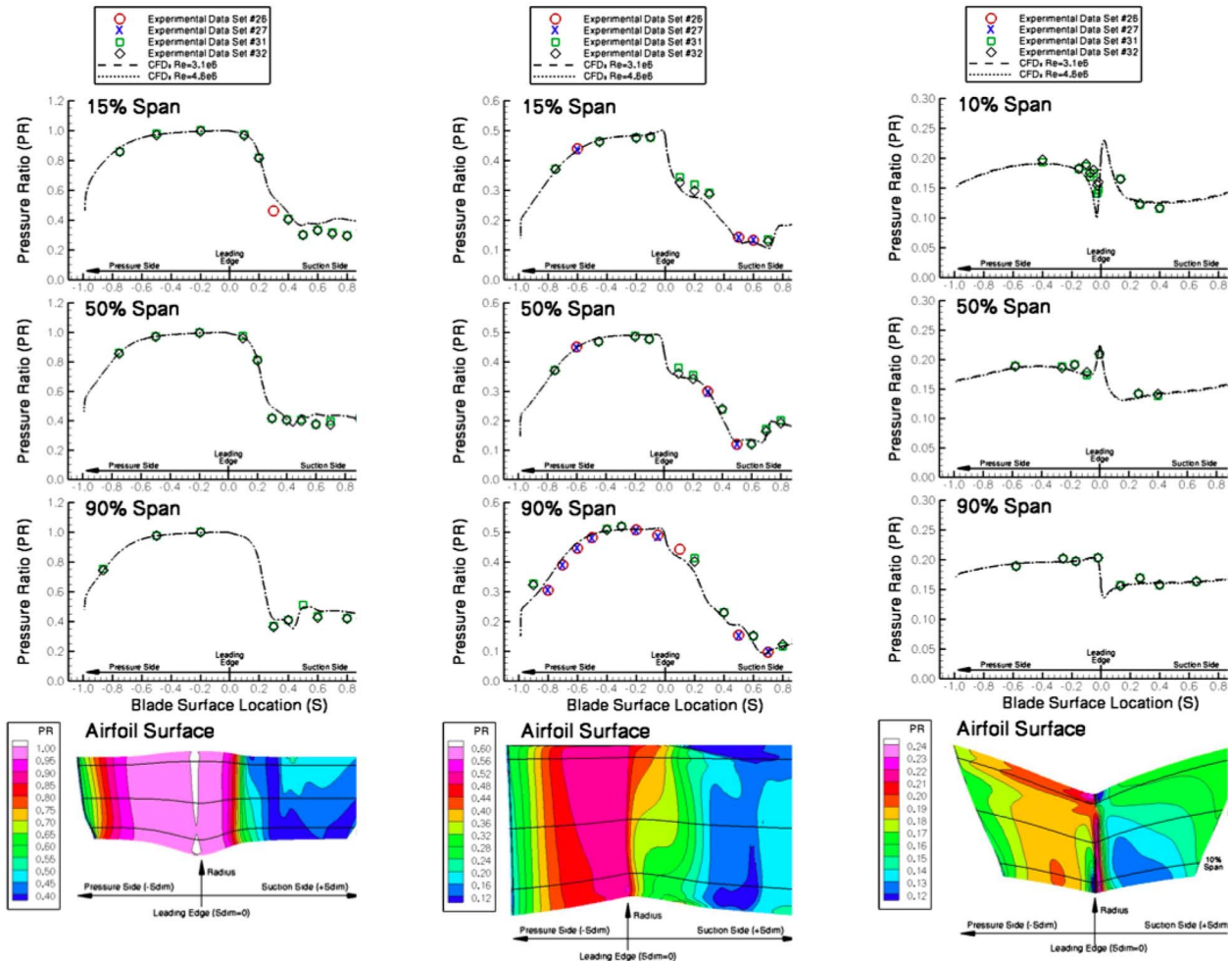


Fig. 2 Measurements and CFD predictions of airfoil pressures (measurements at  $Re/L=6.1 \times 10^6$ )

the most interesting flow-physics takes place between  $S = \pm 0.2$ . While the airfoil shape in this region is fairly uniform in the spanwise direction, the pressure distribution patterns are significantly different. At 50% span, the flow stagnates very near the geometric leading edge ( $S=0$ ) and then accelerates symmetrically around the leading edge ellipse until  $S = \pm 0.1$  where the airfoil begins to turn. This pressure distribution is most representative of that intended for the entire airfoil. At 10% span, the flow stagnates toward the suction side of the geometric leading edge and then must accelerate significantly around the airfoil leading edge geometry toward the pressure-side. At  $S = -0.04$ , the pressure then begins to increase to values similar to those observed at 50% span. At 90% span, the opposite holds true: the flow stagnates slightly toward the pressure-side and then experiences strong acceleration toward the suction-side. The positive angle of attack on the LPV can be observed in the solution contours above 90% span and is associated with the under turning of the HPB exit flow due to the presence of the leakage vortex. The differences in the leading edge pressure distributions between the different spanwise locations, and the agreement of the CFD predictions with the measurements, demonstrates the importance of using a multistage solution methodology to capture the proper aerodynamics in the downstream airfoil-rows.

**HPV Heat Transfer.** The measured and predicted heat transfer distributions on the HPV are shown in Figs. 3 and 4 for both Reynolds number cases. Figure 3 focuses on the HPV airfoil,

making comparisons at 15%, 50%, and 90% span. At any given gauge location, the scatter in the measurement values associated with the different data sets is greater for the  $Re/L=3.1 \times 10^6$  case than with the  $Re/L=4.6 \times 10^6$  case. This is consistent with a comparison of the variability in the facility operating point between the different data sets, shown in Table 1. Because the HPV data scatter is reduced with the  $Re/L=4.6 \times 10^6$  data sets, the accuracy of the predictions can be judged with increased confidence.

The overall agreement between the predictions and the measurements shown in Fig. 3 is very good. The predicted solutions fall within the scatter of measurement points at almost all airfoil measurement locations, and all of the major trends in the measurements are reproduced. As was the case with the pressure distributions, the heat transfer distributions are similar at the different spanwise locations, indicating a reasonably two-dimensional flow across much of the vane. For both Reynolds number cases, the pressure-side prediction distribution at 15% span falls slightly below the measurements.

The airfoil  $St$  prediction contours at the bottom of Fig. 3 show that any influence of near-endwall secondary flows on the airfoil heat transfer is confined to within the 10% span nearest to the endwall. Measurement values at 15% and 90% span confirm this as well. Near both endwalls on the pressure-side,  $St$  levels are augmented slightly within these proximities, as can be seen by the bulging of the contour lines toward the leading edge. There is evidence of the passage vortex on the airfoil suction-side between



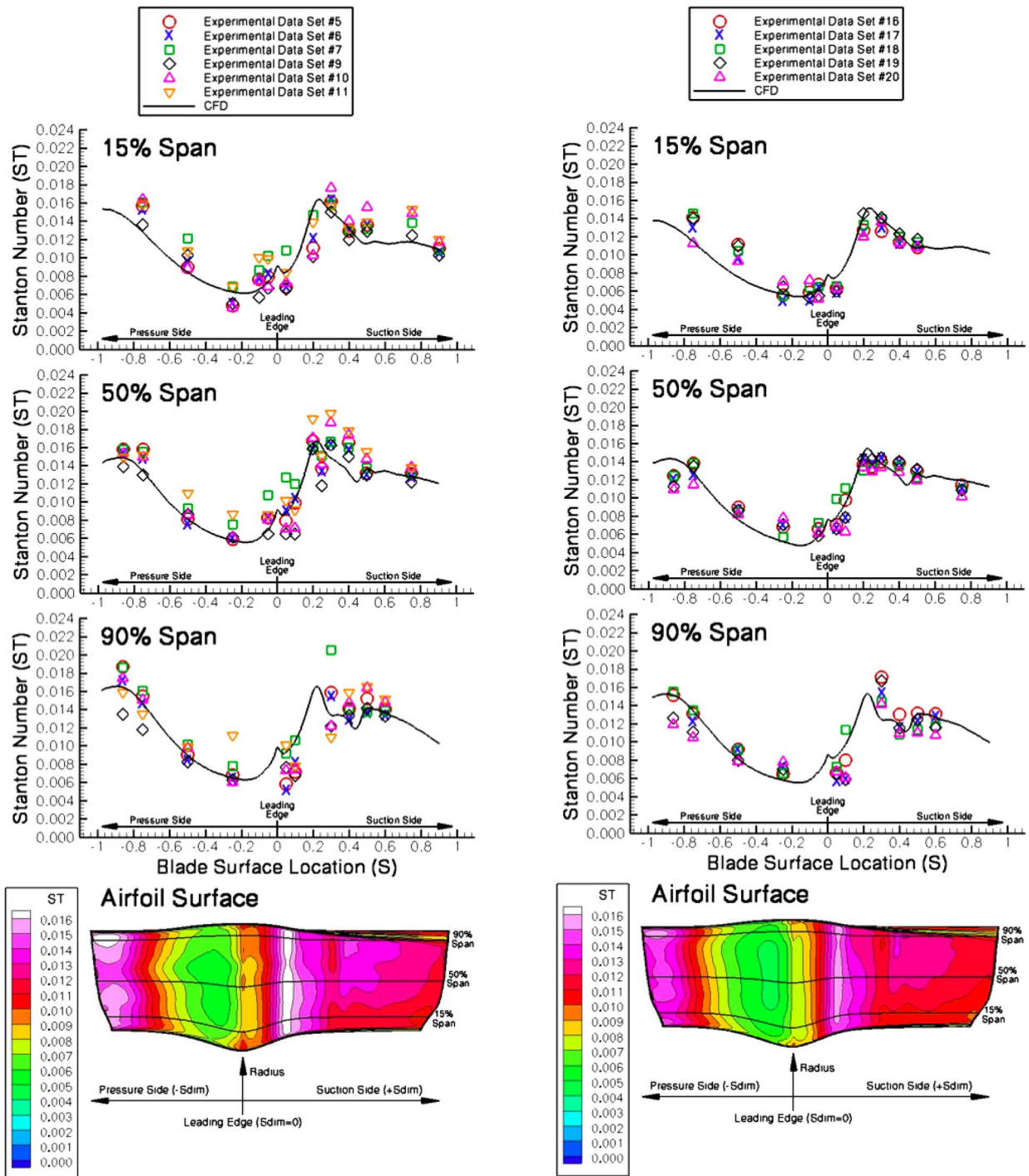


Fig. 3 Measurements and CFD predictions of airfoil heat transfer: high-pressure vane

90% span and the casing. The migration of cooler endwall boundary-layer fluid away from the endwall along the suction surface gives rise to the reduced  $St$  values. The same feature is faintly present near the hub but is confined to within the bottom 5% span.

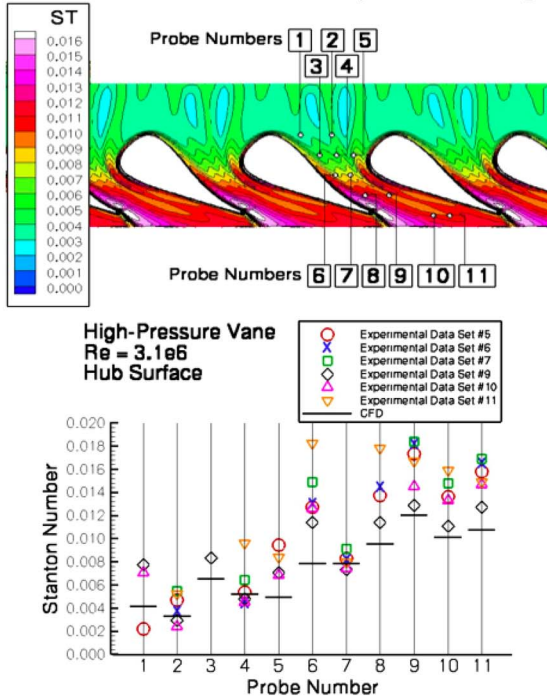
Figure 4 shows comparisons of measured and predicted heat transfer on the HPV inner (hub) and outer (casing) endwalls for both Reynolds number cases. In the upper images of each part of Fig. 4,  $St$  solution contours are shown along with the measurement gauge locations, indicated by small white circles drawn ap-

proximately to the correct scale. In the lower images, the measured  $St$  values from each gauge are shown, along with the CFD prediction at the gauge location. The gauge locations are indexed by number, with the index value increasing first from left-to-right and second from inlet to exit.

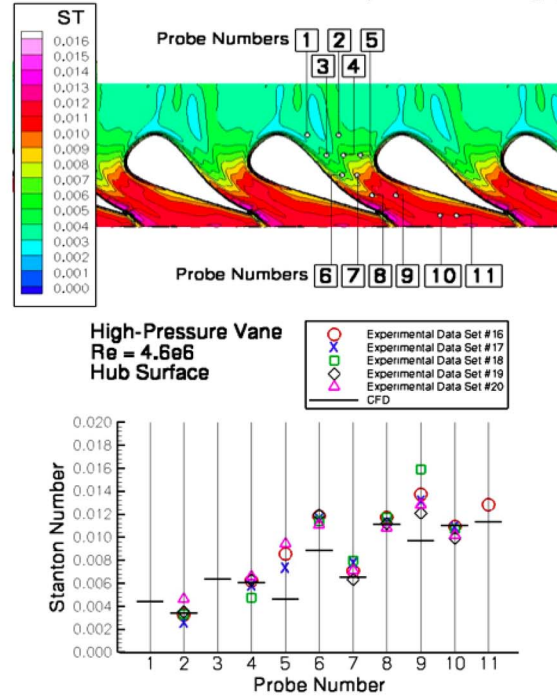
Once again, the measurement scatter is less severe in the  $Re/L=4.6 \times 10^6$  case, making it easier to draw conclusions about the agreement between measurements and predictions. For the hub surface in Fig. 4(b), the  $Re/L=4.6 \times 10^6$  prediction matches



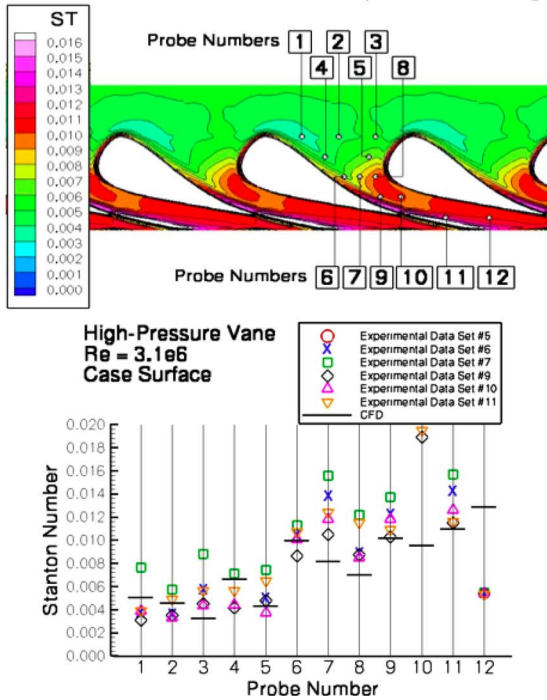
Part A:  $Re/L=3.1E6$  Inner Endwall (Stretched Image)



Part B:  $Re/L=4.6E6$  Inner Endwall (Stretched Image)



Part C:  $Re/L=3.1E6$  Outer Endwall (Stretched Image)



Part D:  $Re/L=4.6E6$  Outer Endwall (Stretched Image)

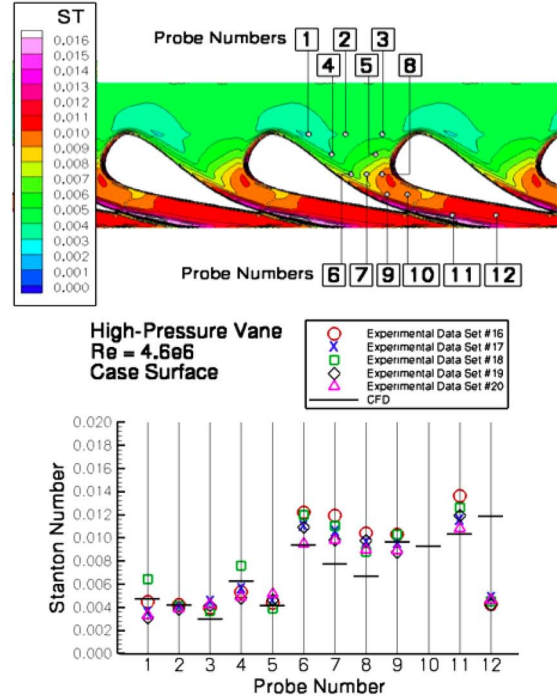


Fig. 4 Measurements and CFD predictions of endwall heat transfer: high-pressure vane

the measurement range at gauges 2, 4, 7, 8, and 10. Gauges 5, 6, 9, and 11 show predictions below the measurements by at most  $3 \times 10^{-3}$  St units. No successful measurements were obtained from gauges 1 and 3 for the  $Re/L=4.6 \times 10^6$  case, while for the  $Re/L=3.1 \times 10^6$  case in Fig. 4(a), the measurements either have large scatter (gauge 1) or only one measurement point (gauge 3). For the outer casing surface in Fig. 4(d), the predicted St value for the  $Re/L=4.6 \times 10^6$  case matches the measurement range at probes 1, 2, 4, 5, 6, and 9, and narrowly misses at gauge locations 3 and 11. At gauges 7 and 8, the predictions fall below the mea-

surement scatter by about  $2 \times 10^{-3}$  St units. The data at gauge 12 are significantly below the prediction. Similar agreement trends are observed throughout the  $Re/L=3.1 \times 10^6$  endwalls, though the trends are more difficult to observe, given the larger measurement scatter.

On both the hub and the casing, the prediction contours of St show similar flow-physics. As the air moves faster through the nozzle with downstream distance, it convects more heat and leads to higher St values. Endwall boundary layers also become thinner as the flow accelerates, thus offering less resistance to heat trans-

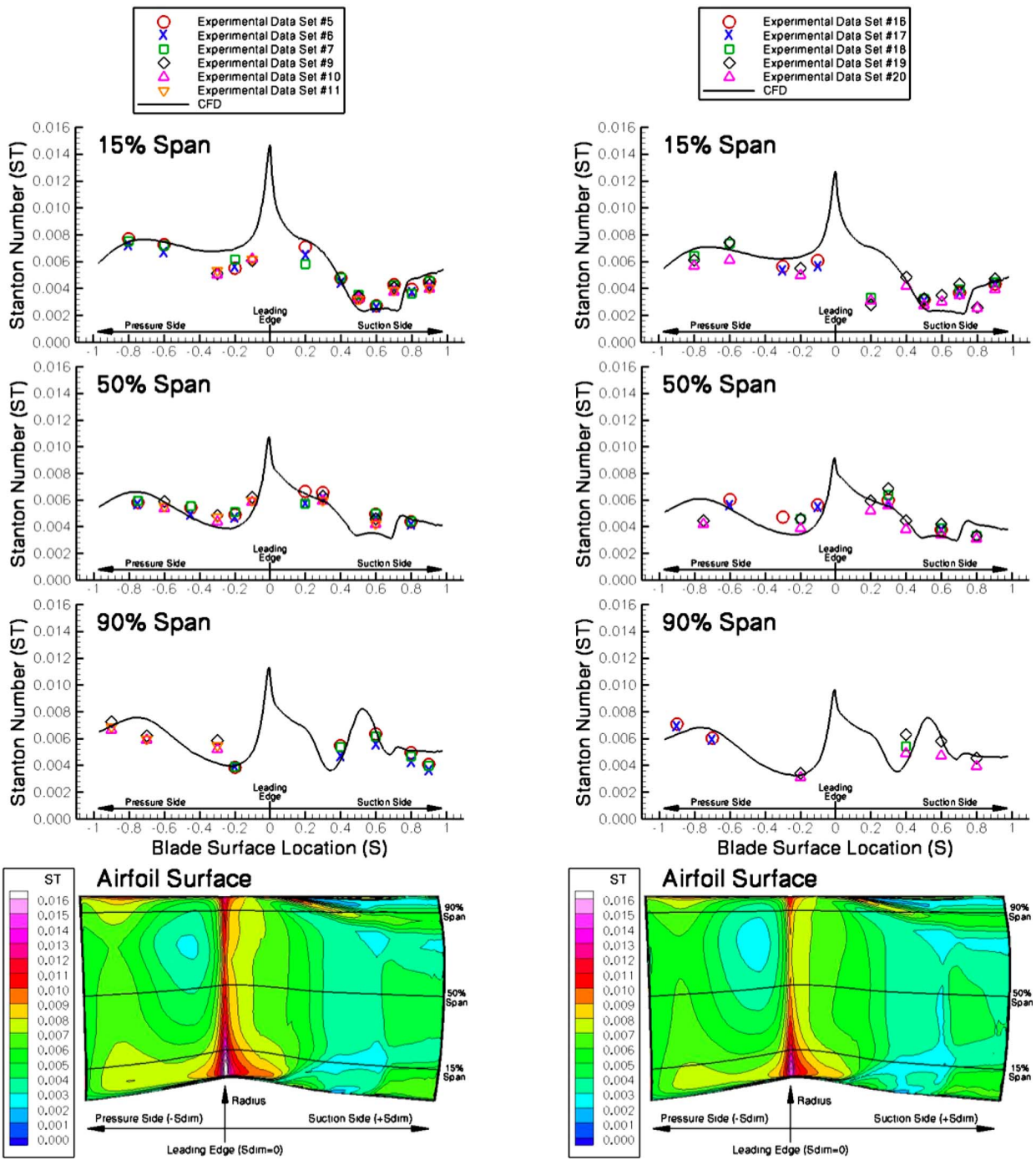


Fig. 5 Measurements and CFD predictions of airfoil heat transfer: high-pressure blade

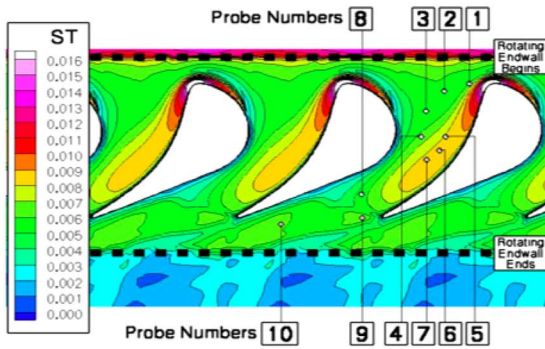
fer. At the same time, differences in the endwall  $St$  contour shapes between the two  $Re/L$  cases indicate that the secondary flow patterns near the endwalls are Reynolds number dependent.

The secondary flow of endwall boundary-layer fluid from the pressure-side of the passage toward the suction-side leaves behind it a void that then entrains in high-temperature fluid from outside the endwall boundary layer. This leads to the increased  $St$  levels present along the pressure-side of the passage, including the highest  $St$  levels observed near the trailing edge and on downstream. The pressure-side region of highest  $St$  is longer and thinner on the casing, due to the larger exit angle compared to the hub. The

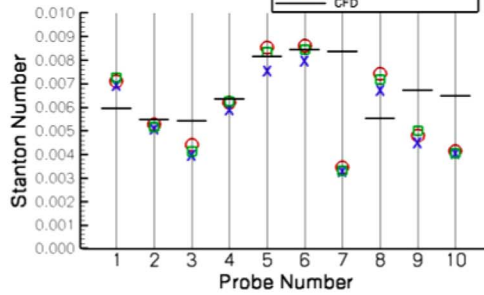
airfoil wake can be observed as the thin contours of reduced  $St$  values adjacent to the downstream region of highest  $St$  and toward the suction-side of the airfoil. Heat transfer levels are reduced in the wake due to the slower-moving fluid that originated in the lower-temperature boundary layer. Elevated heat transfer levels are also present surrounding the leading edge and are associated with a horseshoe vortex structure that is also visible in the airfoil contours shown in Fig. 3.

**HPB Heat Transfer.** Stanton number predictions on the HPB airfoil, hub endwall, and flat tip are presented in Figs. 5 and 6. The

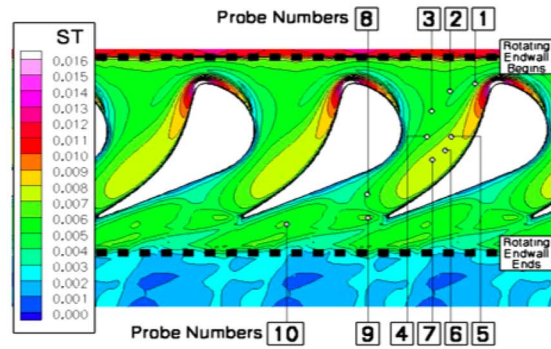
Part A:  $Re/L=3.1E6$  - Inner Endwall (Stretched Image)



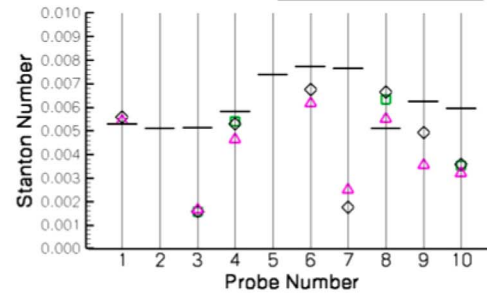
High-Pressure Blade  
 $Re = 3.1e6$   
Hub Surface



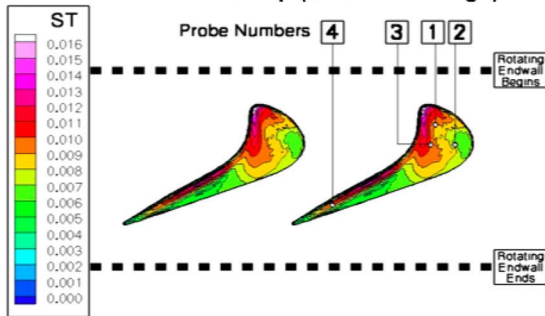
Part B:  $Re/L=4.6E6$  - Inner Endwall (Stretched Image)



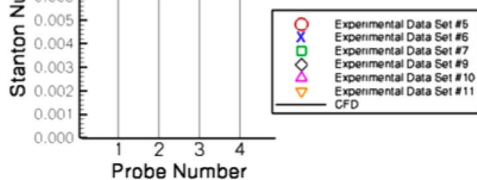
High-Pressure Blade  
 $Re = 4.6e6$   
Hub Surface



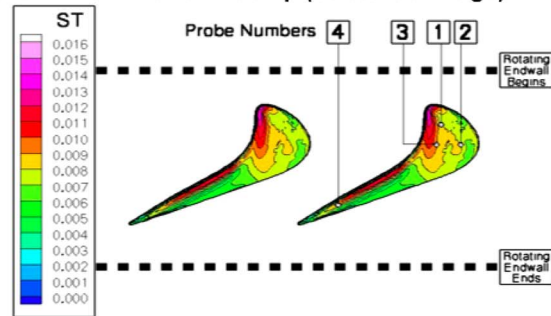
Part C:  $Re/L=3.1E6$  - Flat Tip (Stretched Image)



High-Pressure Blade  
 $Re = 3.1e6$   
Tip Surface



Part D:  $Re/L=4.6E6$  - Flat Tip (Stretched Image)



High-Pressure Blade  
 $Re = 4.6e6$   
Tip Surface

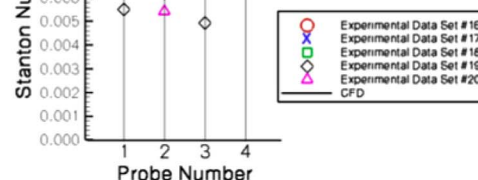


Fig. 6 Measurements and CFD predictions of endwall and tip heat transfer: high-pressure blade

acquisition of heat transfer measurements from the rotating blade is more difficult than with the vane, and so fewer measurement values are available for comparison. In general, there are a greater number of measurement points available for the  $Re/L=3.1 \times 10^6$  case, making it the more attractive case for drawing comparisons on the HPB.

Figure 5 shows good agreement between the measurements and predictions on the airfoil surface at both Reynolds numbers and at all three spanwise locations. For both Reynolds number cases, the predicted  $St$  distribution on the pressure-side falls slightly below the measurements at 50% span, slightly above the measurements

at 15% span, and somewhat in-between measurements at 90% span. On the suction-side of the airfoil, the general shape of the measured distribution is harder to distinguish, but the prediction appears to be representative of the measurements. Measurements are lacking at the leading edge of the airfoil, so the quality of the prediction in that region cannot be judged directly. However, the predictions show a fairly good match of the measurements' magnitudes and trends just outside the leading edge. The greatest discrepancy occurs at  $Re/L=4.6 \times 10^6$ , 15% span,  $S=0.2$ ; however, the measured value at this point appears inconsistent with the



measurements at the same location in the  $Re/L=3.1 \times 10^6$  case.

On the suction-side at  $S=0.7$  and at both 15% and 50% span, the predicted  $St$  curves exhibit a sudden rise in heat transfer, associated with the trailing-edge shock/suction surface interaction. The shock's presence was observed in both the predicted and measured pressure distributions at the same airfoil surface location. The increase in heat transfer due to the shock-boundary layer interaction has been observed in simpler wind tunnel experiments, for example, Refs. [19,20]. The measurements at 15% span show some indication of this feature, while the less-refined measurements at 50% do not. The 15% span measurement values at  $S=0.6$  and  $S=0.8$  are noticeably different between the two  $Re/L$  cases, indicating a Reynolds number dependency for the endwall secondary flow patterns. At 90% span, the leakage vortex is present on the suction-side and in the vicinity of the shock and the abrupt rise in  $St$  is only slightly visible in the prediction.

Many interesting features of the HPB airfoil heat transfer can be observed in the predicted  $St$  contours, shown at the bottom of Fig. 5. The airfoil heat transfer distribution for the HPB is clearly much more three-dimensional than that in the HPV, particularly near the endwalls where secondary flows are present.

The highest  $St$  values occur at the airfoil leading edge, and the highest leading-edge values occur at the root of the airfoil. The augmented  $St$  values at the leading-edge root are due to the horseshoe-vortex, a well-documented fluid dynamics phenomenon caused when the endwall boundary-layer flow stagnates against the airfoil leading edge (see Ref. [21], p 339–341 and Ref. [18], pp. 543–546). The stagnating endwall boundary layer sets up a radial pressure gradient at the leading edge, which draws the airfoil surface fluid toward the endwall. High-temperature freestream fluid then fills the void left by the radially migrated airfoil surface fluid, which leads to increased heat transfer. Because this flow feature is confined to the bottom 10% span of the airfoil, the heat transfer increase associated with the horseshoe vortex is not visible in the measurements.

Downstream of the horseshoe vortex on the suction-side, reduced  $St$  values are observed in a triangular-shaped pattern. These reduced values are associated with the hub secondary flow, which transports cooler endwall boundary-layer fluid from the pressure-side of the passage to the suction-side. Upon reaching the suction-side, the cooler fluid then migrates radially up the airfoil surface, leading to the reduced heat transfer levels observed. There is evidence of this flow feature in the measurements, which can be seen by comparing  $St$  magnitudes at 15% and 50% span for  $0.4 < S < 0.8$ . Around  $S=0.7$ , the reduced  $St$  levels near the hub abruptly increase. Figure 2(b) contours of airfoil static pressure identify this as the location of the trailing-edge shock. Unlike the midspan, the shock line between the root and 15% span takes on noticeable streamwise position variability. This indicates that the shock structure near the endwalls is influenced by secondary flow activity. The accuracy of this finding can only be judged by comparisons with measurement at 15% span, and future measurements in the region would be beneficial toward further validation. For the  $Re/L=3.1 \times 10^6$  case, the 15% span measurements show the shock placement slightly farther upstream than the prediction, while for the  $Re/L=4.6 \times 10^6$  case, the measurements are more ambiguous.

Three-dimensionality in the airfoil heat transfer distribution is also highly visible in Fig. 5 near the tip, associated with the leakage flow and vortex. At any location on the pressure-side 90% span line,  $St$  values increase with increasing radial location. This increase is associated with the entrainment and acceleration of high-temperature freestream fluid from the passage into the tip clearance gap. The elevated heat transfer levels near the tip are most severe toward the aft of the pressure-side, and some evidence of the augmentation can be seen by comparing measured  $St$  values at 90% and 50% span in the vicinity of  $S < -0.75$ .

The leakage vortex manifests itself in Fig. 5 contours along the suction-side and within the top 20% span. Around the 90% span

line and between  $S=0.2$  and 0.5, three distinct contour regions can be seen: a high- $St$  region, oriented at an angle of about 20 deg from the tip, which is sandwiched on its top and bottom by two low- $St$  regions. The bottom low- $St$  region is caused by the obstruction of the passage flow around the leakage vortex. The top low- $St$  region is adjacent to the low-temperature recirculating leakage vortex core. The high  $St$  region is caused by the high temperature leakage fluid from the upstream portion of the gap, which passes over the developing leakage vortex before stagnating against the suction surface and turning downstream. As the leakage vortex grows downstream and separates from the airfoil surface, the core is no longer adjacent to the suction surface, the leakage flow no longer stagnates but instead is entrained around the vortex, and the distinction between the different contour regions is less clear. The comparison of measured and predicted  $St$  at 90% span shows a very good agreement in the vicinity of the leakage vortex for both Reynolds number cases. This was also the case for the airfoil static pressure, shown in Fig. 2(b). At the same time, further  $St$  measurement resolution in the region would be beneficial in confirming the CFD-based interpretation of the heat transfer distribution surrounding the leakage vortex.

Measurements and predictions of  $St$  on the HPB hub and tip are presented in Fig. 6, in a format similar to what was used for the HPV endwalls. For the  $Re/L=3.1 \times 10^6$  case, the comparisons between the measurement and prediction are quite good. The predictions fall within the very-tight scatter of the measurements at probes 2, 4, 5, and 6, and deviate by around  $1 \times 10^{-3}$   $St$  units for probes 1, 3, and 8. The predicted  $St$  contours show that probe 1 is situated in a region of high gradient, thus a slight location change would bring the prediction into agreement with the measurements. The discrepancy is largest at gauge 7, near the center of the passage, and gauges 9 and 10 near the end of the rotor platform are both overpredicted. The gauge 7 measurement values appear to be questionable, however, given their significant difference from nearby measurements at gauges 5 and 6. A flawed gauge at 7 is one possibility. In general, the agreement between the prediction and measurements is similar for the  $Re/L=4.6 \times 10^6$  case, although gauges 2 and 5 are missing measurements, the gauge 3 measurements are inconsistent with the  $Re/L=3.1 \times 10^6$  case, and fewer measurements are available overall.

The contours of predicted  $St$  on the HPB hub, shown in Figs. 6(a) and 6(b), illustrate the influence of the turbine rotor three-dimensional flowfield on the endwall heat transfer. As with the airfoil surface, the highest heat transfer values are located at the leading edge and are associated with the horseshoe vortex structure. The horseshoe vortex acts to entrain high-temperature freestream fluid into the root/hub junction, resulting in the high heat transfer levels. The closest measurement point to the horseshoe vortex footprint is gauge 1, near the leading edge on the pressure-side. For the  $Re/L=3.1 \times 10^6$  case, the measured values from gauge 1 are notably higher than those from gauges 2 and 3, which are situated at a similar axial location but are farther removed from the airfoil.

The prediction hub contours in Fig. 6 show a large region of high  $St$  values, situated across the majority of the pressure-side of the passage. The elevated  $St$  values in this region are primarily due to the secondary flow of the hub boundary layer from the pressure-side of the passage to the suction-side. As the hub boundary layer evacuates the pressure-side of the passage, high-temperature freestream fluid fills the void and leads to increased heat transfer. Gauges 4–6 illustrate this further, with gauges 5 and 6 situated inside the pressure-side region of elevated  $St$  values while gauge 4 falls outside the region. Predictions and measurements match very well at these three locations.

Measurements and predictions of  $St$  on the HPB tip are presented in Figs. 6(c) and 6(d). As was mentioned earlier, the tip geometry investigated was simply a flat tip with uniform clearance height of 2.1% span. Four heat flux gauges were available on the flat-tip geometry. For the  $Re/L=3.1 \times 10^6$  case, measurements



and prediction are in good agreement at gauge 2, situated toward the suction-side of the gap and in fair agreement at gauge 4 near the trailing edge of the gap. For the  $Re/L=4.6 \times 10^6$  case, the prediction falls within the measurement scatter at gauge 4 but overpredicts the heat transfer at gauge location 2. The gauge 2 overprediction also shows an inconsistency with the measurements and predictions from the  $Re/L=3.1 \times 10^6$  case. For gauge locations 1 and 3, both Reynolds number cases show an overprediction of the measurements. These two probes are situated near the leading edge of the tip gap and toward the pressure-side.

The flow-physics of the tip leakage flow through the gap is fairly well understood [22] and the various features of the gap flowfield can be observed in the  $St$  prediction contours of Figs. 6(c) and 6(d). The high-temperature leakage fluid is entrained from the passage into the gap following a direction that includes a large radial component. The entrained leakage flow separates over the sharp pressure-side edge of the gap but because of space constraints is forced to reattach only a short distance downstream of the edge. The reattached leakage flow has yet to lose any of its initial freestream total temperature, and so  $St$  levels are very high, among the highest over the airfoil. Much of the leakage fluid's pre-entrained directional inertia is conserved in the entrainment process, and this dictates the shape of the contours of high  $St$ . At the leading edge, the high  $St$  contours are closely aligned with the inlet flow direction, while on the aft portion of the tip, they orient more with the camber of the airfoil slightly upstream.

The  $St$  contours in Figs. 6(c) and 6(d) show that gauge locations 1, 3, and 4 are positioned right on the edge of the high- $St$  contour regions, where gradients are large and slight position changes produce a different agreement. Additionally, the slightly jagged looking contour lines indicate that the tip gap flowfield is not entirely converged, due to the multistage solution methodology. Near the tip, the boundary condition profiles exchanged between the HPB and LPV buzz slightly with solution iterations, due to the tangentially averaging out of the large and highly 3D leakage vortex. As the rotor exit static pressure boundary condition buzzes near the tip, a slight unsteadiness in the tip gap flowfield and  $St$  solution is observed. The solution buzzing disappears if the rotor exit boundary condition profile is frozen and the single-blade-row solution is converged out.

**LPV Heat Transfer.** Measurements and predictions of  $St$  on the LPV airfoil surface are presented in Fig. 7. Unlike the HPV and HPB, endwall heat transfer measurements were not obtained, and interrogation of the endwall  $St$  predictions revealed very few interesting features. In general, the LPV has very little turning and much lower heat transfer levels due to the reduced hot-gas temperature downstream of the HPB. Maximum  $St$  measurement values for the LPV are approximately half of that from the HPB and one-quarter of that from the HPV. Still, the LPV constitutes a different kind of challenge to the predictions, in that the accuracy is highly dependent on capturing the correct inlet flow conditions via the multistage solution.

The following turbulent flat plate boundary-layer heat transfer correlation is included in Fig. 7 as a reference.

$$Nu_x = 0.0296 Re_x^{4/5} Pr^{1/3} \quad (2)$$

This very famous correlation based on simple "Reynolds Analogy" arguments (see Ref. [23], pp. 393–395, for example) was deemed appropriate because of the LPV's lack of any significant turning. To define the Reynolds number ( $Re_x$ ), the velocity scale was deduced from the local CFD static pressure prediction, the CFD-predicted LPV inlet total pressure and total temperature at the same percent span, and inviscid compressible flow arguments. The local  $S_{dim}$  was used as the length scale, and the Eckert reference temperature was used to determine properties such as density and viscosity. The Nusselt number ( $Nu_x$ ) was then rewritten in the form of  $St$ .

Figure 7 shows that the  $St$  measurements and predictions at the

midspan location are in very good agreement with each other. At 50% span, the flow stagnates with very little incidence angle on the airfoil, and the symmetric-looking prediction curve is testament to the airfoil's symmetric shape. The  $St$  prediction at the airfoil leading edge is overpredicted for both Reynolds number cases. This overprediction may be associated with a variety of causes, including overpredicted inlet freestream turbulence levels, the lack of unsteadiness in the CFD model, or shortcomings in the turbulence production term limiting treatment of Launder and Kato [16]. For the aft half of the airfoil and at 50% span, the measurements appear to be showing signs of a laminar-to-turbulent transition, via increasing  $St$  versus  $S$  location. However, the flat plate correlation falls below the measurements and indicates a turbulent boundary layer downstream of  $S = \pm 0.2$ . The predictions agree very well with the correlation in these regions.

At 10% and 90% span, pressure-side discrepancies between the predictions and measurements can be observed. The discrepancies are consistent between the two Reynolds number cases; thus discussion can be made without direct reference to either case. Two important caveats must be kept in mind when considering the LPV discrepancies. First, the time-averaged measurements were taken in an unsteady environment consistent with turbine's true operation, while the CFD predictions were carried out as a steady multistage solution. This influence is expected to be greater for the LPV than for the HPB because exit flowfield three-dimensionality is more prevalent in the HPB than the HPV. Unsteady CFD predictions of the LPV were beyond the scope of the current study but are currently in development. These predictions, along with those current, should help to determine the importance of unsteadiness in predicting turbine heat transfer, particularly in downstream airfoil-rows. Second, the LPV exit static pressure boundary condition that was applied to the CFD predictions is not necessarily the same as that present in the experimental turbine. Because the HPV is choked, the turbine mass flow rate is fairly insensitive to the specific exit pressure distribution. The mass flow rate distribution through the LPV will depend on the exit pressure distribution, and this will have an impact on the local heat transfer prediction. The CFD exit was specified at the same location as the exit rakes shown in Fig. 1. Static pressure measurements were not available at this location, except at the outer casing; hence, the radial equilibrium relation seemed the logical choice. The predicted total pressure field agreed well with measurements at the rake location.

At 10% span, the pressure-side  $St$  measurements exhibit a steady increase from  $S = -0.05$  to about  $S = -0.5$  and then level off or decrease slightly with farther downstream distance. The pressure-side prediction curve at 10% span also shows signs of this increase, but the  $St$  curve peaks at  $S = -0.08$  and then agrees well with turbulent flat plate correlation farther downstream. Analysis of the CFD solution indicates that the abrupt rise in the predicted  $St$  curve around  $S = -0.05$  is associated with laminar-to-turbulent transition. While no deliberate "transition model" was included in the CFD, the wall integration methodology will predict a transition point, albeit typically prematurely upstream (see Ref. [2], Fig. 2(a), for example). The  $Re/L=4.6 \times 10^6$  measurements show signs of this pressure-side transition slightly farther downstream ( $S = -0.1$ ), but the  $Re/L=3.1 \times 10^6$  measurements do not. The transition is present in the prediction and measurements at 10% span but not at 50% span. Because the airfoil is fairly uniform in its profile shape, the presence of transition is therefore tied to the incidence angle on the airfoil, the location of the stagnation point, and the acceleration around the leading edge toward the pressure-side experienced by the boundary layer. The greater acceleration at 10% span, visible in Fig. 2(c), leads to turbulence suppression and a short laminar segment of the boundary layer. Note that boundary-layer separation around the leading edge was not observed in the predictions at any spanwise location. Evidence of suction-side transition is also present in the measurements at 10% span,  $S = 0.26$ , but the predictions fail to capture this trend.

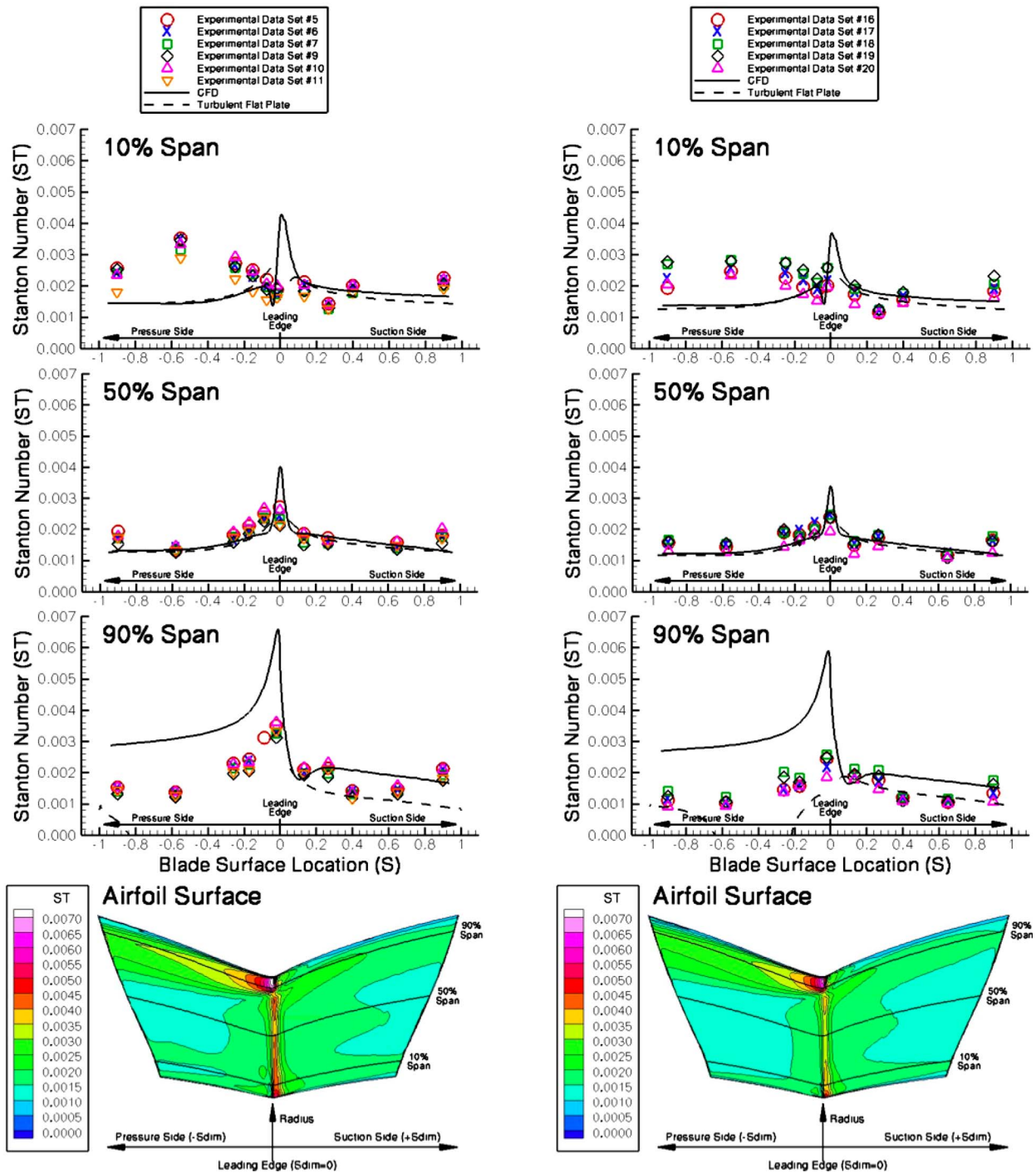


Fig. 7 Measurements and CFD predictions of airfoil heat transfer: low-pressure vane

It is uncertain at this time what mechanism would cause the measured pressure-side heat transfer to continue to rise farther downstream of the transition point at 10% span. Besides the two caveats discussed above, the static pressure at the same location in Fig. 2(c) is well predicted but shifted slightly toward the pressure-side. A slight change in the inlet incidence angle toward the suction-side may be more representative of the unsteady experimental turbine and have an influence on the pressure-side heat transfer. Further measurements in this region would be beneficial in resolving the issue.

At 90% span, the pressure-side prediction curve shows the

same decaying trend as the measurements but is offset approximately  $1.5 \times 10^{-3}$  St units above the measurements. At the same airfoil location, the St prediction contours show a sizable region of increased heat transfer. Flowfield visualization of the LPV CFD prediction revealed that the high St region is associated with flowfield three-dimensionality. The incoming flow stagnates toward the pressure-side of the leading edge then turns radially toward the inner hub as it propagates downstream. The pressure-side stagnation that causes this flow feature is a result of the HPB leakage vortex and its underturned flow. It is reasonable to expect that the

prediction of this high-St region deviates slightly from the data, since the leakage vortex is (a) one of the more challenging flow features to resolve correctly and (b) contributes a significant source of unsteadiness to the LPV, which is not included in the CFD model. Because of the local flowfield's three-dimensionality, the turbulent flat plate correlation curve is an inappropriate descriptor at 90% span.

## Summary and Conclusions

The two primary objectives of this research effort were (1) to develop a better understanding of hot-gas-side heat transfer in high-pressure turbine stages and (2) to extend that understanding into improved turbine heat transfer prediction capabilities, which can ultimately facilitate improved turbine thermal designs with increased operating temperatures and life expectancies. The hot-gas-side heat transfer was measured across the airfoils and endwalls of a modern, transonic, high-pressure,  $1\frac{1}{2}$  stage turbine operating over a range of engine-realistic corrected speeds and pressure ratios, using a short-duration shock-tunnel facility and experimental procedure. CFD solutions of the turbine aerodynamics and heat transfer were obtained using a steady-state, multi-stage, wall integration approach. Detailed comparisons of measured and CFD-predicted static pressure and heat transfer distributions were made across all three airfoils, as well as for the endwalls and tips. In general, the agreement between the measurements and predictions was very good on the HPV and HPB airfoils and moderately good on the HPV and HPB endwalls and tips. The agreement for the LPV airfoil was very good at the midspan but only fair nearer to the endwalls. The predictions were used to identify and understand turbine flow-physics and its influence on the turbine heat transfer field.

Based on the agreement between the measured and predicted turbine heat transfer, and the flow-physics-based explanation of the various heat transfer distribution features, it is concluded that the measurements taken are of high quality and serve as an important stepping stone toward the next-generation turbine thermal designs. It is also concluded that the CFD methodology developed as part of this research is well suited for general turbine hot-gas-side heat transfer predictions in the absence of cooling flow addition and surface roughness. The methodology is also well suited as a foundation upon which the modeling of these two important influences can be built. In addition, the inclusion of unsteadiness in the predictive model should be investigated as a means of improving the prediction accuracy in the downstream airfoil-row (LPV).

## Acknowledgment

The authors would like to thank the technical support staff at the OSU Gas Turbine Lab for their support in producing the experimental data presented in this paper. This work was supported under the GE University Strategic Alliance with help from Robert Bergholz and Fred Buck from GE Transportation.

## Nomenclature

$A_{\text{inlet}}$	= area at the high-pressure vane inlet
$C_p$	= constant Pressure Specific Heat
inlet	= high-pressure vane inlet (subscript)
$\dot{m}$	= turbine mass flow rate
$Nu_x$	= flat plate Nusselt number
$P$	= static pressure
$P_o$	= total pressure (absolute frame)
PR	= ratio of local $P$ to $P_o$ at the high-pressure vane inlet
Pr	= laminar Prandtl number
$\dot{q}_{\text{wall}}$	= local wall heat flux

$Re/L$  = Reynolds number per meter length:

$$Re = \dot{m}/A_{\text{inlet}}/\mu$$

$Re_x$  = flat plate Reynolds number

$S$  = surface distance from the airfoil geometric leading edge to the trailing edge, at constant percent span, nondimensionalized: (0 to +1 on the suction surface, 0 to -1 on the pressure surface)

$S_{\text{dim}}$  = dimensional surface distance from the airfoil geometric leading edge to the trailing edge, at constant percent span

St = Stanton number:  $St = \dot{q}_{\text{wall}}/\dot{m}/A_{\text{inlet}}[(C_p T_o)_{\text{inlet}} - (C_p T)_{\text{wall}}]$

$T$  = static temperature

$T_o$  = total temperature (absolute frame)

wall = At a wall boundary (subscript)

$\mu$  = laminar viscosity

## References

- [1] Haldeman, C. W., Dunn, M. G., Barter, J. W., Green, B. R., and Bergholz, R. F., 2004, "Aerodynamic and Heat-flux Measurements with Predictions on a Modern One and 1/2 Stage High Pressure Turbine," ASME J. Turbomach., **127**, pp. 522-531.
- [2] Tallman, J. A., 2004, "CFD Heat-Transfer Predictions for a High-Pressure Turbine Stage," ASME Paper No. GT2004-53654.
- [3] Dunn, M. G., 2001, "Convective Heat Transfer and Aerodynamics in Axial Flow Turbines," ASME J. Turbomach., **113**, pp. 637-686.
- [4] Giel, P. W., Boyle, R. J., and Bunker, R. S., 2003, "Measurements and Predictions of Heat Transfer on Rotor Blades in a Transonic Turbine Cascade," ASME Paper No. 2003-GT-38839.
- [5] Yang, H., Sumanta, A., Ekkad, S. V., Prakash, C., and Bunker, R. S., 2002, "Flow and Heat Transfer Predictions for a Flat Tip Turbine Blade," ASME Paper No. 2002-GT-30190.
- [6] Arnone, A., Liou, M. S., and Povinelli, L., 1992, "Navier-Stokes Solution of Transonic Cascade Flows Using Non-periodic C-Type Grids," J. Propul. Power, **8**(2), pp. 410-417.
- [7] Chima, R. V. 1991, "Viscous Three-Dimensional Calculation of Transonic Fan Performance," *CFD Techniques for Propulsion Applications*, AGARD Conference Proceedings No. CP-510, AGARD, Neuilly-Sur-Seine, France, February, pp. 21-1 to 21-19; Also NASA TM-103800.
- [8] Polanka, M. D., Hoying, D. A., Meininger, M., and MacArthur, C. D., 2003, "Turbine Tip and Shroud Heat Transfer and Loading Part A: Parameter Effects Including Reynolds Number, Pressure Ratio and Gas to Metal Temperature Ratio," ASME J. Turbomach., **125**, pp. 97-106.
- [9] Polanka, M. D., Clark, J. P., White, A. L., Meininger, M., and Praisner, T. J., 2003, "Turbine Tip and Shroud Heat Transfer and Loading: Part B—Comparisons between Predictions and Experiment Including Unsteady Effects," ASME Paper No. GT2003-38916.
- [10] Haldeman, C. W., 2003, "An Experimental Investigation of Clocking Effects on Turbine Aerodynamics Using a Modern 3-D One and one-half Stage High Pressure Turbine for Code Verification and Flow Model Development," Ph.D. thesis, Ohio State University, Columbus.
- [11] Green, B. R., Barter, J. W., Haldeman, C. W., and Dunn, M. G., 2004, "Time-Averaged and Time-Accurate Aero-Dynamics for the Recessed Tip Cavity of a High-Pressure Turbine Blade and the Outer Stationary Shroud: Comparison of Computational and Experimental Results," ASME Paper No. GT2004-53443.
- [12] Cook, W. J., and Felderman, E. J., 1966, "Reduction of Data from Thin-Film Heat-Transfer Gages: A Concise Numerical Technique," AIAA J., **4**, pp. 561-562.
- [13] Holmes, D. G., Mitchell, B. E., and Lorence, C. B., 1997, "Three Dimensional Linearized Navier-Stokes Calculations for Flutter and Forced Response," Eighth International Symposium on Unsteady Aerodynamics and Aeroelasticity of Turbomachines, Stockholm, Sweden, Sept. 14-18.
- [14] Jameson, A., 1983, *Solution of the Euler Equations for Two Dimensional Transonic Flow by a Multigrid Method*, Princeton University, Princeton, NJ.
- [15] Wilcox, D. C., 1993, *Turbulence Modeling for CFD*, DCW Industries, Inc., La Canada, CA.
- [16] Launder, B. E., and Kato, M., 1993, "Modelling Flow-Induced Oscillations in Turbulent Flow Around a Square Cylinder," *Proceedings of the Fluid Engineering Conference*, Washington, DC.
- [17] Tolpadi, A. K., Tallman, J. A., and El-Gabry, L., 2005, "Turbine Heat Transfer Predictions Using CFD," ASME Paper No. GT2005-68051.
- [18] Lakshminarayana, B., 1996, *Fluid Dynamics and Heat Transfer of Turbomachinery*, Wiley, New York.

- [19] Hayashi, A. S., and Shigeru, A., "Measurement of Heat Transfer Coefficients in Shock Wave-Turbulent Boundary Layer Interaction Regions with a Multi-Layered Thin Film Heat Transfer Gauge," NASA.
- [20] Raghu, S., and Staub, F. W., 1994, "Obtaining the Surface Temperature Distribution in a Shock Wave-Boundary Layer Interaction Region Using a Liquid Crystal Technique," *Exp. Therm. Fluid Sci.*, **9**(3), pp. 283–288.
- [21] Schlichting, H., 2000, *Boundary Layer Theory*, 8th ed., McGraw-Hill, New York.
- [22] Tallman, J. A., 2004, "A Computational Study of Tip Desensitization in Axial Flow Turbines," ASME Paper No. GT2004-53918.
- [23] Incropera, F. P., and Dewitt, D. P., 2002, *Fundamentals of Heat and Mass Transfer*, 5th ed., Wiley, New York.



# Mass/Heat Transfer in Rotating, Smooth, High-Aspect Ratio (4:1) Coolant Channels With Curved Walls

Eashwar Sethuraman  
Sumanta Acharya  
Dimitris E. Nikitopoulos<sup>1</sup>

Turbine Innovation and Energy Research (TIER)  
Center,  
Mechanical Engineering Department,  
Louisiana State University,  
Baton Rouge, LA 70803

*The paper presents an experimental study of heat/mass transfer coefficient in 4:1 aspect ratio smooth channels with nonuniform cross sections. Curved leading and trailing edges are studied for two curvatures of  $9.06\text{ m}^{-1}$  ( $0.23\text{ in.}^{-1}$ ) and  $15.11\text{ m}^{-1}$  ( $0.384\text{ in.}^{-1}$ ) and for two different curvature configurations. One configuration has curved walls with curvature corresponding to the blade profile (positive curvature on both leading and trailing walls) and the other configuration has leading and trailing walls that curve inward into the coolant passage (negative curvature on the leading surface and positive curvature on the trailing surface). A detailed study at  $Re=10,000$  with rotation numbers in the range of  $0-0.07$  is undertaken for the two different curvature configurations. All experiments are done for a  $90\text{ deg}$  passage orientation with respect to the plane of rotation. The experiments are conducted in a rotating two-pass coolant channel facility using the naphthalene sublimation technique. Only the radially outward flow is considered for the present study. The spanwise mass transfer distributions of fully developed regions of the channel walls are also presented. The mass transfer data from the curved wall channels are compared to those from a smooth 4:1 rectangular duct with similar flow parameters. The local mass transfer data are analyzed mainly for the fully developed region, and area-averaged results are presented to delineate the effect of the rotation number. Heat transfer enhancement especially in the leading wall is seen for the lower curvature channels, and there is a subsequent reduction in the higher curvature channel when compared to the 4:1 rectangular smooth channel. This indicates that an optimal channel wall curvature exists for which heat transfer is the highest. [DOI: 10.1115/1.2812327]*

## Introduction

Internal blade cooling involves serpentine passages inside the blade through which coolant air is passed to absorb heat internally. Figure 1 shows a blade cross section and the channels through the blade. The blade is thicker at the midchord and thins out as it goes to the blade trailing edge. Typically, the channel aspect ratios (width:height) change from 1:4 in the midchord up to 10:1 in the trailing edge of the blade. The channel orientation with respect to the direction of rotation also changes as we move from the blade tip to the trailing edge. Moreover, the passage cross sections are not exact squares or rectangles. They are more curved at the blade tip and midchord and become trapezoidal and wedge-like at the blade trailing edges.

The heat transfer and flow patterns inside the channels cannot be predicted only by simulating a square stationary case. Wagner et al. [1] and Johnson et al. [2] studied the flow in smooth square channels (1:1) with rotation and quantified the effects of rotation number ( $R_0 = \Omega D_h / U$ ) and the buoyancy parameter ( $B_0 = (\Delta\rho/\rho) \times (R/D_h) R_0^2$ ) on the heat transfer in rotating channels. Similar research was further done to study the flow patterns with detailed spatial resolution using the mass transfer technique by Park et al. [3] and Kukreja et al. [4]. Rotation induces Coriolis and buoyancy forces, which create secondary flows in the direction perpendicular

to the mean flow direction. In a radially outward flow, both these forces combine to shift the mean flow to the trailing surface of the channel.

Augmentation of heat transfer is mainly due to the mixing of the cooler core of fluid and its movement in the channel due to the forces mentioned above. Figure 2 portrays the rotation-induced forces acting on radially outward-flowing coolant in a heated channel. The buoyancy force is governed by both the centrifugal force acting on the fluid and the density gradient in the fluid. The density gradient is generated due to the difference in temperatures of the fluid near the heated walls and the fluid in the core of the passage. The study presented here uses the naphthalene sublimation technique and the related density gradients are negligible. Therefore, centrifugal buoyancy plays no role in the presented results of this paper, where rotation number effects alone are manifested.

A significant number of studies have been conducted in the past on both smooth and ribbed coolant channels. Zhang et al. [5] experimented with a three-pass serpentine circuit with turbulators oriented normal to the flow, concluding that the normalized Nusselt number is insensitive to the Reynolds number variation. Here, the Reynolds number ( $Re = \rho U D_h / \mu$ ) is based on the hydraulic diameter ( $D_h$ ) of the duct. Heat transfer enhancements have been achieved with the help of rib turbulators and many other forms of turbulence promoters such as vortex generators [6,7], profiled ribs [8,9], and dimples [10]. Changes in channel aspect ratio also affect the heat transfer characteristics. These were studied extensively with the mass transfer method by Agarwal et al. [11] for 1:4 channels, while Refs. [12–14] and others [15] also studied the effects of aspect ratio, with and without ribs using direct heat transfer measurements.

Until a decade back, flow and heat transfers in smooth square

<sup>1</sup>Corresponding author.

Contributed by the International Gas Turbine Institute of ASME for publication in the JOURNAL OF TURBOMACHINERY. Manuscript received July 25, 2006; final manuscript received September 18, 2006; published online January 22, 2009. Review conducted by David Wisler. Paper presented at the ASME Turbo Expo 2006: Land, Sea and Air (GT2006), Barcelona, Spain, May 8–11, 2006.

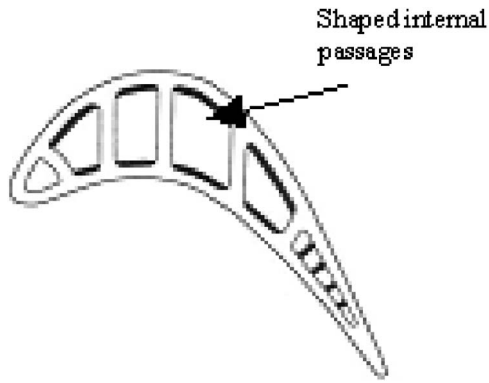


Fig. 1 Blade profile and channel cross section [17]

channels were investigated [16–18]. Higher aspect ratio studies on smooth rectangular channels show a wide range of flow patterns different from the square channel [19–24]. All these studies were conducted on smooth flat walls, with either square or rectangular channel cross section with or without ribs. There is virtually no paper in the literature that has studied the heat transfer aspects of channels with curved walls in the cross section. There have been studies in bends and curved plates by Chung et al. [25], Arnal et al. [26], Kim et al. [27], and Chen et al. [28], in which the flow direction is along the curvature. Under such conditions, Goertler vortex effects may develop. These studies mainly involve the simulation of flows over a blade external surface and flows in the bends of internal cooling channels. Laker et al. [29] and many others studied the flow of coolant through circular ducts, which gives an idea of the fluid flow through curved channels. In reality, the internal channels are not exactly square nor rectangular as shown in Fig. 1. The channels have curved edges and are often trapezoidal in their cross sections depending on the blade profile. Thus, it is important to analyze the heat transfer and flow characteristics inside the turbine blade segment by segment, considering all the parameter changes involved, including the curvature of the channel cross section.

In the present study, two curvature configurations are considered. In the first, both the leading and trailing surfaces have positive curvature (denoted as (( channel) that mimics the natural curvature of the blade. This is a natural configuration to study, but there is no information in this regard in the literature. In the second, the leading surface has negative curvature, while the trailing

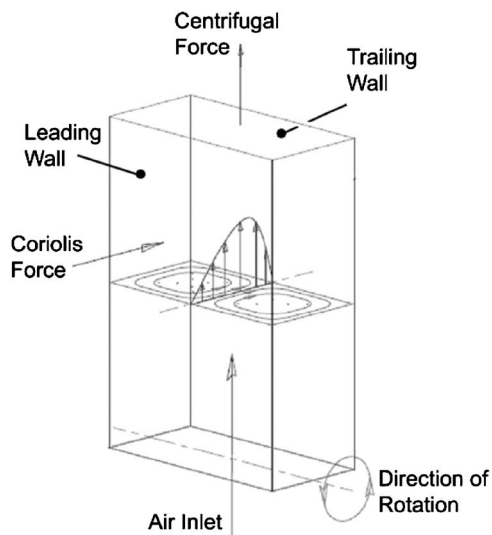


Fig. 2 Basic rotation effects

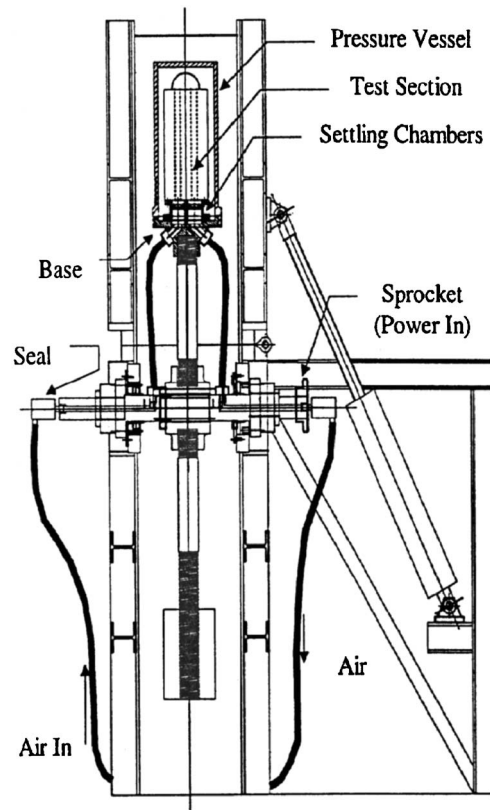


Fig. 3 Test rig

surface has positive curvature, leading to a coolant passage with the leading and trailing surfaces curved inward into the passage. This configuration is denoted as )( channel. The choice of the second curvature is based on the notion that cross-sectional area variations and associated pressure gradients can generate secondary flows that can potentially enhance heat transfer. The )( channel is currently a geometry not encountered in internal coolant passages. Although not immediately of practical relevance, this channel cross-section geometry and the associated results are useful in principle to assess the effect of convex curvature on the mass/heat transfer process under stationary and rotating conditions. However, this geometry may be of practical relevance in the future in designs where internal dividing walls between individual branches of the serpentine cooling channels are approximately parallel to the camber line of the airfoil. In such a design, the dividing wall can be made convex toward the pressure side of the airfoil. Since the outside surface of the pressure side is concave, the corresponding inner wall of the cooling passage is convex; thus, the coolant channel on the suction side of the airfoil can have doubly convex, )(, walls. If there is a heat transfer advantage in such channels, as indeed indicated in the current study, implementation of coolant channels with partitions along the camber line with such cross sections may be viable and advantageous.

The present study uses the naphthalene sublimation technique [30] and the heat to mass transfer analogy to study the effect of curved channel walls with curvature perpendicular to the main flow direction on the mass/heat transfer in outward flowing coolant channels under stationary and rotating conditions. As mentioned previously, rotation number effects are examined in the absence of centrifugal buoyancy.

## Experimental Details

**Rotating Mass Transfer Facility.** The experimental test rig (Fig. 3) for rotating mass transfer studies consists of a rotor with

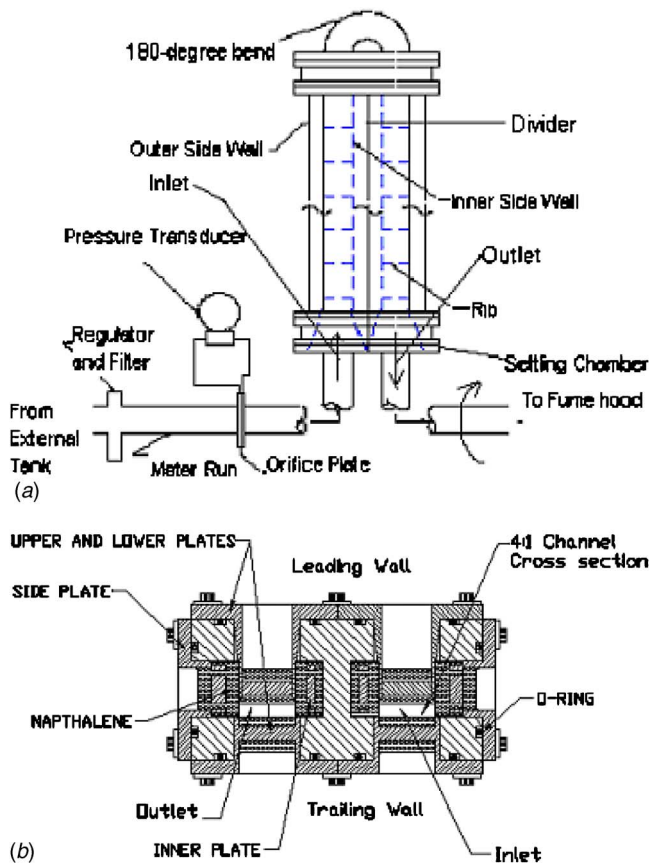


Fig. 4 Test section: (a) general layout and metering, (b) cross section

the test section on one end and counterbalancing weight on the other. The rotation is induced using a hydraulic motor and chain drive mechanism. The test section consists of a single module of serpentine cooling channel whose internal sides are removable plates cast with naphthalene. Compressed air is used as the working fluid. An external reservoir supplies air to the test section to avoid fluctuations in flow due to the compressor. Air flows at the required flow rate through the shaft of the rotor, then through the test section, and back out through the other end of the rotor shaft to an exhaust hood through flexible tubing. A concentric bore orifice is used to measure the mass flow rate in a metering run. Calibrated absolute and differential pressure gauges are used to measure pressure in the channel and across the orifice. The temperature of the naphthalene wall is measured using K-type thermocouples cast into the naphthalene wall. The thermocouple output is recorded and stored in a data logger fitted on the rotating shaft. It is also read simultaneously through a set of slip rings using real time acquisition and by a temperature controller. A differential pressure transducer capable of measuring very low pressures is also fixed onto the test section to study the pressure losses. All the instruments are calibrated for the desired experimental conditions.

Figure 4(a) shows a schematic of the serpentine channel test section and Fig. 4(b) shows its cross-sectional view. For the current study, the radially outward flow coolant passage, also referred to as the inlet channel, is studied for different flow conditions. A 180 deg bend and an outlet flat-walled channel (inward flow) of 4:1 aspect ratio (width:height) are used to complete the serpentine passage. The test section consists of eight removable aluminum plates, four in each pass of the channel, filled with naphthalene. The plates and the bend are secured to the frame in a flangelike manner using O-rings and screws to avoid air leakage. When as-

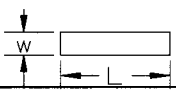
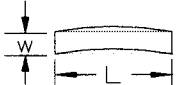
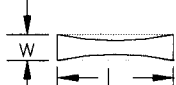
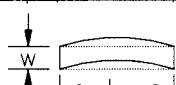
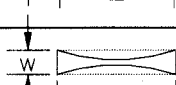
sembled, the test section forms  $25.4 \times 6.35 \times 304.8 \text{ mm}^3$  (width  $\times$  height  $\times$  length) inlet and outlet sections, 38.1 mm apart, that are connected by the 180 deg,  $25.4 \times 6.35 \text{ mm}^2$ , 4:1 rectangular cross-section bend. The radial position of the center of the section is roughly located at 890 mm from the rotating axis. Most of the test section is made of aluminum alloy to reduce weight. The test section is covered with a pressure vessel to allow pressurization. It also diminishes viscous heating as the test section is exposed only to stagnant air and isolated from external disturbances. The rotor and test section are fully enclosed by a cast iron casing for safety purposes. The casing also houses the bearings and supports the rotor shaft.

Table 1 shows the curved cross sections used for the current study. Channels with the two different curvature configurations with curved leading and trailing edges are studied for two curvatures of  $90.6 \text{ m}^{-1}$  ( $0.23 \text{ in.}^{-1}$ ) and  $15.11 \text{ m}^{-1}$  ( $0.384 \text{ in.}^{-1}$ ). A detailed study at  $Re=10,000$  with rotation numbers in the range of 0–0.07 is performed for the different configurations. Positive curvature is defined here as that corresponding to the natural curvature of the blade and is represented by Configurations 2 and 4 in Table 1. The higher curvature ( $R_c$ ) leads to a greater offset ( $e$ ) from the flat configuration (as shown in the schematic in Table 1) and, therefore, the dimensionless curvature can be expressed either as  $e/L$  or by  $L/R_c$ . Both these values are shown in Table 1. For notational convenience, the positive-positive curvature configuration is denoted by the symbol (( with the corresponding  $e/L$  value indicated alongside. The negative-positive curvature configuration is similarly denoted as ). All experiments are done for a 90 deg orientation of the coolant passage relative to the plane of rotation. The mass transfer data from the curved walled channels are compared to those from a smooth 4:1 rectangular duct with similar flow parameters. The local mass transfer data are analyzed mainly for the fully developed region and area averaged to study the effect of rotation number. The fully developed region in the channel consists of  $59 \times 30$  points at a distance of more than 20 hydraulic diameters from the channel entrance. Since the cross sections are symmetric about the wall centerline and the channel is oriented perpendicular to the direction of rotation, the stream-wise averaged plots are shown from the centerline ( $Y/L=0.5$ ) to the outer side (OS) of the wall. The Sherwood number is normalized using the McAdams correlation [31] for a smooth flat-walled channel.

**Casting.** The naphthalene walls are cast by making a mold of highly polished metal backing plates clamped to the channel wall plates using a set of G clamps. The required geometry for the naphthalene surface is obtained by changing the backing plates for casting. For flat smooth surfaces, flat backing plates are used. For a concave surface, convex backing plates are used and vice versa. Similarly, the surface curvature is also determined by the backing plates used. All plates have highly polished casting surfaces. Highly purified naphthalene crystals are melted in heavy walled glass beakers and molten naphthalene is quickly poured into the hollow cavity of the plate frame and the backing plate. The cast plate is kept in a fume hood for at least 8 h to attain thermal equilibrium with the laboratory. To obtain the wall temperature, two thermocouples are cast in the naphthalene in one of the cast plates. The plates are mounted onto the test rig by first inserting the inner sidewall and then the bend, and, at last, the other plates are added onto the test section.

**Data Acquisition.** The mass transfer technique requires measuring the local naphthalene sublimation depth at various points on the naphthalene-coated walls after the experiment. Preliminary analysis and experiments are conducted to decide the positions of interest on the naphthalene walls. The naphthalene sublimated from these points is measured by moving the cast plates under a fixed linear variable differential transducer (LVDT)-type profilometer before and after the experiment is conducted. The cast

**Table 1** The different types of channels used for the current study,  $R_c$ =radius of curvature,  $w=6.35$  mm,  $L=25.4$  mm

SL No.	Section	Hydraulic Dia (mm)	Area (mm <sup>2</sup> )	Segment height (e/L)	Symbol	L/Rc *	Name
1		10.2	161.3	0	□	Infinite	4:1 section
2		10.3	164.2	0.06	(( 0.06	0.23	(( 0.23 section
3		7.7	122.6	0.06	) ( 0.06	0.23	) ( 0.23 section
4		9.7	157.4	0.1	(( 0.1	0.384	(( 0.384 section
5		5.0	81.0	0.1	) ( 0.1	0.384	) ( 0.384 section

plates are moved with the help of a bidirectional traversing table secured onto the platform of a milling machine. The table has a 15.9 mm thick tooling aluminum plate, machined with pin supports and machine screw taps to ensure not only that the walls lie perfectly flat on the mounting plate but also that the scans are repeated at the exact same points. The traverse mechanism is actuated through microstep drive motors with a 0.00127 mm step size using a program ran on a personal computer.

**Data Reduction.** The surface scan takes about 25 min for the leading and trailing walls and 15 min for the two sidewalls. The assembly time per plate onto the test section is about 5 min. For rotating experiments, the rotor is initially rotated for about 40 min to attain a steady state. Except for these conditions, the plates are kept inside a sealed container with naphthalene-saturated atmosphere. Thus, loss of naphthalene due to natural convection only occurs for approximately 45 min at most for a single channel experiment. This loss is near the resolution of the surface measurement and verified experimentally. Nevertheless, this loss is included in the uncertainty analysis.

The surface profiles are deduced with respect to the plane obtained by three fixed points on the walls of each aluminum plate. The difference between the normalized profiles before and after the experiment gives the local naphthalene sublimation depth. This can be used to calculate the mass flux ( $\dot{m}''$ ) at the point and hence the local mass transfer coefficient ( $h_m$ ) given by

$$\dot{m}'' = \rho_s \delta / \Delta t \quad h_m = \dot{m}'' / (\rho_w - \rho_b(x))$$

where  $\rho_s$  is the density of solid naphthalene,  $\delta$  is the local sublimation depth,  $\Delta t$  is the duration of the experiment, and  $\rho_w$  and  $\rho_b(x)$  are the vapor density of the naphthalene at the wall (obtained from the equation of state) and that in bulk (obtained from mass balances), respectively.

The local Sherwood number Sh is then calculated by

$$Sh = h_m D_h / D_{n-a} (P_{duct} / P_{atm}) = h_m D_h Sc / \nu (P_{duct} / P_{atm})$$

where  $D_{n-a}$  is the binary diffusion coefficient for naphthalene in air at 1 atm [32]) and Sc is the Schmidt number defined as the ratio of the kinematic viscosity  $\nu$  of air to this mass diffusivity for naphthalene-air (Sc=2.5), as given by Ref. [33]. The ratio of the pressure in the duct to that in atmosphere ( $P_{duct} / P_{atm}$ ) is used to accommodate the effect of pressure on the diffusion coefficient.

Normalization is done to the Sherwood numbers using the McAdams [31] equation for fully developed flow in a smooth wall pipe,

$$Sh_0 = 0.023 Re^{0.8} Sc^{0.4}$$

where Re is the Reynolds number with respect to the hydraulic diameter of the duct. This expression is analogous to the corresponding heat transfer empirical formula

$$Nu_0 = 0.023 Re^{0.8} Pr^{0.4}$$

Heat and mass transfer results can be analyzed using the analogy (Souza [30])

$$Nu = Sh (Pr / Sc)^{0.4}$$

**Uncertainty Analysis.** Uncertainties for all computed values are estimated using the second-power equation method [34]. Volume flow rate and Reynolds number (Re) uncertainties are estimated to be less than 10% for  $Re > 6000$ . The reported resolution of the LVDT is 0.00127 mm, while the analog-to-digital (A/D) converter is reported to have an accuracy of 0.002 mm in a 12 kHz acquisition rate, 16 bit resolution mode. Experimental tests of accuracy and repeatability for the entire acquisition system indicate a sublimation depth uncertainty of 0.0038 mm, which is therefore the minimum depth that can be measured. Maximum sublimation depths are maintained at about 0.152 mm by varying the duration of the experiment. The maximum subli-



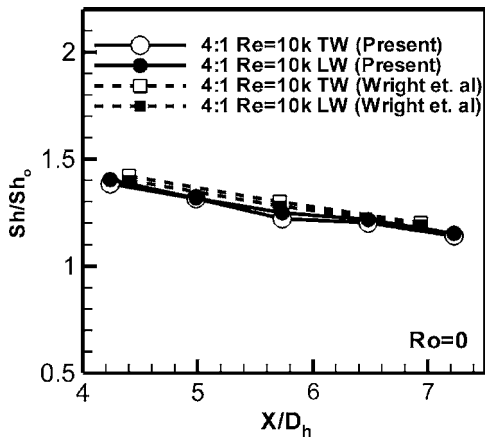


Fig. 5 Comparison of Ref. [23] with present data

mation depth was selected to minimize uncertainties in both depth measurement and changes in duct cross-section area. These uncertainties were found to be 1% and 3%, respectively. The resulting experimental duration was around 120 min for the given set of Reynolds number. The temperature measurement made at the naphthalene wall has an uncertainty of  $+0.5^{\circ}\text{C}$ . The uncertainty due to temperature measurement is found to be less than 9% for the largest temperature errors. The effect of curvature in the depth measurement can be neglected for the calculation of the Sherwood number as the error due to the probe tip curvature on the curved surface of wall was calculated to be less than 0.5% of the sublimation depth measured. Nevertheless, there is a shift of the actual location points along the width of the channel wall, which does not affect the average Sherwood numbers calculated. Thus, the overall uncertainty in average Sherwood number was calculated to be less than 12% and this varies with the Reynolds number (<1%).

## Results and Discussions

**Validation.** The current set of experiments with the flat surfaces was compared with data from the literature. The experiment test section consists of 4:1 single pass smooth channel with a sudden contraction at its entrance. A preliminary test was done to compare the mass/heat transfer data to those reported by Wright et al. [23]. Since the inlet to the test section is different for the two studies, results are compared in the fully developed region. Figure 5 shows the comparison of the fully developed Sherwood number ratio for the 4:1 channel at zero rotation number for the present study with that of Wright et al. [23], and the agreement is well within estimated experimental error. Under rotational conditions (at  $Re=10,000$ ), a comparison with computational data of Murata and Mochizuki [19] is shown in Fig. 6 and the agreement is also very good.

At higher rotation numbers, multiple secondary flow vortices are formed in the high aspect ratio channels. This is confirmed by the computational results of Murata and Mochizuki [19] and Saha and Acharya [20] for a 4:1 rotating channel at higher rotation numbers, where it is shown that multiple secondary flows form in the channel cross section due to the phenomenon of vortex splitting. These complex secondary flows generally enhance heat transfer on both leading and trailing surfaces, as observed by Saha and Acharya [20], but more so on the trailing surface due to the effect of the Coriolis forces. This behavior is confirmed by the present measurements, and as shown in Fig. 7, rotation enhances the mass transfer along both leading and trailing walls although the enhancement along the leading surface is small and relatively insensitive to increases in rotation number, while the corresponding trailing surface exhibits monotonic increase with rotation

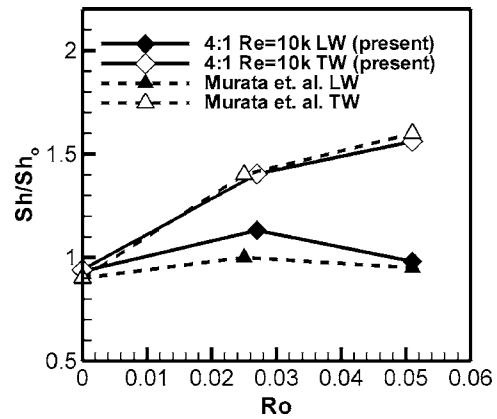


Fig. 6 Comparison of fully developed area-averaged plots for 4:1 rectangular channels with those of Murata and Mochizuki [19]

number. For  $Ro=0.051$ , there is a nearly 50% enhancement of mass/heat transfer along the trailing wall with only a 15% enhancement along the leading surface.

## Curved Surface Results

(( *Section Channels.* The heat/mass transfer results for the given cross sections are represented in terms of normalized Sherwood numbers. Figure 8 shows the fully developed area-averaged plots for the different cross sections in comparison with the 4:1 rectangular channel.

The plots for the lower curvature case, (( 0.06, show enhancement in mass/heat transfer for both the leading and trailing walls with respect to the 4:1 flat channel. While there is a nearly 10% enhancement along the trailing wall (destabilized by rotation), the leading wall has a 20% enhancement for the higher rotation number. Thus, the (( 0.06 curvature case produces modest enhancements in heat transfer along both the stabilized and destabilized surfaces with rotation. However, the higher curvature section, (( 0.1, shows a 10% reduction in mass/heat transfer for low  $Ro$  and about a 20% reduction for the higher  $Ro$  along the leading wall (stabilized by rotation). The trailing wall does not show much of a change in the case of high curvature. This suggests that there may be an optimal curvature for the sections where the mass/heat transfer would be the highest for the leading and trailing walls. The enhancement in mass/heat transfer at low curvatures can be due to the increase in instability due to concave curvature along the leading wall, when secondary flows are generated due to rotation. The destabilizing effects of concave curvatures are shown

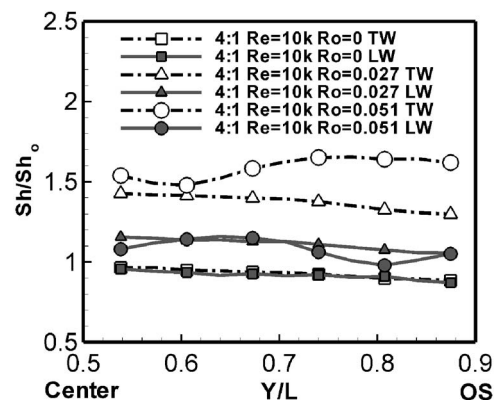


Fig. 7 Streamwise averaged curves of 4:1 rectangular channel for different rotation numbers

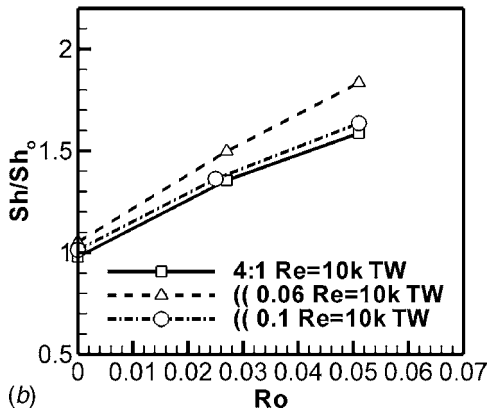
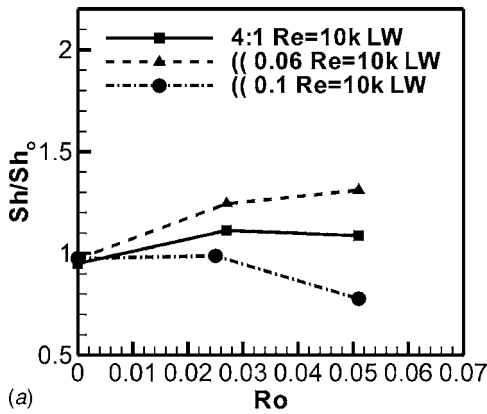


Fig. 8 Fully developed area-averaged plots for (( cross sections at  $Re=10,000$  and  $R_0$  varying from 0 to 0.051

by Kim et al. [27] but for flow along the curvature.

Figure 9 shows the effect of curvature on the spanwise distributions of mass/heat transfer for given rotation numbers. The spanwise variations do not appear to be significant at the lower rotation number. However, at the higher rotation number, spanwise variations of the order of 10–15% appear and spanwise locations of low mass transfer along the leading surface correspond to locations of high mass transfer on the trailing surface and vice versa. This is indicative of a two-roll pattern in half the cross section of the channel or a four-roll pattern in the full cross section. This secondary roll pattern is consistent with the predictions of Saha and Acharya [20] for the flat 4:1 aspect ratio (AR) channel. The lower curvature case appears to enhance the spanwise nonuniformities.

*)( Section Channels.* Streamwise averaged mass/heat transfer results are presented in Fig. 10 for the positive-negative curvature case, denoted by )( . In this case, the restricted area at the centerline may produce counteracting effects. There could be lower velocity in the central restricted region because of the interaction between the opposing boundary layers or a higher velocity because of the area reduction. The former is more likely in the higher curvature stationary duct flow where the distance between the walls is less than 1.5 mm. Indeed, there is evidence of this in Fig. 10 where the mass/heat transfer is reduced toward the center of the duct in the high )( 0.1, curvature case.

Compared to the flat wall case, the )( section shows mass/heat transfer enhancements along the leading and trailing walls for the smaller curvatures, )( 0.06, and these enhancements are highest at the lower rotation number of 0.027. There is a decrease in the mass/heat transfer rate as the rotation number increases and this decrease is steeper along the leading wall of the smaller curvature section. This might be due to the stabilizing effect of the negative

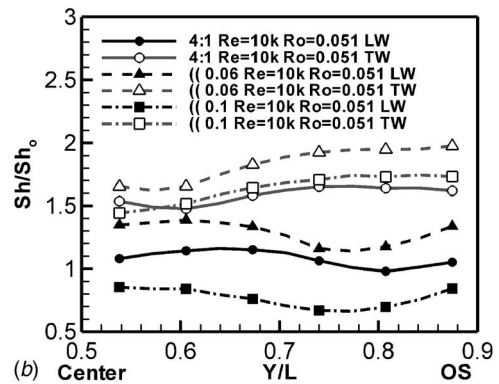
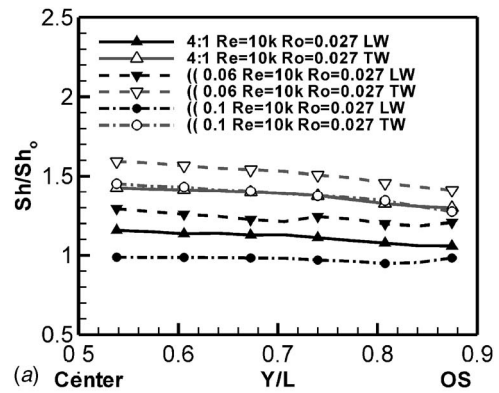


Fig. 9 Streamwise averaged plot for the different cross sections for (a) low and (b) high rotation numbers

curvature along the leading wall, due to which the secondary flow attains more stability in both the leading and trailing walls. The higher curvature )( 0.1 section shows steady increase in the trailing wall mass/heat transfer with increasing rotation number, while the leading wall mass/heat transfer is flat. In general, the destabilized wall displays higher sensitivity to the  $R_0$  number as shown in Fig. 11. It should be noted that the mass transfer rate is consistently lower for the higher wall curvature channel. It is possible that for this more complex cross-sectional geometry, the hydraulic diameter definition used to scale the data may not be the appropriate one.

The streamwise averaged mass/heat transfer data for the )( section for the highest rotation number tested is shown in Fig. 12. The rotation effect is evident for all wall curvatures. The spanwise mass/heat transfer distribution is fairly uniform with the exception of the high curvature case where peak mass/heat transfers occur

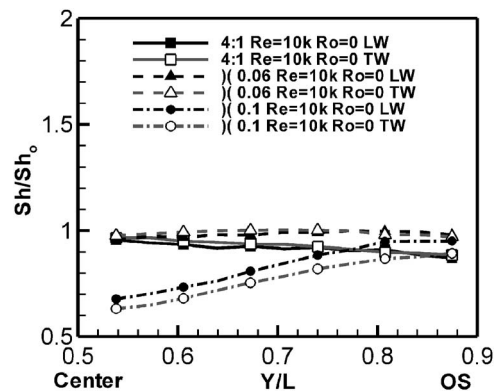


Fig. 10 Comparison between stationary ducts for )( cross-sectioned channels with 4:1 cross section

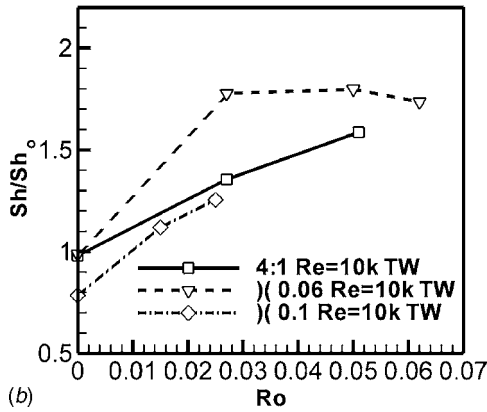
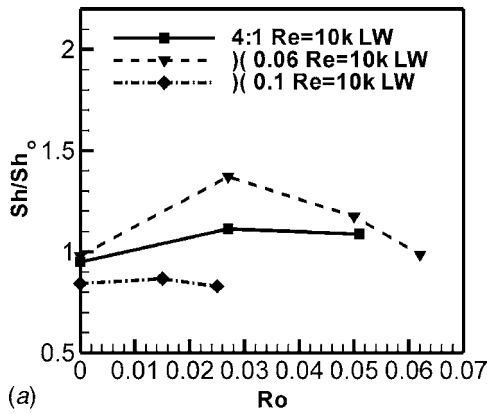


Fig. 11 Fully developed area-averaged plots for (( channels at different  $R_0$

on both leading and trailing walls at off-center locations. As discussed previously regarding the stationary results, this tends to indicate that the flow is decelerated in the central region of the cross section because of interaction of the opposing boundary lay-

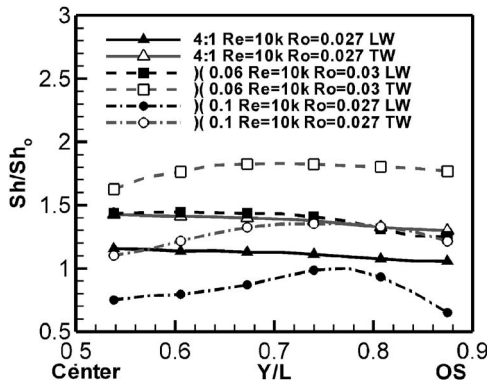


Fig. 12 Comparison of mass/heat transfer from (( cross section and 4:1 flat channel benchmarked at  $R_0=0.03$

Table 2 Comparison of the area-averaged Sherwood number ratios ( $Sh/Sh_0$ ) for all the sections at different rotation numbers

$R_0$	[ ]		((0.06		)(0.06		)((0.1		)((0.1	
	LW	TW	LW	TW	LW	TW	LW	TW	LW	TW
0	0.914	0.925	0.973	1.052	0.980	0.987	0.976	1.014	0.843	0.785
0.027	1.113	1.355	1.244	1.498	1.372	1.777	0.988	1.362	0.829	1.255
0.051	1.087	1.587	1.311	1.835	1.174	1.798	0.778	1.636	x	x

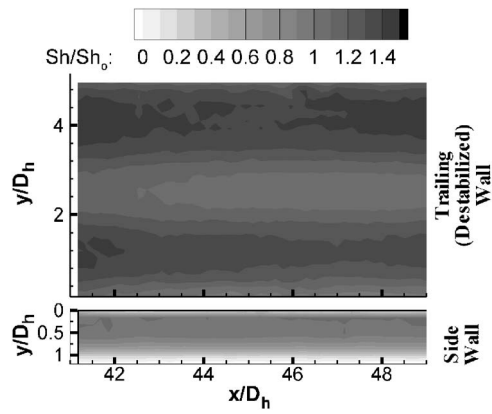


Fig. 13 Sherwood number distribution in the fully developed region of the trailing and the left-side walls of the (( 0.1 channel for  $Re=10,000$  and  $R_0=0.027$

ers in the high curvature case.

Figure 13 depicts the streamwise and spanwise distributions of the normalized Sherwood number in the fully developed region of the trailing (destabilized) and the left-side walls of the high curvature channel. The mass transfer distribution is uniform to a satisfactory effect in the streamwise direction, validating the use of streamwise averaging in the preceding result presentations. The mass transfer distribution exhibits a minimum in the center region of the channel where reduced velocity is expected because of the interacting opposing boundary layers, while peak mass transfer occurs on either side of the centerline. The effect of rotation is observed on the side plate, with high mass/heat transfer on the side of the trailing wall and diminished mass/heat transfer on the side of the leading wall. It is noted that there is an asymmetry of the mass transfer distribution about the centerline. As mentioned previously in the discussion of the stationary case, this asymmetry is attributed to the increased sensitivity of the flow in the high-curvature double-convex cross-section channel to geometrical asymmetry, which, because of the small cross-flow dimension of the channel, is of order of 8% of this dimension. Similar trends of the normalized Sherwood number are observed on the leading wall and on the right-side wall, which are not shown in the interest of brevity.

### Comparison of All Sections

Table 2 gives the Sherwood number ratios for the different configurations at different rotation numbers. The highest mass/heat transfer rates are realized for the smaller curvature (( section at nonzero rotation numbers. Both the (( and the )( show enhancements over the flat wall case at low curvatures and at all rotation numbers. For a rotation number of 0.027, the )( case shows a nearly 30% enhancement along the trailing wall compared to the flat wall case, while for a rotation number of 0.051, there is a nearly 15% enhancement along both leading and trailing walls for the )( case. It is clear that curvature effects cannot be ignored as has been done in the literature, and depending on the rotation



number and curvature value, these effects can be in the range of 15–30% in area-averaged values and higher locally.

## Conclusions

Measurements are reported to document the effect of positive and negative wall curvatures for a 4:1 AR channel. Both (( or positive-positive curvature and )( or positive-negative curvature channels are considered. The following are the major observations of the experimental study:

1. Measurements for a 4:1 AR channel with flat surfaces agree well with reported experimental and computational studies.
2. Mass/heat transfer is sensitive to wall curvature in the 4:1 AR coolant passages considered. Depending on the rotation number and curvature value, these effects can be in the range of 15–30% in area-averaged values and higher locally.
3. For ((channels with smaller curvature, (( 0.06, an enhancement in mass/heat transfer relative to the flat wall channel is seen. This enhancement is of the order of 10–15%. For the same geometry and higher curvature (( 0.1, there is reduction in mass/heat transfer of 20% at the leading wall compared to the 4:1 channel with flat walls.
4. Mass/heat transfer is enhanced in )( channel for the smaller curvature, )( 0.06. This enhancement is highest at lower rotation numbers and steadily decreases as the  $R_0$  increases. For the higher curvature case, there is a reduction in the heat/mass transfer relative to the flat channel case.
5. The comparisons between the low and high wall curvatures indicate that there may be an optimum wall curvature in terms of heat transfer performance.

## Acknowledgment

Support of this effort by the Clean Power and Energy Research Consortium through the Louisiana Board of Regents is gratefully acknowledged.

## Nomenclature

$A$	=	area
$B_0$	=	buoyancy parameter
$D$	=	diameter
$e$	=	segment height
$h$	=	heat transfer coefficient
$L$	=	channel length
$m''$	=	mass flow rate
$Nu$	=	Nusselt number
$P$	=	pressure
$Pr$	=	Prandtl number
$\Delta P$	=	pressure drop
$q''$	=	heat flux per unit area
$R$	=	radius of the rotating arm
$Re$	=	Reynolds number, $Re = \rho U D_h / \mu$
$R_0$	=	rotation number, $R_0 = \Omega D_h / U$
$Sc$	=	Schmidt number
$Sh$	=	Sherwood number
$T$	=	temperature
$t$	=	time
$U$	=	average velocity
$X, x$	=	distance along streamwise direction
$Y$	=	distance along spanwise direction
$\delta$	=	sublimation depth
$\Omega$	=	rotational speed
$\rho$	=	density of naphthalene
$D_{n-a}$	=	naphthalene to air diffusivity coefficient

## Subscripts

$0$	=	smooth conditions
$atm$	=	atmospheric condition
$b$	=	bulk value

duct	=	parameter in the channel
$h$	=	hydraulic
$m$	=	mass transfer parameter
$s$	=	solid (naphthalene)
$w$	=	wall

## References

- [1] Wagner, J. H., Johnson, B. V., and Kopper, F. C., 1991, "Heat Transfer in Rotating Serpentine Passages With Smooth Walls," *ASME J. Turbomach.*, **113**, pp. 321–330.
- [2] Johnson, B. V., Wagner, J. H., and Steuber, G. D., 1993, "Effects of Rotation on Coolant Passage Heat Transfer," NASA Contractor Report No. 4396, Vol. II.
- [3] Park, J. S., Han, J. C., Huang, Y., and Ou, S., 1992, "Heat Transfer Performance Comparisons of Five Different Rectangular Channels With Parallel Angled Ribs," *Int. J. Heat Mass Transfer*, **35**(11), pp. 2891–2903.
- [4] Kukreja, R. T., Park, C. W., and Lau, S. C., 1998, "Heat (Mass) Transfer in a Rotating Two Pass Square Channel-Part-II: Local Transfer Coefficient, Smooth Channel," *Int. J. Rotating Mach.*, **4**(1), pp. 1–15.
- [5] Zhang, N., Chiou, J., Fann, S., and Yang, W.-J., 1993, "Local Heat Transfer Distribution in a Rotating Serpentine Rib-Roughened Flow Passage," *ASME J. Heat Transfer*, **115**, pp. 560–567.
- [6] Myrum, T., Acharya, S., Sinha, S., and Qiu, X., 1996, "The Effect of Placing Vortex Generators Above Ribs in Ribbed Ducts on the Flow, Flow Temperature, and Heat Transfer Behavior," *ASME J. Heat Transfer*, **118**, pp. 294–300.
- [7] Eliades, V., Nikitopoulos, D. E., and Acharya, S., 2001, "Mass Transfer Distribution in Rotating, Two-Pass Ribbed Channels With Vortex Generators," *J. Thermophys. Heat Transfer*, **15**(3), pp. 266–274.
- [8] Acharya, S., Eliades, V., and Nikitopoulos, D. E., 2001, "Heat Transfer Enhancements in Rotating Two-Pass Coolant Channels With Profiled Ribs: Average Results," *ASME J. Turbomach.*, **23**(1), pp. 97–106.
- [9] Nikitopoulos, D. E., Eliades, V., and Acharya, S., 2001, "Heat Transfer Enhancements in Rotating Two-Pass Coolant Channels With Profiled Ribs: Detailed Measurements," *ASME J. Turbomach.*, **23**(1), pp. 107–114.
- [10] Zhou, F., and Acharya, S., 2001, "Mass/Heat Transfer in Dimpled Turbine-Blade Coolant Passages," *Ann. N.Y. Acad. Sci.*, **934**, pp. 424–431.
- [11] Agarwal, P., Acharya, S., and Nikitopoulos, D. E., 2003, "Heat Transfer in 1:4 Rectangular Passages," *ASME J. Turbomach.*, **125**, pp. 726–733.
- [12] Han, J. C., Ou, S., Park, J. S., and Lei, C. K., 1989, "Augmented Heat Transfer in Rectangular Channels of Narrow Aspect Ratios With Rib Turbulators," *Int. J. Heat Mass Transfer*, **32**, pp. 699–1630.
- [13] Han, J. C., 1988, "Heat Transfer and Friction Characteristics in Rectangular Channels With Rib Turbulators," *ASME J. Heat Transfer*, **110**, pp. 321–328.
- [14] Han, J. C., and Zhang, P., 1989, "Pressure Loss Distribution in Three-Pass Rectangular Channels With Rib Turbulators," *ASME J. Turbomach.*, **111**(4), pp. 515–521.
- [15] Zhang, Y. M., Gu, W. Z., and Han, J. C., 1994, "Heat Transfer and Friction in Rectangular Channels With Ribbed or Ribbed-Grooved Walls," *ASME J. Heat Transfer*, **116**(1), pp. 58–65.
- [16] Dutta, S., Andrews, M. J., and Han, J. C., 1996, "Prediction of Turbulent Heat Transfer in Rotating Smooth Square Ducts," *Int. J. Heat Mass Transfer*, **39**(12), pp. 2505–2514.
- [17] Wagner, J. H., Johnson, B. V., Steuber, G. D., and Yeh, F. C., 1992, "Heat Transfer in Rotating Serpentine Passages With Trips Normal to the Flow," *ASME J. Turbomach.*, **114**, pp. 847–857.
- [18] Johnson, B. V., Wagner, J. H., Steuber, G. D., and Yeh, F. C., 1994, "Heat Transfer in Rotating Serpentine Passages With Trips Skewed to the Flow," *ASME J. Turbomach.*, **116**, pp. 113–123.
- [19] Murata, A., and Mochizuki, S., 1999, "Effect of Cross-Sectional Aspect Ratio on Turbulent Heat Transfer in an Orthogonally Rotating Rectangular Smooth Duct," *Int. J. Heat Mass Transfer*, **42**, pp. 3803–3814.
- [20] Saha, A. K., and Acharya, S., 2005, "Unsteady RANS Simulations of Turbulent Flow and Heat Transfer in Ribbed Coolant Passages of Different Aspect Ratios," *Int. J. Heat Mass Transfer*, **48**, pp. 4704–4725.
- [21] Soong, C. Y., Lin, S. T., and Hwang, G. J., 1991, "An Experimental Study of Convective Heat Transfer in Radially Rotating Rectangular Ducts," *ASME J. Heat Transfer*, **113**, pp. 604–611.
- [22] Morris, W. D., and Ghavami-Nasr, G., 1991, "Heat Transfer Measurements in Rectangular Channels With Orthogonal Mode Rotation," *ASME J. Turbomach.*, **113**, pp. 339–345.
- [23] Wright, L. M., Fu, W. L., and Han, J. C., 2005, "Influence of Entrance Geometry on Heat Transfer in Rotating Rectangular Cooling Channels (AR=4:1) With Angled Ribs," *ASME J. Heat Transfer*, **127**, pp. 378–387.
- [24] Griffith, T. S., Al-Hadhrani, L., and Han, J. C., 2002, "Heat Transfer in Rotating Rectangular Cooling Channels (AR=4) With Angled Ribs," *ASME J. Heat Transfer*, **124**, pp. 617–625.
- [25] Chung, J. H., and Hyun, J. M., 1992, "Convective Heat Transfer in the Developing Flow Region of a Square Duct With Strong Curvature," *Int. J. Heat Mass Transfer*, **35**(10), pp. 2537–2550.
- [26] Arnal, M. P., Goering, D. J., and Humphrey, J. A. C., 1992, "Unsteady Laminar Flow Developing in Curved Duct," *Int. J. Heat Mass Transfer*, **13**(4), pp. 347–357.
- [27] Kim, J., Simon, T. W., and Russ, S. G., 1992, "Free-Stream Turbulence and Concave Curvature Effects on Heated, Transitional Boundary Layers," *ASME*

- J. Heat Transfer, **114**(2), pp. 338–347.
- [28] Chen, C. T., and Lin, M. H., 2002, “Effect of Rotation on Goertler Vortices in the Boundary Layer for a Curved Surface,” *Int. J. Numer. Methods Fluids*, **40**(10), pp. 1327–1346.
- [29] Laker, T. S., and Ghiaasiaan, S. M., 2001, “Secondary Flows in a Rotating Serpentine Circular Duct,” *PVP (Am. Soc. Mech. Eng.)*, **424**(1), pp. 155–167.
- [30] Souza-Mendes, P. R., 1991, “The Naphthalene Sublimation Technique,” *Exp. Therm. Fluid Sci.*, **4**, pp. 510–523.
- [31] McAdams, W., 1954, *Heat Transmission*, 3rd. ed., McGraw-Hill, New York.
- [32] Sogin, H. H., and Providence, R. I., 1958, “Sublimation From Disks to Air Streams Flowing Normal to Their Surfaces,” *Trans. ASME*, **80**, pp. 61–69.
- [33] Cho, K., Irvine, T. F., Jr, and Karni, J., 1992, “Measurement of Diffusion Coefficient of Naphthalene Into Air,” *Int. J. Heat Mass Transfer*, **35**(4), pp. 957–966.
- [34] Kline, S. J., and McClintock, F. A., 1953, “Describing Uncertainties in Single-Sample Experiments,” *Mech. Eng. (Am. Soc. Mech. Eng.)*, **75**, pp. 3–8.

# Experimental Investigation of the Clocking Effect in a 1.5-Stage Axial Turbine—Part I: Time-Averaged Results

Sven König

e-mail: koenig.sven@siemens.com

Bernd Stoffel

Turbomachinery Laboratory (TFA),  
Darmstadt University of Technology,  
64287 Darmstadt, Germany

M. Taher Schobeiri

Turbomachinery Performance Laboratory,  
Texas A&M University,  
College Station, TX 77843-3123

*Comprehensive experimental investigations were conducted to get deeper insight into the physics of stator clocking in turbomachines. Different measurement techniques were used to investigate the influence of varying clocking positions on the highly unsteady flow field in a 1.5-stage axial low-pressure (LP) turbine. A Reynolds number typical for LP turbines as well as a two-dimensional blade design were chosen. Stator 2 was developed as a high-lift profile with a separation bubble on the suction side. This paper presents the results that were obtained by means of static pressure tapings and five-hole probes as well as the time-averaged results of unsteady x-wire measurements. The probes were traversed in different measuring planes for ten clocking positions. Depending on the clocking position, a variation in total pressure loss for Stator 2, a change of the rotor exit flow angle, and a dependency of the Stator 2 exit flow angle were found. The influence of these parameters on turbine efficiency was studied. Three main factors affecting the total pressure loss could be separated: the size of the separation bubble, the production of turbulent kinetic energy, and the strength of the periodic fluctuations downstream of Stator 2. [DOI: 10.1115/1.2948968]*

## Introduction

Rotor-stator interactions in multistage turbomachinery cause inherently unsteady flow fields. Additionally, as the lift of blade rows increases, unsteady effects play a more and more important role concerning aerodynamic and structural performance. Wakes from upstream blade rows convect downstream many chord lengths and interact with wakes and airfoils of the following stages. To account for those effects from the beginning of the design process, a profound knowledge of its physics is necessary but not yet available. Clocking (indexing) is one way of influencing the flow field in multistage turbomachinery by changing the relative circumferential position of rotors or stators with the same blade count of adjacent rows.

Huber et al. [1] investigated the loss behavior in a three-stage low-pressure (LP) turbine with identical vane counts for all stator rows. They found a change in turbine efficiency of up to  $\pm 0.5\%$  depending on the relative circumferential position of the two stators. This efficiency variation was called *clocking effect*. The numerical investigations of Griffin et al. [2] showed similar results. Binder et al. [3] studied a five-stage LP turbine and showed that a higher wake defect occurred when the chopped wakes of the upstream rotor hit the leading edge of the second rotor blades, and that higher wake defect was suppressed when the wakes convected through the rotor passage. Ladwig [4] used a cascade wind tunnel to investigate LP turbine blades under steady state flow conditions. With the use of cylindrical bars, steady wakes were generated, impinging on the turbine blades. Ladwig showed that by changing the point of impact of the cylinder wakes, the profile losses of the turbine blades changed. He proposed to use this effect to increase turbine efficiency. Engber and Fottner [5] as well as Acton [6] were able to confirm the results of Ladwig, using a different turbine blade design. Halstead et al. [7] showed

in experimental and numerical investigations of a 1.5-stage turbine that the boundary layer development of the suction side of the second stator is strongly influenced by the relative position of the first stator. The wake induced periodic transition caused by the rotor wakes was the dominant mechanism. If the periodically incoming wakes of the first stator hit the leading edge of the second stator vanes, additional turbulence was transported into the boundary layer of the second stator. The velocity defect and unsteady pressure field also influenced the transition process. The clocking effect is also observed in axial compressors. A good overview of compressor clocking investigations is given by Dorney et al. [8] and Walker et al. [9]. The works by Dorney and Sharma [10], Eulitz and Engel [11], and Dorney et al. [12] give a survey on numerical clocking investigations. Some other numerical work with detailed information about the turbulence modeling is given by Höhn and Heinig [13] as well as Breitbach and Stoffel [14]. Stadtmüller et al. [15] were able to reduce losses by means of a high-lift blade design with a small separation bubble on the suction side. Reinmöller and Niehuis [16] investigated the clocking effect in a 1.5-stage LP turbine with blades of low aspect ratio. A numerical study by Li and He [17] considered aeromechanical aspects of clocking within a 1.5-stage transonic turbine. The focus of the work by Gadea et al. [18] was the time-averaged and time-resolved pressure field of the second stator in a 1.5-stage transonic turbine. They found different optimum clocking positions (clp's) concerning aerodynamics and mechanics. The studies of Halde-mann et al. [19,20] examined the influence of vane/blade spacing and clocking in a 1.5-stage high-pressure (HP) turbine. A change in overall efficiency of 2–3% due to clocking was observed using a variety of independent methods. A more fundamental approach was carried out by Heinke et al. [21]. They studied the influence of clocking within a high-lift turbine cascade without unsteady wakes. The results showed a change in total pressure loss coefficient of the Stator 2 blade row of about 11% depending on the clp. The minimum occurred when the impingement point of the Stator 1 wakes on the Stator 2 vane was shifted 6% of the pitch toward the suction side of Stator 2. Furthermore, a dependency of the Stator 2 deflection angle on the clp was found. König et al. [22],

Contributed by the Turbomachinery Division of ASME for publication in the JOURNAL OF TURBOMACHINERY. Manuscript received September 28, 2006; final manuscript received March 5, 2007; published online January 22, 2009. Review conducted by Dilip Prasad.



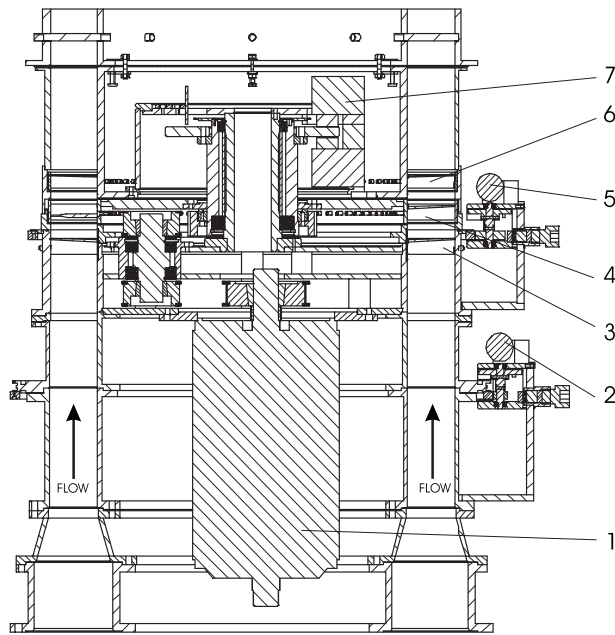


Fig. 1 TU Darmstadt clocking facility

using the same test rig and the same Stator 2 as Heinke, implemented a different Stator 1 and a rotor in such a way that they obtained similar time-averaged inflow parameters for Stator 2. The configuration was the same as the one in the current investigation and the influence of the unsteady rotor wakes on the boundary layer behavior of Stator 2 was studied. Furthermore König and Stoffel [23] studied the applicability of a spoked-wheel wake generator for clocking investigations. Mailach and Vogeler [24] investigated unsteady aerodynamic blade row interactions in a four-stage low-speed compressor. Experiments were carried out for different  $clp$ 's to distinguish between the different periodic influences from surrounding blade rows. A 3D simulation of the unsteady flow in a two-stage turbine was carried out by Bohn et al. [25]. They found a relative efficiency variation of about 0.52%. Billiard et al. [26] investigated the influence of clocking on the heat transfer of the second stator in a 1.5-stage HP turbine. Experimental and numerical clocking investigations in a two-stage LP turbine were carried out by Kryszinski et al. [27]. They found varying efficiency changes along the channel height, with highest values up to 2% close to the hub. Behr et al. [28] used fast response aerodynamic probes (FRAP) to investigate the unsteady flow features within a two-stage HP turbine. Due to the low aspect ratio of the turbine geometry, the flow field was found to be strongly three dimensional and dominated by secondary flow structures.

Authors often present results of clocking investigations in terms of efficiency gain or loss without giving much insight into the complex mechanisms that lead to the efficiency variations. The aim of this two-part paper is to provide a better understanding of the physics of the clocking effect in order to account for it from the beginning of the design process. Furthermore, the detailed experimental results provide a data basis for the validation of turbulence models in respect of their ability to calculate transitional flows with separation.

### Experimental Setup and Aerodynamic Design

Figure 1 shows a schematic of the experimental facility. The flow enters the annular test rig after passing a settling chamber. The vertical test section consists of two stators (3, 6) and one rotor (4). To adjust different  $clp$ 's Stator 1 can be indexed circumferentially relative to Stator 2 by the electric motor (2). Motor (5) allows wake traverses in circumferential direction. A 55 kW water

cooled four quadrant electric generator (1) keeps the revolutions per minute (RPM) of the rotor at a constant level and feeds the surplus power back to the supply system. In case of unallowed mode of operation, the fail safe emergency brake (7) causes a controlled shutdown of the rotor. The details about the experimental setup and the installed equipment are described in more detail by Heinke [29].

Table 1 gives an overview of the geometric and aerodynamic parameters. Stator 2 was designed at MTU Munich as a state-of-the-art high-lift LP turbine airfoil, which, under design flow conditions, has a laminar separation bubble on the suction side. To study the behavior of the separation bubble in detail, the current design slightly differs from the actual turbine blade design to increase the bubble size for the low Mach number flow. The Reynolds number based on exit conditions and cord length of Stator 2 is in the order of 217,000. For the design flow conditions, the flow can be considered incompressible. In the midspan region, secondary flows are negligible and felt seals are applied between rotating parts to minimize leakage flows.

A view on the airfoil geometry profiles and the definition of the  $clp$  is shown in Fig. 2. The dashed-dotted line is the path followed by most of the fluid particles of the Stator 1 wake. On the Stator 2 leading edge, a pressure tapping is used to define the  $clp$ : The smallest measured total pressure on the leading edge indicates  $clp=0.0$ . Due to the distortion of the Stator 1 wake within the rotor passage, this position does not necessarily coincide with the impingement point of the Stator 1 wake on the Stator 2 leading edge. However, numerical calculations show that the two positions are very close. Based on these results, it is assumed that for  $clp=0.0$  the Stator 1 wake hits the leading edge of Stator 2. The  $clp$ 's cover one airfoil pitch at midspan and vary from  $-0.5$  to  $0.5$ . The magnitude of the  $clp$ , given as the fraction of one stator pitch at midspan, is a measure of the circumferential distance between the streamline of the S1 wake core and the streamline leading to the leading edge of S2. Negative values indicate that the Stator 1 wake impinges on the pressure side of S2 and positive values indicate impingement points on the suction side.

### Measurement Techniques

In this paper, three different experimental techniques were used to investigate the influence of clocking on the time-averaged flow field, whereupon the main focus lied on the behavior of Stator 2 subjected to the incoming Stator 1 and rotor wakes. Pressure tapings were applied on the Stator 2 pressure and suction side to measure the static pressure distribution. Profile loss, total and static pressures, flow angles, and flow velocities were measured by five-hole probes and the unsteady flow velocities and flow angles as well as the turbulence quantities by means of an  $x$ -wire probe.

The pressure measurements along the vane surface were performed using a ScaniValve equipment. The pressure sensor was a PDCR22 with a linearity of 0.04% and a pressure range of 70 mbars. A 12 bit analog-to-digital (A/D) converter and a computer with a Pentium II processor were used to carry out the data acquisition.

A PSI9016 pressure scanner with a pressure range of 1 psi and an accuracy of 0.15% (full scale) was used for the five-hole probe measurements. To account for Mach and Reynolds number effects, the probes were calibrated at similar  $Ma$  and  $Re$  numbers as during the experiment. To assess the influence of unsteady wakes on the pneumatic measurements, a variation of the tube length and diameter as well as an error estimation proposed by Kazimierski and Horodko [30] were carried out. It was found that no correction procedure was necessary to account for unsteady effects.

The hot-wire measurements were carried out using a Dantec 55P62  $x$ -wire probe, and an external TC6 temperature probe was used to compensate for temperature variations. The voltage signal was converted using a 12 bit A/D converter. The frequency response of the wires was optimized by a square wave test. A once

**Table 1 Geometry and aerodynamic parameters**

Parameter	Stator 1	Rotor	Stator 2
Geometry			
Tip diameter	881 mm	881 mm	881 mm
Hub diameter	677.5 mm	677.5 mm	677.5 mm
Blade count	66	77	66
Vane blade spacing	35 mm	—	35 mm
Chord length, $C$	42.79 mm	41.01 mm	38.67 mm
Axial chord length, $C_{ax}$	35 mm	35 mm	30 mm
Span, $H$	101.75 mm	101.75 mm	101.75 mm
Pitch at midspan, $s$	37.09 mm	31.79 mm	37.09 mm
Aspect ratio, $H/s$	2.74	3.2	2.74
Geometrical deflection angle	51.7 deg	59.5 deg	69.3 deg
Measured flow parameters			
Mass flow	—	13 kg/s	—
Inlet total temperature, $T_{t_0}$	—	331.6 K	—
Inlet Mach number, $Ma_{c_0}$	—	0.133	—
Inlet flow angle, $\alpha$	—	0.2 deg	—
Inlet turbulence intensity, $Tu_0$	—	2.2%	—
Rotational speed, $n$	—	-1247 rpm	—
Exit Mach number, $Ma_e$	0.217	0.135	0.287
Exit flow angle, $\alpha$	-53.2 deg	11.6 deg	-60.6 deg
Stage pressure ratio, $p_{t_1}/p_{t_3}$	—	1.042	—
Reduced frequency, $f_r = f \frac{C_{S2}}{c_{ax2}}$	—	1.28	—
Flow coefficient, $\phi = \frac{c_{ax2}}{ U }$	—	0.95	—
Stage loading, $\psi = \frac{c_{u2} - c_{u1}}{U}$	—	-1.45	—
Degree of reaction, $R = \frac{\frac{c_2^2 - c_1^2}{2} - U(c_{u2} - c_{u1})}{\frac{c_3^2 - c_1^2}{2} - U(c_{u2} - c_{u1})}$	—	0.3	—
Reynolds number, $Re_{C_{S2}} = \frac{c_3 C_{S2}}{\nu}$	—	217,000	—

per revolution TTL trigger signal allowed ensemble averaging of the measured signal. 150 ensembles were found to be sufficient to resolve the Stator 1 and rotor wakes. The sampling frequency was set to 30 kHz and a low pass filter of 10 kHz was applied. Mea-

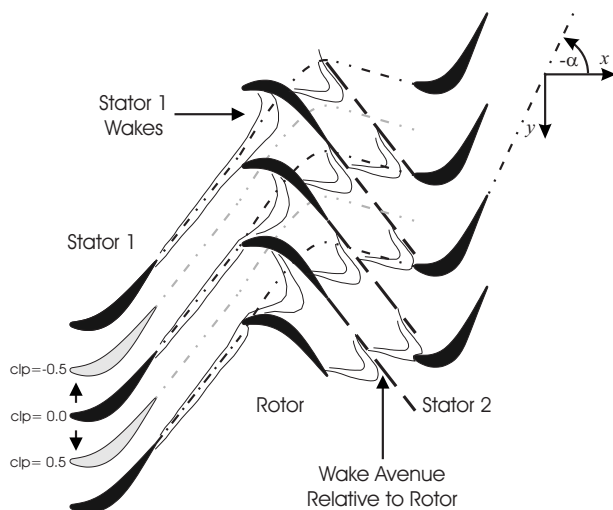


**Fig. 2 Definition of the clp**

urement inaccuracies were mainly due to probe contamination and temperature differences between calibration and experiment, which, due to changes of the density, cannot be completely eliminated by the compensation probe.

To assess the repeatability of the results, at least three measurements were taken for each clp, indicated by means of error bars in the figures being presented. Five-hole probe measurements of four Stator 2 vanes were carried out to find one Stator 2 pitch that represented best the average of the four vanes concerning total pressure loss and deflection angle. To evaluate the influence of the axial probe position, two measurements were carried out in the measuring planes 30 mm and 60 mm downstream of S2. Despite the mixing processes, observable for the local flow variables, the characteristics of the integral curves did not show a dependency on the probe position.

**Time-Averaged Results**

The probe measurements were carried out in five different measuring planes of which the results for the measuring planes 15 mm upstream and 60 mm downstream of S2 are being presented in this paper. The probes were aligned in such a way that their position upstream of S2 for clp=0.0 and  $y/s=0.0$  coincides with the streamline of the Stator 1 wake. The indication for this position was the maximum velocity deficit for clp=0.0. Downstream of S2, using the same procedure, the probes were aligned with the Stator 2 wake for clp=0.0 and  $y/s=0.0$ . In both measuring planes,

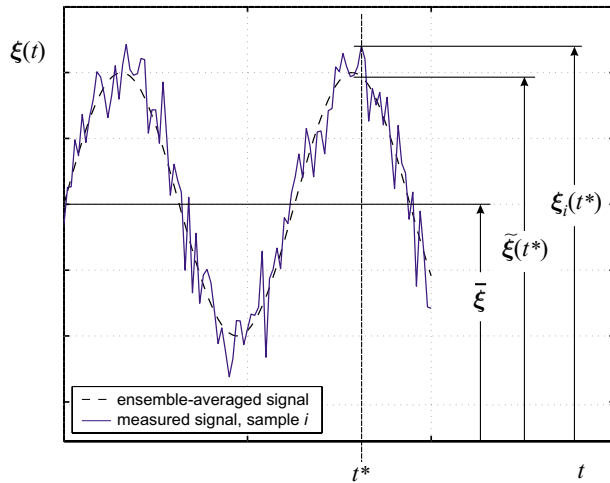


Fig. 3 Illustration of the ensemble-averaging technique

around  $y/s=0.0$ , a symmetrical traverse of 33 measuring points was carried out in circumferential direction over one airfoil pitch at midspan ( $s$ ). Negative values of  $y/s$  indicate probe positions shifted toward the pressure side of S2 and positive values probe positions shifted toward the suction side, respectively. The flow angle  $\alpha$  is measured from the axial direction in mathematical positive sense. The coordinates can be seen in Fig. 2: Downstream of Stator 2,  $y=0$  is located on the streamline of the Stator 2 wakes for  $clp=0.0$ .

To determine the loading of Stator 2, two adjacent vanes were instrumented with static pressure tappings: one on the suction side and one on the pressure side. To avoid interaction between the tappings, they have not been aligned but every other tapping was shifted by 2 mm to the right and left of midspan maintaining a spacing of 2 mm along the vane surface.

Nine different  $clp$ 's were evenly spaced over one airfoil pitch, and one additional  $clp$  was introduced for the case when the impingement point of the Stator 1 wake is shifted 6.3% toward the suction side of Stator 2 ( $clp=0.063$ ). To allow a better survey of the results, not all  $clp$ 's but only a selection of  $clp$ 's is presented in the figures that show the local flow variables. Those are the  $clp$ 's that exhibit the smallest separation bubble ( $clp=-0.125$ ), minimum total pressure loss ( $clp=0.063$ ), maximum total pressure loss ( $clp=-0.375$ ), and the  $clp$ 's that show the most pronounced features for the flow variable being presented. Mean quantities are given in terms of pitch-averaged values defined by

$$\langle \xi \rangle = \frac{1}{s} \int_{-s/2}^{s/2} \xi(y) dy \quad (1)$$

where  $\xi$  corresponds to the flow variable of interest and  $s$  to the stator pitch at midspan.

To get deeper insight into the unsteady nature of the flow field, a separation of the periodic and stochastic fluctuations was carried out by means of the ensemble-averaging technique as illustrated in Fig. 3 using the equation

$$\tilde{\xi}(t) = \frac{1}{N} \sum_{i=1}^N \xi_i(t) \quad (2)$$

The parameter  $\xi_i(t)$  denotes the instantaneous value of ensemble  $i$  and  $N$  corresponds to the total number of measured ensembles. The ensemble-averaged RMS-value reveals information about the stochastic fluctuations of a signal and is defined by

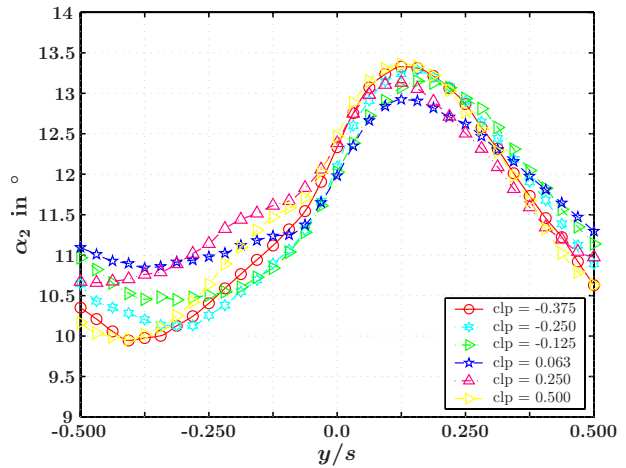


Fig. 4 Flow angle upstream of S2

$$\widetilde{\text{RMS}}(\xi(t)) = \sqrt{\frac{1}{N} \sum_{i=1}^N [\xi_i(t) - \tilde{\xi}(t)]^2} \quad (3)$$

In this paper, only the time average of the RMS-value, for simplification purposes labeled RMS, is subject to investigation.

A measure of the strength of the periodic fluctuations is the  $\text{RMS}_p$ -value of the ensemble-averaged signal given by

$$\text{RMS}_p(\xi) = \sqrt{\frac{1}{M} \sum_{j=1}^M [\tilde{\xi}(t_j^*) - \overline{\tilde{\xi}(t)}]^2} \quad (4)$$

where  $M$  indicates the number of the discrete measuring times  $t_j^*$  and  $\overline{\tilde{\xi}(t)}$  is the time-averaged value of the ensemble-averaged signal.

**Stator 2 Inlet Parameters.** To assess the influence of clocking on Stator 2, its inlet parameters have to be known in detail in order to allow an understanding of the interaction mechanisms that take place within the Stator 2 boundary layer. Furthermore, those parameters may be used as (unsteady) boundary conditions for numerical calculations and for verification purposes when a computation of the whole 1.5-stage turbine is carried out. The measurements were taken 15 mm upstream of Stator 2 and are influenced by the Stator 1 and rotor wake characteristics as well as the potential field of Stator 2. The interaction of those three parameters leads to a complex and highly unsteady flow field that varies for different  $clp$ 's.

In Fig. 4, the Stator 2 inlet flow angle is plotted for six different  $clp$ 's. The higher deflection angle in the region of  $y/s \approx 0.125$  is caused by the Stator 2 potential field, which yields to a deflection of the flow in this region towards the Stator 2 suction side. For negative  $y/s$ , the potential field causes a flow turning towards the Stator 2 pressure side, resulting in smaller deflection angles. Differences due to clocking are caused by the Stator 1 wakes that, because of their velocity deficit, experience a reduced turning within the rotor passage in the absolute frame of reference. This behavior is obvious in the regions  $y/s \approx -0.375$  (reduced deflection angle for  $clp=-0.375$ ) and  $y/s \approx 0.125$  (reduced deflection angle for  $clp=0.063$ ). The pitch-averaged values for all ten  $clp$ 's are shown in Fig. 5. The highest deflection angle occurs for  $clp=0.125$  and the maximum variation of the integral value is 0.23 deg. Three measurements were taken with an  $x$ -wire probe since pneumatic probes are not capable of resolving the highly unsteady flow field in this measuring plane. However, the error bars indicate that the accuracy of the five-hole probe for the measurement of flow angles in the regions of low periodic unsteadiness (downstream of S2, presented later in the paper) could not be



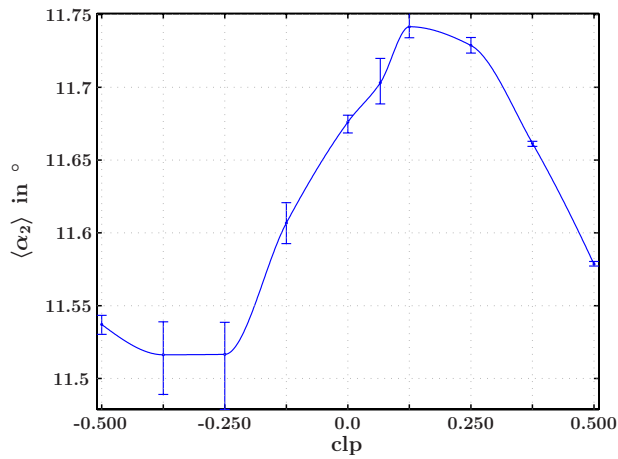


Fig. 5 Pitch-averaged integral flow angle upstream of S2

achieved with the  $x$ -wire probe.

The velocity distribution normalized by its overall mean value upstream of Stator 2 is shown in Figs. 6 and 7 for all ten  $clp$ 's. Since the probe traverse relative to Stator 2 is identical for all  $clp$ 's, the pronounced velocity deficit with changing  $clp$  is caused by the Stator 1 wake flow. As the probe alignment was carried out

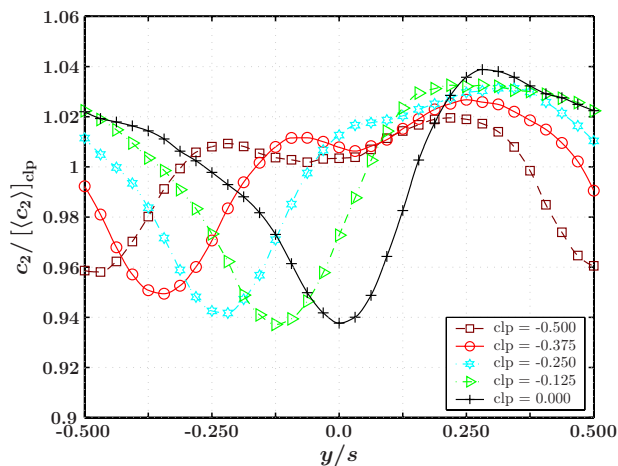


Fig. 6 Normalized absolute velocity upstream of S2; S1 wake impinges on the S2 PS

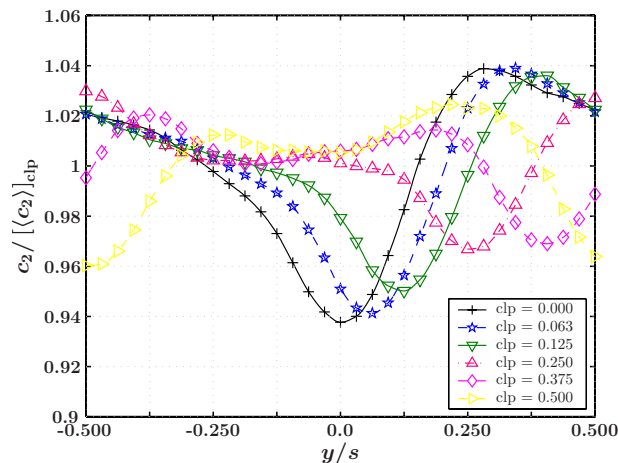


Fig. 7 Normalized absolute velocity upstream of S2; S1 wake impinges on the S2 SS

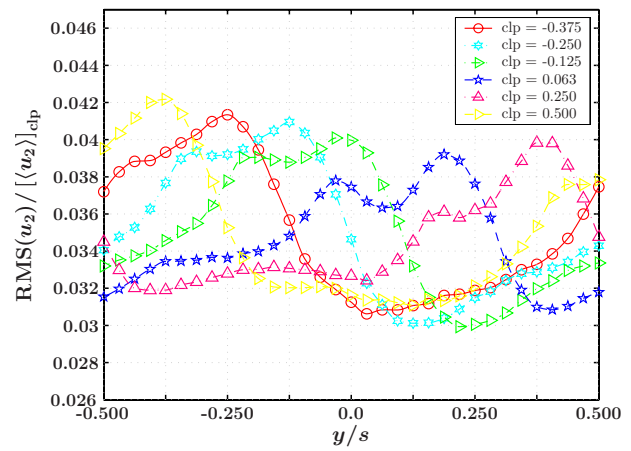


Fig. 8 Normalized stochastic fluctuations in  $x$ -direction upstream of S2

for  $clp=0.0$  in such a way that the minimum velocity was achieved for  $y/s=0.0$  (probe on streamline of the Stator 1 wake), a distinct velocity deficit can be seen at this position. For all other  $clp$ 's, the location of the maximum velocity deficit changes accordingly to the streamline of the Stator 1 wake. The different intensity of the velocity deficit is caused by the superposition of the Stator 1 wake and the Stator 2 potential field. The influence of the latter can be seen in the region  $c_2/[c_2]_{clp} \approx 1-1.02$  and  $y/s \approx -0.25-0.125$  as a dent in the velocity distribution. For  $clp = \pm 0.5$ , the strength of the Stator 2 potential field without the influence of the Stator 1 wakes can be seen in the region mentioned above, since in this case the Stator 1 wakes convect midway between two Stator 2 vanes, which in turn leads to the smallest velocity values for  $y/s = \pm 0.5$ .

The time mean of the ensemble-averaged RMS-value nondimensionalized with the average of the pitch-averaged  $u$ -values of all  $clp$ 's is shown in Figs. 8 and 9 for the two velocity components  $u$  and  $v$ . The axial velocity fluctuations (Fig. 8) show a double peak with a small dent in between at the position of the Stator 1 wake. This double peak nature is typical for wake flows due to the merging boundary layers of the pressure and suction side. The circumferential velocity fluctuations (Fig. 9) exhibit their maximum at the position of maximum velocity deficit, which coincides with the position of the dent in Fig. 8. The maximum is caused by increased mixing in the lateral direction due to the merging pressure and suction side boundary layers. The variable that combines

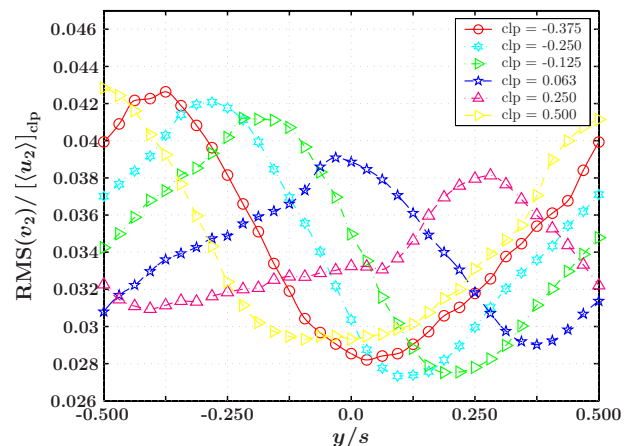


Fig. 9 Normalized stochastic fluctuations in  $y$ -direction upstream of S2

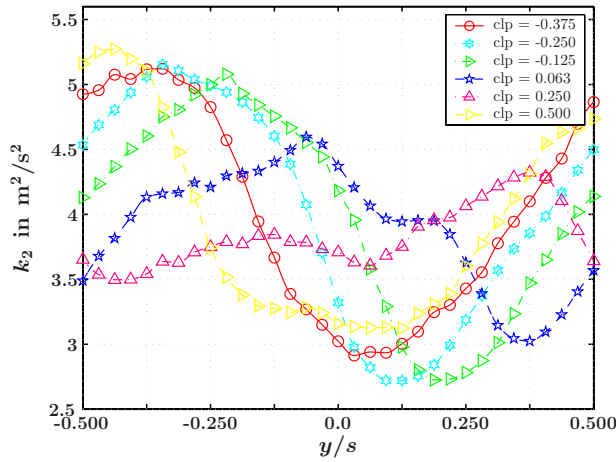


Fig. 10 Turbulent kinetic energy upstream of S2

the velocity fluctuations in both directions is the turbulent kinetic energy  $k$ . It is plotted in Fig. 10 and the curves clearly indicate the superposition of the fluctuations of both velocity components, which results in an almost vanishing of the double peak structure. The overall enhanced fluctuation level in the three figures is caused by the rotor wakes, which produce high unsteadiness and tend to smooth the wake characteristics of Stator 1. Of special interest is the region close to  $y/s=0$ , since this is the portion of the flow that will have the strongest interaction with the Stator 2 boundary layer.  $clp=-0.125$  shows the highest  $u$ -velocity fluctuations in this region whereas the curves of the turbulent kinetic energy lie very close together for the  $clp$ 's ranging from  $clp=-0.125$  to  $clp=0.125$ . This is due to the influence of the  $v$ -velocity fluctuations that exhibit different magnitude in this region for different  $clp$ 's. In Part II [33] of this paper, it will be shown that the stochastic fluctuations within the boundary layer on the Stator 2 leading edge are highest for  $clp=-0.125$ . Obviously, the boundary layer is more susceptible to the velocity fluctuations in the axial direction than to the turbulent kinetic energy of the flow. It will be shown that the amplified  $u$ -fluctuations for  $clp=-0.125$  lead to the shortest separation bubble. It is worth mentioning that not the integral value of the fluctuations but their local value in the region that features the strongest interaction with the Stator 2 boundary layer is the dominant parameter for the length of the separation bubble. The integral value of the turbulent kinetic energy is shown in Fig. 11. The characteristics of the curve

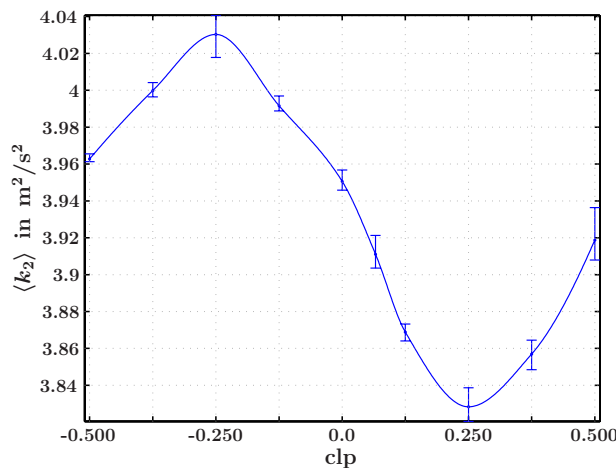


Fig. 11 Pitch-averaged integral turbulent kinetic energy upstream of S2

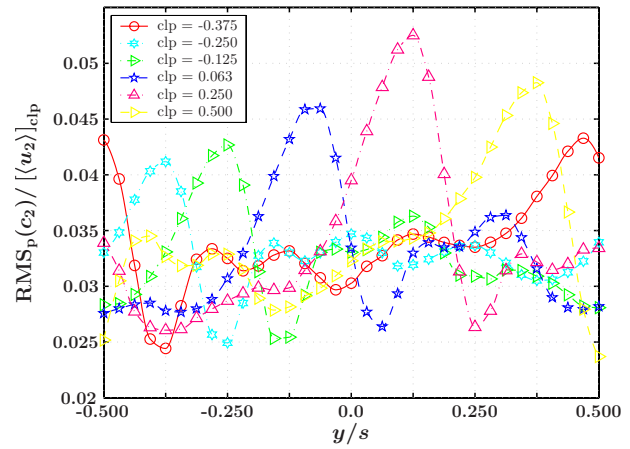


Fig. 12 Normalized periodic fluctuations of the absolute flow velocity upstream of S2

are the same for the integral values of the fluctuations of the two velocity components as well as for the shear stress and indicate highest values for  $clp=-0.25$  and lowest values for  $clp=0.25$ . This behavior is caused by the distortion of the Stator 1 wake within the rotor passage, which, depending on the  $clp$ , reduces or enhances the overall unsteadiness of the flow. The interaction of two different Stator 1 wakes for  $clp=\pm 0.5$  leads to slightly different integral values, which cause the small asymmetry of the curve.

The strength of the periodic fluctuations upstream of Stator 2 is also a function of the  $clp$ . Without any interaction between the Stator 1 and the rotor wakes, the measured velocity signal would, except for a phase shift, remain constant for different lateral probe positions. Besides, the Stator 2 potential field alone does not affect the strength of the periodic fluctuations since there is no periodic motion between the probe and Stator 2. However, it influences the way in which the Stator 1 and rotor wakes interact. In Part II [33] of this paper, it will be shown that the form of the velocity signal changes with varying  $clp$  and probe position. When the probe is affected by the Stator 1 wake, a double peak in the velocity signal appears, which leads to different  $RMS_p$ -values. Figure 12 shows the nondimensionalized periodic  $RMS_p$ -value. For all  $clp$ 's the strength of the periodic fluctuations exhibits its minimum value where the probe is aligned with the streamline of the core of the Stator 1 wake. This behavior is caused by the interaction of the rotor with the low momentum Stator 1 wakes, which leads to a dent in the ensemble-averaged velocity signal that in turn reduces the intensity of the periodic nature of the flow. In the mixing layer between the Stator 1 wake and the main flow, the chopped Stator 1 flow segments enhance the amplitudes of the periodic unsteady flow. For all  $clp$ 's this leads to a pronounced maximum shifted about  $0.125y/s$  in negative  $y$ -direction with respect to the  $RMS_p$  minimum. A less pronounced double peak maximum can be seen shifted about  $0.15y/s$  in positive  $y$ -direction with respect to the  $RMS_p$  minimum. This double peak is caused by the interaction of the Stator 1 wakes within the rotor passage.

**Influence of Clocking on the Static Pressure Distribution of S2.** In Fig. 22, the static pressure coefficient defined by

$$C_p = \frac{[p_{t_{2,FS}}]_{clp} - p_S}{[p_{t_{2,FS}}]_{clp} - [\langle p_3 \rangle]_{clp}} \quad (5)$$

is shown for three different  $clp$ 's on the Stator 2 vane.  $p_S$  is the static pressure along the vane surface  $S$  at midspan,  $[p_{t_{2,FS}}]_{clp}$  is the total pressure upstream of Stator 2 in the freestream region, and  $[\langle p_3 \rangle]_{clp}$  is the static pressure downstream of Stator 2. To assess measurement inaccuracies, three measurements have been

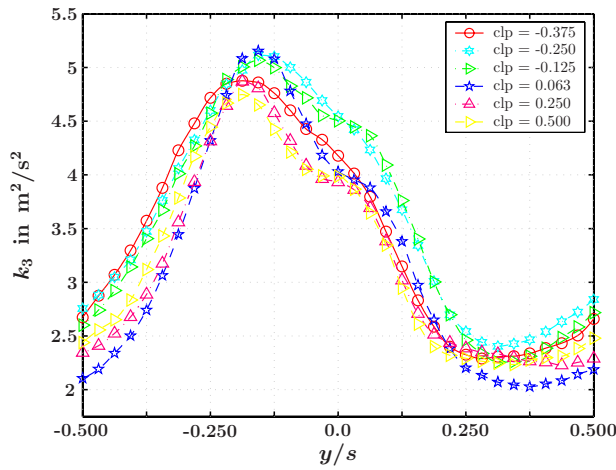


Fig. 13 Turbulent kinetic energy downstream of S2

taken and the error bars are plotted in the two magnified areas in Fig. 22. It can be clearly seen that the measurement accuracy is sufficient to resolve the small changes due to clocking.

The three distributions are very similar but two regions show a dependency on the clp. Close to the leading edge, the lowest pressure is measured for clp=0.0, mainly due to the velocity deficit of the Stator 1 wake. The closer the impingement point of the Stator 1 wake to the leading edge, the smaller are the pressure values. An additional but less pronounced dependency is caused by the small change in incidence angle of about 0.23 deg (compare Fig. 5). The aim of the design process was a distinct separation bubble on the suction side of Stator 2 and in spite of the limited spatial resolution of the pressure tappings (2 mm spacing) the typical distribution of static pressure in separation bubbles is resolved in Fig. 22. The plateau-like region at about 0.5 fraction of surface length indicates the separated region and the strong pressure rise after the plateau the turbulent part of the shear layer above the separation bubble. Good agreement can be found in comparison with the surface mounted hot-film results presented in Part II [33] of this paper: The quasiwall shear stress and its RMS-value indicate the locations of the time-averaged separation, transition, and reattachment points to be at about 0.468, 0.532, and 0.6 fraction of surface length, respectively. The pneumatic measurements as well as the surface mounted hot-film results show that the separation bubble tends to be smaller when the Stator 1 wakes impinge in the region close to the leading edge of Stator 2 and has its smallest value for clp=-0.125. This is caused by the amplified  $u$ -fluctuations for this clp (as mentioned in the previous section) that introduce additional energy into the boundary layer whereby the separated shear layer on the suction side reattaches somewhat downstream, resulting in a reduction in bubble size.

**Influence of Clocking on Turbulent and Periodic Fluctuations Downstream of S2.** As was shown for the Stator 2 inlet parameters, the fluctuations within the flow (stochastic as well as periodic) show a strong dependency on the clp. So, a different interaction with the Stator 2 boundary layer is expected to take place for different clp's, which in turn influence the fluctuations downstream of S2. In Fig. 13, the time-averaged turbulent kinetic energy downstream of S2 is plotted versus one vane pitch. The tendency toward the typical double peak structure observed in wake flows of airfoils is still visible but not well resolved. This is caused by mixing processes that smooth the gradients within the flow field. In the measuring plane closer to the trailing edge of S2 (30 mm downstream of S2, not shown in this paper), a distinct double peak is visible. Despite higher stochastic fluctuations being generated within the suction side boundary layer (compare Ref. [31]), the maximum of turbulent kinetic energy occurs shifted

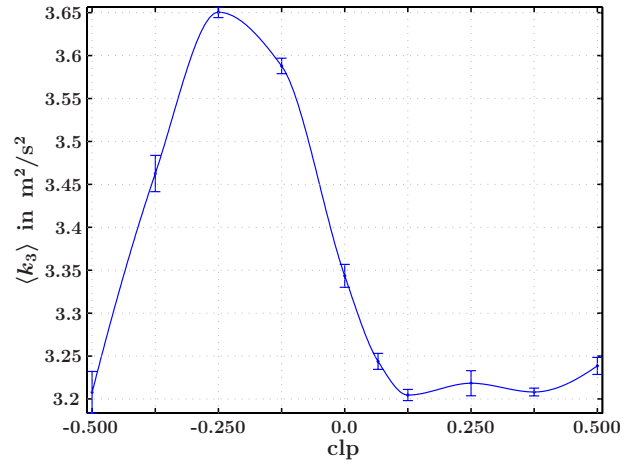


Fig. 14 Pitch-averaged integral turbulent kinetic energy downstream of S2

toward the pressure side (negative  $y/s$ ) for all clp's. This is caused by the higher local values of  $k_2$  for small negative  $y/s$  than for small positive  $y/s$  in Fig. 10 for all clp's. The integral values of turbulent kinetic energy downstream of S2 in Fig. 14 show a similar tendency as the values upstream of S2. The maximum is located at the same position and the minimum in Fig. 11 is situated in the middle of the plateau-like minimum region in Fig. 14. Obviously, the turbulence production upstream of S2 is more dominant than the production of  $k$  within the boundary layer. The relative change of  $\langle k_3 \rangle$  with respect to its mean value is about 13%.

The strength of the periodic fluctuations defined by Eq. (4) is shown in Figs. 15 and 16. The curves of the local values in Fig. 15 clearly indicate that an amplification of the periodic motion takes place within the pressure and suction side boundary layers, which manifest in a double peak characteristic. As shown by König [31], the pressure and suction side boundary layers show a contrarian behavior concerning this amplification process. However, the contribution of the suction side boundary layer is dominant and the integral value of  $\text{RMS}_p$  within the suction side boundary layer shows the same maximum and minimum position as the integral value downstream of S2 in Fig. 16. The local values in Fig. 15 are a superposition of the generated periodic motion within the boundary layer and the local strength of the periodic fluctuations upstream of S2 (compare Fig. 12). This leads, depending on the clp, to an alternation of the position of the absolute maximum in

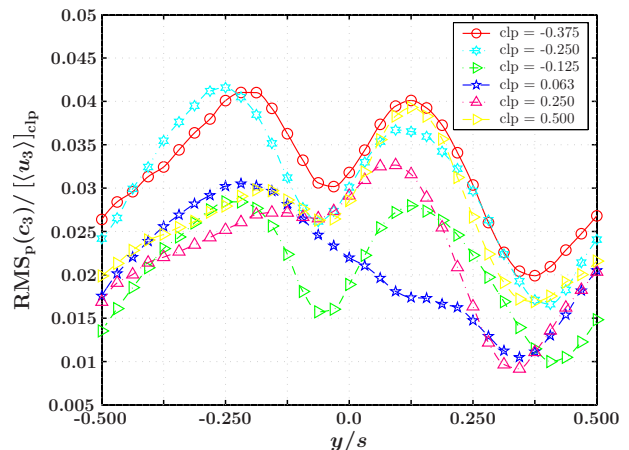


Fig. 15 Normalized periodic fluctuations of the absolute flow velocity downstream of S2



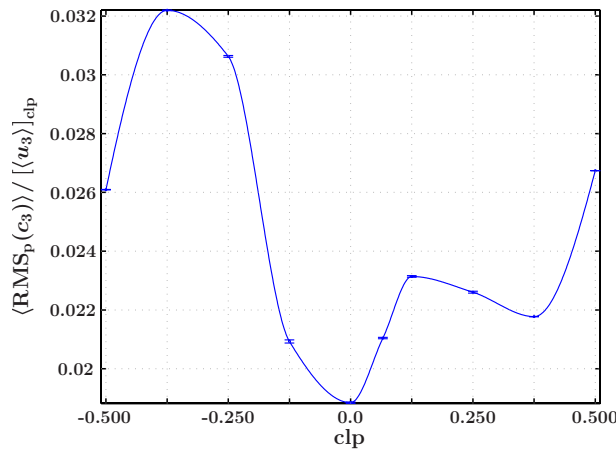


Fig. 16 Pitch-averaged integral normalized periodic fluctuations of the absolute flow velocity downstream of S2

$RMS_p$  from the suction side to the pressure side. The resulting integral values in Fig. 16 show a very strong dependency on the  $clp$ , with a maximum value for  $clp = -0.375$  and a minimum value for  $clp = 0.0$ .

**Influence of Clocking on the Total Pressure Loss of S2.** Usually, the main objective in finding the optimum  $clp$  is the reduction of losses in order to increase the efficiency of the turbomachine. Because of the low Mach number and small pressure ratio occurring in the test facility, a credible thermodynamic measurement of changes in turbine efficiency due to clocking is not possible. However, the changes in total pressure loss can be measured with great accuracy and an estimation of the resulting efficiency change is possible. To measure those changes in the order of only 30 Pa, great care had to be taken to reduce disturbing effects during the measurement. Two five-hole probes shifted by one stator pitch to avoid probe interference were applied to measure the pressures upstream and downstream of S2 simultaneously. This leads to the elimination of pressure variations during the measurement that, despite being very small, would inevitably degrade the results.

In Figs. 17 and 18, the total pressure loss coefficient

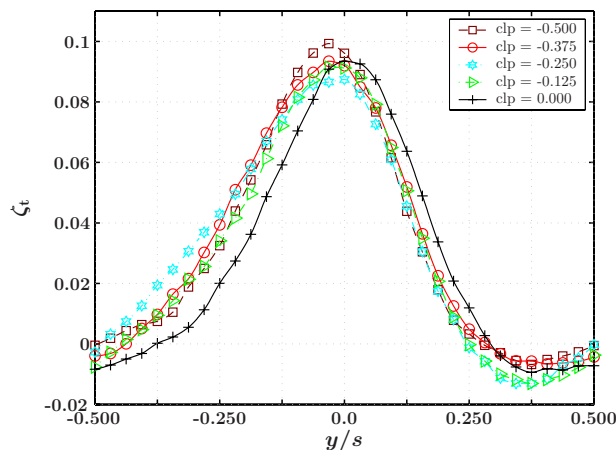


Fig. 17 Total pressure loss coefficient of S2; S1 wake impinges on the S2 PS

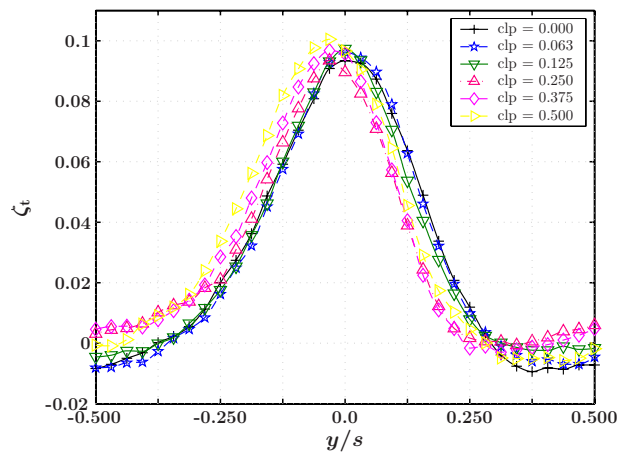


Fig. 18 Total pressure loss coefficient of S2; S1 wake impinges on the S2 SS

$$\zeta_t(y) = \frac{\langle p_{t_2} \rangle - p_{t_3}(y)}{[\langle p_{t_3} \rangle]_{clp} - [\langle p_3 \rangle]_{clp}} \quad (6)$$

is plotted for all ten  $clp$ 's. The squared brackets indicate the mean value over all  $clp$ 's and the angled brackets the pitch-averaged value for each individual  $clp$ . Figure 17 shows those  $clp$ 's where the Stator 1 wake impinges on the pressure side of S2 (negative  $clp$ ). It can be seen that in this case the Stator 1 wake mainly interacts with the Stator 2 pressure side (negative  $y/s$ ), resulting in higher losses in this region compared to  $clp = 0.0$ . Elevated loss values occur for  $clp = -0.25$  and probe positions  $y/s < -0.25$ . On the suction side of S2 (positive  $y/s$ ), the curves for negative  $clp$  lie very close together up to  $y/s \approx 0.25$  since almost no interaction between the Stator 1 wakes and the Stator 2 boundary layer takes place up to this point.

Figure 18 shows those  $clp$ 's where the Stator 1 wake impinges on the suction side of S2 (positive  $clp$ ). In this case, a dependency on the  $clp$  can be seen for positive and negative  $y/s$ . Even though the S1 wakes convect shifted toward the S2 suction surface, their inertia and the strong turning within the S2 passage lead to an interaction with the boundary layer in the rear part of the S2 pressure side for  $clp = 0.25$  to  $clp = 0.5$ . The farther away the S1 wake from the S2 leading edge (increasing  $clp$ ), the stronger this interaction and the higher the losses. For  $clp = 0.0$  to  $clp = 0.125$ , this effect is negligible since the S1 wakes convect very close to the suction side and do not reach the pressure side. For positive  $y/s$ -values up to  $y/s \approx 0.3$  (the intersection point of all six curves), the highest losses occur when the S1 wakes impinge close to the S2 leading edge ( $clp = 0.063$  and  $clp = 0.0$ ).

In both figures, the maximum loss for each individual  $clp$  (observable in the vicinity of  $y/s = 0.0$ ) changes its strength and position depending on the  $clp$ . The strongest maximum occurs when the interaction between the S1 wake and the S2 boundary layer is smallest ( $clp = \pm 0.5$ ) and the least pronounced maximum occurs for  $clp = -0.25$ . This behavior is caused by two different effects: the thickness of the boundary layer at the trailing edge and the resulting mixing losses as well as the profile losses within the S2 boundary layer. The change in position of the maxima is due to a varying deflection angle that leads to a shift of the maximum toward the S2 pressure side for  $|clp| > 0.0$ . This behavior will be discussed in the following subsection. In the region  $y/s \approx \pm 0.5$ , highest loss values are expected when this region is most affected by the S1 wakes ( $clp = \pm 0.5$ ) and smallest loss values when the S1 wakes impinge on the leading edge. Deviations from this behavior are due to the change in deflection angle, which forces the S1 wake further toward negative  $y$ -values and due to the momentum transfer within the S2 passage. The negative  $\zeta_t$ -values close to

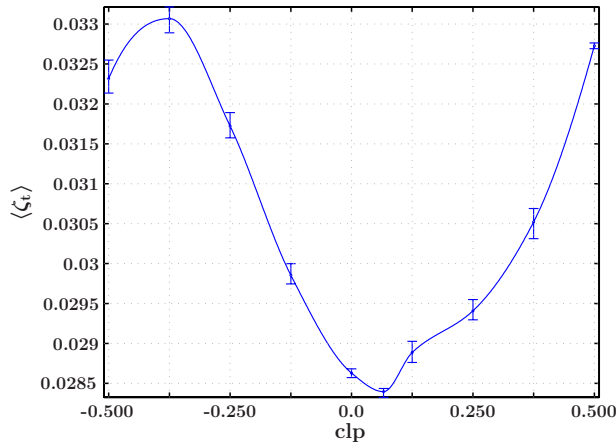


Fig. 19 Pitch-averaged integral total pressure loss coefficient of S2

$y/s = \pm 0.5$  are caused by the fact that the local total pressure downstream of S2 reaches values that are higher than the mean total pressure upstream of S2.

The pitch-averaged value of the total pressure loss for all  $clp$ 's is shown in Fig. 19. Despite the loss variation due to clocking being very small, a great repeatability could be achieved. A distinct maximum can be seen for  $clp = -0.375$  and the minimum occurs for  $clp = 0.063$ . The relative change of  $\langle \zeta_t \rangle$  with respect to its mean value of  $[\langle \zeta_t \rangle]_{clp} = 0.0306$  is about 15%. This change in total pressure loss corresponds to a clocking potential in isentropic total efficiency of about 0.5% points (compare Ref. [31]), which is in good agreement with the expected value from the turbine design at MTU.

For a further analysis of the origin of the losses, substituting  $p_t$  in the numerator of Eq. (6) by the respective dynamic pressures  $p_{dyn}$ , the pitch-averaged value of the change in the kinetic energy of the mean flow is plotted in Fig. 20 versus  $clp$ . The values of  $\zeta_{dyn}$  are negative since, due to the acceleration of the flow, the kinetic energy increases in positive  $x$ -direction. The  $clp$ 's of lowest and highest change in kinetic energy of the mean flow (absolute values) occur for  $clp = -0.25$  and  $clp = 0.25$ , respectively. These positions are in good agreement with the  $clp$ 's of maximum and minimum turbulent kinetic energies downstream of S2 (compare Fig. 14). The energy exchange between the kinetic energy of the mean flow and the kinetic energy of turbulence takes place via the turbulence production tensor defined by

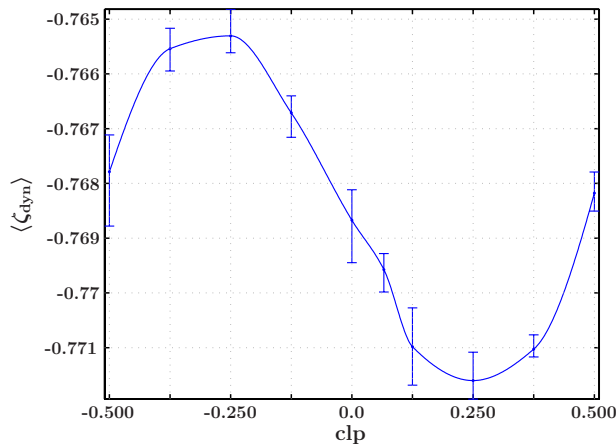


Fig. 20 Pitch-averaged integral dynamic pressure coefficient of S2

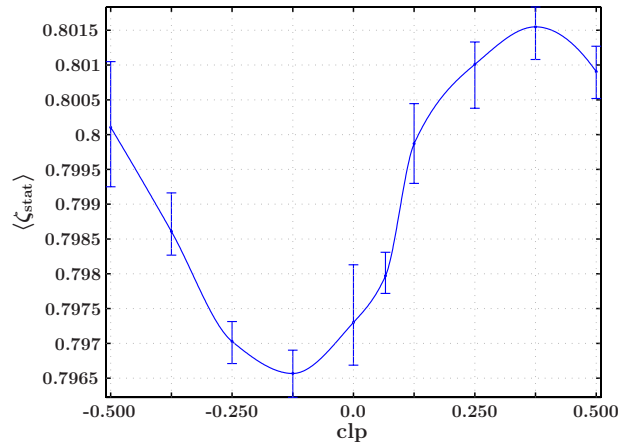


Fig. 21 Pitch-averaged integral static pressure coefficient of S2

$$P_{ij} = - \left( \overline{u'_i u'_k} \frac{\partial \overline{u}_j}{\partial x_k} + \overline{u'_j u'_k} \frac{\partial \overline{u}_i}{\partial x_k} \right) \quad (7)$$

In our case, the energy exchange involves a loss to the mean flow and a profit to the turbulence. This is one important loss mechanism that influences the change in total pressure loss due to clocking. It is anticipated that the turbulence production term balances this exchange of energy between the mean flow and turbulence.

Besides the change in kinetic energy of the mean flow, a second parameter that influences the total pressure loss is the change in static pressure. Substituting the total pressure values in the numerator of Eq. (6) by their static counterparts, the pitch-averaged values are plotted in Fig. 21. Since the accuracy in measuring

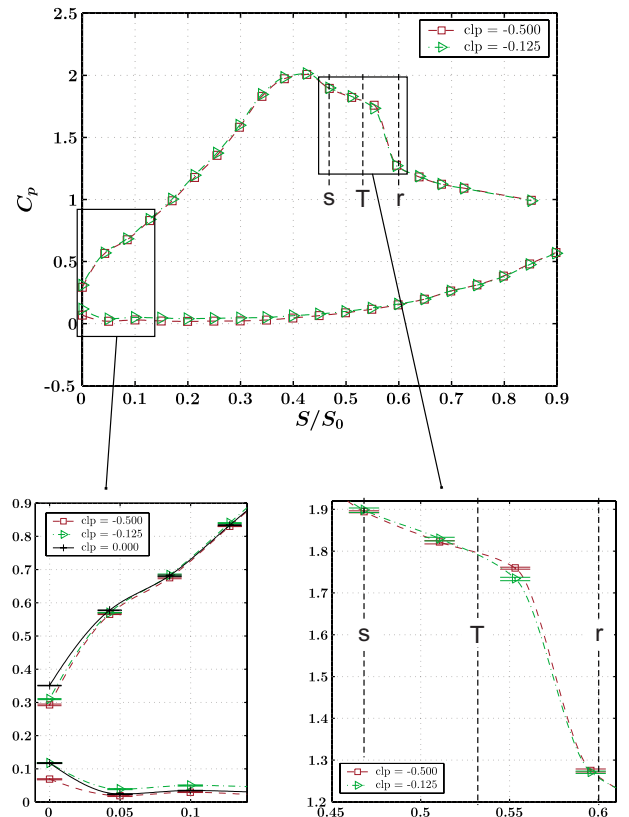


Fig. 22 Time-averaged static pressure distribution for different  $clp$ 's

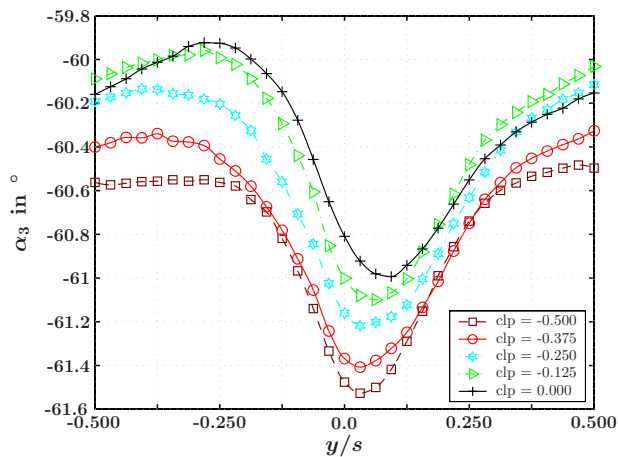


Fig. 23 Flow angle downstream of S2; S1 wake impinges on the S2 PS

static pressures with the five-hole probe is lower than the measurement of total pressures, the error bars are much larger in this case as well as for the measurement of the dynamic pressure (Fig. 20). However, the trend of the curve is still observable: The change in static pressure over the S2 row is smallest for  $clp = -0.125$  and highest for  $clp = 0.375$ . The characteristics of the curve are in good agreement with the size of the separation bubble: The smaller the size of the bubble, the smaller the change in static pressure. This behavior is caused by two different mechanisms: First, a smaller bubble leads to reduced profile losses, and second, a larger throat area due to a reduced bubble size causes a weaker acceleration of the flow within the S2 passage and leads to an energy transfer from the kinetic energy budget of the mean flow.

The change in static pressure due to different  $clp$ 's has a similar value as the change in kinetic energy of the mean flow. Obviously, the losses due to a reduction in bubble size and the losses due to a stronger turbulent production are of the same order of magnitude. A third mechanism that leads to the varying total pressure loss is the strength of the periodic fluctuations downstream of S2. The energy contained in the periodic motion is a loss to the mean flow, which is confirmed by the fact that the pronounced maximum of  $RMS_p$  for  $clp = -0.375$  coincides with the  $clp$  of maximum total pressure loss (compare Figs. 16 and 19). Also, the minima of both curves lie very close together. This suggests the conclusion that the variation of the strength of the periodic fluctuations downstream of S2 is the major loss mechanism. The reason for the variation in the periodic fluctuations will be discussed in Part II [33] of this paper.

**Influence of Clocking on the Deflection Angle Downstream of S2.** In Figs. 23 and 24, the results of the five-hole probe measurements to investigate the influence of the  $clp$  on the deflection angle of the second stator are shown. A layered arrangement of the probe traverses can be seen in Figs. 23 and 24, starting with highest values for  $clp = 0.0$ . For larger  $|clp|$ , the flow angle decreases over most of the airfoil pitch and the position of the maximum deflection angle (most negative value) shifts toward the pressure side of S2 (in negative  $y$ -direction). This behavior is almost symmetrical for positive and negative  $clp$ 's, leading to the maximum integral deflection angle (most negative value) for  $clp = \pm 0.5$  and the minimum integral deflection angle for  $clp = 0.0$  (compare Fig. 25). The higher turning on the suction side and the reduced values on the pressure side of S2 for the local values presented in Figs. 23 and 24 are caused by transport processes behind the profile, which are typical for airfoils. The difference between the maximum and minimum integral deflection angles is about 0.44 deg. The importance of this observation lies in the fact that, for a multistage turbomachine, a changing flow angle downstream of

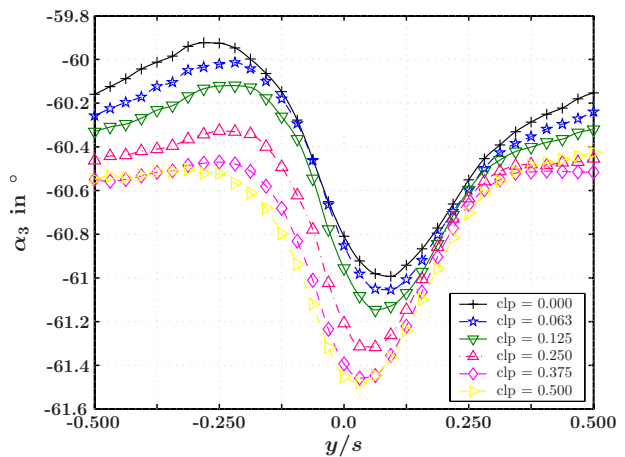


Fig. 24 Flow angle downstream of S2; S1 wake impinges on the S2 SS

S2 leads to different inlet conditions for Rotor 2 that in turn influence the stage efficiency. Furthermore, it gives the designer of the turbomachine the possibility to account for this effect in optimizing the incidence angle of the profile.

**Factors Influencing Turbine Efficiency.** Considering a turbine stage  $i$  (stator  $i$  and rotor  $i$ ) under the influence of a downstream stator row (stator  $i+1$ ) with the same vane count as stator  $i$ , the possible gain in efficiency due to clocking is caused by three main factors. First, a reduction in profile loss of stator  $i+1$  causes, for a fixed inlet total pressure and adiabatic expansion presumed, a higher total pressure at the exit of the machine. Second, favorable changes in flow angle and static pressure in the rotor exit plane lead to a higher total pressure and a lower total temperature downstream of rotor  $i$ . Third, a higher deflection angle of stator  $i+1$  leads to a larger available enthalpy difference for rotor  $i+1$ .

The measured total pressure loss variation includes the effects of a changing profile loss of Stator 2 and the influence of a changing rotor exit total pressure due to a varying rotor exit static pressure. It was already stated that this may cause a variation in total isentropic stage efficiency of up to 0.5% points.

With Euler's turbine equation, the definition of the isentropic total efficiency of a turbine stage reads

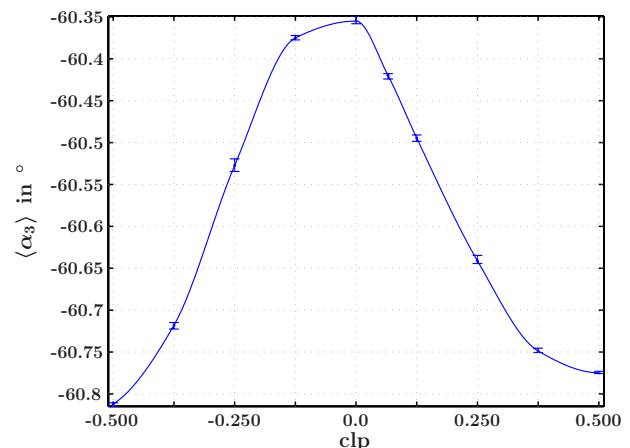


Fig. 25 Pitch-averaged integral flow angle downstream of S2

**Table 2 Uncertainty of selected flow variables**

$C_p$	$\zeta$	$\alpha$	$\overline{c'^2}$	$c$
2.9%	14%	0.75 deg	3%	2%

$$\eta_{T_s} = \frac{\omega(r_{in}c_{u_{in}} - r_{i+1}c_{u_{i+1}})}{\frac{\kappa_i R}{\kappa_i - 1} T_{t_i} \left[ 1 - \left( \frac{p_{t_{i+1}}}{p_{t_i}} \right)^{(\kappa_i - 1)/\kappa_i} \right]} \quad (8)$$

In this equation,  $\omega$  denotes the angular velocity,  $r$  the mean radius of the rotor,  $c_u$  the component of the absolute velocity in circumferential direction,  $\kappa_i$  the representative adiabatic exponent of the stage,  $R$  the gas constant,  $T_{t_i}$  the total temperature at the inlet of the stage, and  $p_{t_i}$  the total pressures. The index  $i$  indicates the inlet of the stage,  $in$  the plane between stator and rotor, and  $i+1$  the exit of the stage. A change in flow angle  $\alpha_{in}$  upstream of the rotor leads, considering  $c_{u_{in}} = c_{in} \sin \alpha_{in}$ , to a change of the stage efficiency as follows:

$$\frac{\partial \eta_{T_s}}{\partial \alpha_{in}} = \frac{\omega r_{in} c_{in}}{\frac{\kappa_i R}{\kappa_i - 1} T_{t_i} \left[ \left( \frac{p_{t_{i+1}}}{p_{t_i}} \right)^{(\kappa_i - 1)/\kappa_i} - 1 \right]} \cos \alpha_{in} \quad (9)$$

In this derivation, it was assumed that small changes in inlet flow angle do not affect the outlet flow angle of the rotor. Similarly, with

$$\frac{\partial \eta_{T_s}}{\partial \alpha_{i+1}} = - \frac{\omega r_{i+1} c_{i+1}}{\frac{\kappa_i R}{\kappa_i - 1} T_{t_i} \left[ \left( \frac{p_{t_{i+1}}}{p_{t_i}} \right)^{(\kappa_i - 1)/\kappa_i} - 1 \right]} \cos \alpha_{i+1} \quad (10)$$

a change in the flow angle downstream of the rotor also affects the turbine efficiency. In Fig. 5, it was shown that the integral flow angle downstream of the rotor shows a dependency of about 0.23 deg on the clp. Since no change of profile loss occurs for the stator of the first stage, a change in efficiency due to clocking is only caused by the variation of this flow angle. The difference in flow angle between clp=0.063 (minimum total pressure loss) and clp=-0.375 (maximum total pressure loss) is about 0.19 deg and a higher deflection is obtained for clp=0.063. Considering Eq. (10), this would lead to an improvement of 0.12% points in efficiency for clp=0.063 compared to clp=-0.375 for the first stage. For the following stages, a superposition of three effects takes place depending on the clp: First, the change in total pressure over the stator vane results in highest efficiency values for clp=0.063 with a clocking potential of 0.5% points. Second, the rotor inlet angle changes, which, considering Eq. (9), leads to a smaller value of turbine efficiency for clp=0.063 compared to clp=-0.375 of about 0.2% points. Third, as for the first stage, the varying rotor exit angle results in an efficiency gain of 0.12% points for clp=0.063 (compare Eq. (10)). Overall, all stages but the first and the last one, experience a clocking potential between the clp of maximum and minimum loss of about 0.42% points. The last stage has a higher clocking potential of about 0.62% points since the negative influence of the reduced stator exit angle for the clp of minimum total pressure loss is not of any relevance.

**Uncertainty Analysis.** To assess the accuracy of the probe measurements, a detailed uncertainty analysis considering inaccuracies due to the measuring equipment, the calibration procedure, and slight fluctuations of the operation point was carried out (compare Ref. [31]). The resulting maximum error bandwidths of the quantities that are being presented in this paper are summarized in Table 2. For derived quantities as the loss coefficient  $\zeta$  and the  $C_p$ -value, the Kline and McClinton [32] method was

applied to determine the corresponding uncertainty. Absolute values as given in Table 2 are of interest mainly for comparison reasons with numerical calculations. For the understanding of the clocking effect, the changes of the flow variables due to different clp's are of much more interest than their absolute values. The inaccuracy of those changes is at least one order of magnitude smaller than that of the absolute values.

## Conclusion

In the present paper, detailed experimental results are presented in order to get a better understanding of the flow physics and interaction mechanisms that take place if two adjacent stator rows with the same vane count are arranged in different circumferential positions (clocking). The experiments were carried out in a 1.5-stage axial turbine with a Reynolds number typical for LP turbines and an inlet Mach number of about 0.13. The main objective of the investigation was to study the interaction of incoming rotor and Stator 1 wakes with Stator 2, a high-lift profile with a separation bubble on the suction side.

In this paper, the behavior of the time-averaged flow quantities for varying clp's is presented in detail. It was found that efficiency variations due to different clp's are caused by changes in rotor exit flow angle, changes in total pressure loss on the Stator 2 vane, and changes in Stator 2 absolute exit flow angle. The alteration of the total pressure loss, which proved to have the strongest influence on efficiency, is determined by three main factors: the length of the separation bubble, the production of turbulence, and the strength of the periodic fluctuations downstream of S2, whereupon the last parameter is the dominant one. Smallest values in total pressure loss occur when the Stator 1 wake impinges slightly shifted towards the suction side of S2 (clp=0.063) and highest values when it convects close to midway between two Stator 1 vanes (clp=-0.375). The change in total isentropic efficiency due to the varying total pressure loss coefficient is in the order of 0.5%. Highest integral deflection angles downstream of S2 occur for the clp close to the total pressure loss maximum and vice versa.

## Acknowledgment

We would like to thank the German Science Foundation (DFG) who has generously granted this project and the German Academic Exchange Service (DAAD) for the financial support during the research stay of the first author at Texas A&M University.

## Nomenclature

- $c$  = flow velocity in absolute frame of reference
- $c'$  = fluctuating velocity component
- $C$  = chord length
- clp = clocking position (fraction of stator pitch at midspan)
- $C_p$  = pressure coefficient
- $f$  = blade passing frequency
- $k$  = turbulent kinetic energy
- Ma = Mach number
- $p$  = static pressure
- $p_{dyn}$  = dynamic pressure
- $p_t$  = total pressure
- $P_{ij}$  = turbulence production tensor
- $r$  = radius
- $R$  = gas constant
- Re = Reynolds number
- RMS = root mean square
- $s$  = stator pitch at midspan
- S1, S2 = Stator 1, Stator 2
- $t$  = time
- $T_t$  = total temperature
- $u$  = velocity component in  $x$ -direction
- $U$  = circumferential velocity



$v$  = velocity component in  $y$ -direction  
 $x$  = coordinate in axial direction  
 $y$  = coordinate in circumferential direction  
 $\alpha$  = flow angle in absolute frame of reference  
 $\eta_{T_s}$  = total isentropic turbine efficiency of stage  $i$   
 $\kappa$  = adiabatic exponent  
 $\nu$  = kinematic viscosity  
 $\bar{\xi}$  = time-averaged value of flow variable  $\xi(t)$   
 $\langle \xi \rangle$  = pitch-averaged value of flow variable  $\xi(y)$   
 $\tilde{\xi}(t)$  = ensemble-averaged value of flow variable  $\xi(t)$   
 $[\xi]_{\text{clp}}$  = arithmetic mean value over all clp  
 $\rho$  = density  
 $\omega$  = angular velocity  
 $\zeta_{\text{dyn}}$  = dynamic pressure coefficient  
 $\zeta_{\text{stat}}$  = static pressure coefficient  
 $\zeta_t$  = total pressure loss coefficient

## Subscripts

0 = measuring plane upstream of S1  
 1 = measuring plane downstream of S1  
 2 = measuring plane 15 mm upstream of S2  
 3 = measuring plane 60 mm downstream of S2  
 ax = axial flow direction  
 $i$  = stage  $i$ , stage inlet  
 in = plane between stator and rotor  
 $i+1$  = stage outlet  
 p = periodic fluctuations  
 u = circumferential direction

## References

- Huber, F. W., Johnson, P. D., Sharma, O. P., Staubach, J. B., and Gaddis, S. W., 1996, "Performance Improvement Through Indexing of Turbine Airfoils: Part I—Experimental Investigation," *ASME J. Turbomach.*, **118**, pp. 630–635.
- Griffin, L. W., Huber, F. M., and Sharma, O. P., 1996, "Performance Improvement Through Indexing Turbine Airfoils: Part 2—Numerical Simulation," *ASME J. Turbomach.*, **118**, pp. 636–642.
- Binder, A., Schröder, T., and Hourmouziadis, J., 1989, "Turbulence Measurements in a Multistage LP-Turbine," *ASME J. Turbomach.*, **111**, pp. 153–161.
- Ladwig, M., 1991, "Experimentelle Untersuchungen zum Einfluß einer inhomogenen Zuströmung auf die Entwicklung des Strömungsfeldes in Turbinenschaukelgittern," Ph.D., thesis, UniBw München, Germany.
- Engber, M., and Fottner, L., 1995, "The Effect of Incoming Wakes on Boundary Layer Transition of a Highly Loaded Turbine Cascade," *AGARD PEP 85th Symposium on Loss Mechanisms and Unsteady Flows in Turbomachines*, Paper No. CP-571.
- Acton, P., 1997, "Untersuchungen des Grenzschichtumschlages an einem hochbelasteten Turbinengitter unter inhomogenen und instationären Zustrombedingungen," Ph.D., thesis, UniBw München, Germany.
- Halstead, D. E., Wisler, D. C., Okiishi, T. H., Walker, G.-J., Hodson, H.-P., Shin, H.-W., 1997, "Boundary Layer Development in Axial Compressors and Turbines—Part I Composite Picture," *ASME J. Turbomach.*, **119**, pp. 114–127.
- Dorney, D. J., et al., 1999, "Full-Annulus Simulations of Airfoil Clocking in a 1.5 Stage Axial Compressor," *Int. J. Turbo Jet Engines*, **16**, pp. 149–160.
- Walker, G. J., Hughes, J. D., and Solomon, W. J., 1998, "Periodic Transition on an Axial Compressor Stator-Incidence and Clocking Effects, Part I and Part II," *ASME Paper No. 98-GT-363 and 98-GT-364*.
- Dorney, D. J., and Sharma, O. P., 1996, "A Study of Turbine Performance Increases Through Airfoil Clocking," *AIAA Paper No. 96-2816*.
- Eulitz, F., and Engel, K., 1998, "Numerical Investigations of Wake Interactions in a Low Pressure Turbine and Its Influence on Loss Mechanisms," *ASME Paper No. 98-GT-563*.
- Dorney, D. J., Sondak, D. L., Stang, U. E. et al., 2001, "Computational Study of Clocking in an Embedded Stage in a 4-Stage Industrial Turbine," *ASME Paper No. 2001-GT-0509*.
- Höhn, W., and Heinig, K., 2000, "Numerical and Experimental Investigation of Unsteady Flow Interaction in a Low-Pressure Multistage Turbine," *ASME J. Turbomach.*, **122**, pp. 628–633.
- Breitbach, C., and Stoffel, B., 2001, "Computation of Wake-Induced Unsteady Flow on a Flat Plate Using Two-Layer Turbulence Models," *Proceedings of the 8th International Symposium on Flow Modelling and Turbulence Measurements*, Tokyo, Japan, Paper No. FMTM2001.
- Stadtmüller, P., Fottner, L., and Fiala, A., 2000, "Experimental and Numerical Investigations of Wake-Induced Transition on a Highly Loaded LP-Turbine at low Reynolds Numbers," *ASME Paper No. 2000-GT-0269*.
- Reinmüller, U., and Niehuis, R., 2002, "Clocking Effects in a 1.5 Stage Axial Turbine-Steady and Unsteady Experimental Investigations Supported by Numerical Simulations," *ASME J. Turbomach.*, **124**, pp. 52–58.
- Li, H. D., and He, L., 2003, "Blade Count and Clocking Effects on Three-Bladerow Interaction in a Transonic Turbine," *ASME J. Turbomach.*, **125**, pp. 632–640.
- Gadea, J., Denos, R., Paniagua, G., Billiard, N., and Sieverding, C. H., 2004, "Effect of Clocking on the Second Stator Pressure Field of a One and Half Stage Transonic Turbine," *ASME Paper No. GT2004-53463*.
- Haldemann, C. W., Krumanaker, M. L., and Dunn, M. G., 2003, "Influence of Clocking and Vane/Blade Spacing on the Unsteady Surface Pressure Loading for a Modern Stage and One-Half Transonic Turbine," *ASME J. Turbomach.*, **125**, pp. 743–753.
- Haldemann, C. W., Dunn, M. G., Barter, J. W., Green, B. R., and Bergholz, R. F., 2005, "Experimental Investigation of Vane Clocking in a One and 1/2 Stage High Pressure Turbine," *ASME J. Turbomach.*, **127**, pp. 512–521.
- Heinke, W., König, S., Matsychock, B., Stoffel, B., Fiala, A., and Heinig, K., 2004, "Experimental Investigations on Steady Wake Effects in a High-Lift Turbine Cascade," *Exp. Fluids*, **37**, pp. 488–496.
- König, S., Heidecke, A., Stoffel, B., Fiala, A., and Engel, K., 2004, "Clocking Effects in a 1.5-Stage Axial Turbine—Boundary Layer Behaviour at Mid-span," *ASME Paper No. GT2004-54055*.
- König, S., and Stoffel, B., 2007, "On the Applicability of a Spoked-Wheel Wake Generator for Clocking Investigations," *ASME J. Fluids Eng.*, **129**, pp. 1469–1477.
- Mailach, R., and Vogeler, K., 2004, "Rotor-Stator Interactions in a Four-Stage Low-Speed Axial Compressor—Part I: Unsteady Profile Pressures and the Effect of Clocking," *ASME J. Turbomach.*, **126**, pp. 507–518.
- Bohn, D., Ren, J., and Sell, M., 2005, "Influence of Stator Clocking on the Unsteady Three-Dimensional Flow in a Two-Stage Turbine," *ASME J. Turbomach.*, **127**, pp. 156–163.
- Billiard, N., Paniagua, G., and Denos, R., 2005, "Effect of Clocking on the Heat Transfer Distribution of a Second Stator Tested in a One and Half Stage HP Turbine," *ASME Paper No. GT2005-68462*.
- Krysinski, J. E., Smolny, A., and Blaszcak, J. R., 2005, "Stator Clocking Effects on 3D Flow in a Two-Stage Low-Pressure Turbine," *ASME Paper No. GT2005-68811*.
- Behr, T., Porreca, T., Mokulys, A., Kalfas, A. I., and Abhari, R. S., 2006, "Multistage Aspects and Unsteady Effects of Stator and Rotor Clocking in an Axial Turbine With Low Aspect Ratio Blading," *ASME J. Turbomach.*, **128**, pp. 11–22.
- Heinke, W., 2002, "Experimentelle Untersuchungen zum Clocking-Effekt an einer stationären Stator-Stator-Anordnung," Ph.D., thesis, TU Darmstadt, Germany.
- Kazimierski, Z., and Horodko, L., 1990, "Total Pressure Averaging by Small-Diameter Tubes in Pulsating Flows," *AIAA J.*, **28**(1), pp. 140–145.
- König, S., 2006, "Untersuchung des Einflusses überlagerter Stator- und Rotor-nachläufe auf den Clocking-Effekt an einer 1.5-stufigen axialen gasturbine," Ph.D., thesis, TU Darmstadt, Germany.
- Kline, S. J., and McClintock, F. A., 1953, "Describing Uncertainties in Single-Sample Experiments," *Mech. Eng. (Am. Soc. Mech. Eng.)*, **75**, pp. 3–8.
- König, S., Stoffel, B., and Schobeiri, M. T., 2009, "Experimental Investigation of the Clocking Effect in a 1.5-Stage Axial Turbine—Part II: Unsteady Results and Boundary Layer Behavior," *ASME J. Turbomach.*, **131**(2), p. 021004.

# Experimental Investigation of the Clocking Effect in a 1.5-Stage Axial Turbine—Part II: Unsteady Results and Boundary Layer Behavior

**Sven König**

e-mail: koenig.sven@siemens.com

**Bernd Stoffel**

Turbomachinery Laboratory (TFA),  
Darmstadt University of Technology,  
64287 Darmstadt, Germany

**M. Taher Schobeiri**

Turbomachinery Performance Laboratory,  
Texas A&M University,  
College Station, TX 77843-3123

*Comprehensive experimental investigations were conducted to get deeper insight into the physics of stator clocking in turbomachines. Different measurement techniques were used to investigate the influence of varying clocking positions on the highly unsteady flow field in a 1.5-stage axial low-pressure (LP) turbine. A Reynolds number typical for LP turbines as well as a two-dimensional blade design were chosen. Stator 2 was developed as a high-lift profile with a separation bubble on the suction side. This paper presents the results that were obtained by means of unsteady x-wire measurements upstream and downstream of Stator 2 and surface mounted hot-film measurements on the Stator 2 suction side. It was found that for the case when the Stator 1 wakes impinge close to the leading edge of Stator 2 the interaction between the Stator 1 and the rotor vortical structures takes place in proximity of the Stator 2 boundary layer, which leads to a shift of the transition point in the upstream direction. The major loss parameter concerning the Stator 2 aerodynamic performance could be attributed to the strength of the periodic fluctuations within the Stator 2 suction side boundary layer. A phase shift in the quasiwall shear stress signal in the front region of the Stator 2 vane was observed for different clocking positions. [DOI: 10.1115/1.2948969]*

## Introduction

Rotor-stator interactions in multistage turbomachinery cause inherently unsteady flow fields. Additionally, as the lift of blade rows increases, unsteady effects play a more and more important role concerning aerodynamic and structural performance. Wakes from upstream blade rows convect downstream many chord lengths and interact with wakes and airfoils of the following stages. To account for those effects from the beginning of the design process, a profound knowledge of its physics is necessary but not yet available. Clocking (indexing) is one way of influencing the flow field in multistage turbomachinery by changing the relative circumferential position of rotors or stators with the same blade count of adjacent rows. A literature survey on the research about the clocking effect in turbomachines is given in Part I of this paper [1]. The current investigation focuses on the influence of unsteady wake effects on the transitional boundary layer (BL) of the second stator in the 1.5-stage turbine.

The significance of the unsteady flow effect on efficiency and performance of compressor and turbine stages was recognized in the early 1970s by several researchers. Fundamental investigations by Pfeil and Herbst [2], Pfeil et al. [3], and Orth [4] studied and quantified the effect of unsteady wake flow on the BL transition along flat plates. Schobeiri and co-workers [5–8] experimentally investigated the effects of the periodic unsteady wake flow and pressure gradient on the BL transition and heat transfer along the concave surface of a constant curvature plate. Liu and Rodi [9] carried out BL and heat transfer measurements on a turbine cascade, which was installed downstream of a squirrel cage type wake generator.

Fottner and co-workers [10,11] and Schulte and Hodson [12] investigated the influence of the unsteady wake flow on the low-pressure (LP) turbine BL. Kaszeta et al. [13] experimentally studied the laminar-turbulent transition process within a channel contoured similar to the suction and pressure surfaces of a LP turbine blade. Lou and Hourmouziadis [14] investigated the mechanism of separation, transition, and reattachment, and the effect of oscillating inlet flow conditions on laminar BL separation along a flat plate under the strong negative pressure gradient similar to the one in a LP turbine. Using a contoured wall to obtain a similar pressure gradient as on the suction side of a LP turbine blade Volino and Hultgren [15] measured the velocity along a flat plate. They showed a strong dependency of the transition length on the Reynolds number and the turbulence intensity.

Using the surface mounted hot-film measurement technique, Fottner and co-workers [10,11], Schröder [16], and Hauelsen et al. [17] documented the strong interaction between the wakes and the suction surface separation bubble on LP turbine blades, both in wind tunnel cascade tests and in a turbine rig. Furthermore, they investigated the BL transition under the influence of periodic wakes along the LP turbine surface and found that the interaction of the wake with the BL greatly affects the loss generation. Halstead et al. [18] used surface mounted hot films to acquire detailed information about the quasiwall shear stress (QWSS) on the blade surface. Investigations by Cardamone et al. [11] and Schröder [16] indicate that the benefit of the wake/BL interaction can be used for the design procedure of modern gas turbine engines to reduce the blade number without altering the stage efficiency. Heinke et al. [19] used surface mounted hot-film probes to investigate the clocking effect in a steady LP turbine cascade. They showed that the size of the separation bubble changed with varying clocking position (clp) and that the shortest separation bubble occurred when the wakes of Stator 1 impinged close to the leading edge of Stator 2. König et al. [20], using the same aerodynamic design, studied the behavior of unsteady rotor and Stator wakes on the

Contributed by the Turbomachinery Division of ASME for publication in the JOURNAL OF TURBOMACHINERY. Manuscript received September 28, 2006; final manuscript received March 5, 2007; published online January 22, 2009. Review conducted by Dilip Prasad.

Stator 2 BL. For different clp's a change of the time dependent behavior of the separation bubble and the transition region could be found. König and Stoffel [26] also investigated the influence of the distortion of the Stator 1 wakes within the rotor passage by means of a spoked-wheel setup.

To account for the clocking effect from the beginning of the design process, a profound knowledge of its physics is necessary. However, the complex interaction mechanisms that result in different stage efficiencies for different clp's are not fully understood. Especially little is known about the way in which the clp affects the unsteady behavior of the BL and in how far the resulting change in profile loss influences the stage efficiency. In Part I of this paper, the changes of the integral values due to the clocking effect are discussed in detail, focusing on parameters such as profile loss, deflection angle, and time-averaged fluctuations. This paper deals with the unsteady mechanisms that lead to the changes of those integral values.

## Experimental Setup and Measurement Techniques

The experimental investigations were performed in the 1.5-stage clocking facility at TU Darmstadt/Germany. Information about the test rig, the experimental setup, and the aerodynamic design are given in Part I of this paper [1]. A view on the airfoil geometry profiles and the definition of the clp is shown in Fig. 2 in Part I of this paper [1]. It is assumed that for clp=0.0, the Stator 1 wakes impinge on the leading edge of Stator 2. The clp's cover one airfoil pitch at midspan and vary from -0.5 to 0.5. The magnitude of the clp, given as the fraction of one stator pitch at midspan, is a measure of the circumferential distance between the streamline of the S1 wake core and the streamline leading to the leading edge of S2. Negative values indicate that the Stator 1 wake impinges on the pressure side of S2 and positive values indicate impingement points on the suction side.

In this paper, two different experimental techniques were used to investigate the influence of clocking on the time-dependent flow field, whereupon the main focus lied on the behavior of Stator 2 subjected to the incoming Stator 1 and rotor wakes. Surface mounted hot-film probes were applied on the Stator 2 suction side to measure the unsteady QWSS. Unsteady flow velocities and flow angles as well as the turbulence quantities were measured by means of an  $x$ -wire probe.

The hot-wire measurements were carried out using a Dantec 55P62  $x$ -wire probe, and an external TC6 temperature probe was used to compensate for temperature variations. The voltage signal was converted using a 12-bit analog-to-digital (A/D) converter. The frequency response of the wires was optimized by a square wave test. A once per revolution TTL trigger signal allowed ensemble averaging of the measured signal. 150 ensembles were found to be sufficient to resolve the Stator 1 and rotor wakes. The sampling frequency was set to 30 kHz and a low pass filter of 10 kHz was applied. Measurement inaccuracies were mainly due to probe contamination and temperature differences between calibration and experiment which, due to changes of the density, cannot be completely eliminated by the compensation probe.

The measurement of wall shear stress using hot-film sensors was originally developed by Bellhouse and Schultz [21] and is now commonly used in turbomachinery applications. The basic idea of this technique is the similarity between the velocity BL and the thermal BL generated by the heated hot-film sensor. To minimize the effects of variations in the gauge and surrounding temperature, the relation between the wall shear stress and the heat transfer by convection to the fluid is expressed by the nondimensional form

$$\tau_{qw} = \left( \frac{E^2 - E_0^2}{E_0^2} \right)^3 \quad (1)$$

where  $\tau_{qw}$  is the QWSS,  $E$  is the output voltage, and  $E_0$  is the voltage under zero flow conditions. Since the gauges were oper-

ated at constant temperature rather than constant overheat the zero voltage  $E_0$  was measured at the same air temperature as the voltage  $E$  during the experiment. To double the spatial resolution of just one hot-film array, two adjacent vanes were equipped on the suction side and two on the pressure side, maintaining the same inflow condition for each clp because of the same stator vane counts. On the two corresponding vanes, the arrays were mounted shifted by half of the array sensor distance, which leads to a spatial resolution of 1.25 mm. To make possible an investigation of the whole BL the sensors cover the whole vane surface on the suction side as well as the pressure side, beginning with the leading edge. For the data representation, the average of the curves of the two corresponding vanes was calculated. To maintain the original vane geometry, the vane surface had to be adjusted and the arrays were glued on lowered by their sensor thickness. The application of the four vanes was carried out by MTU/Munich. A multiplexer was used to scan the output voltages of the 71 sensors sequentially and pass it to the constant temperature anemometer (CTA) bridge. To achieve the same overheat temperature of 60°C for all sensors, deviations in sensor resistances had to be accounted for and each sensor was allocated an individual reference resistance in the anemometer bridge. The frequency response of the hot films was optimized by a square wave test. A once per revolution TTL trigger signal allows ensemble averaging of the measured signal. The sampling frequency was set to 20 kHz. Test measurements were carried out to optimize the number of ensembles required, which led to the number of 100 ensembles. All sensors except the one at 8.0% fraction of surface length were functional.

A discussion of the uncertainty for the probe measurements is given in Part I of this paper.

## Data Processing

To get insight into the unsteady nature of the flow field, a separation of the periodic and stochastic fluctuations was carried out by means of the ensemble-averaging technique using the equation

$$\tilde{\xi}(t) = \frac{1}{N} \sum_{i=1}^N \xi_i(t) \quad (2)$$

The parameter  $\xi_i(t)$  denotes the instantaneous value of ensemble  $i$  and  $N$  corresponds to the total number of measured ensembles. The ensemble-averaged RMS-value reveals information about the stochastic fluctuations of a signal and is defined by

$$\widetilde{\text{RMS}}(\xi(t)) = \sqrt{\frac{1}{N} \sum_{i=1}^N [\xi_i(t) - \tilde{\xi}(t)]^2} \quad (3)$$

Another statistical value, the skewness, represents the degree of asymmetry of a signal around its mean. The ensemble-averaged skewness is given by the equation

$$\widetilde{\text{SKEW}}(\xi(t)) = \frac{(1/N) \sum_{i=1}^N [\xi_i(t) - \tilde{\xi}(t)]^3}{[\widetilde{\text{RMS}}(\xi)]_S^3} \quad (4)$$

where  $[\widetilde{\text{RMS}}(\xi)]_S$  denotes the mean of the RMS-value along the S2 surface coordinate  $S$ .

The influence of unsteady wakes on the Stator 2 BL manifests itself as elevated regions of QWSS in the ensemble-averaged hot-film traces. To follow the trajectories of those perturbations, a nondimensional factor (the "total skewness") is introduced in analogy to the definition of the skewness factor as follows:



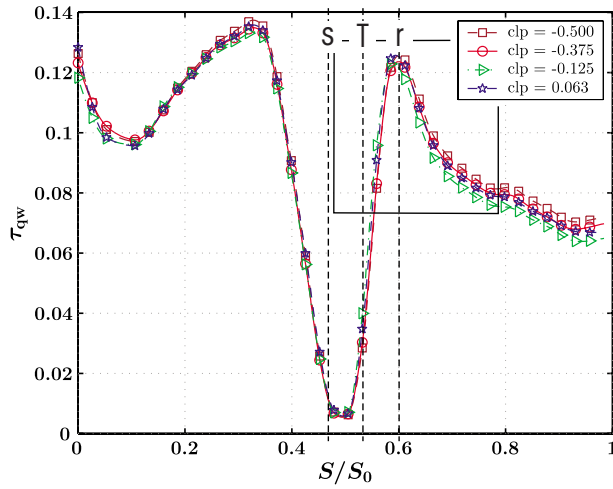


Fig. 1 Time-averaged QWSS along the S2 suction side

$$\widetilde{\text{SKEW}}_t(\xi(t)) = \frac{\left[ \frac{1}{N} \sum_{i=1}^N \left[ \xi_i(t) - \frac{1}{T_m} \int_0^{T_m} \xi_i(t) dt \right]^3 \right]}{\left[ \sqrt{\frac{1}{N} \sum_{i=1}^N \left[ \xi_i(t) - \frac{1}{T_m} \int_0^{T_m} \xi_i(t) dt \right]^2} \right]^3} \quad (5)$$

The subtraction of the time mean (measuring time  $T_m$ ) for each ensemble leads to periodic fluctuations around a value close to 0 and the raise to the power of 3 enhances the signed strength of those fluctuations. The nondimensionalization process compresses the amplitudes of the periodic motion to values around  $\pm 1$  for each sensor. Thereby  $\widetilde{\text{SKEW}}_t(\xi(t))$  leads to an accentuation of the maxima and minima of the original signal and shifts the mean value as well as the strength of the fluctuations for the different sensors in close proximity. That way, it becomes possible to follow the peaks in the original signal—an indication of the wakes generated upstream—in space-time (ST)-diagrams.

### Time-Averaged Boundary Layer Behavior

As shown in Part I of this paper, the Stator 2 vane exhibits a distinct separation bubble on the suction side. The time-averaged size and position of this bubble can also be derived from the time mean of the QWSS and its higher order moments (RMS and skewness). In accordance with the static pressure distribution presented in Part I of this paper, the separation point  $s$  is located near the QWSS minimum ( $S/S_0 \approx 0.468$ ) with values close to zero (compare Fig. 1). The reattachment point  $r$  ( $S/S_0 \approx 0.6$ ) as obtained from the static pressure distribution also shows good agreement with the surface mounted hot-film results: In the latter case, the reattachment point can be seen in Fig. 1 as the location where the drop in QWSS has fully recovered, and in Fig. 3 as the position where the RMS peak passes over into a region of almost constant values. The elevated RMS-values downstream of  $r$  compared to the lower values within the laminar region upstream of  $s$  indicate that the reattached BL is fully turbulent. Due to the increasing BL thickness in the turbulent region the QWSS reduces in streamwise direction for  $S/S_0 > 0.6$  (compare Fig. 1). In the laminar BL, the QWSS is proportional to the BL edge velocity and inverse proportional to the BL thickness. Close to the leading edge ( $S/S_0 < 0.105$ ), the thickening of the BL outbalances the positive velocity gradient, which leads to declining QWSS values. In the region  $0.105 < S/S_0 < 0.33$ , the strong acceleration causes an almost constant BL thickness and rising velocities, resulting in

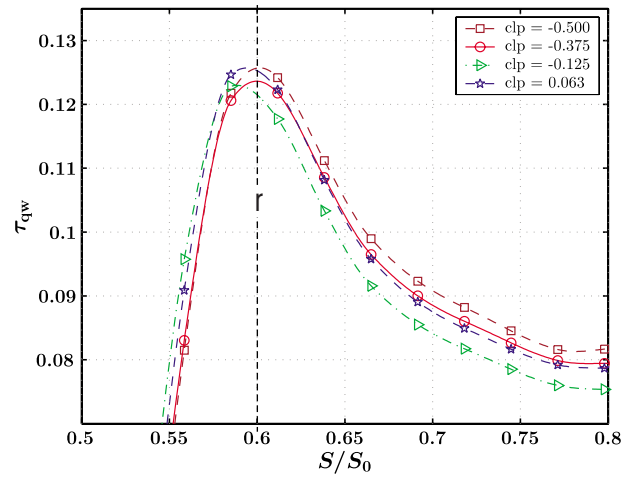


Fig. 2 Time-averaged QWSS along the S2 suction side (reattachment region)

increasing QWSS values. The acceleration decreases in streamwise direction and turns into a deceleration for  $S/S_0 > 0.413$ , which eventually leads to BL separation at  $s$ .

When considering hot-film data high RMS-values are representative for transitional BLs with highest values found where transition is approximately 50% complete (compare Ref. [22]). As can be seen in Fig. 3, this maximum occurs close to midway between the separation and reattachment points around  $S/S_0 \approx 0.532$ . Considering the transition point obtained from the time mean skewness signal in Fig. 4 (zero crossing of the skewness in the transitional region), it is shifted slightly downstream compared to the RMS maximum. Usually the two points are close to each other but this shift is typical in flows with a pronounced separation bubble. Upstream of the separation point  $s$ , skewness values close to zero indicate that, despite the periodical impingement of rotor wakes with elevated turbulence intensity, the BL remains laminar up to this point. In fully turbulent flow, as in laminar flow, the symmetry of the probability density function leads to skewness values close to zero. The point of fully turbulent flow as obtained from the skewness curve in Fig. 4 shows good agreement with the reattachment point derived from the QWSS and its RMS-value. The characteristic of hot-film gauge signals that the positive skew, early in transition, is more obvious than the later negative skew is typical for transitional flows (compare Ref. [22]).

Of special interest for the current investigation is the dependency of the BL behavior on the clp. Considering the QWSS in Fig. 1, only small changes due to the clp occur. Those changes are most obvious in the reattachment region and downstream of the separation bubble, as can be seen in the magnified section in Fig. 2: The steepest gradient in QWSS—an indication for the shortest separation bubble—occurs for  $\text{clp} = -0.125$  and the longest bubble for  $\text{clp} = \pm 0.5$ , respectively. This tendency confirms the results of the static pressure distribution. Downstream of  $r$ , the magnitude of the QWSS correlates with the length of the separation bubble: The shorter the bubble, and hence the transition length, the sooner the fully turbulent BL evolves in streamwise direction (thickening of the BL), which results in reduced QWSS values. That way a decreasing bubble length leads to smaller wall friction downstream of reattachment. The stochastic unsteadiness in terms of the RMS-value presented in Fig. 3 shows a small dependency on the clp in the front region of the vane, where highest values occur for  $\text{clp} = -0.125$ , and in the transition region, where the earliest increase and the soonest decrease of the RMS-values occur for  $\text{clp} = -0.125$ . Considering all clp's, it can be seen that the transition length correlates with the unsteadiness within the Stator 2 BL in close proximity of the leading edge. Furthermore, the latter corre-



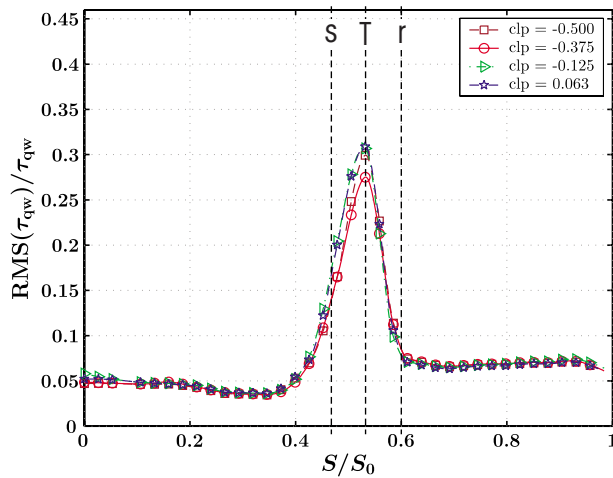


Fig. 3 Time-averaged RMS value (stochastic) along the S2 suction side

lates with the strength of the axial stochastic fluctuations in the leading edge region upstream of S2 (compare Part I of this paper). Obviously, the BL is more susceptible to the velocity fluctuations in the axial direction than to the turbulent kinetic energy of the flow, and those fluctuations are responsible for the length of the separation bubble. The third quantity to characterize the state of the BL, the skewness as plotted in Fig. 4 and discussed in the previous paragraph, shows a stronger dependency on the  $clp$  than the QWSS and its RMS. Even though the change of the transition point obtained from the skewness (zero crossing of the skewness in the transitional region) is more obvious than for the QWSS and its RMS, the end of transition and the relationship between length of transition and  $clp$  correlate with all other measured quantities. However, for the skewness, the limited spatial resolution of the hot-film gauges leads to an overestimation of the movement of the transition point due to the  $clp$ .

In Part I of this paper, it was shown that the intensity of the periodic fluctuations downstream of Stator 2 constitutes the major loss parameter. The  $RMS_p$ -value of the QWSS as defined in Eq. (4) in Part I of this paper is a measure of the strength of those fluctuations within the BL. In Fig. 5, it can be seen that the trend of the  $RMS_p$  curve is similar to the one of the stochastic RMS, values in Fig. 3, with elevated values in the transitional region. However, the dependency of the periodic parts on the  $clp$  is much stronger than for the stochastic parts: Especially in the transitional

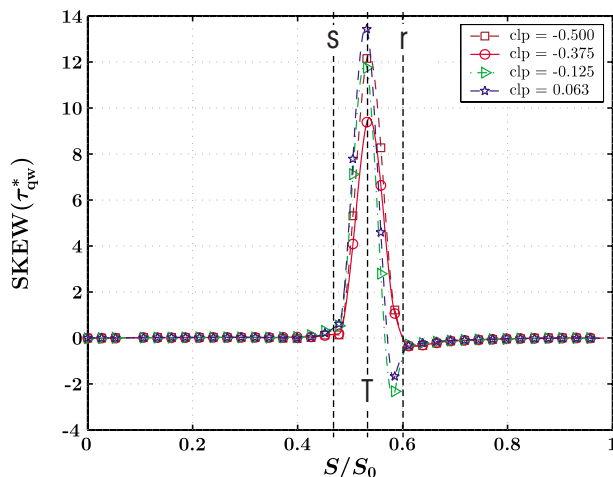


Fig. 4 Time-averaged skewness along the S2 suction side

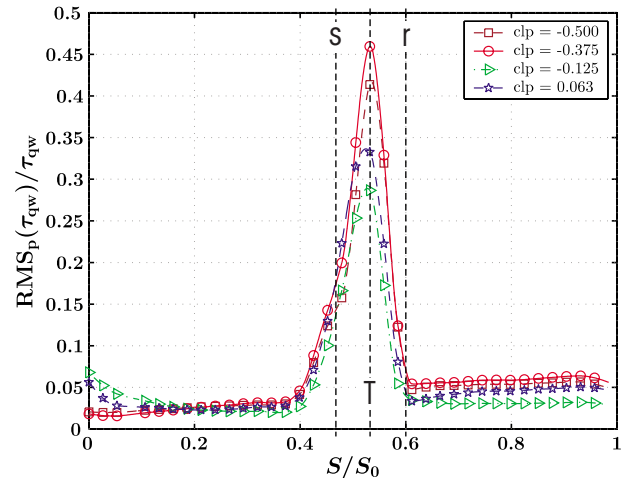


Fig. 5 Time-averaged  $RMS_p$  value (periodic) along the S2 suction side

region and in the turbulent BL, reduced values can be found when the Stator 1 wakes impinge close to the leading edge of Stator 2. In the next section, it will be shown that in this case a strong interaction between the vortical structures of the Stator 1 and the rotor wakes takes place close to the vane surface, which leads to a time-dependent periodical movement of the transition point and a damping of the periodic fluctuations. The integral mean values of the individual curves in Fig. 5 along the surface coordinate  $S$  are presented in Fig. 6. The plot shows the same characteristics as the integral strength of the periodic fluctuations downstream of Stator 2 as presented in Part I of this paper in Fig. 16. Obviously, the damping of the periodic fluctuations within the Stator 2 suction side BL, which is a function of the  $clp$ , is responsible for the strength of the periodic unsteadiness downstream of Stator 2, whereupon the latter is considered the major loss parameter. The sources for this behavior are the interaction mechanisms between the Stator 1 and rotor vortical structures and the Stator 2 BL.

### Unsteady Results

To get deeper insight into the unsteady BL behavior, ST-diagrams of the QWSS, its RMS, and the total skewness are shown in Fig. 7. Sensor positions are indicated by dots at the upper boundary of each figure. As for the time-averaged data, in the ST-diagrams, the results of two neighboring vanes are superimposed to increase the spatial resolution. For different  $clp$ 's the

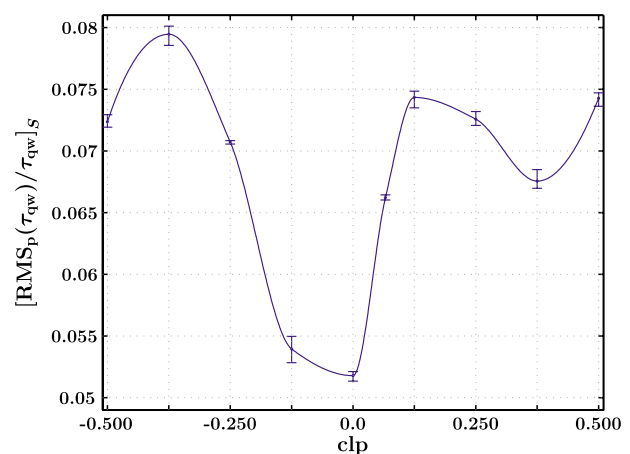


Fig. 6 Integral  $RMS_p$  value (periodic) along the S2 suction side for different  $clp$ 's

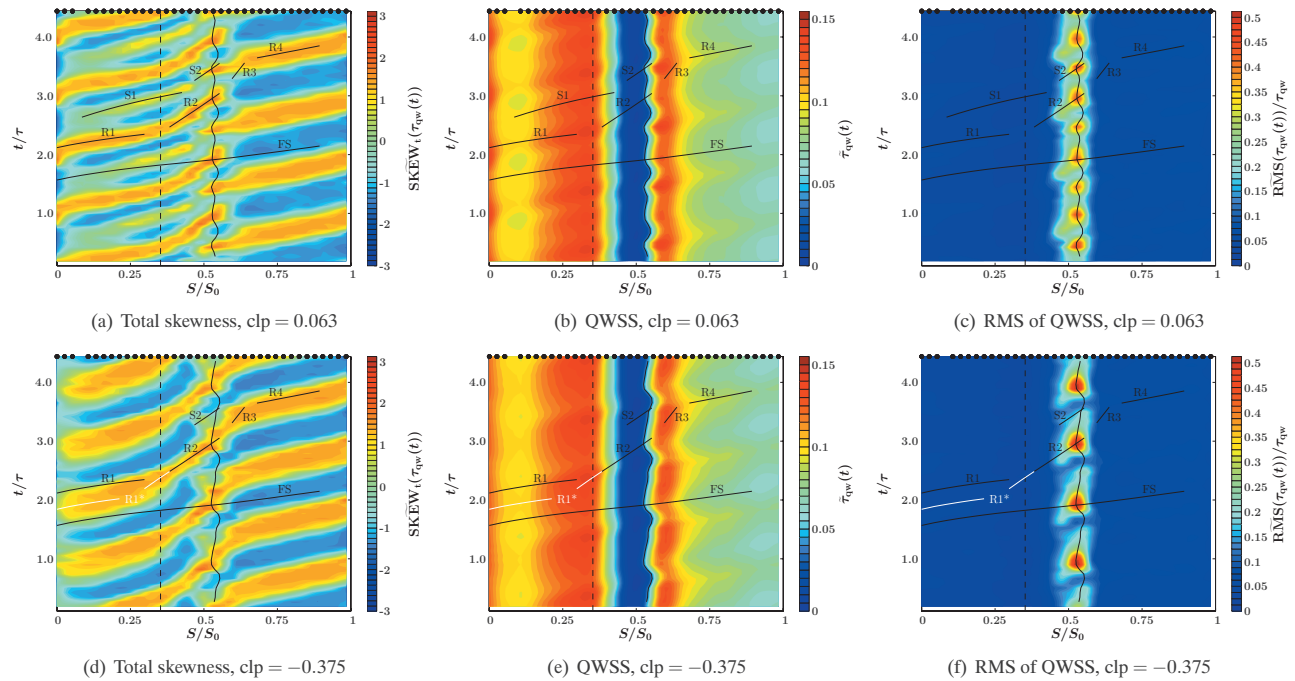


Fig. 7 ST diagrams of ensemble-averaged flow quantities along the Stator 2 suction side

circumferential position of Stator 1 changes but the position of Stator 2 is held constant relative to the rotor. Therefore, the impingement point of the rotor wakes on Stator 2 does not change for varying  $clp$ 's. Characteristic propagation velocities within the Stator 2 BL could be determined analyzing the ensemble-averaged traces of the QWSS, its RMS, and the total skewness. As discussed in "Data Processing," the latter is especially suited to follow the disturbances of the QWSS caused by the periodically incoming Stator 1 and rotor wakes. The characteristic velocities were determined as a function of the local freestream velocity as obtained from the static pressure distribution. Perturbations caused by the Stator 1 wakes are indicated by the letter S and disturbances due to the rotor wakes by the letter R. The trajectory labeled FS shows the flow path of the local freestream velocity. The vertical dashed line indicates the position where the acceleration parameter adopts the value  $3 \times 10^{-6}$ , which implicates that no generation of turbulent spots is possible upstream this point. The solid line in the region  $S/S_0 \approx 0.5$  gives the time-dependent position of the transition point as obtained from the QWSS values. The ST-diagrams are given for the  $clp$ 's of maximum ( $clp = -0.375$ ) and minimum ( $clp = 0.063$ ) total pressure losses.

In Figs. 7(a) and 7(d), the total skewness is shown along the Stator 2 suction surface. Clearly, the influence of the Stator 1 and rotor wakes can be seen as elevated regions of  $SKEW_t(\tau_{qw}(t))$ . Downstream of reattachment, the perturbations of the BL can be attributed to the rotor wakes (R4), and only a negligible phase shift occurs for different  $clp$ 's. In the front region of the vane, the interaction mechanisms between the Stator 1 and rotor wakes lead to a more complex BL behavior: First, for  $clp = 0.063$ , a distinct perturbation due to the Stator 1 wakes can be seen (S1), which does not occur for  $clp = -0.375$ , and second, a phase shift occurs between the propagation velocities of the rotor wakes for different  $clp$ 's (R1 and R1\*). The values of the perturbation velocities are given in Table 1 as a fraction of the BL edge velocity  $c_e$ .

The phase shift in the front region of the vane becomes most obvious considering the ensemble-averaged QWSS on the Stator 2 leading edge in Fig. 8(a). Comparing the position of the QWSS maxima for  $clp = 0.063$  and  $clp = -0.125$ , the phase shift accounts for approximately 35% of the rotor period. For those  $clp$ 's where only a small interaction between the Stator 1 wake segments and

the Stator 2 leading edge takes place (e.g.,  $clp = -0.375$ ), a distinct change in signal pattern with reduced amplitudes can be seen. Downstream of  $S/S_0 \approx 0.05$ , a double peak structure emerges in the QWSS signal when the Stator 1 wakes convect close to the Stator 2 vane. The pronounced phase shift in the front region of the vane reduces in streamwise direction; downstream of  $S/S_0 \approx 0.3$ , the maxima of the QWSS are almost in phase, as can be seen in Figs. 7(a), 7(d), and 8(b).

Considering the ensemble-averaged Stator 2 inlet boundary conditions on the streamline to the Stator 2 leading edge, a consistent behavior can be found compared with the BL response downstream of  $S/S_0 \approx 0.3$ : The dent in the velocity signal between two rotor wake passing events for  $clp = 0.063$  (compare Fig. 8(e)) leads to a similar dent in the QWSS signal in Fig. 8(b). Furthermore, the velocity as well as the QWSS traces are in phase for different  $clp$ 's. The following question arises: Where does the phase shift and the change in signal pattern in the front region of the blade come from? Comparing the results presented in the paper with the results obtained from a spoked wheel setup with the same aerodynamic design (König [23] and König and Stoffel [26]), this behavior can be clearly attributed to the deformation of the Stator 1 wakes within the rotor passage. Besides the interaction of the Stator 1 and the rotor vortical structures, the dependency of the ensemble-averaged inflow angle on the  $clp$  constitutes a major parameter. In Fig. 8(e), it can be seen that the influence of the Stator 1 wakes leads to a time-dependent negative incidence of about 7.2 deg for  $clp = 0.063$ ; the stagnation point is periodically shifted toward the Stator 2 suction side. The superposition of the variation of the Stator 2 inflow angle and the velocity deficit of the rotor wakes, which occur at different times, leads to the strong dependency of the amplitudes in the QWSS signal and the phase shift close to the leading edge. In streamwise direction,

Table 1 Characteristic velocities within the Stator 2 BL

Perturbation velocities as a fraction of $c_e$						
R1	R2	R3	R4	S1	S2	FS
1.0	0.15	0.1	0.7	0.5	0.15	1.0

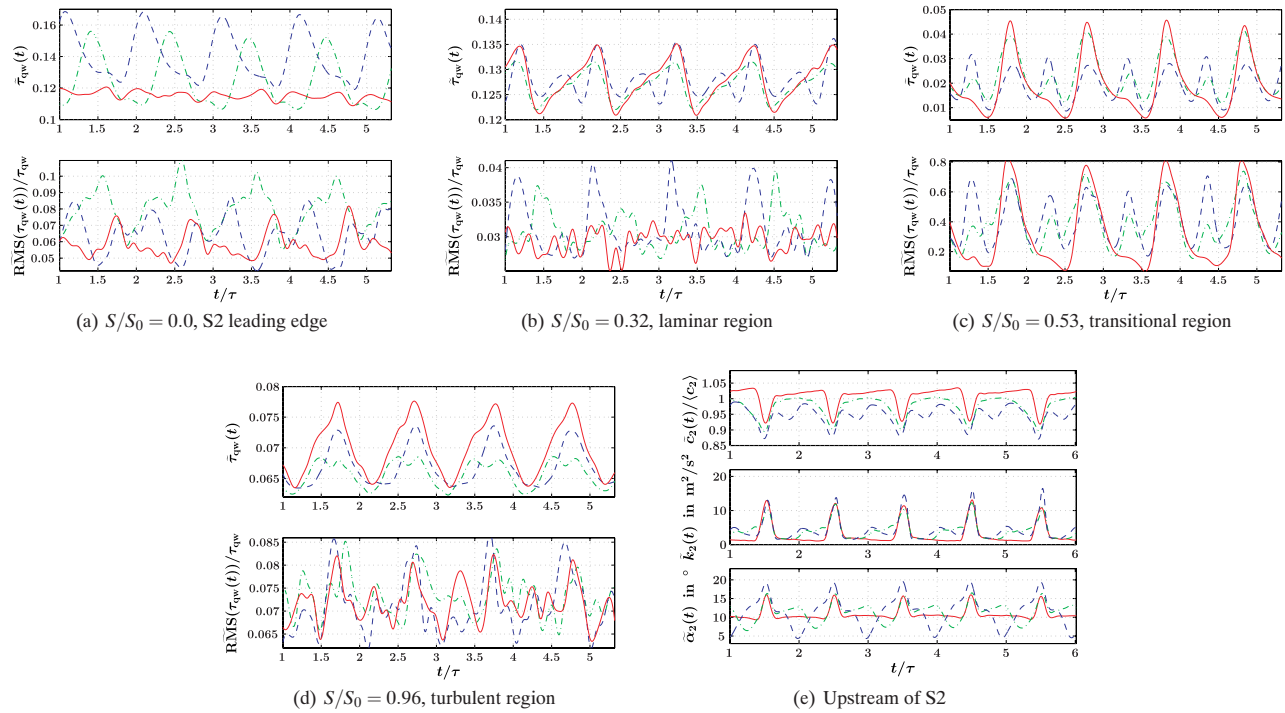


**Fig. 8 Ensemble-averaged time traces along the S2 SS and upstream of S2 (blue/dashed line:  $clp=0.063$ , green/chain dotted line:  $clp=-0.125$ , red/solid line:  $clp=-0.375$ )**

the influence of the incidence angle diminishes and the disturbances introduced at the BL edge play the dominant role for the BL behavior, reducing the phase shift in the direction of the flow.

Considering the characteristic velocities within the Stator 2 BL it is remarkable that only in the front region of the vane (up to  $S/S_0 \approx 0.25$ ) the disturbances due to the rotor wakes convect with the local freestream velocity. In this region the BL disturbances are dominated by the velocity deficit and the enhanced turbulence intensity of the rotor wakes, which convect with the local freestream velocity along the edge of the BL. Approaching the separation bubble, a pronounced deviation from the local freestream velocity occurs, which is caused by the dead water zone within the separation bubble. Such reduced characteristic velocities in proximity of separation bubbles were also observed by Stadtmüller et al. [24], who found a good agreement between the measurements obtained from surface mounted hot-film probes and calculations using the method of characteristics.

The characteristic directions of the QWSS disturbances are most obvious in the ST-diagrams of the total skewness but can also be found in the ST-diagrams of the QWSS. However, considering the RMS-values, the high-frequency disturbances of the BL are much less pronounced in the laminar as well as in the fully turbulent part of the BL (compare Figs. 7(c), 7(f), 8(b), and 8(d)). Elevated RMS-values within the BL are caused by the high turbulence intensity contained in the periodically incoming wakes, which introduce high levels of stochastic unsteadiness at the edge of the BL. However, in close proximity to the wall, viscous effects play the dominant role, leading to a damping of the high-frequency fluctuations. Perturbations of the QWSS are therefore confined to the immediate wall region, whereas the influence of the stochastic fluctuations is more obvious close to the edge of the BL. The investigations of Lou and Hourmouziadis [14] showed that a phase shift occurs between the velocities of the freestream and within the separation bubble. By means of hot-wire traverses, Chakka and Schobeiri [7] found that a phase shift occurs between

the velocity signal and its RMS when analyzing the response of the BL on incoming wakes. Comparing measurements obtained from hot-wire probes and surface mounted hot-film gauges, Griffin and Davies [25] could show that both techniques correlate in close proximity of the wall. Considering those findings, the phase shift between the response of the QWSS and its RMS, which occurs for some  $clp$ 's and some probe positions, is attributed to the damping of the wake turbulence in the viscous sublayer. The characteristic propagation velocities of perturbations of the QWSS are therefore not necessarily linked to the propagation of the high-frequency perturbations. Indeed the latter, as far as detectable in the ST-diagrams, convect with the local freestream velocity.

Neither the ST-diagrams of the QWSS and its RMS nor the corresponding time traces exhibit characteristics of wake induced transition and calming phenomena. In the front region of the vane, the high-frequency perturbations introduced into the BL are damped due to the high flow acceleration, which prevents the generation of turbulent spots; periodically elevated RMS-values on the Stator 2 leading edge almost vanish in streamwise direction (compare Figs. 8(a) and 8(b)). For all  $clp$ 's laminar-turbulent transition occurs abruptly in the shear layer above the separation bubble; in Figs. 7(b) and 7(e), the size of the bubble can be approximated by the blue region. The Stator 1 and rotor wakes, due to their high turbulence intensity, lead to a periodical contraction of the separation bubble and an upstream movement of the transition point, which is indicated by the black solid line in Figs. 7(b) and 7(e). However, for all  $clp$ 's neither the rotor wakes nor the stator wakes are able to completely suppress the separation bubble. When the Stator 1 wakes impinge close to the leading edge of Stator 2 (e.g.,  $clp=0.063$ ), their influence on the transition point can be seen in Fig. 7(b) in Region S2 and in Fig. 8(c). In case that the Stator 1 wakes convect close to midway between two Stator 2 vanes (e.g.,  $clp=-0.375$ ), their influence on the transition point is negligible, which leads to a longer separation bubble in the time mean. The influence of the wake turbulence in the tran-



sitional region can be seen in the ST-diagrams of the RMS-value in Figs. 7(c) and 7(f): The interaction zones of the wake vortical structures with the BL are characterized by elevated RMS regions. As for the QWSS, the influence of the Stator 1 wakes is only detectable when their impingement point is close to the Stator 2 leading edge. In the transitional region, the QWSS and its RMS are in phase, which can be seen in the ST-diagrams and in Fig. 8(c).

Downstream of reattachment, the influence of the wake turbulence on the BL is small since the high-frequency fluctuations in the fully turbulent BL play the dominant role, as can be seen in the RMS traces in Fig. 8(d). However, the time traces of the QWSS show distinct periodic disturbances convecting with 70% of the local freestream velocity. Those disturbances are caused by the rotor wakes and can be seen in the ST-diagrams (R4) and in Fig. 8(d). The reduced disturbance velocities compared to the local freestream velocity are caused by the viscosity in the near wall region: Due to the velocity profile within the BL, the perturbations convect at different speeds, depending on the wall normal distance. Since the sensing volumes of the surface mounted hot-film gauges are prescribed by the thickness of the thermal layer induced by the sensors (which is similar along the vane surface), the sensors sample a larger part of the BL in the (thicker) turbulent region. Investigations at off-design conditions (compare Ref. [23]) confirm this behavior.

## Conclusion

In the present paper, detailed experimental results are presented in order to get a better understanding of the flow physics and interaction mechanisms that take place if two adjacent stator rows with the same vane count are arranged in different circumferential positions (clocking). The experiments were carried out in a 1.5-stage axial turbine with a Reynolds number typical for LP turbines and an inlet Mach number of about 0.13. The main objective of the investigation was to study the interaction of incoming rotor and Stator 1 wakes with Stator 2, a high-lift profile with a separation bubble on the suction side.

In this paper, unsteady results (with focus on the Stator 2 BL) that allow a better understanding of the flow physics leading to the integral changes of the flow variables presented in Part I of this paper are presented. It was found that for all clp's laminar-turbulent transition occurs in the shear layer above the separation bubble whereupon the time-mean length of the bubble changes for different clp's. This behavior could be attributed to the influence of the Stator 1 wakes that lead to a periodical upstream movement of the time-dependent transition point: When the Stator 1 wakes impinge close to the leading edge of Stator 2, the interaction between the Stator 1 and the rotor vortical structures takes place in proximity of the Stator 2 BL and leads to a shift of the transition point in the upstream direction. The movement of the transition point comes along with enhanced stochastic fluctuations in the zone of influence of the Stator 1 and the rotor wakes. It could be shown that the integral strength of the periodic fluctuations within the Stator 2 suction side BL plays the dominant role concerning the Stator 2 aerodynamic performance. Those fluctuations are smallest when the Stator 1 wakes impinge on the leading edge of Stator 2. In the front region of the Stator 2 vane, a phase shift in the QWSS signal that is mainly due to a negative Stator 2 incidence angle in the ensemble-averaged signal, caused by the velocity deficit of the Stator 1 wakes, could be observed.

## Acknowledgment

We would like to thank the German Science Foundation (DFG) who has generously granted this project and the German Academic Exchange Service (DAAD) for the financial support during the research stay of S.K. at Texas A&M University.

## Nomenclature

$[\ ]_S$	= average along the surface coordinate $S$
$c$	= flow velocity in absolute frame of reference
$c_e$	= BL edge velocity
$E$	= measured voltage
$E_0$	= measured voltage at zero flow conditions
$k$	= turbulent kinetic energy
RMS	= root mean square
$s$	= pitch at midspan
$S$	= surface coordinate
$S_0$	= total length of the surface coordinate
S1, S2	= Stator 1, Stator 2
SKEW	= skewness
SKEW <sub>t</sub>	= total skewness
$t$	= time
$\alpha$	= flow angle in absolute frame of reference
$\tilde{\xi}(t)$	= ensemble-averaged value of flow variable $\xi(t)$
$\tau$	= rotor periodic time
$\tau_{qw}^*$	= $(E - E_0)/E_0$ normalized voltage (hot-film gauges)
$\tau_{qw}$	= quasiwall shear stress

## Subscripts

2	= measuring plane 15 mm upstream of S2
p	= periodic fluctuations

## References

- [1] König, S., Stoffel, B., and Schobeiri, M. T., 2009, "Experimental Investigation of the Clocking Effect in a 1.5-Stage Axial Turbine—Part I: Time-Averaged Results," *ASME J. Turbomach.*, **131**(2), p. 021003.
- [2] Pfeil, H., and Herbst, R., 1979, "Transition Procedure of Instationary Boundary Layers," *ASME Paper No. 79-GT-128*.
- [3] Pfeil, H., Herbst, R., and Schröder, T., 1983, "Investigation of the Laminar Turbulent Transition of Boundary Layers Disturbed by Wakes," *ASME J. Eng. Power*, **105**, pp. 130–137.
- [4] Orth, U., 1993, "Unsteady Boundary Layer Transition in Flow Periodically Disturbed by Wakes," *ASME J. Turbomach.*, **115**, pp. 707–713.
- [5] Schobeiri, M. T., and Radke, R. E., 1994, "Effects of Periodic Unsteady Wake Flow and Pressure Gradient on Boundary Layer Transition Along the Concave Surface of a Curved Plate," *ASME Paper No. 94-GT-327*.
- [6] Wright, L., and Schobeiri, M. T., 1999, "The Effect of Periodic Unsteady Flow on Boundary Layer and Heat Transfer on a Curved Surface," *ASME J. Heat Transfer*, **120**, pp. 22–23.
- [7] Chakka, P., and Schobeiri, M. T., 1999, "Modeling Unsteady Boundary Layer Transition on a Curved Plate Under Periodic Unsteady Flow Conditions: Aerodynamic and Heat Transfer Investigations," *ASME J. Turbomach.*, **121**, pp. 88–97.
- [8] Schobeiri, M. T., Read, K., and Lewalle, J., 2003, "Effect of Unsteady Wake Passing Frequency on Boundary Layer Transition, Experimental Investigation and Wavelet Analysis," *ASME J. Fluids Eng.*, **125**, pp. 251–266.
- [9] Liu, X., and Rodi, W., 1991, "Experiments on Transitional Boundary Layers With Wake-Induced Unsteadiness," *J. Fluid Mech.*, **231**, pp. 229–256.
- [10] Brunner, S., Fottner, L., and Schiffer, H.-P., 2000, "Comparison of Two Highly Loaded Turbine Cascades Under the Influence of Wake-Induced Transition," *ASME Paper No. 2000-GT-268*.
- [11] Cardamone, P., Stadtmüller, P., Fottner, L., and Schiffer, H.-P., 2002, "Numerical Investigation of the Wake-Boundary Layer Interaction on a Highly Loaded LP Turbine Cascade Blade," *ASME Paper No. 2002-GT-30367*.
- [12] Schulte, V., and Hodson, H. P., 1996, "Unsteady Wake-Induced Boundary Layer Transition in High Lift LP Turbines," *ASME Paper No. 96-GT-486*.
- [13] Kaszeta, R., Simon, T. W., and Ashpis, D. E., 2001, "Experimental Investigation of Transition to Turbulence as Affected by Passing Wakes," *ASME Paper No. 2001-GT-0195*.
- [14] Lou, W., and Hourmouziadis, J., 2000, "Separation Bubbles Under Steady and Periodic Unsteady Main Flow Conditions," *ASME Paper No. 2000-GT-270*.
- [15] Volino, R. J., and Hultgren, L. S., 2001, "Measurements in Separated and Transitional Boundary Layers Under Low-Pressure Turbine Airfoil Conditions," *ASME J. Turbomach.*, **123**, pp. 189–197.
- [16] Schröder, T., 1989, "Measurements With Hot-Film Probes and Surface Mounted Hot Film Gauges in a Multi-Stage Low Pressure Turbine," *European Propulsion Forum*, Bath, UK.
- [17] Haueisen, V., Hennecke, D. K., and Schröder, T., 1997, "Measurements With Surface Mounted Hot Film Sensors on Boundary Layer Transition in Wake Disturbed Flow," *Paper No. AGARD-CP-598*.
- [18] Halstead, D. E., Wisler, D. C., Okiishi, T. H., Walker, G. H., Hodson, H. P., and Shin, H.-W., 1997, "Boundary Layer Development in Axial Compressors and Turbines—Part 3 of 4," *ASME J. Turbomach.*, **119**, pp. 225–237.
- [19] Heinke, W., König, S., Matyschok, B., Stoffel, B., Fiala, A., and Heinig, K.,



- 2004, "Experimental Investigations on Steady Wake Effects in a High-Lift Turbine Cascade," *Exp. Fluids*, **37**, pp. 488–496.
- [20] König, S., Heidecke, A., Stoffel, B., Fiala, A., Engel, K., 2004, "Clocking Effects in a 1.5-Stage Axial Turbine—Boundary Layer Behaviour at Mid-span," ASME Paper No. GT 2004–54055.
- [21] Bellhouse, B. L., and Schultz, D. L., 1966, "Determination of Mean and Dynamic Skin Friction, Separation and Transition in Low-speed Flow With a Thin-film Heated Element," *J. Fluid Mech.*, **24**, pp. 379–400.
- [22] Howell, R. J., 1999, "Wake-Separation Bubble Interactions in Low Reynolds Number Turbomachinery," Ph.D., thesis, Cambridge University, Cambridge.
- [23] König, S., 2006, "Untersuchung des Einflusses überlagerter Stator- und Rotor-nachläufe auf den Clocking-Effekt an einer 1.5-stufigen axialen Gasturbine," Ph.D., thesis, TU Darmstadt, Germany.
- [24] Stadtmüller, P., Fottner, L., and Fiala, A., 2000, "Experimental and Numerical Investigation of Wake-Induced Transition on a Highly Loaded LP Turbine at Low Reynolds Numbers," ASME Paper No. 2000-GT-0269.
- [25] Griffin, P. C., and Davies, M. R. D., 2002, "On the Use of Hot Film Sensors in the Investigation of Fluid Dynamic Phenomena in the Near Wall Region," 16th Symposium on Measuring Techniques in Transonic and Supersonic Flow in Cascades and Turbomachines, Cambridge, UK.
- [26] König, S., and Stoffel, B., 2007, "On the Applicability of a Spoked-Wheel Wake Generator for Clocking Investigations," *ASME J. Fluids Eng.*, **129**, pp. 1469–1477.

# A Method for Estimating the Influence of Time-Dependent Vane and Blade Pressure Fields on Turbine Rim Seal Ingestion

**Bruce V. Johnson**

**Ralf Jakoby**

Alstom Power,  
CH-5401 Baden, Switzerland

**Dieter E. Bohn**

Institute of Steam and Gas Turbines,  
RWTH Aachen University,  
D-52062 Aachen, Germany

**Didier Cunat**

Turbomeca,  
64511 Bordes Cedex, France

*A method of estimating the turbine rim seal ingestion rates was developed using the time-dependent pressure distributions on the hub of turbines and a simple-orifice model. Previous methods use the time-averaged pressure distribution downstream of the vanes to estimate seal ingestion. The present model uses the pressure distribution near the turbine hub, obtained from 2D time-dependent stage calculations, and a simple-orifice model to estimate the pressure-driven ingress of gas-path fluid into the turbine disk cavity and the egress of cavity fluid to the gas path. The time-dependent pressure distribution provides the influence of both the vane wakes and the bow wave from the blade on the pressure difference between the hub pressure at an azimuthal location and the cavity pressure. Results from the simple-orifice model are used to determine the effective  $C_d$  that matches the cooling effectiveness at radii near the rim seal with the amount of gas-path-ingested flow required to mix with the coolant flow. Cavity ingestion data from rim seal ingestion experiments in a 1.5-stage turbine and numerical simulations for a 1 vane, 2-blade sector of the 16-vane, 32-blade turbine were used to evaluate the method. The experiments and simulations were performed for close-spaced and wide-spaced half stages between both the vane and blade and between the blade and a trailing teardrop-shaped strut. The comparison of the model with a single  $C_d$  for axial gap seals and the experiments showed a reasonable agreement for both close- and wide-spaced stages.*

[DOI: 10.1115/1.2950053]

## Introduction

In the state-of-the-art aircraft and electric power generation gas turbine engines, the high-pressure turbine disks are purged with coolant air through the wheel space. This air reduces the thermal load of the disk and prevents the ingress of hot mainstream gas into the wheel space between the rotating disk and the adjacent stationary casing. As the gas-path temperatures increase, the rim seal cooling flow requirements increase if increased metal temperatures are not allowed. With increased cooling flow to prevent rim seal ingestion, the associated penalties to power output and cycle efficiency from the ideal cycle also increase. As a result, the turbine rim seal region has been identified as one part of the internal cooling air systems (ICAS) where improved technology is likely to result in improved power output and cycle performance.

The effectiveness of the disk cooling and the lifetime of the rotor therefore strongly depend on turbine rim sealing. In the case of the aircraft high-pressure turbine rotor, a modest increase in hot annulus gas concentration in the wheel space is sufficient to decrease the life of the rotor by 50%. On the other hand, reducing the rim sealing flow by half would increase the turbine efficiency by 0.5%, corresponding to a decrease in specific fuel consumption (SFC) of 0.5%.

In gas turbine engines, the internal cooling systems air that is supplied to the turbine to cool the disks is also used to seal the turbine disk cavities and other internal components from the hot primary stream gas path. Discussions of the requirements were presented by Suo [1] and Campbell [2]. The function of maintaining an acceptable thermal environment is becoming more critical

as the trend in gas turbine development has been toward higher turbine pressures, temperatures, and rotation rates in an effort to increase the engine power output and to decrease the engine SFC. As noted, the same cooling air systems may be called upon to perform other functions; therefore the rim seal coolant flow rates have not determined and will not always determine the flow rate in a given circuit. Because the amount of cooling air required to perform these functions significantly influences the efficiency and the power output of the engine, it is imperative that the gas turbine designers have design data and cause/effect models to minimize, or at least optimize, all the internal flow systems' coolant flow rates.

Considerable effort has been devoted (1970–present) to developing thermal design methods for turbine rim seals that incorporate rig data and turbine aerodynamic design data. The methods have become intricate as the physical phenomena associated with the ingestion process have become better understood with an analysis of experimental data and numerical simulation of the turbine stages, including rim seals and the disk-stator cavity.

Much of the work before 1990 was conducted with half turbine stages or with disks without airfoils, investigating one aspect of the rim seal ingestion problem. In the mid 1990s, the European Commission recognized that the internal cooling of gas turbines was critical to the development of more efficient engines and to the European aircraft industry. Consequently, an internal cooling air system–gas turbine (ICAS-GT) research program to improve the design technology for five internal cooling areas of the gas turbine was initiated, as described by Smout et al. [3]. The hot gas ingestion control (Task 1) of ICAS-GT was a combined analytical and experimental project to develop improved technology to control the ingestion of gas path into the cavities of modern gas turbines. Experiments were conducted with a 1.5-stage turbine at RWTH Aachen University (e.g., see Bohn et al. [4]), that had typical first stage vane and blade airfoil profiles. Numerical simu-

Contributed by the International Gas Turbine Institute of ASME for publication in the JOURNAL OF TURBOMACHINERY. Manuscript received March 30, 2007; final manuscript received August 24, 2007; published online January 22, 2009. Review conducted by David Wisler. Paper presented at the ASME Turbo Expo 2006: Land, Sea and Air (GT2005), Barcelona, Spain, May 8–11, 2006.

lations and modeling of the RWTH Aachen University turbine were performed by three industrial partners (e.g., see Jakoby et al. [5]). The present work is part of this modeling effort.

The objective of the present paper is to present an extension to previous modeling methods that incorporates important physical phenomena: the time-dependent pressure variations in the rim seal region between vane and blade stages. Previous experimental, numerical, and modeling work will be reviewed to place the present extension in perspective. Examples of the present model will be presented and comparisons made with experimental data.

## Background

A 1994 survey by Johnson et al. [6] identified the following mechanisms as important for turbine rim seal ingestion:

- disk pumping
- periodic vane/blade pressure field
- 3D geometry in the rim seal region
- asymmetries in the rim seal geometry
- turbulent transport in the platform/outer cavity region
- flow entrainment

Since then,

- 3D, time-dependent flow structure within the disk-stator cavity was shown to be an important factor in the effectiveness of stator and rotor cooling and must be added to the list of important factors influencing turbine rim seal ingestion.

This paper will focus on the description and modeling of the “periodic vane/blade pressure field” and disk pumping ingestion mechanisms. Other physical mechanisms will be discussed as they interact with the vane/blade pressure field mechanism.

Understanding rim seal ingestion has evolved since 1965. The parametric experiments with a rotating disk, stator, and several seal openings from Bayley and Owen [7] provided a correlation for the prevention of ingestion. Extensive flow visualization and pressure distribution disk-cavity-seal experiments by Phadke and Owen [8] were conducted for a number of axisymmetric configurations, with and without axisymmetric external flow fields. These and other experiments are summarized in Owen and Rogers [9]. Correlations were developed for each seal configuration and showed the effects of seal geometry. One measure of no ingestion was that smoke was not ingested into the cavity. The ingestion/no-ingestion limits were characterized as “unsteady.” Unpublished water flow visualization studies with swirling external flow and a disk-cavity-seal rig at United Technologies, circa 1970–1975, showed that the ingress/egress of fluid across the rim cavity seal was unsteady and occurred momentarily over a section of the disk. The term “disk pumping” has been used in the list above to characterize the ingestion mechanisms described in this paragraph and in Refs. [7–9].

Rim seal experiments with CO<sub>2</sub> as a trace gas, a small rim seal cavity, swirling external flow, and several seal configurations by Daniels et al. [10] showed the relationships between coolant flow rate and ingestion flow rate. The extrapolated CO<sub>2</sub> results [10] for 99% cooling effectiveness were in agreement with the Phadke and Owen [8] correlations for their configurations. Although the physical mechanisms for flow ingestion through a rim seal into a disk-stator cavity (without airfoils) are complicated, the mechanism is generally referred to as disk pumping.

Although the details of the mechanisms causing rim seal ingestion were not identified by the aforementioned experiments, several analytical models were developed to explain limits or characteristics of these experiments. A momentum integral analysis by Chew [11] correlated the minimum flow rates required to prevent ingestion. A 1975 turbulent transport “heat or mass diffusion” model by Johnson [12], reprinted in Graber et al. [13], showed a good agreement for the variation of cooling effectiveness with the ratio of coolant flow to ingested flow without cooling flow. How-

ever, the turbulent transport model did not predict the ingested flow rate without an experimental data point to quantify a “lumped” parameter.

The effects of the gas stream pressure downstream of a vane half stage on rim seal ingestion was first published by Abe et al. [14]. Additional experiments by Green and Turner [15] with vanes and a disk to simulate the blade leading edge identified the effects of vane-blade pressure on ingestion.

Several models, based on the pressure distribution downstream of vanes, were developed to estimate ingestion into disk cavities. Chew et al. [16] used correlations for the pressure variation downstream of vanes to develop a model and compared the model to data from Ref. [11]. Numerical studies by Hills et al. [17] show the complex 3D flow details of ingestion. Earlier proprietary models are known to be used by engine manufacturers. More recent models are proposed by Bohn and Wolf [18] and Scanlon et al. [19].

Rim seal experiments with one stage or 1.5 stages have been conducted at RWTH Aachen University, the University of Sussex, and Arizona State University. Results from these experiments further define rim seal ingestion phenomena. References to recent experiments at these three universities are provided in Bohn et al. [4], Gentilhomme et al. [20], and Roy et al. [21]. Results from these experiments have been used to evaluate several models for estimating rim seal ingestion.

Numerical simulation of flow in turbine stages with or without rim seal ingestion varies considerably. A numerical model of the 16-vane, 32-blade, 1.5-stage turbine for one gas path and cooling condition was performed by Volvo Aero under the BriteEuram ICAS-GT program in 1998–2000, reported by Jakoby et al. [5]. Although the results from the complete 3D, 360 deg, time-dependent simulation of the turbine 1.5 stage for flow and cooling were in reasonable agreement with the experiment at RWTH Aachen University [4], the calculation consumed large computing resources and required months to complete. Engine cooling design teams require calculation methods and models that are easier to implement and require less turnaround time.

Numerical 3D simulation of flow in sectors with frozen-rotor-flow calculations, e.g., Bohn et al. [22], shows the ingestion flow patterns. However, the interaction and mixing with the flow in the disk-stator cavity is incomplete. Recent 3D simulations by Foerster et al. [23] were used to develop design correlations.

Numerical 3D time-dependent simulations of a representative sector requires less computing resources and calculation time than calculation of the full 360 deg stage. However, calculations have shown [5] that the calculated cavity stator wall cooling effectiveness can be much greater than the measured due to the uncalculated large-scale mixing between the cavity flow and the ingested flow near the seal. The authors believe that these sector simulations represent the time-dependent gas-path flow accurately and should represent the pressure-driven flow through the seal gap accurately for high Reynolds number flows. The time and effort required to obtain results for this class of simulation are one or 2 orders of magnitude less than those for a full 360 deg. A recent 3D time-dependent sector calculation was used by Okita et al. [24] to investigate innovative rim seal geometries.

The general turbine rim seal modeling statements by Chew et al. [16] and Bayley [25] indicate that the pressure field adjacent to the seal will most strongly influence the ingress and egress of flow through the seal. Reasonably representative time-dependent pressure fields near the seal region can be obtained from 2D time-dependent numerical simulations. In addition, the 2D calculations can be revised with relative ease for various ratios of vanes to blades. Although the consensus from turbine aerodynamics designers/modelers is that the 2- calculations slightly overpredict the unsteady pressure fluctuations, the 2D time-dependent results provide an interactive relationship for the flow field that can be used to determine the spatial and temporal pressure variations across the airfoil gap at various locations between the half stages.

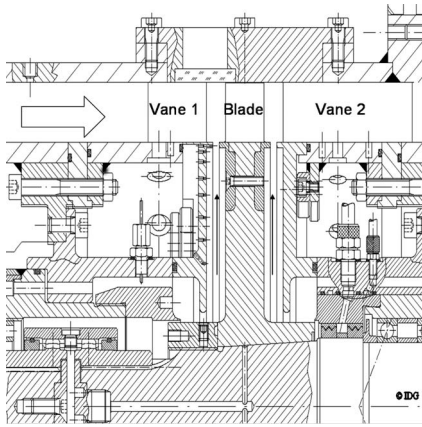


**Fig. 1** Cross section of the RWTH Aachen University test rig with close-spaced arrangement of airfoils

The time-pressure distributions are especially useful in determining the dominant ingestion mechanisms at each intrastage location. Therefore, 2D time-dependent calculations will be used to establish circumferential pressure variations at selected axial locations for the simple-orifice model developed in this paper.

### Experiment and Rig

Data used to evaluate the model described herein were obtained in the turbine rim seal rig at RWTH Aachen University. The rig was described by Bohn et al. [4]. A cross section of the 1.5-stage test rig, employed for the rim seal experiments, is shown in Fig. 1 for reference. Both vane rows consist of 16 airfoils. The rotor has 32 blades. The airfoil shapes for the first vane row and the rotor blade row are derived from the well-known MT1 stage profile, previously used in the public domain. The rig is shown in the close-spaced configuration between the airfoil trailing and leading edges for both half stages with  $G=0.0926$ . For the wide-spaced configuration, the spacing was doubled,  $G=0.1852$ . For both configurations, the seal axial gap ratio,  $G_c$ , was 0.0296 and in the middle of the rotor-stator gap. Figure 2 shows the geometry of the

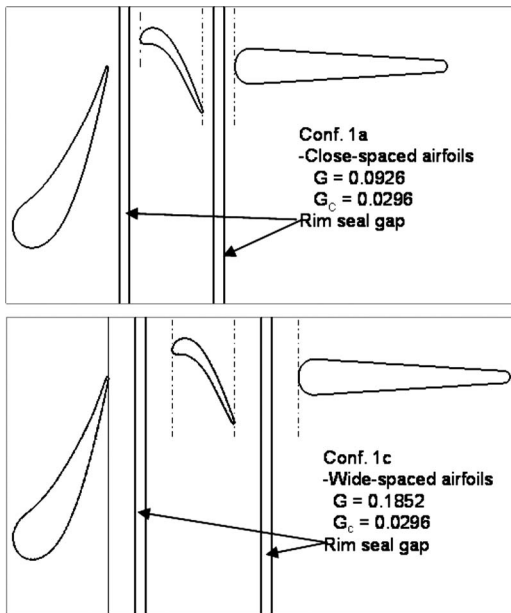


**Fig. 2** Close-spaced (Conf. 1a) and wide-spaced (Conf. 1c) airfoil arrangements for experiments. Axial gap seals are midway between the trailing and leading edges of airfoils.

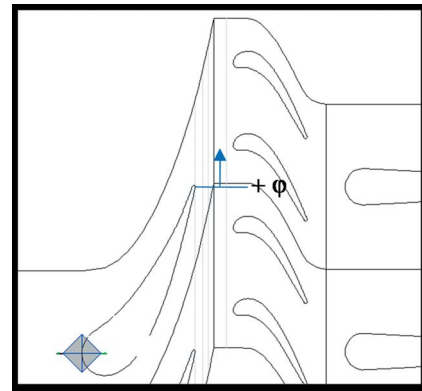


**Fig. 3** Arrangement of airfoils and domains for 2D time-dependent calculations of flow

airfoils and the investigated axial gap rim seals.

The measurement of cooling effectiveness and the pressure distribution at locations on the case and hub walls and on the cavity stator is described by Bohn et al. [22,26,27]. Data from this rig will be compared with the design model, described below.

### Numerical Simulations

2D, time-dependent numerical simulations of the flow field were performed with the FLUENT 5.4 release code at Turbomeca and ABB-Alstom for the experimental rig shown in Fig. 1 and the airfoil and seal arrangements shown in Fig. 2. The calculations were made for the “unrolled” airfoil arrangement shown in Fig. 3. The sliding interface lines were midway between vane 1 and the blade and midway between the blade trailing edge and guide vane 2. The calculations were performed at 10% blade height and were used to estimate the hub pressure distribution. The code was operated with compressible gas, the realizable  $k-\epsilon$  turbulence model and 14120 cells. The time step size was 1/100 of the blade passing time and needed 30–40 passing periods to obtain a converged solution.

**Presentation of Results and Flow Conditions.** Results from the calculations and experiments are presented in dimensionless form to relate the present results with the time-dependent pressure variations from vane-blade interactions to previous rim seal results in quiescent fluid or with swirling flow across the seal. The following parameters are chosen to make the velocity and pressure distributions dimensionless:

- $\Omega R$

(thus, the ingress and egress flow radial velocities through the seal are dimensionless with respect to the hub velocity)

- $q = \rho \Omega^2 R^2 / 2$

With this parameter for pressure, the unsteady and time-averaged pressures are made dimensionless:

$$C_p(\varphi) = (P(\varphi) - P(\varphi)_{av}) / q \quad (1)$$

The first relationship is useful to compare the present results with the correlation in Ref. [7]. Other presentations of the experimental data [4,27] have chosen different velocities to construct their dimensionless parameters.

Calculations were made in the ICAS-GT project for the five operating points of Ref. [27] (Fig. 5) with close vane-blade spacing and for the design condition OP1 for the wide vane-blade spacing. Three of the operating points had similar velocity triangles: the design condition OP1 and two lower rotor speed conditions OP3 and OP4. The other operating points were with the rotor in a modest overspeed, OP5, and a “runaway” overspeed,



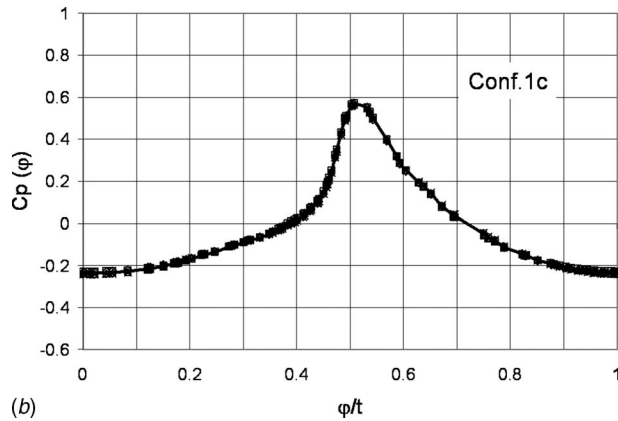
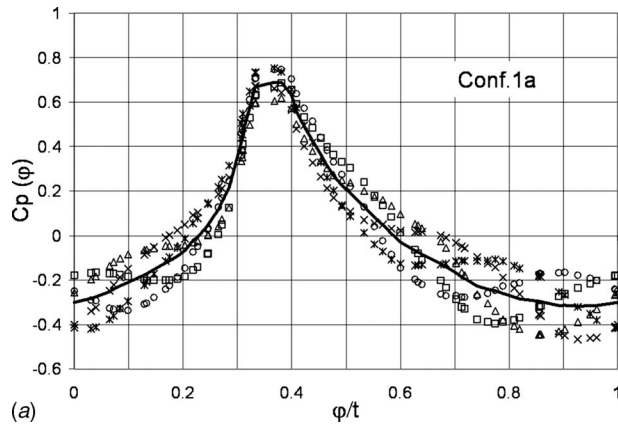


**Fig. 4** Variation of calculated pressure downstream of vane 1 trailing edge with close-spaced (Conf. 1a) and wide-spaced (Conf. 1c) airfoils. Solid line—time averaged; symbols—instantaneous pressures at five equal times in blade passing cycle; variation for Conf. 1c is barely perceptible.

OP2. In this paper, we use calculations for OP1 and OP3 and data from the three operating points with similar velocity triangles.

#### Pressure Variations Downstream of Vane 1 Trailing Edge.

The pressure, velocity, and temperature from the 2D time-dependent calculations were evaluated in detail at selected axial locations. One location was between the vane 1 trailing edge and the upstream edge of the seal. The results for OP1 with both close- and wide-spaced airfoils are shown in Fig. 4. For Conf. 1a, the unsteady variation is approximately 30% of the time-averaged pressure variation across the gap. For Conf. 1c, the unsteady variation is barely perceptible. Note that the peak-to-peak time-averaged variation of  $C_p(\varphi)$  is approximately 0.95 for the close-spaced airfoils and approximately 0.8 for the wide-spaced airfoils at the same distance from the vane trailing edge. Although the 1.5-stage boundary conditions are approximately the same for both numerical simulations, the time-averaged peak-to-peak variation across the vane gap is greater for the close-spaced half stages compared to the wide-spaced half stages. The large differences in the unsteady pressure fields on vanes and blades between close-spaced and wide-spaced half stages are consistent with the unsteady surface pressure measurements on vanes and blades, previously measured by Dring et al. [28]. The axial decay of the rotor pressure asymmetry is quantified and further discussed in Ref. [20].

Results at upstream and downstream edges of seals (Figs. 5 and 6) show the effects of distance from the vane trailing edge and the blade leading edge. For the close-spaced half stages, Conf. 1a (Fig. 5), the time-averaged peak-to-peak variation in  $C_p(\varphi)$  de-

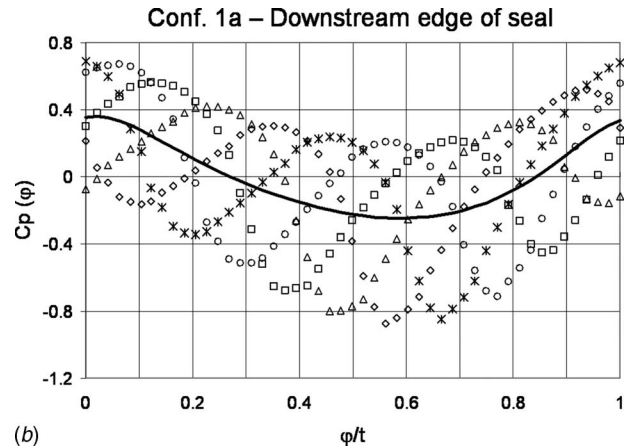
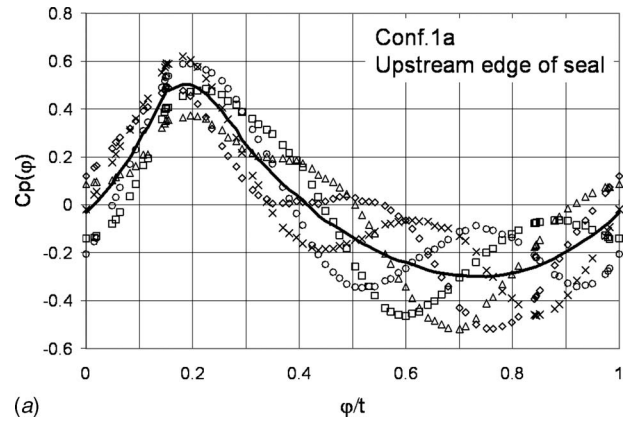


**Fig. 5** Variation of calculated pressure behind Vane 1 with close-spaced airfoils (Conf. 1a) at the upstream and downstream edges of the axial gap seal. The solid line is time averaged; symbols are instantaneous pressures with five blade locations.

creases from the upstream edge of the seal to the downstream edge from 0.8 to 0.6. However, the unsteady variation in  $C_p(\varphi)$  increases from 0.4 to 1.1. Thus the unsteady pressure variation in the rotating coordinate system is likely to be as important to the ingestion process as the vane pressure distribution. Seal locations closer to the blade leading edge are expected to be dominated by the blade pressure field. In our rim seal simple-orifice model, the time-averaged pressure distribution across the vane gap and at the upstream edge of the seal was used for the calculations. An alternative method is to calculate the ingestion characteristics for five or more time locations of the blade and use the average of these results.

For the wide-spaced half stage, Conf. 1c, the peak-to-peak variations of both the time-averaged and the unsteady variation decrease markedly. The time-averaged peak-to-peak variations in  $C_p(\varphi)$  are 0.15 and 0.12 at the seal edges. The unsteady peak-to-peak variation in  $C_p(\varphi)$  are approximately 0.04 (upstream) and 0.10 (downstream). The unsteady variation from the blade is decreased by a factor of 8, compared to the close-spaced stage. The steady variation is decreased by a factor of 2–3. Thus, the effects of stage spacing are quantified, and they are in general agreement with the correlations of Ref. [20].

**Effects of Location on Pressure Distributions Between Blade and Vane 2.** The time-averaged and time-dependent pressure variations between the blade and the second vane are decreased compared to the variations between vane 1 and the blade (Figs. 7 and 8). For both half-stage widths, the flow downstream

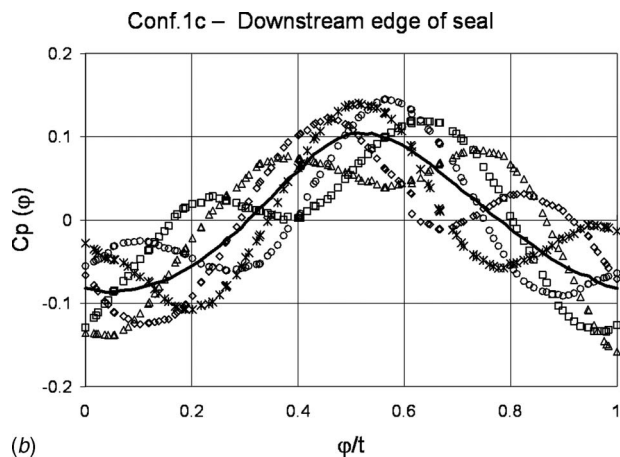
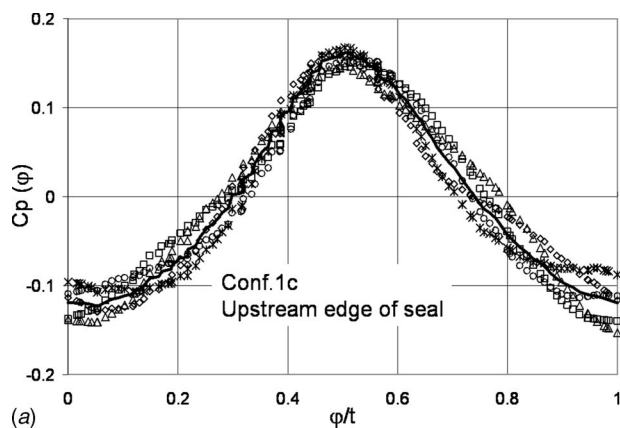


**Fig. 6** Variation of calculated pressure behind vane 1 with wide-spaced airfoils (Conf. 1c) at locations of the upstream and downstream edges of the axial gap seal. The solid line is time averaged; symbols are instantaneous pressures with five blade locations.

of the blade is more axial than swirling from the vane. Thus the velocities and dynamic pressures are decreased. For the close-spaced, half-stage configuration (Fig. 7, Conf. 1a), the time-averaged peak-to-peak variation in  $C_p(\varphi)$  upstream of vane 2 is greater ( $\Delta C_p(\varphi)=0.15$ ) than the unsteady wake effects from the blade ( $\Delta C_p(\varphi)=0.13$ ). Note that the time-averaged peak-to-peak variation in  $C_p(\varphi)$  across the vane gap increases from 0.15 at the upstream edge of the seal to 0.35 at the downstream edge of the seal at the upstream and downstream of the axial gap seal.

For the wide-spaced half stage (Fig. 8, Conf. 1c), the unsteady pressure variation in  $C_p(\varphi)$  decreases from 0.08 at the upstream edge of the seal to 0.04 at the downstream edge of the seal. The gapwise variation of the time-averaged  $C_p(\varphi)$  is approximately 0.08 and 0.22 at these two locations.

**Comments on Numerically-Simulated 2D Results.** The results presented from the simulation of one flow condition and two half-stage spacing for the RWTH Aachen University 1.5-stage turbine quantify the effects of half-stage spacing on the pressure variations near rim seals. These results are consistent with the vane and blade surface pressure measurements presented by Dring et al. [28] for a turbine with somewhat similar velocity triangles, i.e., tangential velocities into the blade at nearly two times wheel speed and near axial flow exiting the blade. The rapid decrease in the airfoil leading edge effects with distance from the airfoil is consistent with the modeling for each half stage in Ref. [20]. The benefit from the 2D time-dependent simulation of the flow field is that the pressure variations from the vane-blade interactions are

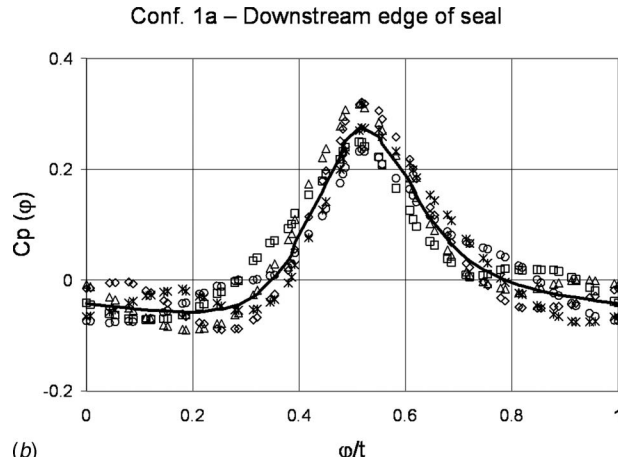
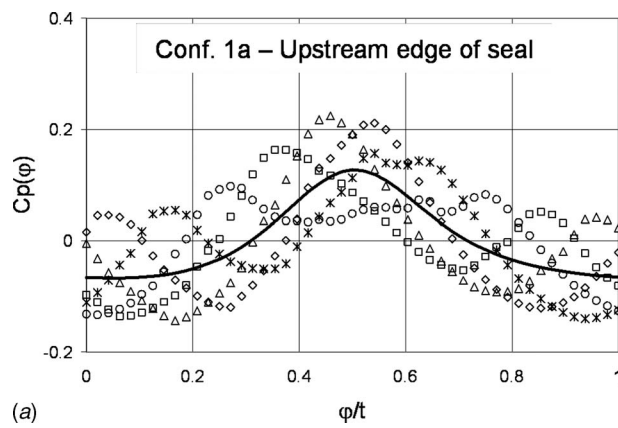


**Fig. 7** Variation of calculated pressure behind the blade with close-spaced airfoils (Conf. 1a) at the upstream and downstream edges of the axial gap seal

shown. The authors believe that the code correctly simulates the airfoil leading edge effects. However, the mixing of the airfoil wakes is dependent in part on the turbulence models in the code. Changing the model will affect the wake mixing and hence the gapwise variation of time-averaged pressure. One comparison of the numerical simulation results and experimental results is shown in the next section.

### Comparison of Measured and Numerically Simulated Pressure Distribution

Pressure data from the RWTH Aachen University turbine (Fig. 1) for the design flow condition (OP1) with close-spaced half stages are compared (Fig. 9) with numerically simulated 2D time-averaged and time-dependent results for a similar flow condition and the identical airfoil geometry. The experimental condition measured was for no coolant flow supplied to the cavity. The time-averaged data were obtained [27] downstream of the vane 1 trailing edge. The gap coordinates for the calculated results are shifted to match the experimental coordinate system. The pressure level for the calculated results was increased by  $C_p(\varphi)=0.04$  to account for differences between the numerical and experimental average pressures. The 2D numerical results bracket the experimental data rather well. An analysis [27] of additional experimental data with moderate coolant flow shows that the pressure distribution is affected by the coolant flow rate. This is also consistent with the stator and rotor data shown by Feiereisen et al. [29] for modest coolant flow rates. The authors' conclusion is that the 2D time-dependent simulations capture the principal effects of

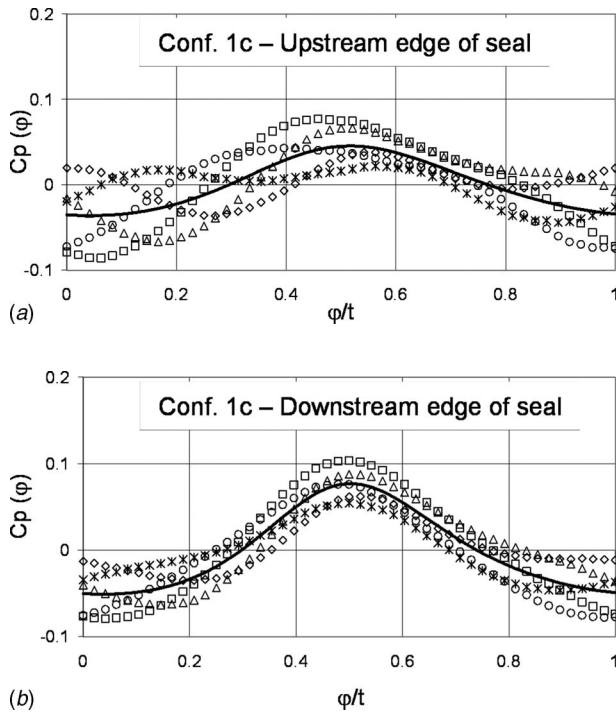


Fig. 8 Variation of calculated pressure behind the blade with wide-spaced airfoils (Conf. 1c) at the upstream and downstream edges of the axial gap seal

half-stage spacing, airfoil shape, and wake mixing and provide a reasonable basis for estimating rim seal ingestion.

### Description of Simple-Orifice Model

The sealing effectiveness of a rim seal is generally defined by the amount of hot gas that penetrates to a stator wall. The sketch (Fig. 10) shows that an interchange of flow between the gas path and the cavity can occur across the seal. A mixing region occurs inside the axial gap with interactions between the gas path, the secondary flow path in the cavity (i.e., outward along the rotor and inward along the stator), and the large cyclonic cells occurring in the disk-stator cavity [5]. The local cooling effectiveness,  $\eta$ , is generally lowest at the outer radius of the stator and increases radially inward [21].

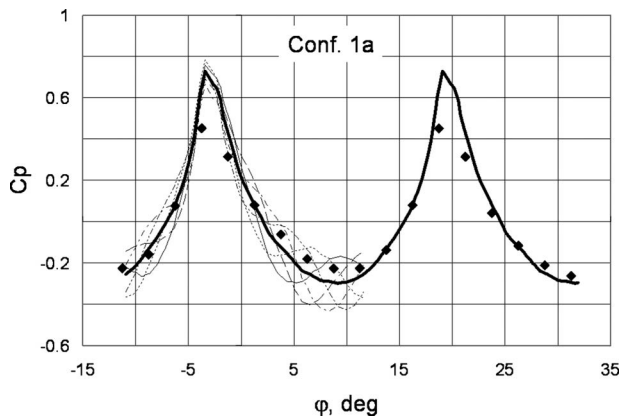


Fig. 9 Comparison of measured and calculated pressure distributions downstream of vane 1 trailing edge with close-spaced airfoils (Conf. 1a). Symbols: measured; heavy line: time averaged; light lines: instantaneous at five blade locations (same calculated results as in Fig. 5).

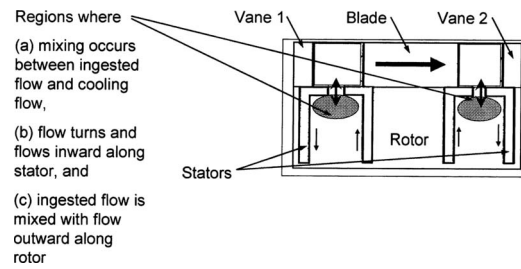


Fig. 10 Sketch of ingestion and mixing processes in an axial gap rim seal

The local cooling effectiveness can be defined in terms of gas path, wall, and coolant temperatures (Eq. (2a)), in terms of the ingested gas-path flow rate and coolant flow rates that are mixed at that location (Eq. (2b)) or in terms of the dimensionless parameters,  $C_w$  and  $C_{w,in}$  (Eq. (2c)),

$$\eta = (T_g - T_w) / (T_g - T_c) \quad (2a)$$

$$\eta = m_c / (m_{in} + m_c) \quad (2b)$$

$$\eta = C_w / (C_w + C_{w,in}) \quad (2c)$$

Experimental cooling effectiveness data can be obtained with temperature measurements to include engine component thermal conduction effects or with trace gases to measure only the ingestion and mixing effects that contribute to cooling effectiveness at a specific location.

**Simple-Orifice Model.** A simple-orifice model was formulated to relate the gas-path ingestion flow rate to the circumferential pressure fields at the seal axial location. This model is expected to be applicable for ingestion conditions that are dominated by stationary and transient pressure variations across the seal caused by vane-blade interactions. The model is similar to previous simple-orifice models except that the current model uses calculated time-dependent results to determine the gas-path circumferential pressure distribution at the axial location of the seal. The pressure distribution will be determined with 2D time-dependent computational fluid dynamics (CFD) codes that can simulate the vane-blade flow field with a combination of stationary and moving airfoils and with a reasonable calculation time. Commercial codes with these characteristics are available.

The following assumptions have been made for our simple-orifice model:

- The model is a “simple orifice,” with the dynamic pressure of the ideal velocity through the orifice equaling the difference between the local gas-path pressure and the “assumed” cavity pressure.
- The model uses either (a) the circumferential, time-averaged gas-path pressure distribution from 2D time-dependent calculations for each turbine stage, seal geometry, and flow condition or (b) several instantaneous circumferential gas-path pressure distributions and averages the results.
- A single  $C_d$  value characterizes the effective orifice area ratio for both the ingress and egress flow and will be a function of seal geometry and gas-path flow condition. The lumped  $C_d$  parameter value will be determined by comparison with experimental data for each class of seal geometry, external flow condition, and disk-cavity flow condition.
- The imprecise use of static pressure differences to estimate radial velocities through the rim seal gap is acknowledged
- The radial pressure difference across the seal caused by the tangential velocity of the flow in the seal is neglected in the model.
- Azimuthal pressure variations on the cavity side of the orifice are neglected.



The ideal radial velocity through the orifice is assumed to be that for a constant density fluid from an infinite reservoir through a nozzle,

$$V\text{-ideal} = \text{sign}\{\text{SQRT}[2\text{abs}(\Delta P)/\rho]\} \quad (3)$$

The  $\Delta P$  term is the absolute value of the pressure difference between the local gas-path static pressure and the assumed cavity static pressure. The flow direction is determined by the sign of  $\Delta P$ .

A Cd value is defined,

$$C_d = V/V\text{-ideal} \quad (4)$$

The range of Cd values can be large and depend on the external flow axial and swirl velocities, the seal geometry, and the rotor speed. Seal gap flow characteristics were determined by Vaughan [30] for a variety of flow conditions. Vaughan's sketches of possible flow patterns indicated that the Cd values may vary from nearly zero to nearly 1. Experiments by Dadkhah reported by Chew et al. [31], indicate that values of 0.5–0.8 were obtained for seals across disk cavities without external flow. Discussion and analysis by Hills [17] and others indicate that values of Cd for seals with axial flow can vary from zero to more than 0.5, depending on the ratio of external flow velocity to seal velocity and the external velocity swirl.

*Calculation Procedure for One Assumed Cavity Pressure.* The sealing effectiveness,  $\eta$ , is calculated for a rim seal with an effective Cd,

1. Determine the gas-path pressure for the vane segment increment from the time-averaged value of the time-dependent 2D flow field across the seal.
2. Assume a cavity pressure.
3. Determine ingress and egress velocity distributions with Eq. (3).
4. Determine the mass flow rate for the vane segment increment (i.e., the product of ideal velocity, Cd, gap width, hub circumference, percent of vane pitch at selected gas-path pressure, and fluid density).
5. Integrate across the one-vane stator segment to determine ingestion flow rate and net flow rate.
6. Calculate seal effectiveness,  $\eta$ .

*Calculation Procedure for Additional Assumed Cavity Pressures*

7. Repeat calculations for a range of cavity pressures to determine the variation of seal effectiveness with Cw

**Comments on the Simple-Orifice Model.** The simple-orifice model has a shortcoming identified in Refs. [17,20] regarding the noninclusion of the inertia terms for the gas path and cavity flow entering the seal region. However, inclusion of these effects for modeling rim seal ingestion requires several simplifying assumptions. A full 3D time-dependent model is required to fully account for these effects [32].

The Cd, determined by comparing modeled gas-path ingestion rates with experimental wall effectiveness data for a given configuration, becomes a lumped parameter. This lumped parameter includes the effects of (a) mixing in the cavity, described in a previous paragraph, (b) seal geometry, and (c) gas-path swirl characteristics. Thus, the Cd obtained is useful in the cooling design for estimating ingestion flow rates for similar turbine designs. The Cd values can be expected to vary with rim cavity radius ratio and evaluation location for the cooling effectiveness. The mixing region location and interaction with the cavity flows, shown in Fig. 10 for an axial gap seal, will depend on seal configuration.

## Simple-Orifice Model Results

**Simple-Orifice Model Calculations for Conf. 1a and OP3.** The variations of time-averaged and time-dependent pressure co-

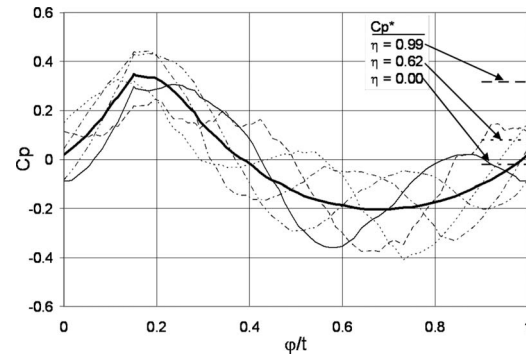


**Fig. 11** Calculated pressure coefficient,  $C_p(\phi)$ , at the upstream edge of seal behind vane 1 with Conf. 1a, OP3, and values of  $C_p^*$  for the cavity-side pressure used to obtain selected seal cooling effectiveness,  $\eta$

efficients,  $C_p(\phi)$ , with vane circumferential location are presented in Fig. 11. The values of  $C_p^*$  used to calculate radial velocity profiles associated with sealing effectiveness,  $\eta$  ( $\eta=0.00$ , 0.62, and 0.99), are also shown. The calculated velocity profiles for the gapwise variation of the time-averaged pressure (Fig. 11) at the upstream edge of the seal with the three values of  $C_p^*$  are shown in Fig. 12.

For the radial velocity profiles with  $\eta=0.00$ , the integral of the velocity across the vane gap under any one of the Cd curves is zero. The zero-net-flow condition was obtained by assuming cavity pressures until the ingress and egress flow rates were equal. Although the process could be automated, finding the desired cooling effectiveness value by adjusting the cavity-side pressure on a worksheet is a 1 min process. Because a yet-to-be-determined constant Cd is assumed for both ingress and egress flows, the calculated cooling effectiveness is only a function of the gas-path pressure variation and the assumed cavity-side pressure. When the Cd for a geometry and class of flow condition is established, the  $m_{in}$  rate calculated is a good estimate for the flow exchange across the rim seal when no cooling flow is supplied. Note in Fig. 11 that the assumed cavity-side pressure coefficient is less than zero, the average pressure across the vane pitch.

The velocity profiles for  $\eta=0.623$  are shown (Fig. 12) because the coolant flow rate is approximately equal  $m_{in}$  for no coolant flow. The assumed cavity-side pressure coefficient (Fig. 11) is greater than zero but approximately 25% of the peak  $C_p$  for this axial location. These axial-gap-averaged profiles can be compared with the shapes of the radial velocity profiles of Ref. [4] at their several axial gap locations. Based on the yet-to-be-determined Cd, we estimate that the calculated flow condition for  $\eta=0.632$  is somewhere between the two experimental flow conditions of Ref. [4].

The velocity profiles for a cavity pressure (Fig. 11) that yielded  $\eta=0.99\%$  show (Fig. 12) the large outward flow region and the small inward flow region and velocity. The assumed cavity-side pressure is slightly less than the peak time-averaged  $C_p$ . However, there is a  $\Delta C_p=0.1$  difference between the peak time-dependent pressure and the peak time-averaged pressure. Thus, complete sealing of the rim seal cavities requires higher coolant flow rates.

Calculations were made for a number of assumed cavity pressures (Fig. 13) and were integrated to produce the variations of  $V^*/(\Omega R)$  and  $V_{in}^*/(\Omega R)$  with cavity pressure. The values of  $C_p^*$  used to calculate the radial velocity profiles of Fig. 12 are shown on the figure.  $V^*$  is the average radial velocity for the coolant flow rate.  $V_{in}^*$  is the average ingress radial velocity for  $m_{in}$ .

**Evaluation of Cd From Experimental Data.** If the simple-orifice model is to be used as a design tool, the Cd values for classes of seals and flow conditions must be available. The evalu-



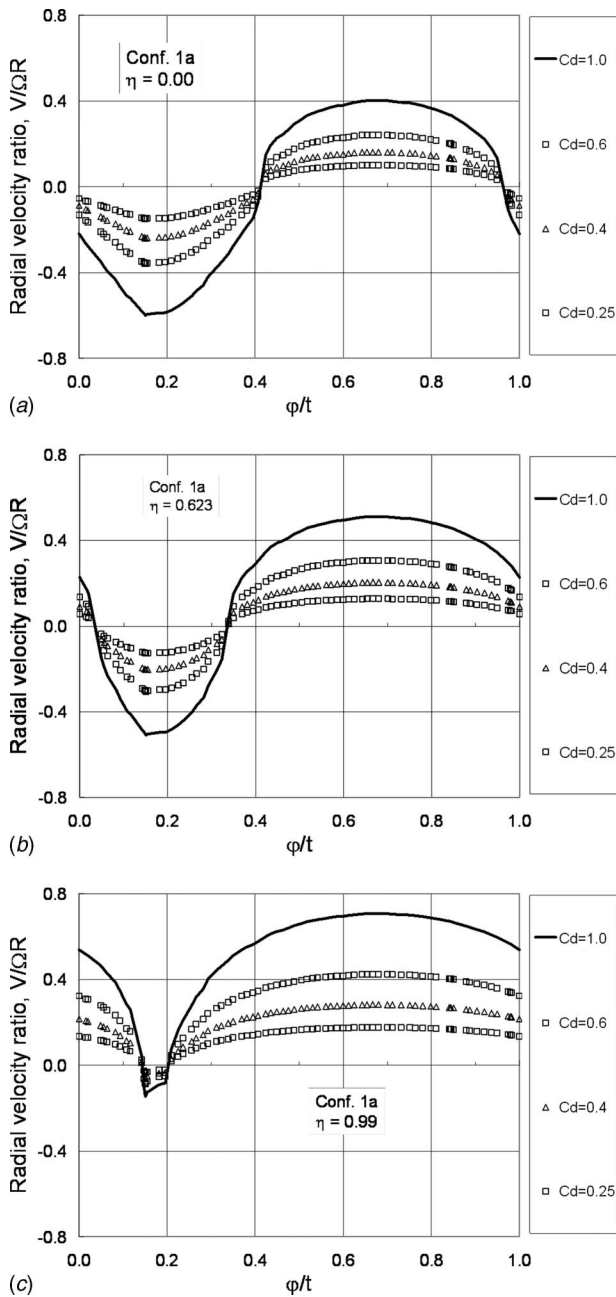


Fig. 12 Calculated velocity distribution across vane pitch for selected cooling effectiveness; vane 1–blade seal with close-spaced airfoils (Conf. 1a)

ation for the axial gap seal of [4,27] was made by comparing the cooling effectiveness obtained from the three different flow conditions with the same velocity triangles (OP1, OP3, and OP4). The Cd and model for OP3 were replotted as the variation of cooling effectiveness with seal velocity ratio,  $V^*/(\Omega R)$  (Fig. 15).

The sealing effectiveness data points at the outermost sampling site on the stator wall,  $r/R=0.952$  [27], are compared with the results from the simple-orifice model for Cd values of 0.3, 0.4, and 0.5 (Fig. 14). Although individual data points are not shown, the data lie within the band shown. From the comparison, the value of Cd=0.4 for the simple-orifice model matches the data rather well.

Values of Cd between 0.30 and 0.43 fit the measured data shown in Fig. 14 for the present model. The data set is the same shown by Scanlon et al. [19]. However, the flow condition range

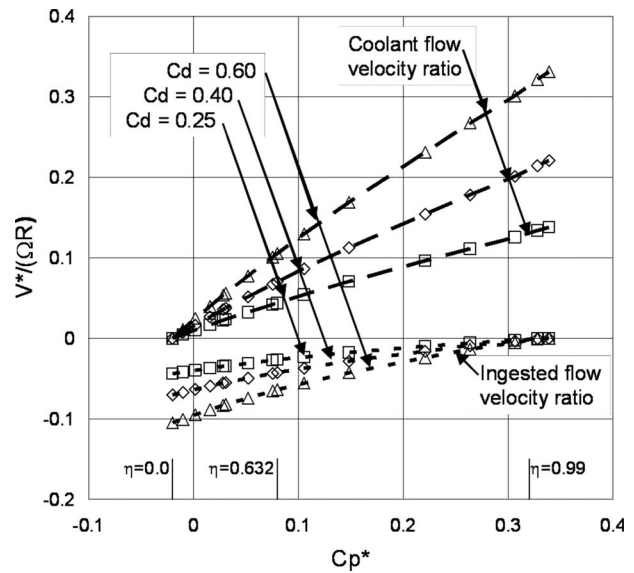


Fig. 13 Variation of ingested flow rates and coolant flow rate with assumed cavity pressure ratio,  $Cp^*$ . Axial gap seal downstream of vane 1 with close-spaced airfoils (Conf. 1a); flow condition OP3; open symbols are ingress  $V_{in}^*$  ( $\Omega R$ ) ratios.

for Ref. [19] included the data points from additional flow conditions and with axial seals with a larger  $G_c$ . The Ref. [19] model was based on the ratio of the average coolant flow velocity to the axial velocity. Our simple-orifice model requires additional 2D time-dependent CFD calculations to produce the hub pressure distribution for the OP2 and OP5 conditions and to estimate the effects of those flow conditions.

The conclusion of the authors is that the model and the single “data matched” value of Cd for the RWTH Aachen University airfoils is applicable to these airfoils and for these turbine stage velocity triangles. The Cd is applicable for the close half-stage spacing where ingestion is dominated by the large time-averaged and time-dependent gapwise pressure variations circumferentially along the seal. Other seal configurations and wide-spaced stages may be dominated by other phenomena.

### Comparison of Simple Orifice Model With a No-Ingestion Correlation and Turbulent Transport Model

The ingested flow rate,  $m_{in}$ , for  $\eta=0.0$ , calculated for the OP3 flow condition is used in the turbulent transport model described

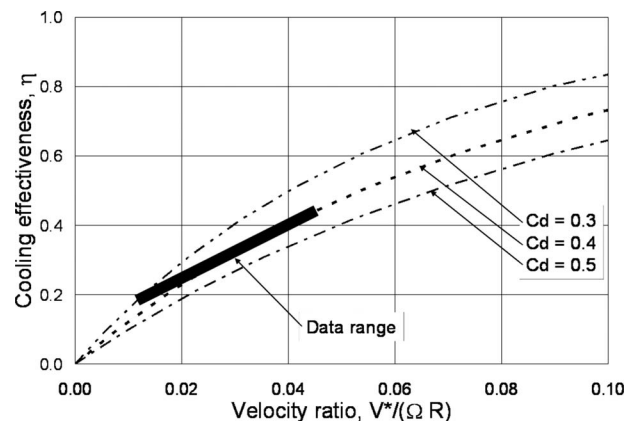
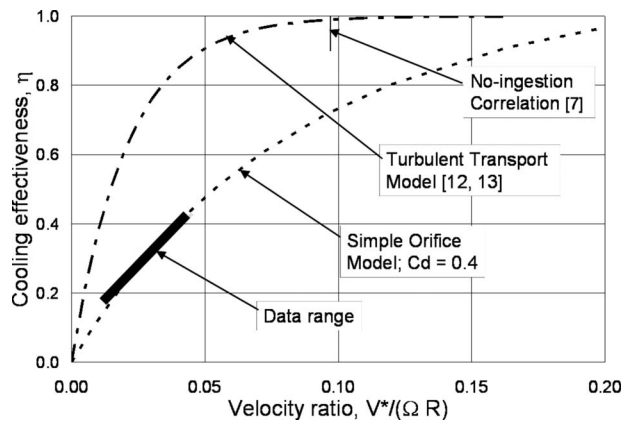


Fig. 14 Evaluation of Cd for simple-orifice model from data calculated for vane 1–blade seal with Conf. 1a and OP3; data from OP1, OP3, and OP4 experimental flow conditions



**Fig. 15 Comparison of simple-orifice model with data for vane 1-blade seal and Conf. 1a and with turbulent transport model**

in Refs. [12,13]. However, the  $C_d$  to quantify the ingested flow rate must be determined by comparison with experimental data, as shown in Fig. 14.

As mentioned in the background material, several correlations and analyses have been made for rim seals without the effects of airfoils. The turbulent transport model [10,12,13] enables a comparison for the partial sealing effects with the simple-orifice model. The early correlation of Bayley and Owen [7] for the prevention of ingestion is used as the coolant flow rate required for 99% cooling effectiveness. This relationship was also found to occur in rotating disk experiments with external swirling flow [10,13] and accurately modeled with the turbulent transport model. The Bayley and Owen correlation of Ref. [7] provides a conservative estimate for disk-stator rim seal flow requirements for the RWTH Aachen University experimental disk Reynolds number. However, the relationship from Ref. [7] is simple in that the velocity ratio,  $V^*/(\Omega R)$ , required to prevent perceivable ingestion, is a constant. More accurate relationships that account for Reynolds number effects [8,9,11] show that lower velocity ratios are required to achieve “no perceivable” ingestion.

The variations of cooling effectiveness from the experimental data and simple-orifice model are compared with the estimated effectiveness for the turbulent transport model (Fig. 15) for the vane 1-blade axial gap seal and Conf. 1a. From the no-ingestion correlation [7] combined with the turbulent transport mode, the experimental and simple-orifice model velocity ratios required to obtain a cooling effectiveness,  $\eta=0.4$ , are 3.5 times that required if ingestion were dominated by disk-cavity flow without airfoils. Thus, the effects of airfoil pressure variations are important for this class of turbines with close-spaced half stages.

The cooling effectiveness from experimental data and the simple-orifice model for the blade-vane 2 seal and Conf. 1c are shown in Fig. 16. Note that cooling effectiveness obtained for the same coolant flow rates as those in Fig. 15 are as high as 0.78. The coolant flow rate to obtain a cooling effectiveness=0.4 is only 1.5 times that for no-ingestion correlation [7] combined with the turbulent transport model. If the vane 2 leading edge radius were smaller and the upstream bow wave penetrated a smaller distance upstream, the rim seal ingestion would have been dominated by disk-stator sealing phenomena rather than the vane 2 pressure field. Thus, the designer must be aware of the dominant mechanism for each sealing application.

### Comparisons With Other Rim Seal Models

Each rim seal ingestion model has advantages and disadvantages. Following are some advantages of using the numerically simulated, time-dependent pressure fields with a simple-orifice model to estimate cavity cooling effectiveness.

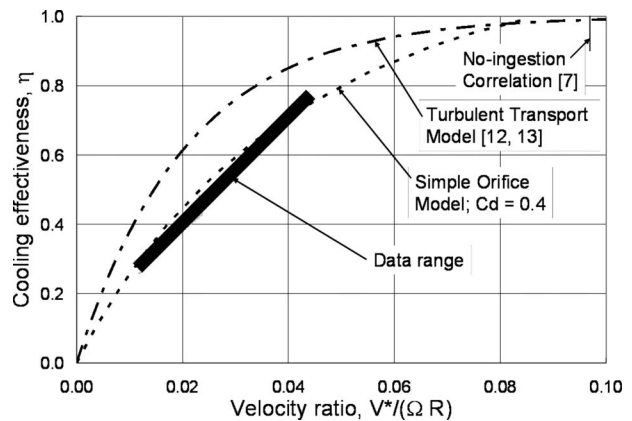


**Fig. 16 Comparison of simple-orifice model with data for blade-vane 2 seal and Conf. 1c and with turbulent transport model**

- The pressure field between vanes and blades are unique to each airfoil shape and operating conditions. Using generalized correlations precludes examining the effects of flow field interactions in detail.
- The simple-orifice model has physically significant limits. For no coolant flow, the cavity approaches the gas-path temperature. At high coolant flow rates, the coolant prevents any ingestion from pressure field sources.
- With modern computer aided design and grid generating programs, the 2D numerical simulations can be obtained with a modest amount of effort.

Of the advantages cited, one author (B.V.J.) believes that the physical insights obtained from the simulations and model give the secondary flow cooling designer a basis for advocating platform and seal design innovations in turbine designs.

The simple orifice model has a weak assumption that ignores the pressure difference across the seal due to the swirl of the flow. Therefore, the pressure differences calculated from the hub pressure and the assumed cavity pressure are not equal to the pressure difference between the hub and the radius of the cavity outer wall.

### Conclusions

The time-dependent pressure field over rim seals can be the dominant physical mechanism for rim seal ingestion. This mechanism becomes dominant when the half stages are closely spaced. The time-dependent pressure field is a less dominant ingestion mechanism when the half-stages are more widely spaced. Conditions can occur where the airfoil-less disk-stator rim seal mechanism will dominate the ingestion.

The simple-orifice model and pressure field results from the 2D time-dependent numerical simulation of the streamline near the turbine hub can be used to estimate the coolant flow rate required to obtain a disk-cavity cooling effectiveness.

The simple-orifice model requires an experimentally determined lumped parameter  $C_d$  for each class of rim seal configuration. The experimental data were in good agreement with  $C_d = 0.4$ . An analysis of the pressure fields generated by the 2D time-dependent numerical simulation can guide the selection of the axial location of the rim seal opening.

### Acknowledgments

The authors gratefully acknowledge the support of the European Commission for the Internal Cooling Air System-Gas Turbines—Hot Gas Ingestion Control Task. The permission of the EC and ICAS-GT partners to publish the paper is gratefully acknowledged. The authors acknowledge the contributions of Dr. B. Bonhoff for initial work on modeling with 2D time-dependent

simulations, B. Rudzinski for experimental data acquisition, and Praktikants at Alstom for providing the data files required for a detailed analysis.

## Nomenclature

- $C_d$  = lumped parameter flow coefficient  
 $C_p(\varphi)$  = pressure coefficient, Eq. (1)  
 $C_p^*$  = pressure coefficient used with simple-orifice model  
 $C_w$  = dimensionless flow parameter,  $m_c/(R\mu)$   
 $C_{w_{in}}$  = dimensionless flow parameter,  $m_{in}/(R\mu)$   
 $G$  = dimensionless cavity gap ratio,  $S/R$   
 $G_c$  = dimensionless seal gap ratio,  $S_c/R$   
 $m_c$  = coolant flow rate, kg/s  
 $m_{in}$  = ingestion flow rate, kg/s  
 $P$  = pressure, Pa  
 $q$  = dynamic pressure of fluid at rotor hub velocity, Pa  
 $R$  = hub radius of stator and rotor, m  
 $Re_\phi$  = disk hub Reynolds number,  $\Omega R^2 \rho / \mu$   
 $S$  = axial gap between stator and rotor, m  
 $S_c$  = axial seal clearance, m  
 $t$  = vane pitch, deg  
 $T_c$  = temperature of the coolant, K  
 $T_g$  = temperature in the gas path, K  
 $T_w$  = cavity wall temperature, K  
 $V$  = average radial velocity across seal gap at  $\varphi$ , m/s  
 $V^*$  = average radial velocity across seal gap and vane pitch, m/s  
 $x$  = axial coordinate, m  
 $\varphi$  = azimuthal coordinate, deg  
 $\eta$  = sealing effectiveness on stator wall near cavity outer radius, Eqs. (2a)–(2c)  
 $\rho$  = fluid density, kg/m<sup>3</sup>  
 $\mu$  = fluid dynamic viscosity, kg/m/s  
 $\Omega$  = rotational rate of disk, rad/s

## References

- [1] Suo, M., 1978, "Turbine Cooling," *Aero-Thermodynamics of Aircraft Gas Turbine Engines*, G. C. Oates ed., Air Force Aero Propulsion Laboratory Report AFAPL-TR-78-52.
- [2] Campbell, D. A., 1978, "Gas Turbine Disc Sealing System Design," Report No. AGARD-CP-237, p. 18.
- [3] Smout, P. D., Chew, J. W., and Childs, P. R. N., 2002, "ICAS-GT: A European Collaborative Research Programme on Internal Cooling Air Systems for Gas Turbines," ASME Paper No. GT-2002-30479.
- [4] Bohn, D. E., Decker, A., Ma, H., and Wolff, M., 2003, "Influence of Sealing Air Mass Flow on the Velocity Distribution In and Inside the Rim Seal of the Upstream Cavity of a 1.5-Stage Turbine," ASME Paper No. GT2003-38459.
- [5] Jakoby, R., Zierer, T., Lindblad, K., Larsson, J., deVito, L., Bohn, D. E., Funcke, J., and Decker, A., 2004, "Numerical Simulation of the Unsteady Flow Field in an Axial Gas Turbine Rim Seal Configuration," ASME Paper No. GT2004-53829.
- [6] Johnson, B. V., Mack, G. J., Paolillo, R. E., and Daniels, W. A., 1994, "Turbine Rim Seal Gas Path Flow Ingestion Mechanisms," AIAA Paper No. AIAA 94-2703.
- [7] Bayley, F. J., and Owen, J., 1970, "The Fluid Dynamics of a Shrouded Disk System With a Radial Outflow of Coolant," ASME J. Eng. Power, **92**, pp. 335–341.
- [8] Phadke, U. P., and Owen, J. M., 1983, "An Investigation of Ingress for an 'Air-Cooled' Shrouded Rotating Disk System With Radial Clearance Seals," ASME J. Eng. Power, **105**, pp. 178–183.
- [9] Owen, J. M., and Rogers, R. H., 1989, *Flow and Heat Transfer in Rotating Disc Systems, Volume 1: Rotor-Stator Systems*, Wiley, New York.
- [10] Daniels, W. A., Johnson, B. V., Graber, D. J., and Martin, R. J., 1992, "Rim Seal Experiments and Analysis for Turbine Applications," ASME J. Turbomach., **114**, pp. 426–432.
- [11] Chew, J. W., 1989, "A Theoretical Study of Ingress for Shrouded Rotating Disc Systems With Radial Outflow," ASME J. Turbomach. **113**, pp. 91–97.
- [12] Johnson, B. V., 1975, "A Turbulent Diffusion Model for Turbine Rim Seal Cavity Seals," UTRC Report No. 75-17.
- [13] Graber, D. J., Daniels, W. A., and Johnson, B. V., 1987, "Disk Pumping Test, Final Report for Period August 1983 to February 1987," Air Force Wright Aeronautical Laboratories, Report No. AFWAL-TR-87-2050.
- [14] Abe, T., Kikuchi, J., and Takeuchi, H., 1979, "An Investigation of Turbine Disk Cooling: Experimental Investigation and Observation of Hot Gas Flow Into a Wheel Space," 13th CIMAG Congress, Vienna, Paper No. GT30.
- [15] Green, T., and Turner, A. B., 1994, "Ingestion Into the Upstream Wheel-space of an Axial Turbine Stage," ASME J. Turbomach., **116**, pp. 327–332.
- [16] Chew, J. W., Green, T., and Turner, A. B., 1994, "Rim Sealing of Rotor-Stator Wheel-spaces in the Presence of External Flow," ASME Paper No. 94-GT-16.
- [17] Hills, N. J., Chew, J. W., Green, T., and Turner, A. B., 1997, "Aerodynamics of Turbine Rim-Seal Ingestion," ASME Paper No. 97-GT-268.
- [18] Bohn, D., and Wolf, M., 2003, "Improved Formulation to Determine Minimum Sealing Flow— $C_w$ , min—for Different Sealing Configurations," ASME Paper No. GT2003-38465.
- [19] Scanlon, T., Wilkes, J., Bohn, D., and Gentilhomme, O., 2004, "A Simple Method for Estimating Ingestion of Annulus Gas Into a Turbine Rotor Stator Cavity in the Presence of External Pressure Variations," ASME Paper No. GT2004-53097.
- [20] Gentilhomme, O., Hills, N. J., Turner, A. B., and Chew, J. W., 2002, "Measurement and Analysis of Ingestion Through a Rim Seal," ASME Paper No. GT-2002-30481.
- [21] Roy, R. P., Feng, J., Narzary, D. Saurabh, P., and Paolillo, R. E., 2004, "Experiments on Gas Ingestion Through Axial-Flow Turbine Rim Seals," ASME Paper No. GT2004-53394.
- [22] Bohn, D., Rudzinski, B., Suerken, N., and Gaertner, W., 2000, "Experimental and Numerical Investigation of the Influence of Rotor Blades on Hot Gas Ingestion into the Upstream Cavity of an Axial Turbine Stage," ASME Paper No. 2000-GT-284.
- [23] Foerster, I., Martens, E., Friedl, W.-H., and Peitsch, D., 2001, "Numerical Study of Hot Gas Ingestion Into an Engine Type High-Pressure Turbine Rotor-Stator Cavity," ASME Paper No. 2001-GT-0114.
- [24] Okita, Y., Nishiura, M., Yamawaki, S., and Hironaka, Y., 2004, "A Novel Cooling Method for Turbine Rotor-Stator Rim Cavities Affected by Mainstream Ingress," ASME Paper No. GT2004-53016.
- [25] Bayley, F. J., 1999, "Flows and Temperatures in Compressor and Turbine Wheel-spaces," Proc. Inst. Mech. Eng., Part C: J. Mech. Eng. Sci., **213**, pp. 451–460.
- [26] Bohn, D., Rudzinski, B., and Suerken, N., 1999, "Influence of Rim Seal Geometry on Hot Gas Ingestion Into the Upstream Cavity of an Axial Turbine Stage," ASME Paper No. 99-GT-248.
- [27] Bohn, D. E., Decker, A., and Ohlendorf, N., 2006, "Influence of a Radial and Axial Rim Seal Geometry on Hot Gas Ingestion into the Upstream Cavity of a 1.5-Stage Turbine," ASME Paper No. GT2006-90453.
- [28] Dring, R. P., Joslyn, H. J., Hardin, L. W., and Wagner, J. H., 1982, "Turbine Rotor-Stator Interactions," ASME J. Eng. Power, **104**, pp. 729–742.
- [29] Feiereisen, J. M., Paolillo, R. E., and Wagner, J., 2000, "UTRC Turbine Rim Seal Ingestion and Platform Cooling Experiments," AIAA Report No. 2000-3371.
- [30] Vaughan, C. M., 1986, "A Numerical Investigation Into the Effect of an External Flow Field on the Sealing of a Rotor-Stator Cavity," Ph.D. thesis, University of Sussex.
- [31] Chew, J. W., Dadkhah, S., and Turner, A. B., 1991, "Rim Sealing of Rotor-Stator Wheel-spaces in the Absence of External Flow," ASME Paper No. 91-GT-33.
- [32] Wang, C.-Z., Johnson, B. V., Cloud, D. E., Paolillo, R. E., Vashist, T. K., and Roy, R., 2006, "Rim Seal Ingestion Characteristics for Axial Gap Rim Seals in a Close-Spaced Turbine Stage From a Numerical Simulation," ASME Paper No. GT2006-90965.



# On the Response of a Strongly Diffusing Flow to Propagating Wakes

**J. P. Gostelow**

Department of Engineering,  
University of Leicester,  
Leicester LE1 7RH, UK  
e-mail: jpg7@le.ac.uk

**R. L. Thomas**

Whittle Laboratory,  
University of Cambridge,  
Cambridge CB3 0DY, UK  
e-mail: rt280@cam.ac.uk

**D. S. Adebayo**

Department of Engineering,  
University of Leicester,  
Leicester LE1 7RH, UK  
e-mail: dsa5@le.ac.uk

*Further evidence on the similarities between transition and separation phenomena occurring in turbomachinery and wind tunnel flows is provided by measurements on a large scale flat plate under a strong adverse pressure gradient. The flat plate has a long laminar separation bubble and is subjected to a range of disturbances with triggering caused by injection of a transverse jet and subsequently by wakes generated by rods moving transversely upstream of the leading edge. Wakes were originally presented individually. Each individual wake provoked a vigorous turbulent patch, resulting in the instantaneous collapse of the separation bubble. This was followed by a very strong, and stable, calmed region. Following the lead given by the experiments of Gutmark and Blackwelder (1987, "On the Structure of Turbulent Spot in a Heated Laminar Boundary Layer," *Exp. Fluids*, 5, pp. 207–229.) on triggered turbulent spots, wakes were then presented in pairs at different wake spacing intervals. In this way wake interaction effects could be investigated in more detail. As in the work on triggered turbulent spots the spacing between impinging wakes was systematically varied; it was found that for close wake spacings the calmed region acted to suppress the turbulence in the following turbulent patch. To investigate whether this phenomenon was a recurring one or whether the flow then reverted back to its unperturbed state, the experiments were repeated with three and four rods instead of two. This has the potential for making available a wide range of variables including direction and speed of rod rotation. It was found that the subsequent wakes were also suppressed by the calming effect. It may be anticipated that this repeating situation is present in a turbomachine, resulting in hidden benefits for blade count and efficiency. There may also conceivably be blade loading advantages while retaining favorable heat transfer conditions in high pressure turbines or stall margin in axial compressors. The inherent and prospective benefits of the calming effect therefore need to be understood thoroughly and new opportunities exploited where this is feasible.*

a [DOI: 10.1115/1.2950054]

## Introduction

Strong diffusion is often required of a flow in practical situations when a high level of loading is indicated. In aircraft, this situation is encountered when high lift is needed from the wing. Improvements required include raising the forward speed while delaying the onset of shock waves. At the same time, the wing loading and the control of this are maximized to improve landing and take-off performance and to reduce weight. The drag needs to be minimized at all times for range and fuel conservation. Wing tip vortices are also a problem, raising safety concerns and potentially reducing the capacity of an airport; radical solutions to this problem are evident in recent generations of passenger aircraft. These issues and constraints have resulted in extensive and sophisticated use of modern computational and experimental techniques in pursuit of improvements in wing shapes. The solutions have to be three dimensional, compressible (including shock wave prediction), and be fully capable of predicting viscous flows in boundary layers, wakes, and regions of separated flow. Aerodynamicists cannot yet claim to have a full capability to predict these flows.

The above considerations also apply to the compressor and turbine blades of modern aircraft engines and gas turbines. Both compressors and turbines may produce shock waves and will

therefore be designed with compressibility in mind. A major consideration is blade count, and hence the weight of the engine, pushing the designer to higher-lift blading. Wing tip vortices take the form of a mix of secondary flows, tip leakage vortices, and generally a much more complex three-dimensional flow field than is encountered on an aircraft wing.

An added complication for turbomachinery blading is that the flows in turbomachines are inherently unsteady. This unsteadiness may take various forms but the most common, and the most severe, tends to be the propagation of wakes from upstream blades through a downstream blade row.

The experimental work described in this paper addresses the propagation of wakes over a surface representing a compressor blade. The initial work was an investigation of triggered turbulent spots over a flat plate and this was extended to single wakes, pairs of wakes, and eventually multiple wakes. The objective was to build up the quality of representation carefully, taking care to obtain as complete an understanding of the physics as was possible at each stage.

Work performed on natural transition, without any stimulation of turbulent spot behavior, has been described in an earlier paper [1]. All subsequent work has also produced time intervals in which the transition was free from stimulation, therefore producing additional data on natural transition.

Work on isolated triggered turbulent spots was then performed. Triggering was achieved using short duration pulses of air from a loudspeaker. This produced additional information on spot spreading rates that permitted extension of the work to highly diffusing conditions conducive to laminar separation [2–4].

This work was extended from loudspeaker triggering of the

Contributed by the International Gas Turbine Institute of ASME for publication in the *JOURNAL OF TURBOMACHINERY*. Manuscript received June 8, 2007; final manuscript received June 28, 2007; published online January 22, 2009. Review conducted by David Wisler. Paper presented at the ASME Turbo Expo 2007: Land, Sea and Air (GT2007), 2007, Montreal, Quebec, Canada, May 14–17, 2007.



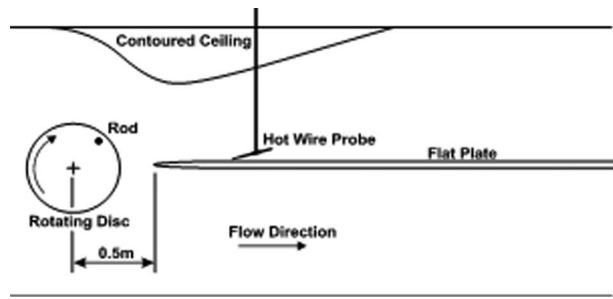


Fig. 1 Flat plate installation with fairing, hot-wire traverse and upstream wake generator

spots to the use of wakes propagating through the flow field. A triggered turbulent spot harbors an attendant calmed region [5] and the very similar interactions of blade wakes sweeping over blade boundary layers result in a particularly strong calmed region [6]. This phenomenon has been exploited in aircraft engine design to significantly reduce cost and weight.

The authors' work on wakes is introduced in Ref. [7]. Wake interaction experiments have involved the systematic variation of spacing between incident upstream wakes. This series of experiments was prompted by the work of Gutmark and Blackwelder [8] who performed similar investigations on triggered turbulent spots. The work of Ref. [8] had demonstrated that when one turbulent spot was closely followed by another at close intervals, such that the following spot entered the calmed region of the initial spot, the celerity and disturbance level of the following spot were reduced. In this work, the celerity has been defined as the feature velocity normalized by the local freestream velocity. This raised the question of whether similar phenomena applied to pairs of wakes with varying time intervals between wakes. A program of work was therefore undertaken with pairs of wakes to establish whether any such effects were present. The outcome of that was that no such effects were noted for the celerity of wake propagation but that the disturbance level of a following wake-induced turbulent patch was reduced in a systematic way, as the interval between wakes became sufficiently low that the following wake entered the calmed region of the initial wake [9].

Following the initial presentation of the work with pairs of wakes, the authors were challenged to demonstrate that the effects observed remained present in the multiwake environment of a turbomachine. This was a reasonable question and the latest work, as presented in this paper, constitutes an attempt to address that question. The approach taken is to present a series of four wakes to the flow. It was found possible to do this at low levels of wake spacing without spurious interference from extraneous wakes.

### Experimental Arrangements

The University of Leicester low-speed research wind tunnel was used for the experiments, which were performed on a flat plate (Fig. 1) in the  $1.00 \times 1.15 \text{ m}^2$  working section. The Reynolds number, based on the plate length of 2.41 m, was constant at  $1.4 \times 10^6$ . The freestream velocity was around 9 m/s at the throat and the turbulence level less than 0.2%.

The ceiling of the test section was contoured to provide the desired strong adverse pressure gradient, providing self-similar conditions with a Hartree [10]  $\beta$  parameter of  $-0.221$  over the  $x$  range between 0.4 m and 0.7 m. The converging section of the wind tunnel included the first 150 mm of the flat plate, terminating at the throat.

The pressure distribution was representative of that of a controlled diffusion compressor blade suction surface at high incidence (Fig. 2). This induced laminar separation in the form of a long laminar separation bubble, which was sufficiently thin to barely influence the pressure distribution. The flat plate, under this

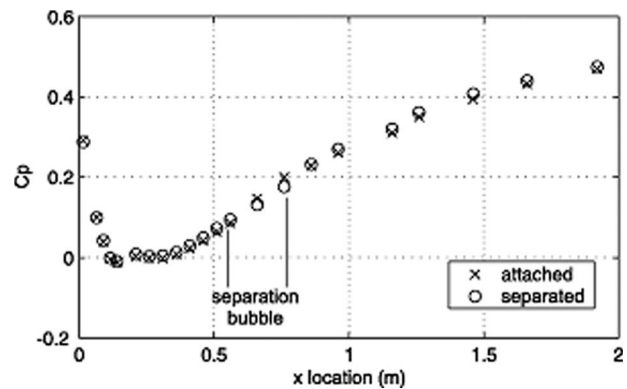


Fig. 2 Pressure distribution along the flat plate

adverse pressure gradient, was subjected to wakes generated by rotating up to four spanwise rods transversely upstream of the working section. The rods were cantilevered from a sidewall disk rotating clockwise at 48 rpm and were mounted at a radius of 270 mm, such that each had a local velocity of 1.36 m/s. Each rod created two impinging wakes for each disk rotation, one moved downwards (toward the plate surface) close to the leading edge of the flat plate, and was designated the primary wake. The second was further upstream and on its return journey; this was designated the secondary wake.

The single wire hot-wire probe was mounted on a computer controlled traverse mechanism. Data were acquired continuously and centerline phase-averaged velocity traces were determined at 27 locations along the plate and distances up to 50 mm normal to the flat plate surface. A photodiode circuit, mounted beside the rotating disk of the wake generator, acted as a triggering mechanism for activating the data acquisition routines. Phase averaging was performed variously over 64 and 128 repetitions, each record consisting of one full rotation of the wake generator. The flat plate was also instrumented with an array of subsurface microphones. Results from these have been reported separately [11].

Postprocessing of the data included the generation of the usual ensemble average velocity and rms of velocity, and intermittency values, calculated using the method previously described in Gos-telow and Thomas [7].

### The Single Wake

The flow was subjected to wakes generated by rods moving transversely upstream of the leading edge. Wakes were initially produced by a single rod. Each individual wake provoked a vigorous turbulent patch, resulting in the instantaneous collapse of the separation bubble. This was followed by a very strong, and stable, calmed region.

Although the upstream disk arrangement has proved to be a very good one, it does have the unusual feature of producing two kinds of wake during each cycle. The "primary wakes" are those in which the rod is relatively close to the leading edge of the flat plate. They give a wake, which has a relatively strong velocity deficit or "negative jet" and a high turbulence level.

As the rod moves a round and traverses the upstream side of the disk, it produces a more mixed out "secondary wake" with a weaker velocity deficit and a weaker turbulence level. Although both wakes represent compressor velocity triangles, the kinematics is different for the two. It has been found that, in general, the primary wakes result in a bypass transition situation with transition inception very close to the leading edge. On the other hand, the secondary wakes result in more of a natural transition with the growth of Tollmien-Schlichting waves and an intermittent transition to turbulence [12].

The passing of each wake above the laminar boundary layer causes the generation of patches of turbulence within the layer

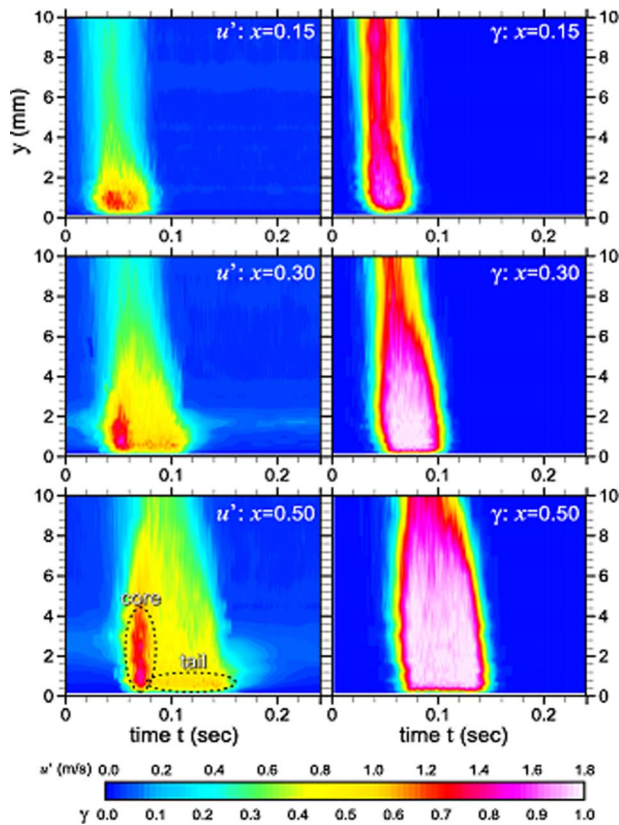


**Fig. 3** rms velocity perturbation,  $u'$ , and intermittency,  $\gamma$ , for a turbulent patch induced by a single primary wake at three chordwise locations. Freestream velocities are  $U_\infty = 8.9$  m/s, 9.0 m/s, and 8.8 m/s, respectively.

directly beneath the footprint of the wake. These patches, or strips, are a spanwise ensemble of merged and merging turbulent spots and exhibit many of the properties of the more traditional turbulent spot [13].

For the primary wake, the progression of the turbulent strip heralds a change in the structure, or internal distribution of kinetic energy, within it, as seen in Fig. 3. The strip develops two distinct regions. The leading edge downstream portion, which remains highly turbulent, is referred to here as the “core.” The remaining and continually expanding region of entraining turbulent spots is referred to as the “tail.” The corresponding difference in value of rms velocity fluctuation corresponds to an aging of the turbulence, and is a direct result of the marriage between strip and freestream wake. The passing of each freestream wake provides a source of turbulence for the boundary layer directly beneath the wake path. If receptive, the boundary layer will accept the kinetic energies, developing and propagating strong single frequency instabilities.

These instabilities become transitional and, as they break down, their content develops harmonics at higher frequencies and lower amplitudes. This process propagates in time with the wake leading edge and at the wake propagation velocity creating new turbulence ahead of the boundary layer strip. The core of the turbulent patch is the region of constantly regenerating turbulence induced by the wake as it travels ahead of the strip, and can be identified as the region with a high rms of velocity. This region also demonstrates the lowest frequency content of the strip as seen from spectral analyses [14]. It propagates at the wake velocity and its trailing edge travels at 50% of the freestream velocity. The tail that develops is a region of older and more mature turbulence that appears with lower rms values and higher frequency harmonics.

From intermittency plots, the entire strip including core and tail regions is seen to be fully turbulent with values above 0.95 throughout.

The secondary wakes develop in a different way with a natural growth process giving rise to a classical intermittency distribution for the transition to turbulence [12].

### Paired Wakes

Gutmark and Blackwelder [8] performed an interesting experiment with the time interval between one triggered turbulent spot and another systematically varied. Close proximity saw the celerity and disturbance level of the following spot diminished. If a wake-induced turbulent patch is really an ensemble of spots, does a wake-induced patch exhibit similar behavior?

Following the lead given by Gutmark and Blackwelder [8], wakes were presented in pairs at different spacing intervals; in this way, it was proposed to investigate wake interaction effects in more details. The spacing between wakes was systematically varied. Plots on a  $y \sim t$  basis of rms velocity perturbation for four streamwise distances, and at each for four different values of proximity,  $\alpha$ , are given in Fig. 4. Various indicators of turbulent activity were examined, including intermittency and rms, as shown in the space-time diagrams of Fig. 5. From these results, no clear variations for celerity were observed as the spacing between wakes was varied. Since the turbulence in the wake interaction situation is imposed and fed from the wake, this was not really surprising.

However, it was found that for close wake spacings (high proximity), the calmed region acted to suppress the turbulence in the following turbulent patch. At the early upstream location of  $x = 0.2$  m, the surrounding boundary layer is laminar. Here, the turbulent strips are newly developed and small in size. Thus, the second of each pair has not grown sufficiently to encroach upon the first turbulent strip. At  $x = 0.4$  m, the contours of rms velocity perturbation show that the turbulent strips have grown in size. For the closest spacing case,  $\alpha = 30$  deg, the second strip has just made contact with the first strip, displaying a slight reduction in rms. The surrounding boundary layer is now highly inflexional, yet still laminar. At  $x = 0.6$  m, the boundary layer is now separated in those areas surrounding the turbulent strips. The strips are now significant in size, with the  $\alpha = 40$  deg case exhibiting contact. The closest case,  $\alpha = 30$  deg, shows a very strong reduction of rms in the second strip. At an  $x$  of 0.8 m, the boundary layer is now reattached and fully turbulent. The second strip of the closest case has propagated into the trailing region of the first strip, merging the two. The cases of  $\alpha = 40$  deg and 50 deg are demonstrating the same behavior as the early  $\alpha = 30$  deg locations.

In Fig. 6, the peak value of rms velocity perturbation has been plotted for all the data against a wake proximity parameter,  $\psi$ , which normalizes the wake temporal spacing by the duration of the turbulent patch. The ordinate shows the peak value of rms velocity normalized to the peak value of rms velocity at the same location in space but for an isolated and hence unsuppressed turbulent strip.

This shows that the trend for rms perturbation to be diminished at close wake spacings is a consistent one. In Fig. 6, the black symbols refer to the four rod configuration described in the next section. Using pairs of rods with systematically varied spacings, a trend had been established for rms velocity disturbance levels to be diminished at close spacings. It was now reasonable to inquire whether such a trend would be maintained for a sequence of wakes, as would occur in a turbomachinery environment.

### Four Wakes

The approach taken to replicating the repeating turbomachinery wake situation, in which wakes recur in a relatively periodic fashion, was to mount four rods on the upstream disk. The rods were carefully selected to produce identical wakes at the measuring



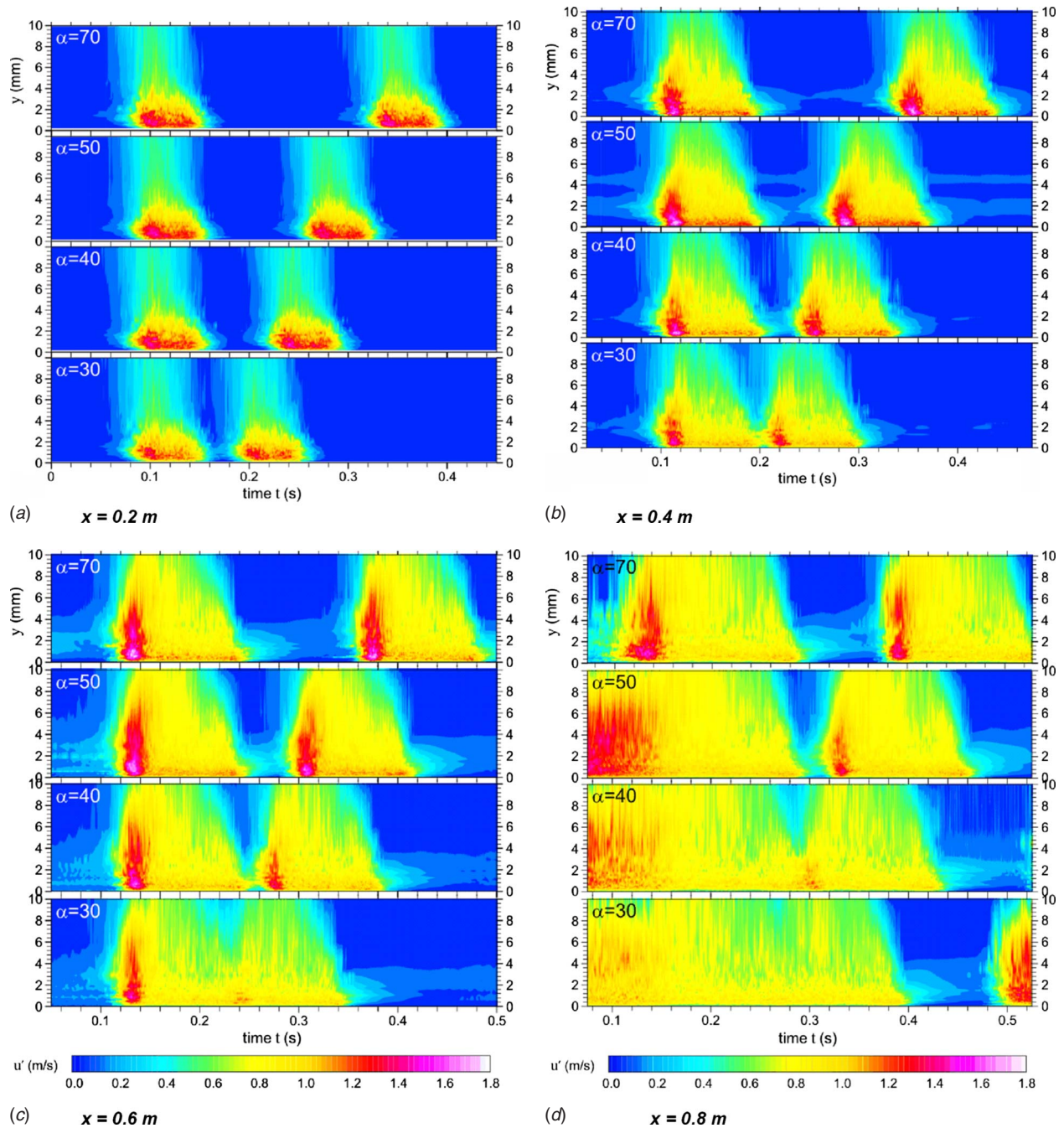


Fig. 4 Effect of increasing wake proximity on rms velocity. (a)  $x=0.2\text{ m}$ ; (b)  $x=0.4\text{ m}$ ; (c)  $x=0.6\text{ m}$ ; (d);  $x=0.8\text{ m}$ .

station. For earlier cases, with one or two rods, the kinematics had not presented a problem, but for four rods the potential for interference between the primary wakes and the secondary wakes existed. It was clear that this was a bigger problem for larger circumferential spacings than for closer spacings and it was found that data could be taken at spacing angles of 30 deg and 40 deg with very little interference. It was therefore decided to undertake a series of tests at these closer spacings to investigate the wake-boundary layer interactions and the calming phenomena.

Results, in the form of rms velocity perturbation plots, are presented for the two angles in Figs. 7 and 8. Each is given for four different  $x$  locations, 0.2 m, 0.4 m, 0.6 m, and 0.8 m. In these plots, the primary wakes are identified in the top plot by a "P" and the secondary wakes by an "S." In this series of plots, it is therefore possible to study the characteristics of natural transition, from

the secondary wakes, bypass transition, from the primary wakes, and at the 0.8 m location natural transition from regions where the flow is undisturbed.

For the 30 deg spacing, the data were taken over a finer grid in the  $x$  direction and a space-time plot of these data is given in Fig. 9. These data, and those of Figs. 7 and 8, show that the leading wake of each group of four has a significant higher rms value than the subsequent wakes. This trend is particularly pronounced for the secondary wakes, which give a natural transition, but is also evident for the primary wakes, which are thought to give a bypass transition.

These trends are set out clearly in Fig. 10, representing the rms activity, at a  $y$  of 1 mm and an  $x$  of 0.8 m, for the spacing of 30 deg. For both primary and secondary wakes, it is clear that it is

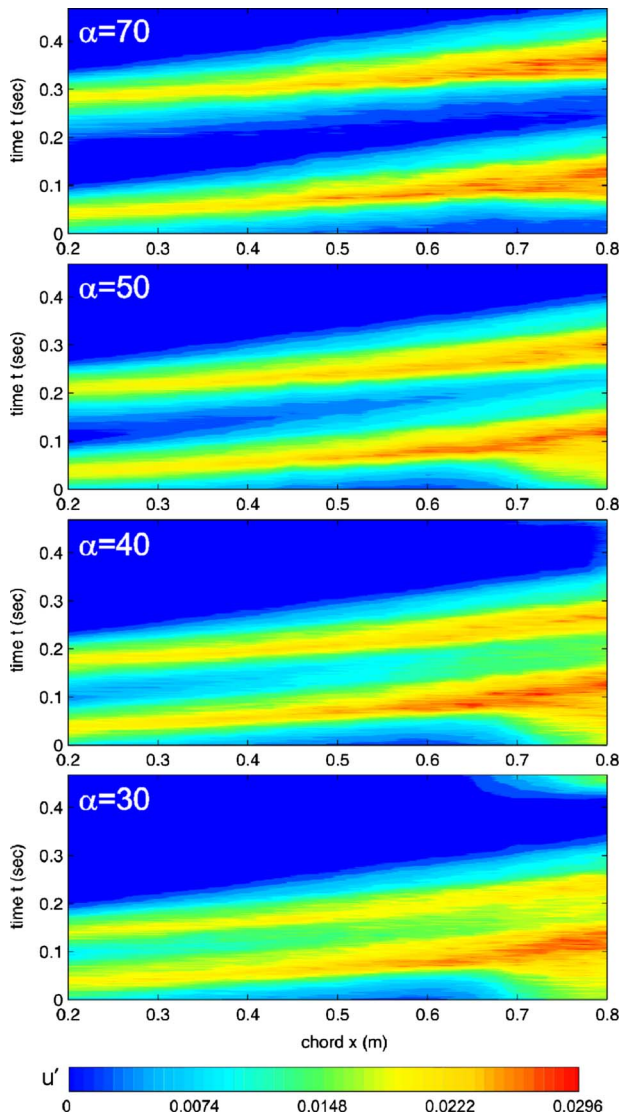


Fig. 5 Space-time plots of rms velocity perturbation for four different wake proximity settings. Data from  $\gamma=2.0$  mm.

the commencement of the turbulence that results in high rms but that the disturbance levels associated with all subsequent wakes are suppressed. As an example, for the primary wakes, the first wake of the series has a rms value of 1.45 m/s, whereas the peak values for the remaining three wakes vary from 0.99 m/s to 1.03 m/s with an average of 1.00 m/s. The disturbance level for the following wakes is very consistent and is, on average, 45% less than that of the first wake.

At this stage, it should be recalled that this behavior is associated with the incursion of the following wake into the calmed region of the leading wake.

As the first of the four wake-induced turbulent strips encounters the natural transition region of the boundary layer, the wake fails to induce fresh turbulence. For this reason the core of the strip begins to age and merge with the surrounding natural transition, resulting in reducing rms of velocity fluctuations. The leading edge of the natural transition, as it develops behind the calmed region of a far-downstream wake, consists of fresh turbulence and is represented as high values of rms.

As was seen in the paired-wake data [9], the following wake-induced turbulent strip of each pair would have identical core and tail features to the initial wake-induced turbulent strip until the calmed regions had grown sufficiently to encounter the turbulent strip leading edges. At this moment, the core of the following wake diminished in rms of velocity to values similar to those of the tail, making the two regions harder to distinguish. This suppression of rms was seen to be the result of the stabilizing influence of the calmed region from the downstream turbulent strip. The strength of this suppression was also seen to be proportional to the distance between each turbulent strip. This suppressive effect of the calmed region was quantified in Ref. [9].

To address the question of whether the stabilizing effects remained present in a multiwake environment, the multiple wake data were analyzed in a similar way to the paired-wake data. The new data were superimposed onto the paired-wake data as black symbols on Fig. 6. The ordinate is nondimensional, and shows the maximum value for  $u'$  in the core of the following strip normalized by the equivalent value for an isolated (unsuppressed) strip. The abscissa represents the turbulent strip spacing, nondimensionalized to one strip width. Unity therefore represents two strips with coincidental edges, i.e., without any space between them; less than unity represents an overlap, and values above unity give an increasing spacing.

Although it was only possible to extract three data points, they

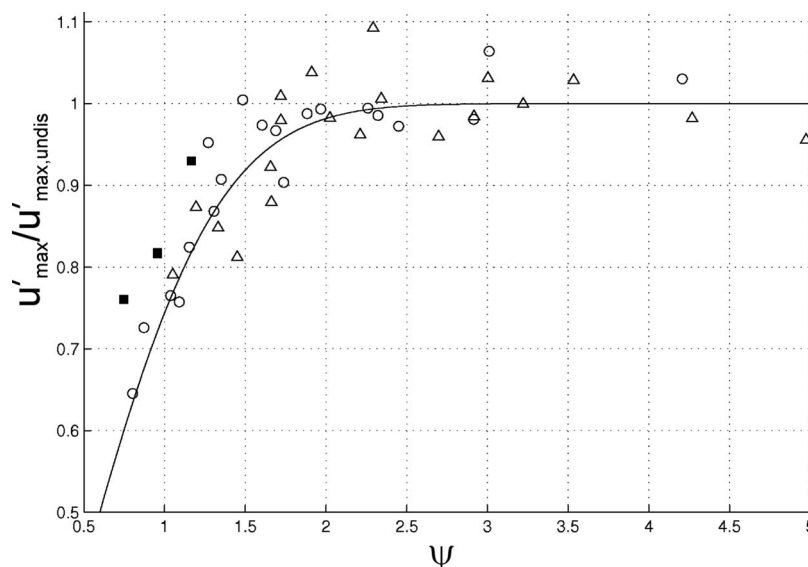


Fig. 6 Variation of peak rms velocity with wake proximity parameter,  $\psi$



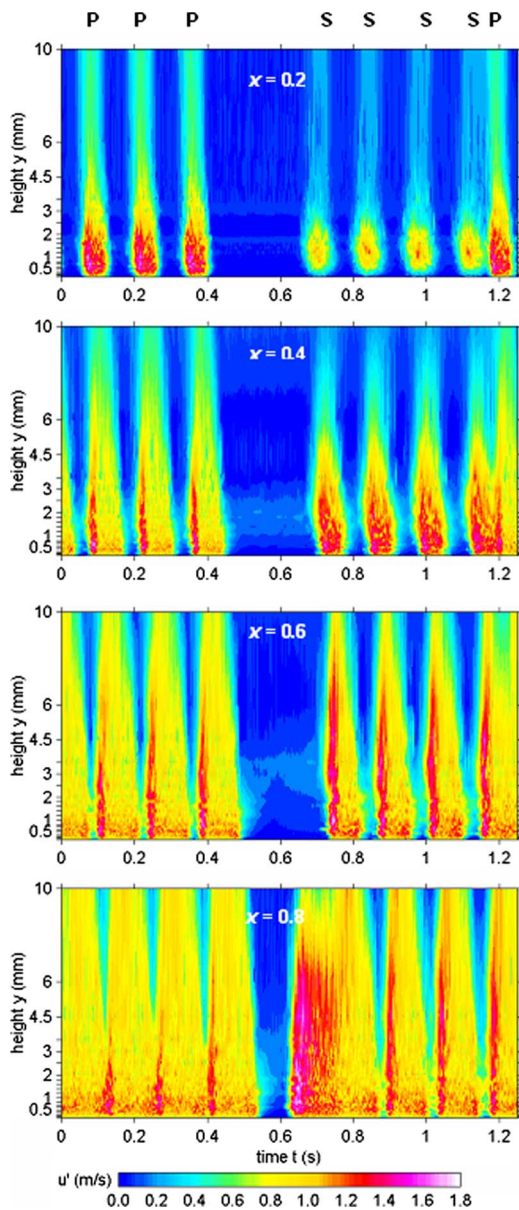


Fig. 7 Four pairs of wakes at 40 deg spacing

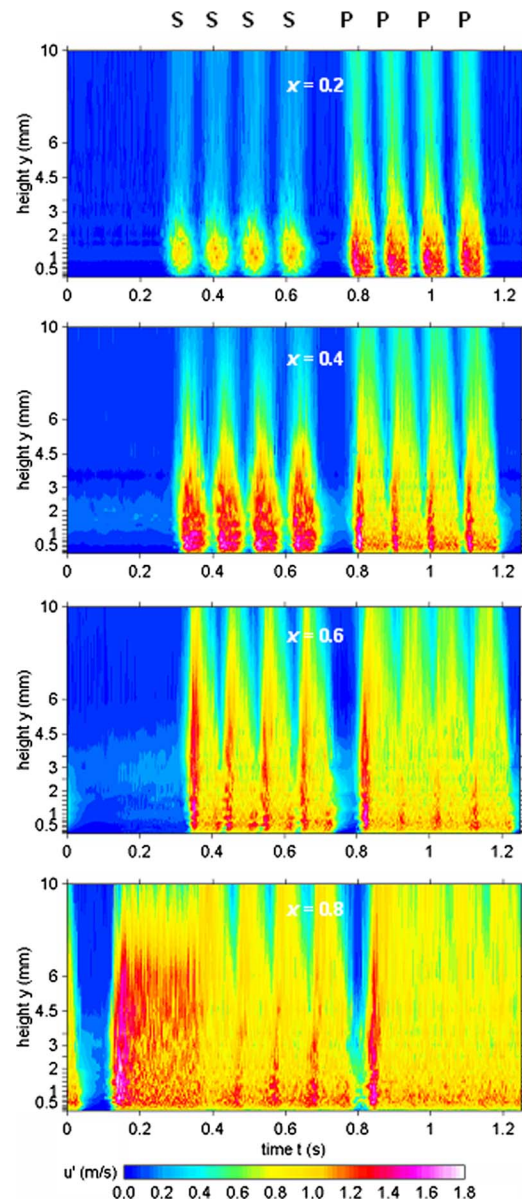


Fig. 8 Four pairs of wakes at 30 deg spacing

are in good agreement with the existing data, lying close to the projected curve fit. More importantly, the values themselves were constant between wake pairings. That is to say, although the new points appear to consistently lie slightly above the curve, the subsequent wake-induced turbulent strips were subjected to a similar degree of suppression or stabilization. There was no visible trend for a reducing suppressive effect with each successive turbulent strip.

This suggests that the strong calmed region induced by a wake interaction effect continues to exercise its stabilizing effect for the repeating wake environment of a turbomachine. Although its effects may not be directly observable, it is likely to be present when wakes follow each other closely. This may be counterintuitive when impressive results have been obtained for widely spaced high lift low pressure turbine blades but nevertheless it is a demonstrated effect that needs to be taken into account. It may also offer further prospective benefits if used judiciously.

## Conclusions

Similarities were observed in the responses of strongly diffusing flows in natural transition, under the stimulus of triggered

turbulent spots, in wake-disturbed boundary layers, and in an environment representative of compressor blading subject to multiple propagating wakes. The approach was to start with a relatively simple arrangement and build up to a more complex one more representative of the turbomachinery flow field.

In almost all turbomachines, wakes from upstream blade rows impinge on downstream blading. Very often, the wake impinges on a laminar boundary layer. Out of this impingement process, and triggered by it, arises a turbulent "strip." The turbulence on the blade surface may arise from a bypass mechanism or from natural growth of the turbulence.

This turbulent strip is nominally two-dimensional but has many of the characteristics of a turbulent spot. The strip is actually a spanwise ensemble of merged and merging turbulent spots. It might therefore be expected to exhibit some of the characteristics of the turbulent spot. One of these characteristics is the calmed region following the turbulent spot. Throughout these investigations, the influence of the calmed region has proved to be very strong. The calmed region and its effects were first noticed in

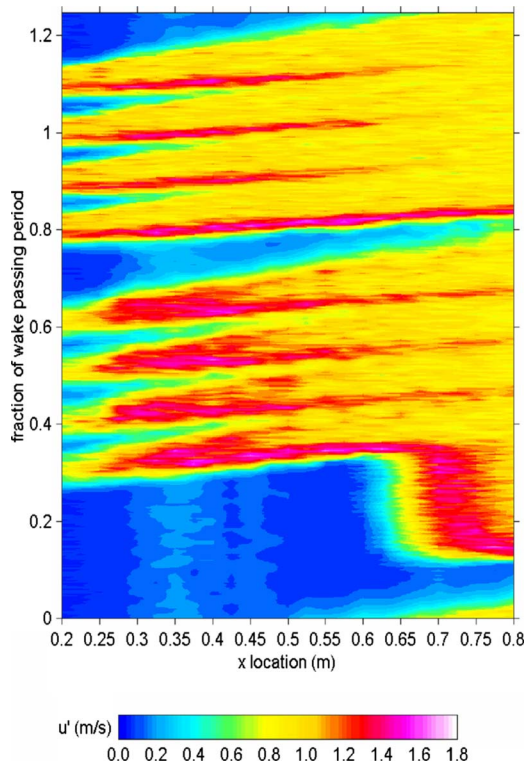


**Fig. 9 Space-time plots of rms velocity perturbation for four rods at 30 deg proximity setting**

investigations of single triggered spots. It has been found to be present in all cases investigated, and is particularly strong after a wake-induced turbulent strip.

When measurements are made in rotating machines, they often reveal such a calmed region, which is an exponential relaxation of the signal from the turbulent patch to the laminar state. This will show up if the time interval between the arrivals of successive wakes is sufficiently large to permit this relaxation. If the interval between wake arrivals is insufficient for this, then it will not be observed and the signal will proceed immediately from one patch of turbulence to the next. It had been assumed that in that situation the flow regime in that domain became turbulent and that the calmed region effect ceased to exist.

Gutmark and Blackwelder [8] were the first to investigate these interaction effects on triggered turbulent spots and their research suggested that when the spacing between the two spots became sufficiently reduced the leading edge celerity and fluctuation lev-

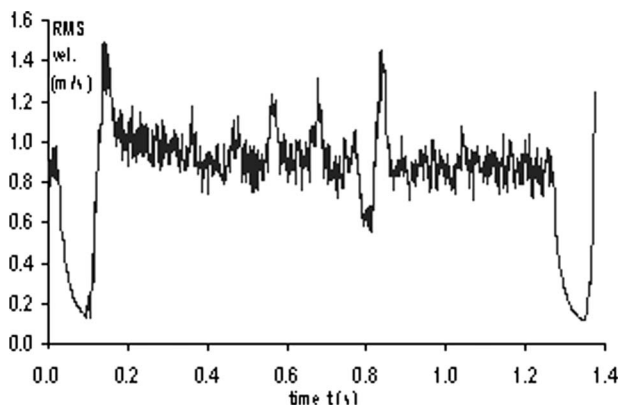


**Fig. 10 Timewise variation of rms velocity perturbation at  $y = 1$  mm,  $x = 0.8$  m, and a wake spacing of 30 deg**

els in the following spot were reduced. The research reported here was an attempt to determine whether similar effects apply to the interactions between turbulent patches in turbomachines as the spacing between upstream wakes is decreased systematically.

Although the impact of the spacing on celerity of the following wake was not observed in these tests, a significant and systematic effect of the closer proximity on the rms turbulence levels of the following wake was observed. As the spacing was reduced, such that the following wake moved into the domain that would have been occupied by the calmed region, its own turbulence intensity was systematically reduced.

By introducing multiple wakes, it was found that the calmed region continues to suppress turbulence in a repetitive wake situation typical of a turbomachine. There, therefore, exist some inherent degree of stabilization and reduced disturbance level due to the calming effect. The strong calmed region induced by a wake interaction effect continues to exercise its stabilizing effect for the repeating wake environment.

It is here suggested that these effects are at work in rotating machines. It had previously been thought that the calming effect needed a sufficient interval between wakes for the calmed region to be manifested and to exert its stabilizing effect. It now appears that that is not the case and that a calming effect remains at work even when its domain coincides with that of the following turbulent patch. This has the effect of reducing the violence of the turbulence and therefore continuing to stabilize the flow. This would almost certainly have a beneficial effect on the efficiency of the machine.

This condition of close proximity between the wake-induced turbulent patches is a common one for turbomachines, especially toward the trailing edge of any blade row. This effect of calming might therefore be expected to be at work in most turbomachines, exerting a beneficial influence at all times. Although this is difficult to detect, the calmed region is acting to suppress disturbances even within the turbulent region of a wake-induced patch. It is therefore acting but undetected in many practical turbomachinery situations resulting in hidden benefits for blade count and efficiency.

The practical benefits of the calmed region have been demonstrated for low pressure turbines; this work suggests that similar benefits, affecting both efficiency and loading capability, might exist for axial compressor blading. These benefits need to be understood thoroughly if they are to be utilized effectively in blade design.

### Acknowledgment

This work was funded by a research grant from the Engineering and Physical Sciences Research Council.

### Nomenclature

- $C_p$  = pressure coefficient,  $(p - p_{ref}) / (P_0 - p_{ref})$
- $L$  = plate length
- $P_0$  = total pressure
- $p$  = static pressure
- $t$  = time
- $u_{x,y,t}$  = instantaneous velocity in space and time
- $x$  = chordwise distance from leading edge
- $y$  = distance normal to plate surface
- $U_\infty$  = freestream velocity
- $u$  = local velocity
- $\alpha$  = paired rod circumferential displacement, deg
- $\beta$  = Hartree pressure gradient parameter
- $\gamma$  = intermittency
- $\psi$  = nondimensional wake spacing

### Superscripts and Subscripts

- ' = prime-rms of value
- $\langle \rangle$  = ensemble average value
- ref = reference value

## References

- [1] Gostelow, J. P., Blunden, A. R., and Walker, G. J., 1994, "Effects of Free-Stream Turbulence and Adverse Pressure Gradients on Boundary Layer Transition," *ASME J. Turbomach.*, **116**, pp. 392–404.
- [2] Gostelow, J. P., Melwani, N., and Walker, G. J., 1996, "Effects of Streamwise Pressure Gradient on Turbulent Spot Development," *ASME J. Turbomach.*, **118**, pp. 737–743.
- [3] D'Ovidio, A., Harkins, J. A., and Gostelow, J. P., 2001, "Turbulent Spot in Strong Adverse Pressure Gradients—Part I: Spot Behaviour," ASME Paper No. 2001-GT-0194.
- [4] D'Ovidio, A., Harkins, J. A., and Gostelow, J. P., 2001, "Turbulent Spot in Strong Adverse Pressure Gradients—Part II: Spot Propagation and Spreading Rates," ASME Paper No. 2001-GT-0406.
- [5] Gostelow, J. P., Walker, G. J., Solomon, W. J., Hong, G., and Melwani, N., 1997, "Investigation of the Calmed Region Behind a Turbulent Spot," *ASME J. Turbomach.*, **119**, pp. 802–809.
- [6] Halstead, D. E., Wisler, D. C., Okiishi, T. H., Walker, G. J., Hodson, H. P., and Shin, H.-W., 1997, "Boundary Layer Development in Axial Compressors and Turbines: Part 1–4," *ASME J. Turbomach.*, **119**(1), pp. 114–127.
- [7] Gostelow, J. P., and Thomas, R. L., 2005, "Response of a Laminar Separation Bubble to an Impinging Wake," *ASME J. Turbomach.*, **127**, pp. 35–42.
- [8] Gutmark, E., and Blackwelder, R.F., 1987, "On the Structure of a Turbulent Spot in a Heated Laminar Boundary Layer," *Exp. Fluids*, **5**, pp. 207–229.
- [9] Thomas, R. L., and Gostelow, J. P., 2005, "The Pervasive Effect of the Calmed Region," ASME Paper No. GT2005-69125.
- [10] Hartree, D. R., 1937, "On an Equation Occurring in Falkner and Skan's Approximate Treatment of the Equations of the Boundary Layer," *Proc. Cambridge Philos. Soc.*, **33**, pp. 225–239.
- [11] Gostelow, J. P., and Thomas, R. L., 2006, "Interactions Between Propagating Wakes and Flow Instabilities in the Presence of a Laminar Separation Bubble," ASME Paper No. GT2006-911935.
- [12] Gostelow, J. P., 2003, "On the Role of Intermittency in the Closure of Laminar Separation Bubbles," *Advances in Fluid Mechanics*, M. Alam, R. Govindarajan, O. N. Ramesh, and K. R. Sreenivas, eds., JNCASR, Bangalore, pp. 188–199.
- [13] van Hest, B. F. A., 1996, "Laminar-Turbulent Transition in Boundary Layers With Adverse Pressure Gradient," Ph.D. thesis, Delft University of Technology.
- [14] Thomas, R. L., 2004, "Closure of a Laminar Separation Bubble by Natural and Wake-Induced Transition," Ph.D. thesis, University of Leicester.



# Film Cooling From a Row of Holes Supplemented With Antivortex Holes

Alok Dhungel

Yiping Lu

Wynn Phillips

Mechanical Engineering Department,  
Louisiana State University,  
Baton Rouge, LA 70803

Srinath V. Ekkad<sup>1</sup>

Mem. ASME  
Mechanical Engineering,  
Virginia Tech,  
Blacksburg, VA 24060  
e-mail: sekkad@vt.edu

James Heidmann

Turbomachinery and Heat Transfer Branch,  
NASA Glenn Research Center,  
Cleveland, OH 44135-3191

*The primary focus of this paper is to study the film cooling performance for a row of cylindrical holes each supplemented with two symmetrical antivortex holes, which branch out from the main holes. The antivortex design was originally developed at NASA-Glenn Research Center by James Heidmann, coauthor of this paper. This “antivortex” design is unique in that it requires only easily machinable round holes, unlike shaped film cooling holes and other advanced concepts. The hole design is intended to counteract the detrimental vorticity associated with standard circular cross-section film cooling holes. The geometry and orientation of the antivortex holes greatly affect the cooling performance downstream, which is thoroughly investigated. By performing experiments at a single mainstream Reynolds number of 9683 based on the freestream velocity and film hole diameter at four different coolant-to-mainstream blowing ratios of 0.5, 1, 1.5, and 2 and using the transient IR thermography technique, detailed film cooling effectiveness and heat transfer coefficients are obtained simultaneously from a single test. When the antivortex holes are nearer the primary film cooling holes and are developing from the base of the primary holes, better film cooling is accomplished as compared to other antivortex hole orientations. When the antivortex holes are laid back in the upstream region, film cooling diminishes considerably. Although an enhancement in heat transfer coefficient is seen in cases with high film cooling effectiveness, the overall heat flux ratio as compared to standard cylindrical holes is much lower. Thus cases with antivortex holes placed near the main holes certainly show promising results. [DOI: 10.1115/1.2950059]*

## Introduction

Advanced gas turbine engines operate at high temperatures (2500–2600°F) to improve thermal efficiency and power output. This temperature range is far above the permissible metal temperature. Cooling of blades is thus indispensable for safe operation, to increase the component life and reduce maintenance costs. Turbine blades are cooled both internally and externally. Internal cooling is achieved by passing the bleed air through several long turbulated serpentine passages with ribs, impingement holes, and pin fins for heat transfer enhancement. External cooling, also known as film cooling, is achieved by ejecting the internal coolant air through discrete holes drilled at several locations on the blade exterior surface. This coolant film protects the outside surface of the blade from the hot combustion gases. Simple angle holes, which are angled only in the flow directions, are used and are sufficient for low temperature operations. For better performance, cooling holes with compound angles, diffuser shaped expansions, and holes in slots are used. Increase in lateral momentum in compound angle holes, decrease in axial velocity in the shaped holes, and reduced jet momentum and 2D jet coverage in slots lead to an increase in cooling efficiency. This jet spreading provides a better lateral coverage; thus a higher laterally averaged cooling efficiency is obtained.

This study aims to investigate the geometry and orientations of supplemental antivortex holes on the film cooling effectiveness and heat transfer over a flat plate and turbine airfoil surfaces. The coolant flow from the antivortex holes reduces the strength of the

kidney shaped pair of vortices generated by the coolant exiting the main hole. This allows for better attachment of the coolant to the blade surface downstream. The basic aim of this study is to optimize such a configuration of antivortex holes, which would minimize the shear stresses and eddies due to mainstream and jet interaction at the sides of the main hole and strengthen the coolant jet from the main holes so as to get a better overall film cooling coverage.

Several studies have investigated compound hole injection. Ligrani et al. [1,2] studied the effects of compound angle injection for a single row and two staggered rows of holes. They pointed out that compound angle injection significantly improved film cooling as compared to simple angled hole keeping all other parameters constant. Sen et al. [3] and Schmidt et al. [4] compared simple angle injection to compound angle injection and shaped hole injection. Although they provided both heat transfer coefficient and film effectiveness results, the former data were very sparse. Ekkad et al. [5,6] provided detailed surface heat transfer measurements using the transient liquid crystal technique. Likewise, there have been a number of studies on film cooling by shaped holes. Makki and Jakubowski [7] used forward-expanded holes and studied its effect. Sen et al. [3] and Schmidt et al. [4] compared simple angled holes and compound angled holes to shaped holes and found out that the shape hole with forward expansion provided significantly larger lateral film coverage than both the other cases. Gritsch et al. [8,9] presented both discharge coefficients and film cooling effectiveness for three hole geometries. They compared simple angle cylindrical holes, fan shaped holes, and laidback fan shaped holes. From their results, they indicated that laidback fan shaped holes provide higher laterally averaged film cooling effectiveness due to increased lateral spreading of jets. Dittmar et al. [10] presented an assessment of various film hole configurations in a simulated turbine surface experiment. They indicated that shaped holes with compound angle produce the best effective cooling compared to the other geometries.

<sup>1</sup>Corresponding author.

Contributed by the International Gas Turbine Institute of ASME for publication in the JOURNAL OF TURBOMACHINERY. Manuscript received June 11, 2007; final manuscript received December 5, 2007; published online January 22, 2009. Review conducted by Je-Chin Han. Paper presented at the ASME Turbo Expo 2007: Land, Sea and Air (GT2007), Montreal, Quebec, Canada, May 14–17, 2007.



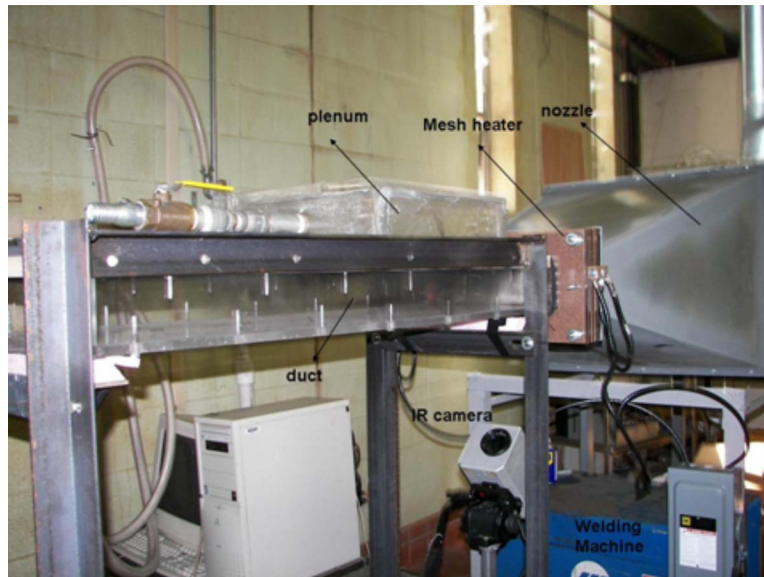


Fig. 1 Experimental set up

Sargison et al. [11] studied a converging slot-hole geometry in which the hole transitions from circular to slot with convergence in the axial direction and divergence laterally. The attempt was to make the three-dimensional nature of the jet into a two-dimensional slot film. The results were aimed at improving effectiveness. Lu et al. [12] introduced a crescent shaped exit geometry and compared it with the base line cylindrical hole exit and the converging slot-hole geometry. They showed that the crescent exit performed well at all blowing ratios producing almost an effectiveness of 0.7–0.9 within three to five hole diameters downstream and high effectiveness values of 0.4 at  $X/D \sim 15$ . The converging hole-slot geometry was also effective and similar to the crescent shape geometry. Most of the above studies with shaped hole focused on reducing the upward momentum of the jets by increasing the hole exit area or transforming the hole to slots. The present study focuses on producing similar results using the antivortex air as supplemental holes without altering the hole exit area.

The present study utilizes a transient infrared thermography technique for obtaining both heat transfer coefficient and film effectiveness from a single test. The transient IR technique, which requires a single test to solve two equations, was proposed by Vedula and Metzger [13] and was demonstrated successfully by Ekkad et al. [14]. Simultaneous  $\eta$  and  $h$  distributions are measured and presented on the flat surface downstream of injection for various blowing ratios for cylindrical holes, shaped holes, and six different cases of cylindrical holes supplemented with antivortex holes. The origin of the design was basically generated at NASA-GRC by Jim Heidmann. A companion computational fluid dynamics (CFD) study by Heidmann and Ekkad [15] evaluates the detailed flow features associated with the antivortex hole design. The experimental results will be compared to the CFD study in that paper.

One concern for this design is the limit on how small the side holes may be from either manufacturing or functional viewpoints. Bunker [16] indicated that film cooling holes may be laser drilled to a very small size, albeit with increasing relative geometrical errors. A greater concern may be the issue of plugging of the side holes from dust and particles in the cooling air. The present study considers side holes half the diameter of the standard-size main hole. However, if needed the entire arrangement may be enlarged by a factor of 2 to keep the smallest hole size the same. In this case, the hole pitch-to-diameter ratio would need to be doubled

(raw pitch increased by a factor of 4) to maintain the coolant hole inlet flow area and approximate coolant flow rate for a given plenum pressure.

### Test Facility

A pictorial view of the experimental setup is shown in Fig. 1. Room temperature air from blower is passed through a converging nozzle, which has its exit attached to the mesh heater. The heater is built with a 304 stainless steel woven wire mesh with a  $20 \mu\text{m}$  wire diameter. The free area of the mesh was 33.6%, which greatly reduced the freestream turbulence before the test section. Figure 2 shows the layout of mesh heater.

The low electrical resistance of the dense wire mesh necessitated the use of a low voltage, high amperage power source. Power was supplied to the heater using a Miller Dialrc 250 AC/DC TIG welding machine. The heater provides a true step rise in the temperature of the mainstream air for the experimental needs. The mainstream temperature is monitored throughout the test. To obtain a desired temperature rise of about  $18^\circ\text{C}$  for the mainstream air, two similar mesh heaters were connected in parallel and placed in line of the 9-cm-high and 30-cm-wide test section.

The test section is made of Plexiglas and has a cross section of 30 cm width and 9 cm height. The top plate of the test section is made of 3-cm-thick ABS. This plate has a replaceable section about 25.4 cm downstream of the test section inlet and the boundary layer trip. This replaceable section can be interchanged to

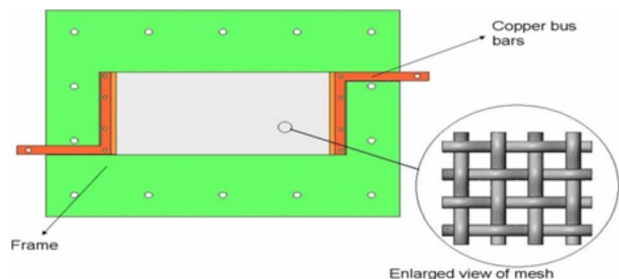


Fig. 2 Layout of mesh heater

change the hole geometry. The 3.2-mm-diameter trip is placed at the entrance to the test section to produce a fully turbulent boundary layer over the test plate. The coolant air is provided from a separate compressed air supply and is metered for flow measurement. When the valve is flipped, the coolant enters a plenum below the test plate and is then ejected through the film cooling holes into the test section. Thermocouples are mounted upstream of the hole row to measure the mainstream temperature and inside one of the holes to measure the coolant exit temperature. The coolant temperature is measured inside only one hole because pretesting showed that all film holes had the same flow rate and temperature conditions.

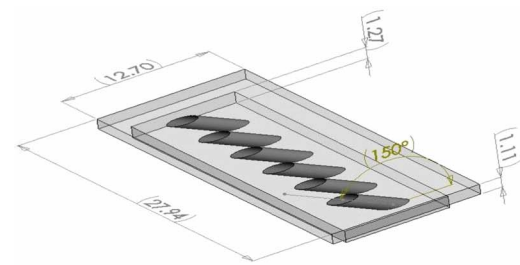
The infrared thermography system used is an FLIR Systems ThermaCAM SC 500. The camera has a range of  $-40$ – $500^{\circ}\text{C}$ . The ThermaCAM 500 utilizes uncooled microbolometer long-wave detectors to sense IR radiation. This makes them ideal for general thermal measurement applications. The SC 500 system provides real time 14 bit digital output, a  $320 \times 240$  pixel detector, precision temperature measurement, internal data storage, and outstanding thermal sensitivity. The camera has following specifications: the field of view and minimum focus distance are  $24 \text{ deg} \times 18 \text{ deg}$  and  $0.5 \text{ m}$ , respectively, the spectral range is  $7.5$ – $13 \mu\text{m}$ , and accuracy is  $\pm 2\%$  or  $2^{\circ}\text{C}$ . The accuracy was further calibrated using a 36-gage thermocouple and adjusting the emissivity and transmissivity to less than  $0.5^{\circ}\text{C}$ . The test surface is viewed through a stretched polyurethane sheet. The sheet is thin enough to cause very little effect on IR transmissivity. The system calibration is conducted using a thermocouple placed on the black painted test surface to act as the benchmark. This thermocouple is used to estimate the emissivity of the test surface. The emissivity of the black painted test when viewed without the window is  $0.96$ . The calibrated transmissivity for the polyurethane sheet was  $0.75$ .

Figure 3(a) shows the base line test plate with film hole geometry used in this study. There are six holes of  $1.27 \text{ cm}$  diameter in each row inclined at  $30 \text{ deg}$  along the flow direction. The hole spacing between adjacent holes is three-hole diameters for all the holes. Figure 3(b) shows the test plate with shaped holes. For these diffuser holes, the hole inclination angle is set at  $30 \text{ deg}$  and the length of the cylindrical inlet portion is twice the diameter of the hole. The hole compound angle is  $15 \text{ deg}$ . Figure 3(c) shows the test plate with the antivortex holes. The orientations and other geometries of the primary film cooling hole are the same as the base line; only the features of the antivortex film cooling holes are altered. Six different geometries are investigated. The details of the geometry are presented in Figs. 4(a) and 4(b) and Table 1.

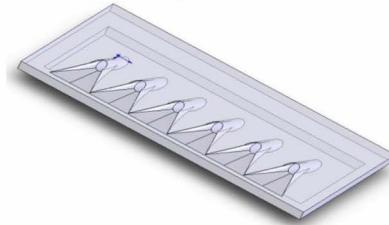
The measured mainstream velocity and freestream turbulence upstream of the hole row using a calibrated single hot wire probe are  $13.8 \text{ m/s}$  and  $2\%$ , respectively. The mainstream Reynolds number ( $Re_d$ ) based on film hole diameter is  $11,000$ . The boundary layer profile measured downstream of the trip is close to the fully turbulent flow profile ( $1/7$ th law). The momentum thickness Reynolds number ( $Re_\theta$ ) just upstream of the hole is  $511$  and the corresponding boundary layer thickness is  $9.87 \text{ mm}$ . Four blowing ratios,  $M=0.5, 1.0, 1.5,$  and  $2.0$ , are tested for all the eight cases.

## Procedure

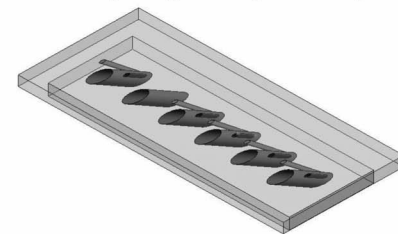
Prior to the actual thermal measurements, calibration of the entire thermography system and the IR signal is required. A thermocouple is mounted on the test surface by aluminum tape. Its location is outside the measurement region to avoid the interference caused by the aluminum tape. The test surface is then sprayed with flat black paint to increase its emissivity. The IR camera is focused on the test surface; the field of view of which also encompasses the thermocouple. The test surface is then heated by the mainstream hot air and thermocouple reading is noted until the plate comes to a steady state. Next, the temperature recorded by the thermocouple is compared to that by the IR camera. A number of factors, such as distance between the front lens and the test surface, relative humidity, and background tempera-



(a) Test plate geometry for baseline case



(b) Test plate geometry with shaped holes



(c) Test plate geometry with anti-vortex holes

**Fig. 3 (a) Test plate geometry for base line case, (b) test plate geometry with shaped holes, and (c) test plate geometry with anti vortex holes**

ture, affect the temperature measured by the IR system. Multiple calibrations at different temperatures should be carried out to minimize the error that creeps in out of these factors. A number of temperatures are used to determine the correct emissivity of the test surface. During the emissivity calculation, polyethylene sheet window was not used. So, the transmissivity value used was 1.

In order to determine the transmissivity of the polyethylene window, similar test was conducted with the window in place. With the known emissivity from the prior test, transmissivity of the window was altered until the IR camera readings coincided with the thermocouple readings. The transmissivity found from this technique matched closely with the factory specified value.

The test starts when the mainstream air is heated with a step rise in temperature by the mesh heater and the coolant air is passed into the film cooling holes exactly at the same time. The temperature measurement also starts at that instant. The mainstream air is typically heated  $18$ – $20^{\circ}\text{C}$  from its prior room conditions. The coolant air that is supplied by a compressed air storage tank is about a degree lower than the room temperature. The hot mainstream air forces the inner test surface to heat gradually while the outside remains unaffected. Thus the test surface was modeled as a semi-infinite solid medium imposed by a sudden transient heating. The entire solid medium was initially at a uniform temperature before the transient test. During the transient heating test, each point on the surface will respond with different temperatures at different times due to different heat transfer rates. Faster time of temperature change in response to the prescribed temperature during the transient test will produce higher heat transfer coefficient and vice versa.

The test surface is modeled as undergoing 1D transient conduction with convective boundary conditions at the wall. Applying

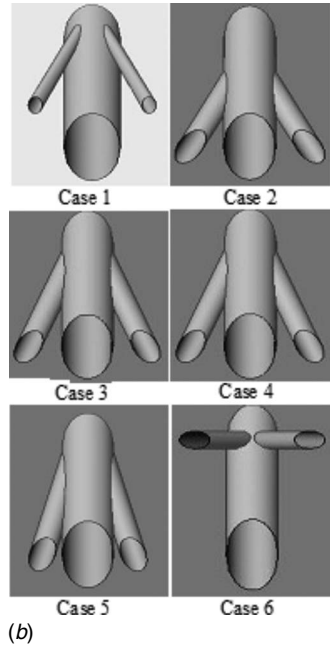
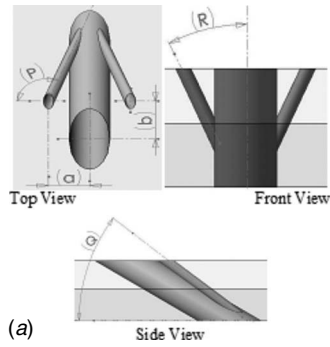


Fig. 4 (a) Generic orthographic views of the anti vortex configurations and (b) top view of the six cases

the prescribed boundary conditions and initial conditions to the problem and solving for the wall temperature response with time at the wall produces a solution of the form

$$\frac{T_w - T_i}{T_\infty - T_i} = 1 - \exp\left(\frac{h^2 \alpha t}{k^2}\right) \operatorname{erfc}\left(\frac{h\sqrt{\alpha t}}{k}\right) \quad (1)$$

where  $h$  is the unknown quantity in the equation with  $T_w$  the wall temperature at time  $t$  after the initiation of the transient test. The material properties,  $\alpha$  ( $0.1076 \times 10^{-6} \text{ m}^2/\text{s}$ ) and  $k$  ( $0.187 \text{ W/m K}$ ), dictate the applicability of the semi-infinite solid

solution. The above equation assumes that the oncoming mainstream flow imposes a step change in air temperature on the surface, which is true; hence the usage of Duhamel's superposition theorem is not needed.

In film cooling situations, the basic convective heat load equation is modified to include the film temperature based on the definition of the local heat flux. The equation becomes

$$\frac{T_w - T_i}{T_f - T_i} = 1 - \exp\left(\frac{h_f^2 \alpha t}{k^2}\right) \operatorname{erfc}\left(\frac{h_f \sqrt{\alpha t}}{k}\right) \quad (2)$$

where  $T_f$  is the local film temperature and is a function of the local mixing between the mainstream and coolant jet near the surface.

Vedula and Metzger [13] presented a method wherein two liquid crystal color change times can be obtained from a single transient test at every location. During the transient test, the liquid crystal coating indicates one surface temperature ( $T_{w1}$ ) at time  $t_1$  and another surface temperature ( $T_{w2}$ ) at time  $t_2$ . Basically, two events are measured at every point, leading to the solution of both  $h$  and  $T_f$  from the simultaneous solution of the two equations:

$$\begin{aligned} \frac{T_{w1} - T_i}{T_f - T_i} &= 1 - \exp\left(\frac{h_f^2 \alpha t_1}{k^2}\right) \operatorname{erfc}\left(\frac{h_f \sqrt{\alpha t_1}}{k}\right) \\ \frac{T_{w2} - T_i}{T_f - T_i} &= 1 - \exp\left(\frac{h_f^2 \alpha t_2}{k^2}\right) \operatorname{erfc}\left(\frac{h_f \sqrt{\alpha t_2}}{k}\right) \end{aligned} \quad (3)$$

In the transient test, the mainstream will be heated and the coolant supply will be near room temperature. The wall temperatures are captured at set instants of time over the entire surface. Twenty separate events are recorded at an equal interval of 2 s and the wall temperatures at every surface location are obtained from the IR images. The mainstream temperature response is also measured. The two equations shown above can be solved simultaneously even with only two known wall temperatures at the same locations and both unknowns  $h$  and  $\eta$  can be determined. This has been demonstrated successfully by Ekkad et al. [14] for a single hole injecting coolant onto a leading edge model. In this study, all the 20 wall temperatures were used for a regression analysis that minimized the error while calculating  $h$  and  $\eta$  in a least squared sense so that the value determined had a best fit for all the data.

The mesh heater was designed to provide a true step change in air temperature at the start of a test. The true step change in mainstream temperature allows the use of the original solution to the transient heating of the wall, Eq. (1). This also helped to reduce the overall time duration of the experiment to under 20 s. The regression technique used to reduce uncertainty in experimental measurements was to collect multiple wall temperature-time data pairs over a broad range of temperatures to use in an over-constrained system of equations to solve for  $h$  and  $\eta$ . The regression analysis put all terms of the conduction equation to the right-hand side of the equation and was solved for all points of data for each pixel. This resulted in a residual error for each time-

Table 1 Tabulated values of detailed geometry of six cases

	Case 1	Case 2	Case 3	Case 4	Case 5	Case 6
$d$ (cm)	0.32	0.63	0.63	0.63	0.63	0.63
$D$ (cm)	1.27	1.27	1.27	1.27	1.27	1.27
$A$	1.27	1.42	1.42	1.42	1.12	1.4
$B$	1.6	0	0	-0.56	0	4.12
$P$	109.16	110.95	106.56	105.67	101.56	0
$Q$	36.76	30	30	26.41	30	90
$R$	24.95	34.74	27.21	27.91	19.43	30.62
Start of antivortex holes	Lower end of the main hole	Middle of the main hole	Lower end of the main hole	Lower end of the main hole	Lower end of the main hole	Lower end of the main hole



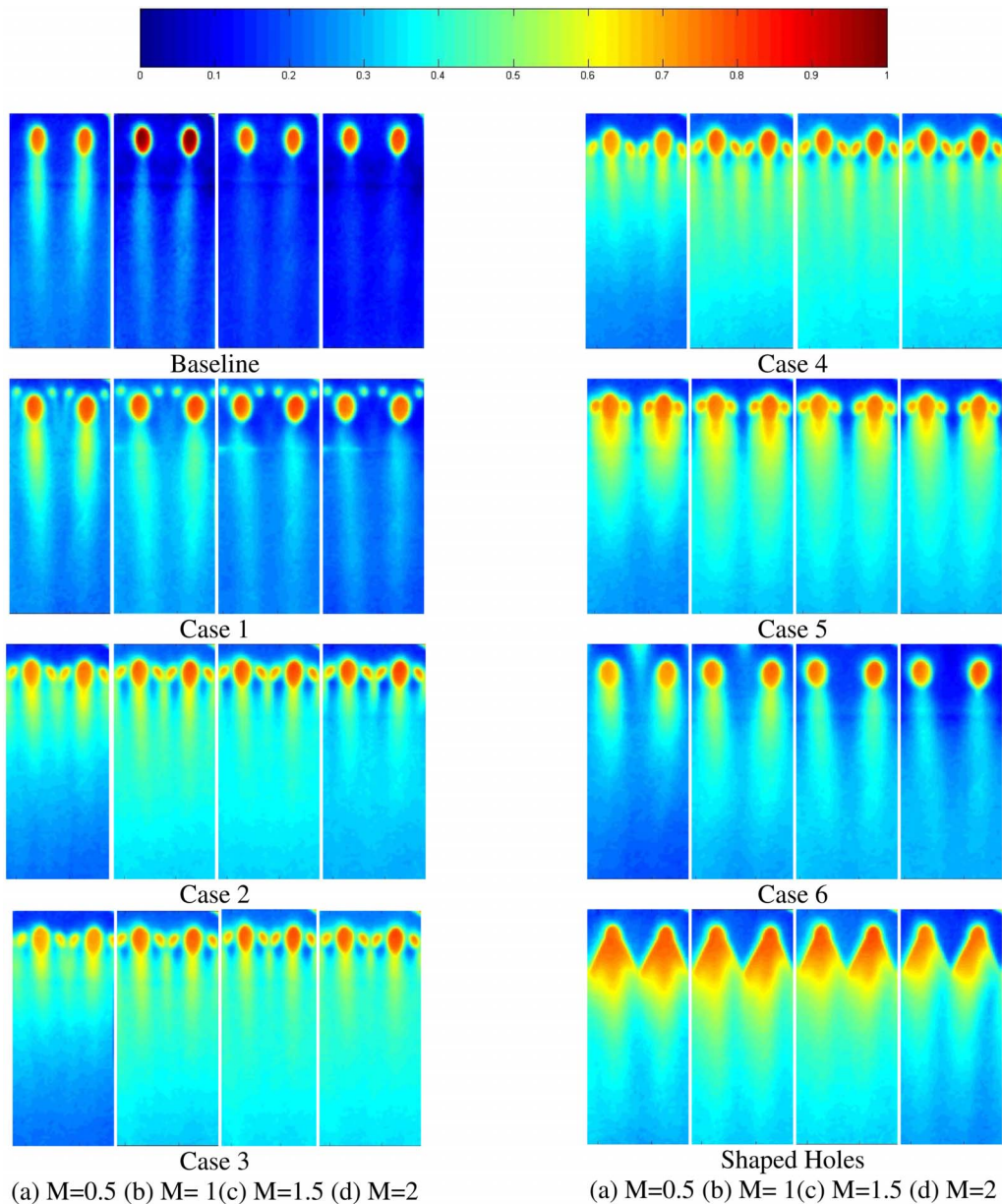


Fig. 5 Detailed film effectiveness distributions for all cases at different blowing ratios

temperature data pair. The residual error was minimized in a least squared sense solving for the heat transfer coefficient that best fits all data.

Uncertainty in the calculation comes from measurement of initial, mainstream, and coolant temperatures. Estimated uncertainty in initial and wall temperature ( $\Delta T_i$ ) is  $\pm 0.5^\circ\text{C}$ , mainstream temperature ( $\Delta T_\infty$ ) is  $\pm 0.5^\circ\text{C}$ , and coolant temperature ( $\Delta T_c$ ) is  $\pm 0.5^\circ\text{C}$ . The camera frame rate is 60 Hz, resulting in a time error of  $\pm 1.6\%$  and the test surface property uncertainty is estimated at  $\pm 3\%$ . The resulting *average* uncertainties using the methodology proposed by Kline and McClintock [17] for heat transfer coefficient and film effectiveness are  $\pm 4.5\%$  and  $\pm 7.0\%$ , respectively. However, uncertainty for local film effectiveness depends on the local value. Uncertainty for effectiveness measurements is  $\pm 0.03$ .

## Results and Discussion

Figure 5 shows the effect of blowing ratio on detailed film effectiveness distributions for all the eight cases. For the base line case, the jet streaks are clearly visible with the highest effective-

ness occurring at  $M=0.5$ . At higher blowing ratios, there is a jet lift-off resulting in lower coverage. There is almost no film effectiveness for  $M=2.0$ . For Case 1, the vortex holes are  $\frac{1}{4}$  the size of the main hole and exit upstream of the main hole. The trend is similar to the base line case except for the higher effectiveness than base line. The antivortex pair causes reduced flow through the main hole and also supplements the overall coverage in the region between the holes. It appears that the antivortex holes produce a small but unsustainable vortex pair counter to the main vortex pair. It is clearly visible that the highest effectiveness occurs at the lower blowing ratio of 0.5. The effect of this antivortex pair appears to mainly reduce the coolant momentum flux from the main holes. For Case 2, the antivortex pair holes are  $\frac{1}{2}$  the size of the main holes and the entry of the antivortex pair is halfway into the main hole. The jet interactions from the two adjacent antivortex holes are very prominent. The best film cooling effectiveness is seen for blowing ratio 1. The two holes from the adjacent antivortex pairs interact between the main holes and produce another jet streak similar to the main holes. Further downstream,

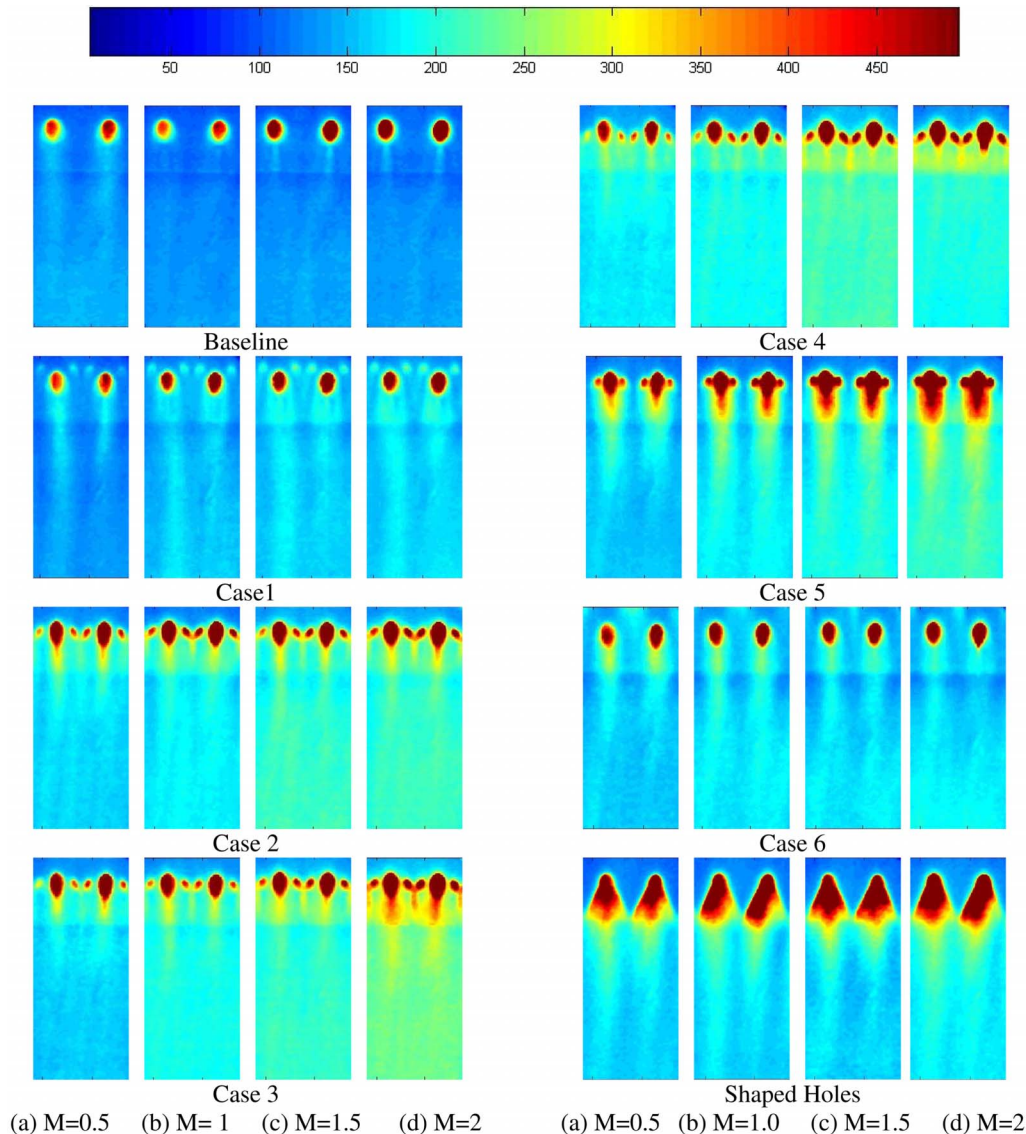


Fig. 6 Detailed heat transfer coefficient distributions for all cases at different blowing ratios

the jet streaks coalesce and produce an almost uniform spanwise effectiveness distribution. However, as the blowing ratio goes beyond  $M=1.0$ , the effectiveness deteriorates rapidly. In Case 3, the antivortex holes emerge out from the base of the main holes and are  $\frac{1}{2}$  the size of the main holes. Thus a more developed coolant flow can be expected from the antivortex holes than Case 2. Higher film cooling effectiveness can be seen even for higher blowing ratios. The spanwise and downstream coverage increases with blowing ratio. The only drawback is that the region adjacent to the main holes remains uncooled for higher blowing ratios. Case 4 is similar to Case 3 except that the exit of antivortex holes is farther downstream than for Case 3. The result looks similar to that of Case 3. Better attachment of the film jets to the surface can be seen even for higher blowing ratio. The additional length to the antivortex pair holes does not provide significant benefit although there are some minor differences between Cases 3 and 4. Case 5 has the exit of antivortex holes very close to the main holes. The jets from the antivortex holes mix with that from the main holes for all blowing ratios and thus create a thicker coolant streak footprint than all the other cases. However, the effectiveness distribution does not show a lateral spread as in Cases 3 and 4. The effectiveness also appears to peak at  $M=1.5$  with similar levels at  $M=2.0$ . Case 6 has its antivortex holes coming laterally outward

from the base of the main film cooling holes. At higher blowing ratio, the antivortex jets seem to lift off clearly. However, the presence of the antivortex holes causes a decrement in the momentum of exit of jet from the main hole (due to less mass flow rate), thus restricting lift off even at a blowing ratio of 1.5. This appears to cause effectiveness to be slightly better than base line but does not contribute to significant effects, as seen for Cases 2–5. For shaped holes, the effectiveness distributions for blowing ratios of 1 and 1.5 indicate better lateral and downstream coverage. The larger exit area in shaped holes reduces the exit velocity of the coolant jet and hence the film remains adhered to the blade surface. At a higher blowing ratio of 2, the coolant jet, however, has greater momentum to lift-off, producing lower effectiveness than for  $M=1.5$ . We also notice the classic diffuser separation phenomena at high blowing ratios, resulting in skewed effectiveness profiles inside the holes.

Figure 6 presents the effect of blowing ratio on detailed heat transfer coefficient ( $h$ ) distributions for the same eight cases. All the cases appear to enhance the heat transfer coefficient as compared to the base line case. The area in the vicinity of the exit of primary and antivortex coolant jets in the downstream region appears to have high heat transfer coefficient. This is due to the result of interaction between the jet (both primary and antivortex)



and the mainstream, which produces region of high turbulence. Except for cases where there is lift-off of the coolant jet, the high heat transfer coefficient region seems to extend far downstream. It appears that Case 5 enhances heat transfer coefficient the most because of the strong interaction between the antivortex pair and the main hole. The higher heat transfer coefficients for the shaped hole may be a direct result of the flow separation inside the shaped hole, leading to larger than expected heat transfer coefficient values.

Figure 7 presents the effect of antivortex hole geometry and orientations on spanwise averaged film effectiveness for each blowing ratio. The downstream exit point of the primary hole is at the location  $x/D=2$ . Results are presented from the downstream edge for the antivortex geometries and  $X/D=5$  for shaped hole case. At a low blowing ratio of  $M=0.5$ , Case 5 with the exit of the antivortex holes near the primary holes clearly provides the highest effectiveness after shaped holes. Effectiveness of Cases 1–4 are also relatively higher than the base line. Case 6 has the lowest relative effectiveness, better than only base line. As the blowing ratio increases to  $M=1.0$ , the effectiveness of Cases 2–5 is almost identical, which is below only shaped holes. The film cooling effectiveness of Case 1 is lower than for Case 6. For a blowing ratio of  $M=1.5$ , Case 4 has the highest effectiveness, which is only slightly better than Cases 3 and 5. Cases 1 and 6 show similar levels of film effectiveness, which is slightly higher than the base line case. For the highest blowing ratio of  $M=2$ , Case 3 produces slightly higher effectiveness than Case 4. The effectiveness of Cases 2 and 5 is also relatively higher and is comparable to that of Cases 4 and 3. The presence of antivortex holes in the nearby region of the main film cooling holes clearly shows an increment in the film cooling effectiveness. This can be attributed to lowering the momentum of the primary coolant jet due to decrease in mass flow rate. A second factor would be better film coverage in space between the two primary holes. As the blowing ratio increases, the antivortex design produces film effectiveness at similar levels as the shaped hole, indicating that the shaped hole can be replaced by antivortex design without any loss to coolant performance.

Figure 8 presents the effect of antivortex hole geometry and orientations on spanwise averaged heat transfer coefficient ratio ( $h/h_0$ ) for each blowing ratio. The local heat transfer coefficient with film cooling ( $h$ ) is normalized by the heat transfer coefficient without holes on a flat surface ( $h_0$ ). The downstream exit point of the primary hole is at the location  $X/D=2$  and for shaped hole at  $X/D=5$ . At a low blowing ratio of  $M=0.5$ , the heat transfer coefficients for Cases 2–5 and shaped holes look similar beyond  $X/D=5$ . These cases also had better film cooling effectiveness. It indicates that the mixing of the mainstream and jet provides a better coverage film but increases local turbulence production, enhancing the heat transfer coefficient. Owing to high film effectiveness and low relative heat transfer coefficient, Case 5 is clearly the best choice, behind shaped holes at this low blowing ratio of  $M=0.5$ . At  $M=1.0$ , Case 5 appears to have the lowest heat transfer coefficient amongst Cases 2–5, which have similar film cooling effectiveness at the same blowing ratio of  $M=1$ . Again for  $M=1.5$ , for cases considered above, Case 5 seems to have the lowest heat transfer coefficient. For  $M=2$ , Case 3 has the highest heat transfer coefficient. For Case 2 the coefficient is less due to the lift-off of the jet. Heat transfer coefficient of Case 4 appears to be lesser than Case 5. In the immediate downstream vicinity of the shaped holes, there is a slight higher heat transfer coefficient but farther downstream, the shaped hole shows lower values than Cases 2–5. It is clear that the antivortex pair enhance heat transfer coefficient over the base line case.

Figure 9 presents the effect of blowing ratio on the overall area-averaged film effectiveness and heat transfer coefficient for all cases. As seen clearly from the plot, film effectiveness is mostly at the same level for increase in blowing ratio from  $M=0.5$  to 1.0 for nearly all cases except Cases 3, 4, and 6, which

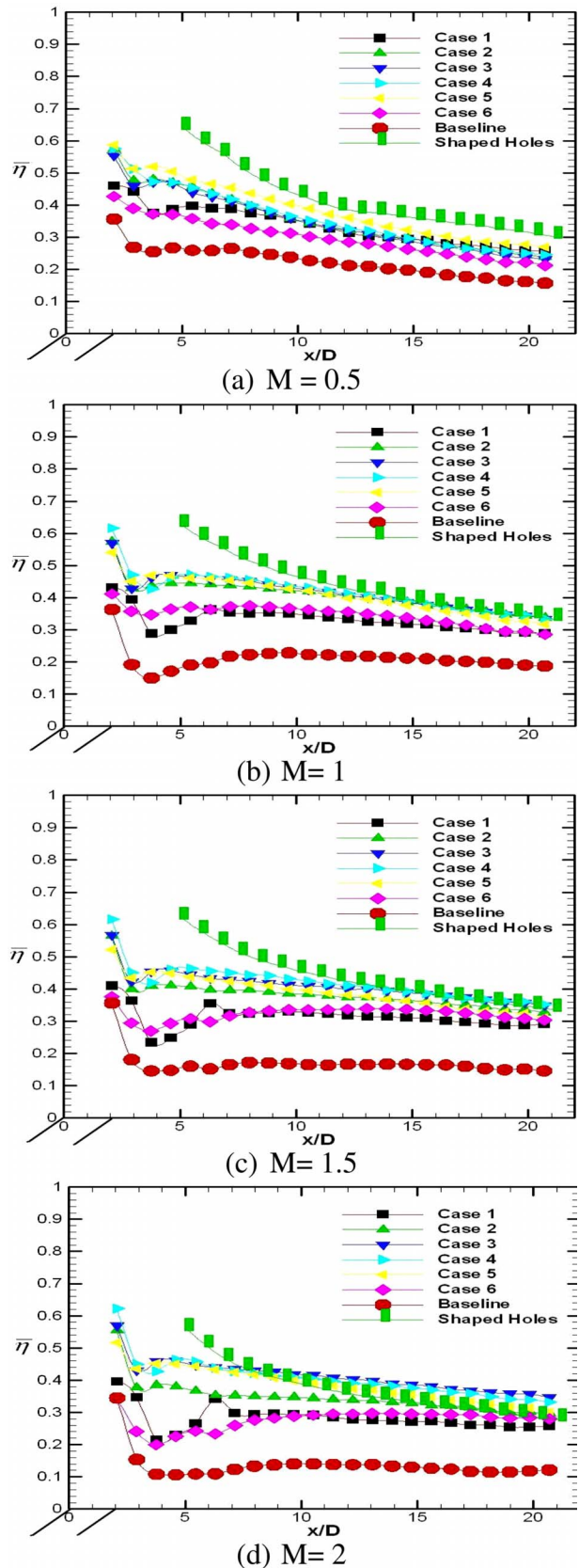
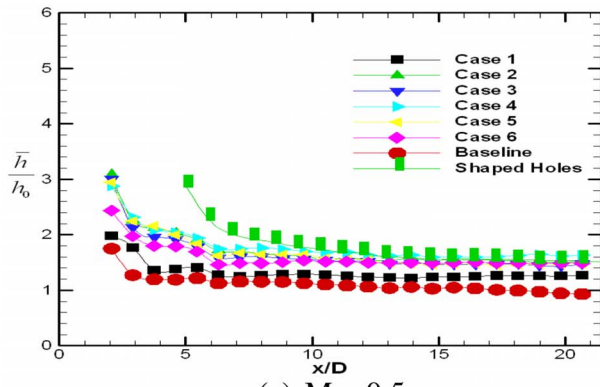


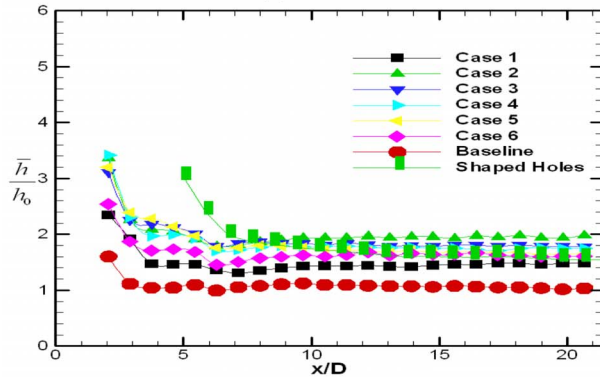
Fig. 7 Effect of hole configuration on spanwise averaged film effectiveness distributions at each blowing ratio

seem to increase a little. From  $M=0.5$  to higher blowing ratios, Cases 2 and 6, base line and shaped holes seem to have lower area-averaged film cooling effectiveness. For other cases, there seems to be no effect of increment in blowing ratio. Heat transfer

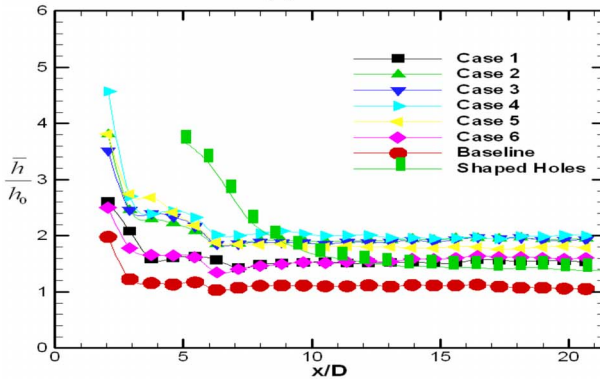




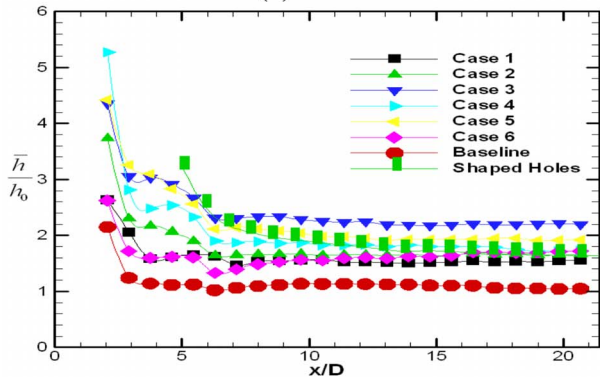
(a)  $M = 0.5$



(b)  $M = 1.0$



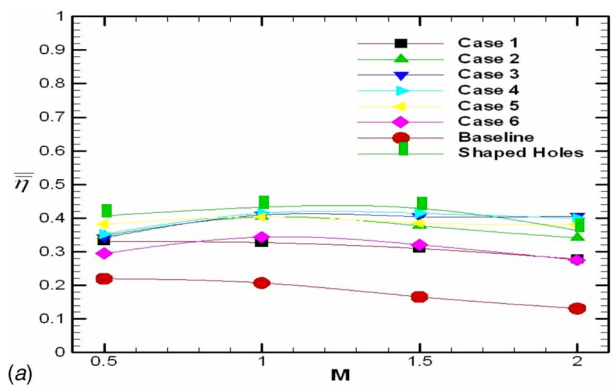
(c)  $M = 1.5$



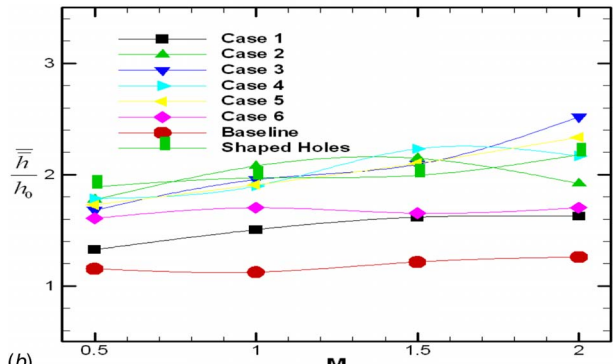
(d)  $M = 2$

**Fig. 8** Effect of hole configuration on spanwise averaged heat transfer coefficient ratio distributions at each blowing ratio

coefficient ratios for Cases 3 and 5 seem to be increasing with increasing blowing ratio. For shaped holes, the ratio seems to be a constant until  $M=1.5$ , after which it starts to increase. For Cases 2 and 4, there seems to be an increase in the ratio when the blowing



(a)



(b)

**Fig. 9** Effect of blowing ratio on (a) overall area-averaged film effectiveness and (b) heat transfer coefficient ratios for all cases

ratio increases from  $M=0.5$  to  $M=1.5$ , after which it decreases.

Figure 10 presents the effect of blowing ratio on overall area-averaged heat flux ratio ( $q''/q''_0$ ) for all three cases. This ratio indicates the reduction in heat flux obtained by introduction of film cooling over the surface. If the value is below 1.0, the effect is positive. If the value is greater than 1.0, then the presence of film cooling is detrimental. The heat flux ratio is calculated based on the formulation presented by Ekkad et al. [6]. The heat transfer ratio with and without film injection ( $h/h_0$ ) and the local film effectiveness are used to calculate the local heat flux ratio.

$$\frac{q''}{q''_0} = \frac{h}{h_0} \left( 1 - \frac{\eta}{\phi} \right)$$

The term  $\phi$  is the overall cooling effectiveness and ranges between 0.5 and 0.7 for typical blade cooling systems. In this study, a typical value of 0.6 is chosen. It is clear from the plot that except for Cases 3 and 1, all other antivortex cases have a positive result. Between  $M=0.5$  and  $M=1$ , Case 5 provides better protection. Cases 4 and 3 work better at blowing ratios between  $M=1$  and  $M=2$ . Overall, it appears that Cases 3–5 all provide much better performance than the base line case.

## Conclusions

A detailed study on the effects of geometry and orientations of antivortex holes branching out from the primary holes on film cooling has been presented. For all the cases, both heat transfer coefficients and film effectiveness were measured using a transient infrared thermography technique. It appears that the presence of antivortex holes reduces the effect of the kidney pair

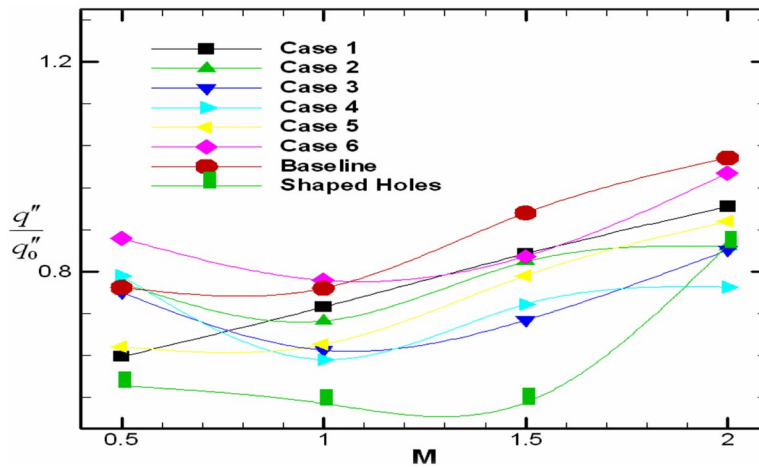


Fig. 10 Effect of blowing ratio on overall heat flux ratio for different cases

vortices and also reduces the momentum of the main jet, hence bettering the film coverage in both downstream and lateral directions. Cases 3–5 are clearly the better choices for their low overall heat flux ratio. Case 5, however, may pose a problem in structural integrity for there is a very narrow piece of material that separates the main hole from the antivortex holes. Cases 3 and 4 clearly are closer in overall performance to the industry standard diffuser shaped holes especially at  $M > 0.5$  and may be a good alternative in terms of manufacturability to the shaped hole, which is the best performer of all cases.

### Acknowledgment

The authors would like to acknowledge funding for the program NASA-EPSCoR DART subprogram. The director is Dr. John Wefel. The work was generated through a collaborative effort with NASA-GRC to work on the antivortex film hole design proposed by Dr. Jim Heidmann, coauthor of the paper.

### Nomenclature

- $a$  = center to center distance between main and antivortex holes ( $x$ -direction)
- $b$  = center to center distance between main and anti vortex holes ( $y$ -direction)
- $c_p$  = specific heat (kJ/kg K)
- $d$  = side hole diameter (cm)
- $D$  = main hole diameter (cm)
- $h_0$  = local heat transfer coefficient without film injection ( $W/m^2 K$ )
- $h$  = local heat transfer coefficient with film injection ( $W/m^2 K$ )
- $k$  = thermal conductivity of test surface ( $W/m K$ )
- $L$  = length of film hole (m)
- $M$  = blowing ratio  $= \rho_c V_c / \rho_\infty V_\infty$
- $P$  = angle of antivortex holes measured in top plane
- $q''$  = surface heat flux ( $W/m^2$ )
- $Q$  = angle of antivortex holes measured in side plane
- $R$  = angle of antivortex holes measured in front plane
- $Re$  = freestream Reynolds number ( $V_\infty d / \nu$ )
- $\rho_c$  = coolant density ( $Kg/m^3$ )
- $\rho_\infty$  = mainstream density ( $Kg/m^3$ )
- $t$  = time (s)
- $T_c$  = coolant temperature (K)
- $T_f$  = film temperature (K)

- $T_i$  = test surface initial temperature (K)
- $T_r$  = reference temperature (K)
- $T_\infty$  = mainstream temperature (K)
- $Tu$  = free-stream mean turbulence intensity (%)
- $T_w$  = local wall temperature (K)
- $U_c$  = coolant velocity (m/s)
- $U_\infty$  = mainstream velocity (m/s)
- $x$  = streamwise distance along the test plate (m)
- $y$  = coordinate normal to surface (m)
- $\eta$  = film cooling effectiveness
- $\phi$  = nondimensional temperature  $= (T_c - T_\infty) / (T_w - T_\infty)$
- $\nu$  = kinematic viscosity of mainstream ( $m^2/s$ )
- $\alpha$  = thermal diffusivity ( $m^2/s$ )

### References

- [1] Ligrani, P. M., Wigle, J. M., Ciriello, S., and Jackson, S. W., 1994 "Film-Cooling From Holes With Compound Angle Orientations: Part 1-Results Downstream of Two Staggered Rows of Holes With 3d Spanwise Spacing," ASME J. Heat Transfer, **116**(2), pp. 341–352.
- [2] Ligrani, P. M., Wigle, J. M., and Jackson, S. W., 1994 "Film-Cooling From Holes With Compound Angle Orientations: Part 2-Results Downstream of a Single Row of Holes With 6d Spanwise Spacing," ASME J. Heat Transfer, **116**(2), pp. 353–362.
- [3] Sen, B., Schmidt, D. L., and Bogard, D. G., 1996 "Film Cooling With Compound Angle Holes: Heat Transfer," ASME J. Turbomach., **118**(4), pp. 801–807.
- [4] Schmidt, D. L., Sen, B., and Bogard, D. G., 1996 "Film Cooling With Compound Angle Holes: Adiabatic Effectiveness," ASME J. Turbomach., **118**(4), pp. 807–813.
- [5] Ekkad, S. V., Zapata, D., and Han, J. C., 1997 "Heat Transfer Coefficients Over a Flat Surface With Air and CO<sub>2</sub> Injection Through Compound Angle Holes Using a Transient Liquid Crystal Image Method," ASME J. Turbomach., **119**(3), pp. 580–586.
- [6] Ekkad, S. V., Zapata, D., and Han, J. C., 1997 "Film Effectiveness Over a Flat Surface With Air and CO<sub>2</sub> Injection Through Compound Angle Holes Using a Transient Liquid Crystal Image Method," ASME J. Turbomach., **119**(3), pp. 587–593.
- [7] Makki, Y., and Jakubowski, G., 1986, "An Experimental Study of Film Cooling From Diffused Trapezoidal Shaped Holes," AIAA Paper No. 86–1326.
- [8] Gritsch, M., Schulz, A., and Wittig, S., 1998 "Heat Transfer Coefficient Measurements of Film Cooling Holes With Expanded Slots," ASME Paper No. 98-GT-28.
- [9] Gritsch, M., Schulz, A., and Wittig, S., 1988 "Adiabatic Wall Effectiveness Measurements of Film Cooling Holes With Expanded Exits," ASME J. Turbomach., **120**(3), pp. 549–556.
- [10] Dittmar, J., Schulz, A., and Wittig, S., 2002, "Assessment of Various Film Cooling Configurations Including Shaped and Compound Angle Holes Based on Large Scale Experiments," ASME Paper No. GT-2002-30176.

- [11] Sargison, J. E., Guo, S. M., Oldfield, M. L. G., Lock, G. D., and Rawlinson, A. J., 2002, "Flow Visualization of a Converging Slot-Hole Film Cooling Geometry," ASME Paper No. GT 2002-30177.
- [12] Lu, Y., Fauchaux, D., and Ekkad, S. V., 2005, "Film Cooling Measurements for Novel Hole Configurations," ASME Paper No. HT2005-72396.
- [13] Vedula, R. J., and Metzger, D. E., 1991, "A Method for the Simultaneous Determination of Local Effectiveness and Heat Transfer Distributions in a Three Temperature Convective Situations," ASME Paper No. 91-GT-345.
- [14] Ekkad, S. V., Ou, S., and Rivir, R. B., 2004, "A Transient Infrared Thermography Method for Simultaneous Film Cooling Effectiveness and Heat Transfer Coefficient Measurements From a Single Test," ASME J. Turbomach. **126**, pp. 546–553.
- [15] Heidmann, J., and Ekkad, S. V., 2007, "A Novel Anti-Vortex Turbine Film Cooling Hole Concept," ASME Paper No. GT2007-27528.
- [16] Bunker, R. S., 2005, "A Review of Shaped Hole Turbine Film-Cooling Technology," ASME J. Heat Transfer, **127**, pp. 441–453.
- [17] Kline, S. J., and McClintock, F. A., 1953, "Describing Uncertainties in Single Sample Experiments," Mech. Eng. (Am. Soc. Mech. Eng.), **75**, pp. 3–8.



# Effects of Combustor Exit Profiles on Vane Aerodynamic Loading and Heat Transfer in a High Pressure Turbine

M. D. Barringer

K. A. Thole

Department of Mechanical and Nuclear  
Engineering,  
The Pennsylvania State University,  
University Park, PA 16802

M. D. Polanka

Air Force Research Laboratory,  
Turbines Branch,  
WPAFB, OH 45433

*The flow and thermal fields exiting gas turbine combustors dictate the overall performance of the downstream turbine. The goal of this work was to investigate the effects of engine representative combustor exit profiles on high pressure turbine vane aerodynamics and heat transfer. The various profiles were produced using a nonreacting turbine inlet profile generator in the Turbine Research Facility (TRF) located at the Air Force Research Laboratory (AFRL). This paper reports how the pressure loading and heat transfer along the vane surface was affected by different turbine inlet pressure and temperature profiles at different span locations. The results indicate that the inlet total pressure profiles affected the aerodynamic loading by as much as 10%. The results also reveal that the combination of different total pressure and total temperature profiles significantly affected the vane heat transfer relative to a baseline test with uniform inlet total pressure and total temperature. Near the inner diameter endwall, the baseline heat transfer was reduced 30–40% over the majority of the vane surface. Near the outer diameter endwall, it was found that certain inlet profiles could increase the baseline heat transfer by 10–20%, while other profiles resulted in a decrease in the baseline heat transfer by 25–35%. This study also shows the importance of knowing an accurate prediction of the local flow driving temperature when determining vane surface heat transfer.*

[DOI: 10.1115/1.2950051]

## Introduction

The desire to continuously improve the performance and working life of aircraft gas turbine engines has led to the need for more advanced engine hardware that is capable of surviving in very intense flow and thermal environments. Improvements in engine performance can come in the form of increasing thrust production while increasing the working life of the individual engine components. Increasing the thrust can be accomplished by increasing the gas working temperature of the turbine section. As a result of the push for higher temperatures, the gas temperatures exiting combustors of modern engines are well above the melting point of the metal alloy engine components. The durability and maintainability of these engine parts are therefore primary concerns of gas turbine engine designers. Of particular interest is the interface between the combustor and turbine sections where the high pressure turbine vanes are subjected to the very harsh, highly turbulent, and nonuniform flow fields exiting the combustor.

The complexity of the combustor exit flow stems from the intense flow interactions that take place within the central chamber of the combustor. This chamber consists primarily of inlet flow swirlers, fuel nozzles, inner diameter (ID) and outer diameter (OD) annular liners, and an overall exit contraction. The annular liners typically contain primary holes and dilution holes that inject large amounts of air into the central chamber to first help stabilize combustion and then to dilute the combustion products to reduce the overall gas temperature to a level acceptable for the turbine hardware. The liners also contain film cooling holes and slots that inject cooling air along the liner walls to form a protective layer of insulating air that shields the metal from the relatively hot com-

bustion gas. As the individual flow streams travel down the length of the chamber, they combine and interact with one another, resulting in a highly nonuniform flow structure at the combustor exit. The spatial variations in temperature impose nonuniform heat transfer on the high pressure turbine vanes and blades that can result in local melting and cracking of the metal and can thus permanently damage strategic cooling features. The elevated turbulence levels act to intensify this heat transfer by increasing local convection heat transfer coefficients to the vane surface. The spatial variations in the pressure at the combustor exit can result in nonuniform aerodynamic loading that can increase local thermal-mechanical stresses.

Turbine engine designers have been forced to prepare for the worst case when designing the high pressure vanes and blades without knowing exactly how the combustor exit profiles affect the hardware. For example, some designers currently use a radial pressure profile consistent with a standard turbulent boundary layer as the inlet condition to the turbine while designing their vanes and blades. However, more realistic combustor exit flows can result in turbine inlet profiles and secondary flow development that is significantly different from what has been used as a design condition. A better understanding of how the combustor exit flow alters the flow development and heat transfer within the downstream turbine is needed. This understanding can be accomplished by studying how different combustor exit profile shapes impact the downstream turbine components.

The primary research objective of this paper was to study the effects of several radial pressure and temperature profiles on high pressure turbine vane aerodynamic loading and heat transfer. The profiles analyzed in this study were produced by the nonreacting inlet profile generator (combustor simulator) that is located in the Turbine Research Facility (TRF) at the Air Force Research Laboratory (AFRL) and described in Barringer et al. [1].

Contributed by the International Gas Turbine Division of ASME for publication in the JOURNAL OF TURBOMACHINERY. Manuscript received October 10, 2006; final manuscript received December 3, 2007; published online January 23, 2009. Review conducted by Je-Chin Han. Paper presented at the ASME Turbo Expo 2006: Land, Sea and Air (GT2006), Barcelona, Spain, May 8–11, 2006.

## Relevant Past Studies

Several studies have been performed to analyze and model the flow and thermal fields within aircraft engine combustors and turbines. Few studies, however, have focused on how the combustor exit environment affects the performance of the downstream turbine. Rather, most studies have been isolated to analyzing either the combustor section or the turbine section alone. Studying the interaction of the combustor exit flow with the turbine is crucial to fully understanding how the vanes and blades are influenced by different realistic inlet conditions. This understanding will help turbine designers improve their own research and development work. The following is a review of some past and recent studies that have focused on the interface between the combustor and turbine sections.

The effect of different inlet radial temperature profiles on the aerodynamic performance of a transonic turbine stage was investigated by Cattafesta [2] using the MIT blow-down Turbine facility. Tests with similar corrected flow conditions but with different temperature profiles changed the overall turbine efficiency by 2%. Shang et al. [3] conducted similar tests using a full turbine stage in the same facility to study the influence of inlet temperature distortion on rotor blade heat transfer. It was found that changing the stage inlet turbulence intensity from 0.5–8% did not influence the rotor blade surface heat flux. Radial thermal distortions near midspan, with peak temperatures 10% larger than the mean, resulted in significant augmentation of local blade heat transfer along the pressure side (PS) in the tip and hub regions. This radial temperature distortion resulted in Nusselt numbers 10% higher than those measured with uniform conditions within the tip region and 50% higher within the hub region. The Nusselt numbers measured at midspan were nearly the same with and without the radial temperature distortion.

Chana et al. [4] conducted research using a nonuniform inlet temperature generator at the QinetiQ transient turbine research facility. Cold gas was injected upstream of the turbine section at the hub and tip to shape the temperature profile in the radial direction and through turbulence rods inserted into the main flow to shape it in the circumferential direction. Results showed that vane heat transfer was affected by the presence of the nonuniform temperature profile on the suction surface of the turbine nozzle guide vanes. Povey et al. [5] conducted similar research in the same QinetiQ facility and outlined a thorough review of recent and past studies involving high pressure experimental facilities used to simulate and study combustor exit flows, some of which are mentioned in this literature review. An important finding from their study was the significant augmentation to the vane heat transfer when comparing uniform turbine inlet temperature profiles to the vane heat transfer measured when the inlet temperature profile possessed maximum nonuniform conditions of  $T/T_{av}$  near 10%. Their study also discussed a method to determine the vane surface and endwall heat transfer driving temperature based on knowledge of the Nusselt number with uniform inlet temperature and inlet temperature distortion. Their method assumes that the heat transfer coefficient is unchanged with and without the inlet temperature distortion.

Krishnamoorthy et al. [6] investigated the effect of combustor exit turbulence on a downstream turbine vane cascade. Their results indicated that the effect of high turbulence at the combustor exit was to reduce the cooling effectiveness on the vane by 10%. It was also shown that the effect of temperature nonuniformities at the combustor exit was to reduce the overall cooling effectiveness on the vane by as much as 21%. Van Fossen and Bunker [7] studied heat transfer augmentation in the stagnation region of a flat plate with an elliptical leading edge. The test article was located downstream of an arc segment of a dual-annular combustor. The swirl driven combustor flow produced turbulence intensities up to approximately 32% with length scales near 1.3 cm. Aug-

mentation of heat transfer was found to be very significant in the range of 34–59%. No effect of circumferential position with respect to the upstream swirlers was found.

There have been few investigations into the effects of inlet profiles on endwall secondary flow development. These are important as they distribute the temperature field and generate turbulence. As shown in the literature, the secondary flows present within turbine vane passages originate at the leading edge vane-endwall junction. The horseshoe vortex that forms at this leading edge junction splits into two vortices, one of which progresses to the vane PS and one to the suction side (SS). The PS leg of the horseshoe vortex travels down the endwall along the upstream portion of the PS of the vane during which it merges with and becomes the passage vortex. This passage vortex crosses over the channel along the endwall toward the SS of the adjacent vane. It then travels down the endwall along the latter portion of the SS of this adjacent vane. The SS leg of the horseshoe vortex is much smaller in size relative to the PS vortex and passage vortex. This SS leg travels along the endwall corner of the vane suction surface until it is overcome by the passage vortex.

Studies by Hermanson and Thole [8] have shown that the total pressure field is a driving force in the development of secondary flows and heat transfer present in turbine vane passages. They also reported that a counter-rotating vortex can exist, in addition to the passage vortex, within the vane passage that can drive fluid away from the endwall and toward midspan. This counter-rotating vortex was found for an inlet total pressure profile containing a positive inflection point in the spanwise direction near the endwall.

Colban et al. [9] studied the effects of varying FC flow through the liner and exit junction slot in a large scale, low speed combustor simulator on the adiabatic effectiveness, and secondary flow development within a downstream turbine cascade. Results showed that varying the coolant injection through the liner led to different total pressure profiles entering the downstream turbine section. Measurements showed that the coolant exiting the liner and slot accumulated along the SS of the vane and endwall and that increasing the FC flow through the liner did not result in a continual increase in adiabatic effectiveness values.

Their study also documented the vane passage secondary flow vectors for different vane inlet total pressure profiles and confirmed the presence of a counter-rotating vortex located above the passage vortex when the vane inlet pressure profile contains a slight forward facing peak near the endwall. This is illustrated in Fig. 1, which shows secondary flow vectors within the vane passage (at approximately  $X/C=0.35$ ) for two different vane inlet pressure profiles. The type A profiles, shown in Fig. 1(a), possess the typical shape of a turbulent boundary layer with lower total pressure near the endwall relative to midspan, and the type B profiles, shown in Fig. 1(b), contain a forward facing inflection point. This inflection point is caused by the injection of high flow out of the cooling liner holes resulting in a high total pressure region near the endwall at  $Z/Sp=0.1$  relative to midspan. The size and location are dependent on the amount of coolant ejected.

To summarize, the current research to date suggests that certain heat transfer trends within the turbine section are due to nonuniform inlet temperature and pressure conditions. Studies have reported significant augmentation of heat transfer along the SS of the vanes and the PS of the blades in both the hub and tip regions with insignificant changes noted near midspan. Also, the literature contains few experimental data that document total pressure profiles at the combustor exit. The goal of this work is not only to verify some of the important trends found in the literature but, more importantly, to enhance the understanding of the impact of more realistic turbine inlet profiles. In addition to representative combustor exit temperature profiles, realistic pressure profiles are also studied to quantify the effects of both on high pressure turbine vane heat transfer and aerodynamics. This study will provide some new insight to further enhance future turbine development.

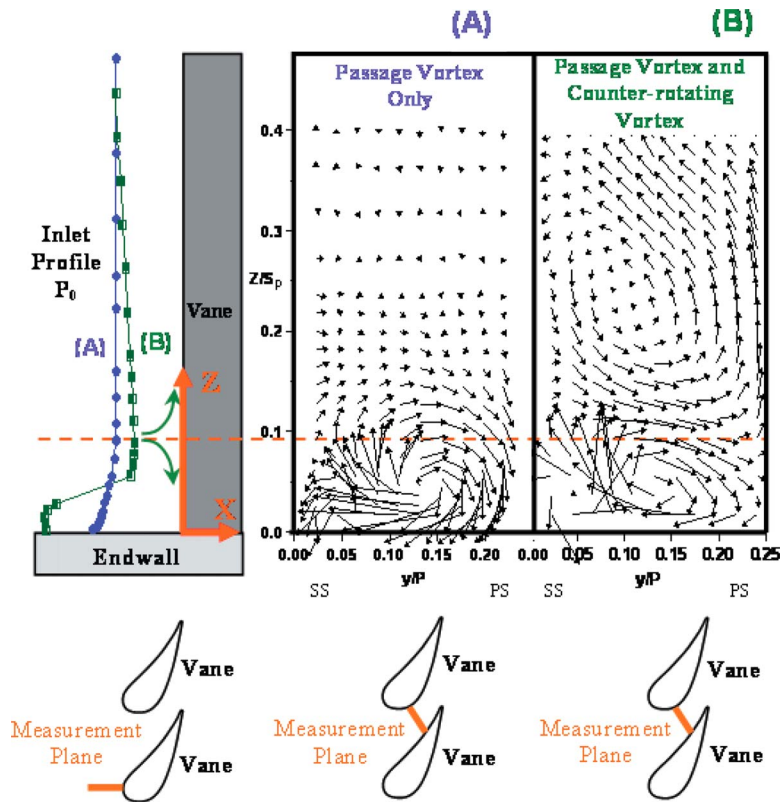


Fig. 1 Velocity contours within the vane passage ( $X/C=0.35$ ) from Colban et al. [9] showing secondary flow vectors and their corresponding vane inlet total pressure profiles for (A) a turbulent boundary layer and (B) a forward facing inflection point near the endwall

### Experimental Facility and Instrumentation

The experimental facility used in this study is the TRF at the AFRL at Wright Patterson Air Force Base in Dayton, Ohio. The TRF, documented in Haldeman et al. [10], is a short duration blow-down test facility that can match engine Reynolds number, Mach number, pressure ratio, gas to metal temperature ratio, corrected speed, and corrected mass flow. The facility is shown in Fig. 2, and it consisted primarily of a large supply tank, a turbine test section, and two large vacuum tanks. The turbine test section was a true scale, fully annular, half turbine stage, consisting of high pressure vanes.

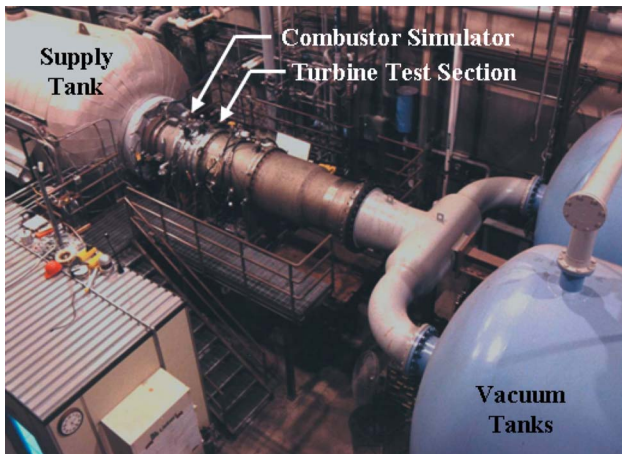
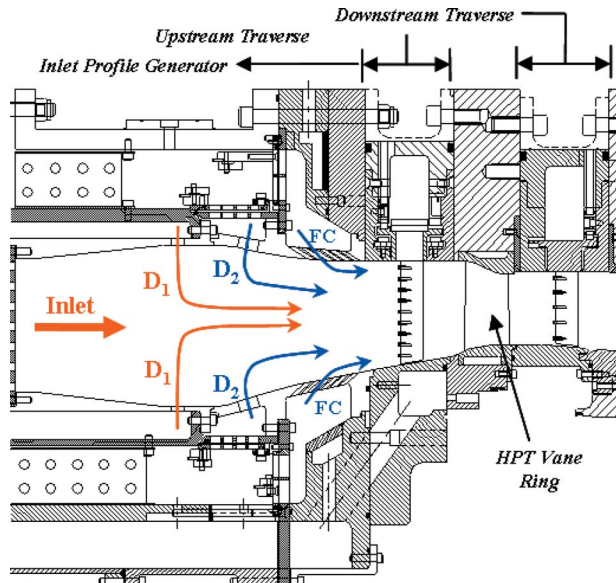


Fig. 2 Photograph of the TRF facility

Prior to testing, nitrogen gas was pressurized and heated within the supply tank, while the turbine section and vacuum tanks were evacuated. Testing began by activating the main valve located in the supply tank, at which time the gas flowed from the supply tank through the turbine test section and into the vacuum tanks. The mass flow rate was set by controlling the turbine pressure ratio using a variable area isolation valve that was located downstream of the main test section. The duration of a typical test was nominally 5 s. Due to the short test duration, all instrumentation measurements are recorded simultaneously in real time onto data storage units. The TRF facility was capable of simultaneously acquiring data across 200 12 bit channels with a maximum frequency response of 100 kHz and 200 16 bit channels with a maximum frequency response of 200 kHz. Signal conditioning on each channel took place using low pass filters and built-in amplifiers. All data reduction was performed at a later time.

The turbine inlet profile generator (combustor simulator) that was used in this study was designed and installed into the TRF facility to allow turbine testing to be performed with more realistic turbine inlet profiles of pressure, temperature, and turbulence intensity. Prior to installing the simulator, the temperature and pressure profiles at the inlet of the turbine section were nearly uniform in the radial and circumferential directions. The design of the simulator is documented in Barringer et al. [11]. The simulator essentially divides the supply tank flow into multiple concentric annular flow paths and directs each flow stream to a central annular chamber, similar to an actual aeroengine combustor. A magnified view of this central annular chamber is shown in Fig. 3 which highlights the general paths for the flow streams that inject flow into the chamber. These include the flow passing through the inlet, two rows of in-line opposed dilution holes ( $D_1$  and  $D_2$ ), and six staggered rows of film cooling (FC) holes. The influence of a





**Fig. 3** Drawing of the combustor simulator central chamber indicating the general flow paths

particular flow stream over the turbine inlet profile can extend over a large radial range or it can be concentrated to a small local region. The effects of the film cooling flow were found to be evident in radial regions near the ID endwall at  $0.0 < Z/S < 0.2$  and near the OD endwall at  $0.8 < Z/S < 1.0$ . The effect of the inlet core flow and dilution flows were found to be present over a larger span region of  $0.2 < Z/S < 0.8$ .

The turbine inlet and exit conditions were measured using multiple instrumentation rakes located on traverse rings upstream and downstream of the turbine section. The rakes, shown in Fig. 4, contained multiple thermocouples or multiple pressure transducers that were spaced to obtain measurements over equal annular flow areas. Most of the tests discussed in this study involved circumferentially traversing these rakes by approximately 90 deg during the blowdown to obtain both radial and circumferential profiles. However a few tests were performed in which the rakes were traversed by only 32 deg to allow a larger number of data points to be taken across multiple vane pitches. For the turbine inlet profiles being analyzed in the current study, a temperature rake containing seven 0.0254 mm diameter thermocouple beads with a thermal time constant of approximately 1.1 ms was used. Two pressure rakes were also used, each containing nine pressure

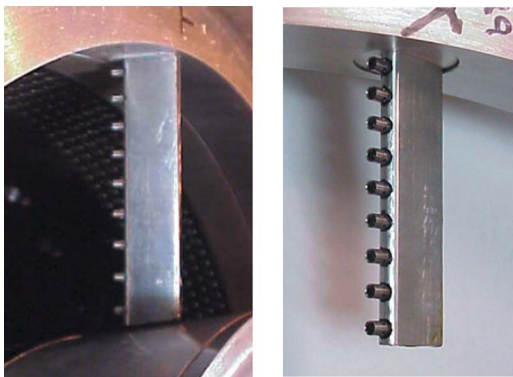


**Fig. 4** Instrumentation rakes mounted in the upstream (left) and downstream (right) traverses

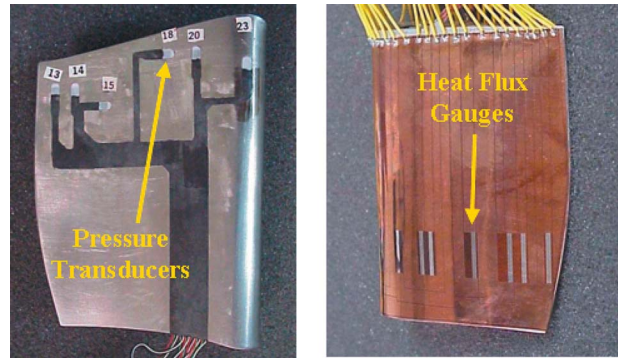


**Fig. 5** Photographs of TRF vanes that were instrumented with pressure gauges (left) and HFGs (right)

transducers. Note that no boundary layer measurements were taken as these probes were fixed radially. All flow measurements were sampled at 20 kHz.

The pressure along the surface of several uncooled turbine vanes was measured using the 700 kPa miniature Kulite pressure transducers shown in Fig. 5. The transducers were mounted flush with the vane surface along both the suction and pressure surfaces. Two vane span locations were selected for making surface pressure measurements including  $Z/Sp=0.5$  near midspan and  $Z/Sp=0.9$  near the OD. The Kulite transducers were also used to take static pressure measurements on the ID and OD endwalls at the vane inlet and exit. The total uncertainty associated with these measured pressures is at most 0.40% full scale.

The heat flux along the pressure and suction surfaces of several uncooled vanes was measured using thin film Oxford heat flux gauges (HFGs) [12] that are also shown in Fig. 5. Three span locations were selected for taking surface heat flux measurements including  $Z/Sp=0.24$  near the ID,  $Z/Sp=0.60$  near midspan, and  $Z/Sp=0.90$  near the OD. The gauges at  $Z/Sp=0.24$  and  $0.60$  had a spanwise extent of  $\Delta Z/Sp=0.15$ , while the spanwise extent of the gauges at  $Z/Sp=0.90$  was  $\Delta Z/Sp=0.03$ . Thermocouple beads with a diameter of 0.0254 mm were embedded into the vane metal directly beneath each HFG such that the beads were flushed with the vane surface.

By utilizing a semi-infinite solid analysis, the heat flux to the vane surface was calculated. The convection heat transfer coefficient,  $h$ , was then determined by dividing the local measured heat flux by the driving temperature. The driving temperature associated with the local heat flux was defined as the difference between the local vane surface temperature,  $T_w$ , and the adiabatic wall temperature,  $T_{aw}$ , in the vicinity of the gauge. The adiabatic wall temperature was calculated using the recovery factor and was based on the flow total temperature at the vane inlet at the same span location as the gauge. Typical values for this driving temperature difference were approximately 50–60 K. This driving temperature was then used to determine the local convection heat transfer coefficient on the vane surface. With  $h$  known, the length scale chosen for the Nusselt number was the vane axial chord length. The local Nusselt number was then obtained with the gas properties as taken from the local film temperature. This temperature was defined as the linear mean of the local vane surface temperature and the total temperature of the flow at the vane inlet at the same span location as the gauge.

Based on the uncertainties in the measurement of the HFG resistance and the uncertainty in calibration from resistance to temperature, the surface temperature uncertainty for the heat flux measurement was calculated to be  $\pm 0.8$  K for the HFGs. A jitter analysis described by Moffat [13] was then performed through the reduction scheme to obtain the uncertainty in the surface heat flux. This resulted in uncertainties in heat flux between  $700 \text{ W/m}^2$  and  $2000 \text{ W/m}^2$  depending on the gauge. The heat transfer coefficient

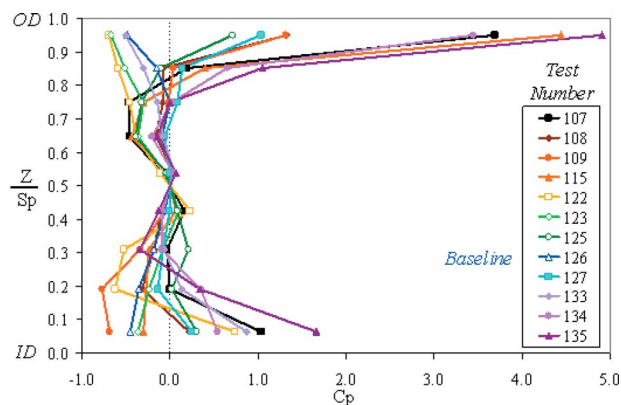


**Fig. 6 Plot of several radial pressure profiles at the turbine vane inlet**

uncertainty was determined to be about  $30 \text{ W/m}^2 \text{ K}$  for the thin film gauges based on an uncertainty in flow temperature of  $0.7 \text{ K}$  along with the hysteresis in the measurement. This resulted in Nusselt number uncertainties between 5% and 9% depending on the location. The repeatability of these runs had a similar variation of 8–10%.

### Test Conditions

The turbine inlet profiles that were analyzed for this study were generated during a series of benchmark tests to verify that the inlet profile generator operated as desired. The flow conditions corresponding to the verification tests are presented in Barringer et al. [1], which documents the overall operating range of the turbine inlet profile generator. The mean flow conditions at the turbine inlet for all of the profiles presented in this study correspond to  $Re=2.1 \times 10^5$  and a Mach number of 0.1. The turbulence intensity associated with these turbine inlet profiles was also documented during the verification tests and was found to be in an elevated range between 20% and 30%, while the length scales were found to be between 1.5 cm and 1.9 cm. The longitudinal integral length scales were determined to be approximately 30% of the vane pitch or 2.3 times the vane leading edge diameter.

To document the effects of different turbine inlet profiles on turbine vane aerodynamics and heat transfer, a baseline test case was selected to make comparisons. The baseline that was chosen is test 126, which is characterized by both a relatively uniform radial pressure profile and a relatively uniform radial temperature profile. The turbulence intensity of the flow entering the turbine vane near midspan was at an elevated level near 21% for the baseline test 126. Comparisons of heat transfer and pressure loading are reported relative to those measured for the baseline case. The maximum percent deviations above and below the baseline results are also reported.

### Aerodynamic Measurements at Midspan and in the Outer Diameter Region

Several radial pressure profiles at the turbine vane inlet are shown in Fig. 6. The profiles are plotted in terms of a normalized total pressure coefficient  $C_p$  defined as the local total pressure subtracted by the midspan total pressure all divided by the average dynamic pressure at the vane inlet. Note that by this definition  $C_p=0$  at midspan. These radial profiles have been circumferentially (spatially) averaged across one full vane pitch along lines of constant radius that are spaced at equal annular flow areas and represent the mean vane inlet conditions. As shown in a previous investigation [1] there is about a 1% variation in the pressure and temperature profiles in the pitch variation, so essentially these profiles are circumferentially uniform.

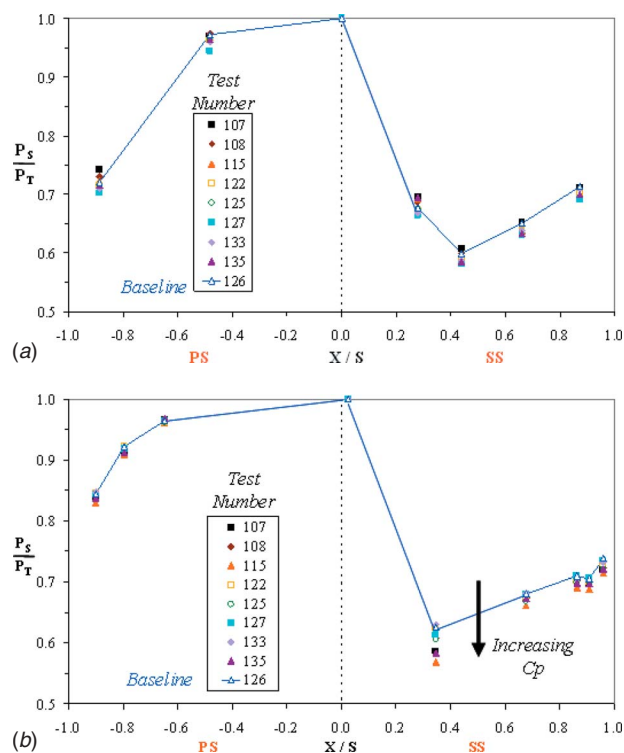


**Fig. 7 Plot of the vane surface pressure at (a)  $Z/Sp=0.50$  and (b)  $Z/Sp=0.90$**

A wide variety of radial profile shapes can be seen, including some that contain sharp gradients near the ID and OD endwalls. These gradients were the result of varying the amount of upstream film coolant being injected into the mainstream flow along the endwalls. As discussed in the previous paper [1], real engines exhibit  $C_p$ 's in the range of  $-0.5 < C_p < 2.0$ , and this investigation covers a range somewhat larger than that. The peak  $C_p$  value near the ID and OD endwalls was found previously [1] to be directly related to the film cooling momentum flux ratio where an increase in this ratio resulted in an increase in the peak  $C_p$  value. It does have to be noted that the exact location and peak value of  $C_p$  is unknown as the rakes represent only specific discrete points. However, as discussed in a previous work [1], real engines exhibit  $C_p$ 's in the range of  $0.5 < C_p < 2.0$ , so this investigation clearly covers that range and furthermore gives the designer some insight into whether any benefit could be obtained from utilizing even a larger range. It is also important to note that a negative  $C_p$  value does not indicate that the flow is in the reverse (upstream) direction; it simply means that the local total pressure is less than that at the midspan. This behavior can be seen for the baseline test 126 that possesses slightly less total pressure near the ID and OD endwalls (compared to the midspan) due to an absence of film coolant along the ID and OD endwalls for this particular test.

The corresponding pressure along the surface of the turbine vanes for these radial inlet pressure profiles is plotted in Fig. 7 at  $Z/Sp=0.50$  and  $Z/Sp=0.90$ . Surface pressure measurements were not taken in the near ID endwall region. The ratio of the local vane surface static pressure,  $P_s$ , to the total pressure of the flow at the vane inlet,  $P_T$ , is plotted versus the vane surface distance,  $X/S$ , along both the SS and PS. Note that the normalizing total pressure,  $P_T$ , used in Fig. 7 is the surface pressure measured at the leading edge of the vane at  $X/S=0.0$  at the same corresponding span location. In Fig. 7 it can be seen that the effect of the surface pressure loading due to the inlet pressure profiles was less significant at the midspan than at the OD region location at  $Z/Sp=0.90$ . This was due in part to small changes in the midspan  $C_p$  for these cases, coupled with the fact that the vane geometry in the

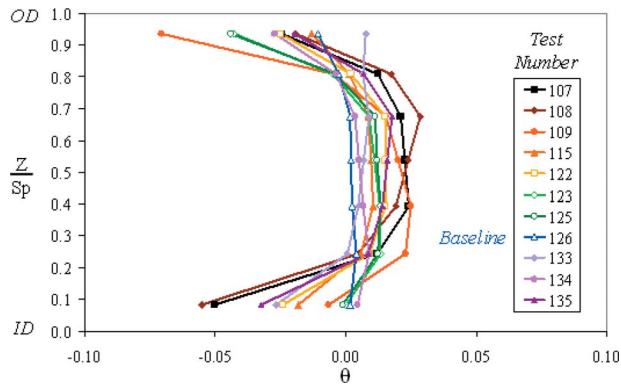


**Fig. 8** Plot of several radial temperature profiles at the turbine vane inlet

midspan region is nearly two dimensional. Therefore limited secondary flow changes are expected at midspan. The maximum percent deviation of  $P_S/P_T$  from the baseline test that was observed at  $Z/Sp=0.50$  was approximately 3.0% for test 107, which occurred on the PS of the vane near the trailing edge at  $X/S = -0.89$ .

More significant differences occur at  $Z/Sp=0.90$ . The data on the vane SS indicate that the different inlet pressure profiles had a significant impact on the surface pressure from  $X/S=0.35$  to the trailing edge. Figure 7(b) indicates that the most significant effect of the different inlet pressure profiles occurs on the vane suction surface near  $X/S=0.35$ , which is close to the minimum passage area for this vane geometry. At this location, test 115 (containing a large  $C_p$  peak value near 4.5) resulted in a maximum  $P_S/P_T$  deviation of 9.1% below the baseline test (over three times the maximum at midspan), and test 133 (containing a negative  $C_p$  peak value near  $-0.5$ ) resulted in a maximum deviation of 0.7% above the baseline test. These two tests resulted in a  $P_S/P_T$  pressure ratio range of approximately 9.8% at this  $X/S$  surface location, thus illustrating that the local aerodynamic loading of the vane can change as much as 10% depending on the inlet total pressure profile.

At 90% span, Fig. 7(b) also shows that the percent deviation from the baseline test was relatively small on the PS of the vane (similar to most locations on the PS at midspan). In general, an increase in the pressure profile  $C_p$  peak along the endwall resulted in a decrease in the ratio of  $P_S/P_T$ . These results indicate that higher momentum fluid along the OD endwall results in an increase in the aerodynamic loading of the vane at this span. It is believed that the secondary flows are moving lower pressure fluid from the lower span into this region on the SS consistent with the work of Colban et al. [8]. One additional comment is that the total pressure at the 90% span stagnation location, used as the reference for determining the loading, is at a lower level than midspan, giving rise to a higher loaded airfoil.

### Heat Transfer Measurements in the Inner and Outer Diameter Regions

Several different radial temperature profiles at the turbine vane inlet are shown in Fig. 8. The profiles are plotted in terms of a nondimensional temperature coefficient  $\theta$  defined as the local total temperature subtracted by the average total temperature entering the turbine, all divided by the same average temperature. These radial profiles have been circumferentially averaged across one full vane pitch along lines of constant radius that are spaced at equal annular flow areas. The average temperature at the simulator exit was determined by integrating the spanwise profile from the seven headed rake from hub to tip. To obtain a better approximation of this average temperature, the temperature data were extrapolated to the endwalls using a constant slope between the out-

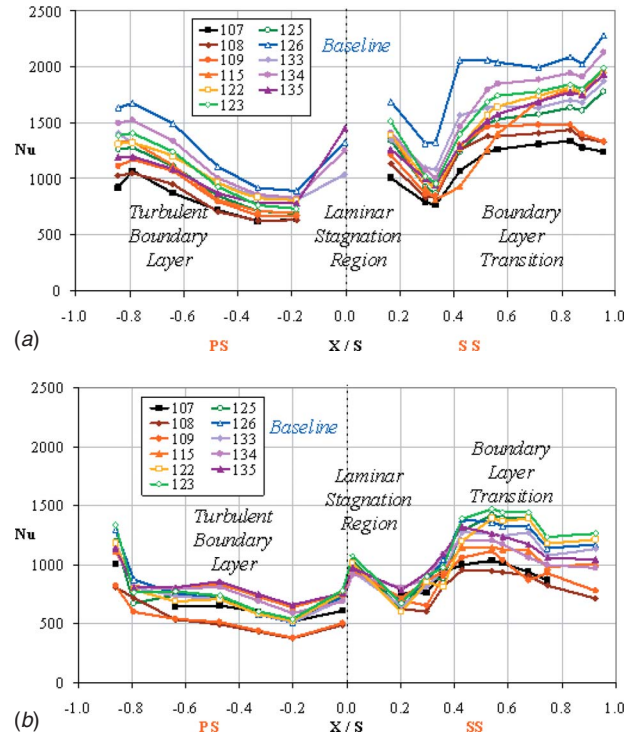


**Fig. 9** Nusselt number distribution along the vane surface in the ID region at (a)  $Z/Sp=0.24$  and in the OD region at (b)  $Z/Sp=0.90$

ermost and second outermost data points. The actual average temperature varied for each test but was in the range of 380–435 K.

The inlet temperature profiles include some that contain considerable gradients along the endwalls (tests 107 and 108) and some that are nearly uniform over the entire span (baseline case test 126). Figure 8 shows that the most significant differences occur in the two span regions  $0 < Z/Sp < 0.25$  and  $0.75 < Z/Sp < 1.0$ . Again this was attributed to the varying amounts of upstream film coolant being injected along the ID and OD endwalls at different momentum flux ratios and different temperatures relative to the core flow. The midspan region indicates more uniform temperature distributions compared to the ID and OD regions, with the variations resulting from differing upstream dilution flow injections. The shape of the profiles are consistent with engine combustor profiles, as discussed in an earlier work [1], with the overall minimum to maximum magnitude variation in  $\theta$  being slightly less in this investigation than in the engine.

The corresponding heat transfer distribution along the vane surface for the different inlet temperature profiles is shown in Fig. 9 in terms of the Nusselt number, which is a dimensionless temperature gradient at the wall surface. The Nu distributions near the ID at  $Z/Sp=0.24$  are shown in Fig. 9(a), while Fig. 9(b) shows the Nu heat transfer distributions near the OD at  $Z/Sp=0.90$ . The results in the ID and OD regions only are presented to focus on the locations where the heat transfer was significantly altered as seen in Fig. 9 shows. The midspan gauges showed similar trends as seen at 24%. It can also be seen in Fig. 9 that the overall heat transfer variations and levels are higher at  $Z/Sp=0.24$  compared to  $Z/Sp=0.90$ . This can be explained in part by recognizing that the HFGs located at the  $Z/Sp=0.24$  span position extend from approximately  $Z/Sp=0.20$  to 0.35, and therefore their measurements were influenced by the higher turbulent flow that dominates the midspan region. In addition the location of the passage vortex exiting the vane row could be contributing to the higher levels. For all of the tests, the Nu distributions showed elevated levels



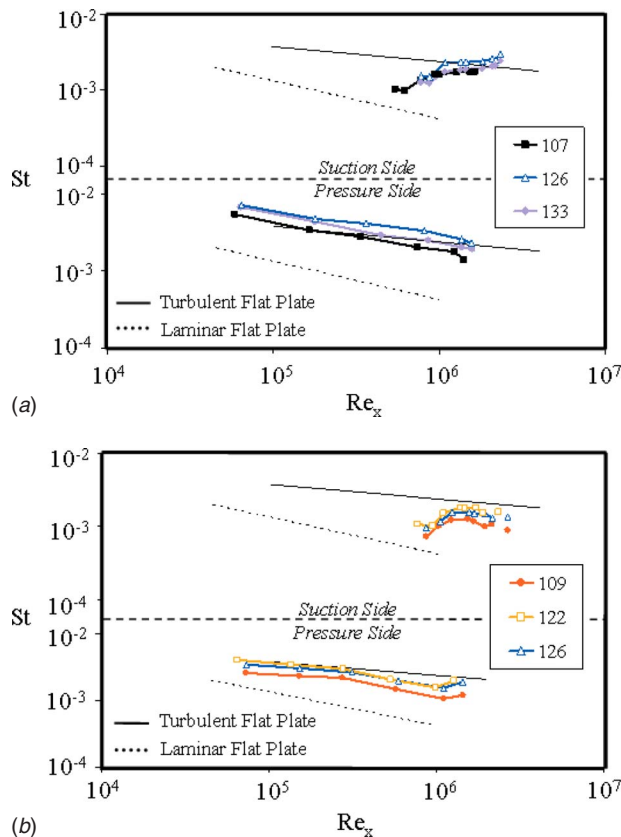


**Fig. 10** Plot of the Stanton number versus Reynolds number along the vane surface at (a)  $Z/Sp=0.24$  and (b)  $Z/Sp=0.90$

near the leading edge stagnation region where the flow was within the laminar flow regime. The  $Nu$  levels then decreased with increasing distance from the leading edge on both the pressure and suction surfaces. It is evident from Fig. 9 that transition to a turbulent boundary layer begins on the suction surface near  $X/S=0.3$  at both span locations. This transition region extended over the majority of the suction surface toward the trailing edge. The  $Nu$  distribution on the PS of the vane from  $X/S=-0.3$  to the trailing edge was indicative of a turbulent boundary layer.

The heat transfer along the surface of the vane for the baseline test 126 is also illustrated in Fig. 10 in the form of Stanton number versus Reynolds number based on surface distance from the leading edge,  $Re_x$ . The data in Fig. 10 correspond to PS gauges between  $-1.0 < X/S < -0.2$  and SS gauges at  $0.3 < X/S < 1.0$ . The vane leading edge region data were not included in the figure. The velocity scale used for both the Stanton and Reynolds numbers was the local freestream velocity. For the 24% gauges the Mach number at 50% span was used to aid this calculation as the Mach number at 24% span was unknown. The thermodynamic fluid properties were evaluated at the local film temperature. Data are plotted for both span locations at  $Z/Sp=0.24$  and  $0.90$  and both the PS and SS of the vane. Also plotted in this figure are the Stanton number correlations for laminar and turbulent flows over a flat plate. Figure 10(a) compares the baseline test results to the heat transfer results from tests 107 and 133, which were selected to illustrate the full  $St$  range of the data at  $Z/Sp=0.24$ . Figure 10(b) compares the baseline test results to the heat transfer results from tests 109 and 122, which were also selected to illustrate the full Stanton number range of the data at  $Z/Sp=0.90$ .

The results shown in Fig. 10 are important for two reasons. First, they show that on the PS the Stanton numbers follow the general slope of the turbulent correlation. Therefore, although the levels of heat transfer differ at the two spans, both pressure sur-

faces are fully turbulent. Second, they show that on the SS the Stanton numbers appear to make a transition from a laminar behavior to a turbulent behavior, and this agrees with the  $Nu$  distribution for the SS.

The overall variation in  $Nu$  from test to test is considerable at both span locations and was attributed to the different vane inlet profiles effect. This will be discussed more in the next section. Near the ID, at  $Z/Sp=0.24$ , it can be seen that the  $Nu$  distribution along the vane surface for the baseline case is consistently higher than the other test cases on both the pressure and suction surfaces. It was found that at this span location the different inlet profiles reduced the baseline heat transfer by 30–40% over the majority of the vane surface with a maximum reduction of 48% for test 107, which has a  $C_p=1.0$  and a  $\theta=-0.05$ . At 90% span, it was found that certain inlet profiles could increase the baseline heat transfer by 10–20% over the majority of the vane surface, for example, test 122 which has a  $C_p=0.75$  and  $\theta=-0.002$ . While other inlet profiles resulted in a decrease in the baseline heat transfer by 25–35% over the majority of the vane surface, for example, test 109 which also has a  $C_p=1.0$  and a  $\theta=-0.007$  but on the OD side.

### Influence of Inlet Profiles

Returning to the results shown in Fig. 9(a), an investigation was performed into the effects on the vane heat transfer due to temperature profiles shown in Fig. 8. As the temperature profile shifts from a flat profile like the baseline test 126 to a slightly shaped profile like test 123, to a higher gradient profile like test 122, to the largest gradient shape tested like test 108, the Nusselt number clearly decreases across the majority of the airfoil. Creating the greatest thermal profile is clearly beneficial in reducing the heat transfer for this span. This phenomenon occurred on both surfaces, leaving the baseline test (126) as the highest heat loaded case.

The isolated effect of the turbine inlet pressure profile on the vane surface heat transfer was determined by comparing the Nusselt number curves in Fig. 9 for tests having similar inlet temperature profiles but different inlet pressure profiles. For example, in the ID region near  $Z/Sp=0.24$ , Fig. 8 shows that tests 126 and 134 had very similar inlet temperature profiles that possessed moderate gradients near the endwalls, but Fig. 6 shows that these same two tests had inlet pressure profiles with different positive  $C_p$  peak values. In Fig. 9(a) it can be seen that test 135 (with a higher  $C_p$ ) resulted in lower Nusselt numbers at this span location. A similar result was also found when comparing test 123 to 125, test 122 to 135, and also test 108 to 107. This led to an important conclusion that at  $Z/Sp=0.24$  the test possessing a larger peak  $C_p$  value near the ID endwall resulted in lower Nusselt numbers for tests with similar inlet temperature profiles. This decrease was readily apparent along the entire PS. It also occurred on the SS but was most prevalent aft of  $X/S>0.4$ .

This observation is consistent with previous findings in the literature. For example, it was found within the work of Hermanson and Thole [8] and Colban et al. [9] that the turbine vane inlet pressure profile near the endwall directly affects the development of the secondary flows that exist within the turbine vane passage. The secondary flow vectors shown in Fig. 1 dictate the heat transfer along the vane surface and endwall region. The forward facing peak in the radial inlet pressure profile produced two vortices as the flow approaches and reached the leading edge of the vane. The span location that separated these two vortices was dictated by the span location of the  $C_p$  peak in the inlet pressure profile. It is believed that the relative size and strength of these two vortices directly depend on both the peak  $C_p$  value and the spanwise thickness of the forward facing region of the pressure profile. For this set of experiments it was not possible to determine the exact location of the peak in the spanwise total pressure at the inlet, but it is believed to be less than 10% span from either endwall due in part to the results of the computational fluid dynamics (CFD) work documented in Kunze et al. [14]. Due to the fact that the ID

and OD endwalls possess different contraction geometries, the secondary flow development will be slightly different on the ID versus the OD. However it was the overall flow changes with respect to a typical boundary layer behavior that was significant.

For a test case without utilizing the simulator film coolant jets along the endwall, like the baseline test 126, the turbine vane inlet pressure profile took the shape of a standard turbulent boundary layer profile (type A). In Fig. 1 it can be seen that the passage vortex for these inlet pressure profiles would have a slight impact on the flowfield at the  $Z/Sp=0.24$  span location. Therefore, the heat transfer measurements taken at this span were only slightly impacted by the passage vortex structure and therefore the dominant driver for heat transfer was the temperature found at about 24% span. However for a test similar to 134 that had a similar temperature profile (as shown in Fig. 8) but a significant peak in the pressure profile (type B), the existence of the counter-rotating vortex will directly impact the development of the passage vortex, for example, by confining it to a span region closer to the endwall or by reducing its vorticity, as seen in Fig. 1. This change in flow structure will have a definitive change in the heat transfer at 24% span as indicated in the reduction of the Nusselt number shown in Fig. 9(a).

Focusing next on the OD region, examining the temperature and pressure profiles at 90% span helps to understand why the Nusselt number increased in some cases and decreased in others. On the SS, the cases with higher Nusselt numbers than the baseline case were those that have negative  $C_p$  values near the OD endwall. Again this does not imply that an inlet profile that has a higher midspan total pressure causes a reverse flow at the endwall. However it infers that this condition would result in a more typical turbulent boundary layer. What these results suggest is that to keep the Nusselt numbers relatively low near the endwall, some high total pressure fluid is desirable to buffer the hot flow away from the endwall to avoid this increase in heat transfer. In practice, the cases with negative  $C_p$  result in strong type A profiles. These cases thereby generated a larger and stronger passage vortex, as indicated in Fig. 1, and thus increased the 90% heat transfer levels particularly aft of  $X/S > 0.4$ , as shown in Fig. 9(b). By increasing the near wall  $C_p$ , the passage vortex is broken up somewhat and the hottest midspan gases were not able to reach the endwall region.

On the PS, the low  $C_p$  cases also resulted in elevated PS Nusselt numbers but are joined by the very high  $C_p$  cases (tests 135, 107, and 134). These latter cases correspond to the type B inlet pressure profiles, but due to the very high  $C_p$  values, they resulted in the formation of a stronger passage vortex and a larger counter-rotating vortex system. It is believed that these two vortices caused the elevated heat transfer in the 90% region particularly on the PS. This is further enhanced by the stagnation region in between the vortices, as indicated in Fig. 1. While the exact location of the stagnation line was unknown, it can be expected that the strength of the vortices (as well as the size of the stagnation region) would increase with increasing  $C_p$  values and thus heat transfer.

The position of these vortices helps to explain some of the differences in trends between the 90% and 24% span locations. While at 24%, the higher  $C_p$  peaked pressure profile resulted in the lower Nu, this trend did not hold true at the 90% span. Clearly the highest  $C_p$  profiles caused an increase in the heat transfer, which suggests that there may be an optimum profile. In Fig. 9(b), test 108 displayed the lowest Nusselt number along the entire vane surface at 90%. This run was characterized by having a temperature profile with large radial gradients, which was previously shown to benefit the heat transfer at 24% as well. It furthermore has a high, but not extremely high,  $C_p$  value along the OD endwall. Its value is closer to 1.0, and while there are not enough runs within this  $C_p$  range to determine the exact optimum, clearly increasing the value to a  $C_p$  of 3.0 (test 107) is detrimental. This was also consistent with the results at the 24% span as the ID  $C_p$

**Table 1 Range of span locations that influence the driving temperature at  $Z/Sp=0.24$  and  $Z/Sp=90$**

Side of vane	Range of span locations (%)			
	Suction side		Pressure side	
Profile type	A	B	A	B
24% Span	24	24–35	24	10–24
90% Span	90–100	85–90	85–90	90–95

profiles were all less than 2.0. So for the ID profiles, increasing the  $C_p$  was still a benefit as they did not reach this “peak” benefit value. Since tests at higher  $C_p$  were not run on the ID, it is uncertain if these Nu levels would subsequently decrease, but it is believed that they would.

As the pressure profile increases from a case like test 122 toward test 126, the strength of the passage vortex decreases. Clearly there is some condition where the strength of this vortex will be near zero. This would be the ideal condition for reducing the secondary flows but not necessarily for achieving the lowest Nu. As the  $C_p$  value continues to increase, the passage vortex will form again as a pressure gradient was established as the flow approached the wall. Now, however, at the spanwise position of the peak  $C_p$  value, an inflection point was created, serving to swirl the rest of the flow back toward midspan. This served to circulate the hot flow away from the endwall, keeping the endwall cooler. As shown in Fig. 1, between these two vortices there was also a stagnation region formed, which served to increase the heat transfer in this region. At the highest  $C_p$ , this stagnation region can be expected to be large, elevating the local heat transfer. Likewise the strength of the two vortices would be expected to increase, further enhancing the Nusselt number.

### Influence of Driving Temperature

Utilizing the velocity vector trends shown in Fig. 1 and keeping in mind that the inflection points for the inlet profiles examined in this study are believed to be slightly closer to the endwall, a range of span locations that influence the local driving temperature was developed in Table 1. This table was built by determining where the secondary flow circulation patterns would bring the flow based on the velocity vector distribution shown in Fig. 1. It is understood that the values given in Table 1 are not exact, but they can be used as a general method to help determine how significant the impact of driving temperature is for the predicted Nusselt numbers. For example, for a type A profile at 24% there was relatively minimal secondary flow so the inlet profile at 24% would continue through the vane uninterrupted. The single point values indicate that a span range to average over was unnecessary, and the inlet total temperature at that same span location may be used as a good indicator of the true driving temperature. However at the 90% span Fig. 1 indicates a vortex with size in the 85–100% span moving fluid down the SS and up the PS of the airfoil.

For nonuniform vane inlet temperature profiles, a relatively warmer or cooler flow circulated from one span location to another span location changes the value of the driving temperature that should be used to determine the local values of  $h$  and Nu. The method of determining this driving temperature discussed in Povey et al. [5] could not be used in the current study since the technique assumed that the convection heat transfer coefficient was unchanged with and without vane inlet temperature distortion. In the current study, the inlet total pressure profiles vary significantly from one test to the next. This variation affects the secondary flow patterns within the vane passage and therefore also changes the local convection heat transfer coefficient from test to test.

To illustrate the effect of the secondary flow circulation patterns on the driving temperature, the Nusselt number distributions at both span locations are plotted in Fig. 11 for a test with a type A

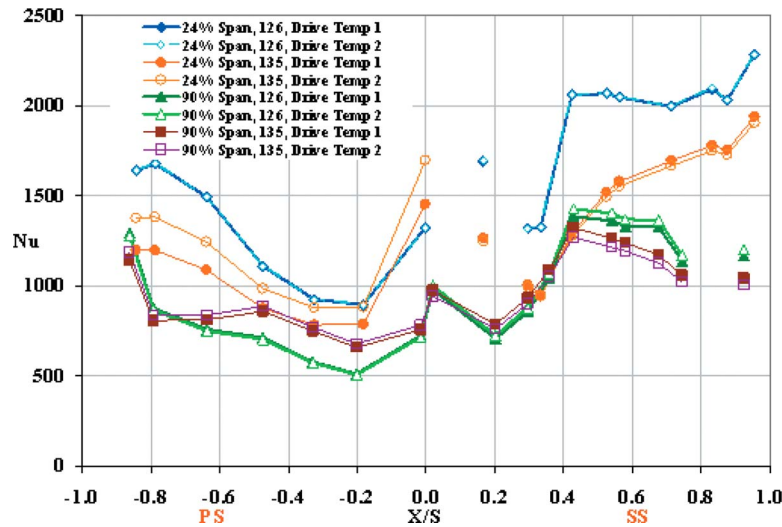


Fig. 11 Plot showing the effect of driving temperature on Nusselt number at the  $Z/Sp=0.24$  and  $Z/Sp=0.90$  measurement locations for a vane inlet pressure profile corresponding to type A (test 126) and type B (test 135)

inlet pressure profile (Test 126) and a type B inlet pressure profile (test 135). The Nusselt number distribution is plotted for two different driving temperatures. The first driving temperature, designated as “Drive Temp 1,” is the original driving temperature defined in the nomenclature and used in Fig. 9. The second driving temperature, designated as “Drive Temp 2,” is also the original driving temperature definition but utilizes  $T_{aw}$  based on the mean flow temperature within the vane span range described in Table 1.

Figure 11 shows this comparison for the baseline test 126, which had nearly uniform inlet profiles of both pressure and temperature. As expected for a case where the vane inlet flow temperature does not vary significantly in the span direction, the change in driving temperature was small and the impact on the predicted Nusselt number was also small at both span locations. However, the combination of a significant pressure profile causing more secondary flow circulation coupled with a significant thermal gradient in the temperature profile will affect the true driving temperature. Figure 11 also shows this comparison for test 135, which exhibited these types of profiles. The effect of the two different driving temperatures on Nu for test 135 was noticeable over the majority of the vane surface at both span locations. At  $Z/Sp=0.90$  these changes were on average near  $-4\%$  on the SS and  $+4\%$  on the PS. At  $Z/Sp=0.24$  the changes in Nu were on average near  $-2\%$  on the SS and  $+12\%$  on the PS. This indicates that the SS Nusselt number would have been overpredicted by approximately 3% had the more correct driving temperature not been taken into account, and the PS Nu was substantially underpredicted without accounting for the secondary flow effects.

## Conclusions

Several different temperature and pressure radial profiles representative of those exiting aeroengine combustors were investigated to determine their effects on high pressure turbine vane heat transfer and aerodynamic loading. The profiles were generated using a turbine inlet profile generator located in the TRF at the AFRL. Surface pressure measurements were analyzed at two span locations including midspan at  $Z/Sp=0.50$  and near the OD at  $Z/Sp=0.90$ . Heat flux measurements were analyzed near the ID and OD endwalls at  $Z/Sp=0.24$  and  $0.90$ .

The surface pressure measurements showed that increasing the Cp at the inlet to 4.5 increased the baseline aerodynamic loading as much as 9% near the OD endwall. This percentage was defined as the local deviation of the quantity  $P_S/P_T$  from the baseline test, which was characterized by a nearly uniform inlet pressure. These

same profiles had far less effect at midspan, only resulting in increases of 3%. The different inlet temperature and pressure profiles altered the vane surface heat transfer significantly along both the PS and SS of the vanes. Near the ID endwall at  $Z/Sp=0.24$ , increasing the Cp of the inlet profile reduced the baseline heat transfer up to 30–40% over the majority of the vane surface. Near the OD endwall, at  $Z/Sp=0.90$ , it was found that negative Cp inlet profiles could increase the baseline heat transfer by 10–20% over the majority of the vane surface, while profiles with moderate Cp values of around 1.0 resulted in a decrease in the baseline heat transfer by 25–35%. The isolated effect of the inlet pressure profile on vane heat transfer showed that the pressure profile plays an important role in the vane heat transfer. In general, an increase in the pressure profile Cp peak value for similar inlet temperature profiles leads to a reduction in the Nusselt number distribution over large portions of the pressure and suction surfaces of the vanes up to some optimum value. It is suggested that there is an ideal pressure profile somewhere around a Cp of 1.0 for reducing the secondary flows and thus the heat load to the turbine. It is also suggested that the temperature profile with the largest radial gradients provides the greatest heat transfer benefit.

The authors recommend that traditional models of passage vortex evolution developed for typical boundary layer profiles (type A) should not be applied for turbine vane inlet flows that contain forward facing pressure regions with inflection points near the endwalls (type B profiles). The heat transfer within the vane passage will be significantly different between type A and B inlet profiles due to the different secondary flow development, vortex strength, and vortex size within the passage.

The vane inlet pressure profile near the endwalls will directly influence the secondary flow circulation patterns that exist within the vane passage. The size and strength of the vortices within the passage will dictate the thermal migration in the spanwise direction, which will in turn affect the heat transfer driving temperature at the surface of the vanes and endwalls. This paper provided a description of this thermal migration process for different inlet pressure profile types and showed that very close attention must be paid to the driving temperature being used when predicting the Nusselt number distribution along the vane surface and endwalls. Otherwise, turbines operating with inlet profiles similar to those considered in this study could be exposed to local heat transfer significantly different from that intended or expected.



## Acknowledgment

The authors would like to thank Michael Kobelak, Terry Gillaugh, and Dr. Douglas Rabe from the AFRL/PRTE Technology Evaluation Branch for their guidance and help in conducting these experiments and to Robert Free for the installation of the HFGs on the vanes as well as for the manufacture of the rakes. The authors would also like to thank the Air Force Research Laboratory at Wright Patterson Air Force Base for funding and sponsoring this research effort.

## Nomenclature

- $C$  = vane axial chord length  
 $C_p$  = pressure coefficient,  $C_p = (P_t - P_{t_{ms}}) / (1/2 \rho_{av} U_{av}^2)$   
 $d$  = hole diameter  
 $h$  = convection heat transfer coefficient,  $h = q'' / (T_{aw} - T_w)$   
 $Nu$  = Nusselt Number,  $Nu = h_{local} C / k_f$   
 $P$  = pressure or vane pitch  
 $PS$  = pressure side  
 $q''$  = heat flux  
 $Re$  = Reynolds number,  $Re = U_{av} C / \nu_{av}$   
 $S$  = total vane surface length  
 $Sp$  = vane span  
 $SS$  = suction side  
 $St$  = Stanton number,  $St = h_{local} / (\rho_f C_p U_{local})$   
 $T$  = temperature  
 $U$  = velocity  
 $X$  = axial direction or surface distance  
 $Y$  = pitch direction  
 $Z$  = span direction

## Greek

- $\nu$  = kinematic viscosity  
 $\rho$  = density  
 $\theta$  = nondimensional temperature,  $\theta = (T - T_{av}) / T_{av}$

## Subscripts

- $av$  = mean or average conditions  
 $aw$  = adiabatic wall  
 $f$  = film conditions  
 $FC$  = film cooling

- $MS$  = midspan  
 $S$  = flow static conditions  
 $T$  = flow total conditions  
 $w$  = vane wall surface  
 $x$  = surface distance along vane

## References

- [1] Barringer, M., Thole, K., and Polanka, M., 2007, "Experimental Evaluation of an Inlet Profile Generator for High Pressure Turbine Tests," *ASME J. Turbomach.*, **129**, pp. 382–393.
- [2] Cattafesta, L., 1988, "An Experimental Investigation of the Effects of Inlet Radial Temperature Profiles on the Aerodynamic Performance of a Transonic Turbine Stage," MS thesis, MIT.
- [3] Shang, T., Guenette, G., Epstein, A., and Saxer, A., 1995, "The Influence of Inlet Temperature Distortion on Rotor Heat Transfer in a Transonic Turbine," AIAA Paper No. 95-3042.
- [4] Chana, K., Hurriion, J., and Jones, T., 2003, "The Design, Development and Testing of a Non-Uniform Inlet Temperature Generator for the QinetiQ Transient Turbine Research Facility," ASME Paper No. 2003-GT-38469.
- [5] Povey, T., Chana, K., Jones, T., and Hurriion, J., 2005, "The Effect of Hot-Streaks on HP Vane Surface and Endwall Heat Transfer: An Experimental and Numerical Study," ASME Paper No. GT2005-69066.
- [6] Krishnamoorthy, V., Pai, B., and Sukhatme, S., 1988, "Influence of Upstream Flow Conditions on the Heat Transfer to Nozzle Guide Vanes," *ASME J. Turbomach.*, **110**, pp. 412–416.
- [7] Van Fossen, J., and Bunker, R., 2002, "Augmentation of Stagnation Region Heat Transfer Due to Turbulence from an Advanced Dual-Annular Combustor," ASME Paper No. GT2002-30184.
- [8] Hermanson, K., and Thole, K., 2000, "Effect of Inlet Conditions on Endwall Secondary Flows," *J. Propul. Power*, **16**(2), pp. 286–296.
- [9] Colban, W., Thole, K., and Zess, G., 2002, "Combustor Turbine Interface Studies—Part 2: Flow and Thermal Field Measurements," ASME Paper No. 2002-GT-30527.
- [10] Haldeman, C. W., Dunn, M. G., MacArthur, C. D., and Murawski, C. G., 1992, "The USAF Advanced Turbine Aerothermal Research Rig (ATARR)," *NATO AGARD Propulsion and Energetics Panel Conference Proceedings 527*, Antalya, Turkey.
- [11] Barringer, M., Thole, K., and Polanka, M., 2004, "Developing a Combustor Simulator for Investigating High Pressure Turbine Aerodynamics and Heat Transfer," ASME Paper No. GT2004-53613.
- [12] Jones, T. V., 1995, "The Thin Film Heat Transfer Gauge: A History and New Developments," *Proc. Inst. Mech. Eng., Part C: J. Mech. Eng. Sci.*, **209**(C510), p. 150–160.
- [13] Moffat, R. J., 1982, "Contributions to the Theory of a Single-Sample Uncertainty Analysis," *ASME J. Fluids Eng.*, **107**, pp. 153–160.
- [14] Kunze, V. R., Wolff, M., Barringer, M. D., Thole, K. A., and Polanka, M. D., 2006, "Numerical Insight Into Flow and Thermal Patterns Within an Inlet Profile Generator Comparing to Experimental Results," ASME Paper No. GT-2006-90276.

# An Experimental Study of Combustor Exit Profile Shapes on Endwall Heat Transfer in High Pressure Turbine Vanes

M. D. Barringer

K. A. Thole

Department of Mechanical and Nuclear  
Engineering,  
Pennsylvania State University,  
University Park, PA 16802

M. D. Polanka

Turbines Branch,  
Turbine Engine Division,  
Air Force Research Laboratory,  
WPAFB, OH 45433

*The design and development of current and future gas turbine engines for aircraft propulsion have focused on operating the high pressure turbine at increasingly elevated temperatures and pressures. The drive toward thermal operating conditions near theoretical stoichiometric limits as well as increasingly stringent requirements on reducing harmful emissions both equate to the temperature profiles exiting combustors and entering turbines becoming less peaked than in the past. This drive has placed emphasis on determining how different types of inlet temperature and pressure profiles affect the first stage airfoil endwalls. The goal of the current study was to investigate how different radial profiles of temperature and pressure affect the heat transfer along the vane endwall in a high pressure turbine. Testing was performed in the Turbine Research Facility located at the Air Force Research Laboratory using an inlet profile generator. Results indicate that the convection heat transfer coefficients are influenced by both the inlet pressure profile shape and the location along the endwall. The heat transfer driving temperature for inlet profiles that are nonuniform in temperature is also discussed.*

[DOI: 10.1115/1.2950072]

## Introduction

The performance and durability of the hot section within gas turbine engines are critical operational issues that present many design and research challenges. The hot section of these engines includes both the combustion chamber and the high pressure turbine, the latter of which includes the endwall regions under investigation in this study. Considering that the hot gas temperatures are well above the melting point of the metal turbine hardware, the heat transfer to and aerodynamic loading of these platform regions is of great interest to engine designers. Long exposure to these elevated temperatures can result in the hardware experiencing thermal and mechanical fatigue, which can be better managed if the true turbine inlet conditions are well known and understood.

The spatial profiles of pressure and temperature that exit the combustor and enter the high pressure turbine play an important role in the operation of the engine. These profiles can be nearly uniform or can possess significant gradients near the inner and outer diameter endwalls. Some inlet pressure profiles have relatively high total pressure near the endwall compared to midspan, and some have relatively low total pressure near the endwall compared to midspan. As the flow passes through the turbine passages, these inlet pressure profiles can result in flow migration from the endwall toward midspan or from midspan toward the endwall. From a heat transfer perspective, the critical issue then is what part of the flow field affects a given region on the endwall or airfoil surface, and how does this influence change based on the inlet profiles.

The radial shape of a typical turbulent boundary layer profile has decreasing total pressure from midspan to the endwall. This turbulent boundary layer profile has often been used as an inlet condition in designing turbine vane and blade hardware. The be-

havior and influence, however, of more realistic inlet profile shapes need to be examined in the endwall region. The primary research objective for this paper was to investigate how different radial profiles of temperature and pressure affect the heat transfer along the vane endwall in a high pressure turbine. Testing was performed in the Turbine Research Facility (TRF) located at the Air Force Research Laboratory (AFRL) using a turbine inlet profile generator.

## Review of Relevant Literature

Within the recent past, turbine design has focused on incorporating strategically placed cooling holes and slots that serve to directly reduce the heat transfer in certain regions along airfoil surfaces and their endwalls. In addition, contouring the shape of the junction that joins the vanes to the endwalls was performed in studies by Zess and Thole [1] and Lethander et al. [2] to reduce the intensity of secondary flow circulation patterns that take place within the vane passage. Hermanson and Thole [3] showed that these secondary flows can redirect warmer fluid near the midspan toward the endwall and can redirect the cooling flow along the endwall toward midspan, which in turn reduces the benefit of the coolant.

There have been a large number of experimental and computational studies that have focused on turbine vane and blade endwall aerodynamics and heat transfer. Early work performed by Munk and Prim [4], Lakshminarayana [5], and Langston [6] focused on improving the understanding of the secondary flow patterns that develop within airfoil turning passages. It was shown that an inlet flow field consistent with a turbulent boundary layer resulted in the production of secondary flows, which have a direct impact on the primary passage flow by circulating it toward or away from the endwalls. If the inlet total pressure is uniform, the streamline patterns remain unchanged and the secondary flow vortices do not develop.

Several studies have further investigated the influence of the inlet flow field on the development of these secondary flows and vortices. Computational studies by Hermanson and Thole [3]

Contributed by the International Gas Turbine Institute of ASME for publication in the JOURNAL OF TURBOMACHINERY. Manuscript received July 26, 2007; final manuscript received December 5, 2007; published online January 23, 2009. Review conducted by David Wisler. Paper presented at the ASME Turbo Expo 2007: Land, Sea and Air (GT2007), Montreal, Quebec, Canada, May 14–17, 2007.

showed that the total pressure field is the driving force in the development of secondary flows and heat transfer present in turbine vane passages. They also reported that a counter-rotating vortex (CRV) can exist, in addition to the passage vortex (PV), within the vane passage that can drive fluid away from the endwall and toward midspan. This counter-rotating vortex was found for an inlet total pressure profile containing a positive inflection point (IP) in the spanwise direction near the endwall. Colban et al. [7,8] experimentally confirmed the existence of this counter-rotating PV by studying the effects of varying the film cooling flow through the liner and exit junction slot in a large-scale combustor simulator. Their study documented the passage secondary flow vectors for different vane inlet total pressure profiles and reported a counter-rotating vortex located above the PV for a vane inlet pressure profile containing a positive IP near the endwall.

Kost and Nicklas [9] also found that coolant injected along the vane endwall significantly affected the secondary flow development by strengthening the formation of the leading edge horseshoe vortex (HSV). The increased vortex strength depended on the axial location of the injection with respect to the leading edge stagnation point. They also found that coolant injected through an upstream slot and endwall film cooling holes acted to reduce the endwall cross flow (ECF) and PV by altering the endwall boundary layer thickness. In a study by Kang et al. [10] it was found that a relatively high vane exit Reynolds number ( $Re=1.2 \times 10^6$ ) resulted in the vane PV lifting off the endwall and onto the vane suction surface. The same result was not found for a lower exit Reynolds number ( $Re=6.0 \times 10^5$ ). The vortex lift-off resulted in a decrease in the endwall static pressure, thus causing a different surface heat transfer pattern compared to the lower exit Reynolds number. The high Reynolds number case resulted in the peak heat transfer occurring near the suction surface endwall interface, but for the low Reynolds number the peak occurred more toward midpassage. The separation of the boundary layer occurred farther upstream of the stagnation point for the high Reynolds number case.

The vane passage secondary flow development and endwall heat transfer were also found to be influenced by high freestream turbulence in a study by Radomsky and Thole [11]. They reported a region of high heat transfer upstream of the vane stagnation point corresponding to the formation of the HSV. The center of this HSV was found to be physically closer to the vane surface for high freestream turbulence (19.5%) compared to low freestream turbulence (0.6%). The difference in location was attributed to the elevated turbulence increasing the near wall approach velocities resulting in the vortex being pushed closer to the vane. Within the vane passage, relatively high Stanton numbers were found near the suction surface, while further downstream within the passage the Stanton numbers became aligned with the flow direction. Elevated freestream turbulence levels were found to increase the heat transfer over the entire endwall, with the exception of near the trailing edge where there was little reported augmentation. They reported that the secondary flows dominated the heat transfer near the trailing edge rather than freestream turbulence.

Blair [12] reported that secondary flows direct coolant along the vane endwall across the channel from the pressure surface toward the suction surface. This cross-passage pressure gradient results in increased cooling near the vane-endwall junction along the suction side and reduced cooling near the vane-endwall junction along the pressure side. The extent of the endwall cooling increased somewhat with increased coolant mass flow. Data recorded near the pressure surface showed a more rapid decrease in the film effectiveness compared to the midpassage. With no upstream coolant injection, the heat transfer was greater near the leading edges of both the suction and pressure surfaces than in the midpassage region. This increase in heat transfer was attributed to the leading edge vortex distorting the endwall boundary layer.

Haldeman and Dunn [13] performed heat transfer measurements in a full stage high pressure turbine. For the vane inner

endwall, the results showed that the Stanton number increased significantly through the passage with increasing axial chord. In the pitch direction, the magnitude of the heat transfer was highest for gauge locations nearest to the pressure and suction surfaces compared to gauges located near midpassage. They also reported that the vane-endwall Stanton numbers were in a similar elevated range as the airfoil itself. Similar results were found by Povey et al. [14] who studied the effects of radial inlet temperature distortion on vane and endwall heat transfer in a high pressure turbine facility. Their results also showed that the endwall Nusselt numbers increased with increasing distance within the passage. They also reported similar elevated Nusselt numbers along the endwall as the vane surface. They reported a large decrease in heat transfer along the hub and casing endwalls with inlet temperature distortion compared to an inlet temperature profile that was nearly uniform. The decrease in Nusselt number along the midpassage hub endwall was between 30% and 50%, while along the midpassage casing endwall it was between 25% and 35%. This reduction in heat transfer was attributed to lower local total temperatures of the flow near the endwalls rather than a decrease in the heat transfer coefficient. They found that this reduction in heat transfer was similar for two different circumferential clocking positions of a hot streak, which suggested that the relative circumferential position of the hot streak and vane did not affect the endwall heat transfer.

A study by Nicklas [15] reported that the front part of a transonic turbine vane passage without endwall film cooling experiences relatively constant levels of heat transfer coefficients. Graziani et al. [16] found similar results for the inlet region of a large-scale blade endwall. They reported that the area of influence of the HSV is larger for a relatively thicker inlet boundary layer. They reported elevated heat transfer along the endwall near the airfoil leading edge as well as similar minimum and maximum Stanton numbers for the thick and thin inlet boundary layers. The lowest values of Stanton number were reported near the pressure surface for both inlet boundary layers. The highest values of heat transfer on the endwall were found in the blade wake region for both inlet boundary layer types.

There are relatively few studies in the current literature that have investigated the effects of different realistic inlet temperature and pressure profiles on vane-endwall heat transfer. The temperature profiles exiting combustors and entering turbines become less peaked than in the past and become more spatially uniform. This trend is primarily due to operating the engine hot section closer and closer to its stoichiometric theoretical limits. As the combustor exit thermal fields become more uniform, the hot mainstream gases are in closer proximity to the vane-endwall regions. This has placed great emphasis on the need for a better understanding of how different types of inlet temperature and pressure profiles affect the flow and thermal migration within the first stage turbine passages, especially near the endwalls. The goal of the current study is to examine several different turbine inlet profiles and their corresponding endwall heat transfer levels.

## Test Facility and Instrumentation

All testing in the current study was performed at the TRF, which is located in the AFRL at Wright Patterson Air Force Base. This facility operates in a short duration blowdown manner in which several aerothermal engine parameters are matched. These nondimensional parameters include Reynolds number, Mach number, pressure ratio, gas to metal temperature ratio, and corrected mass flow. A photograph of the facility is shown in Fig. 1 and it consists primarily of a large supply tank, a turbine test section, and two large vacuum tanks. The facility has been fully documented by Haldeman et al. [17].

The nitrogen gas working fluid is pressurized and heated within the supply tank prior to testing and the turbine section and vacuum tanks are evacuated. Testing then begins by activating the supply tank main valve, at which time the gas flows through the



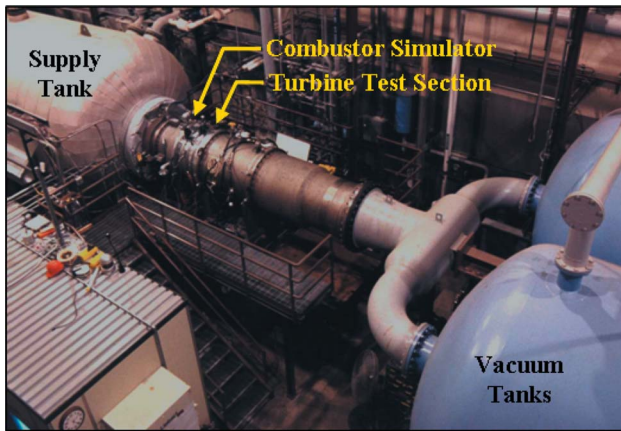


Fig. 1 Photograph of the TRF facility

turbine test section and into the vacuum tanks. The mass flow rate is set by controlling the turbine pressure ratio using a variable area isolation valve located downstream of the main test section. The duration of the tests in the current study was approximately 5 s, which was dependent on the size of the turbine being tested. Due to the short test duration, all instrumentation measurements were recorded simultaneously in real time onto data storage units. The data were simultaneously acquired across 200 12 bit channels having a maximum frequency response of 100 kHz and 200 16 bit channels having a maximum frequency response of 200 kHz. Signal conditioning on each channel was performed using low pass filters and built-in amplifiers. All data reduction was performed at a later time.

The turbine test section is a true scale, fully annular, half turbine stage and for this particular study, it was operated in a vane only configuration, as shown in the facility drawing in Fig. 2. The turbine inlet profile generator, documented by Barringer et al. [18], was used in the current study to allow turbine testing to be performed with inlet profiles of pressure and temperature representative of those exiting engine combustors including realistic turbulence intensities and length scales. Several different radial and some circumferential profiles of temperature and pressure were obtained from General Electric, Pratt & Whitney Engines, and the Air Force Research Laboratory during the design phase of the inlet profile generator. These engine profile data in conjunction with several combustor simulator exit pressure profiles docu-

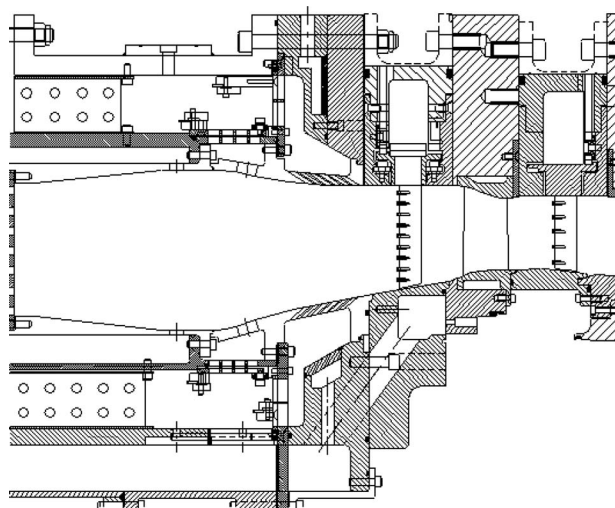


Fig. 2 Drawing of the TRF test rig in a vane only configuration with the inlet profile generator

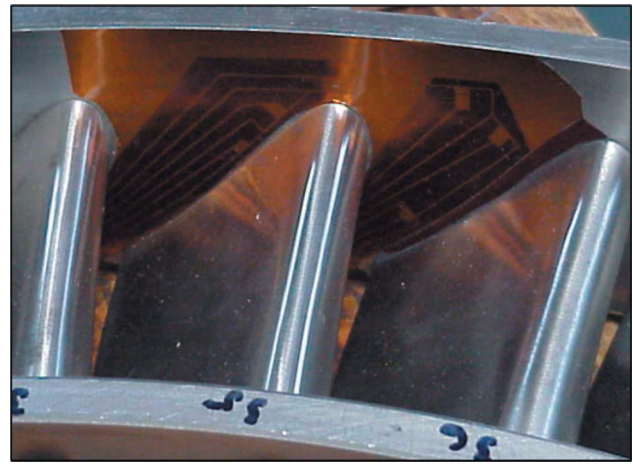


Fig. 3 Photograph of the turbine vane OD endwall instrumented with thin film heat flux gauges

mented by Colban et al. [7,8] were studied to help determine the proper radial profile shapes that the simulator should be capable of producing.

The inlet profile generator can also be seen in Fig. 2 upstream of the test vane ring. The generator operates by mimicking an aeroengine combustor in which it injects several different flow streams at different temperatures into a central chamber via dilution holes and film cooling holes. The injection flow rates, momentum flux ratios, and temperatures of the different flow streams are varied depending on the desired turbine inlet profile shapes.

The turbine inlet and exit profiles were measured using several instrumentation rakes located on traverse rings upstream and downstream of the turbine section. The rakes contain multiple thermocouples or multiple pressure transducers that are spaced to obtain measurements over equal annular flow areas. The tests discussed in this study involved circumferentially traversing these rakes by approximately 90 deg during the blowdown to obtain both radial and circumferential data. For the turbine inlet profiles being analyzed in the current study a temperature rake was used that contained seven 0.0254 mm diameter thermocouple beads with a thermal time constant of approximately 1.1 ms. Two pressure rakes were also used each containing nine miniature high frequency pressure transducers. All flow and thermal measurements were sampled at 20 kHz. The heat flux along the outer diameter (OD) endwall was measured using Oxford thin film heat flux gauges [19]. Heat flux measurements were not taken along the inner diameter (ID) endwall. The layout of the individual gauges can be seen in the photograph in Fig. 3. Seven gauges were placed near the vane passage inlet, along the pressure side of the vanes, and near the passage exit, as shown in the schematic in Fig. 4.

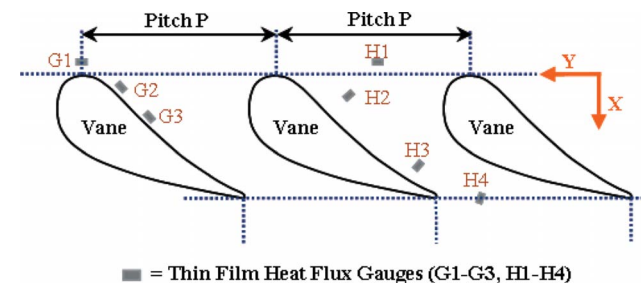
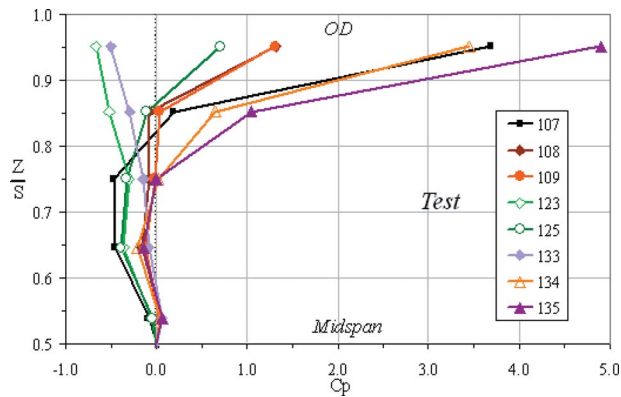


Fig. 4 Schematic of the OD endwall indicating the locations of the thin film heat flux gauges



**Fig. 5 Radial total pressure profiles measured at the vane inlet near the OD**

Based on the uncertainties in the measurement of the heat flux gauge resistance and the uncertainty in calibration from resistance to temperature, the surface temperature uncertainty for the heat flux measurement was calculated to be  $\pm 0.8$  K for the heat flux gauges. A jitter analysis, described by Moffat [20], was then performed through the reduction scheme to obtain the uncertainty in the surface heat flux. This resulted in uncertainties in heat flux up to  $2000 \text{ W/m}^2$  depending on the gauge. The uncertainty in flow temperature is approximately 0.7 K. The uncertainty in the end-wall heat transfer coefficient was determined to be approximately  $30 \text{ W/m}^2 \text{ K}$  for the thin film gauges based on uniform inlet temperature profiles. This corresponded to Nusselt number uncertainties between 5% and 9% depending on location. The uncertainty in the endwall heat transfer coefficient for nonuniform inlet temperature profiles is discussed in the following sections.

### Vane Inlet Conditions

The pressure and temperature profiles that are analyzed in this study were generated during a series of tests whose flow conditions are reported in more detail by Barringer et al. [18]. To summarize the test conditions, the flow at the turbine inlet for all of the profiles presented in this study corresponds to a mean Reynolds number of  $\text{Re} = 2.1 \times 10^5$  and a mean axial Mach number of  $M = 0.1$ . The turbulence intensity associated with these turbine inlet profiles was found to be in an elevated range between  $\text{Tu} = 20\text{--}30\%$ . The longitudinal integral length scale was found to be near 30% of the vane pitch, which corresponds to 2.3 times the vane leading edge diameter.

Several radial total pressure profiles at the turbine vane inlet are shown in Fig. 5 from midspan ( $Z/S = 0.5$ ) to the OD endwall ( $Z/S = 1.0$ ). The profiles are plotted in terms of a normalized total pressure coefficient  $C_p$  defined as the local total pressure subtracted by the midspan total pressure all divided by the average dynamic pressure at the vane inlet. Note that by this definition  $C_p = 0$  at midspan. These radial profiles have been circumferentially (spatially) averaged across one full vane pitch along lines of constant radius that are spaced at equal annular flow areas and represent the mean vane inlet conditions. The test numbers are a numeric record of the facility settings used within the inlet profile generator and supply tank. These settings were summarized in tabular form by Barringer et al. [18] for each test number. Each test is different since the inlet profile generator settings are different for each test. The settings within the inlet profile generator control the mass flow rate and temperature of the film cooling flow, dilution flow, and core mainstream flow. These different settings result in different pressure and temperature profile shapes entering the vanes.

A range of pressure profile shapes can be seen including some that contain sharp gradients near the OD endwall in Fig. 5. These

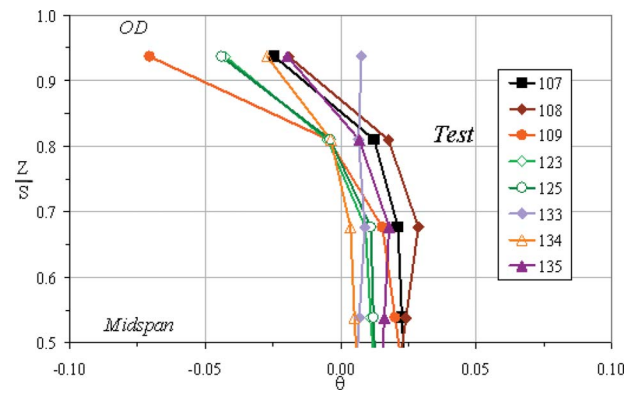


**Fig. 6 Radial total temperature profiles corresponding to the pressure profiles in Fig. 5**

gradients are the result of varying amounts of upstream film coolant being injected into the mainstream flow along the endwall. The  $C_p$  values near the OD endwalls at  $Z/S = 0.95$  were found to be directly related to the upstream film cooling momentum flux ratio where an increase in this ratio resulted in an increase in the maximum  $C_p$  value [18]. It is important to note that a negative  $C_p$  value does not mean that the flow is in the reverse upstream direction; it simply means that the local total pressure is less than that at the midspan. This behavior can be seen for Tests 123 and 133, which possess slightly less total pressure near the OD endwall (compared to the midspan). This profile behavior is characteristic of a turbulent boundary layer in that the total pressure decreases with increasing proximity to the endwall. This is in contrast to the pressure profiles for Tests 107, 108, 109, 125, 134, and 135; all of which are characterized by positive  $C_p$  values at  $Z/S = 0.95$  indicating that an increase in total pressure takes place near the endwall. It is expected that all of these pressure profile shapes exhibit a similar trend closer to the endwall in which a negative gradient should be present.

The radial total temperature profiles at the turbine vane inlet corresponding to the total pressure profiles in Fig. 5 are shown in Fig. 6. The temperature profiles are plotted in terms of a nondimensional total temperature coefficient  $\theta$  defined in the Nomenclature. These radial temperature profiles have also been circumferentially averaged across one full vane pitch along lines of constant radius that are spaced at equal annular flow areas. It can be seen that one of the temperature profiles is nearly uniform in the radial direction from midspan to the OD endwall, Test 133. The remaining thermal profiles, however, contain moderate to significant gradients near the endwall. These endwall gradients were found to scale with the upstream film cooling momentum flux ratio and the film coolant temperature [18]. The shapes of the pressure and temperature profiles near midspan are more uniform than near the endwall, which is a result of the intense mixing of the dilution flow in the upstream inlet profile generator.

### Secondary Flow Patterns

There are several means by which the inlet total pressure profile can alter the vane-endwall heat transfer. It can change the local boundary layer thickness and turbulence intensity. The inlet pressure profile can also affect the secondary flow vorticity (rotation direction), turnover rate, vortex size, and vortex trajectory. All of these physical mechanisms influence the convective heat transfer coefficients along the endwall.

The different total pressure profiles at the vane inlet result in different secondary flow development within the vane passage. The HSV that forms at the vane leading edge junction will have a range of flow circulation patterns within the vane passage depending on whether the inlet total pressure profile near the endwall is consistent with a typical turbulent boundary layer ( $C_p < 0$ ), has



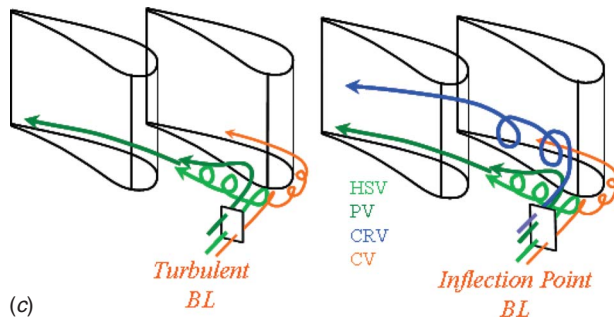
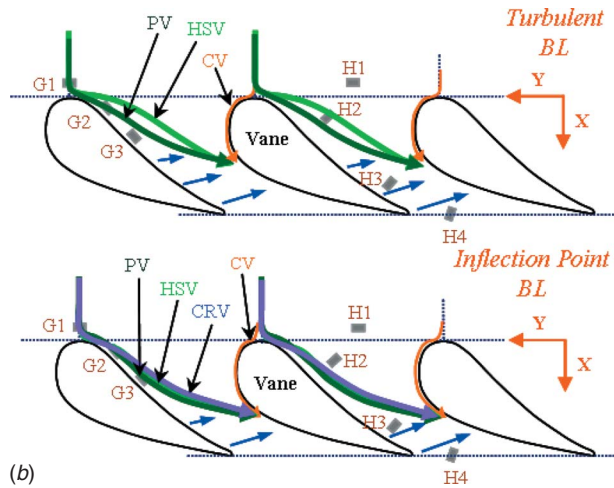
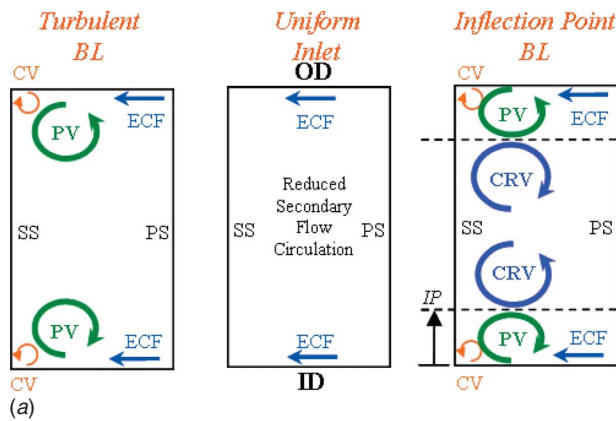


**Fig. 7 Schematics illustrating secondary flow patterns that develop within the vane passage including (a) a cross-passage view near midaxial chord looking downstream, (b) a span view looking toward the endwall, and (c) an isometric view upstream looking downstream**

nearly uniform pressure ( $C_p \approx 0$ ), or contains a forward facing IP ( $C_p > 0$ ). The schematic shown in Fig. 7(a) illustrates the different circulation patterns within the vane passage near midaxial chord for these three pressure profile scenarios.

For the turbulent boundary layer scenario ( $C_p < 0$ ), a PV and suction side corner vortex (CV) form near the endwalls circulating mainstream flow and ECF along the endwall toward the suction side of the vane. The PV is considerably larger than the CV and also directs flow from the endwall toward the midspan. For the near uniform inlet condition scenario ( $C_p \approx 0$ ) with near uniform total pressure, there is no significant secondary flow pattern present within the vane passage. For the inlet boundary layer scenario with an IP in total pressure ( $C_p > 0$ ), the PV and CV will

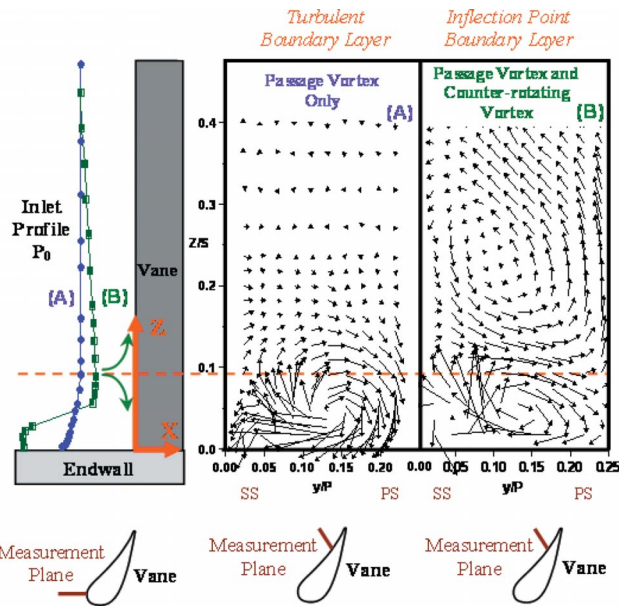


**Fig. 8 Velocity contours within the vane passage ( $X/C=0.35$ ) from Colban et al. [8] showing secondary flow vectors and their corresponding vane inlet total pressure profiles for (a) a turbulent boundary layer and (b) a forward facing IP boundary layer near the endwall**

form as well as a CRV, which is larger in size than the PV. The CRV develops in this case since the inlet total pressure profile has an IP that is located near the endwall, typically somewhere between 0% and 15% of the vane span. The span location where the PV and CRV become tangent corresponds to the general span location of the IP.

The schematics shown in Figs. 7(b) and 7(c) show conceptually that when the total pressure near the endwall at the vane inlet is less than the midspan total pressure, then the near endwall flow field contains both (1) the HSV that develops near the vane leading edge and (2) the PV that forms from fluid entering the vane inlet that passes over top of the HSV and then down into the relatively lower pressure region along the endwall behind the HSV. The pressure side portion of the HSV combines with this PV into one vortex near midaxial chord, and then finally this combined PV crosses over the passage toward the suction side of the adjacent vane where it continues until it reaches the vane passage exit. The suction side portion of the HSV remains relatively small and close to the suction side endwall junction where it is eventually overcome by the PV. Note that in Fig. 7(a), the passage vortex that is shown refers to the combined PV. When the total pressure near the endwall at the vane inlet is larger than the midspan total pressure and contains an IP near the endwall, then the near endwall flow field contains (1) and (2) just described but also contains the CRV. The CRV develops from fluid entering the vane that is above the IP and rotates in an opposite direction compared to the combined PV.

The concepts that are illustrated in Fig. 7 were developed based on the findings from both Hermanson and Thole [3] and Colban et al. [8]. Experimental data from the study of Colban et al. [8] are shown in Fig. 8 including example secondary flow vectors within the vane passage for two different types of vane inlet pressure profiles. Their study confirmed the presence of a counter-rotating vortex located above the PV when the vane inlet pressure profile contains a slight forward facing IP near the endwall. This is illustrated in Fig. 8, which shows secondary flow vectors within the vane passage at approximately  $X/C=0.35$ . The turbulent bound-



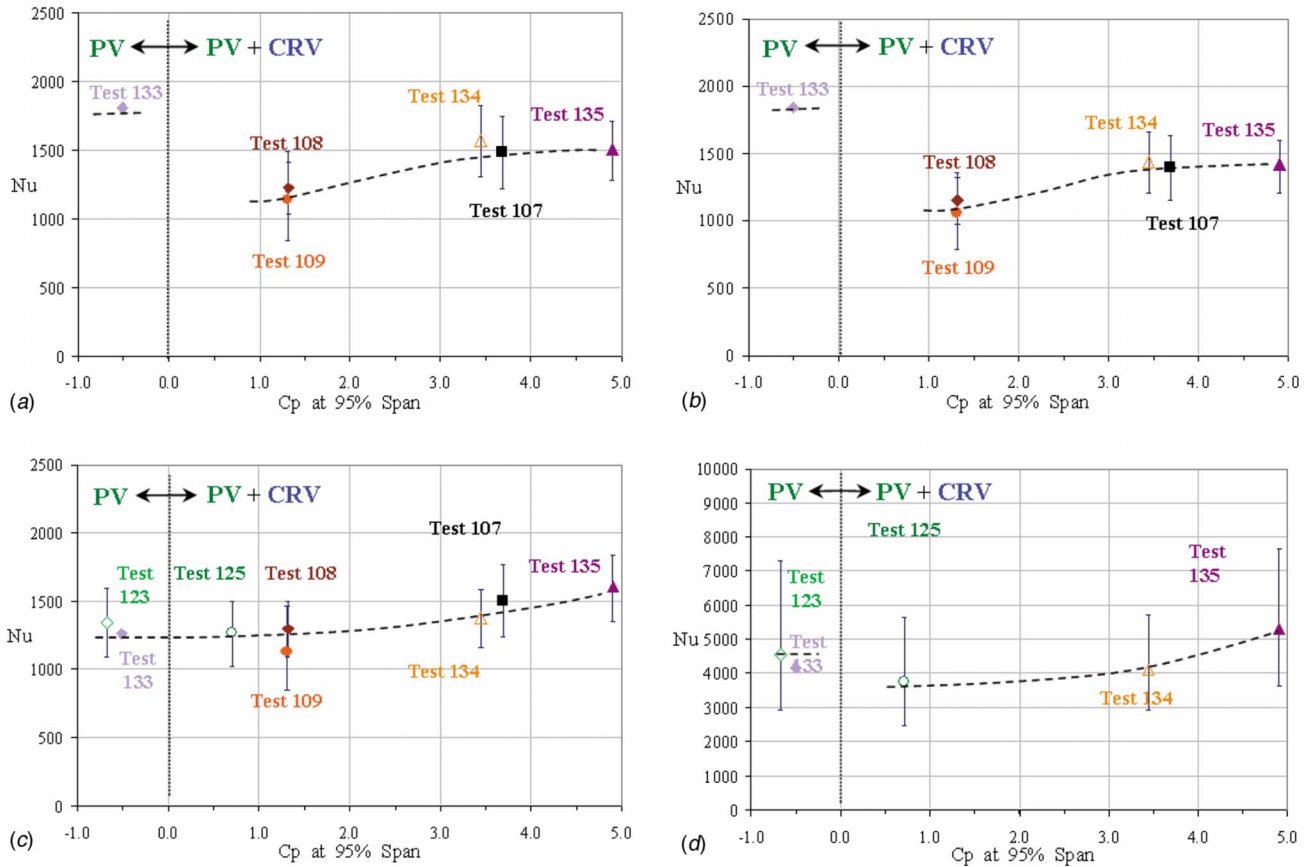


**Fig. 9 Nusselt number scaling for heat flux gauge (a) G1 near vane stagnation, (b) G2 near the vane pressure side leading edge, (c) H1 at the passage inlet near midpitch, and (d) H2 near the passage inlet near midpitch**

ary layer profile has lower total pressure near the endwall relative to midspan, and the IP profile has higher total pressure near the endwall at  $Z/S=0.1$  relative to midspan.

The inlet total temperature profile can also alter the vane-endwall heat transfer. Inlet temperature profiles that are nearly uniform in shape result in fluid temperatures near the endwall that are very similar to the hot midspan flow, which results in increased wall temperatures. Inlet temperature profiles with negative thermal gradients near the endwall have fluid temperatures near the wall that are cooler than the hot midspan flow, which results in reduced endwall metal temperatures for the same convection coefficient. Depending on the corresponding inlet pressure profile shape, the fluid near the wall can be circulated toward midspan or the fluid near midspan can be circulated toward the endwall.

### Endwall Heat Transfer Measurements

The heat transfer measurements taken on the OD endwall are reported in this section for the different inlet profiles shown in Figs. 5 and 6. The heat transfer for each of the seven heat flux gauges is documented in Figs. 9 and 10 in the form of Nusselt number, which is defined in the Nomenclature. The convective heat transfer coefficient was obtained by dividing the measured heat flux by an appropriate driving temperature. The driving temperature associated with the local heat flux was defined as the difference between the measured wall surface temperature ( $T_w$ ) and the total temperature of the freestream ( $T_\infty$ ) in the vicinity of the heat flux gauge, which is now discussed.

The issue of how to determine  $T_\infty$  near the individual heat flux gauges is a challenging problem since detailed flow and thermal field data within the vane passage could not be taken for the various inlet profiles. Simply using the mean flow temperature

that enters the turbine vane as a driving temperature for all endwall surface locations and regions has been done in many past studies involving turbine heat transfer but a better approximation of the true driving temperature must be estimated for realistic inlet conditions that are not uniform. It was decided that the mean flow temperature at the vane inlet in the span range  $0.75 < Z/S < 1.0$  was a more accurate definition for  $T_\infty$  since the flow field in this span region significantly affects the endwall region. This definition is used consistently for all gauges and for all tests discussed below. However, its applicability is also examined in this section at different locations along the endwall.

For inlet flows where the near endwall total pressure has  $C_p < 0$ , the PV circulates fluid within approximately 20% of the vane span toward the endwall throughout the passage [21]. Near the leading edge region, when  $C_p > 0$  the fluid between the IP span location and endwall is circulated toward the endwall. However, at axial locations within the passage where the edges of the PV and CRV vortices interact with one another, the endwall is not limited to the inlet profile flow temperatures between the endwall and the IP. At these axial locations, the endwall can see temperatures from fluid that originated farther away from the endwall at the vane inlet. For example, the CRV can circulate fluid near midspan toward the IP span location and then the PV can circulate a portion of this same fluid layer toward the endwall. Note, however, that this overall circulation from CRV to PV to endwall would take place over a finite streamwise distance, and this distance may change slightly depending on the size and strength of the vortices. The secondary flow patterns emphasize that the endwall driving temperature is dependent on the location within the passage as well as the inlet pressure and temperature profile shapes.

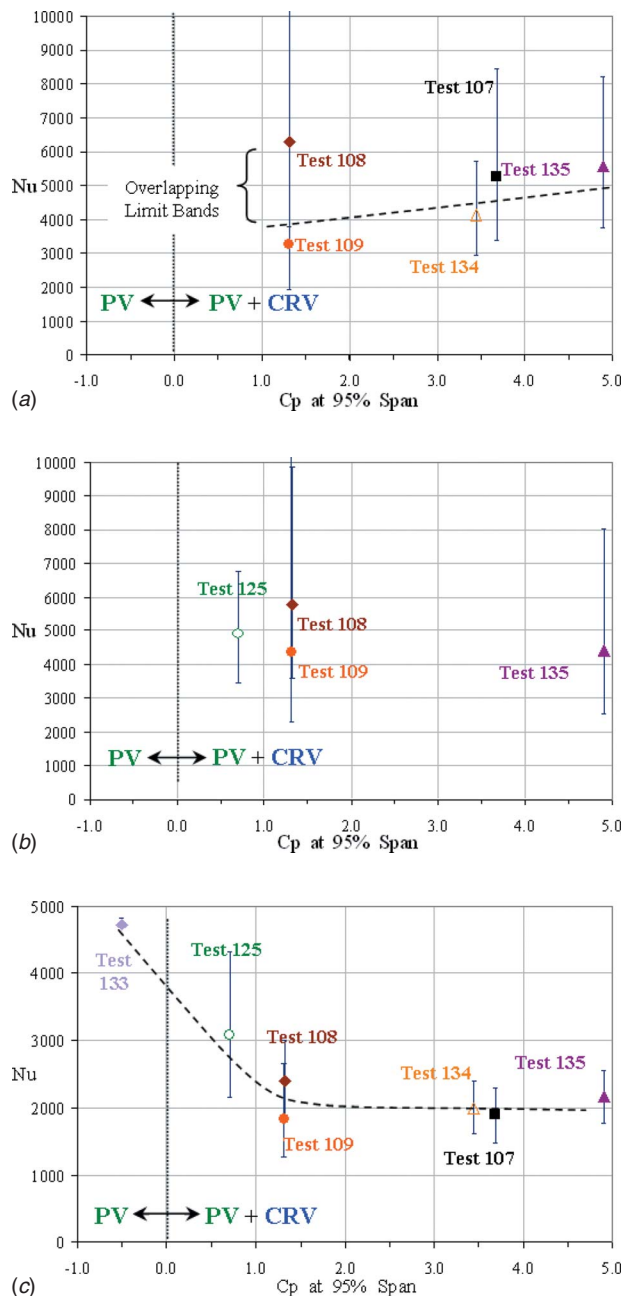


**Fig. 10** Nusselt number scaling for heat flux gauge (a) G3 near the vane pressure side at midaxial chord, (b) H3 near the vane pressure side trailing edge, and (c) H4 near the vane passage exit

No matter how  $T_\infty$  is defined, the convection heat transfer coefficient  $h$  at a given endwall location should be very similar for two inlet pressure profiles that have nearly the same shape and  $C_p$  values, as long as they also both have nearly the same inlet Reynolds number and Mach number. In other words, if two different tests have the same inlet  $C_p$  value near the endwall, for example, Tests 108 and 109 in which  $C_p \approx 1.3$  at  $Z/S=0.95$ , but one test resulted in  $\theta=-0.02$  (Test 108) near the endwall and the other test resulted in  $\theta=-0.07$  (Test 109) near the endwall, then the convection coefficient  $h$  should be nearly the same value, since  $h$  itself is not a function of temperature.

Figures 9(a)–9(d) and 10(a)–10(c) compare the Nusselt number with the  $C_p$  value measured at  $Z/S=0.95$  near the OD endwall. The available data points that are plotted correspond to the previ-

ously mentioned driving temperature definition for the convective heat transfer coefficients. The plus and minus bands on each data point correspond to the Nusselt number that would occur at the maximum and minimum measured flow temperatures at the vane inlet in the span range  $0.75 < Z/S < 1.0$ . The plus and minus bands do not represent error bars. The dashed curve represents the general trend in Nusselt number as a function of the  $C_p$  value near the endwall. As the inlet total pressure profile near the endwall is changed, the pressure field that drives the local flow also changes, including a change in the secondary flow. This will directly impact the convection heat transfer coefficients near the endwall. The magnitude and sign of the change in  $h$  depend on the magnitude of the change in the inlet total pressure and the location within the vane passage.

The heat transfer measurements taken near the vane leading edge stagnation region are shown in Fig. 9(a) for heat flux Gauge G1 that is positioned at  $X/C=-0.12$  (see Fig. 4). This location should be close to the position where the HSV begins to form. It can be seen in Fig. 9(a) that the limit bands for Test 133 are very small, which is due to the near uniform temperature profile near the OD for this particular test. It can also be seen that the data points for Tests 108 and 109 are very similar in Nu, which implies that the driving temperature definition mentioned previously is consistent (since the driving temperature value is different for these two test conditions). The fact that Tests 108 and 109 have nearly identical pressure profiles near the OD endwall suggests that very similar convection heat transfer coefficients should be present, and this is the case. Similar  $h$  values are also seen for Tests 134 and 107, which have similar  $C_p$  values ( $C_p \approx 3.5$ ) at  $Z/S=0.95$ . The Nu data point for Test 134 is slightly higher than for Test 107 but agreement still occurs within the limit bands.

The results in Figs. 9(a) and 9(b) indicate that the heat transfer coefficient near the vane leading edge stagnation region is higher for an inlet profile with  $C_p$  less than but nearly equal to zero, as compared to an inlet profile with  $C_p > 0$ . Between  $-0.5 < C_p < 1.2$  there is a clear reduction in Nu. It is believed that this reduction in Nu is the result of the HSV separation point moving in the axial direction, relative to the vane stagnation point, due to a change in the endwall inlet  $C_p$  value. Both Figs. 9(a) and 9(b) show that for inlet profiles with  $C_p > 0$ , as the total pressure is increased along the OD endwall the value of  $h$  increases, which is a result of the velocity increasing in magnitude.

Figure 9(b) shows that the heat transfer results for heat flux Gauge G2 are slightly lower but very similar to G1 (Fig. 9(a)). Heat flux Gauge G2 is positioned near the vane pressure side leading edge at  $X/C=0.06$  (see Fig. 4). The evident similarity in heat transfer behavior between Gauges G1 and G2 is due to their close endwall proximity. It is believed that Gauge G2 is only slightly influenced by the edge of the PV and HSV, and therefore the same driving temperature definition is applicable. Again, there is good agreement in the Nusselt number values between Tests 108 and 109 and between Tests 107 and 134.

The results for Gauge H1 located at the passage inlet near midpitch (see Fig. 4) are shown in Fig. 9(c). This gauge location is not significantly affected by the secondary flow development as one would expect. As  $C_p$  is increased, the local streamwise velocity near the passage inlet increases and results in a continuous increase in the convection heat transfer coefficient. Another important result is that the magnitudes of the Nusselt numbers for Gauge H1 are comparable to those measured for Gauges G1 and G2, which are also located near the passage inlet. This finding is in agreement with the results reported by Nicklas [13] and Graziani et al. [14] in that the front part of the airfoil passage experiences near constant levels of heat transfer coefficients.

The Nusselt number results for Gauge H2 at  $X/C=0.12$  near midpitch (see Fig. 4) are reported in Fig. 9(d). The levels reported for this gauge are three to four times higher than those reported at the passage inlet for Gauges G1, G2, and H1. This increase is attributed in part to flow acceleration from the vane passage inlet

to the gauge location, but it is also attributed to the HSV and PV passing over and circulating fluid into the endwall near the gauge location. The general trend shown for Gauge H2 is similar to that of Gauge H1 in that an increase in the inlet profile  $C_p$  results in an increase in  $h$ . This similarity is expected. Since the Nusselt numbers for Tests 123 and 133 in Fig. 9(d) are similar, this implies that the originally defined driving temperature is still applicable at this location for  $C_p < 0$ . For Gauge H2, between  $-0.5 < C_p < 0.7$  there is a small reduction in Nu. This reduction is similar to the reduction reported for Gauges G1 and G2 between  $-0.5 < C_p < 1.2$  and was attributed to the weakening of the HSV and the PV as the inlet total pressure profile near the endwall approaches uniform conditions (as  $C_p$  approaches  $C_p = 0.0$ ).

The heat transfer results for heat flux Gauge G3 within the passage at  $X/C = 0.3$  (see Fig. 4) are shown in Fig. 10(a). The Nusselt numbers at this location are also nearly three to four times higher than those measured near the leading edge stagnation region. This increase was again attributed in part to the flow accelerating between the passage inlet and  $X/C = 0.3$  but also because of the PV passing near the gauge in which freestream fluid is circulated toward the endwall gauge location. Figure 10(a) shows the available data for this gauge, which corresponds to only inlet pressure profiles with  $C_p > 0$  near the endwall. This particular gauge was not operating properly during the other tests. For the available data, it can be seen that the previously mentioned driving temperature definition is not very accurate at this gauge location for the  $C_p$  values tested since the Nu values for Tests 108 and 109 ( $C_p = 1.3$ ) as well as those for Tests 107 and 134 ( $C_p \approx 3.5$ ) are considerably different. However, the true Nu values for this set of tests should be within their overlapping bands.

The large limit bands in Figs. 10(a) and 10(b) are a result of the relatively higher heat flux values and higher wall temperatures measured at these two gauge locations. The lower limit band is calculated by using the largest driving temperature, which is between  $T_w$  and the maximum fluid temperature at the vane inlet between  $0.75 < Z/S < 1.0$ . The upper limit band is calculated by using the smallest driving temperature, which is between  $T_w$  and the minimum fluid temperature at the vane inlet between  $0.75 < Z/S < 1.0$ .

The true Nu values for Tests 108 and 109 in Figs. 10(a) and 10(b) as well as for Tests 107 and 134 in Fig. 10(a) may, in fact, never fall within their overlapping bands at this location. This is due to the fact that within the vane passage the PV and CRV vortices complete more than one rotation (turn over cycle) and some of this fluid comes in contact with the lower temperature walls, which can change the true driving temperature to something other than the difference between the measured wall temperature and the average of the inlet temperature profile over a certain span region. This is the reason that it is impossible to know for certain what the true  $T_\infty$  is for the gauges downstream of the leading edge region within the passage without having well resolved flow field data within the passage or detailed accurate predictions from computational fluids dynamics (CFD). This also emphasizes how difficult these heat transfer measurements are, but more importantly how difficult it is for the engine designer to estimate the right values and use them in their hardware life prediction tools. Turbine designers must be made aware that this is a key reason why the turbine endwalls can see significant thermal fatigue and melting in real engine hardware. An underestimation of the true driving temperature, which can easily take place as shown by the large limit bands, can cause significant hardware failure.

The fluid that reaches Gauge G3 comes from a span location further away from the endwall than for Gauges G1 and G2. In other words, the part of the vane inlet flow field at a span location consistent with the PV is being directed toward this endwall gauge location (see Fig. 7(c)). The PV essentially circulates warmer fluid into this gauge location. For endwall inlet profiles having  $C_p > 0$ , as  $C_p$  is increased the PV and CRV increase in strength and are pushed somewhat closer to the vane pressure side (closer to G3)

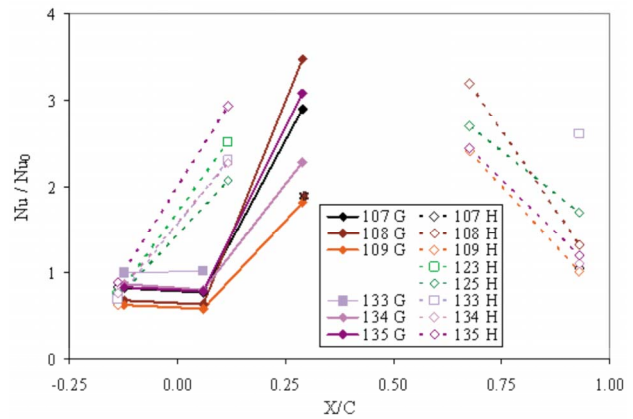


**Fig. 11 Nusselt number augmentation versus  $X/C$  for each heat flux gauge**

prior to crossing the channel to the adjacent vane, which takes place farther downstream within the passage, as was illustrated conceptually in Fig. 7. This results in increased  $h$  values near this gauge location.

The Nusselt numbers for Gauge H3 within the passage at  $X/C = 0.68$  near midpitch (see Fig. 4) are reported in Fig. 10(b). Gauge H3 experiences the most elevated heat transfer coefficients. This is a result of the gauge being located near the throat of the vane passage and therefore the fluid velocities are relatively high. This gauge location should not be significantly influenced by the secondary flows, and the quantity of available data points shown in Fig. 10(b) is not large enough to draw conclusive comments regarding a trend involving the inlet total pressure profile.

The results for heat flux Gauge H4 near the vane passage exit (see Fig. 4) are shown in Fig. 10(c). In general, this gauge reports that the heat transfer coefficients are larger for inlet profiles with a total pressure coefficient  $C_p$  that is less than but nearly equal to zero. It can be seen that as the  $C_p$  value is increased, the Nu values decrease and then level out. It is believed that as the inlet total pressure along the OD endwall is increased at the vane inlet, the secondary flow PV trajectory is being shifted away from the heat flux gauge location and thus a reduction in the heat transfer coefficient is observed.

### Heat Transfer Augmentation

The OD endwall heat transfer is presented in augmentation form in Fig. 11. The augmentation is with respect to the heat transfer coefficient  $Nu_0$  determined in the endwall stagnation region measured with Gauge G1 for Test 133, which had near uniform inlet temperature and an endwall  $C_p = -0.5$  at  $Z/S = 0.95$ . The data points connected with solid lines and solid symbols correspond to heat flux Gauges G1–G3 that are positioned at a pitch location near the pressure side of the vane upstream of midaxial chord. The data points connected with dashed lines and open symbols correspond to heat flux Gauges H1–H4 that are positioned at a pitch location closer to midpitch and are distributed from the passage inlet to the passage exit.

It can be seen from Fig. 11 that the heat transfer coefficient depends on both the location within the vane passage and the inlet profiles. The augmentation near the passage inlet for a given inlet profile is nearly the same for Gauges G1 and H1 with values ranging from  $Nu/Nu_0 = 0.6$  to 1.0 depending on the profile. This helps illustrate that inlet profiles that have a total pressure coefficient  $C_p$  value less than but close to zero result in higher endwall heat transfer near the passage inlet than inlet profiles with  $C_p > 0$ . It can also be seen that this  $Nu/Nu_0$  range is similar for Gauge G2, which is a result of the similar heat transfer behavior between G1 and G2 that was shown in Fig. 9. These three gauges



have Nusselt numbers consistent with the stagnation region Nusselt numbers on the airfoil surface, as reported by Barringer et al. [22].

Downstream of Gauge G2 within the region  $0.12 < X/C < 0.68$  the augmentation for Gauges G3, H2, and H3 shows a significant rise in  $Nu/Nu_0$  for both pitch locations. This increase in Nusselt number is due in part to the flow accelerating within the passage but also because of the secondary flow vortices intensifying the local flowfield in the vicinity of the gauges. The Nusselt number in this region is thus the highest experienced within the vane section. It is important to note that since the driving temperature definition was not very accurate for Gauge G3, the data points for Tests 108 and 109 at  $X/C=0.3$  should be nearly the same at an augmentation level just below 2.0, as indicated by the star (\*) symbol in Fig. 11.

Near the passage exit at  $X/C=0.93$ , Test 133 resulted in elevated Nusselt numbers similar in magnitude to the other test data shown in Fig. 11 between  $0.12 < X/C < 0.68$ . However, at  $X/C=0.93$  Tests 108, 109, 125, and 134 all resulted in significantly lower augmentation levels than Test 133, and it is interesting that these tests all include inlet pressure profiles with  $C_p > 0$ . The decrease in augmentation that is seen from  $X/C=0.68-0.93$  can be explained by the flow decelerating from the vane passage throat to the passage exit. However, the decrease in augmentation at  $X/C=0.93$  between Test 133 and tests 108, 109, 125, and 134 is an indication that as the inlet total pressure along the OD endwall is increased at the vane inlet, the secondary flow PV trajectory is being shifted away from the heat flux gauge location and thus a reduction in the heat transfer coefficient is observed.

An important result from Fig. 11 is that relative to uniform inlet conditions (Test 133) the heat transfer does decrease at the passage inlet and near the passage exit when nonuniform inlet conditions are present at the vane inlet. This finding is consistent with the results from Povey et al. [14]. The uniform inlet conditions result in warmer fluid being near the endwall surface as well as a reduction in secondary flow circulation.

## Conclusions

Several different turbine inlet pressure and temperature profiles were investigated to determine their effect on the heat transfer along the OD endwall in a high pressure turbine vane ring. The inlet profiles resulted in a wide range of Nusselt numbers at different locations on the endwall. Near the vane passage inlet as well as the passage exit, the inlet pressure profiles consistent with the shape of a standard turbulent boundary layer resulted in higher Nusselt numbers than inlet profiles with IPs that have higher total pressure near the endwall relative to midspan. At the passage inlet near midpitch, as the total pressure along the endwall was increased a continuous increase in the convection heat transfer coefficient was observed. The endwall gauge locations near the passage inlet near midpitch are more influenced by changes in the inlet Reynolds number than changes in secondary flow patterns.

Some other general trends that were found include relatively uniform heat transfer levels near the passage inlet for both the stagnation and midpitch regions. Along the vane pressure surface the heat transfer levels increase significantly with increasing distance into the passage. The data also showed that near midpitch the rise in heat transfer with increasing distance into the passage occurred closer to the passage inlet compared to further downstream for the gauges located near the pressure side surface of the vane.

For realistic turbine inlet profiles that contain significant gradients near the endwalls in both pressure and temperature, the assumption of a constant freestream temperature throughout the passage as a heat transfer driving mechanism can lead to significant underprediction or overprediction of the true local heat transfer coefficients. The secondary flows that develop near the endwalls vary in strength, size, and trajectory depending on the inlet pressure profile. This results in different driving temperatures for dif-

ferent locations along the endwall, especially in the front half of the passage. However, the secondary flow circulation patterns can be used along with the physical limits of the inlet temperature profile near the endwall as a guide in estimating the true driving temperature and heat transfer trends.

The results from this study are considered useful to turbine engine designers since they show how different inlet profiles affect the convection heat transfer coefficient at several different locations along the OD endwall of a high pressure turbine. The heat transfer trends reported here will allow better design and placement of film cooling holes and slots in the endwall region, both upstream of the vane and within the vane passage since they show the dependency of Nusselt number on the turbine inlet profile and location within the vane passage. This work also emphasizes how difficult this type of heat transfer measurement is, and how challenging it is to predict accurate convection heat transfer coefficients when nonuniform inlet conditions are present. The underprediction of these coefficients and subsequent use in hardware life prediction tools can result in significant thermal fatigue and melting in real engine hardware.

## Acknowledgment

The authors would like to thank the AFRL Technology Evaluation Branch for their help in conducting these experiments. The authors would also like to thank Dr. Richard Anthony for the manufacture of the heat flux gauges and Robert Free for installation of the heat flux gauges. The authors would also like to thank the Air Force Research Laboratory at Wright Patterson Air Force Base for funding and sponsoring this research effort.

## Nomenclature

$C$	= specific heat or vane axial chord length
$C_p$	= pressure coefficient, $C_p = (P_t - P_{t_{ms}}) / \frac{1}{2} \rho_{ave} U_{ave}^2$
$h$	= convection coefficient, $h = q'' / (T_\infty - T_w)$
$k$	= thermal conductivity
$M$	= Mach number
$Nu$	= Nusselt Number, $Nu = hC / k_f = q''C / (T_\infty - T_w)k_f$
$P$	= pressure or vane pitch
$q''$	= heat flux
$Re$	= Reynolds number, $Re = U_{ave}C / \nu_{ave}$
$S$	= vane span or total vane surface length
$T$	= temperature
$Tu$	= turbulence intensity, $Tu = U_{rms} / U_{ave}$
$U$	= velocity
$X, Y, Z$	= axial, pitch, and span directions

## Greek

$\nu$	= kinematic viscosity
$\rho$	= density
$\theta$	= nondimensional temperature, $\theta = (T - T_{ave}) / T_{ave}$

## Subscripts

0	= heat flux from Gauge G1 for uniform inlet conditions
$\infty$	= freestream or mainstream
ave	= mean or average conditions
$f$	= film conditions
MS	= midspan
rms	= root mean square
$s$	= flow static conditions
$t$	= flow total conditions
$w$	= wall surface
$x$	= axial distance with respect to stagnation

## References

- [1] Zess, G., and Thole, K., 1999, "Computational Design and Experimental Evaluation of Using a Leading Edge Fillet on a Gas Turbine Vane," ASME Paper No. 2001-GT-0404.

- [2] Lethander, A., Thole, K., Zess, G., and Wagner, J., 2003, "Optimizing the Vane-Endwall Junction to Reduce Adiabatic Wall Temperatures in a Turbine Vane Passage," ASME Paper No. GT2003-38940.
- [3] Hermanson, K., and Thole, K., 2000, "Effect of Inlet Conditions on Endwall Secondary Flows," *J. Propul. Power*, **16**(2), pp. 286–296.
- [4] Munk, M., and Prim, R. C., 1947, "On the Multiplicity of Steady Gas Flows Having the Same Streamline Pattern," *Proc. Natl. Acad. Sci. U.S.A.*, **33**, pp. 137–141.
- [5] Lakshminarayana, B., 1975, "Effects of Inlet Temperature Gradients on Turbomachinery Performance," *ASME J. Eng. Power*, **97**, pp. 64–74.
- [6] Langston, L. S., 1980, "Crossflows in a Turbine Cascade Passage," *ASME J. Eng. Power*, **102**, pp. 866–874.
- [7] Colban, W. F., Thole, K. A., and Zess, G., 2002, "Combustor-Turbine Interface Studies-Part 1: Endwall Effectiveness Measurements," ASME Paper No. GT2002-30526.
- [8] Colban, W. F., Thole, K. A., and Zess, G., 2002, "Combustor-Turbine Interface Studies-Part 2: Flow and Thermal Field Measurements," ASME Paper No. GT2002-30527.
- [9] Kost, F., and Nicklas, M., 2001, "Film-Cooled Turbine Endwall in a Transonic Flow Field: Part I-Aerodynamic Measurements," ASME Paper No. 2001-GT-0145.
- [10] Kang, M., Kohli, A., and Thole, K. A., 1999, "Heat Transfer and Flowfield Measurements in the Leading Edge Region of a Stator Vane Endwall," *ASME J. Turbomach.*, **121**(3), pp. 558–568.
- [11] Radomsky, R., and Thole, K. A., 2000, "High Freestream Turbulence Effects in the Endwall Leading Edge Region," *ASME J. Turbomach.*, **122**, pp. 699–708.
- [12] Blair, M. F., 1974, "An Experimental Study of Heat Transfer and Film Cooling on Large-Scale Turbine Endwalls," *ASME J. Heat Transfer*, **96**(4), pp. 524–529.
- [13] Haldeman, C., and Dunn, M., 2004, "Heat-Transfer Measurements and Predictions for the Vane and Blade of a Rotating High-Pressure Turbine Stage," *ASME J. Turbomach.*, **126**, pp. 101–109.
- [14] Povey, T., Chana, K., Jones, T., and Hurrian, J., 2005, "The Effect of Hot-Streaks on HP Vane Surface and Endwall Heat Transfer: An Experimental and Numerical Study," ASME Paper No. GT2005-69066.
- [15] Nicklas, M., 2001, "Film-Cooled Turbine Endwall in a Transonic Flow Field: Part II-Heat Transfer and Film-Cooling Effectiveness Measurements," ASME Paper No. 2001-GT-0146.
- [16] Graziani, R., Blair, M., Taylor, J., and Mayle, R., 1980, "An Experimental Study of Endwall and Airfoil Surface Heat Transfer in a Large Scale Turbine Blade Cascade," *ASME J. Eng. Power*, **102**, pp. 257–267.
- [17] Haldeman, C. W., Dunn, M. G., MacArthur, C. D., and Murawski, C. G., 1992, "The USAF Advanced Turbine Aerothermal Research Rig (ATARR)," *NATO AGARD Propulsion and Energetics Panel Conference Proceedings*, Vol. 527, Antalya, Turkey.
- [18] Barringer, M. D., Thole, K. A., and Polanka, M. D., 2007, "Experimental Evaluation of an Inlet Profile Generator for High-Pressure Turbine Tests," *ASME J. Turbomach.*, **129**(2), pp. 382–393.
- [19] Jones, T. V., 1995, "The Thin Film Heat Transfer Gauge-A History and New Developments," *Proc. Inst. Mech. Eng., Part C: J. Mech. Eng. Sci.*, **209**(C510), pp. 150–160.
- [20] Moffat, R. J., 1982, "Contributions to the Theory of a Single-Sample Uncertainty Analysis," *ASME J. Fluids Eng.*, **104**, pp. 250–260.
- [21] Kang, M., and Thole, K. A., 2000, "Flowfield Measurements in the Endwall Region of a Stator Vane," *ASME J. Turbomach.*, **122**, pp. 458–466.
- [22] Barringer, M. D., Thole, K. A., and Polanka, M. D., 2009, "Effects of Combustor Exit Profiles on Vane Aerodynamic Loading and Heat Transfer in a High Pressure Turbine," *ASME J. Turbomach.*, **131**(2), p. 021008.

# Migration of Combustor Exit Profiles Through High Pressure Turbine Vanes

M. D. Barringer  
K. A. Thole

Department of Mechanical and Nuclear  
Engineering,  
Pennsylvania State University,  
University Park, PA 16802

M. D. Polanka  
J. P. Clark  
P. J. Koch

Turbines Branch,  
Turbine Engine Division,  
Air Force Research Laboratory,  
WPAFB, OH 45433

*The high pressure turbine stage within gas turbine engines is exposed to combustor exit flows that are nonuniform in both stagnation pressure and temperature. These highly turbulent flows typically enter the first stage vanes with significant spatial gradients near the inner and outer diameter endwalls. These gradients can result in secondary flow development within the vane passage that is different than what classical secondary flow models predict. The heat transfer between the working fluid and the turbine vane surface and endwalls is directly related to the secondary flows. The goal of the current study was to examine the migration of different inlet radial temperature and pressure profiles through the high turbine vane of a modern turbine engine. The tests were performed using an inlet profile generator located in the Turbine Research Facility at the Air Force Research Laboratory. Comparisons of area-averaged radial exit profiles are reported as well as profiles at three vane pitch locations to document the circumferential variation in the profiles. The results show that the shape of the total pressure profile near the endwalls at the inlet of the vane can alter the redistribution of stagnation enthalpy through the airfoil passage significantly. Total pressure loss and exit flow angle variations are also examined for the different inlet profiles. [DOI: 10.1115/1.2950076]*

## Introduction

The performance of gas turbine engines is highly dependent on the operation and durability of the hot section, which includes the combustor and high pressure turbine. The vanes and blades of the high pressure turbine must operate in a very harsh flow environment that includes elevated turbulence and significant spatial gradients of pressure and temperature. The flow and thermal field gradients are most prevalent at the turbine inlet along the inner diameter (ID) and outer diameter (OD) endwalls. Their shape and complexity originate from intense flow interactions that take place within the upstream combustor section. The spatial variations in pressure and temperature at the turbine inlet result in nonuniform heat transfer to the vanes and blades that can damage the components. The high turbulence typically found at the exit of an aeroengine combustor acts to intensify this heat transfer by increasing local convection heat transfer coefficients.

The mean radial flow and thermal profiles that enter the high pressure turbine can have gradients near the ID and OD endwalls that are either positive or negative. This means that the local total pressure or total temperature near the endwalls can be larger or smaller than that near midspan. Typically, turbine durability engineers prepare for the worst case when designing the high pressure vanes and blades without knowing specifically how the combustor exit profiles are redistributed from vane inlet to blade inlet. For example, designers often use a radial pressure profile consistent with a flat plate turbulent boundary layer as the inlet condition to the turbine and assume a temperature drop across the vane due to cooling for a given combustor exit temperature variation. A turbulent boundary layer is characterized by decreasing total pressure with increasing proximity to the endwall. However, more realistic combustor exit flows can result in turbine inlet profiles that are significantly different than that. For example, some turbines experience inlet conditions where there is an increase in total pressure

near the endwall that is caused by a combination of combustor liner film cooling and a contraction at the combustion chamber exit. Additionally, the one dimensional analyses often used to assess temperature redistribution are known to be lacking. So, what is needed are accurate experimental studies with realistic vane inlet profiles and modern turbine geometries coupled with Reynolds-averaged Navier–Stokes (RANS)-based numerical analyses.

## Relevant Past Studies

Computational and experimental studies have been performed that have investigated certain effects of turbine inlet profiles. One of the earliest studies was performed by Munk and Prim [1] in 1947 who showed mathematically that streamline patterns would remain unchanged in a vane passage with respect to variations in inlet total enthalpy provided the inlet total pressure field was constant. This finding is applicable to a hot streak propagating through a vane passage. The presence of the hot streak does not affect the pressure field in the vane passage provided the inlet total pressure field remains unchanged. Langston [2] showed in 1980 that a flat plate turbulent boundary layer at the inlet of a turbine vane separates near the endwall and forms a horseshoe vortex. The part of the vortex proceeding to the pressure side of the vane develops into a passage vortex, and the portion that proceeds to the suction side of the vane develops into a relatively smaller and weaker counter-rotating vortex. This counter-rotating vortex is sometimes referred to as a corner vortex since it is restricted to the endwall junction region along the vane suction side. These secondary flow vortices have a direct impact on the migration of the primary flow by circulating it toward or away from the endwalls and vane surfaces.

Studies by Hermanson and Thole [3] have shown that the total pressure field is the driving force in the development of secondary flows and heat transfer present in turbine vane passages. Colban et al. [4] studied the effects of varying film cooling flow through the liner and exit junction slot of a large-scale, low speed combustor simulator on the adiabatic effectiveness and secondary flow development within a downstream turbine cascade. Their study documented the vane passage secondary flow vectors for different vane

Contributed by the International Gas Turbine Institute of ASME for publication in the JOURNAL OF TURBOMACHINERY. Manuscript received July 26, 2007; final manuscript received January 3, 2008; published online January 23, 2009. Review conducted by David Wisler. Paper presented at the ASME Turbo Expo 2007: Land, Sea and Air (GT2007), Montreal, QC, Canada, May 14–17, 2007.



inlet total pressure profiles and reported a counter-rotating vortex located above the passage vortex for a vane inlet pressure profile containing an inflection point near the endwall.

Computational studies performed by Boyle and Giel [5] and Dorney and Schwab [6] as well as experimental studies performed by Cattafesta [7], Shang et al. [8], Chana et al. [9], and Povey et al. [10] have all showed that heat transfer to turbine vanes and blades is affected by the presence of a nonuniform inlet temperature profile. The heat load to the vane and endwall regions is typically reduced when a nonuniform temperature profile consistent with a combustor exit is present at the inlet of the turbine stage, relative to a uniform turbine inlet temperature profile. The heat load to the rotor blades, however, typically increases especially along the pressure side. This result was first determined from studies performed by Butler et al. [11] and later verified by Saxer and Giles [12].

The current literature to date suggests that certain heat transfer trends within the turbine section are due to nonuniform inlet temperature and pressure conditions. Studies including Barringer et al. [13], Shang et al. [8], Chana et al. [9], Butler et al. [11], and Saxer and Giles [12] have reported significant augmentation of heat transfer along the suction side of the vanes and the pressure side of the blades in both the hub and tip regions using nonuniform inlet temperature profiles. The literature, however, contains little experimental data that documents the effects of realistic total pressure profiles at the turbine inlet.

An improved understanding of how these realistic turbine inlet profiles affect the flow development and heat transfer within the turbine is needed. This can, in part, be accomplished by studying how different radial profiles of total pressure and temperature are redistributed as the flow passes through the high pressure vane passages. The goal of the current study is to examine the migration of different turbine inlet profiles by analyzing both the vane inlet and corresponding exit profile shapes. The results from this study will aid turbine designers by providing them with an improved picture of what blade inlet profiles they should anticipate for certain combustor exit profile shapes.

## Experimental Facility

The experimental facility used in this study is the Turbine Research Facility (TRF) located within the Air Force Research Laboratory (AFRL) at Wright Patterson Air Force Base. This facility operates in a short duration blowdown manner in which several aerothermal engine parameters are matched. These nondimensional parameters include Reynolds number, Mach number, pressure ratio, gas to metal temperature ratio, and corrected mass flow. The facility consists primarily of a large supply tank, a turbine test section, and two large vacuum tanks. The facility is described in more details in Haldeman et al. [14]; however, a brief summary of its operation is provided here.

The working fluid (nitrogen gas) is pressurized and heated within the supply tank prior to testing while at the same time the turbine section and vacuum tanks are evacuated. Testing then begins by activating the supply tank main valve, at which time the gas flows through the turbine test section and into the vacuum tanks. The mass flow rate of the working fluid is set by a variable area isolation valve located downstream of the main test section, which controls the turbine pressure ratio. The duration of the tests in the current study was approximately 5 s, which was dependent on the size of the turbine being tested. Due to the short test duration, all measurements were recorded simultaneously in real time. The data were simultaneously acquired across multiple 12 bit channels having a maximum frequency response of 100 kHz and multiple 16 bit channels having a maximum frequency response of 200 kHz. Signal conditioning on each channel was performed using low pass filters and built-in amplifiers. All data processing was performed at a later time.

The turbine test section is a true scale, fully annular, single turbine stage consisting of vanes and blades. The tests in the cur-

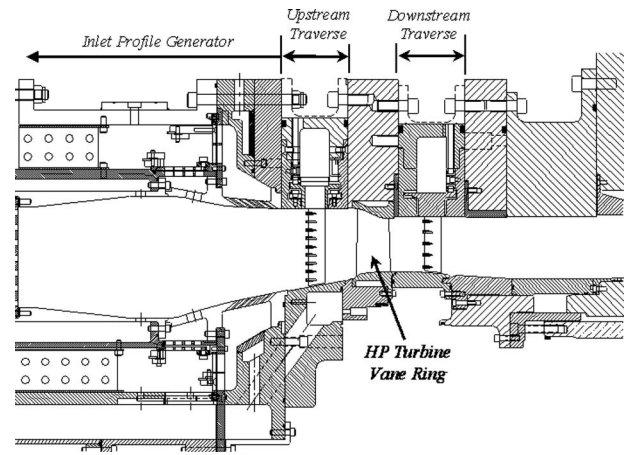


Fig. 1 Drawing of the TRF test rig in a vane-only configuration with the inlet profile generator

rent study were performed using a vane only configuration, as shown in the facility drawing in Fig. 1. The turbine inlet profile generator, documented in Barringer et al. [15], was used in the current study to allow turbine testing with inlet profiles of pressure and temperature representative of those exiting engine combustors as well as realistic turbulence intensities and length scales. The inlet profile generator can also be seen in Fig. 1 upstream of the test vane ring. The generator operates by mimicking an aeroengine combustor in which it injects several different flow streams at different temperatures into a central chamber via dilution holes and film cooling holes. The injection flow rates, momentum flux ratios, and temperatures of the different flow streams are varied depending on the desired turbine inlet profile shapes.

The turbine inlet and exit profiles are measured using multiple instrumentation rakes located on traverse rings upstream and downstream of the turbine section. The rakes, shown in Fig. 2, contain multiple thermocouples or pressure transducers that are spaced to obtain measurements over equal annular flow areas. The tests discussed in this study involved traversing these rakes by approximately 90 deg during the blowdown to obtain both radial and circumferential data. For the turbine inlet profiles being analyzed in the current study, a temperature rake was used containing seven 0.0254 mm diameter thermocouple beads with a thermal time constant of approximately 1.1 ms. Two pressure rakes were also used each containing nine miniature high frequency pressure transducers. All flow and thermal measurements were sampled at 20 kHz.

The pressure transducers were calibrated in situ prior to each test using a Ruska standard. A typical calibration uncertainty for

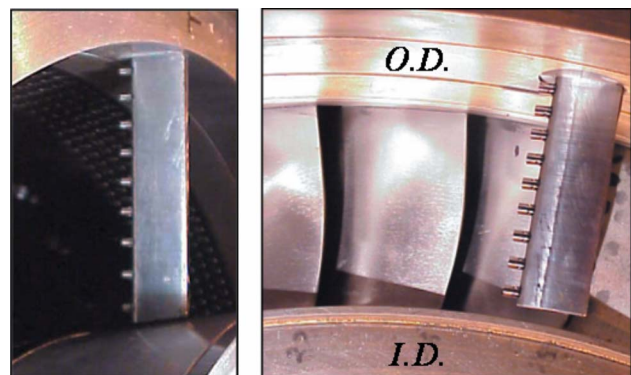


Fig. 2 Instrumentation rakes mounted in the upstream (left) and downstream (right) traverses

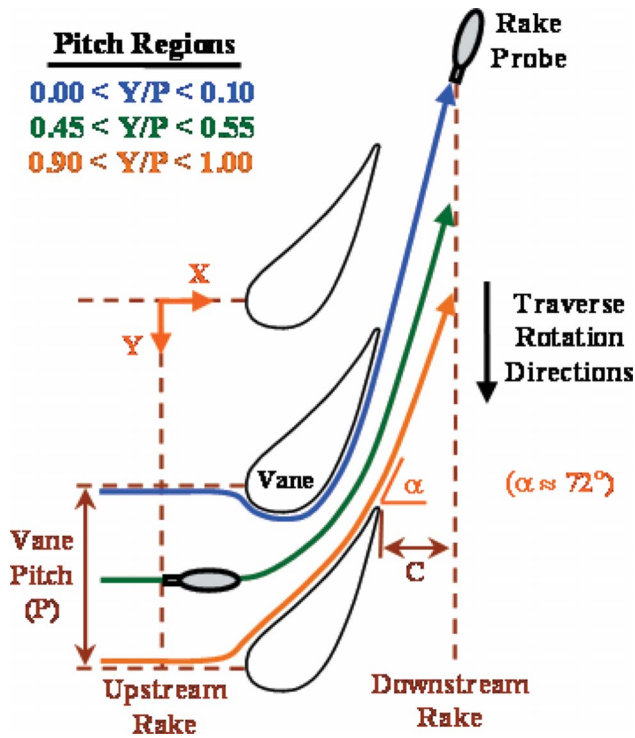


Fig. 3 Schematic showing the three different flow path regions and measurement locations

the transducers was less than 0.05% of full scale. The overall uncertainty for these transducers was raised 0.40% due to the short term drift known to exist between time of calibration and time of the run. The thermocouple wire used to manufacture the beads was calibrated in a Kaye temperature bath against a platinum RTD standard accurate to 0.01 K. The 0.0254 mm beads in the rakes were calibrated to an accuracy of 1.5 K.

### Test Conditions and Measurements

The pressure and temperature profiles that are analyzed in this study were generated during a series of tests whose flow conditions are reported in more details in Barringer et al. [15]. To summarize, the mean flow conditions at the turbine inlet for all of the profiles presented in this study correspond to a mean Reynolds number of  $Re=2.1 \times 10^5$  and a mean axial Mach number of  $M=0.1$ . The turbulence intensity associated with these turbine inlet profiles was also documented during testing and was found to be in an elevated range between  $Tu=20-30\%$ . For a baseline test case with nearly uniform inlet pressure and temperature, the turbulence intensity was determined to be approximately 21% and the longitudinal integral length scale was approximately 30% of the vane pitch or 2.3 times the vane leading edge diameter.

To study the migration of the flow in both the radial and circumferential directions as it passes through the vane passage, three pitch regions are considered. The schematic shown in Fig. 3 highlights the locations of the three different flow pitch regions. The uppermost streamline is centered at  $Y/P=0.05$  and is indicative of the flow conditions present near the suction side of the vane between  $0.00 < Y/P < 0.10$ . The flow path region in the middle is centered at  $Y/P=0.50$  and is representative of the flow conditions that are present near the midpassage between  $0.45 < Y/P < 0.55$ . The lowermost streamline is centered at  $Y/P=0.95$  and is indicative of the flow conditions that are present near the pressure side of the vane between  $0.90 < Y/P < 1.00$ .

The vanes have a nominal exit flow angle of  $\alpha=72$  deg and the downstream traverse rakes are aligned according to this same angle. The axial distances from the trailing edge of the vanes to

the downstream rake measurement location and from the leading edge to the upstream rake measurement location are both approximately equal to one vane axial chord length. During rotation, the traverses move from the suction side of the vane toward the pressure side.

### Computational Techniques

In an effort to supplement the experimental data obtained in this study, the flow through the turbine vane was analyzed via the 3D time-accurate RANS solver of Dorney and Davis [16]. The flow solver is itself a further development of the Rai code [17,18]. The solver is second order accurate in time and third order accurate in space, and numerical closure is obtained via a modified version of the Baldwin-Lomax algebraic turbulence model [16].

In a previous study, Praisner et al. [19] demonstrated the grid counts as well as the viscous and cooling model details necessary to predict the redistribution of stagnation quantities in turning ducts as well as modern high pressure turbine stages. The results of that previous study were used as a guide for the simulations performed here both in terms of grid-count and turbulence-model selection. Accordingly, an O-H grid was employed with counts for the O-grid of  $161 \times 40 \times 49$  in the axial, circumferential, and radial directions, respectively. For the H-grid, the grid counts were  $100 \times 41 \times 49$ . The near-wall grid spacing was set at  $0.25 \mu\text{m}$  to minimize the local grid Reynolds number based on wall units, which was everywhere less than unity. As regards to the viscous model employed here, Praisner et al. [19] noted that the redistribution of 1D profiles was as adequately captured with an algebraic turbulence model as it was with more computationally expensive two equation turbulence models. So, the use of the Baldwin-Lomax turbulence model [16] is justified given the goals of the current study.

A pair of simulations was performed, and experimentally determined boundary conditions consistent with Profiles B and D (to be discussed in the next section) were used to obtain flow solutions. These profiles were selected for code validation because they represented the extreme variation of the profiles tested in the experiment. The experimental data used for boundary conditions included the inlet total pressure and temperature, the inlet flow angle, and the vane exit static pressure. Additionally, an isothermal wall thermal boundary condition was employed, and the wall temperature was set at a level consistent with time-averaged measurements made with thin-film heat flux gauges on the vane and endwall surfaces. Results of the simulations were postprocessed in a manner consistent with the experimental measurements via tools available in the AFRL Turbine Design and Analysis System, which has been previously described [20,21].

### Turbine Vane Inlet Flow

Four radial profiles of total pressure measured at the turbine vane inlet are shown in Fig. 4. Each profile that is shown represents the mean conditions across three vane pitches. The pitchwise uniformity of the four inlet total pressure profiles in the circumferential direction was found to be excellent from vane to vane. This uniformity revealed that the radial profiles measured upstream of the vane were nearly the same for each of the three pitch regions. This is important in making comparisons of the exit profiles because it ensures that the same inlet conditions are present for each pitch. The total pressure has been normalized by use of the total pressure coefficient  $C_p$ , which references the local total pressure to the midspan total pressure and divides the result by the mean dynamic pressure of the flow entering the vane passage. A positive value of  $C_p$  indicates that the local total pressure is larger than that measured at the midspan, and a negative value of  $C_p$  indicates that the local total pressure is smaller than that measured at the midspan. This pressure normalization is helpful in illustrating the important gradients that are typically found in turbine inlet pressure profiles near the endwalls.

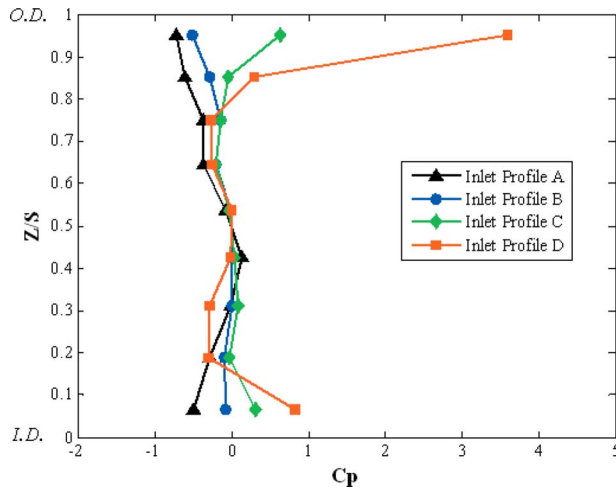


Fig. 4 Radial profiles of total pressure at the vane inlet

The first total pressure profile in Fig. 4 to be considered is Inlet Profile A, which is characterized by a parabolic shape with a maximum total pressure at  $Z/S=0.43$  near midspan and lower total pressures near both the ID and OD endwalls. Inlet Profile A is characteristic of flow having a turbulent boundary layer profile on both the ID and OD endwalls. Inlet Profile B is characterized by near uniform total pressure over the majority of the vane span with slightly lower total pressure near the OD endwall. Inlet Profile C possesses near uniform total pressure over the majority of the vane span but has higher total pressure near both the ID and OD endwalls. Inlet Profile D is also characterized by near uniform total pressure over the majority of the vane span but has much higher total pressure near the ID and OD endwalls.

This set of four inlet pressure profiles was considered important for the current investigation, since it included both lower and higher total pressure scenarios near both endwalls relative to midspan. The difference in total pressure near the endwalls was the result of varying amounts of film cooling that entered the turbine along the endwalls. The near uniform pressure that is present near the midspan region is the result of intense dilution mixing that is present upstream and typically found in combustor exit flows.

The corresponding total temperature profiles measured upstream of the vanes are shown in Fig. 5. These radial profiles are also spatial averages of the temperature conditions in the circumferential direction across the inlet of three vane pitches. The total

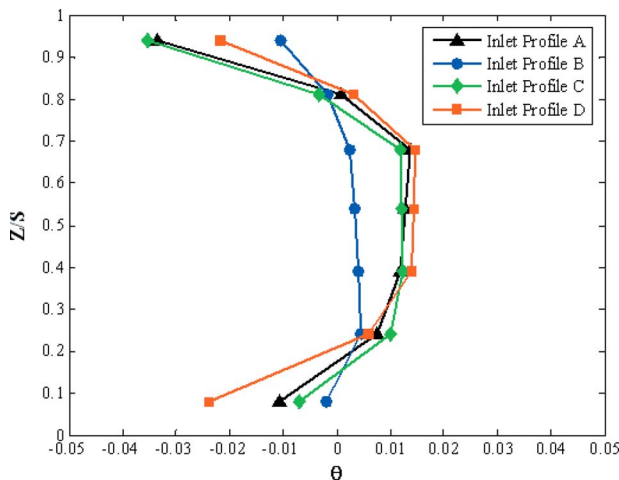


Fig. 5 Radial inlet profiles of total temperature corresponding to the pressure profiles in Fig. 4

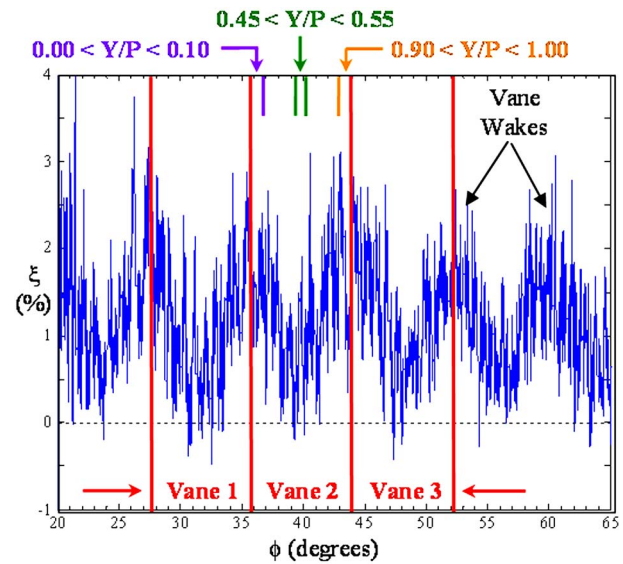


Fig. 6 Total pressure loss across the vanes at  $Z/S=0.19$  for Inlet Profile B

temperature has been normalized by the use of a temperature coefficient  $\theta$ , which references the local total temperature to the average temperature measured upstream of the vanes. These spanwise thermal profiles were also found to be near uniform in the pitch direction. The thermal Inlet Profiles A and C are almost identical with warmer fluid near midspan and cooler fluid near the endwalls. The thermal Inlet Profile B is more uniform across the span, and the thermal Inlet Profile D is a near symmetric profile about midspan with warmer fluid near midspan and cooler fluid near the endwalls.

### Turbine Vane Exit Flow

The relative position of the upstream and downstream traverse rakes with respect to the vanes was verified by comparing their rotational timing to the wake profiles measured downstream of the vanes. Figure 6 shows an example of a wake profile measured downstream of multiple vanes for Inlet Profile B (near uniform inlet conditions) at a span location of  $Z/S=0.19$ . The total pressure loss, defined in the Nomenclature, is plotted versus traverse rotation angle for several vane pitches.

A low value of loss ( $\xi$ ) implies that the total pressure measured downstream of the vane is nearly the same as the total pressure measured upstream at the vane inlet. A low value of loss, therefore, takes place near midpitch ( $Y/P=0.50$ ) in which the flow experiences a little pressure drop as it passes through the vane passage. A higher loss corresponds to a lower total pressure relative to that measured upstream of the vane at the same pitch location. Higher values of loss exist in pitch regions in the vicinity of the vane airfoil trailing edge, for example, near the vane suction side ( $Y/P=0.05$ ) or near the vane pressure side ( $Y/P=0.95$ ). The three flow path pitch regions are also indicated near the top of Fig. 6 for one of the vane passages to illustrate how the vane wake profile shape corresponds to each region. The total pressure loss across the vanes at this span location ( $Z/S=0.19$ ) was found to be within  $0 < \xi < 3\%$  with a mean value of  $\bar{\xi} = 1.25\%$ .

The total pressure loss across the vanes was also investigated for Inlet Profile B as a function of vane span location for multiple vane pitches, as shown in Fig. 7. Figure 7(a) indicates that the wake profile shape is more evident near the ID compared to the midspan region and near the OD. This result was also found for each of the four inlet pressure profiles studied. This is explained



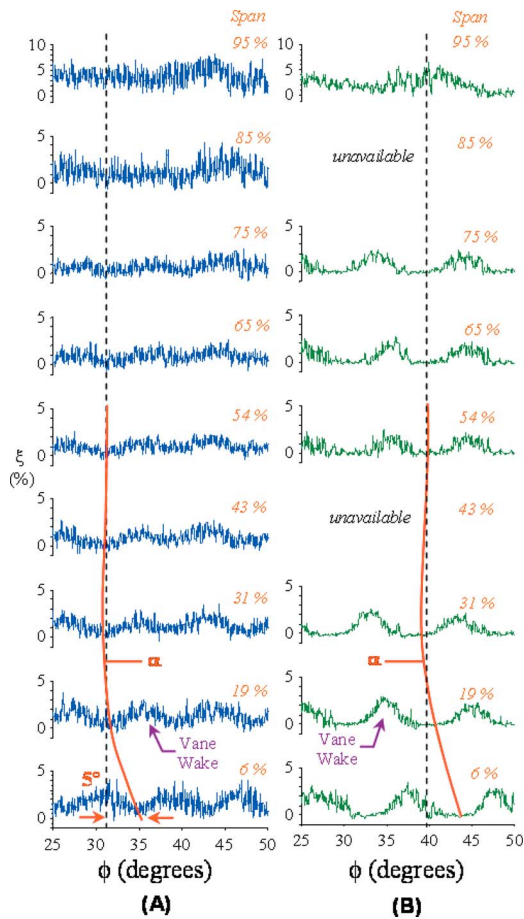


**Fig. 7 Total pressure loss  $\xi$ (%) across the vane for Inlet Profile B with high freestream turbulence 21% (a) and low freestream turbulence 1% (b), shown for three vane pitches**

by the fact that the vane exit velocities near the ID are higher than at the midspan and OD. These higher exit velocities were verified by both measurements of the vane exit static pressure and the results of RANS simulations. The higher exit velocities near the ID are a consequence of radial equilibrium considerations at the exit. Therefore, the wake profile should be more noticeable near the ID.

It can also be seen in Fig. 7(a) that the wake profile at  $Z/S = 0.06$  is nearly 180 deg out of phase with the wakes near midspan. This phase shift can be verified by examining the alignment of the wake peaks and valleys at 6% span versus 19% span. It was determined that this phase shift in wake profile was due to a change in the vane exit flow angle  $\alpha$  of approximately  $\Delta\alpha = 5.0$  deg between midspan and the ID endwall. The solid line in Fig. 7(a) is an estimate of the radial profile shape of the exit flow angle from the ID endwall to the OD endwall.

Figure 7(b) is a comparison of the total pressure loss across the same vane ring when testing with uniform inlet conditions but with low freestream turbulence near 1%. This low freestream turbulence data was taken during a study by Urbassik et al. [22], and when it is compared to the data in Fig. 7(a) from the current study, it can be seen that the high freestream turbulence is resulting in less total pressure being recovered downstream of the vanes. This is evident by first examining the region of the data traces near  $\xi = 0\%$  at each span location. For the low freestream turbulence case, the data traces exhibit zero loss over a larger range of circumferential traverse rotation than the high freestream turbulence case. Second, integrating the total pressure loss over both the vane pitch and radius yields an overall mean loss of  $\bar{\xi} = 1.20\%$  for the

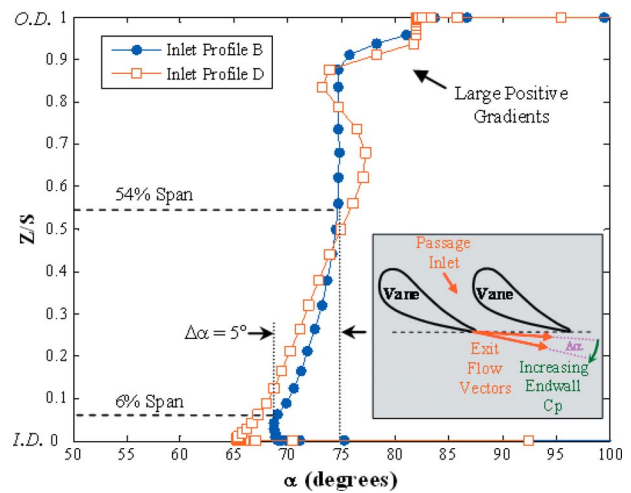


**Fig. 8 CFD prediction of the exit flow angle as a function of vane span**

high turbulence case (Inlet Profile B) and  $\bar{\xi} = 0.81\%$  for the low turbulence case. The higher turbulence is resulting in the exit flow loss profiles being more mixed out. In addition, when comparing Fig. 7(a) to Fig. 7(b), it can be seen that the rms of the loss traces is much less for the lower turbulence case. This is consistent with the lower level of random unsteadiness expected in the low turbulence case.

All of these results are consistent with the findings by Ames et al. [23] who reported that high freestream turbulence acted to enhance the mixing downstream of a turbine vane as well as broaden the wakes and increase the losses. They also reported that as the flow developed from  $\frac{1}{4}$  to  $\frac{1}{2}$  axial chord downstream of the vane, the wakes spread and decreased in amplitude and that this spreading was more pronounced at a high freestream turbulence condition ( $\sim 15\%$ ) relative to a low freestream turbulence condition ( $\sim 1\%$ ).

It is also evident from Fig. 7(a) that the total pressure loss in the vicinity of the OD endwall at 95% span is much higher than the loss measured at all other span locations. Note the scale used at this span location ( $Z/S = 0.95$ ) is  $0 < \xi < 10\%$  loss, while the scale used at all other span locations was  $0 < \xi < 5\%$  loss. This difference in plot was included to fully display the larger loss measured at  $Z/S = 0.95$  while also ensuring that the wakes at the other span locations were identifiable. It was determined that the large pressure loss near the OD corresponded to the same span region in which a sharp change in the vane exit flow angle was predicted. Since the loss profiles are mixed out circumferentially from midspan to the OD, the shift in exit flow angle is not clearly evident from the wake profiles in Fig. 7(a). However, a prediction of the exit flow angle as a function of span location for Inlet Profile B is presented in Fig. 8. The prediction of the overall shift in exit flow angle between  $0.06 < Z/S < 0.54$  for Inlet Profile B is approximately  $\Delta\alpha = 5$  deg, which compares well with the data in Fig. 7(a). In the span region  $0.50 < Z/S < 0.85$ ,  $\alpha$  is predicted to be uniform near  $\alpha = 74$  deg, which is also consistent with the data. At span locations above  $Z/S > 0.85$ , a large positive gradient is present, which is believed to correspond to the large pressure loss measured near the OD.

A comparison is also made in Fig. 8 between the exit flow angles for Inlet Profiles B and D, which have very different pressure profile shapes. Inlet Profile B has near uniform total pressure across the span and Inlet Profile D has uniform total pressure near midspan but has much higher total pressure near both the ID and OD endwalls. Figure 8 shows that the exit flow angle experienced for Inlet Profile D near the ID endwall is several degrees lower than that corresponding to Inlet Profile B. This reduction in exit

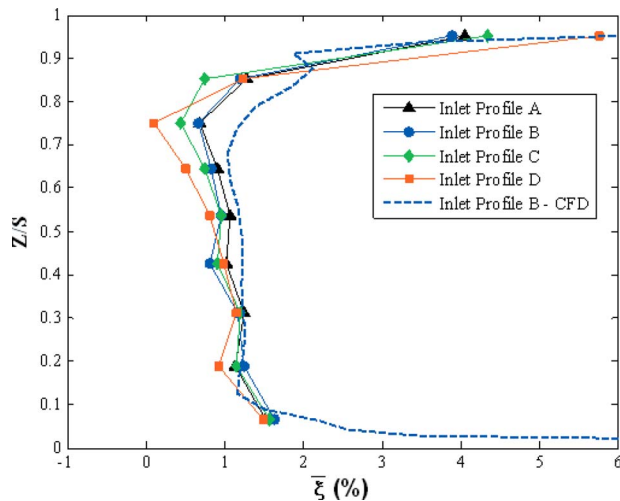


**Fig. 9 Average total pressure loss as a function of span location for the different inlet profiles**

flow angle is physically explained in the schematic shown in Fig. 8. As the total pressure is increased at the vane passage inlet near the ID endwall, the momentum of the fluid entering the passage also increases. At these higher inlet pressures, the momentum of the fluid becomes large enough to overcome the cross passage pressure gradient from pressure side to suction side. This results in the flow not following the curvature of the suction side of the vane near the passage exit as closely as it would at lower inlet pressures (lower inlet momentum), thus reducing the exit flow angle. In addition, the relatively high pressure region near the passage exit along the pressure side increases as the passage inlet total pressure increases. This forces the flow leaving the passage along the vane pressure side to turn more in the axial direction into the relatively lower pressure region along the suction side.

Near the OD within the span region  $0.85 < Z/S < 0.95$ , both inlet profiles are predicted to have large positive gradients in the exit flow angle. This implies that the large total pressure loss experienced near the OD at the vane exit is not associated with the vane inlet flow conditions. The loss is more likely due to the vane and endwall geometry in this span region producing strong secondary flows. In general, this high pressure turbine vane results in an exit flow angle that increases with increasing span location due to the vane metal angle slightly increasing from hub to tip. The important result is that the different inlet pressure profiles result in different exit flow angle profiles by altering the fluids inlet momentum.

The average total pressure loss across the vanes at each measured span location is plotted in Fig. 9 for each inlet pressure profile. It can be seen that the loss is higher near the endwalls compared to midspan for each inlet profile. This is a result of the flow near the endwalls interacting with three wall surfaces (vane pressure side, vane suction side, and endwall) as compared to the midspan flow that interacts with only two wall surfaces (vane pressure side and vane suction side). The endwall acts to reduce the fluid momentum by increasing its aerodynamic drag. The presence of secondary flow vortices near the endwall and vane hub and tip surfaces also contributes to the higher loss experienced near the platforms.

The mean loss measured near the OD endwall at  $Z/S=0.95$  is considerably higher than that measured near the ID endwall at  $Z/S=0.06$  for each inlet profile. However, the simulation results, also shown in Fig. 9, for Inlet Profile B shows that the mean loss also becomes large at span locations close to the ID endwall. The agreement between the simulation and the data for Inlet Profile B

**Table 1 Average total pressure loss near the OD as a function of the inlet total pressure coefficient**

Inlet profile	$C_p$	$\bar{\xi}$ (%)
A	-0.72	4.05
B	-0.51	3.90
C	0.64	4.35
D	3.61	5.77

in Fig. 9 is relatively good, and it is believed that the measured data would also show an increase in near wall mean loss if data were taken at spans between  $0 < Z/S < 0.06$ .

The inlet profile shape does not significantly affect the mean loss values near the ID endwall at  $Z/S=0.06$  but does affect the mean loss values near the OD endwall at  $Z/S=0.95$ . Table 1 shows that the mean loss measured near the OD endwall at  $Z/S=0.95$  scales well with the value of the total pressure coefficient  $C_p$  measured at the vane inlet at the same span location. An increase in the inlet  $C_p$  coefficient value leads to an increase in the mean total pressure loss. It is believed that the loss at  $Z/S=0.95$  is minimized when the inlet total pressure  $C_p=0$ . It is also believed that a similar relationship exists near the ID endwall below the span location  $Z/S=0.06$ , where it is believed that the effect between different inlet profiles becomes more pronounced.

### Pressure Profile Migration

The redistribution of total pressure for Inlet Profile A as the flow passes through the vanes is shown in Fig. 10(a). The pressure profile measured downstream near midpitch has a similar shape to that of the inlet profile from  $0.06 < Z/S < 0.75$ ; however, it possesses a large total pressure loss near the OD endwall. The two pressure profiles measured downstream near the suction and pressure sides of the vane are very similar in shape to one another and each have similar large total pressure losses near the OD endwall as does the midpitch profile. This implies that the flow is nearly uniform in the circumferential direction as it exits the vane near the OD but at a lower total pressure compared to the upstream OD. This pitchwise uniformity is consistent with the relatively weak wake formation shown near the OD in Fig. 7(a).

A similar negative total pressure gradient very close to the ID endwall within the span region  $0.0 < Z/S < 0.06$  was observed in the results of the simulations (Fig. 9). The pitchwise uniformity near the OD was not found between  $0.0 < Z/S < 0.55$ . In this span region, rather, the midpitch exit profile shows relatively high pressure compared to the two exit profiles near the vane surfaces. This behavior is consistent with the stronger wake formation present near the ID in Fig. 7(a) and the gradual decrease in wake strength that is present with increasing span location.

The subsequent effect of changing the radial shape of Inlet Profile A by increasing the total pressure near both the ID and OD endwalls and how this influences the shape of the downstream pressure profiles are shown in Figs. 10(a)–10(d). As the upstream total pressure is increased along the endwalls, there is a general shift to the right toward increasing total pressure values for each of the downstream exit profiles. In addition, the three downstream profiles tend to become more uniform in the pitch direction over the majority of the vane span. For example, this is evident in the reduction of the wake strength near the ID at  $Z/S=0.20$  when comparing the results for Inlet Profile A to the results for Inlet Profile D. It is clear from Fig. 10 that obtaining a relatively uniform exit pressure profile for this vane as an inlet condition to the downstream blade may not be possible, at least not without a very large total pressure near the endwalls at the combustor exit and vane inlet. This large total pressure at the inlet would be needed to overcome the large pressure loss experienced near the endwalls as the flow passes through the vane passage.

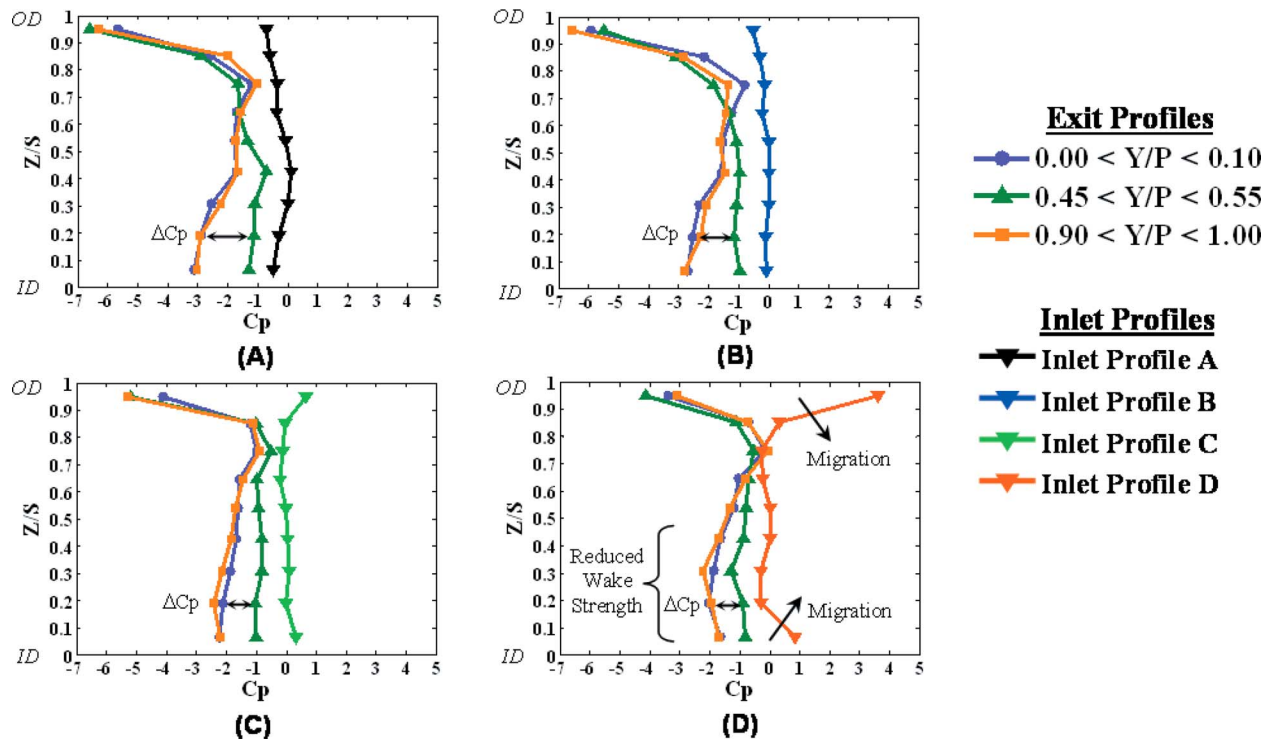


Fig. 10 Radial total pressure profiles measured at the vane exit for (a) Inlet profile A, (b) Inlet Profile B, (c) Inlet Profile C, and (d) Inlet Profile D

Another important finding was that Inlet Profiles C and D, which possess high total pressure near the endwalls at the inlet, result in fluid near the endwall migrating toward midspan, which is at a relatively lower total pressure. This migration is evident in comparing the exit profile  $C_p$  values and shapes in the span region  $0.06 < Z/S < 0.30$  as well as near  $Z/S=0.75$  between Inlet Profiles A, B, C, and D. In the case of Inlet Profile D, this is resulting in total pressures at  $Z/S=0.75$  that are actually slightly higher for the exit profiles than for the vane inlet profile. Near the ID within the span region  $0.0 < Z/S < 0.30$ , in going from Inlet Profile A to Inlet Profile D, the total pressure gradients of the exit profiles have reversed direction from a decreasing  $C_p$  trend to an increasing  $C_p$  trend. In general, over the majority of the vane span, the pressure profiles at the vane exit within the pitch regions  $0.0 < Y/P < 0.1$  and  $0.9 < Y/P < 1.0$  are similar for each of the inlet pressure profiles, except near the OD. In the OD endwall region, the secondary flow losses are stronger along the vane pressure surface for Inlet Profiles A, B, and C. Figure 10(d) indicates that when the inlet total pressure near the OD endwall is very large, these secondary flow losses are similar along both vane surfaces (both pitch regions close to the vane surfaces).

The strength and size of these secondary flows near the endwalls are dependent on the inlet pressure profile shape near the endwall as well as the physical shape of the endwall and vane. Since the measurements were made one axial chord downstream of the vane passage exit, then the data are representative of vortex behavior (shape and size) near the passage exit. This means the vortices have already felt the influence of the endwall shapes and the vane turning, as well as the slight twist in vane metal angle. The larger the total pressure along the endwall (relative to midspan) at the vane inlet, the stronger these vortices become.

### Temperature Profile Migration

The thermal migration of the inlet total temperature profiles as the flow passes through the vanes is now discussed using Fig. 11. The first temperature profile to be considered is that corresponding to Inlet Profile A, which is shown in Figure 11(a). This inlet

temperature profile has warmer fluid near midspan and cooler fluid near the endwalls. The three corresponding exit temperature profiles are nearly identical to one another across most of the span, which implies that almost uniform thermal conditions exist in the circumferential direction at the vane exit. It is believed that this pitchwise uniformity is the result of the elevated freestream turbulence and secondary flow mixing that occurs within the passage, which was also evident in the pressure and wake profiles discussed earlier. The similarity between the three exit profiles is an observation that is also present for Inlet Profiles B, C, and D shown in Fig. 11(b)–11(d). In addition, it is evident from Figs. 11(a)–11(d) that the mean flow temperature,  $T_{ave}$ , upstream at the vane inlet is larger than the mean flow temperature downstream at the vane exit. The difference between the two average flow temperatures is a measure of the total heat that is lost from the flow into the vane and endwall metal surfaces.

The three exit temperature profiles resulting from inlet Profile C are very similar to each other, and they are also similar to the exit temperature profile shapes for inlet Profile A. This is a result of Inlet Profiles A and C having similar temperature and pressure profile shapes over most of the vane span. The only noteworthy difference for Inlet Profile C takes place near the OD endwall where the reduction in flow temperature across the vane is larger for Inlet Profile C than for Inlet Profile A. This difference is attributed to Inlet Profile C having a positive  $C_p$  value of approximately  $C_p=1.0$  near the OD endwall, as compared to  $C_p=-1.0$  for Inlet Profile A. The positive  $C_p$  value means that the turbine inlet pressure profile near the OD contains a forward facing pressure profile inflection point near the endwall. This results in a secondary flow structure that is different than for a typical turbulent boundary layer, in that it circulates flow toward both the endwall and midspan. As the flow passes through the turbine vane, this OD high pressure region directs colder fluid near the endwall toward the relatively lower total pressure midspan. This redistribution of colder fluid significantly reduces the fluid temperature from the OD endwall and into the midspan region.

A small increase in flow temperature is observed from the vane



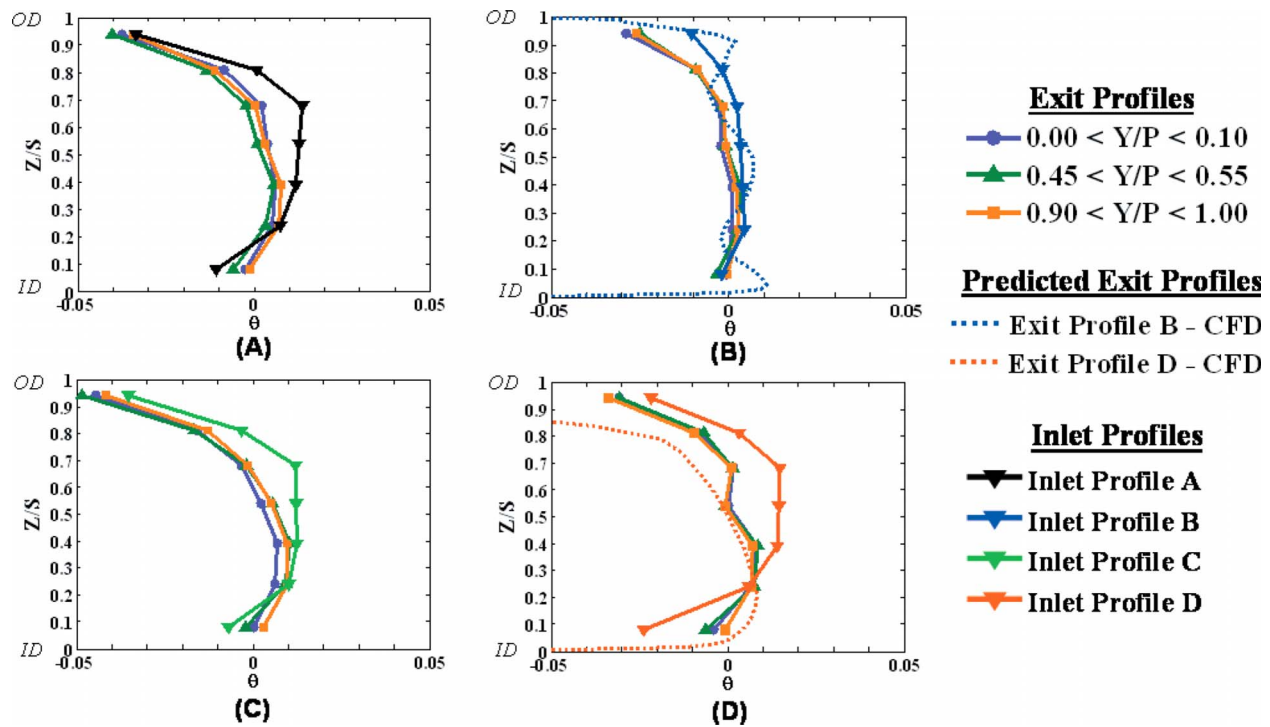


Fig. 11 Radial total temperature profiles measured at the vane exit for (a) Inlet Profile A, (b) Inlet Profile b, (c) Inlet Profile C, and (d) Inlet Profile D

inlet to the vane exit near the ID for each of the inlet profiles, with the exception of Inlet Profile B. Since Inlet Profile B has near uniform inlet pressure near the ID, the exit temperature profile near the ID should be similar to the inlet temperature profile, which is also near uniform, and the results in Fig. 11(b) verify that to be true. This result is consistent with the predictions of Munk and Prim [1]. Results of the simulations of the mean temperature profile at the vane exit plane for inlet Profiles B and D are also included in Fig. 11. In the simulation, a small increase in flow temperature is observed near the ID for inlet Profile B and a larger increase in flow temperature is seen for inlet Profile D. It is believed that the increase in flow temperature near the ID is caused by a migration of warmer fluid near midspan toward the ID endwall via secondary flow circulation within the vane passage.

Secondary flow vectors are plotted in Fig. 12 over contours of normalized exit temperature for the flow simulation with inlet Profiles B and D. The cutting plane was taken at an axial plane at 12% axial chord downstream of the vane trailing edge. The secondary flow vectors were calculated by subtracting the component of the local velocity parallel to the midspan, midpassage flow direction from the local flow vector [24]. Then, these secondary flow vectors were resolved into components on the cutting plane. These figures clearly show the wake regions. Within these wakes, the secondary flow vectors show a large movement of flow from the OD to the ID. The color contours indicate that this flow is carrying cold fluid from the OD wall down toward the ID. As shown in Figure 12(a), inlet Profile B results in far less thermal migration toward the ID than in inlet Profile D (Figure 12(b)). This is consistent with the exit temperature profiles determined both experimentally and computationally. This migration is caused by secondary flow development as the remnants of the passage vortices are still readily discernible at span locations of 0.1 and 0.9 percent in this wake region, as shown in the figure. Consequently, it is believed that these passage vortices, which develop from the vane leading edge horseshoe vortices, are more dominant within the passage.

The same increase in fluid temperature from the vane inlet to the vane exit is not seen near the OD endwall, but rather a reduc-

tion in temperature occurs for all four measured inlet profiles. Again, this is consistent with secondary flow migration toward the ID endwall. The differences in the measured exit temperature profiles with changing inlet profile are consistent with variations in the level of migration of OD flow toward the ID. Again, this is related to differences in the severity of the secondary flows. Since secondary flows are driven by radial and circumferential gradients in static pressure within the passage, it is instructive to consider the change in airfoil loading resulting from one profile versus another. Figure 13 is a plot of the static pressure on the vane normalized by the upstream total pressure ( $P_1$ ). Both the pressure and suction surfaces are shown for both Inlet Profiles B and D. Clearly, it can be seen that the loading changes from ID to OD. This pressure variation has a profound effect on the radial and circumferential gradients in the velocity vectors within the passage. Again, this is consistent with the general conclusions of Munk and Prim [1]. Also note that the difference in static pressure between inlet Profiles B and D is significantly different near the OD driving even more flow down the vane span for inlet Profile D.

## Conclusions

Several different radial profiles of pressure and temperature were analyzed at the inlet and exit of a fully annular high pressure turbine vane ring. The redistribution of the inlet profiles as the flow passed through the vane passages was examined and several important results were found. As the upstream total pressure is increased along the endwalls, there is an increase in total pressure loss across the vanes. The downstream pressure profiles taken within different vane pitch regions also tend to become more uniform in the pitch direction over the majority of the vane span. This result suggests that the secondary flow vortices are becoming stronger and are affecting a larger span and pitch region within the vane passage.

A temperature decrease was noticed near the OD and into the midspan region for each of the inlet profiles studied. As the total pressure near the OD endwall was increased, this temperature

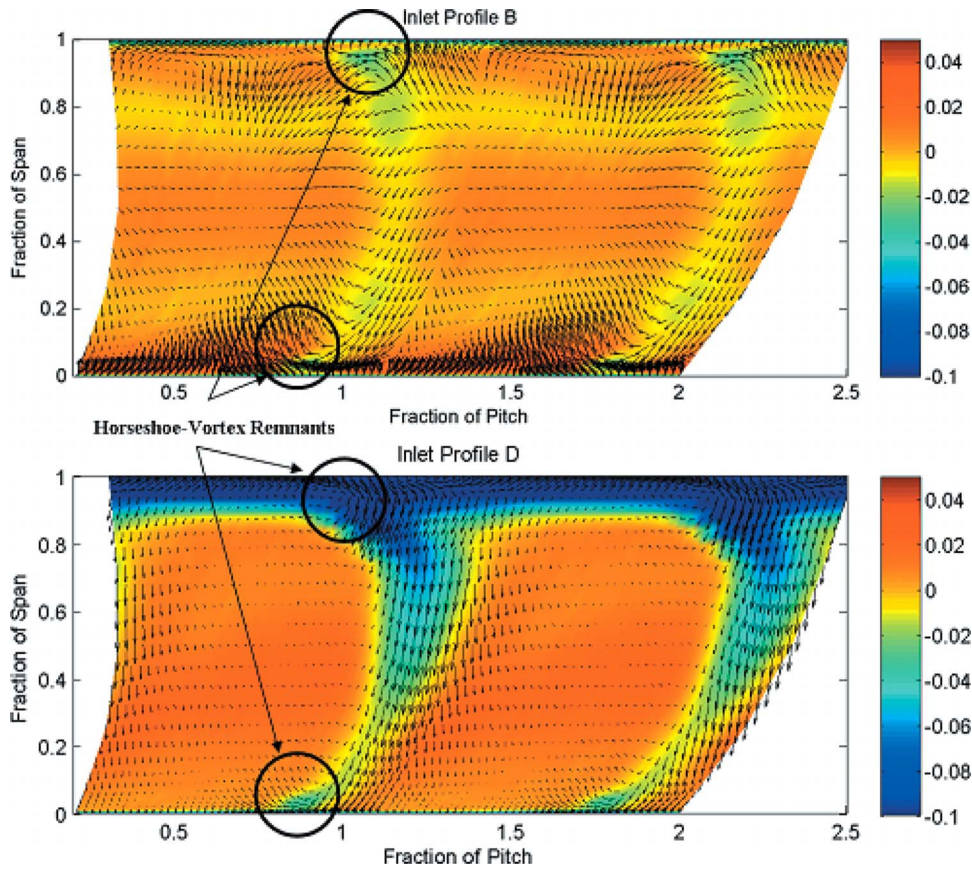


Fig. 12 Secondary flow vectors over contours of nondimensional exit temperature  $\theta$  near the vane exit plane for Inlet Profiles B and D

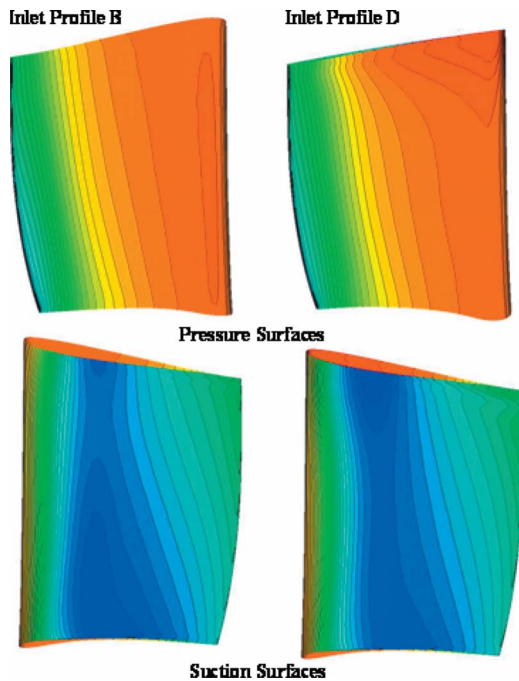


Fig. 13 Static pressure, normalized by  $P_1$  of the vane airfoil for Inlet Profiles B and D on the pressure surfaces and suction surfaces

reduction grew larger. This was caused by relatively cool fluid at a relatively high total pressure near the OD endwall being circulated toward the warmer and lower pressure midspan region. A temperature increase was observed near the ID for three of the four inlet profiles examined in this study. The one case in which there was no temperature increase was for a uniform inlet pressure field with uniform inlet temperature, and therefore no change in temperature was expected. For the other three cases, the increase in fluid temperature was attributed to the vane passage secondary flows directing the warmer core flow toward the ID endwall. The difference between the ID and OD exit temperature profile behavior is believed to be caused by the difference in the vane airfoil aerodynamic loading near the ID versus the OD. This spanwise difference in aerodynamic loading resulted in a different vane passage fluid migration and therefore changed the secondary flow circulation pattern.

Another important result from this study is that an increase in the total pressure along the endwalls at the vane inlet results in a decrease in the vane exit flow angle near the endwalls. This reduction in exit flow angle caused the flow to be oriented more in the axial direction. A relatively large pressure loss and change in exit flow angle were experienced near the OD for all of the inlet pressure profiles that were considered. This was attributed to large secondary flow vortices present within this span region. The exit flow angle results from this study are important when considering the design of a film cooling pattern located on the endwall platforms downstream of the vane. The results from this study are also important for considering the design of the downstream blade, which is heavily dependent on an accurate accounting of thermal conditions entering the airfoil row.

## Acknowledgment

The authors would like to thank AFRL/PRTT and PRTE for their help in conducting these experiments as well as Robert Free for assembling the instrumentation rakes. The authors would also like to thank the Air Force Research Laboratory at Wright-Patterson Air Force Base for funding and sponsoring this research effort.

## Nomenclature

- $C$  = axial chord length of vane  
 $C_p$  = pressure coefficient,  
 $C_p = (P - P_{MS1}) / (1/2 \rho_{AVE} U_{AVE}^2 |_1)$   
 $P$  = total pressure, or vane pitch  
 $Re$  = Reynolds number,  $Re = U_{ave} \cdot C / \nu_{ave}$   
 $S$  = vane span, or total vane surface length  
 $T$  = total temperature  
TDC = top dead center of turbine vane ring  
 $Tu$  = turbulence intensity,  $Tu = U_{rms} / U_{ave}$   
 $U$  = velocity  
 $X, Y, Z$  = axial, pitch, and span directions

## Greek

- $\alpha$  = vane exit flow angle  
 $\phi$  = circumferential location with respect to TDC  
 $\nu$  = kinematic viscosity  
 $\rho$  = density  
 $\theta$  = nondimensional temperature,  
 $\theta = (T - T_{ave1}) / (T_{ave1})$   
 $\xi$  = percent total pressure loss,  $\xi = 100 \cdot (P_1 - P_2) / P_1$   
 $\bar{\xi}, \bar{\xi}$  = mean and overall loss,  $\bar{\xi} = \int_{\phi=0}^{\phi=P} \xi d\phi$ ,  
 $\bar{\xi} = \int_{r=ID}^{r=OD} \int_{\phi=0}^{\phi=P} \xi d\phi dr$

## Subscripts

- 1 = upstream of vane  
2 = downstream of vane  
ave = mean, or average conditions across vane pitch or span  
ms = midspan

## References

- [1] Munk, M., and Prim, R. C., 1947, "On the Multiplicity of Steady Gas Flows Having the Same Streamline Pattern," *Proc. Natl. Acad. Sci. U.S.A.*, **33**, pp. 137–141.
- [2] Langston, L. S., 1980, "Crossflows in a Turbine Cascade Passage," *ASME J. Eng. Power*, **102**, pp. 866–874.
- [3] Hermanson, K., and Thole, K. A., 1999, "Effect of Inlet Profiles on Endwall Secondary Flows," *J. Propul. Power*, **16**(2), pp. 286–296.
- [4] Colban, W., Thole, K., and Zess, G., 2002, "Combustor Turbine Interface Studies—Part 2: Flow and Thermal Field Measurements," *ASME Paper No. 2002-GT-30527*.
- [5] Boyle, R., and Giel, P., 1997, "Prediction of Nonuniform Inlet Temperature Effects on Vane and Rotor Heat Transfer," *ASME Paper No. 97-GT-133*.
- [6] Dorney, D., and Schwab, J., 1996, "Unsteady Numerical Simulations of Radial Temperature Profile Redistribution in a Single-Stage Turbine," *ASME J. Turbomach.*, **118**, pp. 783–791.
- [7] Cattafesta, L., 1988, "An Experimental Investigation of the Effects of Inlet Radial Temperature Profiles on the Aerodynamic Performance of a Transonic Turbine Stage," MS thesis, M.I.T., Cambridge.
- [8] Shang, T., Guenette, G., Epstein, A., and Saxer, A., 1995, "The Influence of Inlet Temperature Distortion on Rotor Heat Transfer in a Transonic Turbine," *AIAA Paper No. 95-3042*.
- [9] Chana, K., Hurriion, J., and Jones, T., 2003, "The Design, Development and Testing of a Non-Uniform Inlet Temperature Generator for the QinetiQ Transient Turbine Research Facility," *ASME Paper No. 2003-GT-38469*.
- [10] Povey, T., Chana, K., Jones, T., and Hurriion, J., 2005, "The Effect of Hot-Streaks on HP Vane Surface and Endwall Heat Transfer: An Experimental and Numerical Study," *ASME Paper No. GT2005-69066*.
- [11] Butler, T. L., Sharma, O. P., Joslyn, H. D., and Dring, R. P., 1989, "Redistribution of an Inlet Temperature Distortion in an Axial Flow Turbine Stage," *J. Propul. Power*, **5**(1), pp. 64–71.
- [12] Saxer, A., and Giles, M., 1990, "Inlet Radial Temperature Redistribution in a Transonic Turbine Stage," *AIAA Paper No. 90-1543*.
- [13] Barringer, M. D., Thole, K. A., and Polanka, M. D., 2009, "An Experimental Study of Combustor Exit Profile Shapes on Endwall Heat Transfer in High Pressure Turbine Vanes," *ASME J. Turbomach.*, **131**(2), p. 021009.
- [14] Haldeeman, C. W., Dunn, M. G., MacArthur, C. D., and Murawski, C. G., 1992, "The USAF Advanced Turbine Aerothermal Research Rig (ATARR)," *NATO AGARD Propulsion and Energetics Panel Conference Proceedings*, Vol. 527, Antalya, Turkey.
- [15] Barringer, M. D., Thole, K. A., and Polanka, M. D., 2007, "Experimental Evaluation of an Inlet Profile Generator for High-Pressure Turbine Tests," *ASME J. Turbomach.*, **129**(2), pp. 382–393.
- [16] Dorney, D. J., and Davis, R. L., 1992, "Navier–Stokes Analysis of Turbine Blade Heat Transfer and Performance," *ASME J. Turbomach.*, **114**, pp. 795–806.
- [17] Rai, M. M., 1987, "Navier–Stokes Simulations of Rotor-Stator Interaction Using Patched and Overlaid Grids," *J. Propul. Power*, **3**, pp. 387–396.
- [18] Rai, M. M., and Madavan, N. K., 1990, "Multi-Airfoil Navier–Stokes Simulations of Turbine Rotor-Stator Interaction," *ASME J. Turbomach.*, **112**, pp. 377–384.
- [19] Praisner, T. J., Magowan, J. W., and Clark, J. P., 2003, "Predictions of Temperature Redistribution in a Turning Duct and in High-Pressure Turbines," *ASME Paper No. GT2003-38317*.
- [20] Clark, J. P., and Grover, E. A., 2006, "Assessing Convergence in Predictions of Periodic-Unsteady Flowfields," *ASME Paper No. GT2006-90735*.
- [21] Johnson, P. D., 2005, "Consortium Turbine Research Rig, Aerothermal and Mechanical Design," *AFRL Technical Report No. AFRL-PR-WP-TR-2005-2157*.
- [22] Urbassik, R. M., Wolff, J. M., and Polanka, M. D., 2006, "Unsteady Aerodynamics and Interactions Between a High Pressure Turbine Vane and Rotor," *ASME J. Turbomach.*, **128**, pp. 35–72.
- [23] Ames, F. E., Johnson, J. D., and Fiala, N. J., 2006, "The Influence of Aero-Derivative Combustor Turbulence and Reynolds Number on Vane Aerodynamic Losses, Secondary Flows, and Wake Growth," *ASME Paper No. GT2006-90168*.
- [24] Cumpsty, N. A., 1989, *Compressor Aerodynamics*, Longmans, New York, p. 316.



# Analysis of Turbulent Flow in 180 deg Turning Ducts With and Without Guide Vanes

Jiang Luo

Eli H. Razinsky

Solar Turbines Incorporated,  
A Caterpillar Company,  
San Diego, CA 92101

*This paper presents a numerical study of the turbulent flows through a number of 2D and 3D 180 deg U-ducts, with and without guide vanes, using the Reynolds-averaged Navier-Stokes method. Computations have been first carried out for a 2D U-duct flow ( $W/H = 1.0$ ) with four turbulence models (V2F,  $k-\epsilon$ , shear stress transport (SST), and Reynolds stress). The models' capability for predicting streamline curvature effects on turbulence and separation has been assessed, using flow and turbulence data. The effects of adding a guide vane inside the bend have been analyzed to reduce/avoid flow separation. Three vanes with different radial locations have been studied, and the mechanism for pressure loss reduction has been examined. Analyses have been performed for turbulent flows in 3D U-ducts with square cross section and sharp 180 deg turning ( $W/D = 0.2$ ), similar to the U-bends in typical turbine blade cooling passages. The predictions are compared with the data of outer-wall pressure. The effects of the guide vane and outer-wall shape on the flow separation, secondary-flow vortices, and pressure loss have been evaluated. The combined vane and uniform cross section area are found to improve the flow distribution and reduce the pressure loss significantly.*

[DOI: 10.1115/1.2987239]

## 1 Introduction

The steady increase in turbine inlet temperature over the past several decades has significantly enhanced the performance of gas turbine engines. The tendency for higher turbine inlet temperature continues and poses considerable challenges for the analysis and design of turbine cooling schemes [1–4]. In a typical cooled turbine blade, multiple channels (aligned with the airfoil spanwise direction) are connected by 180 deg bends to produce a serpentine passage. The total flow resistance through the multipass passage determines the coolant flow rate at a given supply pressure. Therefore, a designer's predictive capability for this passage flow resistance is critical to achieve an accurate prediction of blade cooling. The 180 deg bend is known to cause a substantial increase in pressure loss and heat transfer due to the usually excessive flow separation, mixing, impingement, and enhanced turbulence inside and downstream of the sharp  $U$ -turn.

There have been numerous studies on curved duct flows. It is well known that the streamline curvature has surprisingly large effects on turbulent flows that simple eddy-viscosity models fail to account for [5]. The turbulence is suppressed by the convex curvature but amplified by the concave curvature. The magnitude of this curvature effect may be indicated by a parameter  $\delta/R$ , the ratio of the shear layer thickness to the radius of curvature [5]. Most of the earlier studies dealt with turbulent flows with mild to moderate curvatures (with  $\delta/R \sim 0.01-0.1$ ).

Typical  $U$ -bends in turbine cooling passages, however, experience much stronger curvature, with  $\delta/R \sim 1$  or higher, especially around the inner-wall (divider) tip. Metzger et al. [6] studied the pressure loss through sharp 180 deg turns ( $W/D = 0.2$ ) in a range of geometry combinations typical in blade cooling design. They studied the effects of the channel aspect ratio, the turn clearance, and the Reynolds number. Han et al. [7] observed significantly higher heat/mass transfer after the sharp 180 deg turns in two-pass

channels. There have been extensive experimental efforts by Wagner et al. [8], Iacovides et al. [9], Liou et al. [10], and Zhou and Acharya [11], with more studies listed in Refs. [2,12].

Many numerical studies have been published for 180 deg  $U$ -duct flows. Shih and Sultanian [13] reviewed the Reynolds-averaged Navier-Stokes (RANS) computations of  $U$ -duct flows related to turbine blade internal cooling. Various eddy-viscosity models (e.g.,  $k-\epsilon$  and  $k-\omega$ ) and differential Reynolds stress models (RSMs) have been employed [13–24]. The RSMs are often observed to be the best turbulence closure for  $U$ -duct flows, e.g., in Refs. [19–23]. The advantages of the RSM over eddy-viscosity models in a 2D  $U$ -duct flow were discussed in Ref. [22]. Han and Chen [12] examined the RSM results of various blade cooling passages, including the effects of blade rotation, rib geometry, and channel aspect ratio on heat transfer enhancement.

The turbulent flows inside blade serpentine cooling passages are very complex, due to the excessive flow separation (inherently unsteady), re-attachment, and secondary flows generated by ribs, rotation, and sharp 180 deg turns [1–4]. This complexity poses challenges to all the RANS turbulence models, including the RSM. To overcome such limitation, Sewall and Tafti [25] employed large-eddy-simulation (LES) for a two-pass  $U$ -duct flow with ribs. Their LES results displayed excellent agreement with heat transfer and pressure loss data. However, the LES method remains time consuming and expensive for industry design practice, in spite of the rapidly increasing computer speed and memory.

The V2F model [26] appears to be a good compromise between the superior yet stiff RSMs and the usually robust eddy-viscosity models. It solves the system of equations for  $k$ ,  $\epsilon$ , and two additional quantities,  $\overline{v^2}$ , the wall-normal Reynolds stress component, and  $F_{22}$ , the redistribution term in the equation of  $\overline{v^2}$ . There has been growing interest in the V2F model in the turbomachinery community (e.g., Refs. [27–29]). However, its performance for curved flows has not been fully assessed. In this paper, the V2F model as in Ref. [30] will be compared with other models for  $U$ -bend flows.

There have been only a few studies on turning vanes inside  $U$ -ducts published in the open literature. Rao et al. [31] carried out

Contributed by the International Gas Turbine Institute of ASME for publication in the JOURNAL OF TURBOMACHINERY. Manuscript received August 13, 2007; final manuscript received May 5, 2008; published online January 29, 2009. Review conducted by David Wisler. Paper presented at the ASME Turbo Expo 2007: Land, Sea and Air (GT2007), May 14–17, 2007, Montreal, QC, Canada.

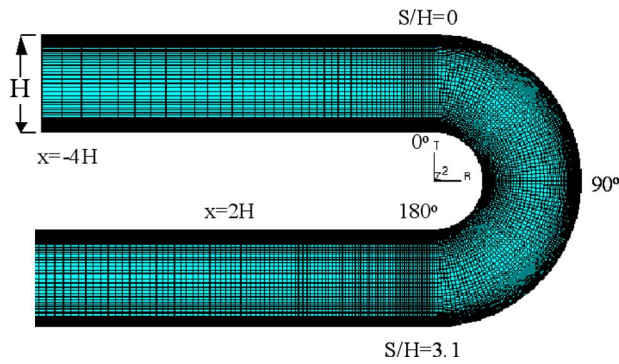


Fig. 1 Mesh for 2D *U*-bend ( $R_i=0.5H$ ,  $R_o=1.5H$ )

an experimental study on various guide vanes inside a sharp 180 deg bend. They observed that the shape and position of vanes significantly affected the pressure loss. The information on guide vanes inside 180 deg bends remains limited and further studies are needed.

The objectives of this paper are as follows: (1) to assess the accuracy of the V2F, SST,  $k-\epsilon$ , and Reynolds stress models for a 2D *U*-duct flow with strong curvature effects; (2) to study the effects of guide vanes inside the 2D *U*-duct; and (3) to study the effects of guide vanes in 3D *U*-duct flows with very small turn radius, and the impact of the outer-wall shape.

## 2 Solver and Turbulence Models

The flow solver used is the commercial computational fluid dynamics (CFD) package STAR-CD [30]. STAR-CD is an implicit finite volume solver that employs a variant of the SIMPLE algorithm for velocity-pressure correction. The convective fluxes in the mean-flow and turbulence equations are discretized with a second-order accurate differencing scheme called monotone advection and reconstruction (MARS). The MARS scheme is blended (50%/50%) with the first-order accurate upwind differencing (UD) scheme to ensure convergence for all the cases. The numerical diffusion error, introduced by the blended MARS-UD scheme, is negligible with the present fine meshes. The convergence criteria (maximum residual tolerance in STAR-CD) are set to  $1 \times 10^{-4}$  for both flow and turbulence variables. The difference in the mass flow rates at the inlet and exit is less than 0.01% in the final solutions.

The eddy viscosity ( $\mu_t$ ) is from three low-Reynolds-number (LRN) models: (1) Launder–Spalding’s  $k-\epsilon$  model with the LRN function of Lien and Leschziner, (2) Menter’s SST  $k-\omega$  model, and (3) Durbin’s V2F model. The Gibson–Launder’s RSM equations predict the Reynolds stress components directly. The details

for the four models can be found in Ref. [30]. Note that the RSM here is not a LRN model because the wall function is used to bridge the near-wall region ( $y^+ < 40$ ), the only option for RSM in STAR-CD.

## 3 Results and Discussion

CFD analyses have been performed for the turbulent flows in 2D and 3D *U*-ducts, with and without flow guide vanes. The predictions of mean flow and turbulence will be compared with available data. The effects of turning vanes will be assessed on the flow separation in both 2D and 3D ducts and the secondary-flow vortices in 3D ducts.

**3.1 2D *U*-Duct Flow.** The Reynolds number modeled is the same as in the test [32],  $Re=1$ . The inlet flow has thick turbulent boundary layers on the inner and outer walls, with  $\delta/H=0.35, 0.30$ , respectively, at  $x=-1H$ . The computational mesh (Fig. 1) starts from  $x=-4H$  and ends at  $x=12H$ . The inlet boundary conditions of both flow and turbulence were specified to match the measured profiles very well, as in Ref. [22]. The mesh size, with a total of  $291 \times 141$  (streamwise  $\times$  radial) cells, has proved to provide grid-independent solutions [22]. The first grid near the wall is located around  $y^+=1$  to satisfy the requirements of the LRN models. Note that this  $291 \times 141$  mesh was not used in the RSM computation. Instead, a second mesh of  $291 \times 101$  cells was used there. It has fewer radial cells and larger near-wall spacing around  $y^+=40$  because the wall function is used.

The predicted velocity contours are shown in Fig. 2. The difference lies in the downstream separation size, as indicated by the blue color near the inner wall. The  $k-\epsilon$  model predicts the smallest separation zone, while the RSM shows the largest one. This is consistent with earlier observations, e.g., in Ref. [22], in spite of the differences in the CFD codes and near-wall treatment for the models. The SST and V2F predictions are similar, with the recirculation significantly larger than the  $k-\epsilon$  prediction but smaller than the RSM prediction.

The  $k-\epsilon$  prediction shows turbulence amplification near the convex wall, while the RSM predicts a large damping of turbulence there, Fig. 3. The V2F and SST predictions are similar to the RSM prediction but with less degree of turbulence damping near the convex wall and turbulence amplification near the concave wall. All the models show very high turbulence downstream near the inner wall, as a result of flow separation.

The upstream thick boundary layers largely disappear once inside the bend, Fig. 4(a)). All the models underpredict the turbulence enhancement near the concave wall, Fig. 4(b)). Improvement was shown in an earlier RSM prediction with the  $\epsilon$  equation modified to account for the nonequilibrium flow with large eddies near the concave wall [23]. Nevertheless, this comparison exposes

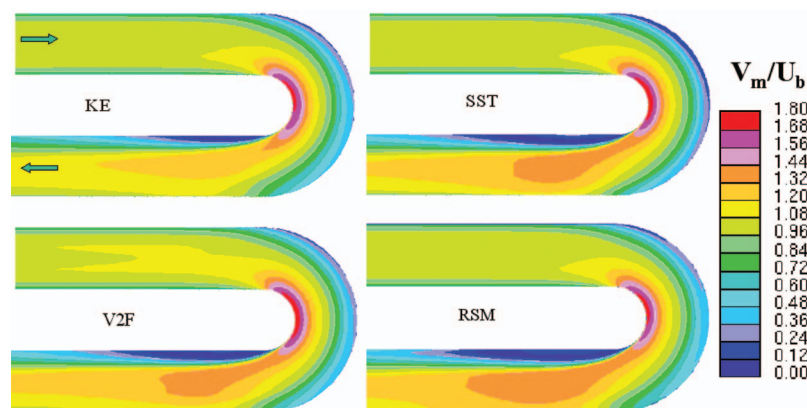


Fig. 2 Velocity ( $V_m/U_b$ ) contours predicted by the models

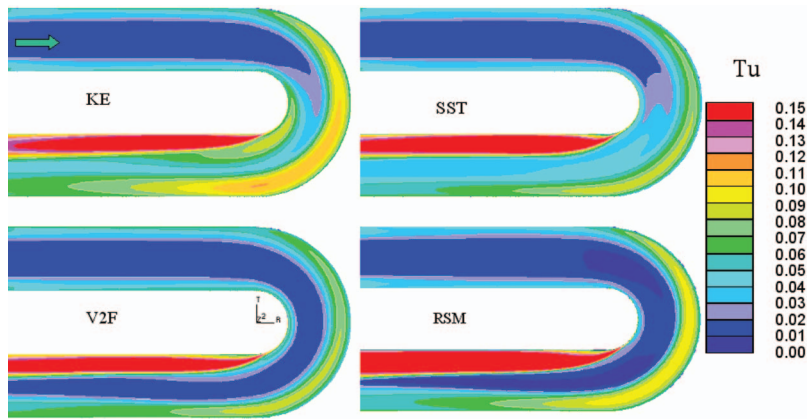


Fig. 3 Predicted turbulence level (Tu) contours

the limitation of RANS modeling of  $U$ -duct flows, even with the RSM. A LES solution may be needed to capture the energetic large eddies induced by the concave curvature.

Due to the adverse pressure gradient and diminished turbulence, the flow separates around  $\theta=150$  deg on the inner wall [32]. The velocity profiles ( $U/U_b$ ) at  $x=1H$  downstream are shown in Fig. 5. The extent of separation is seen to be inversely proportional to the turbulence level upstream. The RSM, V2F, and SST models predict the lower levels of turbulence upstream (Fig. 3), hence the larger separations downstream. The  $k-\epsilon$  model underpredicts the separation, resulting in a poor prediction of  $U/U_b$  across the channel.

The wall pressure distribution ( $C_p$ ) and pressure loss ( $C_{p1}-C_{p2}$ ) are largely determined by the extent of separation, which dictates the effective throughflow area and hence the pressure recovery characteristics. The pressure loss is seriously underpredicted by the  $k-\epsilon$  model due to its underprediction of flow separation, Fig. 6. Compared with the data ( $C_{p1}-C_{p2}=0.45$ ), the pressure loss has been underpredicted 39%, 29%, 22%, and 6%, by the  $k-\epsilon$ , SST, V2F, and RSMs, respectively. The V2F model provides more accurate prediction than the  $k-\epsilon$  and SST models. Without using eddy viscosity, the RSM provides the best prediction for the pressure loss.

While the mean flow is dominated by the pressure gradient, the effect of turbulence is still important, especially when the flow begins to decelerate and separate. The RSM captures the turbulence damping and hence lower  $C_f$  on the convex wall, in the best agreement with the data, Fig. 7(a). Though the RSM predicts

excessive recirculation downstream, the STAR-CD code outputs close-to-zero values of  $C_f$  rather than negative values, due to the use of wall function.

It should be noted that the V2F model predicts an overshoot of  $C_f$  downstream of the flow re-attachment ( $S/H=4.7$ ), Fig. 7(a). This is caused by an unphysically high level turbulence near the wall, including the viscous sublayer. Further investigation is needed to fully understand it. The Reynolds analogy indicates that the V2F would also overpredict the heat transfer rate after flow re-attachment. The  $C_f$  values on the outer wall display smaller differences among the models, Fig. 7(b). Though the data inside the bend are not available, it is likely that all the models underpredict  $C_f$  since the turbulence enhancement has been underpredicted there (Fig. 4(b)). The RSM yields the best prediction of  $C_f$  downstream of the bend.

**3.2 2D  $U$ -Duct Flows With Turning Vanes.** A study was carried out to assess the impact of flow guide vanes inside the  $U$ -bend. Figure 8 displays three vanes with similar shape but different locations in the channel span. The vanes extend  $1.5H$  upstream and downstream, locating, respectively, at 50% (Vane 1), 34% (Vane 2), and 20% (Vane 3) radially between the inner and outer walls. The vanes' downstream length was determined using the measured extent of separation ( $\sim x=1.5H$ ). The upstream length was set to avoid turning-induced incidence at the leading edge. The vanes are modeled as idealized baffles with zero thickness. This preserves the key flow features including forced flow turning and the boundary layer growth on both sides of the vane,

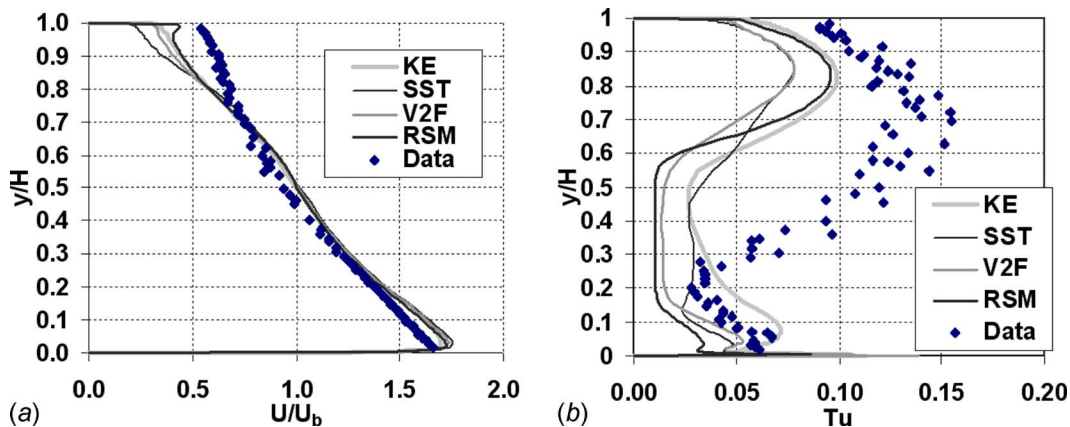


Fig. 4 Profiles at 90 deg section: predictions versus data ( $y/H=0$  at inner wall;  $y/H=1.0$  at outer wall). (a)  $U/U_b$  and (b) Tu.



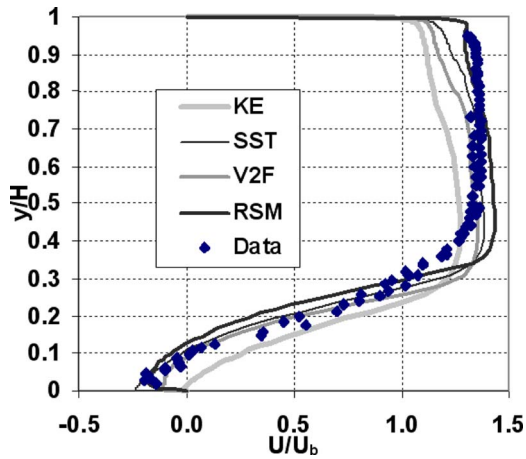


Fig. 5 Velocity ( $U/U_b$ ) profiles at  $x=1H$  downstream

without involving the additional effects of the vane profile. All the analyses were obtained with the Reynolds stress model, as it provided the best prediction earlier. The grids are refined near the vanes to have near-wall spacing around  $y^+=40$ , as wall functions are used.

Figure 9 shows the velocity contours without and with the vanes. It is evident that the presence of a flow guide vane substantially improves the flow distribution through the bend, particularly in the downstream. With the forced flow splitting and turning by the vanes, the downstream separation is now avoided. The velocity contour for Vane 1 (midchannel) shows much reduced flow acceleration and deceleration around the inner wall. Indeed, it shows more uniform flow speed inside the two subchannels and downstream.

While the flow still experiences significant acceleration and deceleration on the convex side of Vane 3 (20% radially), it does not separate off the vane. This is due to the increased radius of 180 deg turning and the new boundary layer that is much thinner and hence “healthier” than the original one on the duct inner wall. The new boundary layer, on all the vanes’ convex side, also has additional benefit of much lower  $\delta/R$ , meaning the turbulence damping is less significant than the original one with high  $\delta/R$ .

It is interesting to note that the guide vanes also modify the turbulence characteristics inside and downstream of the bend, Fig. 10. The high level turbulence downstream is now absent with the vanes. This is because the flow separation and associated turbulence generation have been eliminated from the downstream. Near the outer wall, the vane has also subdued the turbulence amplification. This is most likely caused by the reduction of flow shear

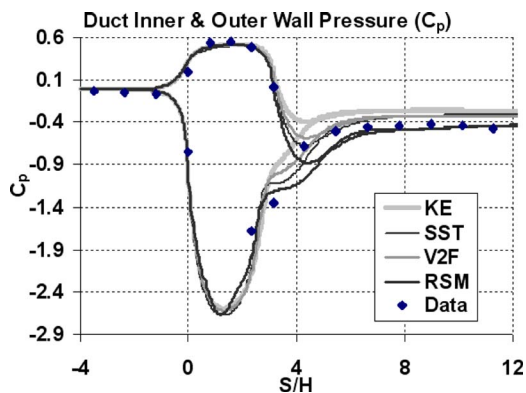


Fig. 6 Wall pressure ( $C_p$ ) distribution through the bend: predictions versus data ( $S/H=0$  at  $\theta=0^\circ$ ;  $S/H=3.1$  at  $\theta=180$  deg)

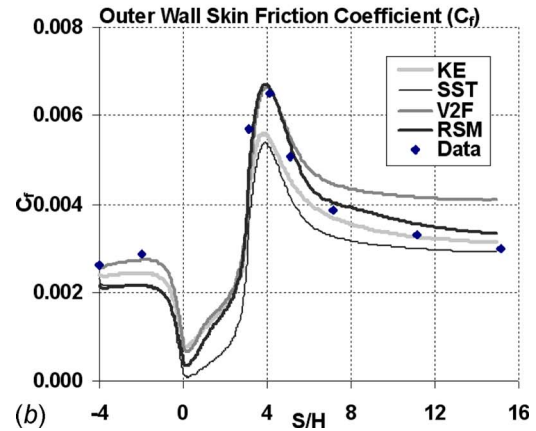
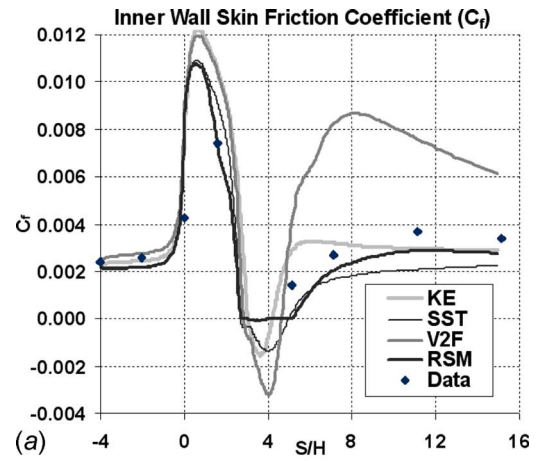


Fig. 7 Skin friction coefficients: predictions versus data: (a) inner wall and (b) outer wall

strain (hence the turbulence production) inside the subchannel between the vane and the outer wall, as shown earlier in the more uniform velocity distribution (Fig. 9). The growth of turbulent kinetic energy inside the boundary layers on the vanes and the wakes is also visible.

The predicted velocity profiles downstream at  $\theta=180$  deg, with and without vanes, are shown in Fig. 11. It is clear that the channel has been split into two subchannels with very thin boundary layers on both sides of the vane. All three vanes have succeeded in avoiding the flow separation near the duct inner wall, leading to much improved velocity profiles across the duct. The impact near

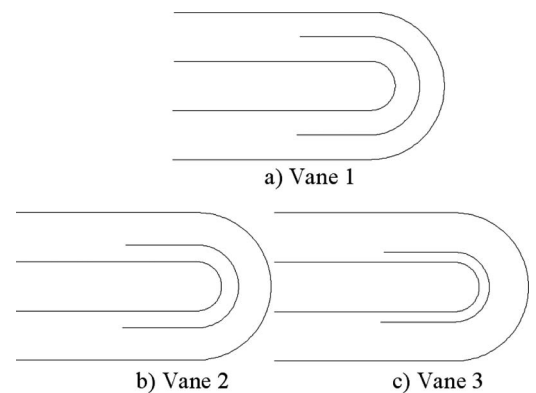


Fig. 8 Three flow guide vanes inside the U-bend: 50%, 34%, and 20% locations (measured from the inner wall)

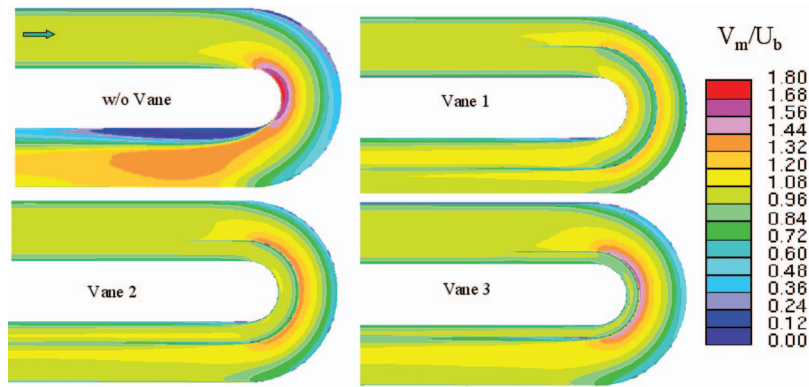


Fig. 9 Predicted velocity ( $V_m/U_b$ ) contours: without vane and with different vanes (all by the RSM)

the duct outer wall is small, as seen earlier in Fig. 9.

The improvement to the flow distribution can be further appreciated at  $2H$  downstream of the bend, Fig. 12. The predicted velocity profile with each vane is much less skewed than the measured profile without vane. Indeed, the profiles with vanes show velocity around  $U_b$  over much of the height. By avoiding the separation, the vanes also greatly reduce the generation of turbulence, Fig. 12(b)). For the baseline case without vane, the RSM severely underpredicts the rate of flow recovery from separation at  $x=2H$ . This underprediction is probably caused by the deficiency of the RSM equations, separated flow unsteadiness and three-dimensionality.

The presence of turning vanes has substantially modified the pressure on both duct walls (Fig. 13). Due to the flow splitting and turning by the vane, the flow acceleration near the inner wall (shown as the large dip in  $C_p$  plot) is substantially reduced. The lowest  $C_p$  value is increased by about 60% by Vane 1 and has been further increased by Vanes 2 and 3, as they are placed closer to the inner wall. With the vanes, the radial pressure gradient between the duct walls and the streamwise pressure gradient, especially near the inner wall, have been cut significantly. This results in much improved flow distribution seen earlier. Compared with the case without vane, the pressure loss ( $C_{p1}-C_{p2}$ ) has been cut by 56%, 58%, and 53% by Vanes 1, 2, 3, respectively.

Each vane is effective in avoiding the sharp increase (due to the flow acceleration) and decrease (due to the flow deceleration) of  $C_f$  on the inner wall inside the bend, Fig. 14(a)). The impact of the vanes on the outer-wall skin friction is also significant (Fig. 14(b)). The peak values of  $C_f$  near  $S/H=4$  and downstream are

much reduced, indicating slower flow near the outer wall. This is due to the increase of effective flow area by the elimination of flow blockage (separation) near the inner wall at the bend exit.

**3.3 3D Square  $U$ -Duct Flows.** A series of CFD analyses was carried out for 3D  $U$ -duct flows without and with guide vanes. The square  $U$ -duct without vane (baseline case) is modeled after the test geometry of Rao et al. [31]. The inner-wall (divider) thickness is 0.2 of the duct hydraulic diameter, i.e.,  $W/D=0.2$ , Fig. 15. The divider tip is a semicircle with  $R_t=0.1D$ . Compared with the 2D case with  $W/H=1.0$ , this represents a much sharper turning. The clearance between the divider tip and the outer wall at  $\theta=90$  deg location is  $1.0D$ . Hence the 90 deg cross section area is also  $1.0D^2$ , the same as that in the straight region.

The Reynolds number based on the bulk velocity and duct hydraulic diameter is around 17,000, considerably lower than the 2D case ( $Re=1 \times 10^6$ ). The flow before the  $U$ -turn is modeled as fully developed turbulent flow as in the experiment. All analyses have been performed using the V2F model due to its overall accuracy and robustness. Earlier analyses with the RSM experienced convergence difficulty, possibly due to the RSM stiffness and the use of wall function in this low Reynolds number flow. Further investigation with the RSM will be conducted.

**3.4 Straight-Corner  $U$ -Ducts With and Without Vane.** The baseline configuration (Case 1) with square cross section is shown in Fig. 15(a)). Due to its geometric symmetry, only half of the duct is meshed, with the computational inlet and exit located at 13 diameters away from the turn. Based on the published information

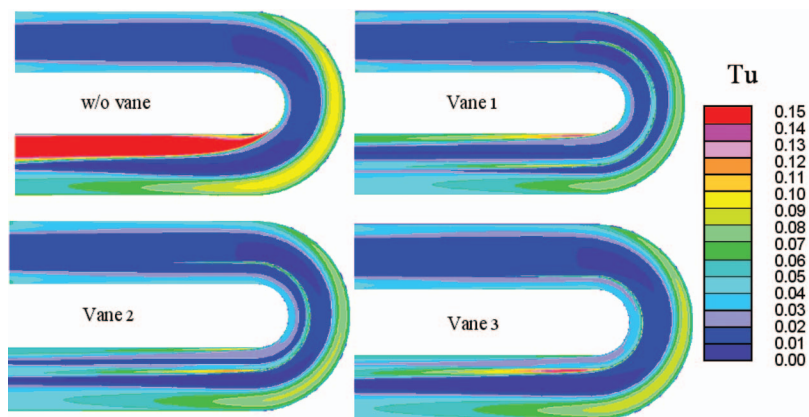


Fig. 10 RSM-predicted turbulence level ( $Tu$ ) contours: without and with different vanes

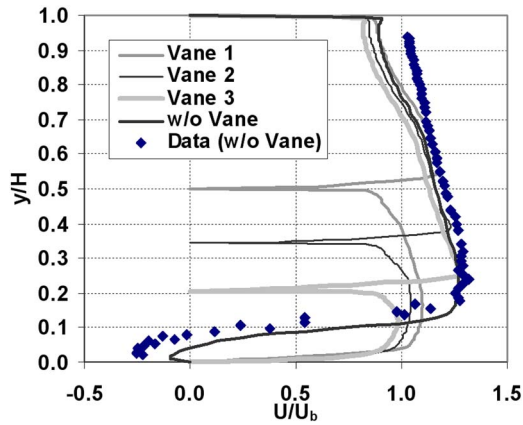


Fig. 11 Longitudinal velocity profiles at 180 deg section: RSM predictions without and with vanes versus data (without vane)

and an internal study [33], the mesh count is  $220 \times 70 \times 35$  (539,000 cells), which is equivalent to  $220 \times 70 \times 70 (1.08 \times 10^6)$  cells for the full duct. Further refinement of the mesh (to 750,000 cells) has resulted in little variation in the solution ( $<0.2\%$  in pressure loss). The grids are refined near the 180 deg turning region to capture large velocity and pressure gradients. Near-wall spacing is maintained at  $y^+ \sim 1$  to meet the low-Reynolds-number requirement of the V2F model.

The planar view for the duct with a turning vane (Case 2) is shown in Fig. 15(b)). Like Vane 1 in the 2D  $U$ -duct, this vane

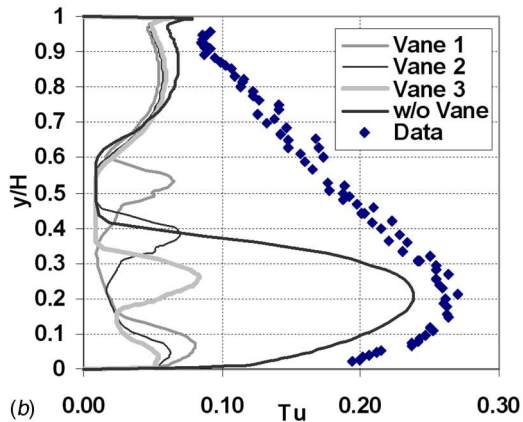
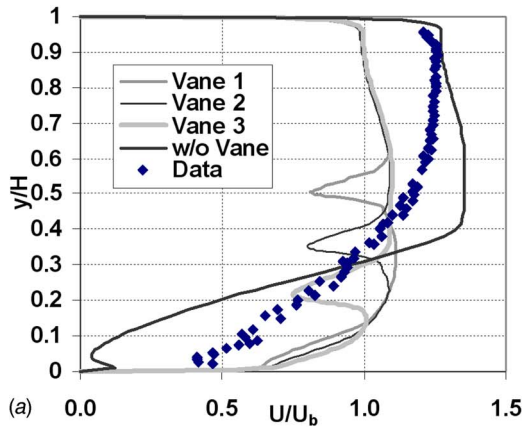


Fig. 12 Profiles at  $x=2H$  downstream of 180 deg section ( $S/H=5.1$ ): RSM predictions (without and with vanes) versus data (without vane). (a) Longitudinal velocity and (b) turbulence level.

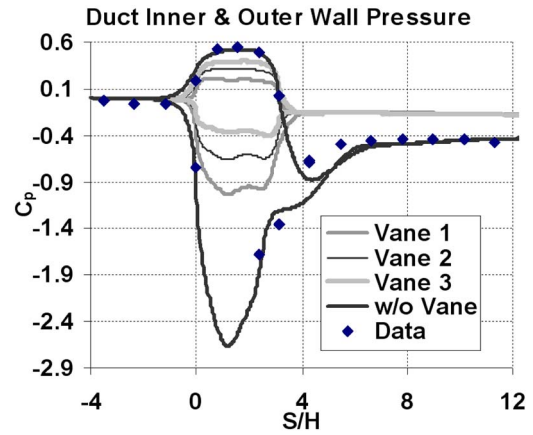


Fig. 13 Wall pressure distributions: RSM predictions (without and with vanes) versus data (without vane)

extends  $1.5D$  upstream and downstream of the turn and is located in the center of the channel. It has a height of  $1.0D$  in the full duct. The vane is again modeled as baffle with zero thickness for simplicity, while preserving the important flow features. The grids are refined near the vane (Fig. 15(c)) to resolve its boundary layers (with  $y^+ \sim 1$ ). Hence the total mesh account for Case 2 is 770,000.

The predicted velocity vectors on the symmetry section of the duct without vane are shown in Fig. 16(a)). The sharp  $U$ -turn causes an excessive flow separation (indicated by the reversed

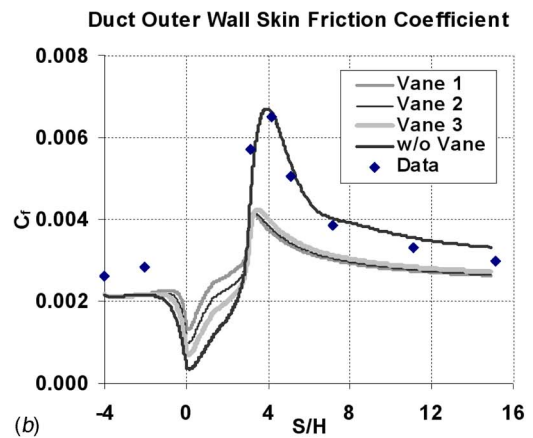
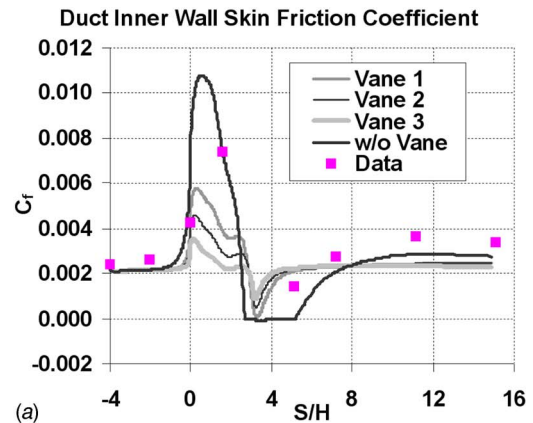


Fig. 14 Duct skin friction coefficients ( $C_f$ ): RSM predictions (with and without vanes) versus data (without vane). (a) inner wall and (b) outer wall.



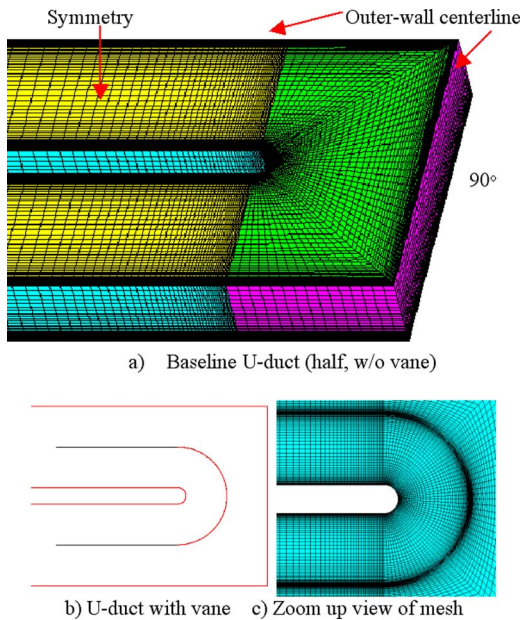


Fig. 15 Mesh for 3D U-Ducts without and with vane ( $R_i = 0.1D$ )

vectors and blue color) off the divider tip. The separation starts well before the divider tip midpoint ( $\theta=90$  deg). As a result of the current much smaller radius ( $R_i=0.1D$ ), the flow recirculation is extensive, much larger than the 2D case ( $R_i=0.5D$ ). Two recirculation zones are also visible in the 90 deg corners. The blockage due to the separation pushes the flow toward the outer wall, downstream of the bend. In addition to causing pressure loss, the separated flow is less energetic/effective in cooling than the attached flow and should be avoided or minimized.

Downstream of the divider, the flow is improved substantially

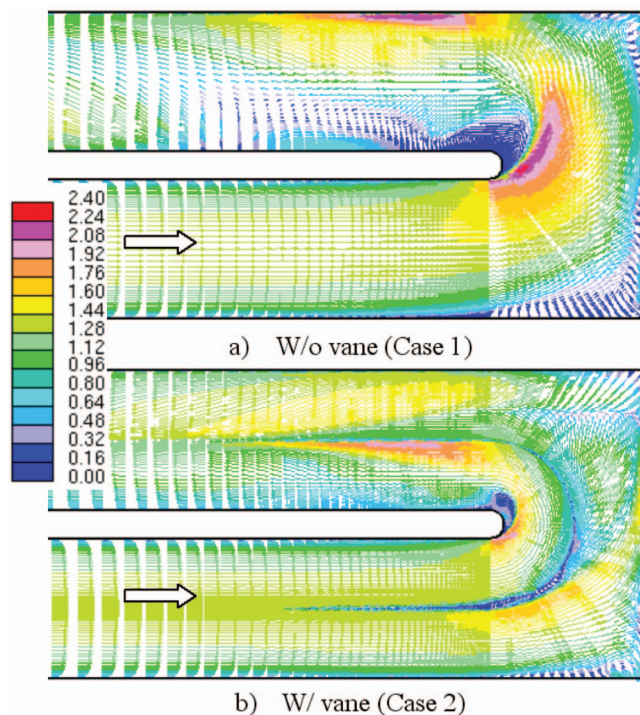


Fig. 16 Predicted velocity contour ( $V_m/U_b$ ) on symmetry section of the straight-corner duct: without and with vane

by the turning vane, Fig. 16(b)). The vane splits the duct into two, with about 49% mass flow through the inner half channel and 51% through the outer half. Much of the low speed and separated flow region is absent. The flow is seen to stay attached on the convex side of the vane, probably due to the large increase of turning radius (from  $0.1D$  of the divider tip to  $0.6D$  of the vane). Due to the vane extension downstream of the bend, the flow is forced to stay attached close to the inner wall. However, the vane is unable to avoid the separation completely near the divider tip, unlike those in the 2D cases. Along the concave (inner) side of the vane, there exist small separation bubbles, caused by local adverse pressure gradients.

Secondary flow is generated whenever a shear layer is turned through a duct or cascade. Figure 17(a) shows a Dean-type secondary-flow vortex on the 90 deg section, inside the bend of the current half duct. Due to the upstream thick boundary layer on the bottom wall and the radial pressure gradient between the inner and outer walls inside the bend, the near-wall flow migrates toward the inner wall, rolling up into a distinct vortex with clockwise rotation. The secondary-flow vectors are plotted using the two velocity components projected on the cross section (normalized by  $U_b$ ).

The guide vane splits the channel into two, resulting in two smaller but still distinct vortices, Fig. 17(b)). The predicted mass-averaged secondary-flow kinetic energy (SKE) coefficient at  $\theta = 90$  deg is now 0.53, a 38% drop from 0.85 of Case 1 in Fig. 17(a)). Therefore, the vane is able to reduce the strength of secondary-flow vortices by a large degree. Figure 17(c) shows the growth and decay of secondary flows inside the original U-bend. Significant secondary flow is visible at 2D downstream. However, the vane greatly reduces the growth of secondary-flow vortices in the bend and downstream, Fig. 17(d)), in consistency with the predicted reduction in SKE. Indeed, these vortices have largely disappeared by 1D downstream.

The pressure distributions along the inner- and outer-wall centerlines (i.e., intersection line with the symmetry plane) are shown in Fig. 18. Note the inner-wall streamline coordinate inside the bend is scaled up to match the outer-wall  $x/D$ , for easy comparison. The inner-wall  $C_p$  curve shows a very sharp drop into the bend and retarded recovery later. The flat portion (i.e., no pressure recovery) of this  $C_p$  curve, dipping at  $\sim -4.6$ , corresponds with the extensive separation off the divider tip before  $\theta=90$  deg, Fig. 16(a)). The prediction of Case 1 is in good agreement with the data, except in the separated flow inside the bend and immediate downstream. The predicted pressure loss coefficient ( $C_{p1} - C_{p2}$ ) of the entire duct is 3.26, which is about 4% off the data of 3.4 [31]. Hence the V2F model shows much better accuracy here than its prediction of 2D flows earlier. This is because the 3D flow loss is due to both the secondary flows and the separation. The latter appears to be dictated by the very small radius of the divider tip and is less affected by turbulence and curvature effects.

The vane leads to a significant reduction in the pressure gradient between the two walls, as in the 2D cases. This lower radial pressure gradient helps to reduce the secondary-flow energy. Compared with Case 1 without vane, the loss has been lowered by 22% due to the vane. Rao et al. [31] observed an improvement of 12% with a similar but shorter turning vane (with thickness). The additional benefit here appears to be brought by the idealized vane (zero thickness) and the absence of thick wake due to its zero thickness.

**3.5 Round-Corner U-Ducts With and Without Vane.** Two more configurations with round corners, without and with the vane (Cases 3 and 4, Fig. 19), have been studied for the effects of the cross section area distribution. The outer wall is now a semi-circle with radius of  $1.1D$ . This keeps the clearance between the divider tip and outer wall to be  $1D$  through the bend, so that the cross section area is constant at  $D^2$  in the entire duct.

The recirculation zones in the former sharp corners near the



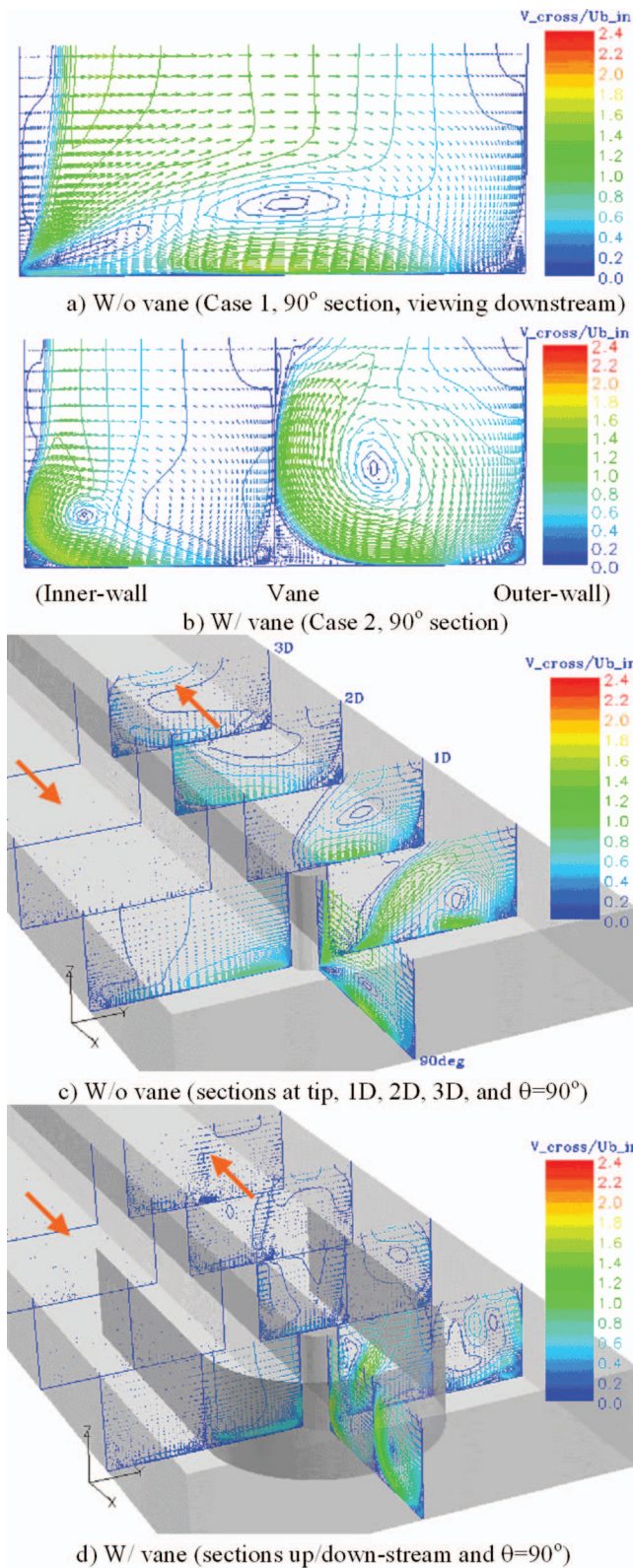


Fig. 17 Secondary-flow vectors on the sections inside the straight-corner duct: without and with vane

outer wall have now disappeared, Fig. 19(a). The vane greatly reduces the separation off the divider tip and downstream, Fig. 19(b). The resultant flow is much more uniform through the bend. This means improved cooling flow distribution and effectiveness. The vane splits the mass flow into 44% through the inner

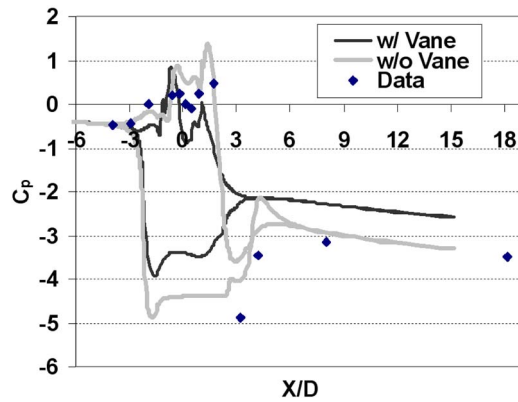


Fig. 18 Pressure distributions on the centerlines of inner and outer walls ( $x/D=0$  at  $\theta=90$  deg), without and with vane: predictions versus data (Case 1 without vane; outer wall only)

half channel and 56% through the outer half. Note that the mass flow in the outer channel (Case 4) increases by 5% from Case 2. This is attributed to the lower flow resistance in the outer channel due to the reduction of separation (Fig. 19(b) versus Figure 16(b)) and secondary flow there (Fig. 20(a) versus Figure 17(b)).

The secondary-flow vectors for Case 3 are not shown here, as they are largely similar to those of Case 1. However, the combination of vane and uniform cross section area has resulted in a sharply weakened Dean vortex in the outer half channel, Fig. 20(a). The elimination of the sharp 90 deg corner of the outer wall is the only change from Case 2 to Case 4, hence the cause for reducing the second Dean vortex strength from Fig. 17(b) to Fig. 20(a). The growth of secondary flow through the bend is much mitigated by the vane and the change of outer-wall shape, Fig. 20(b). The secondary flow has largely decayed by 1D downstream.

The decay of SKE is summarized in Fig. 21. The SKE coeffi-

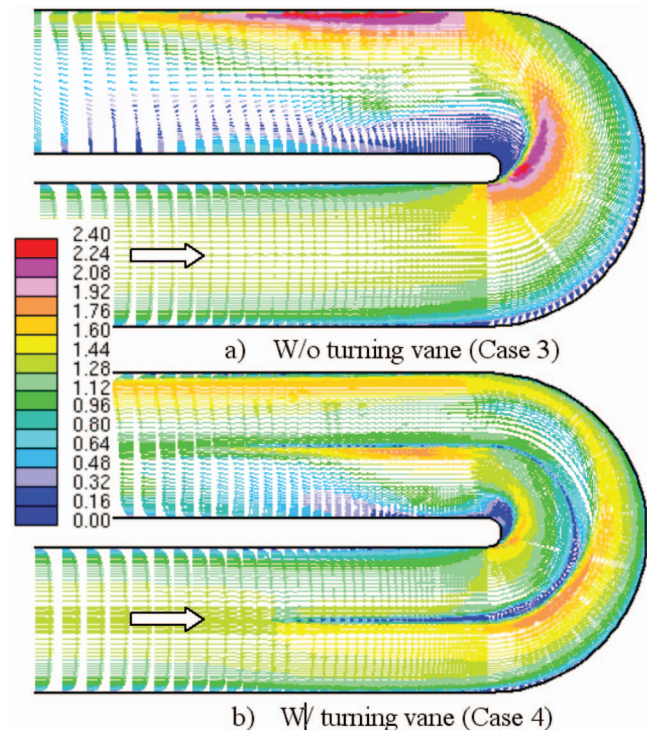
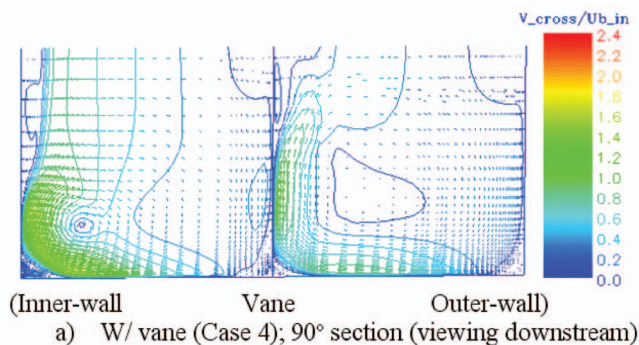
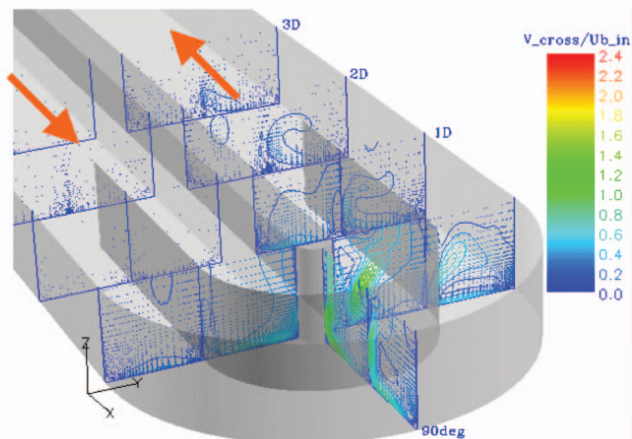


Fig. 19 Velocity contour ( $V_m/U_b$ ) on symmetry section of round-corner duct ( $R_i=0.1D$ ,  $R_o=1.1D$ ): without and with vane



a) W/ vane (Case 4); 90° section (viewing downstream)



b) W/ vane (sections up/down-stream and inside bend)

Fig. 20 Secondary-flow vectors on sections in Case 4

coefficients are mass-averaged values on the sections. Compared with Case 1, Case 3 shows weaker secondary flow at  $\theta=90$  deg (12% lower SKE) and downstream. The vane in Case 2 leads to a large reduction in SKE (38% lower at  $\theta=90$  deg) from Case 1. With the vane and uniform cross section area, Case 4 shows a drastic 73% reduction in SKE at 90 deg section from Case 1 and much weaker secondary flow downstream.

The pressure distributions along the inner- and outer-wall centerlines for Cases 3 and 4 are shown in Fig. 22. The absence of corner flow separations removes the kinks from the outer-wall  $C_p$  curve. Again, the flat portion of inner wall  $C_p$  curve ( $\sim -4.6$ ) reflects the extensive separation off the divider tip, Fig. 19(a)). The vane leads to a substantial reduction in the radial pressure gradient. The combination of vane and uniform cross section is seen to produce much better pressure recovery downstream of the bend.

A comparison of Fig. 22 with Fig. 18 shows that the rounding

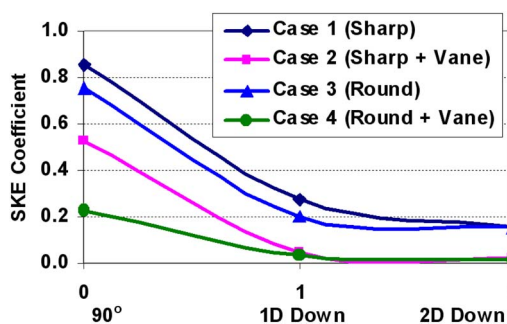


Fig. 21 Decay of secondary-flow kinetic energy through the  $U$ -ducts (three sections: 90 deg, 1D and 2D downstream)

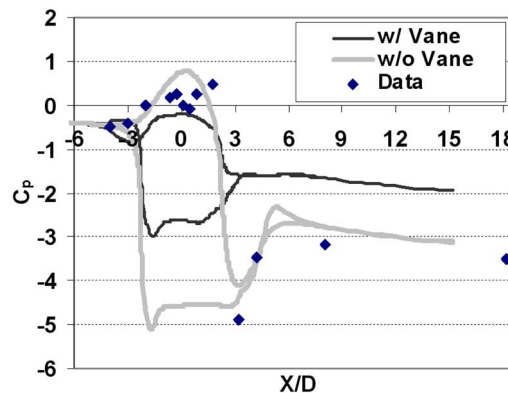


Fig. 22 Pressure on the centerlines of inner and outer walls (Cases 3 and 4): predictions versus data (Case 1; outer wall)

of the outer wall (Case 3) has resulted in 5% lower loss. It also helps the vane achieve a larger reduction of pressure loss (37%, Case 4 over Case 3 versus 22% for Case 2 over Case 1). The largest improvement is achieved in Case 4 with both the vane and uniform cross section area, due to its smaller separation (Fig. 19(b)) and weaker secondary flows (Fig. 20). Compared with the baseline Case 1, the predicted pressure loss of Case 4 is 41% lower. It is encouraging to see such an improvement can be obtained using the insight from CFD results and the guidance from flow physics.

#### 4 Conclusions

Turbulence modeling is critical for predicting pressure loss through 2D  $U$ -duct flows with large curvature effects. The  $k-\epsilon$  model severely underpredicts the loss, mainly due to its underprediction of separation and curvature effects. The V2F and SST models have shown significantly better predictions than the  $k-\epsilon$  model. The Reynolds stress model overall provides the closest agreement with the data, but with some deficiency for flow separation and re-attachment.

The current simulations have demonstrated that a proper guide vane can greatly improve the flow distribution through the 2D  $U$ -bend. Each one of the three idealized vanes is capable of avoiding the downstream flow separation and achieving more than 50% reduction in pressure loss.

The V2F prediction of the overall pressure loss in the 3D  $U$ -duct flow, with sharp 180 deg turning as in typical blade cooling passages, is in close agreement with the data. The midchannel vane is shown to be very effective for flow improvement. It has significantly reduced the flow separation off the divider, the growth of secondary-flow vortices, and the overall pressure loss.

Additional reduction in secondary-flow loss has been achieved by modifying the outer-wall shape. The combined vane and uniform cross-section area has led to much weaker secondary-flow vortices and smaller separation, resulting in a substantial reduction in pressure loss.

The present study indicates that the RANS CFD technique with advanced turbulence models, while having limited accuracy of local properties inside separation, can be used effectively in the design environment for optimizing  $U$ -bends and guide vanes in the turbine cooling passage.

#### Acknowledgment

We would like to thank Solar Turbines Inc. for permission to publish this work.

#### Nomenclature

$$C_p = \text{pressure coefficient, } (P - P_1)/0.5\rho U_b^2$$



$C_f$  = skin friction coefficient,  $\tau_w/0.5\rho U_b^2$  ( $\tau_w$  = wall shear stress)  
 $D$  = hydraulic diameter of 3D duct  
 $H$  = Height of 2D U-duct (Fig. 1)  
 $k$  = turbulent kinetic energy  
 $P$  = static pressure on surface  
 $R$  = wall curvature radius  
 $R_i/R_o$  = inner-/outer-wall radius  
 $Re$  = Reynolds number based on  $D$  or  $H$  and  $U_b$   
 $S$  = distance from bend entrance along 2D duct centerline ( $S=0$  at entrance,  $\theta=0$  deg;  $S=3.1 H$  at  $\theta=180$  deg)  
SKE = secondary-flow kinetic energy coefficient:  $(u_s^2 + v_s^2)/U_b^2$   
 $Tu$  = turbulence intensity/level,  $Tu = \sqrt{2/3k}/U_b$   
 $U$  = longitudinal mean-flow velocity  
 $U_b$  = bulk velocity of mean-flow at inlet  
 $V_m/V_{cross}$  = total/secondary-flow velocity magnitude  
 $u_s, v_s$  = secondary-flow velocity components  
 $W$  = divider wall thickness  
 $x$  = longitudinal coordinate for 2D duct ( $x < 0$  upstream  $x > 0$  downstream of bend) coordinate along outer-wall centerline of 3D duct ( $x=0.0$  at  $\theta=90$  deg)  
 $y$  = radial coordinate (measured from inner wall)  
 $y^+$  = nondimensional distance from wall  
 $\delta$  = shear/boundary layer thickness  
 $\varepsilon$  = dissipation rate of turbulent energy  
 $\theta$  = angle into bend measured from bend entrance  
 $\mu_t$  = turbulent eddy viscosity  
 $\rho$  = density

## Subscript

1, 2 = duct inlet, exit condition

## References

- [1] Lakshminarayana, B., 1996, *Fluid Dynamics and Heat Transfer of Turbomachinery*, Wiley, New York.
- [2] Han, J. C., Dutta, S., and Ekkad, S. V., 2000, *Gas Turbine Heat Transfer and Cooling Technology*, Taylor & Francis, New York.
- [3] Dunn, M. G., 2001, "Convective Heat Transfer and Aerodynamics in Axial Flow Turbines," *ASME J. Turbomach.*, **123**, pp. 637–686.
- [4] Shih, T. I.-P., and Chyu, M. K., 2006, "Special Section: Turbine Science and Technology," *J. Propul. Power*, **22**, pp. 225–396.
- [5] Bradshaw, P., 1973, "Effects of Streamline Curvature on Turbulent Flow," *AGARDograph No. 169*.
- [6] Metzger, D. E., Plevich, C. W., and Fan, C. S., 1984, "Pressure Loss Through Sharp 180 deg Turns in Smooth Rectangular Channels," *ASME J. Eng. Gas Turbines Power*, **106**, pp. 677–681.
- [7] Han, J. C., Chandra, P. R., and Lau, S. C., 1988, "Local Heat/Mass Transfer Distributions Around Sharp 180 deg Turns in Two-Pass Smooth and Rib-Roughened Channels," *ASME J. Heat Transfer*, **110**, pp. 91–98.
- [8] Wagner, J. H., Johnson, B. V., and Hajek, T., 1991, "Heat Transfer in Rotating Passages With Smooth Walls and Radial Outward Flow," *ASME J. Turbomach.*, **113**, pp. 42–51.
- [9] Iacovides, H., Kounadis, D., Launder, B. E., and Xu, Z., 2006, "Experimental Study of the Thermal Development in a Rotating Square-Ended U-Bend," *ASME Paper No. GT2006-90846*.
- [10] Liou, T.-M., Hwang, Y.-S., and Chen, M.-Y., 2005, "Characteristics of Pressure, Flow, and Heat Transfer in Rotating Internal Cooling Passages With Attached-Detached Ribs," *ASME Paper No. GT2005-68661*.
- [11] Zhou, F., and Acharya, S., 2006, "Heat Transfer at High Rotation Numbers in a Two-Pass 4:1 Aspect Ratio Rectangular Channel With 45-deg Skewed Ribs," *ASME Paper No. GT2006-90391*.
- [12] Han, J.-C., and Chen, H.-C., 2006, "Turbine Blade Internal Cooling Passages With Rib Turbulators," *J. Propul. Power*, **22**(2), pp. 226–248.
- [13] Shih, T. I.-P., and Sultanian, B. K., 2001, "Computation of Internal and Film Cooling," *Gas Turbine Heat Transfer*, B. Sundén and M. Faghri, eds., WIT, Ashurst, Southampton.
- [14] Iacovides, H., Launder, B. E., and Li, H., 1996, "The Computation of Flow Development Through Stationary and Rotating U-Ducts of Strong Curvature," *Int. J. Heat Fluid Flow*, **17**, pp. 22–33.
- [15] Rigby, D. L., Ameri, A. A., and Steinthorsson, E., 1996, "Internal Passage Heat Transfer Prediction Using Multi-Block Grids and a  $k-\omega$  Turbulence Model," *ASME Paper No. 96-GT-188*.
- [16] Bonhoff, B., Tomm, U., Johnson, B. V., and Jennions, I., 1997, "Heat Transfer Predictions for Rotating U-Shaped Coolant Channels With Skewed Ribs and With Smooth Walls," *ASME Paper No. 97-GT-162*.
- [17] Shih, T. I.-P., Lin, Y.-L., Stephens, M. A., Chyu, M. K., and Civinskis, K. C., 1998, "Flow and Heat Transfer in a Ribbed U-Duct Under Typical Engine Conditions," *ASME Paper No. 98-GT-213*.
- [18] Rumsey, C. L., Gatski, T. B., and Morrison, J., 2000, "Turbulence Model Predictions of Strongly Curved Flow in a U-Duct," *AIAA J.*, **38**(8), pp. 1394–1402.
- [19] Al-Qahtani, M. S., Jang, Y. J., Chen, H. C., and Han, J. C., 2002, "Prediction of Flow and Heat Transfer in Rotating Two-Pass Rectangular Channels With 45-Degree Rib Turbulators," *ASME J. Turbomach.*, **124**, pp. 242–250.
- [20] Su, G., Chen, H. C., Han, J. C., and Heidmann, J. D., 2004, "Computation of Flow and Heat Transfer in Two-Pass Rotating Rectangular Channels With 45-deg Angled Ribs by Reynolds Stress Turbulence Model," *ASME Paper No. GT2004-53662*.
- [21] Sleiti, A. K., and Kapat, J. S., 2004, "Fluid Flow and Heat Transfer in Rotating Curved Duct at High Rotation and Density Ratios," *ASME Paper No. GT2004-53028*.
- [22] Luo, J., and Lakshminarayana, B., 1997, "Prediction of Strongly Curved Turbulent Duct Flows With Reynolds Stress Model," *AIAA J.*, **35**(1), pp. 91–98.
- [23] Luo, J., and Lakshminarayana, B., 1997, "Analysis of Streamline Curvature Effects on Wall-Bounded Turbulent Flows," *AIAA J.*, **35**(8), pp. 1273–1279.
- [24] Amano, R. S., Song, B., and Reza, M. S., 2005, "A Study on Flow and Heat Transfer in Strongly Curved U-Bend," *ASME Paper No. GT2005-68005*.
- [25] Sewall, E. A., and Tafti, D. K., 2005, "Large Eddy Simulation of Flow and Heat Transfer in the 180° Bend Region of a Stationary Ribbed Gas Turbine Internal Cooling Duct," *ASME Paper No. GT2005-68518*.
- [26] Durbin, P. A., 1991, "Near-Wall Turbulence Closure Modeling Without Damping Functions," *Theor. Comput. Fluid Dyn.*, **3**, pp. 1–13.
- [27] Medic, G., and Durbin, P. A., 2002, "Toward Improved Prediction of Heat Transfer on Turbine Blades," *ASME J. Turbomach.*, **124**, pp. 187–192.
- [28] Ibrahim, M., Kochuparambil, B. J., Ekkad, S. V., and Simon, T. W., 2005, "CFD for Jet Impingement Heat Transfer With Single Jets and Arrays," *ASME Paper No. GT2005-68341*.
- [29] Luo, J., and Razinsky, E. H., 2007, "Conjugate Heat Transfer Analysis of a Cooled Turbine Vane With the V2F Turbulence Model," *ASME J. Turbomach.*, **129**, pp. 773–781, Paper No. GT2006-91109.
- [30] STAR-CD: Methodology, 2005, CD-adapco Group, New York.
- [31] Rao, D. V. R., Babu, C. S., and Prabhu, S. V., 2004, "Effect of Turn Region Treatments on the Pressure Loss Distribution in a Smooth Square Channel With a Sharp 180° Bend," *Int. J. Rotating Mach.*, **10**, pp. 459–468.
- [32] Monson, D. J., Seegmiller, H. L., McConnaughey, P. K., and Chen, Y. S., 1990, "Comparison of Experiment With Calculations Using Curvature-Corrected Zero and Two Equation Turbulence Models for a 2-D U-Duct," *AIAA Paper No. 90-1484*.
- [33] Spivey, S. K., 2005, "Numerical Analysis of Geometric Effects on Pressure Drop in 180° Turning Channels," *Solar Turbines Internal Report*.

# Forced Convection Heat Transfer in Channels With Rib Turbulators Inclined at 45 deg

**Giovanni Tanda**  
Full Professor

**Roberto Abram**  
Ph.D. student

DIPTM/TEC,  
University of Genova,  
via all'Opera Pia 15a,  
I-16145 Genova, Italy

*Local and average Nusselt numbers and friction factors are presented for rectangular channels with an aspect ratio of 5 and angled rib turbulators inclined at 45 deg with parallel orientations on one and two surfaces of the channel. The convective fluid was air, and the Reynolds number varied from 9000 to 35,500. The ratio of rib height to hydraulic diameter was 0.09, with the rib pitch-to-height ratio equal to 13.33 or 6.66. Experiments were based on the use of heating foils (for the attainment of uniform heat flux condition) and of the steady-state liquid crystal thermography (for the identification of isotherm lines and the reconstruction of local heat transfer coefficient). Local results showed quasiperiodic profiles of Nusselt number in the streamwise direction, whose features were strongly affected by the value of rib pitch and by the spanwise coordinate. For all the investigated geometries a heat transfer augmentation, relative to the fully developed smooth channel, was found; when inclined rib turbulators were placed on two opposite surfaces of the channel, the full-surface Nusselt number was higher (by 10–19%) than that for the one-ribbed wall channel, but pressure drop penalties also increased by a factor of about 3. For both the one- and two-ribbed wall channels, the best heat transfer performance for a constant pumping power, in the explored range of Reynolds number, was generally achieved by the larger rib pitch-to-height ratio (=13.33).*

[DOI: 10.1115/1.2987241]

## 1 Introduction

Modern high-performance gas turbine engines operate at high entry gas temperature, well above the allowable metal temperature. Therefore, highly efficient cooling technologies (film cooling, impingement cooling, and internal cooling) are required for vanes and blades of advanced gas turbines. Internal cooling is achieved by passing the coolant through passages inside the blades. The specific technology has developed from simple smooth cooling passages to very complex geometries, involving a great number of different circuit designs and flow path surfaces. Rib turbulators, periodically deployed along the main direction of the flow, were one of the first improvements of blade internal cooling.

Many parameters affect the performance of rib-roughened channels: the shape and dimensions of the channel (including constant and variable cross section channels and multiple sharp turns), the rib characteristics (including shape, size, location, and thermal conductivity), the convective flow characteristics (through the Reynolds and Prandtl numbers), and the rotation of the blade (through the rotation number and the wall-to-coolant density ratio). Among these parameters, the role played by the rib installation has often been recognized as the most important. Consequently, a considerable amount of literature work has been devoted in evaluating heat transfer and friction characteristics of stationary straight channels with various forms of turbulators.

First studies of heat transfer and friction in rib-roughened passages (see, e.g., Refs. [1–6]) were addressed to the gas cooling technology of nuclear reactors and, from the 1980s, specifically to the turbine blade internal cooling design. Typical investigated geometries consisted of annular or rectangular channels with continuous, regularly spaced, transverse ribs on one or two opposite sides, with air as the working fluid. The most important parameters were found to be the rib pitch-to-height ratio  $p/e$ , the rib height-to-hydraulic diameter ratio  $e/D$ , the aspect ratio (AR) of

the rectangular channel (defined as the ratio between the width  $W$  of the ribbed side and the channel height  $H$ ), and the Reynolds number  $Re$ . The ribs were typically square in cross section, with height  $e$  from 5% to 10% of the channel hydraulic diameter  $D$ . These studies showed that there is an optimum rib pitch-to-height ratio  $p/e$  that maximizes the heat transfer coefficient (and unfortunately the pressure drop). For too small rib pitch-to-height ratios the flow that separates after each rib does not reattach in the inter-rib region where a weak recirculating flow, resulting in low heat transfer conditions, occurs. For too large rib spacings the reattachment point at the wall is reached and a boundary layer begins to grow before the succeeding rib is encountered, reducing the heat transfer. At the optimum value  $p/e$  the flow does reattach close to the next rib: This value was found to be in the 6–15 range for annular passages ribbed only on the inner side [1] and about 10 for rectangular channels ribbed on two opposite sides [4,6]. The corresponding average Nusselt number of the rib-roughened passages, with the unribbed channel as a reference under the same mass flow rate constraint, is generally two to three times higher with about 3- to 18-fold pressure drop penalty.

The inclination of ribs can lead to superior heat transfer performance because of the secondary flow induced by the rib angle. This secondary flow has the form of two counter-rotating vortices, aligned with the inclined ribs, which carry cold fluid from the central core region toward the ribbed walls. These cells, interacting with the main flow, affect the flow reattachment and recirculation between ribs and interrupt boundary layer growth downstream of the reattachment regions. Early studies of heat transfer performance of square/rectangular channels with angled ribs [4,7–12] drew the guidelines for the appropriate thermal design of a channel with angled rib turbulators. In square channels (AR = 1) ribbed on two opposite sides and smooth on the other sides, with  $p/e=10-20$  and  $e/D=0.063$ , the highest Nu, accompanied by the highest  $f$ , occurred at a rib angle-of-attack  $\alpha$  (relative to the main flow direction) between 60 deg and 75 deg, whereas the best performance for a constant pumping power occurred at an angle-of-attack between 30 deg and 45 deg [7,10]. For rectangular chan-

Manuscript received September 13, 2007; final manuscript received July 25, 2008; published January 29, 2009. Review conducted by Je-Chin Han.

nels ( $p/e=10-20$  and  $e/D=0.047-0.102$ ) with an AR larger than 2 (ribbed on the wider sides), it was found that angling the ribs has a smaller impact on heat transfer performance, with lower pressure drop but similar (for  $\alpha=75-45$  deg) or lower ( $\alpha=30-20$  deg) heat transfer coefficient as compared with transverse ribs [4,8,11]. Conversely, the rib angle effect is more important for the narrow aspect ratio channels ( $AR=\frac{1}{2}$  and  $\frac{1}{4}$ ), with similar or slightly higher pressure drop as compared with transverse ribs but significantly higher heat transfer coefficients [9,11]. Detailed local heat/mass transfer distributions for square channels with angled ribs ( $\alpha=60$  deg,  $p/e=10$ , and  $e/D=0.0625$ ) showed remarkable spanwise variations of the average heat/mass transfer coefficient due to the interaction of oblique secondary flows with the main flow over the ribbed wall [12]; moreover, the average heat/mass transfer coefficient on the ribs (when thermally active) turned out to be higher than that on the exposed surfaces between ribs.

Since the 45 deg orientation of rib turbulators (relative to the main flow direction) appears to be the most common in practice today, the majority of recent research papers are focused (mainly or only) on this geometry [13-36]. Straight, stationary, ribbed channels are still extensively studied [14,16-18,20,22,26,28,29,31,34], while Refs. [19,21,25,27,30,32] addressed the effect of 45 deg angled rib turbulators on heat transfer in straight rotating channels and Refs. [13,15,23,24,33,35,36] dealt with heat transfer in multipass channels with and without rotation. Some of these studies provided further insight into the flow features by means of detailed velocity measurements and flow visualizations with nonintrusive tools [18,22,28] as well as numerical simulations with different turbulence models [21,23,27,28,34].

Despite the large mass of studies dealing with channels with 45 deg angled ribs, some issues still remain unresolved. For instance, whereas the ideal rib pitch-to-height ratio  $p/e$  for channels with transverse ribs is approximately equal to 10, irrespective of the value of the channel AR [35], angling the ribs (by 45 deg) gives the best thermal performance again at  $p/e=10$  for  $AR=1$  [17] (only heat transfer from ribs is considered). As AR is reduced, the ideal  $p/e$  is still equal to 10 if the performance comparison with the smooth channel is based on the total heat transfer area; conversely, the optimum  $p/e$  is lowered to 3 and 2.5 (for  $AR=0.5$  and 0.25, respectively) when the comparison is based on the projected area [35,36] (heat transfer from ribs and inter-rib regions). These studies also indicated that the optimum rib spacing is very sensitive to other parameters, such as the rib height-to-hydraulic diameter ratio  $e/D$  and the thermal conductivity of ribs (i.e., if the ribs exchange heat with convective fluid or not). Seemingly, no systematic studies on the effect of the rib spacing on heat transfer for AR values larger than 1 are available in literature. A further less investigated aspect concerns the effect of the number of ribbed walls on heat transfer and friction characteristics in a channel. Most literature papers consider square or rectangular channels with ribs on two opposite walls, the other walls remaining smooth. Chandra et al. [37,38] found that both the heat transfer coefficient and the friction factor increase with an increasing number of ribbed walls, but the relative increase in heat transfer is lower than the relative increase in friction factor. For instance, for a square channel (with transverse ribs,  $p/e=8$  and  $e/D=0.0625$ ) at  $Re=30,000$ , two-ribbed walls give a heat transfer increase on the ribbed wall of about 6%, which corresponds to a channel-averaged heat transfer increase of about 26% over the one-ribbed wall (1RW) case, whereas the friction factor increases by 72%. Similar considerations apply to rectangular channels with  $AR=2$  and same rib arrangement, except for the case of the channel with one-ribbed wall (ribs on the wider side), which performs better than the two-ribbed wall (2RW) channel (with ribs on the short sides). The above results seem to suggest that the heat transfer

performance of one-ribbed wall channels (per unit pumping power) could be potentially similar or superior to the two-ribbed wall channels (with less manufacturing efforts).

Another important issue in the experimental heat transfer investigation of ribbed channels is the adopted measuring technique. A large number of investigations have been performed by the standard heater plates/foils and thermocouple technique [4,6-11,13,15,17,22,24,25,32-38] or the naphthalene sublimation technique [5,12,19,20,30]. The former provides accurate but discrete or regionally averaged results; the latter requires special effort for the test section preparation and the evaluation of the local amount of naphthalene leaving the surface.

In general, detailed maps of the local heat transfer coefficient in channels with ribs/turbulators can be obtained by using optical techniques, such as the infrared thermographic technique [29,31,39] and the liquid crystal (LC) technique [14,16,26,28,40-44]. In particular, LC techniques, more economical and affordable than the infrared thermal imaging method, can be classified into two categories: the steady method and the transient method. The steady LC method allows the entire surface to be mapped from one LC image using a color processing system. To overcome the problem of limited color play range, the heat flux into the surface can be adjusted so as to move the color band to different locations and thus progressively map the heat transfer coefficient over the entire test section. The transient LC method is based on the fact that when the test surface of a uniform initial temperature is suddenly exposed to a uniformly heated or cooled flow, the magnitudes of the time-varying surface temperature is governed by transient heat conduction penetrating into a semi-infinite solid (see, for instance, Refs. [16,40]).

In this paper, local and average heat transfer coefficients in a rib-roughened rectangular channel ( $AR=5$  and hydraulic diameter  $D=0.033$  m) are presented. Configurations include sequences of continuous 45 deg angled ribs having square cross sections (rib height  $e=3$  mm and  $e/D=0.09$ ). Ribs were regularly spaced, first over one side of the channel (the wider one), heated at uniform heat flux (the other sides remaining smooth and unheated) and second over two sides of the channel, namely, the heated side and the opposite one. In the latter configuration, the ribs on the opposite walls were arranged in-line. Two values of the rib pitch  $p$  were considered ( $p=40$  mm and 20 mm), so as to yield two values of the rib pitch-to-height ( $p/e=13.33$  and 6.66), the Reynolds number  $Re$  ranging from 9000 to 35,500. Ribs, made of balsa wood, were considered to be nearly adiabatic for the thermal boundary condition; therefore attention was focused on local and average heat transfer coefficients on the inter-rib regions of the heated plate. The study was performed by using the steady-state liquid crystal technique.

## 2 Experimental Apparatus and Procedure

**2.1 Experimental Setup.** The description of the experimental apparatus is facilitated by reference to Fig. 1. The main components are the wind tunnel, the test section, the heating arrangement, and the instrumentation.

An open-circuit suction-type wind tunnel was used for this study. Air, drawn at room temperature, passed through a filter and entered a rectangular channel (width  $W=0.1$  m, height  $H=0.02$  m,  $AR=5$ , and hydraulic diameter  $D=0.033$  m) in which the test section was fitted. The rectangular channel consisted of a hydrodynamic development section, the test section, and the exit section. This duct was followed by a long circular pipe, which contained a control valve and a Venturi flowmeter and terminated at the blower inlet. The air discharged from the blower was ducted out of the laboratory room.

The test section was a rectangular channel as wide and high as the entry and exit sections and delimited by a thin heated plate (width  $W=0.1$  m and length  $L=0.28$  m) and lateral and frontal unheated Plexiglas walls. The plate was made of 0.5 mm thick



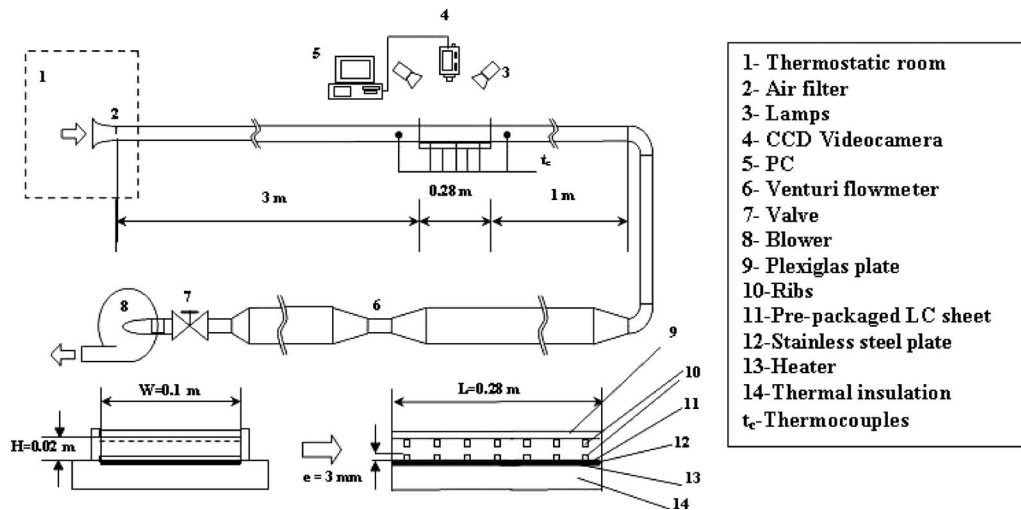


Fig. 1 Schematic layout of the experimental setup and test section

stainless steel to which a plane heater had been attached to provide a controllable uniform heat flux. A thin LC sheet was applied on the side opposite to the heater to measure local wall temperature. The side walls of the test section were covered with thermal insulation layers in order to convey as much as possible the electric power dissipated by the heater to the convective air flow. Power was supplied by an adjustable dc source and measured by a voltmeter and an amperometer. Fine-gauge thermocouples were placed inside the rectangular channel directly exposed to the airflow and in several places inside the channel wall material. These sensors were used to measure the air temperature at the test section inlet, estimate conduction heat losses to the surroundings, and control the attainment of the steady-state conditions. Pressure taps, connected to a common alcohol manometer, were located at the inlet and outlet of the test section in the streamwise direction. A Venturi flowmeter was used for the measurement of the mass flow rate.

Thermosensitive cholesteric liquid crystals were used to measure temperature distributions on the heated surface. The prepackaged LC sheet (0.15 mm thick) consisted of a thermochromic liquid crystal layer on a black background applied onto a Mylar film and backed with a pressure-sensitive adhesive. The color distribution of the liquid crystals was observed by a charge coupled device (CCD) videocamera through the Plexiglas wall opposite to the heated surface and stored in a PC via an IEEE 1394 interface. Four 100 W lamps were used to illuminate the test section during image storing. The lamps were switched on only for the time strictly required for image acquisition to prevent radiant heating of the test surface.

**2.2 Rib Configurations.** Ribs, made of balsa wood, had a square section (side  $e$  is equal to 3 mm) and a blockage ratio  $e/H=0.15$  ( $e/D=0.09$ ). Owing to their low thermal conductivity, ribs were considered to be virtually adiabatic and their function was to generate turbulence in the airflow in order to increase the inter-rib heat transfer. They were glued at periodic streamwise stations (longitudinal rib pitch  $p=40$  mm or 20 mm, giving rib pitch-to-height values  $p/e$  of 13.33 and 6.66, respectively), as shown in Fig. 2. After preliminary tests conducted for a smooth asymmetrically heated channel, two different test sessions were performed: (i) with 45 deg angled parallel ribs glued only on the heated plate, the opposite adiabatic plate being flat, and (ii) with 45 deg angle, parallel ribs glued symmetrically (in-line) on the heated plate and on the opposite adiabatic plate. Case (i) is referred as the one-ribbed wall channel, while case (ii) is termed the two-ribbed wall channel. For practical reasons (direct visualization of LC colors on the heated plate through the opposite trans-

parent wall) the heating of both the ribbed walls in case (ii) was not feasible. However, on the basis of results presented in Ref. [45], the absence of heating of one of the two facing ribbed walls is expected to affect only slightly the heat transfer coefficients of the heated ribbed wall. For both cases (i) and (ii), the remaining walls are unheated.

**2.3 Calibration of Thermosensitive Liquid Crystals.** The relationship between the color and the temperature of the thermosensitive liquid crystals was found by a calibration experiment. The calibration test was carried out by gradually heating a 5 mm thick aluminum plate (calibration plate) covered by a LC film identical to that used in the experiments. The calibration plate was placed in the test section and equipped with ten fine-gauge type-K thermocouples calibrated to  $\pm 0.1$  K. The thermocouples, housed in small holes drilled in the material at different positions as close to the surface as possible, were used to measure the wall temperature and the degree of surface temperature uniformity. The inlet and outlet passages of the test section were blocked during the calibration test in order to promote isothermal conditions inside the test section. For a given wall temperature, the corresponding color image displayed by the LCs was digitized and processed in order to obtain, pixel by pixel, the hue, saturation, and intensity (HSI) contents from the red, green, and blue (RGB) domain. Among the new parameters (HSI) only hue was retained since it was found to be the only one correlated with the surface temperature [46]. The hue-temperature correlation of calibration data depends not only on the type of LCs but also on the recording angle and on the features of the illumination and of the test section (presence of transparent or reflecting walls). LCs here employed had a red start temperature of 30°C with a bandwidth of 4°C. The hue-temperature correlation was found to be fairly linear and repeatable in the range from 31.5°C to 32.5°C (hue in the 70–140 range): This field of hue was therefore selected for the quantitative

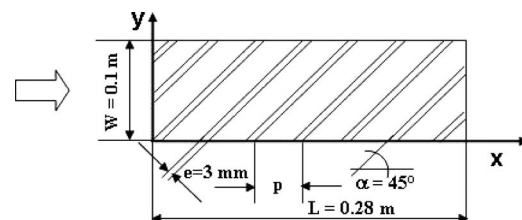


Fig. 2 Geometry of the rib-roughened heated surface

analysis of each LC image. The corresponding calibration line has an uncertainty band (at the 95% confidence interval) of  $\pm 0.2$  K.

**2.4 Operating Procedure and Data Reduction.** After the rib array had been set and the airflow had been adjusted to a prescribed velocity, the dc was supplied to the heater. The surface temperature was maintained within the thermosensitivity region of the liquid crystals by controlling the input power delivered to the heater. Once steady-state conditions were reached, input power, thermocouple readings, and the LC images were recorded. The image of the colored pattern of LCs was taken by the CCD videocamera and converted by the frame grabber to a BMP file for subsequent manipulation by standard graphical packages and by the algorithm for the RGB to HSI pixel-by-pixel conversion. A convolution filter was used to minimize the effects of image defects producing, in isolated pixels, values of hue not correlated with the surface temperature. The final step consisted in applying custom-made software to convert the hue into the surface temperature in order to extract the local heat transfer coefficient according to the following relationship:

$$h = q_{\text{conv}} / (T_{\text{LC}} - T_{\text{air},x}) \quad (1)$$

where  $q_{\text{conv}}$  is the convective heat flux, assumed to be uniformly distributed over the heated plate,  $T_{\text{LC}}$  is the surface temperature detected by the LCs, and  $T_{\text{air},x}$  is the bulk temperature of the air at the  $x$ -position along the streamwise direction.

The convective heat flux was evaluated as follows:

$$q_{\text{conv}} = (Q_{\text{el}} - Q_{\text{rad}} - Q_{\text{dis}} - Q_{\text{ribs}}) / A \quad (2)$$

where  $Q_{\text{el}}$  is the measured input power to the heater,  $Q_{\text{rad}}$  is the calculated radiative heat transfer rate to the surroundings,  $Q_{\text{dis}}$  is the calculated heat transfer rate dissipated through the insulation on the rear face of the heater, and  $A$  is the area of the plate surface exposed to the airflow. The term  $Q_{\text{ribs}}$  takes into account the heat dissipation from the ribs. Even though the ribs were deemed to be adiabatic owing to their low thermal conductance, the conventional one-dimensional fin model was applied to estimate (by an iterative procedure, assuming the heat transfer coefficient along the rib to be equal to the average heat transfer coefficient over the baseplate) the amount of heat transfer rate delivered to the airflow from their sides. The sum of  $Q_{\text{rad}}$ ,  $Q_{\text{dis}}$ , and  $Q_{\text{ribs}}$  was typically equal to 15–25% of  $Q_{\text{el}}$  for  $p/e=6.66$  and to 10–20% for  $p/e=13.33$ .

The bulk temperature of air at the  $x$ -position was calculated by the following equation:

$$T_{\text{air},x} = T_{\text{air},0} + (Q_{\text{el}} - Q_{\text{dis}} - Q_{\text{rad}})(x/L) / (m' c_p) \quad (3)$$

where  $T_{\text{air},0}$  is the air temperature measured at the entrance of the test section (where the flow is isothermal),  $c_p$  is the air specific heat,  $m'$  is the mass flow rate, and  $L$  is the heated surface length.

The convective heat flux  $q_{\text{conv}}$  varied from about 400 W/m<sup>2</sup> to 2500 W/m<sup>2</sup> depending on the test conditions; air temperature increases along the test section were typically within 3 K in the presence of average plate-to-air temperature differences of about 11–15 K.

As previously explained, only points with the hue within the 70–140 range were processed; outside the selected hue interval, no information is gained. Therefore, in those cases, tests were repeated at the same air flow rate and for 7–15 different values of the input power so as to move the color pattern toward the regions not previously monitored and to locally extract the values of the heat transfer coefficient. Another important issue is the resolution of the LC images. When the whole test section is pictured inside a single image, after digitizing and filtering processes the resolution is about 0.87 mm/pixel. This can be enhanced by increasing the magnification of the videocamera (up to 0.31 mm/pixel) but in this case only a reduced region of the test surface is framed, and numerous images therefore have to be stored and linked in order to reconstruct the heat transfer coefficient over the entire test sur-

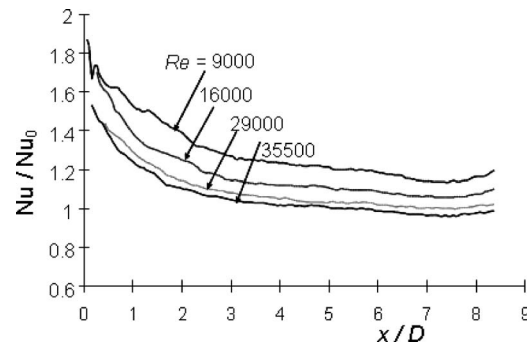


**Fig. 3 Smooth channel normalized Nusselt number**

face. Since this last procedure is lengthy and demanding, the majority of image acquisitions in this study were obtained from full-field pictures.

Experimental data were recast in dimensionless form, introducing the Nusselt number  $Nu$  and the Reynolds number  $Re$  as follows:

$$Nu = hD/k \quad (4)$$

$$Re = GD/\mu \quad (5)$$

where  $G = m' / (WH)$  is the air mass velocity in the channel (air mass flow rate per unit area) and  $D = 2WH / (W + H)$  is the channel hydraulic diameter.

To obtain a dimensionless representation of the pressure drop  $\Delta P$  due to the ribs, the friction factor  $f$ , based on adiabatic conditions (i.e., test without heating), was introduced according to the Fanning definition:

$$f = (\Delta P / L') D \rho / (2G^2) \quad (6)$$

where  $L'$  is the axial distance between the two pressure taps, approximately equal to the test section length  $L$ . Thermal conductivity  $k$ , dynamic viscosity  $\mu$ , and density  $\rho$  of air were evaluated at the film temperature.

Uncertainty analysis was performed by applying the estimation method proposed by Moffat [47]. The uncertainty (at the 95% confidence level) in local  $h$  values was estimated to be  $\pm 6\%$ . This value takes into account the effects of measuring errors in voltage, current, and LC thermographic readings and of thermal conduction, along transverse and longitudinal directions, inside the stainless steel heated plate. The Reynolds number had a calculated uncertainty of  $\pm 4\%$ . Finally, the uncertainty in the friction factor  $f$  was estimated to be  $\pm 8\%$  at the lowest Reynolds numbers and  $\pm 4\%$  at the highest Reynolds numbers.

### 3 Results and Discussion

**3.1 The Smooth Channel.** For the purpose of comparison, preliminary tests for the baseline condition of a smooth channel (without ribs) with asymmetric heating have been performed.

The local Nusselt number  $Nu$  was normalized by the Nusselt number  $Nu_0$  for fully developed turbulent flow in smooth circular tubes given by the well known Dittus–Boelter correlation

$$Nu_0 = 0.023 Re^{0.8} Pr^{0.4} \quad (7)$$

Even though Eq. (7) tends to overestimate the average heat transfer for a channel with an asymmetric heating by 10–20% [48], its assumption is a standard practice in literature regardless of the thermal boundary condition applied to the walls. The test conditions allowed a complete development of the flow field of the fluid entering the test section (about 90 hydraulic diameters) while the test section length (8.4 hydraulic diameter) could not be sufficient to attain the fully developed thermal field, the preceding section of the channel being unheated. Inspection of Fig. 3, where

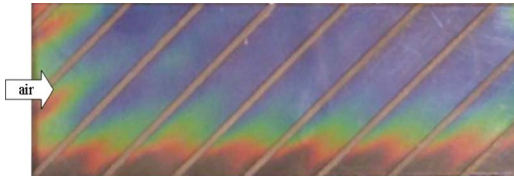


Fig. 4 Typical liquid crystal image for the ribbed heated plate

the distributions of the normalized local Nu number are presented, reveals the entry effects persist up to about five to seven diameters at the highest Re values and probably over the whole test section at the lowest Re values.

### 3.2 The Ribbed Channels

**3.2.1 Local Heat Transfer Coefficient.** The flow pattern generated by the 45 deg angled ribs is typically three dimensional, owing to the interactions of the oblique secondary flows with the main flow over the ribbed wall. This can lead to significant spanwise variations of the local heat transfer coefficient, especially for channels having a low aspect ratio.

A typical liquid crystal image, recorded for the one-ribbed-wall channel, is presented in Fig. 4: The main flow is from the left to the right. The color changes in each inter-rib region as one moves along the direction parallel to the ribs reflect the 3D character of the flow and thermal fields. From the processing of a set of LC images, the map of the heat transfer coefficient on the heated wall is recovered, as shown in Fig. 5, for  $p/e=13.33$  and  $Re=29,000$ . Inspection of the figure shows a higher heat transfer performance in the upstream acute angle region, where the secondary flow brings core air to the wall and low heat transfer coefficients in the downstream, opposite, acute angle corner.

Figures 6 and 7 show the streamwise Nusselt number values. Each plot reports the Nu distributions along the  $x$  direction (normalized by the hydraulic diameter  $D$ ) at four different spanwise coordinates  $y$  (normalized by the channel width  $W$ ). For both the rib pitch-to-height ratios and the one-ribbed and two-ribbed wall channels, Nu distributions are reported for the lowest and highest Re of the explored range.

Generally speaking, a development region is observed from the entrance up to about three to four diameters in the streamwise direction. Beyond the entrance region, the inter-rib Nu numbers exhibit a nearly periodic distribution whose features are strongly related to the rib pitch-to-height ratio and to the spanwise coordinate.

When  $p/e$  is relatively high ( $=13.33$ , Fig. 6), Nu values initially decrease, owing to a recirculating flow region just downstream of the rib. As the main flow reattaches on the wall, a relative maximum is reached; then, the gradual redevelopment of flow is accompanied by a further decrease in Nu values. An abrupt increase is observed immediately upstream of the downstream rib due to the flow recirculation caused by the presence of the obstacle. The effect of the secondary flow induced by rib inclination is respon-

sible for the spanwise variation in Nu with significant reductions (up to about 50%) along the  $y$  coordinate for both the Re values. The extent of this reduction grows with the distance from the inlet section. A further consequence of the secondary flow is the damping of the streamwise Nu variations: As  $y/W$  increases from 0.1 to 0.25, the  $x$ -distributions of the heat transfer coefficient become flatter since the flow reattachment and subsequent boundary layer growth are inhibited; beyond  $y/W=0.25$ , periodic variations of Nu along  $x$  provide similar excursions.

The same considerations apply to the one-ribbed wall and the two-ribbed wall channels; in the latter case the presence of the ribs on both sides is expected to affect more deeply the flow field and, in principle, also the heat transfer characteristic of the heated wall. Inspection of Fig. 6 reveals that, when ribs are glued on two opposite walls, the local heat transfer distributions are qualitatively similar to those shown by the one-ribbed wall channel, but local values are generally higher for any Re and location.

The inter-rib streamwise distributions of Nu for the lower value of  $p/e$  ( $=6.66$ , Fig. 7) are characterized by a minimum value just downstream of each rib, followed by a gradual increase up to the following rib. The presence of a relative Nu maximum in the inter-rib region, denoting the flow reattachment on the wall, is observed only at the spanwise coordinate  $y/W=0.1$ , which is very close to the channel side forming with ribs the upstream acute angles. Elsewhere, secondary flow effects, in conjunction with the relatively short rib pitch  $p$ , do not permit the flow to reattach on the wall. Excursions of Nu along each inter-rib region seemingly increase with Re number, while passing from one to two-ribbed walls increases the local Nu values and their variations along  $x$ , probably due to the higher level of turbulence.

Finally, for all rib configurations, the mean inter-rib Nu values typically increase with  $x$  when the spanwise coordinate  $y/W$  is low, decrease with  $x$  when  $y/W$  is high, and remain constant along the centerline ( $y/W=0.5$ ).

**3.2.2 Regionally and Full-Surface Averaged Heat Transfer Coefficient and Friction Factor.** First, local Nusselt number values were spatially averaged over each wall region between two consecutive ribs (module). The distributions of the per-module mean Nu value along the streamwise coordinate (identified by the module number  $N_x$ ) are presented in Fig. 8 ( $p/e=13.33$ ) and Fig. 9 ( $p/e=6.66$ ). Owing to the specific features of the rib installations, the geometry repeats itself identically from the 3rd to the 6th module for  $p/e=13.33$  and from the 5th to the 13th module for  $p/e=6.66$ . Within these intervals, the per-module mean Nu appears to be unaffected by the streamwise coordinate for any experimental condition, except for channels with  $p/e=6.66$  at medium-high Re, for which Nu exhibits an irregular variation with  $N_x$  from the 9th to the 13th module.

The integration of local Nu values over the whole heat transfer area (the area of the heated wall not covered by the ribs) gives the full-surface Nusselt number that allows a direct comparison of heat transfer performance to be performed. To quantify the degree

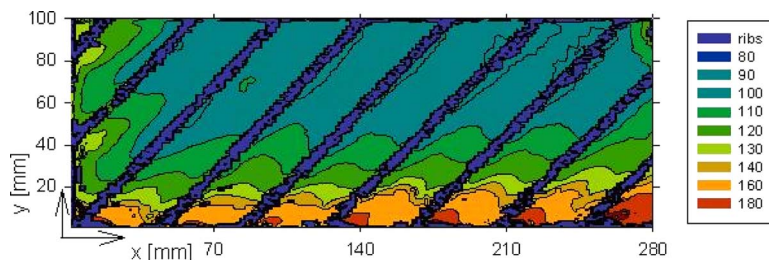


Fig. 5 Local heat transfer coefficient  $h$  ( $W/m^2 K$ ) along the ribbed heated surface for  $p/e=13.33$ ,  $Re=29,000$ , 1RW channel



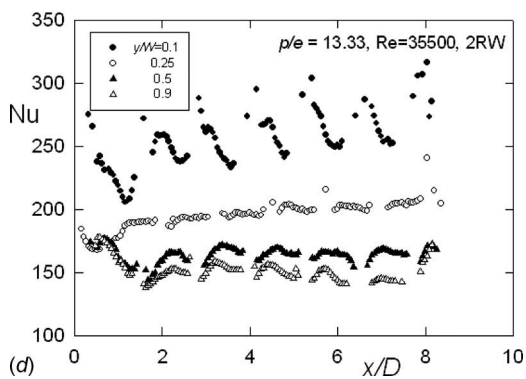
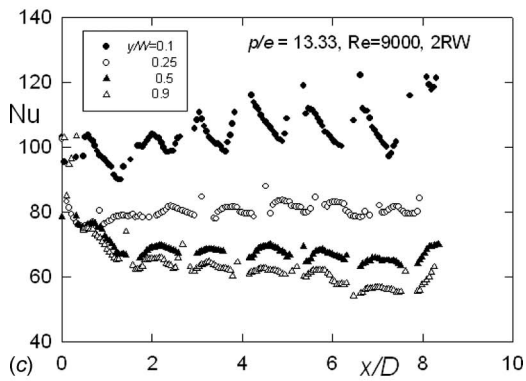
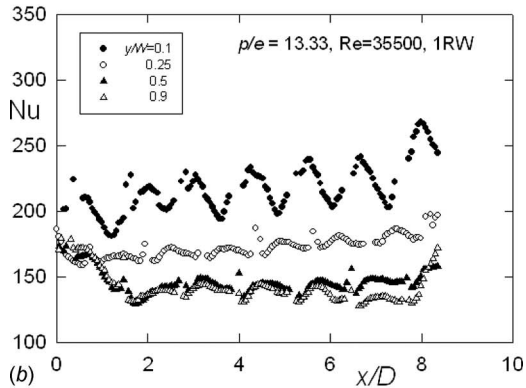
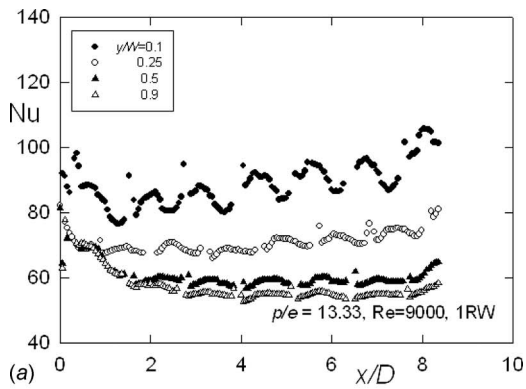


Fig. 6 Streamwise Nusselt number at various spanwise stations for  $p/e=13.33$ . 1RW channel: (a)  $Re=9000$  and (b)  $Re=35,500$ ; 2RW channel: (c)  $Re=9000$  and (d)  $Re=35,500$ .

of heat transfer enhancement relative to the smooth channel, the full-surface Nusselt number was normalized by the Nusselt number  $Nu_0$  given by the Dittus–Boelter correlation (Eq. (7)).

Figure 10 shows the normalized Nusselt number versus the

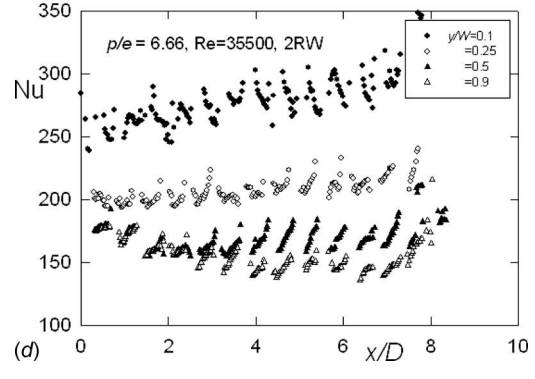
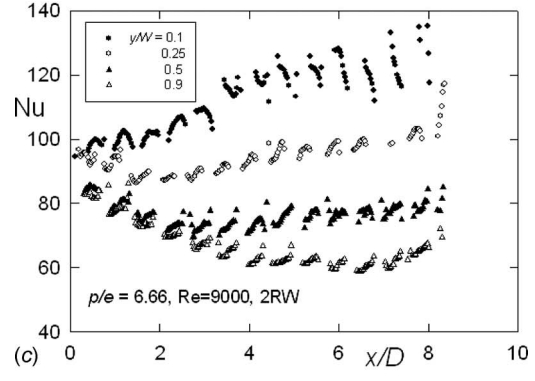
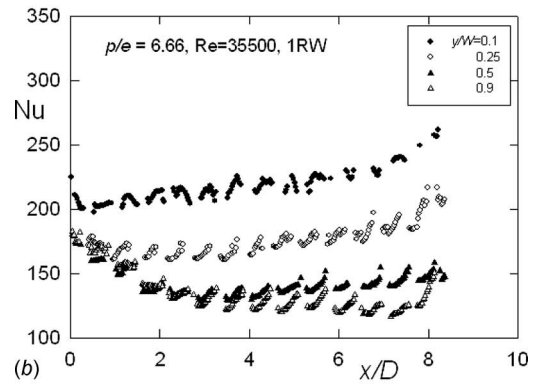
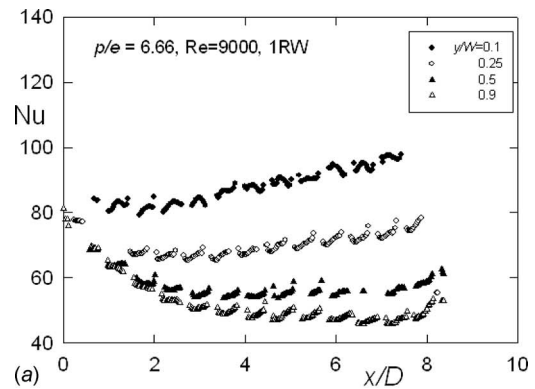


Fig. 7 Streamwise Nusselt number at various spanwise stations for  $p/e=6.66$ . 1RW channel: (a)  $Re=9000$  and (b)  $Re=35,500$ ; 2RW channel: (c)  $Re=9000$  and (d)  $Re=35,500$ .

Reynolds number for all the investigated geometries. The heat transfer augmentation is in the 1.8–2.7 range and decreases with  $Re$ , as typically occurs in rib-roughened channels. When ribs are applied to the heated plate only, the larger rib pitch ( $p/e=13.33$ ) provides slightly higher heat transfer than the smaller rib pitch

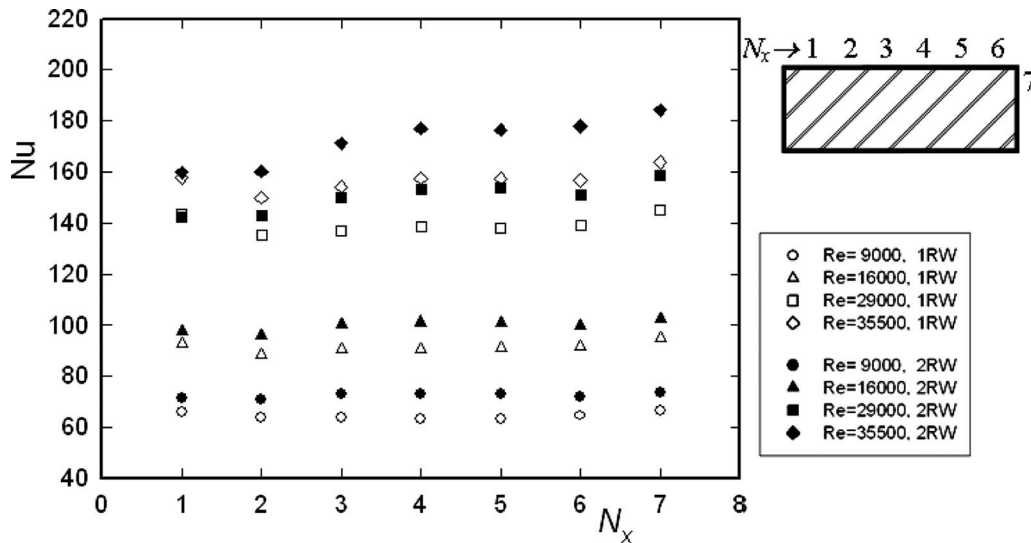


Fig. 8 Per-module Nusselt number for  $p/e=13.33$ . Open symbols: 1RW channel; filled symbols: 2RW channel.

( $p/e=6.66$ ) by +6% on average. The rib adding on the opposite plate increases the turbulence level for both the rib pitch values with enhanced heat transfer coefficient as compared with the one-ribbed wall case (+10% for  $p/e=13.33$  and +19% for  $p/e=6.66$ ). It is interesting to note that the two-ribbed wall channel heat transfer results indicate slightly higher heat transfer coefficients (by 4% on average) for the surface with a smaller rib pitch ( $p/e=6.66$ ) than those for the larger rib pitch surface ( $p/e=13.33$ ). It is conjectured that the secondary flow features are affected both by the rib pitch and the number of ribbed walls; in particular, the optimal rib pitch-to-height ratio, which accommodates the maximum heat transfer, may be larger when only one wall of the channel is ribbed.

Fanning friction factor of the ribbed channels, calculated according to Eq. (6), was normalized by the friction factor  $f_0$  for the fully developed turbulent flow in smooth circular tubes proposed by Blasius:

$$f_0 = 0.046 \text{Re}^{-0.2} \quad (8)$$

As expected, the normalized friction factor, shown in Fig. 11, increases with increasing Reynolds number. For the one-ribbed wall channel, the lower rib pitch gives the higher pressure drop in conjunction with, as observed previously, the lower average heat transfer coefficient; it can be concluded that the ribbed geometry with the lower rib pitch ( $p/e=6.66$ ) performs worse than that with the higher rib pitch ( $p/e=13.33$ ). When ribs are present on two opposite walls, the friction factor ratio  $f/f_0$  is greatly enhanced, becoming about three times higher as compared with the one-ribbed wall channel. For the lower rib pitch geometry ( $p/e=6.66$ ),  $f$  values are from 12 to 14 times the corresponding smooth-channel values. At the higher rib pitch ( $p/e=13.33$ ), the degree of enhancement of the friction factor, relative to the smooth channel, is between 9 and 11. Thus, the higher rib pitch provides a slightly lower heat transfer (about -4%) but with a significant reduction in the pressure drop (about -25%).

Normalized Nusselt number and friction factor results are plotted together in Fig. 12; they correspond to the Re values of

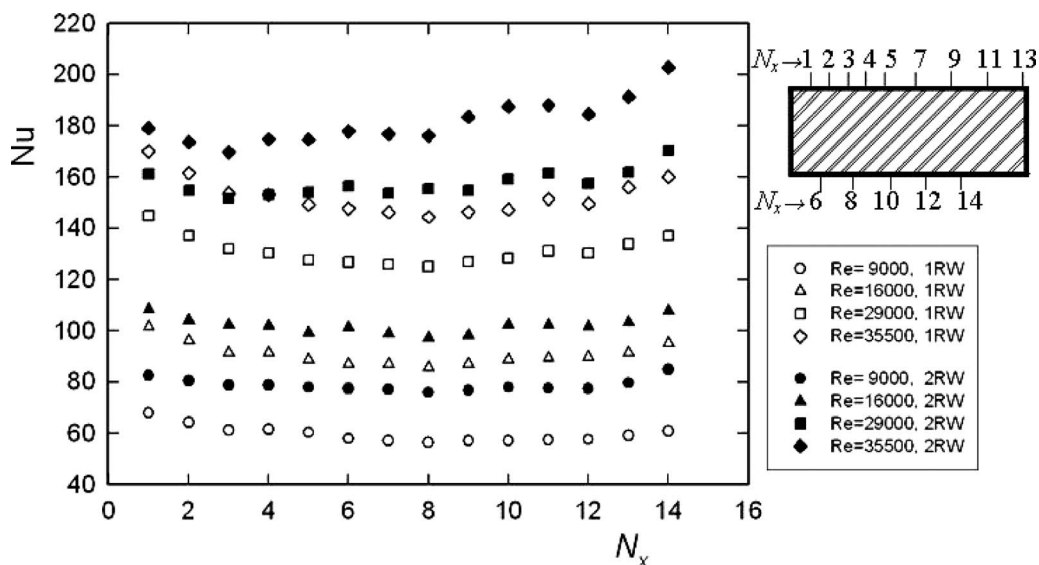


Fig. 9 Per-module Nusselt number for  $p/e=6.66$ . Open symbols: 1RW channel; filled symbols: 2RW channel.

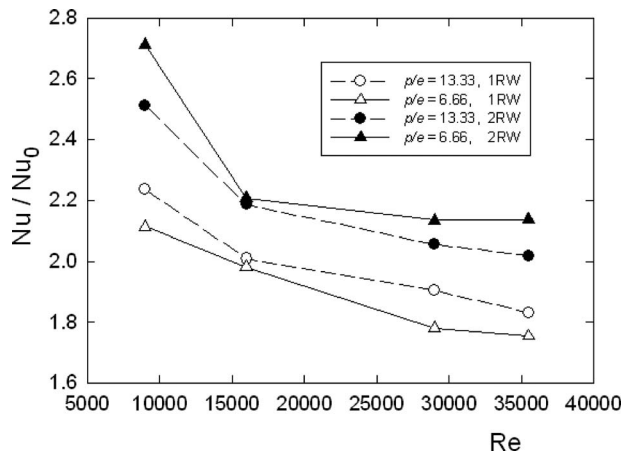


Fig. 10 Normalized full-surface Nusselt number versus the Reynolds number. Open symbols: 1RW channel; filled symbols: 2RW channel.

16,000, 29,000, and 35,500. Data from Park et al. [11] for a two-ribbed wall channel with  $AR=4$ ,  $p/e=10$ ,  $e/D=0.078$ , and  $\alpha=45$  deg, from Chandra et al. [37] for a one-ribbed wall channel with  $AR=2$ ,  $p/e=8$ ,  $e/D=0.0625$ , and  $\alpha=90$  deg, and from Tanda [44] for a one-ribbed wall channel with  $AR=5$ ,  $p/e=13.33$ ,  $e/D=0.09$ , and  $\alpha=90$  deg were added in the graph since the geometric and operating conditions were very similar to those considered here ( $AR=5$ ,  $p/e=6.66$  and  $13.33$ ,  $e/D=0.09$ , and  $\alpha=45$  deg). Experiments reported in Refs. [11,37] were performed in a Re range wider than the present data; therefore, to facilitate the comparison, only reference data obtained for similar Re values were plotted. Inspection of the figure reveals that, for the one-ribbed wall channel, the angled ribs with  $p/e=13.33$  provide slightly lower Nu values than those for the transverse ribs at the same  $p/e$ ,  $AR$ ,  $e/D$ , and similar Re. This heat transfer reduction (about  $-5\%$ , on average) is compensated by the marked friction factor reduction (about  $-30\%$ , on average) obtained by angling the ribs. Data from Ref. [37] show friction factors generally higher than the present data (probably due to the transverse installation of ribs) but lower than those from Ref. [44] (probably due to the reduced aspect ratio of the channel). Conversely, normalized Nu values from Ref. [37] largely exceed the present data and those taken from Ref. [44]: It is worth noting that Chandra et al. [37] include in the full-surface Nu number the contribution of ribs

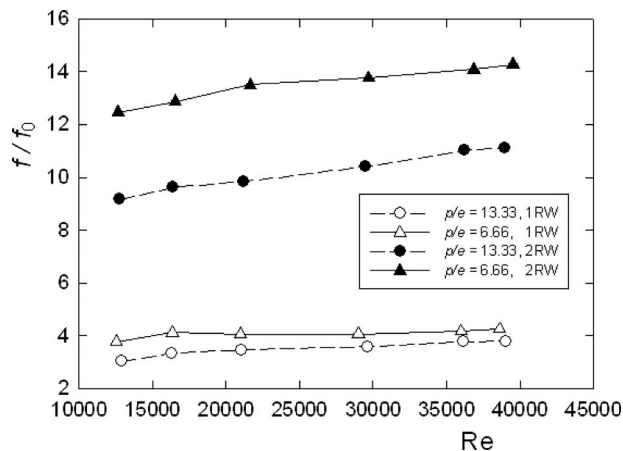


Fig. 11 Normalized friction factor versus the Reynolds number. Open symbols: 1RW channel; filled symbols: 2RW channel.

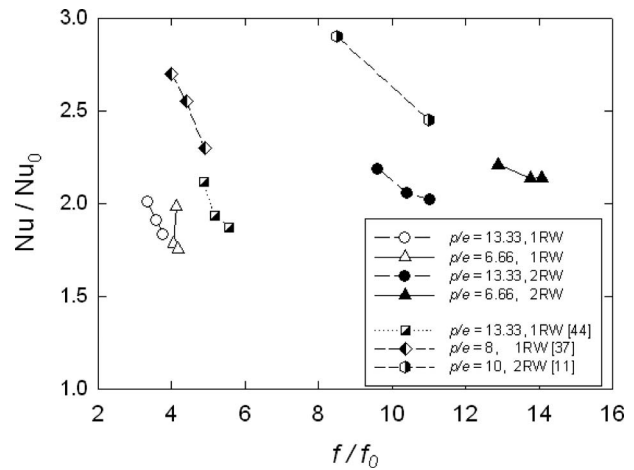


Fig. 12 Normalized full-surface Nusselt number versus the normalized friction factor. Open symbols: 1RW channel; filled symbols: 2RW channel; and semi-filled symbols: literature data from Park et al. [11] (2RW,  $AR=4$ ,  $p/e=10$ ,  $e/D=0.078$ , and  $\alpha=45$  deg), from Chandra et al. [37] (1RW,  $AR=2$ ,  $p/e=8$ ,  $e/D=0.0625$ , and  $\alpha=90$  deg), and from Tanda [44] (1RW,  $AR=5$ ,  $p/e=13.33$ ,  $e/D=0.09$ , and  $\alpha=90$  deg).

(whose heat transfer coefficient is generally higher than that from the inter-rib region, see, for instance, Refs. [12,17,49]), while present results (and those from Ref. [44]) refer only to the exposed surface between ribs. The two-ribbed wall channel with 45 deg angled ribs and  $p/e=13.33$  denotes similar friction factors as those obtained in Ref. [11] with the same rib inclination and very close values of the other parameters; again, the higher normalized Nu values found in Ref. [11] as compared with the present data can probably be ascribed to the contribution of ribs to overall heat transfer.

A criterion to evaluate the performance of the rib-roughened channels is to estimate the quantity  $Nu/Nu_0$  according to the same power required to pump the convective fluid inside the ribbed (enhanced) and the smooth (reference) channels. In order to comply with this constraint, the mass flow rates passing through the enhanced and reference channels cannot be the same; the assumption of constant pumping power leads to

$$f_0 Re_0^3 = f Re^3 \quad (9)$$

where  $Re_0$  is the value of the Reynolds number for the reference channel. If Eq. (8) is used to correlate  $f_0$  and  $Re_0$ , it follows that

$$Re_0 = (21.74f Re^3)^{0.357} \quad (10)$$

with  $Re_0$  representing the value to be used in Eq. (7) to evaluate  $Nu_0$ .

The value of  $Nu/Nu_0$  reported in Fig. 13 (where the abscissa  $Re_0$  was chosen as a convenient reference for all the ribbed channels) can determine whether or not a given geometry is potentially advantageous under the requirement that the pumping power must be the same. Among the one-ribbed wall configurations, 45 deg angled ribs with  $p/e=13.33$  perform better than transverse ribs of same dimensions and pitch (data from Ref. [44]) and than 45 deg angled ribs with  $p/e=6.66$ , with levels of heat transfer enhancement, for the investigated range of Reynolds number between 1.25 and 1.45. The same  $p/e$  ratio (13.33) gives a higher heat transfer performance (relative to the  $p/e=6.66$  geometry) even for the two-ribbed wall channel, with augmentations of Nu number, relative to the smooth channel at the same pumping power, from 1.02 to 1.15. At the highest Reynolds number values, the effect of  $p/e$  on the heat transfer performance becomes poorly discernible.



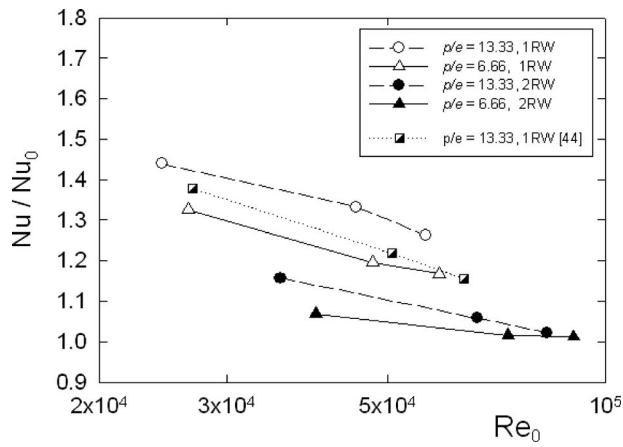


**Fig. 13 Normalized full-surface Nusselt number versus the smooth-channel Reynolds number for fixed pumping powers. Open symbols: 1RW channel; filled symbols: 2RW channel; and semi-filled symbols: literature data from Tanda [44] (1RW, AR=5,  $p/e=13.33$ ,  $e/D=0.09$ , and  $\alpha=90$  deg).**

#### 4 Conclusions

Heat transfer characteristics of rectangular channels (AR=5) with 45 deg angled parallel ribs have been experimentally investigated by means of the steady-state liquid crystal thermography. The parallel ribs have been installed either onto one wall of the channel or, in-line, onto two opposite walls. Based on the results, the following conclusions are drawn.

After a relatively short entrance region, the local Nusselt number attains a nearly periodic distribution along the streamwise direction, with features markedly affected by the rib pitch and the spanwise coordinate. When the rib pitch is relatively high, a relative maximum in each inter-rib region probably occurs at the re-attachment point; for the lower rib pitch, the typical inter-rib Nu values first decrease just downstream of each rib and then increase up to the following rib. Spanwise Nusselt number values decrease along the rib direction (from the acute upstream angle to the acute downstream angle) because of the secondary flow induced by rib inclination.

The per-module mean Nu values appear to be unaffected by the streamwise coordinate for any experimental condition, except for channels with  $p/e=6.66$  at medium-high Re, for which Nu exhibits an irregular variation with  $N_x$  from the 9th to the 13th module.

Heat transfer augmentations, relative to the smooth channel, are in the 1.8–2.7 range and decrease with Re, as typically occurs in rib-roughened channels. The full-surface normalized Nu values are typically higher (by 10–19%) when the channel is ribbed on two opposite walls rather than on one wall only, but friction factor becomes about three times higher. Ribs with  $p/e$  of 13.33 give higher heat transfer coefficients and lower friction factors than those with  $p/e=6.66$  for the one-ribbed wall channel; when ribs are present on two opposite walls, both heat transfer coefficients and friction factors are higher for the lower  $p/e$  value.

Heat transfer performance, relative to a smooth channel with the same pumping power, is generally better for the higher rib pitch-to-height ratio ( $p/e=13.33$ ) regardless of the number of ribbed walls (one or two).

#### Nomenclature

$A$	= heated surface area
AR	= channel aspect ratio, $W/H$
$c_p$	= specific heat (at constant pressure) of air
$D$	= channel hydraulic diameter of the rectangular channel, $2WH/(W+H)$
$e$	= rib height

$f$	= Fanning friction factor $(\Delta P/L')D\rho/(2G^2)$
$f_0$	= Fanning friction factor for the reference (un-ribbed) channel
$k$	= thermal conductivity of air
$G$	= air mass velocity, $m'/(WH)$
$H$	= channel height
$h$	= convective heat transfer coefficient
$L$	= length of the heated surface
$L'$	= distance between the pressure taps
$m'$	= air mass flow rate
Nu	= Nusselt number
$Nu_0$	= Nusselt number for the fully developed flow in the reference (unribbed) channel
$N_x$	= module number
Pr	= Prandtl number
$p$	= rib pitch
$\Delta P$	= pressure drop across the test section
$q_{conv}$	= convective heat flux
$Q_{el}$	= input power to the heater
$Q_{rad}$	= radiation heat transfer rate
$Q_{dis}$	= conduction heat transfer rate
$Q_{ribs}$	= heat transfer rate from ribs
Re	= Reynolds number, $GD/\mu$
$Re_0$	= Reynolds number for the reference channel
$T_{LC}$	= surface temperature (by liquid crystals)
$T_{air,x}$	= air bulk temperature
$T_{air,0}$	= inlet air temperature
$W$	= channel width
$x$	= streamwise coordinate
$y$	= spanwise coordinate

#### Greek Symbols

$\alpha$	= rib angle-of-attack
$\rho$	= density of air
$\mu$	= dynamic viscosity of air

#### References

- [1] Wilkie, D., 1966, "Forced Convection Heat Transfer From Surfaces Roughened by Transverse Ribs," *Proceedings of the Third International Heat Transfer Conference*, Chicago, Vol. 1, pp. 1–19.
- [2] Burggraf, F., 1970, "Experimental Heat Transfer and Pressure Drop With Two-Dimensional Turbulence Promoter Applied to Two Opposite Walls of a Square Tube," *Augmentation of Convective Heat and Mass Transfer*, A. E. Bergles and R. L. Webb, eds., ASME, New York, pp. 70–79.
- [3] Dalle Donne, M., and Meyer, L., 1977, "Turbulent Convective Heat Transfer From Rough Surfaces With Two-Dimensional Rectangular Ribs," *Int. J. Heat Mass Transfer*, **20**, pp. 583–620.
- [4] Han, J. C., Glickmann, L. R., and Rohsenow, W. M., 1978, "An Investigation of Heat Transfer and Friction for Rib-Roughened Surfaces," *Int. J. Heat Mass Transfer*, **21**, pp. 1143–1156.
- [5] Sparrow, E. M., and Tao, W. Q., 1983, "Enhanced Heat Transfer in a Flat Rectangular Duct With Streamwise-Periodic Disturbances at One Principal Wall," *ASME J. Heat Transfer*, **105**, pp. 851–861.
- [6] Han, J. C., 1984, "Heat Transfer and Friction in Channels With Two Opposite Rib-Roughened Walls," *ASME J. Heat Transfer*, **106**, pp. 774–781.
- [7] Han, J. C., Park, J. S., and Lei, C. K., 1985, "Heat Transfer Enhancement in Channels With Turbulence Promoters," *ASME J. Eng. Gas Turbines Power*, **107**, pp. 628–635.
- [8] Han, J. C., and Park, J. S., 1988, "Developing Heat Transfer in Rectangular Channels With Rib Turbulators," *Int. J. Heat Mass Transfer*, **31**, pp. 183–195.
- [9] Han, J. C., Ou, S., Park, J. S., and Lei, C. K., 1989, "Augmented Heat Transfer in Rectangular Channels of Narrow Aspect Ratios With Rib Turbulators," *Int. J. Heat Mass Transfer*, **32**, pp. 1619–1630.
- [10] Han, J. C., Zhang, Y. M., and Lee, C. P., 1991, "Augmented Heat Transfer in Square Channels With Parallel, Crossed, and V-Shaped Angled Ribs," *ASME J. Heat Transfer*, **113**, pp. 590–596.
- [11] Park, J. S., Han, J. C., Huang, Y., Ou, S., and Boyle, R. J., 1992, "Heat Transfer Performance Comparisons of Five Different Rectangular Channels With Parallel Angled Ribs," *Int. J. Heat Mass Transfer*, **35**, pp. 2891–2903.
- [12] Kukeja, R. T., Lau, S. C., and McMillin, R. D., 1993, "Local Heat/Mass Transfer Distribution in a Square Channel With Full and V-Shaped Ribs," *Int. J. Heat Mass Transfer*, **36**, pp. 2013–2020.
- [13] Johnson, B. V., Wagner, J. H., Steuber, G. D., and Yeh, F. C., 1994, "Heat Transfer in Rotating Serpentine Passage With Trips Skewed to the Flow," *ASME J. Turbomach.*, **116**, pp. 113–123.
- [14] Taslim, M. E., Li, T., and Kercher, D. M., 1996, "Experimental Heat Transfer

- and Friction in Channels Roughened With Angled, V-Shaped, and Discrete Ribs on Two Opposite Walls," *ASME J. Turbomach.*, **118**, pp. 20–28.
- [15] Mochizuki, S., Murata, A., and Fukunaga, M., 1997, "Effects of Rib Arrangements on Pressure Drop and Heat Transfer in a Rib-Roughened Channel With a Sharp 180 deg Turn," *ASME J. Turbomach.*, **119**, pp. 610–616.
- [16] Wang, Z., Ireland, P. T., Kohler, S. T., and Chew, J. W., 1998, "Heat Transfer Measurements to a Gas Turbine Cooling Passage With Inclined Ribs," *ASME J. Turbomach.*, **120**, pp. 63–69.
- [17] Taslim, M. E., and Lengkon, A., 1998, "45 deg Staggered Rib Heat Transfer Coefficient Measurements in a Square Channel," *ASME J. Turbomach.*, **120**, pp. 571–580.
- [18] Bonhoff, B., Parneix, S., Leusch, J., Johnson, B. V., Schabacker, J., and Bölc, A., 1999, "Experimental and Numerical Study of Developed Flow and Heat Transfer in Coolant Channels With 45 deg Ribs," *Int. J. Heat Fluid Flow*, **20**, pp. 311–319.
- [19] Park, C. W., Yoon, C., and Lau, S. C., 2000, "Heat (Mass) Transfer in a Diagonally Oriented Rotating Two-Pass Channel With Rib-Roughened Walls," *ASME J. Heat Transfer*, **122**, pp. 208–211.
- [20] Cho, H. H., Wu, S. J., and Kwon, H. J., 2000, "Local Heat/Mass Transfer Measurements in a Rectangular Duct With Discrete Ribs," *ASME J. Turbomach.*, **122**, pp. 579–586.
- [21] Jang, Y. J., Chen, H. C., and Han, J. C., 2001, "Flow and Heat Transfer in a Rotating Square Channel With 45 deg Angled Ribs by Reynolds Stress Turbulence Model," *ASME J. Turbomach.*, **123**, pp. 124–132.
- [22] Kiml, R., Mochizuki, S., and Murata, A., 2001, "Effects of Rib Arrangements on Heat Transfer and Flow Behavior in a Rectangular Rib-Roughened Passage: Application to Cooling of Gas Turbine Blade Trailing Edge," *ASME J. Heat Transfer*, **123**, pp. 675–681.
- [23] Al-Qahtani, M., Jang, Y. J., Chen, H. C., and Han, J. C., 2002, "Prediction of Flow and Heat Transfer in Rotating Two-Pass Rectangular Channels With 45-deg Rib Turbulators," *ASME J. Turbomach.*, **124**, pp. 242–250.
- [24] Azad, G. S., Uddin, M. J., Han, J. C., Moon, H. C., and Glezer, B., 2002, "Heat Transfer in a Two-Pass Rectangular Rotating Channel With 45-deg Angled Rib Turbulators," *ASME J. Turbomach.*, **124**, pp. 251–259.
- [25] Griffith, T. S., Al-Hadhrani, L., and Han, J. C., 2002, "Heat Transfer in Rotating Rectangular Cooling Channels (AR=4) With Angled Ribs," *ASME J. Heat Transfer*, **124**, pp. 617–625.
- [26] Bailey, J., and Bunker, R. S., 2003, "Heat Transfer and Friction in Channels With Very High Blockage 45° Staggered Turbulators," *Proceedings of the ASME Turbo Expo 2003 Power for Land, Sea and Air*, Atlanta, GA, Jun. 16–19.
- [27] Al-Qahtani, M., Chen, H. C., and Han, J. C., 2003, "A Numerical Study of Flow and Heat Transfer in Rotating Rectangular Channels (AR=4) with 45 deg Rib Turbulators by Reynolds Stress Turbulence Model," *ASME J. Heat Transfer*, **125**, pp. 19–26.
- [28] Iacovides, H., Kelemenis, G., and Raisee, M., 2003, "Flow and Heat Transfer in Straight Cooling Passages With Inclined Ribs on Opposite Walls: An Experimental and Computational Study," *Exp. Therm. Fluid Sci.*, **27**, pp. 283–294.
- [29] Ligrani, P. M., and Mahmood, G. I., 2003, "Spatially Resolved Heat Transfer and Friction Factors in a Rectangular Channel With 45-deg Angled Crossed-Rib Turbulators," *ASME J. Turbomach.*, **125**, pp. 575–584.
- [30] Agarwal, P., Acharya, S., and Nikitopoulos, D. E., 2003, "Heat Transfer in 1:4 Rectangular Passages With Rotation," *ASME J. Turbomach.*, **125**, pp. 726–733.
- [31] Won, S. Y., Burgess, N. K., Peddicord, S., and Ligrani, P. M., 2004, "Spatially Resolved Surface Heat Transfer for Parallel Rib Turbulators With 45 deg Orientations Including Test Surface Conduction Analysis," *ASME J. Heat Transfer*, **126**, pp. 193–201.
- [32] Wright, L. M., Fu, W. L., and Han, J. C., 2004, "Thermal Performance of Angled, V-Shaped and W-Shaped Rib Turbulators in Rotating Rectangular Cooling Channels (AR=4:1)," *ASME J. Turbomach.*, **126**, pp. 604–614.
- [33] Fu, W. L., Wright, L. M., and Han, J. C., 2005, "Heat Transfer in Two-Pass Rotating Rectangular Channels (AR=1:2 and AR=1:4) With 45 deg Angled Rib Turbulators," *ASME J. Turbomach.*, **127**, pp. 164–174.
- [34] Lu, B., and Jiang, P. X., 2006, "Experimental and Numerical Investigation of Convection Heat Transfer in a Rectangular Channel With Angled Ribs," *Exp. Therm. Fluid Sci.*, **30**, pp. 513–521.
- [35] Liu, Y. H., Wright, L. M., Fu, W. L., and Han, J. C., 2007, "Rib Spacing Effect on Heat Transfer in Rotating Two-Pass Ribbed Channels (AR=1:2)," *J. Thermophys. Heat Transfer*, **21**, pp. 582–595.
- [36] Huh, M., Liu, Y. H., Han, J. C., and Chopra, S., 2008, "Effect of Rib Spacing on Heat Transfer in a Two-Pass Rectangular Channel (AR=1:4) With a Sharp Entrance at High Rotation Number," *Proceedings of the ASME Turbo Expo 2008 for Land, Sea and Air*, Berlin, Germany, June 9–13.
- [37] Chandra, P. R., Niland, M. E., and Han, J. C., 1997, "Turbulent Flow Heat Transfer and Friction in a Rectangular Channel With Varying Numbers of Ribbed Walls," *ASME J. Turbomach.*, **119**, pp. 374–380.
- [38] Chandra, P. R., Alexander, C. R., and Han, J. C., 2003, "Heat Transfer and Friction Behaviours in Rectangular Channels With Varying Number of Ribbed Walls," *Int. J. Heat Mass Transfer*, **46**, pp. 481–495.
- [39] Aliaga, D., Lamb, J. P., and Klein, D. E., 1994, "Convective Heat Transfer Distributions Over Plates With Square Ribs From Infrared Thermography Measurements," *Int. J. Heat Mass Transfer*, **37**, pp. 363–374.
- [40] Ekkad, S. V., and Han, J. C., 1997, "Detailed Heat Transfer Distributions in Two-Pass Square Channels With Rib Turbulators," *Int. J. Heat Mass Transfer*, **40**, pp. 2525–2537.
- [41] Liou, T. M., Chen, C. C., and Tsai, T. W., 2000, "Heat Transfer and Fluid Flow in a Square Duct With 12 Different Shaped Vortex Generators," *ASME J. Heat Transfer*, **122**, pp. 327–335.
- [42] Gao, X., and Sundén, B., 2001, "Heat Transfer and Pressure Drop Measurements in Rib-Roughened Rectangular Ducts Distribution in Rectangular Ducts With V-Shaped Ribs," *Exp. Therm. Fluid Sci.*, **25**, pp. 25–34.
- [43] Tanda, G., 2001, "Heat Transfer and Pressure Drop in a Rectangular Channel With Diamond-Shaped Elements," *Int. J. Heat Mass Transfer*, **44**, pp. 3529–3541.
- [44] Tanda, G., 2004, "Heat Transfer in Rectangular Channels With Transverse and V-Shaped Broken Ribs," *Int. J. Heat Mass Transfer*, **47**, pp. 229–243.
- [45] Han, J. C., Zhang, Y. M., and Lee, C. P., 1992, "Influence of Surface Heat Flux Ratio on Heat Transfer Augmentation in Square Channels With Parallel, Crossed, and V-Shaped Angled Ribs," *ASME J. Turbomach.*, **114**, pp. 872–880.
- [46] Camci, C., Kim, K., and Hippensteele, S. A., 1992, "A New Hue Capturing Technique for the Quantitative Interpretation of Liquid Crystal Images Used in Convective Heat Transfer Studies," *ASME J. Turbomach.*, **114**, pp. 765–775.
- [47] Moffat, R. J., 1988, "Describing the Uncertainties in Experimental Results," *Exp. Therm. Fluid Sci.*, **1**, pp. 3–17.
- [48] Sparrow, E. M., Lloyd, J. R., and Hixon, C. W., 1966, "Experiments on Turbulent Heat Transfer in an Asymmetrically Heated Rectangular Duct," *ASME J. Heat Transfer*, **88**, pp. 170–174.
- [49] Taslim, M. E., and Wadsworth, C. M., 1997, "An Experimental Investigation of the Rib Surface-Averaged Heat Transfer Coefficient in a Rib-Roughened Square Passage," *ASME J. Turbomach.*, **119**, pp. 381–389.

# Unsteady Simulation of an Axial Compressor Stage With Casing and Blade Passive Treatments

**Nicolas Gourdain**

Computational Fluid Dynamics Team,  
CERFACS,  
42 Avenue Gaspard Coriolis,  
Toulouse 31057, France

**Francis Leboeuf**

Laboratoire de Mécanique des Fluides et  
d'Acoustique,  
UMR CNRS 5509,  
University of Lyon,  
36 Avenue Guy de Collongue,  
Ecully 69034, France

*This paper deals with the numerical simulation of technologies to increase the compressor performances. The objective is to extend the stable operating range of an axial compressor stage using passive control devices located in the tip region. First, the behavior of the tip leakage flow is investigated in the compressor without control. The simulation shows an increase in the interaction between the tip leakage flow and the main flow when the mass flow is reduced, a phenomenon responsible for the development of a large flow blockage region at the rotor leading edge. A separation of the rotor suction side boundary layer is also observed at near stall conditions. Then, two approaches are tested in order to control these flows in the tip region. The first one is a casing treatment with nonaxisymmetric slots. The method showed a good ability to control the tip leakage flow but failed to reduce the boundary layer separation on the suction side. However, an increase in the operability was observed but with a penalty for the efficiency. The second approach is a blade treatment that consists of a longitudinal groove built in the tip of each rotor blade. The simulation pointed out that the device is able to control partially all the critical flows with no penalty for the efficiency. Finally, some recommendations for the design of passive treatments are presented. [DOI: 10.1115/1.2988156]*

*Keywords:* compressor, tip leakage flow, casing treatment, groove, slots

## 1 Introduction

The prediction of the surge line position is a key parameter for the design of compressors. Rotating stall and surge have been studied for 50 years [1] but the basic mechanisms linked to these unstable flows are not yet fully understood. To keep a gas turbine safe, compressors are designed with a large surge margin. The main drawback of this is the waste of high pressure ratio and high efficiency operating range. Today, objectives in terms of pollutant emissions and costs are responsible for a greater emphasis on efficiency, requiring the system weight and the specific consumption to be reduced. Thus it is necessary to increase the efficiency of the compression system without crossing the stability limit.

The design of the compressor is often based on simplified model when the surge margin is to be determined. The advantage of these models is to provide reasonably accurate data for the whole system with few computational resources. For example, the model of Moore and Greitzer [2] based on the Helmholtz resonator principle gives valuable information about the selection of the instability (rotating stall or surge) and also the aerodynamic evolution after the stall inception point. On the same spirit, the model of Spakovszky [3] provides valuable data concerning the stability of different modes in the compressor, which can then be used for testing flow control strategies such as air injection or blowing. However, two limitations are associated with these methods. The first one is that simplified models are not able to predict accurately the position of the surge line. Hence it is really difficult for designers to reduce the surge margin. The second drawback is that no precise information can be delivered by 1D and 2D models about the 3D mechanisms that take place in the compressor with or without a control strategy. Today, thanks to the development of the computational power and the numerical methods, the use of computational fluid dynamics (CFD) turns out to be a suitable tool to predict and study complex flows near the stall.

Many studies have recently shown numerical simulation of ro-

tating stall [4,5] or surge [6,7]. Using such methods the flow control method can be optimized using simulation and fewer configurations, which then have to be tested experimentally. The expected effect is a reduction in the development time and costs. Another advantage of the CFD approach is that it provides a large database that can be used to analyze the physical mechanisms induced by the control methods. For the past few years, a large number of investigations were carried out and showed that several elements play a role in the development of rotating stall and surge. He [8] pointed out that rotor-stator interactions have an influence for the selection of the number of rotating stall cells. Other authors such as Crook et al. [9] and Hoying [10] showed that the tip leakage region exhibits usually the first signs of instabilities, even if mechanisms are different in a subsonic compressor [11] or in a transonic compressor [12]. Today, a large effort is developed by industrials and research centers to control the flow and increase the stability of compressors.

Three main ways can be found in literature for the enhancement of compressor performances. Some authors proposed to use active control such as blowing [6] or air injection [13]. These techniques are flexible but not easy to implement in a modern gas turbine engine since cost and weight are increased by the control installation. The second method is to decrease the surge margin with a better engine control of the fuel-air ratio and the compressor rotating speed. A specific tool based on a signal treatment has been presented by Wadia et al. [14] to obtain such a result. The main advantage of this technique is that it can be used for existing gas turbine engines so as to improve fuel economy or to increase the acceleration rate of aircrafts. Finally, passive methods are the third solution to increase compressor performances. Different designs of passive methods have been proposed such as axisymmetric grooves [15] or nonaxisymmetric casing treatment [16]. Some authors combine also many technologies. For example, Hathaway [17] proposed to use casing bleed and injection at the same time. This self-recirculating casing treatment leads to an important extension of the stable operating range [18]. It is well established that passive treatments represent a promising way for industrial applications since the integration cost is moderate with respect to

Manuscript received December 18, 2007; final manuscript received May 19, 2008; published online January 29, 2009. Review conducted by Nick Cumpsty.



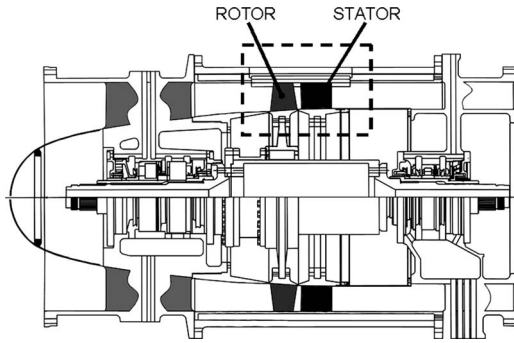


Fig. 1 Schematic view of the compressor rig

the benefits of the technology. Unfortunately, some studies also show that some compressors exhibit no increase in the performance even with a casing treatment geometry [19] that has been through the optimization process.

The present work focuses on two aspects. The first objective is the investigation of the role of the tip flow in an axial compressor. The second objective is the flow control in the tip region with passive control methods. A specific feature of this work is that it takes into account the stator behind the rotor, so the role of the rotor-stator interactions can be explored. Section 2 of this paper deals with the description of the compressor test case and the numerical methodology. In Section 3, results from the simulation are analyzed. First, the reference case (without control) is investigated, and the role of the tip leakage flow near the stall inception point is underlined. Then two kinds of passive methods are tested. The first method consists of a casing treatment with nonaxisymmetric slots while the second one is based on a longitudinal groove in the tip of each rotor blade. Positive and negative impacts of each technology on the tip flow are also explained in this section. Section 4 draws conclusions on the capacity of the tested methods to increase the operability of the compressor. In addition, some recommendations are also presented for the design of future passive control methods.

## 2 Part I: Compressor Test Case and Numerical Methodology

**2.1 Description of the Experimental Compressor.** The test case considered for this study is the Cme2 compressor located at the LEMFI laboratory [20]. Figure 1 shows a view of the compressor and the dashed box pointed out the simulated part of the machine. This axial compressor was designed by SNECMA in 1995 to provide representative unsteady rotor-stator interactions encountered in a modern high pressure multistage compressor. This is a single-stage machine with 30 blades in the rotor and 40 blades in the stator. Four struts are also located upstream of the compressor at the entrance of the inlet duct. The measured nominal rotation speed is  $6330 \pm 14$  rpm, which corresponds to a relative Mach number at a tip of 0.534. Table 1 gives some information about its aerodynamic performances and its main geometric characteristics. At the nominal operating point, the flow characteristics are  $10.5 \pm 0.1$  kg s<sup>-1</sup> for the mass flow and 1.152 for the total-to-total pressure ratio. The tip clearance represents 0.8% of the rotor span. The compressor test facility is equipped with a laser Doppler velocimeter (LDV) and crossed hot-film probes. Previous experimental work has shown that the casing region exhibits the first signs of instabilities [20]. A numerical simulation has also underlined that the rotating stall is initiated in the tip leakage region [21].

**2.2 Numerical Parameters.** The flow solver used for this study is the ELSA software developed by ONERA and CERFACS [22]. The code solves the unsteady Reynolds-averaged Navier–Stokes equations using a cell centered approach on multiblock

Table 1 Compressor description

Nominal pressure ratio	1.152
Nominal mass flow	10.50 kg s <sup>-1</sup>
Measured efficiency	0.92
Nominal rot. speed	6330 rpm
Blade passing frequency	3165 Hz
Rotor speed at the tip	182.0 m s <sup>-1</sup>
Shaft power	180 kW
Tip radius	0.275 m
No. of rotor blades	30
No. of stator blades	40
Rotor blade chord	84 mm
Stator blade chord	77 mm
Tip clearance	0.5 mm
Hub to tip ratio	0.78

structured meshes. For this study, convective fluxes are estimated thanks to a second order centered scheme with scalar artificial dissipation [23], and diffusive fluxes are estimated with a second order center scheme. A second order dual time stepping (DTS) method is considered for the time integration [24]. The time marching for the inner loop is performed by an efficient implicit time integration scheme. This method is based on the backward Euler scheme and a scalar lower-upper symmetric successive over-relaxation (LU-SSOR) method. Convergence acceleration techniques such as local time stepping method are also used. To converge correctly, the number of subiterations for the inner loop is defined to obtain two orders of reduction for the residual magnitude. The turbulent viscosity is computed with the two equation model of Wilcox [25] based on a  $k-\omega$  formulation. The flow is assumed to be fully turbulent (since the Reynolds number based on the chord is about  $Re \approx 5 \times 10^5$ ).

To capture correctly all dominant frequencies, the number of physical time steps has been chosen with a particular care. Let us define  $f_{\max}$  as the maximum frequency that can be computed. Two criteria  $f_{\max}(1)$  and  $f_{\max}(2)$  are used in this study. The first criterion  $f_{\max}(1)$  is only linked to the dimension of the time step  $\Delta t$  (Shannon theorem) such that

$$f_{\max}(1) = 1/2\Delta t \quad (1)$$

The time step  $\Delta t$  can be expressed as a multiple  $k$  of the blade passing frequency (BPF) given by Eq. (2). In this case, the criterion  $f_{\max}(1)$  is given by Eq. (3).

$$f_{\text{BPF}} = N_R \Omega_R / 2\pi \quad (2)$$

$$f_{\max}(1) = k \cdot f_{\text{BPF}} / 2 \quad (3)$$

with  $k$  an integer.

It will be shown later that the choice of this maximum frequency may be performed according to the flow physics in the rotor-stator context and that it underlines the details of the spatial mesh. This second criterion  $f_{\max}(2)$  is based on physical considerations in order to properly capture the rotating structures. In a turbomachine stage, tangential modes are induced by the rotor-stator interactions. The Tyler and Sofrin model [26] is used to predict the development of these structures. Each tangential mode  $m$  in the flow is linked to a spatial wavelength  $\lambda_m$  according to Eq. (4). Then the theoretical circumferential speed of the wavelength  $\lambda_m$  can be deduced from the circumferential speed  $\Omega_m$  of the spatial mode  $m$  given by Eq. (5).

$$m = 2\pi \cdot r / \lambda_m = aN_R + bN_S \quad (4)$$

with  $a$  and  $b$  as relative integers.

The rotational frequency of the  $m$ -order mode is therefore given by

$$\Omega_m = 2\pi \cdot f_m / m = aN_R \cdot \Omega_R / m \quad (5)$$

The theorem of Shannon makes it easy to relate the smallest circumferential dimension of the mesh  $L_\theta$  to the smallest wavelength  $\lambda_{\min}$  that this mesh can compute. The relation  $\lambda_{\min} = 2 \cdot L_\theta$  is a minimum condition, but, owing to numerical errors, more than two mesh cells are generally needed to compute properly a wavelength. For this application, the greatest mesh dimension in the circumferential direction of a blade passage is about 1 mm, implying that  $\lambda_{\min} = 2$  mm. From Eq. (4), the rotor mode number  $a_{\max}$  can be estimated for a given stator mode number  $b$  and a minimum spatial wavelength  $\lambda_{\min}$  according to Eq. (6). Then, Eq. (7) enables the maximum frequency to be computed from the mesh.

$$a_{\max} = [(2\pi \cdot r / \lambda_{\min}) - bN_S] / N_R \quad (6)$$

$$f_{\max}(2) = a_{\max} \Omega_R N_R / 2\pi = a_{\max} f_{\text{BPF}} \quad (7)$$

If only temporal modes of the rotor ( $b=0$ ) are considered at hub ( $r=r_{\text{hub}}$ ), the maximum frequency that can be computed with this mesh is found to be around  $22.2f_{\text{BPF}}$ . To have a reasonable calculation time, the time step coherencies are chosen in combination with the mesh density to compute correctly at least the rotor fundamental frequencies. In the present case, the unsteady flow is computed with 51 time steps by rotor passage (i.e.,  $f_{\max}(1) = 25f_{\text{BPF}}$ ).

**2.3 Compressor Numerical Model.** Previous work has shown that the whole compression system plays a role in the selection of the most unstable frequency during surge or rotating stall [3]. However, in the present study, only a good estimation of the stability limit is wanted. In this case, the dimensions of ducts do not have a major impact [21]. Thus for practical reasons of CPU resources, the whole domain of the experimental facility is not simulated; only a part of the ducts and of the compressor circumference is simulated. The four struts of the inlet duct are not taken into account. A particular feature of the present compressor is the periodicity between the number of the rotor and stator blades. Thus only three rotor passages and four stator passages are considered for the simulation (a 36 deg sector). The consequence is that no tangential wavelength greater than a tenth of the circumference can develop. Thus this model is not able to compute correctly a rotating stall phenomenon, although the rotor-stator periodicity is correctly considered. It is assumed that a good description of the deterministic stresses is sufficient to compute the stability limit and obtain a correct flow behavior, at least before the massive stall occurs.

The flow domain is discretized with a multiblock strategy. Views of the calculation domain and of the mesh are presented in Fig. 2. In order to avoid numerical difficulties (reflection on the boundary conditions), the computational domain extends 0.6 radius of the compressor upstream of the rotor and 0.5 radius downstream of the stator. These values have been chosen to be consistent with the wavelength dimensions that can develop during a stall process. An *O-H* meshing strategy has been used for each passage of the compressor. The dimensions of the rotor mesh are 108, 169, and 67 points, respectively in the axial, tangential, and radial directions. Similarly, the mesh dimensions of the stator are 115, 161, and 57. In order to reduce the CPU cost, a wall law approach is applied. The minimum cell size is equal to  $40 \mu\text{m}$ , which corresponds to a mean computed distance  $y^+$  of 20. A more detailed description of this wall law method can be found in Ref. [27].

Due to the minimum cell size, the number of mesh points to discretize the tip gap in the radial direction is constrained and only 11 points are considered. A join with nonmatching points is used between the tip mesh and the passage mesh in order to relax constraints on the mesh design. The total number of nodes for the configuration without control device is  $3.57 \times 10^6$ . A standard condition of spatial periodicity is considered for the lateral bound-

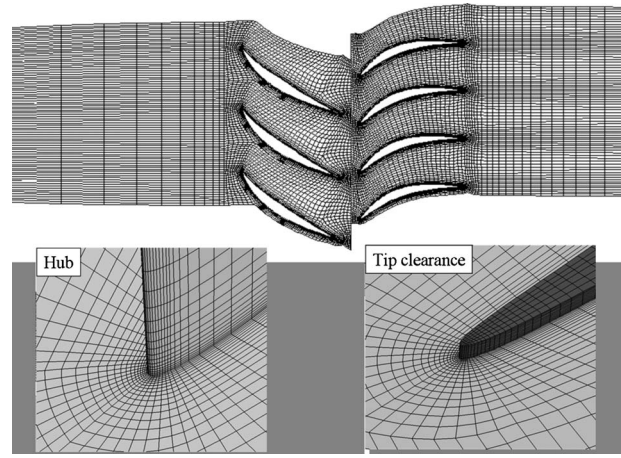


**Fig. 2 Calculation domain (up) and mesh details at the rotor leading edge (bottom)**

aries. The inlet and outlet boundary conditions are key parameters for the simulation of the unsteady flow in such a compressor, especially when the prediction of the stability limit is expected. A previous study has been performed to define the best boundary conditions to avoid numerical problems at near stall conditions and to represent correctly the flow upstream and downstream of the computational domain [5].

The inlet flow has constant and uniform stagnation pressure and temperature:  $P_{i0} = 101,325$  Pa,  $T_0 = 288$  K, and  $\alpha = 0$  deg. At the outlet, a throttle condition given by Eq. (8) is coupled with a simplified radial equilibrium following Eq. (9). To describe the characteristic of the compressor from the choked point to the stall inception point, the value of the throttle parameter  $\lambda$  is progressively increased. Calculations have been performed on a Cray xd1 supercomputer with 8 Opteron processors.

$$P_{s_{\text{out}}} = P_{\text{inf}} + \lambda \cdot Q^2 \quad (8)$$

$$\frac{\partial P_s}{\partial r} = \rho \frac{V_\theta^2}{r} \quad (9)$$

### 3 Part II: Unsteady Simulation of the Compressor Stage

**3.1 Simulation of the Compressor (Reference Case).** The first step is to consider only the compressor with no passive control. For convenience, results shown in this paper are presented in a nondimensional form

$$P_s = P_{s_{\text{dim}}} / P_{i0}, \quad V = V_{\text{dim}} / \sqrt{\gamma R T_{i0}}$$

The aim is to describe more precisely the compressor characteristic at the nominal rotation speed and to obtain data concerning the flow close to the stall inception point. For a typical simulation, the CPU time for one operating point (i.e., one value of the throttle parameter) is 140 h and the memory cost is 6.7 Gbytes. Starting from a steady solution, the simulation reached a periodic state after 2.5 rotor revolutions, i.e., 75 rotor blade passages (Fig. 3). The outlet mass flow history in a stator passage is also used to quantify the unsteadiness of the flow at the outlet. At a near stall point ( $\Phi = 0.83$ ), the signal oscillation represents 1.7% of the mean mass flow. This oscillation of the mass flow is the consequence of the rotor-stator waves that still exist on the downstream boundary.

The first thing is to evaluate the capacity of the model to compute the surge line position. Nevertheless an assumption is necessary to estimate the stability of an operating point. The experimental time needed to obtain instabilities can be very important, more

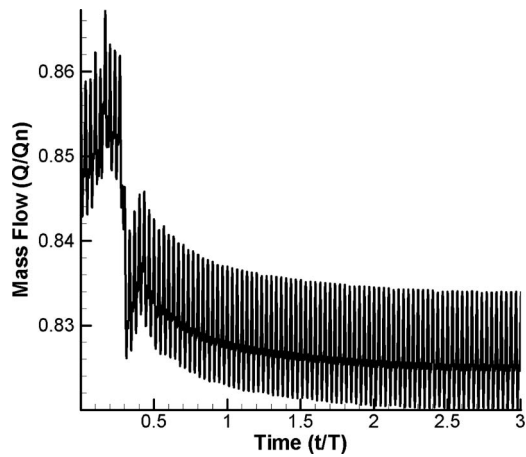


Fig. 3 Mass flow evolution at the outlet of the compressor ( $\Phi=0.83$ )

than hundred of revolutions. For practical reason of time, only three rotor revolutions are computed for each value of the throttle parameter. If a periodic state is reached at the end of the computation, the point is assumed to be stable. With this assumption, the numerical stall inception point is found at  $\Phi=0.813$  (Fig. 4). The dashed line in Fig. 4 indicates the transient from the last converged point to the first point where the stable operating point is in the rotating stall. The experimental stall inception point is found at  $\Phi=0.816$ . Thus numerical simulations and experimental results match correctly. A comparison between the computed characteristic and the experimental data shows that the pressure ratio is slightly underestimated by the simulation (about  $-7\%$  at some points). The main reason for that is the use of a high artificial dissipation value (to stabilize the calculation at near stall conditions) that leads to a loss of information in terms of pressure rise. Moreover the wall law function also induces an overestimation of the wall friction in this case, which means a reduction in pressure ratio and efficiency. Despite these differences, locations of the pressure ratio peak and of the surge line are well computed. A way to explore in order to improve the quality of these results could be the low Reynolds method. Unfortunately this approach has not been tested in the present context mainly because it needs a very fine mesh and thus a higher CPU consumption (more mesh points and smaller time step). Typically more than 25 mesh points are required in a boundary layer with this method (that means more than 100 points in the radial direction). So it is assumed that a wall law calculation is more suitable than a low Reynolds calcu-

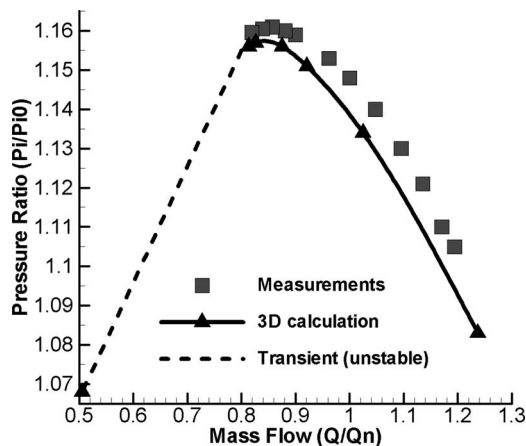
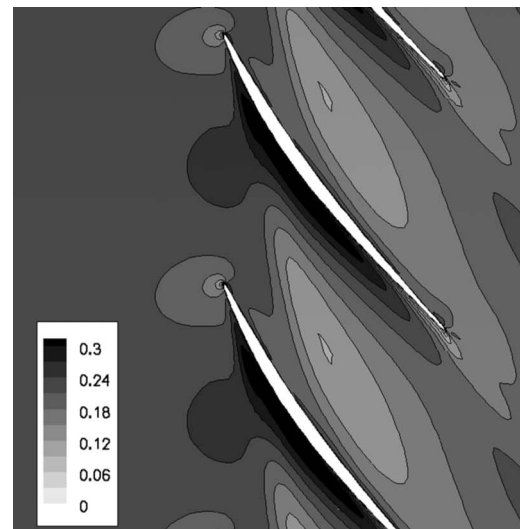
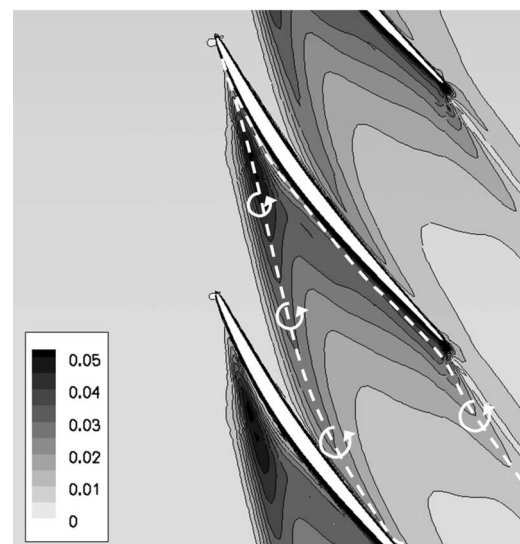


Fig. 4 Pressure ratio evolution with respect to mass flow



(a)



(b)

Fig. 5 Time averaged solution of the axial velocity (a) and relative helicity (b) in the rotor at the nominal operating point ( $\Phi=1.03$ )— $h/H=98\%$

lation with a lack of point in the boundary layers.

Figures 5 and 7 show the time averaged results of axial velocity and helicity flow fields, respectively, at the nominal operating point ( $\Phi=1.03$ ) and at a near stall point ( $\Phi=0.83$ ). The definition of the helicity computed with relative velocity is given by Eq. (10). Helicity shows the vorticity of the relative flow field in the direction of the relative flow directions; it is helpful in showing secondary vortex structures. The dashed lines plotted in Figs. 5 and 6 show the trajectory of the main vortices observed near the casing.

$$He_r = W \text{ rot } W \quad (10)$$

At the nominal point (Fig. 5), only a small region of flow blockage is observed near the casing. A high intensity vortex develops near the leading edge of the rotor and is driven by the main flow in the channel. As a consequence of the low static pressure in the vortex core, it tends to capture all the low kinetic energy material of the near region around it. As the low kinetic energy is generally associated with high level of entropy for the regions close to the solid walls, the losses tend to accumulate in the core of the vortex.



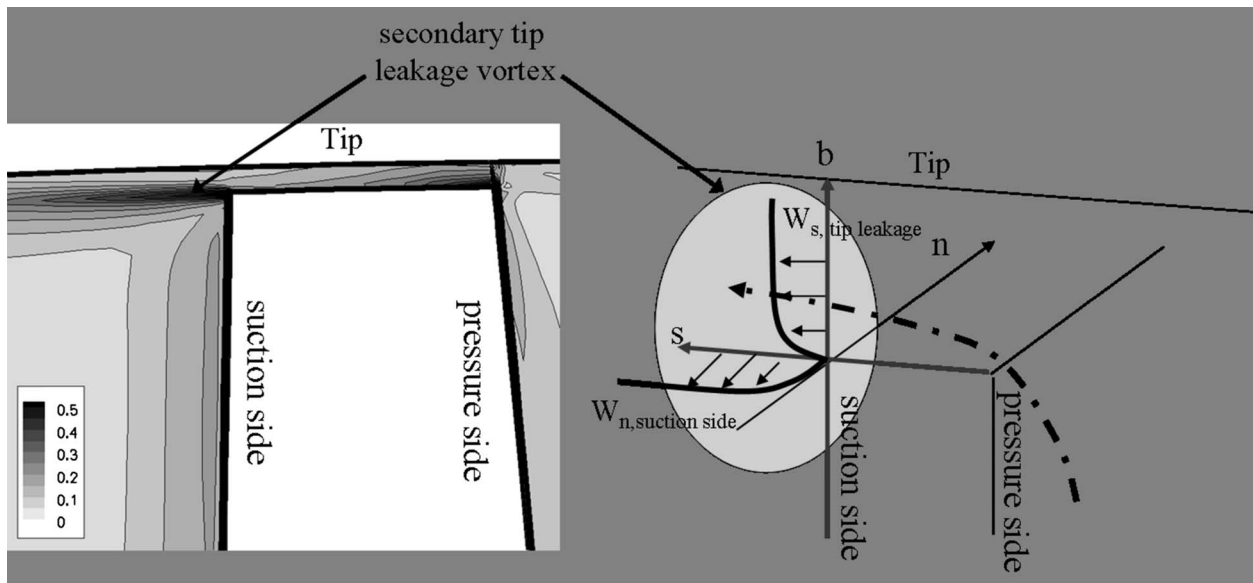


Fig. 6 Model of the tip leakage vortex and comparison with the simulation (helicity flow field at  $x/C=50\%$ )

Indeed the trajectory of this vortex is correlated with the deficit of axial momentum in the channel. In this case, it is assumed that this vortex is the result of a separation line on the casing. The flow injection from the tip leakage is driven by the pressure gradient between the pressure side and the suction side. The maximum gradient is located near the leading edge of the rotor, so it explains why this vortex develops at this location. Due to the competition with the main flow, the tip leakage jet loses its momentum in the rotor passage and separates from the casing wall toward the hub. The vortex observed in the channel is thus induced by this separation line [28].

A second vortex is also observed along the rotor suction side. A model is proposed in Fig. 6 to explain the development of this flow structure. This is a consequence of the tip clearance jet flow that emerges from the blade suction side and that loses its momentum around the location of this second vortex. According to the model, the interaction between the tip leakage boundary layer and the suction side boundary layer induces the development of a high helicity region just under the tip leakage jet, near the blade suction side. The development of this vortex can be explained by Eq. (11) that shows the transport equation of the vortex component  $\Psi_s$  in the velocity direction. The term  $\Psi_b(\partial W_s / \partial b)$  is linked to the vortex production on the rotor suction side while the term  $\Psi_b W_s K_{sb}$  corresponds to the development of a vortex on the pressure side, but it is found to be small in this case. A similar phenomenon has already been pointed out in axial turbines by Billonnet et al. [29] and in transonic compressors by Caro et al. [30]. This tip leakage vortex is then also associated with a local loss of kinetic energy and flow blockage. Apart from this vortex, no sign of massive boundary layer separation is highlighted. To sum up, at the nominal operating point, two phenomena are mainly induced by the tip leakage flow. The first one is the separation line at the casing led by the flow injection at the rotor leading edge and the second phenomenon is the tip leakage vortex located near the suction side of the rotor.

$$\rho W_s^2 \frac{\partial}{\partial s} \left( \frac{\Psi_s}{\rho W_s} \right) \approx \Psi_b \frac{\partial W_s}{\partial b} - \Psi_b W_s K_{sb} > 0 \quad (11)$$

$s$ ,  $n$ , and  $b$  are local coordinates linked to the velocity vector direction ( $s$  is tangent to the flow direction).

At a mass flow near stall (Fig. 7), a region of high helicity and low axial momentum is detected at the rotor entrance near the casing. The high incidence on the leading edge generates a high

pressure gradient that tends to push the tip clearance flow upstream of the rotor. An angle of almost 90 deg between the incoming flow in absolute coordinates and the tip clearance jet is observed. Since the intensity of the tip clearance jet is very high, the separation line at the casing is moved further in the rotor passage. In this case, the jet loses its momentum near the leading edge of the next rotor blade, thereby generating the accumulation of low axial momentum observed in this region. The intensity of the flow blockage is due to the massive separation that occurs at this point. A similar phenomenon has been observed by Suder and Celestina [31] for a transonic compressor operating at part-speed conditions. They found experimentally and numerically that a vortex, which is not created directly by the tip gap, develops in the middle of the rotor passage near the end wall region and causes flow blockage at near stall conditions.

A second region of the flow blockage is also noticed on the last 50% of the rotor chord. It is mainly induced by the separation of the boundary layer on the suction side due to the high flow incidence at the rotor inlet and the tip leakage flow injection along the rotor chord. As a consequence, the flow angle at the leading edge of the stator is periodically increased, and a separation of the stator suction side boundary layer occurs. It is responsible for large potential effects that lead to a deficit of axial momentum in the rotor-stator inter-row region. At near stall conditions, two regions of low axial momentum have been pointed out near the casing by this study. The objective is now to increase the compressor stability thanks to a control of the flow in these regions.

### 3.2 Simulation of the Compressor With Casing Treatment.

The first tested method to control the tip flow is a casing treatment with nonaxisymmetric slots. The design of the slot is largely based on previous authors' recommendations such as Wilke and Kau [16] and Lu et al. [32]. The treatment is composed of 110 slots that are built equally spaced around the circumference of the rotor (Fig. 8). Thus, the number of slots for each rotor passage is not an integer ( $110/30 \approx 3.67$ ). The cavity is split in two segments: the upstream part of the slot is purely axial and the second one is inclined of 45 deg with respect to the axial direction. Each slot extends from upstream of the rotor to 25% of the rotor axial chord. The expected effect is to drive the flow from the second segment of the slot to the upstream of the rotor.

The slot mesh is connected to the rotor passage mesh with sliding interfaces. The 2D interpolation coefficients used by the

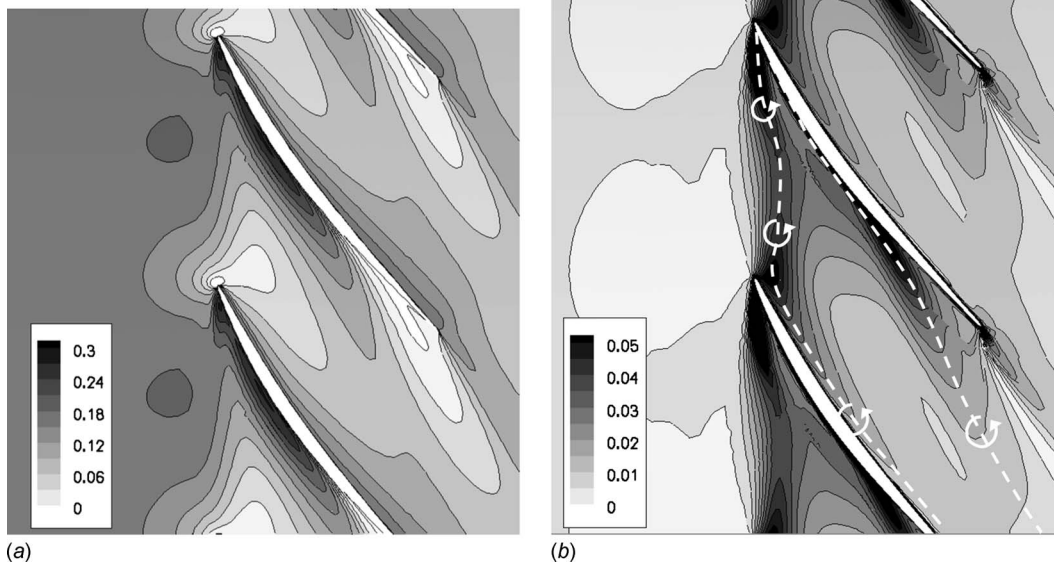


**Fig. 7 Time averaged solution of the axial velocity (a) and helicity (b) in the rotor at near stall condition and for the reference case ( $\Phi=0.83$ )– $h/H=98\%$**

method are computed for each time step. For this reason, a higher memory is requested (+30%) compared with the smooth wall case simulation. This boundary condition is conservative in the case of a plane interface, which is roughly the case here. The number of mesh points is 350,000 for a 36 deg sector of the casing treatment (11 slots).

The outlet mass flow evolution for a near stall point ( $\Phi = 0.83$ ) is shown in Fig. 9. A smooth wall unsteady solution is used as an initial field for the casing treatment computation. In this case, a periodic state is reached after only 1.5 rotor revolutions. The mass flow variation at  $\Phi=0.83$  is 2.2% of the mean mass flow. It means that unsteadiness at the compressor outlet is increased with respect to the reference case. The impact on performances of the nonaxisymmetric slots is presented in Fig. 10. The last stable point with casing treatment is computed at  $\Phi = 0.789$  ( $\Phi=0.813$  for the smooth wall case). An increase of 6% of the operability range  $\Delta Q (=Q_{max} - Q_{stall})$  is thus achieved due to this flow control. The casing treatment has also a positive impact on the pressure ratio since a slight increase in the maximum total-to-total pressure ratio is observed (+0.6%).

Axial velocity and relative helicity are shown in Fig. 11 for a

near stall operating point ( $\Phi=0.83$ ). As expected, the blocked flow region near the leading edge of the rotor is largely reduced by the casing treatment (compared with Fig. 7). The mechanism involved is the circulating flow inside the slot, mainly led by the static pressure gradient (Fig. 12). The maximum recirculation effect is observed when the rear part of the slot is located at the pressure side of a rotor blade and the forward part is above the suction side of the leading edge. The deviated flow leads to an increase in the axial momentum near the casing at the rotor entrance, and thus reduced tendency to stall in this region. In fact, the effect is similar to a pulsating jet with a periodic flow removal in the rotor passage and a periodic flow injection at the rotor inlet. The pulsating frequency is determined by the number of slots and the blade passing frequency while the momentum of the jet is fixed by the geometry of the casing treatment slot. The main effect of this jet is the periodic reduction in the pressure gradient between the pressure side and the suction side because the tip clearance vortex is pushed downstream in the passage. This mechanism is responsible for a modification of the separation line position at the casing, below the slot position. Moreover, periodic blowing and injection lead to an increase in the radial momentum

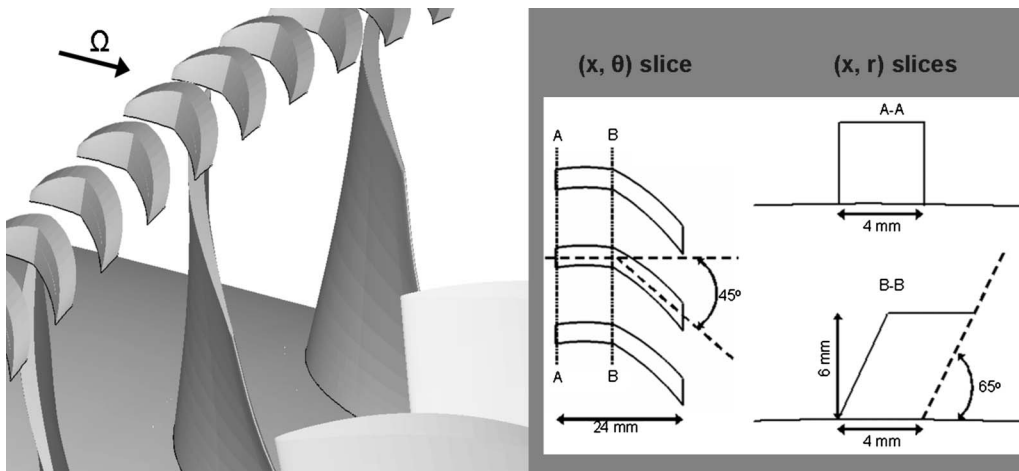


**Fig. 8 Design of the casing treatment and integration with the compressor stage**

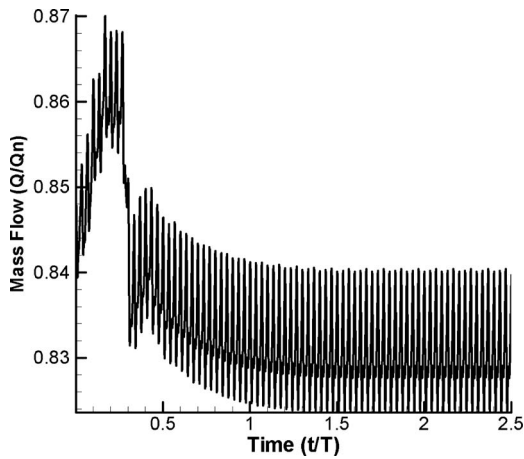


Fig. 9 Mass flow evolution at the outlet of the compressor with casing treatment ( $\Phi=0.83$ )

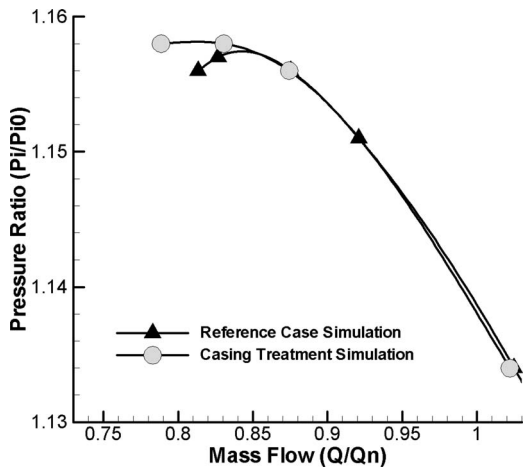


Fig. 10 Pressure ratio evolution with respect to the mass flow

near the tip and cut the vortices that develop near the end wall. The flow blockage is then removed from the leading edge of the rotor blades.

Unfortunately the separation of the boundary layer on the suction side of the rotor blade is badly affected by the slots. The separation point of the suction side boundary layer moves forward with respect to the reference case. Moreover, this stall leads to a strong deviation of the flow in the rotor passage and thus to an increase in the flow angle at the stator leading edge. The result is a massive region of the blocked flow at the rear part of the rotor. This phenomenon limits the extension of the stable operating range.

To sum up this part, it can be said that the casing treatment enables a reduction in the blockage induced by the separation line at the casing (near the leading edge of the rotor) but failed to control the separation of the suction side boundary layer. Indeed the extension of the stable operating range is a little bit less important compared with the result found by Lu et al. [32] for a similar compressor. It is assumed that the control of the tip leakage flow is not sufficient in this case to obtain an important increase in the stability.

### 3.3 Simulation of the Compressor With Longitudinal Groove

The second method is a blade treatment with a groove built in the head of each rotor blade (Fig. 13). The longitudinal groove extends between the leading edge and the trailing edge of the rotor blade. The rotor walls around the groove are idealized walls with a null thickness (groove extends from the pressure side to the suction side). The potential consequence of this assumption is a bad description of the local losses on the top walls around the groove. Moreover, it is also assumed that the main effect induced by the groove on the rotor flow depends mainly on the cavity geometry; the groove thickness probably has an influence and thus further investigations are required to investigate this point. In the present case, the groove depth evolves from 0.5 mm at the leading edge to 1.4 mm at 50% of the rotor axial chord. The mesh of the groove has 93, 9, and 17 points, respectively, in the axial, tangential, and radial directions. The first expected effect of this device is a reduction in the tip jet intensity, which develops at the rotor leading edge. A second effect on the suction side boundary layer separation is also expected.

The mass flow history for a near stall point ( $\Phi=0.83$ ) is shown in Fig. 14. A smooth wall unsteady solution is used as an initial field for the longitudinal groove simulation. A periodic state is

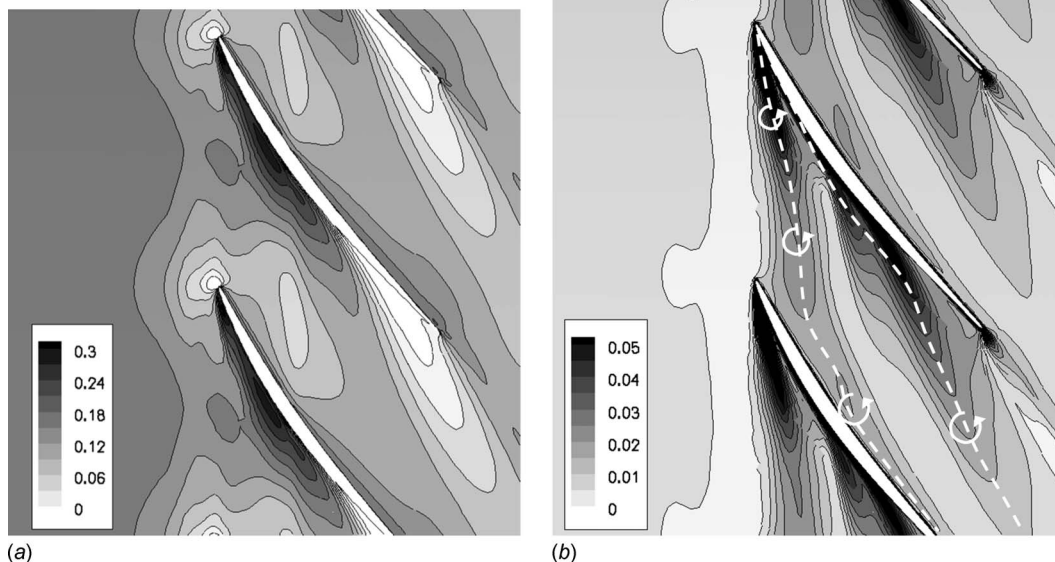


Fig. 11 Time averaged solution of the axial velocity (a) and helicity (b) in the rotor at near stall condition and with a casing treatment ( $\Phi=0.83$ )— $h/H=98\%$



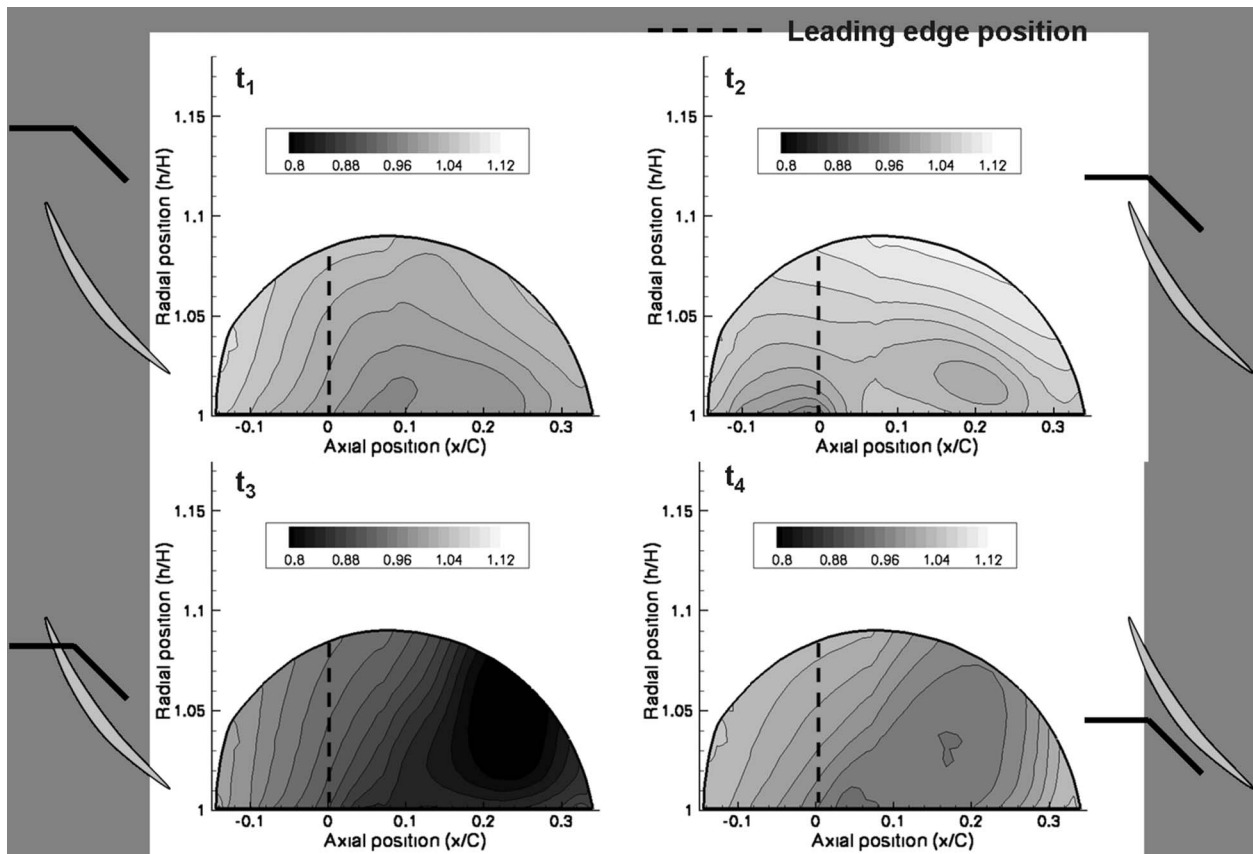


Fig. 12 Instantaneous solution of the static pressure in an axial slot (meridian view)

reached after one revolution of the rotor. At this point, the mass flow variation represents 1.5% of the mean mass flow. Thus, the level of unsteadiness is reduced with respect to the casing treatment case and also with respect to the smooth wall case. The pressure ratio evolution with respect to the mass flow is shown in Fig. 15. The characteristic of the compressor with grooves is

shifted toward the left, and the last stable point is found at  $\Phi = 0.779$ . It corresponds to an extension of 8% for the operability range but with quasi-no-impact on the maximum pressure ratio.

Axial velocity and relative helicity are shown in Fig. 16 in the grooved rotor for a near stall operating point of the smooth casing ( $\Phi = 0.83$ ). Two effects of the longitudinal groove are observed.

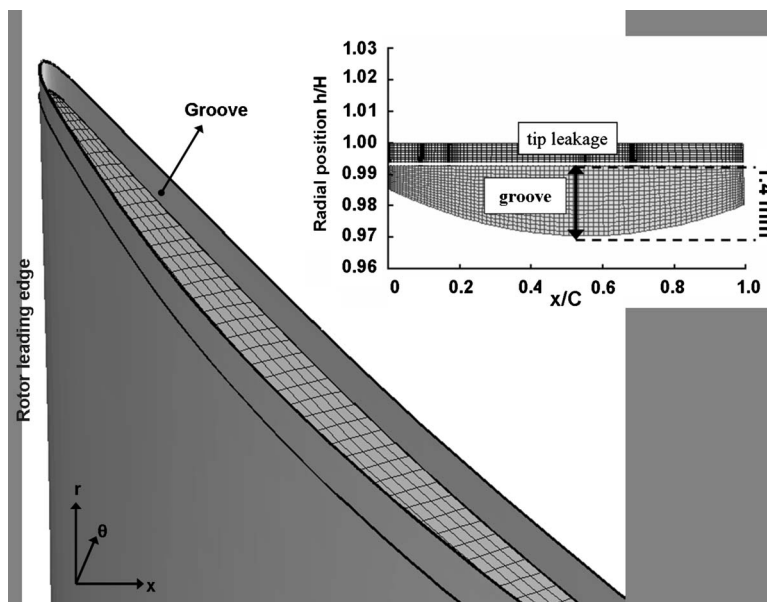


Fig. 13 Design of the longitudinal groove inside a rotor blade

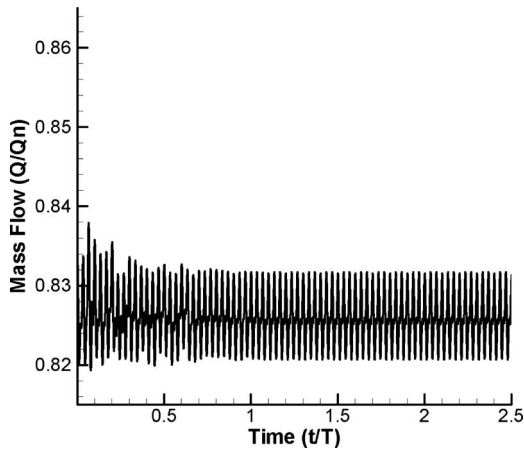


Fig. 14 Mass flow evolution at the outlet of the compressor with longitudinal groove ( $\Phi=0.83$ )

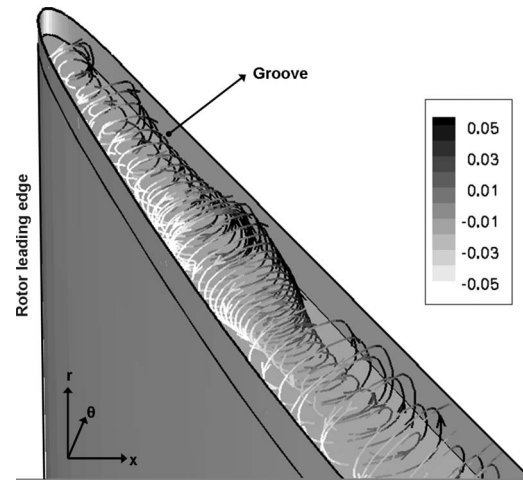


Fig. 17 Streamlines in a rotor groove from a time averaged solution of the radial velocity ( $\Phi=0.83$ )

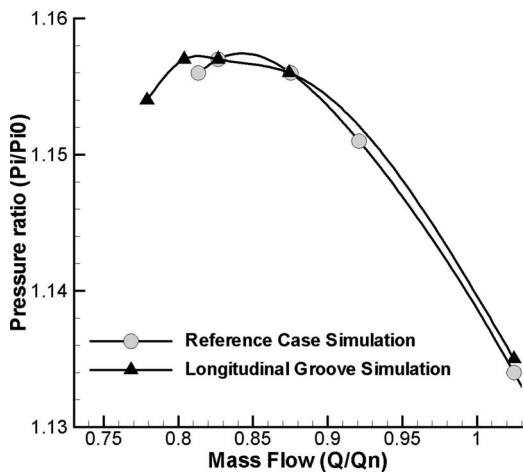


Fig. 15 Pressure ratio evolution with respect to the mass flow

The first one is that the separation line at the casing is moved toward the middle of the rotor passage. Thus, the low axial momentum region is removed from the leading edge of the rotor. The strength of the vortex is not reduced in the way it was for the casing treatment, but the vortex trajectory is close to the trajectory at the nominal operating point. The passage is no longer blocked at the entrance by the clearance vortex, and the flow angle at the rotor leading edge is therefore reduced. The second effect is the reduction in the blocked region induced by the suction side boundary layer separation, with its helicity field showing clearly that the separation point is moved toward the trailing edge of the rotor. A consequence is a reduction in the periodic increase in the incidence angle at the stator leading edge and a consequent reduction in the separated region on the stator suction side. This mechanism explains the reduction in the unsteadiness at the stator exit.

The main effect of this control method is the generation of a strong vortex inside the groove (Fig. 17). This vortex modifies the structure of the tip leakage flow mainly because of an increase in the turbulent kinetic energy. As it can be seen in Fig. 18, the groove leads to a large increase in the turbulent kinetic energy in the tip leakage region (up to 100% in some positions). According

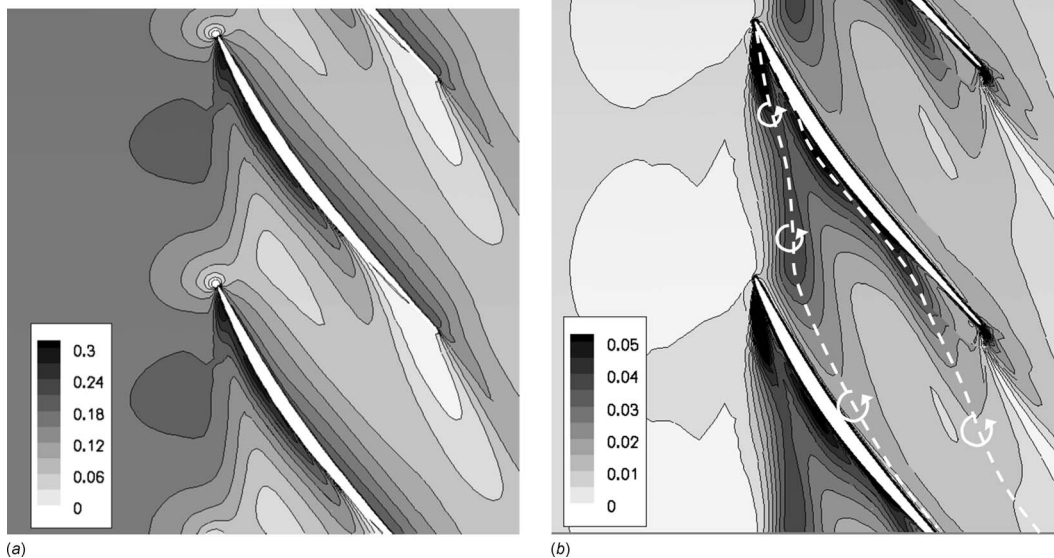


Fig. 16 Time averaged solution of the axial velocity (a) and helicity (b) in the rotor at near stall condition and with longitudinal grooves ( $\Phi=0.83$ )

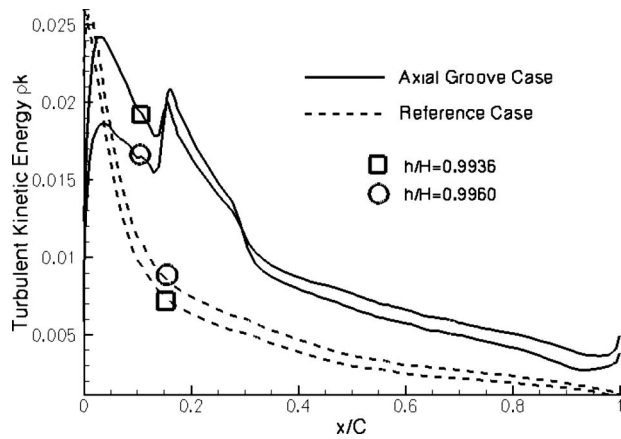


Fig. 18 Level of turbulent kinetic energy in the tip gap at a near stall point ( $\Phi=0.83$ )

to the work of Shabbir and Adamczyk [15], the axial pressure force is balanced only by the axial viscous shear force near the casing. An increase in the turbulent kinetic energy corresponds to an increase in the turbulent viscosity and thus leads to an increase in the viscous shear forces. This raised shear force can be used to balance the axial pressure gradient and thus to improve the stability of the flow near the casing. An effect of the device is also to remove the boundary layer of the rotor head and thus to reduce the tip leakage vortex (cf. Fig. 6). Finally, the simulation shows that a partial control of the two low axial momentum regions is achieved with the longitudinal grooves, and a positive effect on the stability is observed.

#### 4 Part III: Discussion

In order to compare the different devices, it is interesting to show their impact on a given stimulus. In the present case, it is assumed that the tip leakage flows are the main point of interest. As it has been shown, two regions of low axial momentum are observed near the casing when no control is applied just before instabilities occur. In fact, more than the tip leakage flow features, it is assumed that the total flow blockage (zero or negative axial momentum) in the rotor passage is the most useful indicator to estimate the capacity of the compressor to operate safely. Basically flow blockage areas at the rotor outlet represent the regions where the adverse pressure gradient is no longer balanced by the shear stress forces and the convective acceleration. The consequence is that the flow direction can change locally and lead to the development of large stalled flow regions. Figure 19 shows the mean value of the flow blockage in the rotor, expressed in percentage of the total passage area, with respect to the axial position. Controlled cases are indicated only for the near stall point ( $\Phi=0.83$ ), and two operating points are shown for the reference case ( $\Phi=1.03$  and  $\Phi=0.83$ ). For the smooth wall case and at nominal operating conditions, the total blocked area represents less than 0.1% of the total passage area, except around the position  $x/C=0.3$  for which the flow blockage is 0.6% (due to the tip leakage flow). At a reduced mass flow, the flow blockage increases and is more than 1% of the total area in two regions, near the leading edge ( $x/C=0.15$ ) and near the trailing edge ( $x/C=0.75$ ). The phenomena responsible for these flow blockage areas have been pointed out by the simulation and correspond to two mechanisms. The first one is linked to the separation line at the casing induced by the tip leakage flow injection at the leading edge of the rotor. The second one is the boundary layer separation on the suction side of the rotor induced mainly by the strong flow incidence. When no control is used, Fig. 19 shows clearly that the flow blockage near the rotor leading edge is the most important (more than 1.5% at near stall conditions).

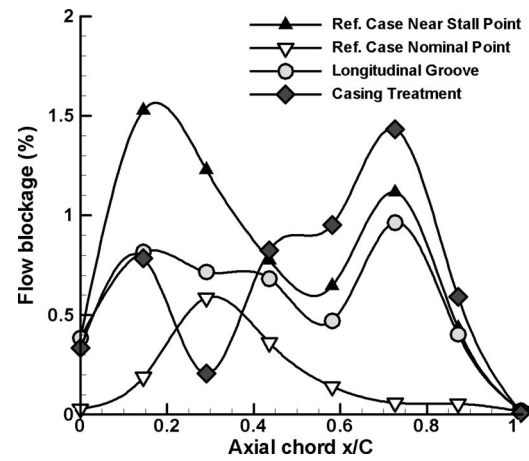


Fig. 19 Comparison of the control method impact on the mean flow blockage in the rotor

The simulated casing treatment configuration proves that a good control of this region can be achieved since the leading edge flow blockage is decreased to less than 0.8%. Unfortunately, it also leads to an increase in the flow blockage around  $x/C=0.75$  that becomes higher in the case of casing treatment (the flow blockage becomes 1.4% compared with 1.1% in the smooth wall case). It explains why the casing treatment does not succeed to extend operability of the compressor more than 6%. In the case of the longitudinal groove, the flow blockage is reduced for all axial positions. At near stall conditions, the flow blockage is nowhere more than 1% of the total area for a given axial position. However, like for the casing treatment case, the maximum blockage is now located around  $x/C=0.75$  (the flow blockage is 0.9%) while the flow blockage near the leading edge is considerably reduced (0.8%). Unlike the casing treatment, the blade treatment shows a capacity to control partially the suction side boundary layer separation, which explains why a better extension of the operability is observed with grooves (+8%). Unfortunately, this separation is not completely removed and is responsible for a periodic increase in the flow incidence at the stator leading edge. The growth of the stator potential effects induces a large deficit of axial momentum in the rotor-stator inter-row region, and a periodic coupling is then observed between the separation of the suction side boundary layer in the rotor and the potential effects of the stator. At the stall inception point, this stator potential interaction effect leads to a massive boundary layer separation on the entire rotor chord. It is interesting because it highlights clearly that a control of the tip leakage flow is not sufficient to increase stability and performances. A better control of the suction side boundary layer has to be done for this compressor (for example, with boundary layer blowing).

Finally, another point of interest is the impact of the tested passive methods on the efficiency of the compressor. Figure 20 shows a comparison of isentropic efficiency for the different configurations. The casing treatment has a negative effect on the efficiency of up to -2% at partial mass flow (with respect to the reference case). Even if an increase in the stability and the pressure ratio is observed, the benefit induced by the casing treatment is balanced by losses inside the slots. The simulation shows that the longitudinal groove has almost no impact on the efficiency, implying that losses induced by grooves are balanced by the control of the end wall flows.

#### 5 Conclusion

A numerical method has been presented to simulate the flow in a stage of an axial compressor. A criterion based on the Tyler and Sofrin relation has also been proposed to choose the time step for



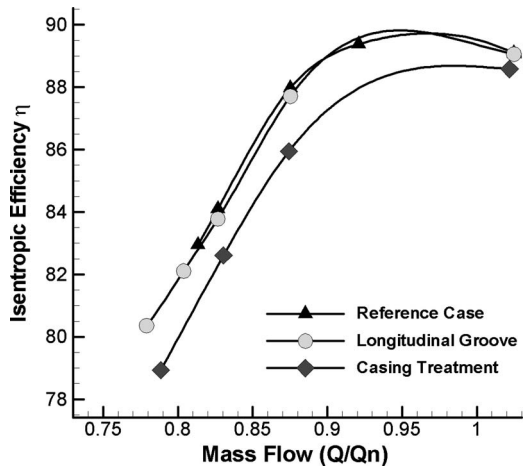


**Fig. 20 Comparison of the isentropic efficiency with the different control strategies**

unsteady simulations in connection with the spatial mesh size in the circumferential direction. Then a study has been performed without any treatment to investigate the behavior of the tip leakage flow at conditions near the stall. The comparison with experiments shows that the numerical model is able to compute correctly the stability limit and the performances of the compressor.

Two destabilizing effects induced by the tip leakage flow have been pointed out in the casing region based on the simulation results. The first phenomenon is a flow blockage that develops near the rotor leading edge. The second is a separation of the rotor suction side boundary layer, amplified by the stator potential effects. A scenario has been proposed to explain the loss of stability that involves both mechanisms.

To increase stability, two strategies of the passive control have been tested. The first method is based on nonaxisymmetric slots in the casing. The simulation of this casing treatment shows a good control of the separation line at the casing but with a penalty for efficiency. The impact of the casing treatment is limited to a slight extension of the operability (+6%). A second passive method composed of a longitudinal groove in the rotor blade has been tested. The simulation shows that the device is able to control partially both types of blockage. Results in terms of stability are thus better than with casing treatment (+8% for the operability) with no penalty for the efficiency.

The present study shows that a good control of the tip leakage flow is not sufficient in some cases. In literature casing treatment is often applied for transonic configurations. In most of these compressors, a vortex induced by the tip leakage flow interacts with the passage shock and is responsible for a flow blockage near the casing ("tip blockage stall" phenomenon). A casing treatment is thus a solution to increase stability since the slots lead to a reduction in the jet intensity in the tip leakage region. Nevertheless in some cases, a classical boundary layer separation occurs ("blade tip stall" phenomenon). This kind of stall is amplified when the stator starts to interact and the casing treatment is not able to extend the stable operating range for these configurations. Further investigations are thus required to test the capacity of longitudinal grooves to control the different tip leakage phenomena in the case of a transonic compressor. A coupling between a blade treatment and a casing treatment should also be explored.

### Acknowledgment

Writing a paper involves the help of many people. Important contributions have been provided by Hubert Miton (LEMF) for supplying experimental data and Jean-François Bousuge (CERFACS) for helpful recommendations about the numerical choices. These people are gratefully acknowledged. No numerical study

can be achieved without a good support from the software developers. Thanks to Marc Montagnac from CERFACS for developing efficient methods in the ELSA code that was used for this study. Authors also thank anonymous reviewers and Nick Cumpsty for very helpful comments and suggestions. Finally, thanks to SNECMA for giving authorization to use the Cme2 compressor geometry.

### Nomenclature

#### Latin Letters

- $C$  = rotor axial chord
- $f$  = frequency
- $h$  = radial position
- $H$  = compressor span
- He = helicity
- $K$  = curvature
- $m$  = tangential mode
- $N_{R,S}$  = number of blades ( $R$ , rotor  $S$ , stator)
- $P_i$  = total pressure
- $P_s$  = static pressure
- $r$  = radius
- $R$  = gas constant ( $c_p - c_v = 287.0 \text{ J K}^{-1}$ )
- $Q$  = mass flow
- $Q_n$  = nominal operating point ( $Q_n = 10.5 \text{ kg s}^{-1}$ )
- $t$  = time
- $T$  = rotor passing period ( $2\pi/\Omega_{\text{rotor}}$ )
- $T_i$  = total temperature
- $U_\tau$  = friction velocity
- $V_{x,r,\theta}$  = absolute velocity components
- $W_{x,r,\theta}$  = relative velocity components
- $x$  = axial position
- $y$  = distance to the wall
- $y^+$  = nondimensional distance to the wall ( $y \cdot U_\tau / \nu$ )

#### Greek Letters

- $\gamma$  = gas constant ( $c_p/c_v = 1.4$ )
- $\lambda$  = throttle parameter, wavelength
- $\nu$  = kinematic velocity
- $\rho$  = density
- $\Phi$  = mass flow coefficient ( $=Q/Q_n$ )
- $\Psi$  = vortex vector ( $=\text{rot } W$ )
- $\Omega$  = rotation speed

#### Subscripts

- 0 = upstream state
- BPF = blade passing frequency (3165 Hz)
- out = outlet state

### References

- [1] Pamreen, R. C., 1993, *Compressor Surge and Stall*, Concepts ETI, White River Junction, VT.
- [2] Moore, F. K., and Greitzer, E.M., 1985, "A Theory of Post-Stall Transients in Axial Compression Systems, Part I: Development of Equations, Part II: Applications," ASME Paper Nos. 85-GT-171 and 85-GT-172.
- [3] Spakovszky, Z., 2001, "Application of Axial and Radial Compressor Dynamic System Modeling," Ph.D. thesis, Massachusetts Institute of Technology, Cambridge, MA.
- [4] Schmidtmann, O., and Anders, J. M., 2001, "Route to Surge for a Throttled Compressor: A Numerical Study," *J. Fluids Struct.*, **15**, pp. 1105–1121.
- [5] Gourdain, N., Burguburu, S., Leboeuf, F., and Miton, H., 2006, "Numerical Simulation of Rotating Stall in a Subsonic Compressor," *Aerosp. Sci. Technol.*, **10**, pp. 9–18.
- [6] Niazi, S., 2000, "Numerical Simulation of Rotating Stall and Surge Alleviation in Axial Compressor," Ph.D. thesis, Georgia Institute of Technology, Atlanta, GA.
- [7] Tauveron, N., Ferrand, P., Leboeuf, F., Gourdain, N., and Burguburu, S., 2006, "A Numerical Contribution to the Analysis of Surge Inception and Development in Axial Compressors," *Proceedings of the 11th ISUAAAT*, Moscow, Russia.
- [8] He, L., 1997, "Computational Study of Rotating-Stall Inception in Axial Compressors," *J. Propul. Power*, **13**, pp. 31–38.
- [9] Crook, A. J., Greitzer, E. M., Tan, C. S., and Adamczyk, J. J., 1993, "Numerical

- cal Simulation of Compressor Endwall and Casing Treatment Flow Phenomena," *ASME J. Turbomach.*, **115**(3), pp. 501–512.
- [10] Hoying, D. A., 1996, "Blade Passage Flow Structure Effects on Axial Compressor Rotating Stall Inception," Ph.D. thesis, Massachusetts Institute of Technology, Cambridge, MA.
- [11] Inoue, M., Kuroumaru, M., Yoshida, S., Minami, T., Yamada, K., and Furukawa, M., 2004, "Effect of Tip Clearance on Stall Evolution Process in a Low-Speed Axial Compressor Stage," *ASME Paper No. GT2004-53354*.
- [12] Bergner, J., Hennecke, D. K., and Hah, C., 2005, "Tip Clearance Variations of an Axial High-Speed Single Stage Transonic Compressor," Paper No. ISABE-2005-1096.
- [13] Scheidler, S., and Mundt, C., 2004, "Active Stability Control of the Compressor System in a Twin-Spool Turbofan Engine by Air Injection," *Proceedings of the Tenth International Symposium on Transport Phenomena and Dynamics of Rotating Machinery*, Honolulu, HI.
- [14] Wadia, A. R., Dhingra, M., Neumeier, Y., and Prasad, J. V. R., 2007, "Compressor Stability Management," *Proceedings of the 18th Symposium on Air-breathing Engines*, Beijing, China, Paper No. ISABE-2007-1352.
- [15] Shabbir, A., and Adamczyk, J. J., 2004, "Flow Mechanism for Stall Margin Improvement Due to Circumferential Casing Grooves on Axial Compressors," *ASME Paper No. GT2004-53903*.
- [16] Wilke, I., and Kau, H. P., 2004, "A Numerical Investigation of the Flow Mechanisms in a High Pressure Compressor Front Stage With Axial Slots," *ASME J. Turbomach.*, **126**(3), pp. 339–349.
- [17] Hathaway, M., 2002, "Self Recirculating Casing Treatment Concept for Enhanced Compressor," *ASME Paper No. 2002-30368*.
- [18] Iyengar, V., Sankar, L., and Niazi, S., 2005, "Assessment of the Self Recirculating Casing Treatment Concept to Axial Compressors," *AIAA Paper No. 2005-0632*.
- [19] Brignole, G., Kau, H. P., and Wilke, I., 2005, "Numerical Evaluation of Important Parameters Ruling the Effectiveness of Casing Treatments in Transonic Compressor," Paper No. ISABE-2005-1095.
- [20] Michon, G. J., Miton, H., and Ouayahya, N., 2005, "Experimental Study of the Unsteady Flows and Turbulence Structure in an Axial Compressor From Design to Rotating Stall Conditions," *Proceedings of the Sixth European Conference on Turbomachinery*, Lille, France, Paper No. 015-03/39.
- [21] Gourdain, N., Burguburu, S., and Leboeuf, F., 2005, "Rotating Stall Simulation and Analysis in an Axial Compressor," *ISABE Paper No. 2005-1138*.
- [22] Cambier, L., and Gazaix, M., 2002, "An Efficient Object Oriented Solution to CFD Complexity," *AIAA Paper No. 2002-0108*.
- [23] Jameson, A., Schmidt, W., and Turkel, E., 1981, "Numerical Solution of the Euler Equations by Finite Volume Methods Using Runge-Kutta Time Stepping Schemes," *AIAA Paper No. 81-1259*.
- [24] Jameson, A., 1991, "Time Dependent Calculation Using Multigrid With Application to Unsteady Flow Past Airfoils and Wings," *AIAA Paper No. 91-1596*.
- [25] Wilcox, D. C., 1988, "Reassessment of the Scale Determining Equation for Advanced Turbulence Models," *AIAA J.*, **26**(11), pp. 1299–1310.
- [26] Tyler, J. M., and Sofrin, T. G., 1962, "Axial Flow Compressor Noise Studies," *Soc. Automot. Eng. [Spec. Publ.]*, **70**, pp. 309–332.
- [27] Goncalves, E., 2001, "Implantation et Validation de Loi de Paroi Dans un Code Navier–Stokes," Ph.D. thesis, Ecole Nationale Supérieure de l'Aéronautique et de l'Espace, Toulouse, France.
- [28] Perrin, G., Leboeuf, F., and Dawes, W. N., 1992, "Analysis of Three-Dimensional Viscous Flow in a Supersonic Axial Flow Compressor Rotor, With Emphasis on Tip Leakage Flow," *Proceedings of the ASME Turbo Expo*, Cologne, Germany.
- [29] Billonnet, G., Couailler, V., Vuillot, A. M., and Heider, R., 1992, "Analysis of Three-Dimensional Viscous Flow Including Tip Clearance Phenomena in Axial Turbines," *Recent Advances in Compressor and Turbine Aerothermodynamics*, SFM, Paris, France.
- [30] Caro, J., Ferrand, P., Aubert, S., and Kozuch, L., 2003, "Inlet Conditions Effect on Tip Clearance Vortex in Transonic Compressors," *Proceedings of the Fifth European Conference on Turbomachinery*, Prague, Czech Republic.
- [31] Suder, K. L., and Celestina, M. L., 1994, "Experimental and Computational Investigation of Tip Clearance Flow in a Transonic Axial Compressor," *ASME Paper No. 94-GT-365*.
- [32] Lu, X., Chu, W., Zhu, J., and Wu, Y., 2006, "Experimental and Numerical Investigation of a Subsonic Compressor With Bend Skewed Slot Casing Treatment," *ASME Paper No. 2006-90026*.

# On the Coupling of Inverse Design and Optimization Techniques for the Multiobjective, Multipoint Design of Turbomachinery Blades

**Duccio Bonaiuti**

Advanced Design Technology Ltd.,  
Monticello House,  
45 Russell Square,  
London WC1B 4JP, United Kingdom

**Mehrdad Zangeneh**

Department of Mechanical Engineering,  
University College London,  
London WC1E 7JE, United Kingdom

*Automatic optimization techniques have been used in recent years for the aerodynamic and mechanical design of turbomachine components. Despite the many advantages, their use is usually limited to simple applications in industrial practice, because of their high computational cost. In this paper, an optimization strategy is presented, which enables the three-dimensional multipoint, multiobjective aerodynamic optimization of turbomachinery blades in a time frame compatible with industrial standards. The design strategy is based on the coupling of three-dimensional inverse design, response surface method, multiobjective evolutionary algorithms, and computational fluid dynamics analyses. The blade parametrization is performed by means of a three-dimensional inverse design method, where aerodynamic parameters, such as the blade loading, are used to describe the blade shape. Such a parametrization allows for a direct control of the aerodynamic flow field and performance, leading to a major advantage in the optimization process. The design method was applied to the redesign of a centrifugal and of an axial compressor stage. The two examples confirmed the validity of the design strategy to perform the three-dimensional optimization of turbomachine components, accounting for both design and off-design performance, in a time-efficient manner. The coupling of response functions and inverse design parametrization also allowed for an easy sensitivity analysis of the impact of the design parameters on the performance ones, contributing to the development of design guidelines that can be exploited for similar design applications.*

[DOI: 10.1115/1.2950065]

## Introduction

The increasing market pressure on turbomachinery manufacturers to reduce the development and design time and their associated costs is forcing turbomachinery industries to review their design systems and to consider alternative approaches for the aerodynamic design of turbomachine blades.

One approach that has been considered is based on automating the conventional design process by coupling an optimization method, CAD based blade generators and a computational fluid dynamics (CFD) code. Many companies in the turbomachinery industry from aeroengines (Sonoda et al. [1], Shahpar and Radford [2], Arnone et al. [3], Burguburu et al. [4]) to gas turbines (Kammerer et al. [5], Buche et al. [6]) to industrial applications (Sieverding et al. [7], Benini and Tourlidakis [8], Bonaiuti and Pediroda [9]) are trying to exploit the time saving potential of such a strategy and to integrate it into their design systems.

The major advantages of this approach are the reduction of man cost and the development of a design process, which relies more on a systematic methodology rather than on individual experienced designers.

Despite these attractive features, automatic optimization strategies present some drawbacks. The main one is the high computational cost, which is due to the large number of simulations required. This is related to the large number of geometrical parameters necessary to accurately represent the blade geometry and to the shape of the objective function to be optimized, which

is usually quite complex since there is not a direct relationship between the geometrical design parameters and the aerodynamic performance.

Turbomachine designs are usually multiobjective problems, where several performance parameters must be considered in the optimization process. Multiobjective optimization algorithms require an even larger number of simulations making such techniques impractical in an industrial framework. This problem becomes exacerbated when dealing with multipoint problems, where performance parameters must be evaluated at different operating conditions, thus requiring multiple CFD simulations for each configuration to analyze.

The high computational cost limits the use of automatic optimizations to 2D or simple 3D design problems in standard design processes, relegating the more complex optimizations only to research programs.

Another major drawback of optimization strategies is that at the end of each optimization, despite the large number of CFD simulations, it is difficult to derive a general know-how that can be exploited for similar design problems.

All these drawbacks are related to the parametric description of the blade, which is conventionally performed by means of purely geometrical parameters: The blade surface or blade camber and thickness distribution are usually parametrized by means of B-spline or Bezier control points.

A possible solution to this problem is to use a blade parametrization based on an inverse design method. Inverse design methods have been widely used for the aerodynamic design of both centrifugal (Zangeneh [10]) and axial (Watanabe and Harada [11]) turbomachines, proving this technique to be a valuable alternative to the iterative use of direct methods.

The main advantage of the inverse design approach is the closer relationship between the design parameters and the aerodynamic

Contributed by the International Gas Turbine Institute of ASME for publication in the JOURNAL OF TURBOMACHINERY. Manuscript received June 25, 2007; final manuscript received October 11, 2007; published online January 29, 2009. Review conducted by David Wisler. Paper presented at the ASME Turbo Expo 2006: Land, Sea and Air (GT2006), 2006, Barcelona, Spain, May 8–11, 2007.



flow field, and then a more direct control of the aerodynamic performance. Therefore, the use of an inverse method to parametrize the blade geometry in an optimization system reduces the complexity of the objective function with a potential reduction of the overall optimization time.

As also evident from the present work, the number of design parameters required to efficiently describe the blade shape is usually less than with a direct approach, further simplifying the design task.

Design specifications such as the design mass flow rate and the work coefficient or flow turning are directly imposed in the inverse design parameterization, while in the conventional approach such parameters have to be considered as constraints, which reduces the optimization convergence rate.

At the end of the design process, instead of the optimal combination of geometrical control points, the optimal blade loading distribution is obtained. This is a general result and can be applied to similar design problems without repeating the optimization process.

In this paper, an optimization strategy is presented where the blade parametrization is based on a three-dimensional inverse design method. The blade shape is described by a mix of geometrical and aerodynamic parameters. On the basis of the above considerations, such parametrization allows the use of a simplified representation of the optimization functions. In the present work, the response surface methodology (RSM) is used to generate an approximated model of the objective functions.

The use of such a strategy allows a simple and efficient sensitivity analysis of the impact of the single design parameters and of their interaction on the machine performance (Lecerf et al. [12], Bonaiuti et al. [13], Kawagishi and Kudo [14]). This feature is crucial to understand the flow physics behind the design problem, thus contributing to the increase of know-how.

After the RSM model is built, a multiobjective genetic algorithm is applied to the approximated response functions in order to determine the optimal set of design configurations (Pareto front). The designer can then choose a design solution considering the trade-off between different aerodynamic performances.

This optimization strategy was applied to the design of a centrifugal compressor stage and a single stage axial compressor. Design and off-design performances were analyzed and optimized in both cases.

The purpose of the present paper is to show the capability of this design strategy to perform the three-dimensional, multiobjective, multipoint aerodynamic optimization of turbomachinery components in a time frame compatible with industrial standards. The two examples also highlight how the design method can be used to develop design know-how, which can be exploited for similar applications.

## Description of the Design Strategy

**Optimization Process.** Generally speaking, a design process can be considered as the optimization of the functions correlating the performance parameters  $P_j$  to the design factors  $X_i$ :

$$P_j = P_j(X_i), \quad i = 1, N, \quad j = 1, M \quad (1)$$

In the present study, the design factors are the parameters used to define the blade geometry. The blade parametrization is performed by means of an inverse design method, described in the next paragraph. The performance parameters are the turbomachine performances whose actual value is given by an aerodynamic analysis, such as a CFD evaluation.

In the engineering design, statistical techniques have been widely used in order to build approximations of these functions. In the present work, the response surface methodology (RSM) (Myers [15]) coupled with the design of experiment (DOE) technique (Taguchi [16]) was applied.

The RSM approximates the objective functions with polynomi-

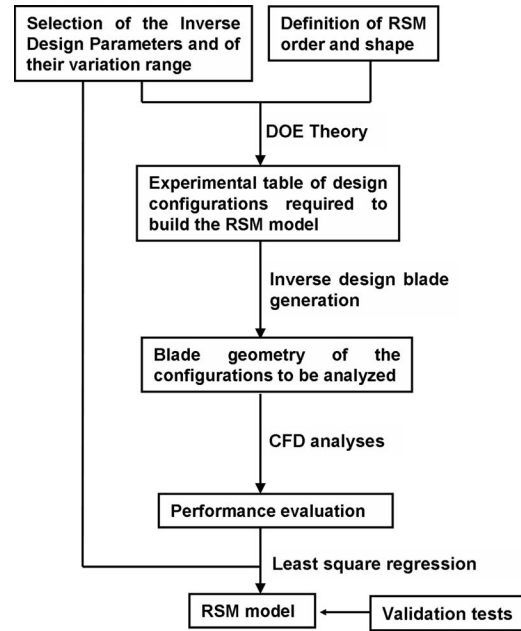


Fig. 1 Response surface model building scheme

als (response surfaces), whose order and shape must be chosen beforehand. In common practice, a first- or second-order polynomial function is usually used:

$$P_j = \beta_0^j + \sum_{i=0}^n \beta_i^j X_i + \sum_{i=0}^n \beta_{ii}^j X_i^2 + \sum_{i \neq j}^n \beta_{ij}^j X_i X_j \quad (2)$$

The polynomial coefficients  $\beta_0$ ,  $\beta_i$ ,  $\beta_{ii}$ , and  $\beta_{ij}$  are determined by means of a standard least-squares regression, which minimizes the sum of the square of the deviations of the predicted values from the actual ones for a set of points. The DOE theory provides the sampling points, at which to perform the tests, in order to minimize the necessary number of simulations. For numerical stability, the range of variation of the design parameters is usually scaled to span  $[-1, +1]$ .

In the present case, once the DOE theory has selected the configurations to be analyzed, the inverse design code is used to build the relative blade geometries and CFD analyses are performed to determine their performance parameters. The approximated response functions correlating the aerodynamic performance to the blade design parameters are then obtained by means of the least-squares regression.

The validity of the model is verified through the analysis of two parameters:  $R^2$  (the ratio of the model sum of squares to the total sum of squares) and  $R_{adj}^2$  ( $R^2$  adjusted to the number of parameters in the model).

A sketch of the process used to build the response surface model is reported in Fig. 1.

An important feature of the present optimization strategy is that more than one performance parameters can be analyzed simultaneously and they can even be selected or changed after the CFD analyses. The number of performance parameters to investigate does not affect the computational cost, which solely depends on the number of design parameters and on the selected RSM model.

From the analysis of the approximated model, it is possible to quantify the impact of the design parameters (coefficients  $\beta_i$  and  $\beta_{ii}$ ) and of their interactions (coefficients  $\beta_{ij}$ ) on each performance parameter.

After all the models have been created, a multiobjective genetic algorithm can be applied, imposing as competing objective functions two or more performance parameters. The convergence of this optimization process is very fast since the objective functions

are calculated using the RSM models and no further CFD evaluations are required. As a result, the Pareto front of the optimal solutions is determined. Then, depending on the design specifications, the best compromise between different performance parameters is chosen on the Pareto front.

**Blade Parametrization.** The commercial software TURBODESIGN<sup>-1</sup> is used to parametrically describe the blade geometry. TURBODESIGN<sup>-1</sup> (Zangeneh [17]) is a three-dimensional inviscid inverse design method, where the distribution of the circumferentially averaged swirl velocity ( $rV_\theta$ ) is prescribed on the meridional channel of the blade and the corresponding blade shape is computed iteratively.

The circulation distribution is specified by imposing the spanwise  $rV_\theta$  distribution at leading and trailing edges and the meridional derivative of the circulation  $drV_\theta/dm$  (blade loading) inside the blade channel. The input design parameters required by the program are the following:

- meridional channel shape in terms of hub, shroud, leading and trailing edge contours.
- normal/tangential thickness distribution.
- fluid properties and design specifications.
- inlet flow conditions in terms of spanwise distributions of total temperature and velocity components.
- exit  $rV_\theta$  spanwise distribution. By controlling its value, the Euler work coefficient (rotor) or the inviscid flow turning (stator) is controlled.
- blade loading distribution ( $drV_\theta/dm$ ). It is imposed at two or more span locations. The code then automatically interpolates spanwise to obtain the two-dimensional distribution over the meridional channel.
- stacking condition. The stacking condition must be imposed at a chordwise location between the leading edge and the trailing edge. Everywhere else the blade is free to adjust itself according to the loading specifications.

**CFD Analysis.** The CFD analyses were performed using the TRAF code (Arnone et al. [18]), a fully viscous, multigrid, multi-row code developed at the University of Florence. The space discretization is based on a cell-centered finite volume scheme and the system of governing equations is advanced in time using the explicit four-stage Runge–Kutta scheme. Implicit residual smoothing, local time stepping, and multigrid technique are used to reduce the computational cost. In this analysis, the algebraic model of Baldwin–Lomax was used for the turbulence closure.

Boundary conditions are imposed on the solid walls, on the periodic boundaries, at inlet (total pressure, total temperature, and flow angles), and at the outlet (static pressure at the hub) of the computational domain.

The code has been widely validated for the analysis of both centrifugal (Arnone et al. [19], Bonaiuti et al. [20]) and axial (Arnone et al. [21,22]) compressors.

## Analysis of a Centrifugal Compressor Stage

**Description of the Test Case.** The centrifugal compressor under consideration is composed of a shrouded impeller and of a vaneless diffuser. A sketch of the compressor is shown in Fig. 2, while the main geometrical and design specifications are reported in Table 1.

**Optimization Target and Design Parametrization.** The goal of this analysis is to study the effect of some of the major aerodynamic and geometrical parameters on the compressor design and off-design performance and to determine their optimal combination. The following performance parameters were considered:

- efficiency at design point  $\eta_{des}$  and peak efficiency  $\eta_{PE}$ . The efficiency values were calculated in the middle of the vaneless diffuser (see Fig. 1), in order to take into account the

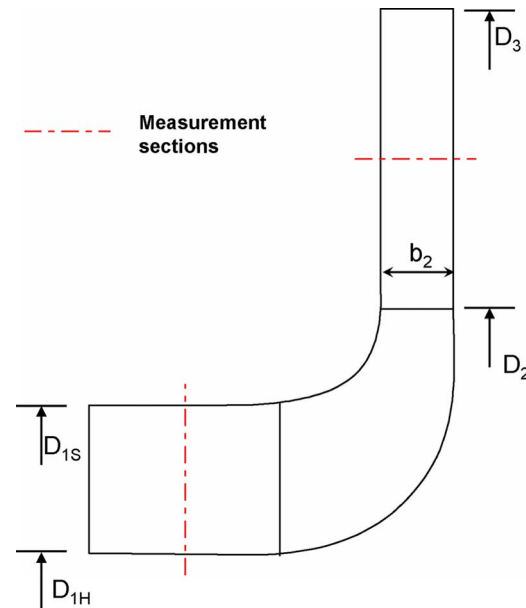


Fig. 2 Sketch of the centrifugal compressor stage

diffuser mixing losses. It was not possible to use a downstream station since the occurrence of wall recirculations in some configurations spoiled the efficiency calculation, thus compromising the validity of the RSM model.

- efficiency at 80% of the design point mass flow rate (parameter  $\eta_{80}$ ). Since it is not possible to identify the stall margin by means of steady-state CFD analyses, this parameter was used to characterize the aerodynamic performance at low mass flow rates.
- the *choke margin*, defined as  $(\Phi_{ch} - \Phi_{des})/\Phi_{des}$ .
- the work coefficient at design point  $\tau_{des}$ . The Euler work coefficient is imposed in the blade parametrization. This parameter was monitored to control if viscous effects significantly affect the value of the actual work coefficient.

The sizing of the compressor was considered optimized and the one-dimensional design parameters specified in Table 1 were not altered during the optimization. The analysis was then focused on the blade loading, stacking condition, and meridional channel shape.

Table 1 Geometrical data and design specifications of the centrifugal compressor

Geometrical specifications	
Impeller type	Shrouded
Impeller exit diameter $D_2$	500 mm
Inlet hub diameter $D_{1H}$	175 mm
Inlet shroud diameter $D_{1S}$	372 mm
Diffuser exit diameter $D_3$	900 mm
Impeller exit width $b_2$	42 mm
Blade number	17
Design specifications	
Rotational speed	9550 rpm
Inlet total temperature	288 K
Inlet total pressure	101,325 Pa
Design flow coefficient $\Phi_{des}$	0.1416
Design work coefficient $\tau_{des}$	0.63
Peripheral Mach number $M_u$	0.735

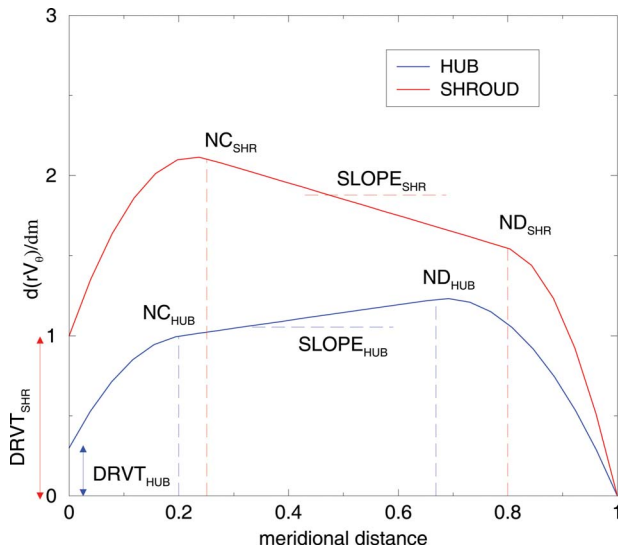


Fig. 3 Blade loading parametrization

The blade loading was controlled by specifying the distribution of  $drV_{\theta}/dm$  on the hub and shroud sections. Both distributions were parametrized by means of the three-segment method, which employs a combination of two parabolic curves and an intermediate linear line. Four parameters are required to control each distribution (see Fig. 3):

- NC: intersection between the first parabolic distribution and the linear segment.
- ND: intersection between the linear segment and the second parabola.
- SLOPE: slope of the linear line. This parameter controls the loading distribution type: A positive value leads to a fore-loaded distribution, and a negative one leads to an aft-loaded distribution.
- DRVT: blade loading at the leading edge. This parameter controls the flow incidence and then the inlet blade angle. If set to zero, a zero-incidence condition is imposed at the design mass flow rate.

A total of eight parameters were then used for the control of the blade loading. A linear stacking condition was imposed at the trailing edge of the blade. Its slope was allowed to vary from  $-10$  deg to  $+10$  deg, as shown in Fig. 4.

The meridional channel was parametrized by means of cubic splines. The control points used to describe the hub and shroud contours are shown in Fig. 5. Four meridional channel parameters were analyzed:

- the axial length. The control points were simultaneously shifted axially in order to change its value. The two extreme distributions are plotted in Fig. 5.
- the leading edge sweep angle. A variation range from  $15$  deg to  $45$  deg was considered.

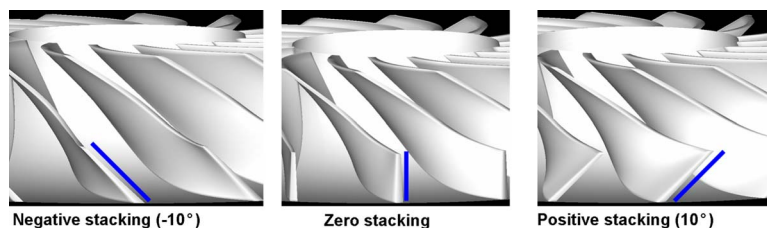


Fig. 4 Stacking parametrization

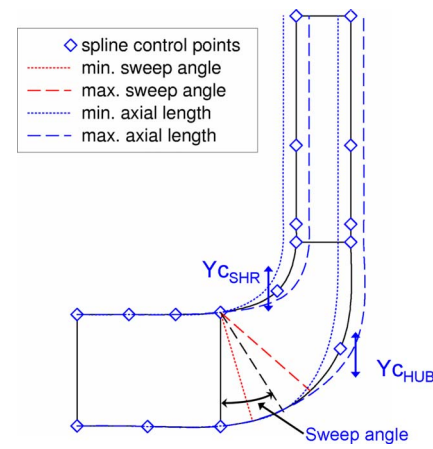


Fig. 5 Meridional channel parametrization

- the radial position of the two cubic spline control points inside the impeller region (parameters  $Y_{C_{HUB}}$  and  $Y_{C_{SHR}}$  in Fig. 5).

The impeller blade thickness distribution was not altered during the analysis.

**Design Strategy and Computational Details.** The analysis was split into two parts: First, the blade loading and stacking parameters were investigated and an optimal configuration was selected. Then, centering the design space on the optimized configuration, the effect of the four meridional channel parameters was studied.

The main reason of this approach was to simplify the analysis of the results at the cost of losing the effect of the interactions between the meridional channel parameters and the blade loading ones. Furthermore, in the authors' experience, the RSM model tends to lack of reliability when dealing with too many design parameters whose number should be limited to less than 10.

For the first analysis, a linear approximation model was used, where only some selected interactions were included in the model. Considering the large number of design parameters involved in this study, a simple linear model was considered more appropriate both for simplifying the analysis and for reducing the number of simulations required to generate the DOE database. As a drawback, the quadratic term is neglected in the response surface functions.

The second analysis was performed considering a full quadratic response surface where all the interactions were taken into account.

In order to create the two databases, the DOE theory provided the set of configurations (experimental table) to be analyzed, which consisted of 33 tests for the first analysis and of 25 tests for the second one.

For each configuration to be analyzed, CFD calculations were



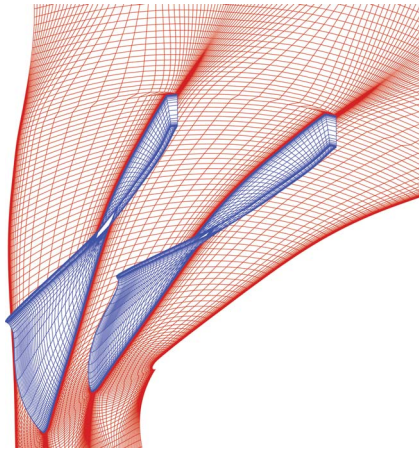


Fig. 6 3D view of the compressor grid

carried out for a predefined set of backpressures in order to describe the whole characteristic curve. Interpolations were then performed to obtain the values of the performance parameters of interest.

All the configurations were analyzed using an H-type grid with  $133 \times 45 \times 45$  grid points in the streamwise, pitchwise, and spanwise directions, respectively. Grid clustering was imposed close to the blade/walls in order to have a  $Y^+ \approx 1$ . An example of computational grid is shown in Fig. 6.

**Analysis of the Results.** All the approximated models in both the analyses presented high values of  $R^2$  (above 99%) and of  $R^2_{adj}$  (95–99%), thus confirming that, despite its simplicity, the present approach is able to well represent the design problem.

As expected, the work coefficient is not significantly affected by the design parameters and among the tested configurations its maximum variation was lower than 1%.

All the configurations presented a flat efficiency curve shape around the design point, leading the analyses of  $\eta_{des}$  and of  $\eta_{PE}$  almost to coincide. Only the latter parameter was then considered in the postprocessing.

For both these analyses, once the response surfaces were created, a multiobjective optimization was performed considering as competing objective functions the efficiency at 80% of design point  $\eta_{80}$  and the choke margin. Therefore, the resulting Pareto front consists of configurations maximizing the choke, the stall margin or a compromise between the two.

Different choices of the objective functions would have led to optimized configurations with different characteristics (i.e., maximizing the peak efficiency).

The Pareto front obtained from the first analysis is shown in Fig. 7. The axes report the percent variation of the performance parameters with respect to the baseline configuration. An optimal configuration providing a balanced improvement in both the performances was selected and used as baseline for the second analysis.

Figure 8 reports the Pareto front of the second analysis. The choice of the optimal solution on the Pareto front depends on the specific impeller requirements. In the present case, the choke margin improvement achieved in the first analysis was considered satisfactory and the final configuration was chosen in order to maximize the efficiency  $\eta_{80}$ , without penalizing the choke.

The comparison of the geometrical and design parameters between the final design and the initial baseline configuration is shown in Fig. 9, while Fig. 10 reports the comparison of the efficiency curves.

With respect to the baseline configuration, the final design pre-

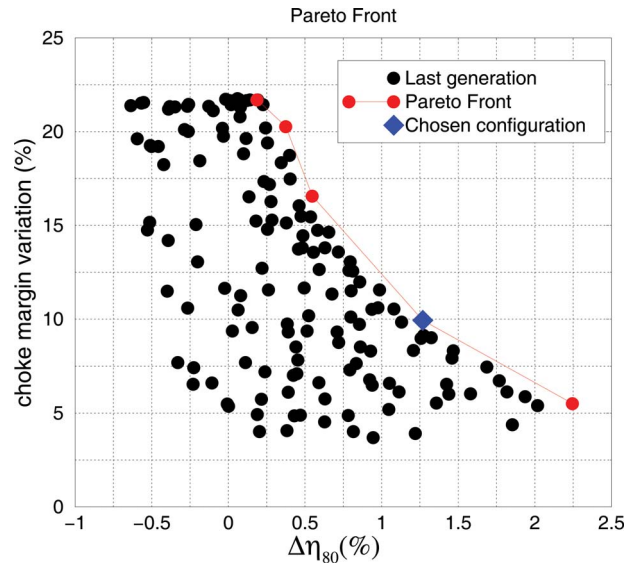


Fig. 7 Pareto front of the first analysis

sents a higher efficiency (around 3% at design point) and a wider choke margin. Even if the stall was not investigated in detail, the higher efficiency at low mass flow rates indicates a better stall margin.

Figures 11–13 report the comparison of the secondary flow development on the blade pressure and suction side and on the impeller casing, at design point.

The baseline configuration is characterized by a strong secondary flow on the blade pressure side (see Fig. 11), which, once it reaches the impeller casing, moves toward the suction side (see Fig. 13) and mixes with the secondary flow on the blade suction side (Fig. 12). As a result, a separation takes place on the shroud suction side corner, as shown in Fig. 13. Such recirculation tends to increase at low mass flow rates and extends to the downstream diffuser.

The redesigned configuration presents a much reduced secondary flow development and the corner separation has been completely suppressed.

In order to understand the improvements in performance and in the flow field, it is useful to analyze the surface response models

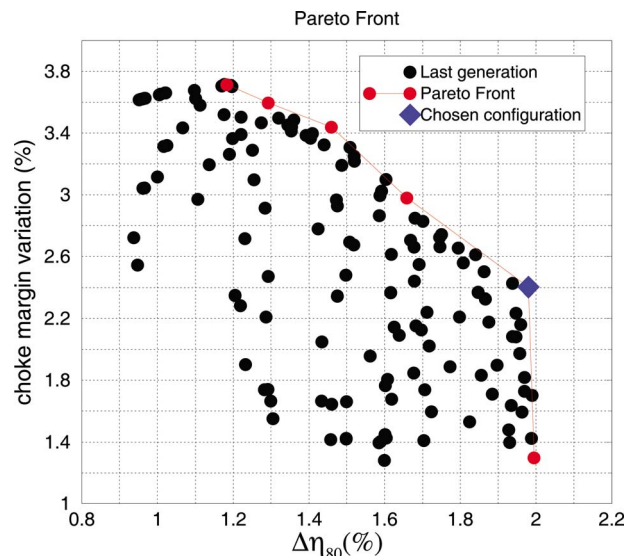


Fig. 8 Pareto front of the second analysis

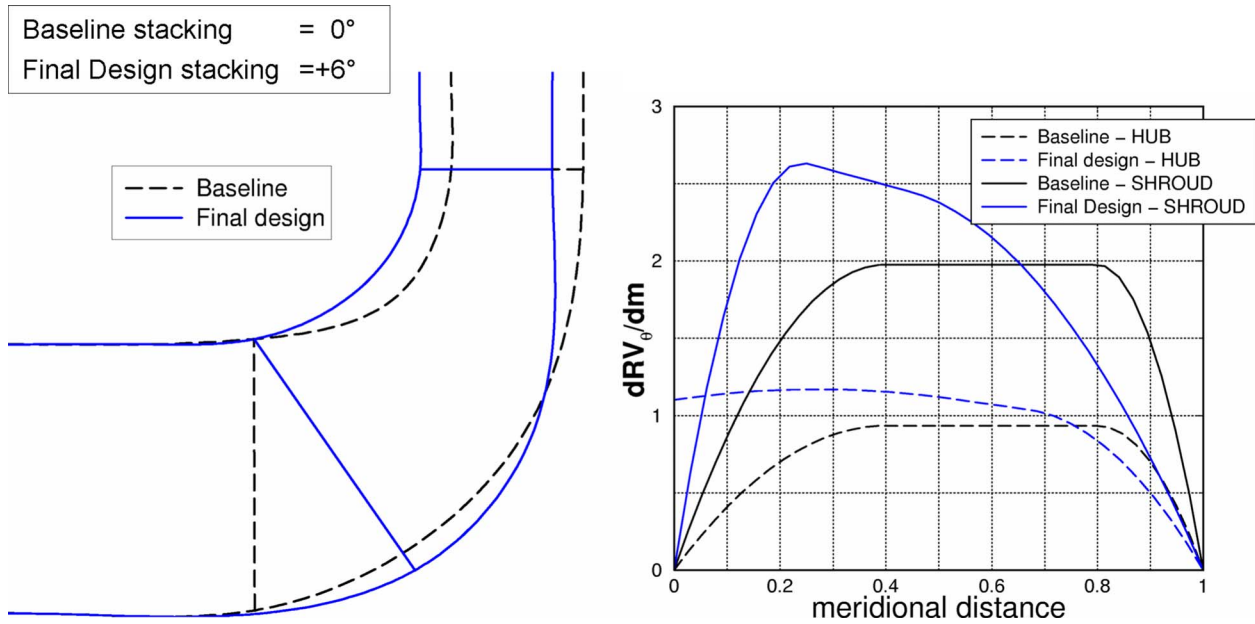


Fig. 9 Comparison of the meridional contour and blade loading distribution between the baseline and final design

and to identify the impact of each design parameter on the performance ones. Figure 14 reports the main effect of the first analysis design parameters on the compressor performances. Such graphs are built by setting all the other design parameters to the default value and plotting the dependence of the performance parameters

from a single design factor.

The blade loading parameters suggest that an aft-loaded distribution at the hub (high values of  $NC_{hub}$ ,  $ND_{hub}$ , and  $SLOPE_{hub}$ ) and a fore-loaded one at the shroud (small values of  $NC_{shr}$ ,  $ND_{shr}$ , and  $SLOPE_{shr}$ ), coupled with a positive stacking, contribute to improve the compressor efficiency (both  $\eta_{PE}$  and  $\eta_{80}$ ).

This is in agreement with the previous work of one of the authors (Zangeneh et al. [23]), where it was shown how such a loading distribution and stacking condition contribute to suppress the secondary flow, and then to increase the efficiency, of an impeller with characteristics similar to the present one.

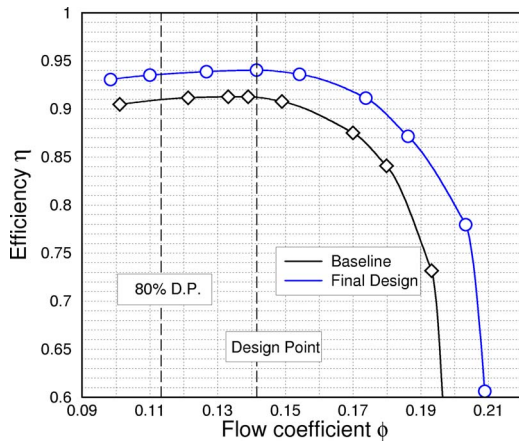


Fig. 10 Comparison of the baseline and final design efficiency curves (CFD analysis)

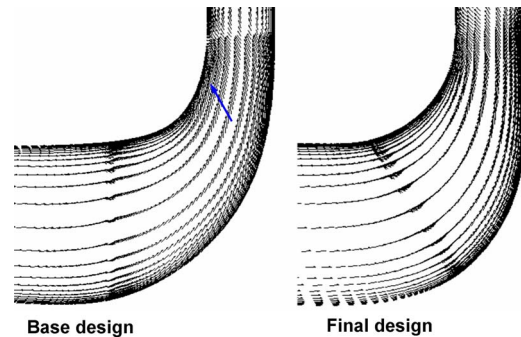


Fig. 12 Secondary flow on the blade suction side at design point

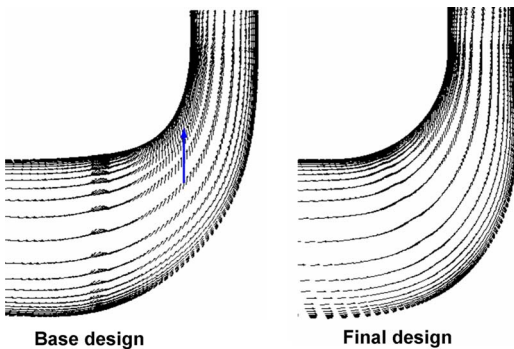


Fig. 11 Secondary flow on the blade pressure side at design point

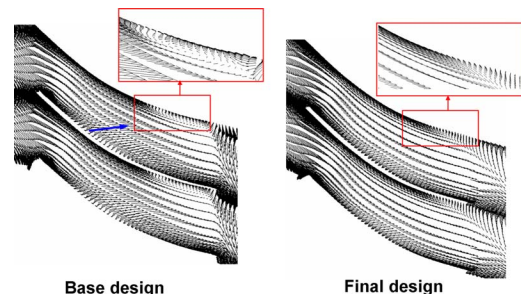
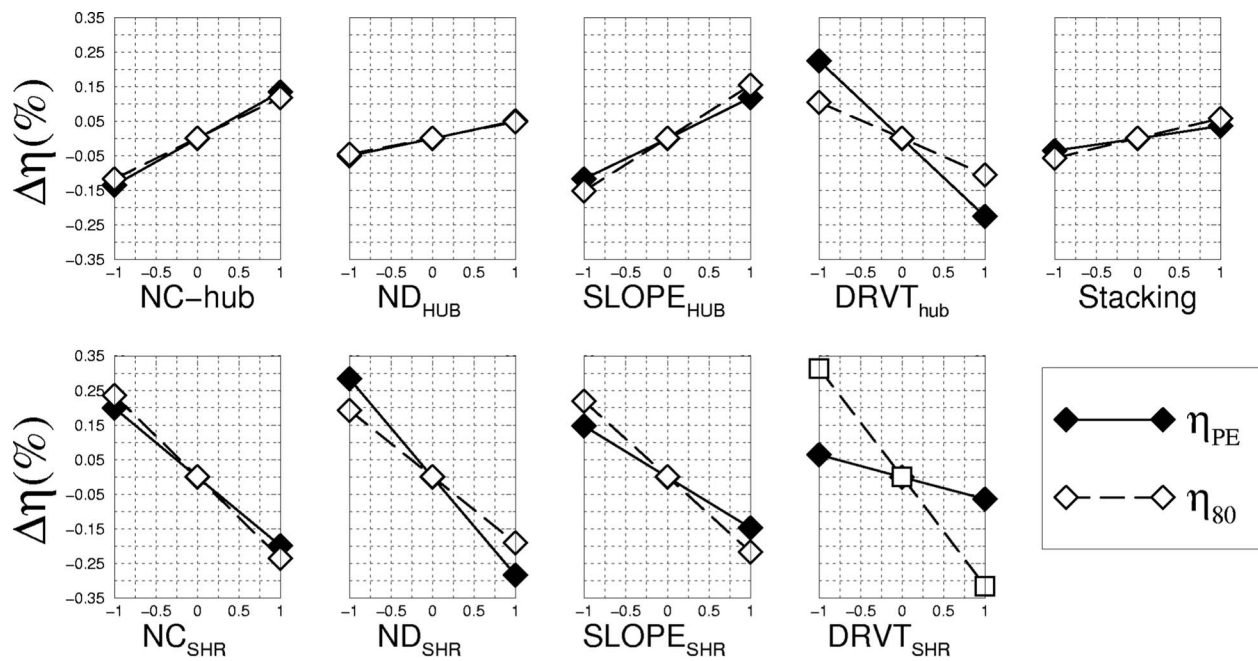
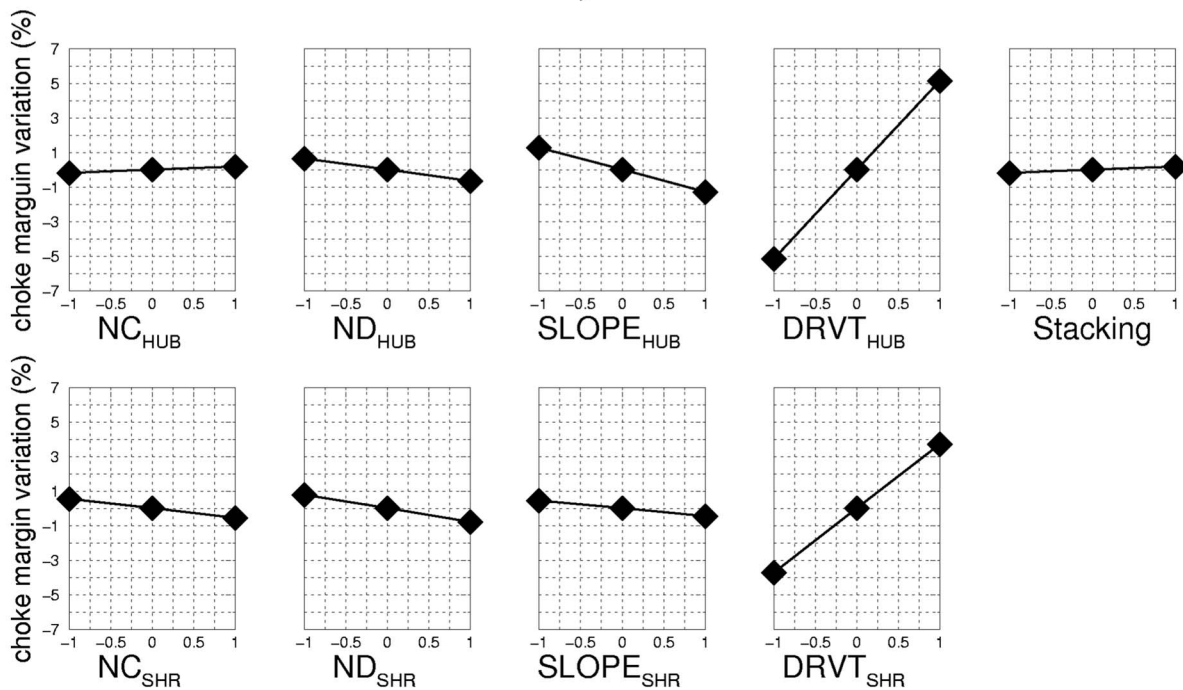


Fig. 13 Secondary flow on the tip section at design point



a)



b)

Fig. 14 Main effect of blade loading and stacking parameters on the peak and stall efficiencies (a) and the choke margin (b)

Positive values of hub and shroud leading edge loadings ( $DRVT_{hub}$  and  $DRVT_{shr}$ ) deteriorate both the peak efficiency  $\eta_{PE}$  and the efficiency at 80% of design point  $\eta_{80}$ .

A high value of  $DRVT_{hub}$  increases the pressure coefficient gap between the hub and the shroud of the pressure side (see Fig. 16), thus increasing the secondary flow on the blade pressure side (see also Zangeneh et al. [23]), especially on the inlet part of the blade.

A positive  $DRVT_{shr}$  is more harmful at low mass flow rates (see effect on  $\eta_{80}$ ), since it increases the local flow incidence, which may cause separation on the shroud suction side and lead to an early impeller stall.

As expected, Fig. 14(b) indicates that  $DRVT_{hub}$  and  $DRVT_{shr}$  are the most important parameters affecting the choke margin: High values of such parameters reduce the inlet blade angle and



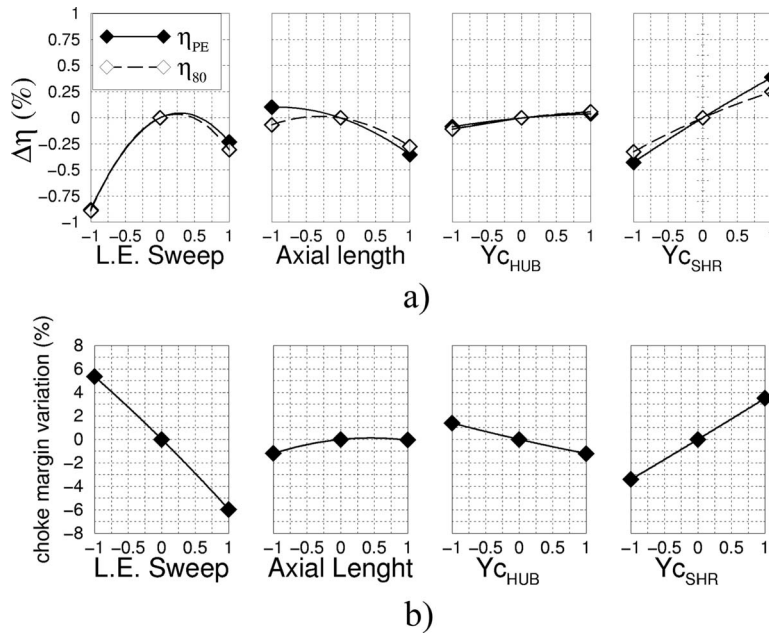


**Fig. 15 Main effects of the meridional channel parameters on peak and stall efficiencies (a) and choke margin (b)**

then increase the impeller throat area. Fore-loading the blade also contributes to enlarge the throat area and then to increase the choke margin, while the stacking condition does not provide a significant contribution.

As shown in Fig. 9, the final configuration presents a high fore-loading at the shroud and a more aft-loaded hub, with high incidence only on the hub section. This resulted to be the best compromise in order to improve both the choke margin and the efficiency at low mass flow rates.

From the analysis of the meridional channel parameters (see Fig. 15(a)), it can be observed that a reduced axial length with high leading edge sweep angle and steeper hub and shroud contours (higher values of  $Y_{c_{hub}}$  and  $Y_{c_{shr}}$ ) has a beneficial effect on the impeller efficiency. The reason is that the resulting meridional shape leads to an overall flow path with reduced streamline curvature. According to the secondary flow theory (Cumpsty [24]), high streamline curvatures are responsible for the secondary flow development on the blade surfaces, which plays an important role in the flow field of the impeller under investigation.

On the other hand, a high value of the leading edge sweep angle

reduces the throat area, thus penalizing the choke margin (see Fig. 15(b)). Variations of  $Y_{c_{hub}}$  and  $Y_{c_{shr}}$ , which increase the channel size, also contribute to increase the choke margin, while the axial length does not affect it significantly.

The final design, according to the optimal point selected on the Pareto front, presents meridional channel modifications which improve the efficiency (higher sweep, reduced axial length, and high values of  $Y_{c_{hub}}$  and  $Y_{c_{shr}}$ ), without penalizing the choke margin.

### Analysis of an Axial Compressor Stage

**Description of the Test-Case.** The axial compressor under investigation is the HP9 single-stage compressor (Ginder and Harris [25]). A sketch of the compressor is shown in Fig. 17, while the main design and geometrical specifications are reported in Table 2.

**Optimization Target and Parametrization.** The purpose of this study is to perform a simplified analysis of the effect of the rotor and stator loading distributions on the compressor performance at design and off-design conditions. The goal is to determine a loading distribution type that can be used as a reference for the design of similar axial compressor stages.

In analogy with the centrifugal compressor analysis, both the rotor and stator blade loadings were imposed only at the hub and shroud. A linear interpolation was then performed to obtain the loading distribution over the meridional channel.

In order to simplify the analysis, each loading distribution was controlled by means of a single parameter: NC and ND were fixed and the parameter SLOPE was allowed to vary from a negative

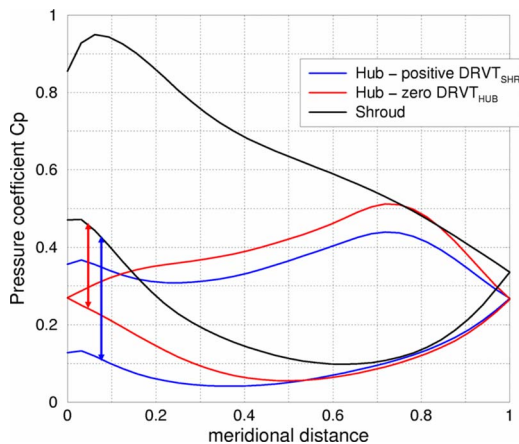


**Fig. 16 Effect of hub leading edge loading on the blade distribution of the reduced pressure coefficient at design point**

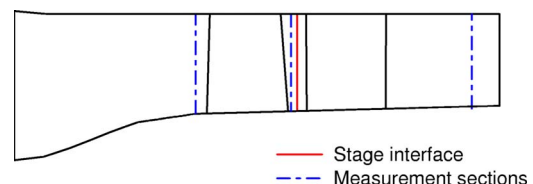


**Fig. 17 Sketch of the HP9 axial compressor stage**

**Table 2 Geometrical data and design specification of the HP9 compressor stage**

Geometrical specifications	
Outer diameter	518.2 mm
Hub diameter (rotor inlet)	436.6 mm
Hub diameter (diffuser exit)	440.5 mm
Rotor blade number	41
Stator blade number	73
Rotor tip clearance	0.25% of blade height
Design specifications	
Rotational speed	9626.5 rpm
Inlet total temperature	288 K
Inlet total pressure	101,325 Pa
Stator exit swirl	0 deg
Rotor Reynolds number	$0.7 \times 10^6$
Design point flow coefficient $\Phi_{des}$	0.549
Design point work coefficient $\tau_{des}$	0.355
Degree of reaction	$\approx 0.8$

value to a positive one in order to determine the fore-loading or aft-loading of the section (see Fig. 18(a)). Four parameters were then necessary to determine the loading of the four sections (rotor hub, rotor shroud, stator hub, and stator shroud).

The inter-row vortex distribution was also modified in the analysis: Starting from a spanwise constant  $rV_\theta$  distribution (free vortex), a linear variation was allowed (see Fig. 18(b)), while keeping unaltered the value of the rotor Euler work. The slope of the inter-row  $rV_\theta$  distribution (angle  $\alpha_{RVT}$  in Fig. 18(b)) could vary from a negative value (more work performed at the hub than at the shroud) to a positive one (specific work increasing along the span).

Both rotor and stator were radially stacked at midchord. The meridional channel contour and the thickness distributions were not changed during the analysis. A total of five parameters were then investigated in this analysis.

In order to characterize the design and off-design performances, of the compressor, the following parameters were monitored:

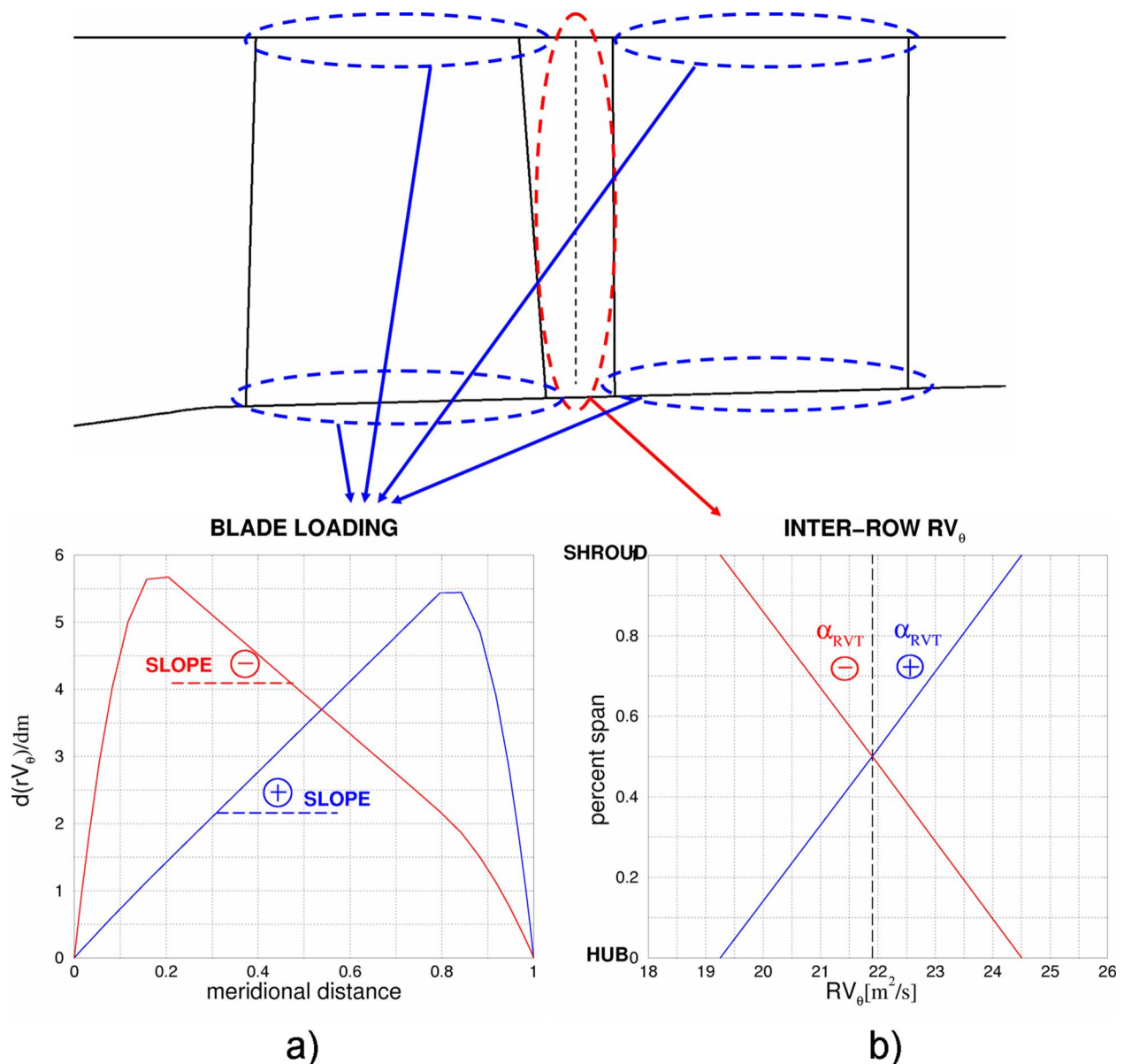


**Fig. 18 (a) Blade loading parametrization; (b) inter-row  $RV_\theta$  parametrization**

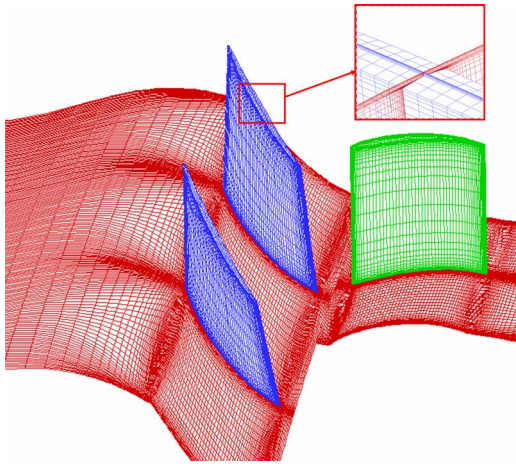


Fig. 19 3D view of the computational grid

- rotor efficiency at 90%, 100%, and 110% of the design mass flow rate
- stator loss coefficient at 90%, 100%, and 110% of the design mass flow rate
- stage efficiency at 90%, 100%, and 110% of the design mass flow rate
- work coefficient at design point  $\tau_{des}$

Efficiency and loss coefficient values were calculated using the measurement sections shown in Fig. 17.

**Design Strategy and Computational Details.** The analysis was performed using a full quadratic RSM model, which led to an experimental table of 28 configurations.

For each configuration, stage CFD analyses were carried out for a set of backpressures to describe the operating range from the choke to 80% of the design mass flow rate, in order to allow the calculation of the performance parameters via interpolation.

The physical domain was subdivided into two blocks: the first one representing the rotor domain, and the second one representing the stator. A computational grid with  $129 \times 61 \times 53$  grid points was used for the rotor domain and one with  $129 \times 53 \times 53$  grid points for the stator one. The mixing plane approach was used to set the boundary conditions at the interface between the two blocks.

Grid clustering was applied in order to have a  $Y^+ \approx 1$  on the walls and blades. A 3D view of the grid is shown in Fig. 19. Eight cells were posed inside the rotor tip clearance region.

**Analysis of the Results.** High values of  $R^2$  (above 99%) and of  $R^2_{adj}$  (above 97%) were obtained also in this analysis, further confirming the validity of the proposed design strategy.

The main effects of the design factors on the single performance parameters, resulting from the analysis of the response surfaces, are shown in Figs. 20–23. Only the design parameters that have a significant impact on the specific performance are reported.

Figure 20 highlights that fore-loading the rotor (both at hub and shroud) improves the rotor efficiency, while from Fig. 21, it can be noticed that fore-loading the stator has a beneficial effect in reducing the stator losses. This is effective at all the operating conditions and also results in an improvement of the compressor efficiency (see Fig. 22).

A negative slope of the inter-row  $rV_\theta$  (higher loading at the hub than at the shroud) reduces the overall work performed at the rotor shroud section, thus reducing the tip clearance flow. Its effect cannot be detected at the compressor interstage (no effect on rotor efficiency) but at the stage exit where the flow mixing is completed and the mixing losses are considered. Such a distribution then reduces the stator loss coefficient (see Fig. 21) and increases the stage efficiency (see Fig. 22), especially at low mass flow rates, where the clearance flow is more extended.

Figure 22 reports the effect of the design parameters on the compressor efficiency. Since the compressor is characterized by a high degree of reaction, the rotor is the more critical component and it has a dominant role in determining the stage efficiency.

The rotor loading distribution also affects the work coefficient. Figure 23 reports the dependency of the design point work coefficient from the hub and shroud loading parameters. Fore-loading the blade reduces the adverse pressure gradient in the rear part of the blade suction side, leading to a more gradual flow deceleration. This limits the boundary layer growth and reduces the possibilities of flow separation in the trailing-edge region. Consequently, the viscous flow deviation at the rotor exit is smaller and the resulting work coefficient is closer to the Euler value than was imposed in the inverse design parametrization of the blade.

This also explains the effect of the rotor loading on the stator loss coefficient (see Fig. 21): Considering the same mass flow rate, the rotor exit absolute flow angle (and then the stator incidence) is higher for a fore-loaded configuration. As a result, the

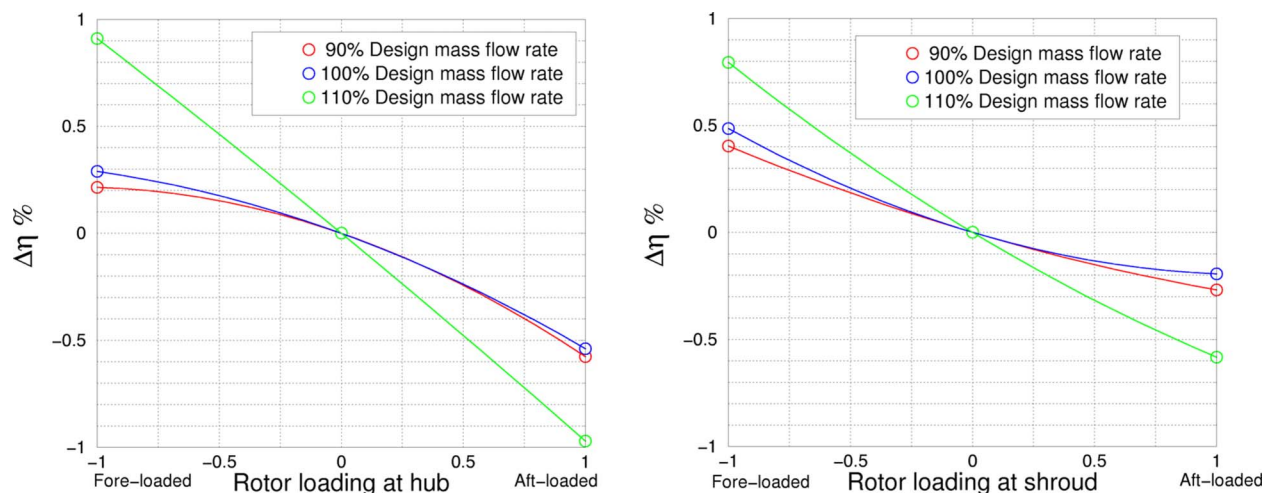


Fig. 20 Effect of the design parameters on the rotor efficiency



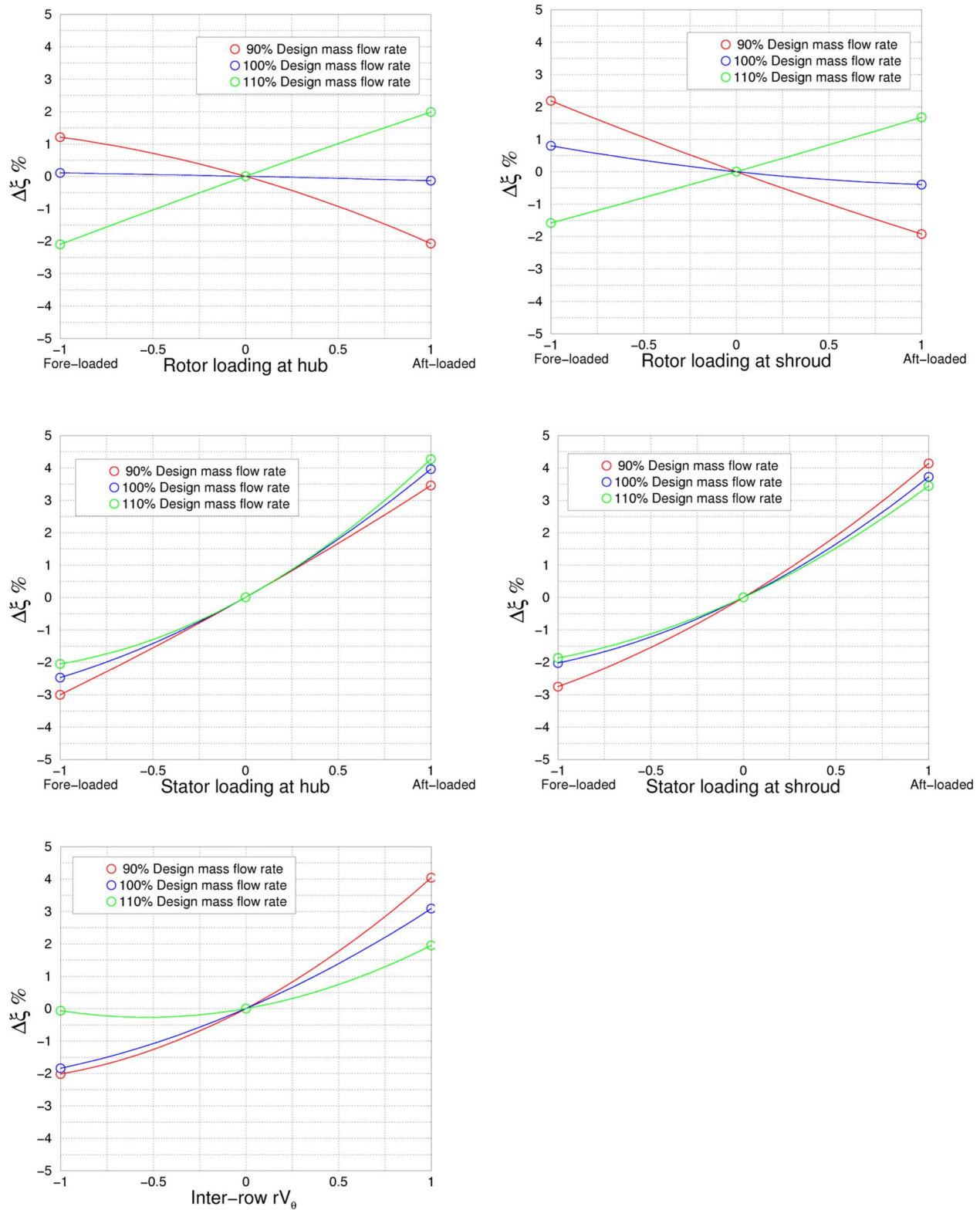


Fig. 21 Effect of the design parameters on the stator loss coefficient

stator loss coefficient curve is shifted toward higher mass flow rates, as reported in Fig. 24. A fore-loaded rotor then leads to lower stator losses at high mass flow rates and vice versa, as shown in Fig. 21. From Fig. 24, it can also be noticed that the rotor loading does not affect the minimum value of the loss

coefficient.

The multiobjective genetic algorithm was run imposing as competing objective functions the compressor efficiency at 90% and at 110% of design point mass flow rate. The work coefficient was not constrained during the optimization; its value was then ad-

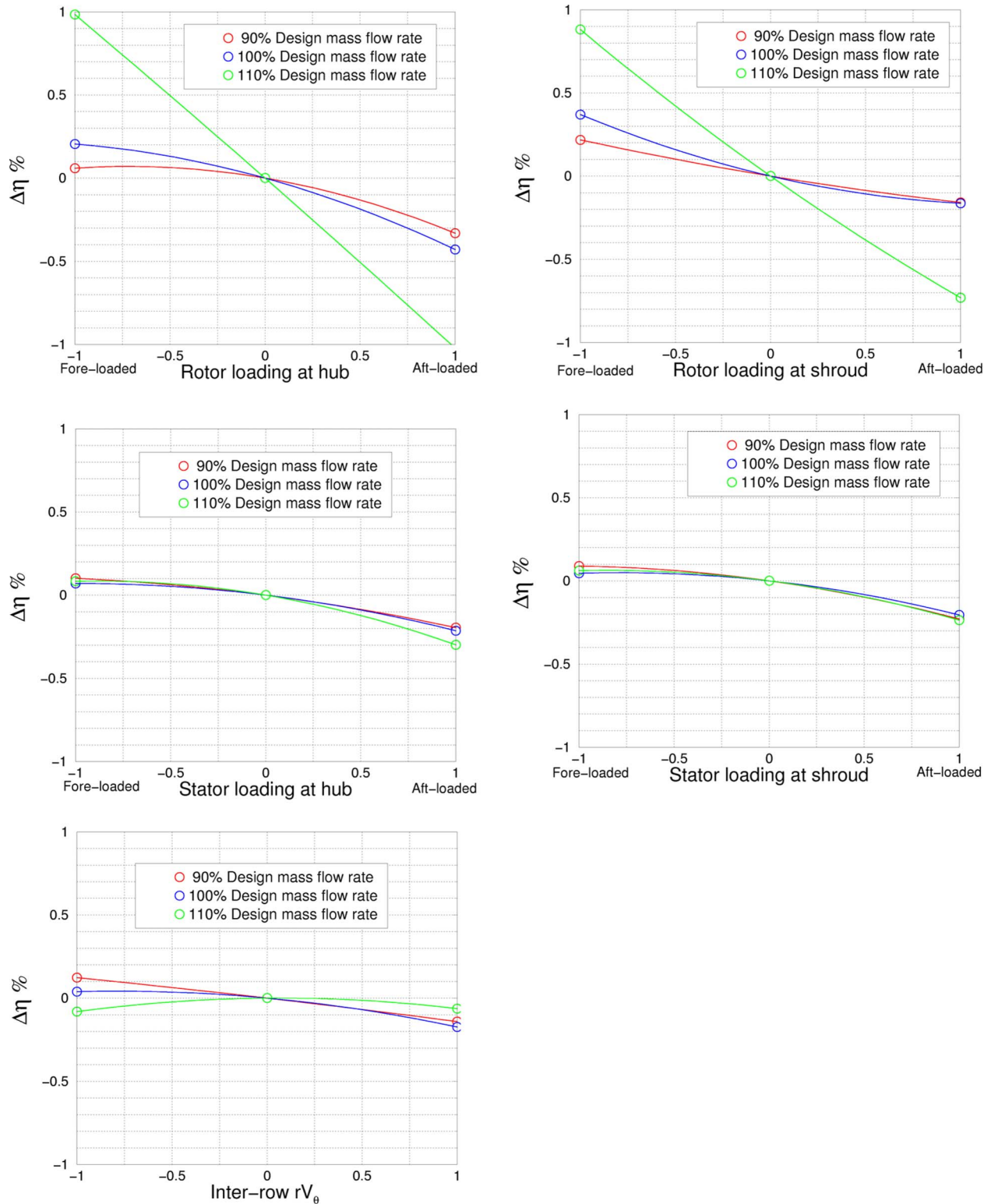


Fig. 22 Effect of the design parameters on the stage efficiency

justed afterwards for the optimized configuration by reducing the  $rV_\theta$  value in the design parametrization. The resulting Pareto front and the chosen configuration are reported in Fig. 25.

The final design is characterized by a high-loading of both stator and rotor and by a negative value of the inter-row  $rV_\theta$  slope.

The comparison of the loading distributions with respect to the baseline configuration is shown in Fig. 26, while Fig. 27 reports the comparison of the rotor blade pressure distributions at different span sections. Similar results were found for the stator.

The optimized configuration presents pressure/velocity distribu-

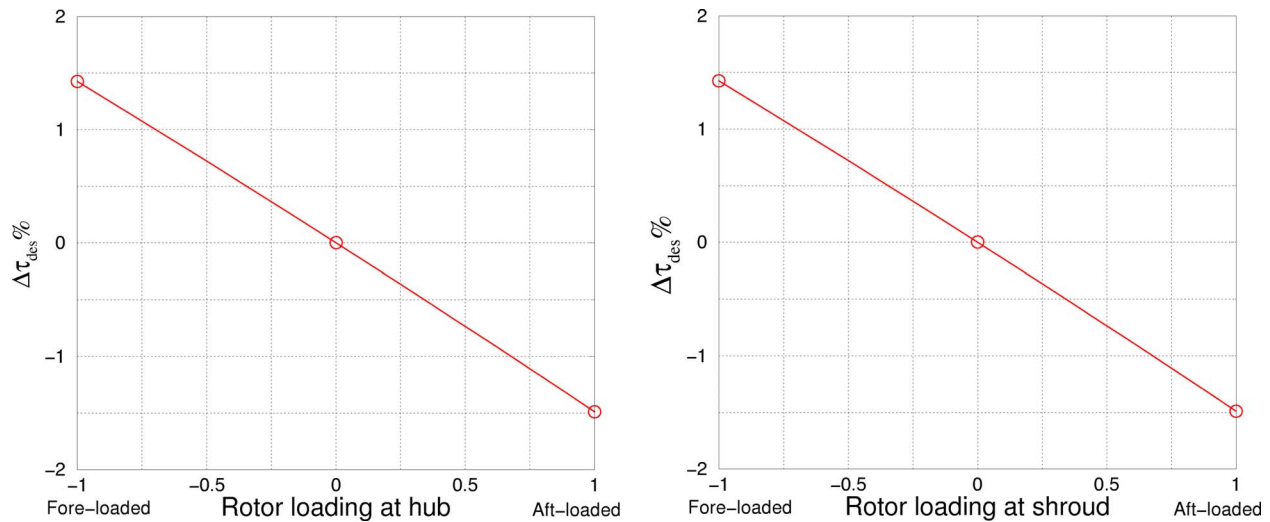


Fig. 23 Effect of the design parameters on the rotor work coefficient

tions similar to the ones of the controlled diffusion airfoils (CDAs): The suction side has a peak Mach number in the first 10–15% of the chord followed by a steep deceleration that becomes smoother toward the trailing edge, while a flat Mach number distribution characterizes the blade pressure side.

The comparison of the compressor performance between the baseline and the final design are reported in Fig. 28. The optimized configuration presents higher stage efficiency (about 2.3% at 110% design point and 1.3% at 90% design point) and a wider operating range.

The improvements in efficiency and flow range brought by the use of fore-loaded pressure distributions are in agreement with recent 2D studies (Sieverding et al. [7], Buche et al. [26]) and 3D studies (Terauchi et al. [27]) on axial compressors.

The averaged flow angle at the compressor exit, also shown in Fig. 28, is smaller for the optimized configuration over the whole operating range, further confirming that the fore-loading of the blade, in this case of the stator, leads to a better flow guidance.

Since the compressor is characterized by a small work coefficient, no extended secondary flows were found in any of the analyzed configurations. The most critical region is the hub suction side of the rotor, near the trailing edge. As shown in Fig. 29, the

final design presents a smaller secondary flow development where the hub corner separation is almost completely suppressed.

### Conclusions

The paper presents a design strategy based on the coupling of multiobjective optimization algorithms, RSM, and CFD analyses, where the blade parametrization is performed by means of a three-dimensional inverse design method. As also confirmed by the case studies reported in this paper, this design method is capable of performing the three-dimensional, multipoint, multiobjective optimization of turbomachinery blades in a time frame compatible with industrial standards.

The use of an inverse-based blade parametrization reduces the complexity of the correlations between design parameters and performance parameters, which can be represented by simple response surface models. Optimization algorithms can then be directly applied to the RSM models.

Such an approach leads to a substantial reduction of the computational cost, since CFD analyses must be performed only to evaluate the set of configurations (experimental table) that are required to build up the approximation models. Once the RSM function is selected, the total number of configurations to analyze

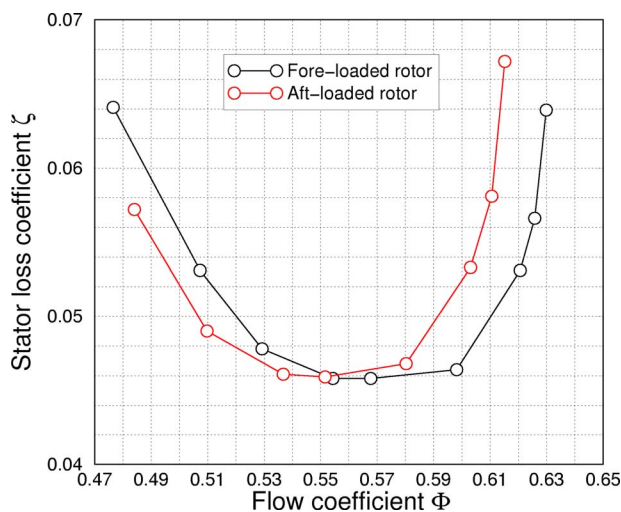


Fig. 24 Comparison of the stator loss coefficient curve between two configurations differing only for the rotor loading

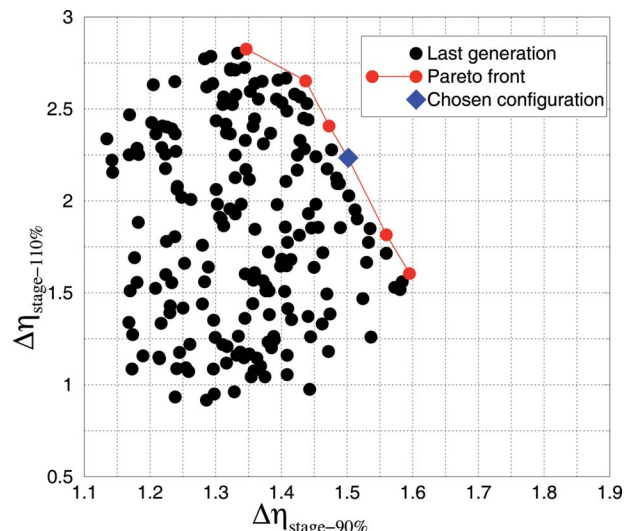


Fig. 25 Pareto front of the axial compressor analysis



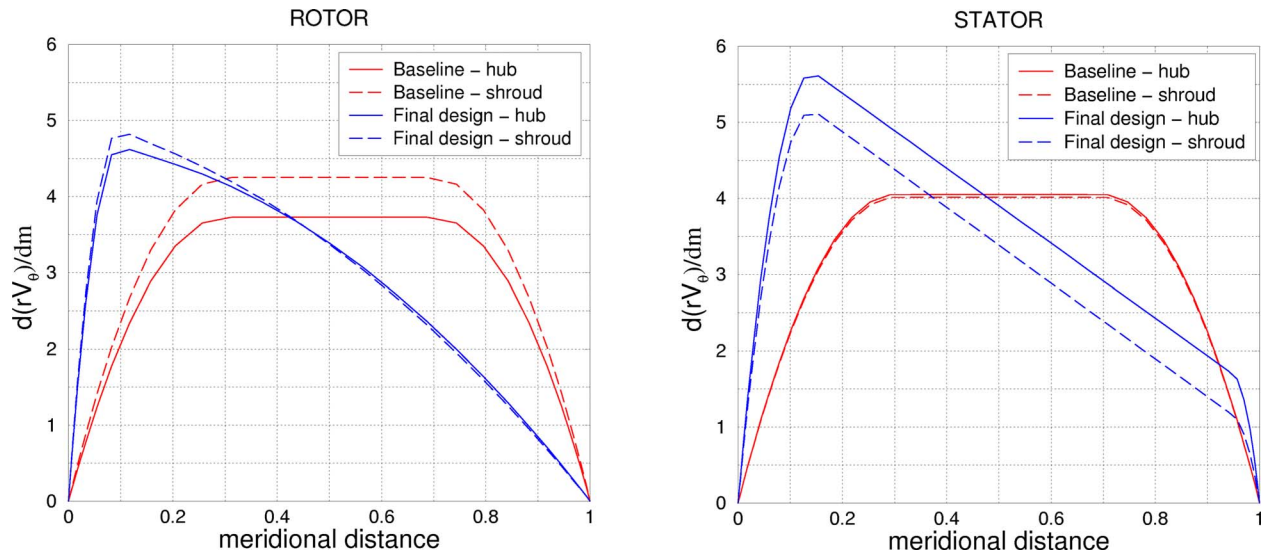


Fig. 26 Comparison of the blade loading distributions between baseline and final design

depends only on the number of design parameters, which, with the inverse parametrization, is considerably lower than with the conventional parametrization. The number of performance parameters that are investigated does not affect the size of the experimental table and several performances of interest can be simultaneously analyzed.

Once the models are built, optimization algorithms are applied to the RSM models, with negligible computational cost. In the present work, a multiobjective genetic algorithm was used. As a result, the set of optimal solutions was obtained (Pareto front) representing the best trade-off between competing performance

parameters. The Pareto front can be used as a dynamic database: Depending on the specific requirements, a different design configuration is selected, which privileges the maximization of a particular performance parameter.

Since the number of configurations to be analyzed is substantially reduced with respect to conventional optimization strategies, this allows to perform optimizations based on more computational-expensive CFD analyses. In the present case, a multipoint aerodynamic analysis was performed, where both design and off-design operating conditions were investigated.

Although the examples reported in this paper analyze only aerodynamic performance, the method is suitable for multi-disciplinary optimizations, where stress and vibration analyses can be coupled with the aerodynamic ones.

The design strategy also allows an easy sensitivity analysis aimed at quantifying the impact of the design factors and of their interaction on the performance parameters. Since the inverse-design blade parameters have an aerodynamic meaning, the design factors can be directly related to the flow physics. As also shown in this paper, the sensitivity analysis is then used to generate design know-how and to define design rules of general validity, which can be exploited for similar design problems.

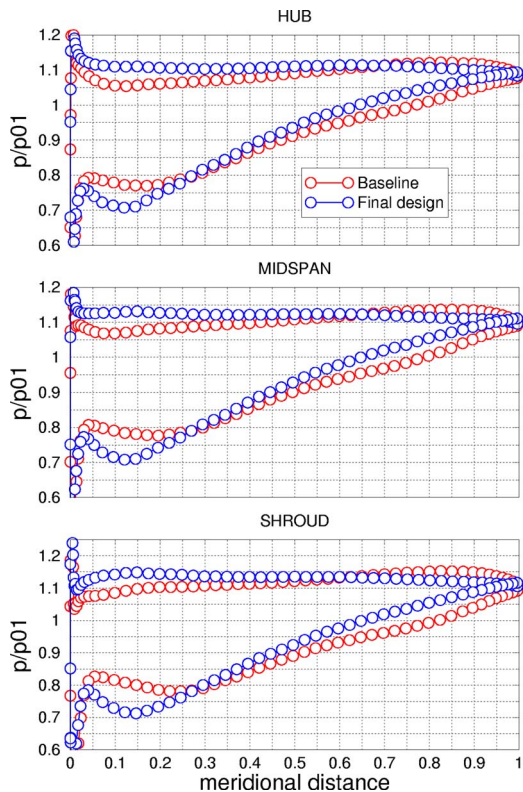


Fig. 27 Comparison of the rotor blade pressure distribution between baseline and final design

### Acknowledgment

The authors would like to thank Mr. Nicolas Potier and Ms. Isabelle Delaunay for their help, and Professor Andrea Arnore for his help in the use of the TRAF code.

### Nomenclature

- $\eta$  = adiabatic efficiency
- $\Phi \equiv \frac{4Q_1}{\pi D_2^2 U_2} \frac{V_x}{U_2}$  = flow coefficient (centrifugal, axial compressor)
- $\tau \equiv \frac{h_{02} - h_{01}}{U_2^2}$  = work coefficient
- $\zeta \equiv \frac{P_{03} - P_{02}}{1/2 \rho_2 V_2^2}$  = stator loss coefficient
- $M_u = \frac{U_2}{a_{0t}}$  = peripheral Mach number
- $a_{0t}$  = sound speed based on the inlet total conditions
- $h_0$  = stagnation enthalpy

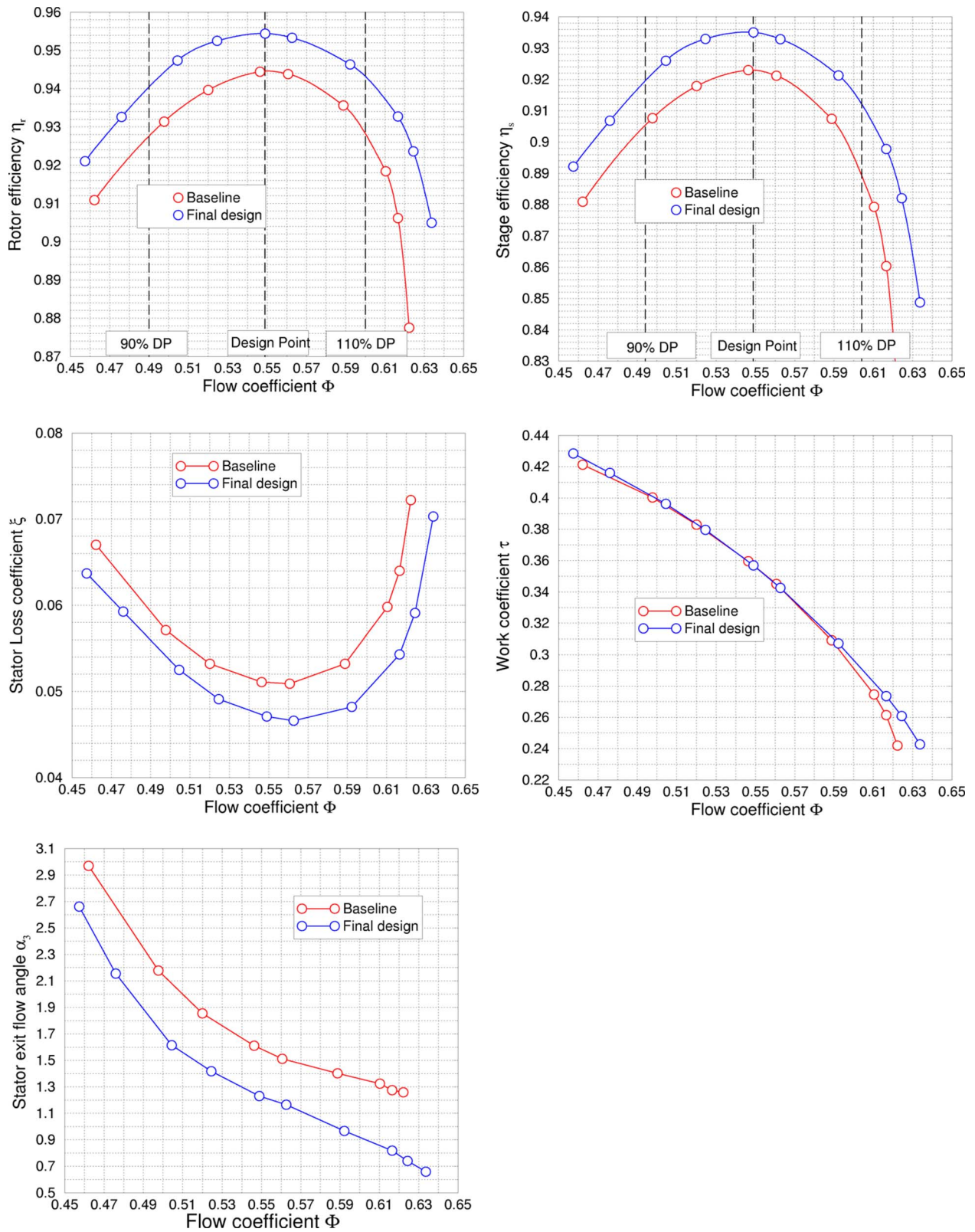
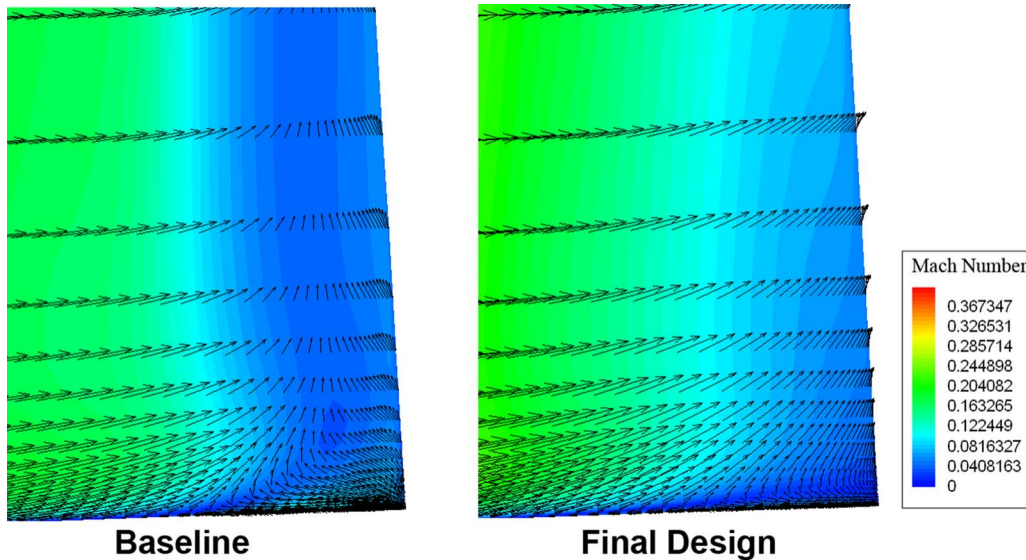


Fig. 28 Comparison of the compressor performance between baseline and final design



**Fig. 29 Mach number distribution and velocity vectors on the hub trailing-edge region of the rotor suction side**

$Q$  = volume flow rate  
 $U_2$  = impeller/rotor peripheral velocity at the shroud trailing edge  
 $x, r, \theta$  = cylindrical coordinates  
 $V$  = absolute velocity  
 $P$  = total pressure  
 $p$  = static pressure

#### Subscripts

1 = rotor/impeller inlet  
 2 = rotor/impeller exit  
 3 = stator/diffuser exit  
 des = design point  
 pe = peak efficiency  
 ch = choke

#### References

- [1] Sonoda, T., Yamaguchi, Y., Arima, T., Olhofer, M., Sendhoff, B., and Schreiber, H., 2003, "Advanced High Turning Compressor Airfoils for Low Reynolds Number Condition," ASME Paper No. GT2003-38458.
- [2] Shahpar, S., and Radford, D., 1999, "Application of the FAITH Linear Design System to a Compressor Blade," *Proceedings of ISAABE Conference*, ISABE 99-7045.
- [3] Arnone, A., Bonaiuti, D., Focacci, A., Pacciani, R., Scotti, A., and Spano, E., 2004, "Parametric Optimization of a High-Lift Turbine Vane," ASME Paper No. GT2004-54308.
- [4] Burguburu, S., Toussaint, C., Bonhomme, C., and Leroy, G., 2003, "Numerical Optimization of Turbomachinery Bladings," ASME Paper No. GT2003-38310.
- [5] Kammerer, S., Mayer, J. F., Paffrath, M., Wever, U., and Jung, A. R., "Three-Dimensional Optimization of Turbomachinery Bladings Using Sensitivity Analysis," ASME Paper No. GT2003-38037.
- [6] Buche, D., Guidati, G., and Stoll, P., 2003, "Automated Design Optimization of Compressor Blades for Stationary, Large-Scale Turbomachinery," ASME Paper No. 2003-38421.
- [7] Sieverding, F., Casey, M., Ribi, B., and Meyer, M., 2003, "Design of Industrial Axial Compressor Blade Sections for Optimal Range and Performance," ASME Paper No. GT2003-38036.
- [8] Benini, E., and Tourlidakis, A., 2001, "Design Optimization of Vaned Diffusers of Centrifugal Compressors Using Genetic Algorithms," AIAA Paper No. 2001-2583.
- [9] Bonaiuti, D., and Pediroda, V., 2001, "Aerodynamic Optimization of an Industrial Centrifugal Compressor Impeller Using Genetic Algorithms," *Proceedings of Eurogen 2001*.
- [10] Zangeneh, M., 1994, "Inviscid-Viscous Interaction Method for Three-Dimensional Inverse Design of Centrifugal Impellers," ASME J. Turbomach., **116**, pp. 280-290.
- [11] Watanabe, H., and Harada, H., 1999, "Suppression of Secondary Flows in a Turbine Nozzle With Controlled Stacking Shape and Exit Circulation by 3D Inverse Design Method," ASME Paper No. 99-GT-72.
- [12] Lecerf, N., Jeannel, D., and Laude, A., 2003, "A Robust Design Methodology for High-Pressure Compressor Through-flow Optimization," ASME Paper No. GT2003-38264.
- [13] Bonaiuti, D., Arnone, A., Ermini, M., and Baldassarre, L., 2006, "Analysis and Optimization of Transonic Centrifugal Compressor Impellers Using the Design of Experiments Technique," ASME J. Turbomach., **128**, pp. 786-797.
- [14] Kawagishi, H., and Kudo, K., 2005, "Development of Global Optimization Method for Design of Turbine Stages," ASME Paper No. GT2005-68290.
- [15] Myers, R. H., 1999, "Response Surface Methodology—Current Status and Future Direction," J. Quality Technol., **31**(1), pp. 30-44.
- [16] Taguchi, G., 1976, *Design of Experiment*, Maruzen, Tokyo.
- [17] Zangeneh, M., 1991, "A 3D Design Method for Radial and Mixed-Flow Turbomachinery Blades," Int. J. Numer. Methods Fluids, **13**, pp. 599-624.
- [18] Arnone, A., Liou, M. S., and Povinelli, L. A., 1992, "Navier-Stokes Solution of Transonic Cascade Flow Using Non-Periodic C-type Grids," J. Propul. Power, **8**, pp. 410-417.
- [19] Arnone, A., Bonaiuti, D., Boncinelli, P., Ermini, M., Milani, A., Baldassarre, L., and Camatti, M., 2002, "CFD Applications to Industrial Centrifugal Compressor Design," ASME Paper No. GT-2002-30393.
- [20] Bonaiuti, D., Arnone, A., Hah, C., and Hayami, H., 2002, "Development of Secondary Flow Field in a Low Solidity Diffuser in a Transonic Centrifugal Compressor Stage," ASME Paper No. GT-2002-30371.
- [21] Arnone, A., 1994, "Viscous Analysis of Three-Dimensional Rotor Flows Using a Multigrid Method," ASME J. Turbomach., **116**, pp. 435-445.
- [22] Arnone, A., Carnevale, E., and Marconcini, M., 1997, "Grid Dependency Study for the NASA Rotor 37 Compressor Blade," ASME Paper No. 97-GT-384.
- [23] Zangeneh, M., Goto, A., and Harada, H., 1998, "On the Design Criteria for Suppression of Secondary Flows in Centrifugal and Mixed-Flow Impellers," ASME J. Turbomach., **120**, pp. 723-735.
- [24] Cumpsty, N. A., 1989, *Compressor Aerodynamics*, Longmans, Green, New York.
- [25] Ginder, R. B., and Harris, D., 1990, "Test-Case E/CO-3 Single Subsonic Compressor Stage," AGARD AR-275.
- [26] Buche, D., Guidati, G., and Stoll, P., 2003, "Automated Design Optimization of Compressor Blades for Stationary, Large-Scale Turbomachinery," ASME Paper No. GT2003-38421.
- [27] Terauchi, K., Kariya, D., Maeda, S., and Yoshiura, K., 2005, "Redesign of an 11-Stage Axial Compressor for Industrial Gas Turbines," ASME Paper No. GT2005-68689.



# Experiments on the Physical Mechanism of Heat Transfer Augmentation by Freestream Turbulence at a Cylinder Stagnation Point

**A. C. Nix**

Department of Mechanical and Aerospace  
Engineering,  
West Virginia University,  
Morgantown, WV 26506-6106  
e-mail: andrew.nix@mail.wvu.edu

**T. E. Diller**

Fellow ASME  
Department of Mechanical Engineering,  
Virginia Polytechnic Institute and State  
University,  
Blacksburg, VA 24061  
e-mail: tdiller@vt.edu

*Detailed time records of velocity and heat flux were measured near the stagnation point of a cylinder in low-speed airflow. The freestream turbulence was controlled using five different grids positioned to match the characteristics from previous heat flux experiments at NASA Glenn using the same wind tunnel. A hot wire was used to measure the cross-flow velocity at a range of positions in front of the stagnation point. This gave the average velocity and fluctuating component including the turbulence intensity and integral length scale. The heat flux was measured with a heat flux microsensor located on the stagnation line underneath the hot-wire probe. This gave the average heat flux and the fluctuating component simultaneous with the velocity signal, including the heat flux turbulence intensity and the coherence with the velocity. The coherence between the signals allowed identification of the crucial positions for measurement of the integral length scale and turbulence intensity for prediction of the time-averaged surface heat flux. The frequencies corresponded to the most energetic frequencies of the turbulence, indicating the importance of the penetration of the turbulent eddies from the freestream through the boundary layer to the surface. The distance from the surface was slightly less than the local value of length scale, indicating the crucial role of the turbulence in augmenting the heat flux. The resulting predictions of the analytical model matched well with the measured heat transfer augmentation. [DOI: 10.1115/1.2950079]*

## Introduction

As engine manufacturers strive to raise turbine inlet air temperatures upwards to 3000°F (1650°C), they are limited by the life capability of the turbine airfoils. Understanding and predicting the heat transfer to the turbine blades are critical to designing and implementing the cooling system to maintain the material temperatures within the required operational limits. One of the main unknowns in the heat transfer prediction capability is the effect of the freestream turbulence generated in the combustor. A cylinder in crossflow provides a good model for the effect of turbulence at the leading edge of turbine blades, which is typically the region of highest heat transfer. Because of the thin boundary layer and high flow acceleration, the stagnation region boundary layer is laminar in nature with freestream flow unsteadiness superimposed by the turbulence. Because the boundary layer is very thin in the stagnation region, the length scale of the turbulence is generally much larger than the boundary layer thickness. The cylinder experimental model is used in the present research to develop increased understanding of the detailed mechanism of the heat transfer augmentation.

## Background

It is well known that freestream turbulence augments the time-averaged stagnation heat transfer on cylinders, although there is considerable scatter in the experimental data. Cascade experimen-

tal results demonstrate similar augmentation for blade models in a low-speed cascade [1]. Two important parameters used to correlate the experimental results are the turbulence intensity and the cylinder Reynolds number, which are often used as the product  $Tu \sqrt{Re}$  [2]. The length scale of the turbulence, however, has also been shown to have an important impact on the heat transfer augmentation [1,3].

The nature of the freestream turbulence in the vicinity of a stagnation point has been studied by Bearman [4], who measured all three components of the velocity as the flow approached a two-dimensional bluff body. The most striking increase in unsteadiness was measured for the  $w'$  component in the direction transverse to the flow. The largest increases in heat transfer were found for the smallest length scales of the turbulence. This was explained by vortex stretching of the turbulence.

Further evidence of the importance of vortex amplification on stagnation heat transfer was provided by Van Fossen and Simoneau [5]. They used wires oriented perpendicular to a downstream cylinder to generate vorticity. The flow was documented with hot wires and smoke visualization, while the steady heat transfer on the cylinder was visualized with liquid crystals. The heat transfer was lowest in the region directly in the wake of the wires, where the turbulent unsteadiness was highest, but the flow from the vortex pair was away from the cylinder. The highest heat transfer was recorded in between the wires, where the vortex pair induced flow toward the cylinder.

Van Fossen et al. [6] studied the influence of turbulence length scale on heat transfer on a cylinder. A correlation, which included the ratio of the integral length scale to the leading edge diameter was developed:

Contributed by the International Gas Turbine Institute of ASME for publication in the JOURNAL OF TURBOMACHINERY. Manuscript received July 30, 2007; final manuscript received August 30, 2007; published online January 29, 2009. Review conducted by David Wisler. Paper presented at the ASME Turbo Expo 2005: Land, Sea and Air (GT2005), Reno, NV, June 6–9, 2005.

$$\frac{h_{\text{turb}}}{h_{\text{lam}}} = 1 + 0.00792 \sqrt{\text{TuRe}_d^{0.8} \left(\frac{\Lambda_x}{d}\right)^{-0.574}} \quad (1)$$

where  $\Lambda_x$  represents the integral length scale and Tu the freestream turbulence intensity measured at the cylinder location with the cylinder removed. This indicates that the heat transfer augmentation becomes larger as the length scale is decreased.

Magari and LaGraff [7] used a small cylinder as a wake generator in front of a larger model cylinder to create local turbulence intensities from 9% to 21%, depending on the flow conditions used. Unfortunately, length scales could not be measured. The heat flux at several locations around the ceramic model cylinder was measured using thin-film surface temperature sensors in combination with a transient thermal model to calculate the corresponding heat flux. The turbulence intensity of the heat flux signal was between 15% and 25%. Power spectra and cross correlations of the resulting heat flux demonstrated similar frequency content and some correlation between sensors at different locations around the cylinder.

Ching and O'Brien [8] glued a Kapton sheet with a thin-film temperature sensor onto a heated copper strip at the stagnation point of a cylinder. Unsteady heat flux was calculated from the temperature fluctuations using finite-difference solutions of the one-dimensional unsteady conduction equation. Average heat transfer was measured from the power to the heater. Turbulent heat flux intensities of about 20% were measured for a grid-generated freestream turbulence intensity of 8% (measured without the cylinder present). A hot wire placed 2.5 mm above the sensor was used to record the simultaneous fluctuations of velocity. Power spectra showed similar broadband frequency content for both signals. Cross correlations demonstrated very little lag between the velocity and heat flux signals. No information on the length scale of the turbulence was reported.

Time-resolved heat flux measurements were made at the stagnation point of a large air jet by Simmons et al. [9] using a heat flux microsensor. A hot-film sensor was mounted about 5 mm above the heat flux sensor to simultaneously measure the local velocity. A grid was used at the exit of the jet to increase the turbulence, but the length scale was not measured. The freestream turbulent intensity was 11.3% in the free jet. The corresponding heat flux turbulent intensity was 10.3%. The coherence between the velocity and heat flux signals showed a peak of about 0.25 at a frequency of about 200 Hz.

Dullenkopf and Mayle [10] presented a correlation that introduced the idea of an "effective" turbulence level. Fluctuations at high frequencies (small scale) are viscously damped, while disturbances at low frequency (large scale) are seen as quasi-steady, similar to bulk flow pulsations, which in the mean do not affect heat transfer. Only a small frequency band around a dominant frequency is effective at increasing heat transfer.

Cascade experiments were performed by several groups to document the effects of large-scale freestream turbulence in low-speed turbine vane cascades (Ames [11,12], Radomsky and Thole [13], and Wang et al. [14]). Freestream turbulence was shown to significantly augment heat transfer in the laminar flow regions of the blade (stagnation point, pressure surface, and favorable pressure gradient region of the suction surface). Heat transfer augmentation was reported to be highest in the stagnation region and on the pressure surface.

Holmberg et al. [15,16] performed measurements of unsteady surface heat flux with a hot wire collocated with the heat flux gage. Coherence between freestream velocity and surface heat flux was found to be useful in determining the scale and frequency range of turbulent structures interacting with surface heat flux.

Research by Nix et al. [17] detailed time-resolved measurements of heat flux and velocity at three locations on the pressure and suction surfaces of a transonic turbine blade in a linear cascade. Engine combustor turbulence was simulated to match the measured conditions of Van Fossen and Bunker [18]. Coherence

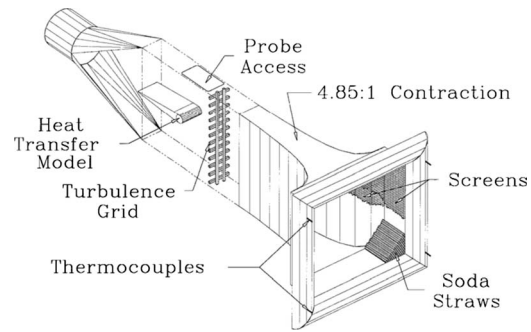


Fig. 1 Wind tunnel and turbulence grid

was measured between the velocity and heat flux signals near the most energetic frequency of the turbulence at the wall. This leads to a new analytical model based on surface renewal by the turbulent mixing through the boundary layer. The model was directly applied to the time-averaged heat transfer results measured, as well as to results reported by other research groups. The model results matched very well with the experiments for laminar boundary layers. One set of cylinder data from NASA Glenn was used as an example of the match between the model and experiments. A number of questions were not addressed, however, including the influence of different length scales and the different locations above the surface for correlation of the velocity and heat flux signals. These important considerations are investigated in the present report.

## Experimental Facility and Instrumentation

The experiments were performed at the facilities of NASA Glenn during the summer of 1995. The tunnel and grids are described in a report by Van Fossen et al. [6].

**Wind Tunnel.** The experiments were performed in the wind tunnel at NASA Glenn shown in Fig. 1. Air is drawn into the flow-conditioning section of the tunnel by the laboratory exhaust system. This section consists of screens on either side of 19.7 cm long soda straws. The air then passes through a 4.85:1 contraction before entering the 15.2 cm wide by 68.6 cm high test section. The velocity used was approximately 45 m/s for all of the tests. Without the turbulence grids, the turbulence intensity was less than 0.5%.

**Turbulence Grids.** Five different turbulence grids were used. Each was a square bar, square mesh grid with identical open areas of 60.5%. The square grids were labeled Grids 1–4 and Grid 6. The grid numbering except for Grid 6 corresponds to that used in Ref. [6]. The purpose of the different grids was to provide different turbulent length scales over a range of intensities to study independently the different effects on the cylinder heat transfer.

The size of the grid elements,  $b$ , is listed in Table 1 along with the distance from the grid to the stagnation point of the cylinder,  $x$ . The turbulence intensities and length scales created by the grids were determined with a standard, 5  $\mu\text{m}$ , single-sensor hot wire oriented normal to the flow direction. The hot-wire signals were linearized with analog linearizers. The frequency response of the

Table 1 Grid characteristics

Grid	$b$ (cm)	$x/b$	Tu (%)	$\Lambda_x$ (cm)
1	1.27	39.4	8.3	1.9
2	0.61	47.0	7.3	1.2
3	0.32	42.4	7.5	0.54
4	0.16	75.0	4.5	0.42
6	2.54	48.5	6.9	4.2

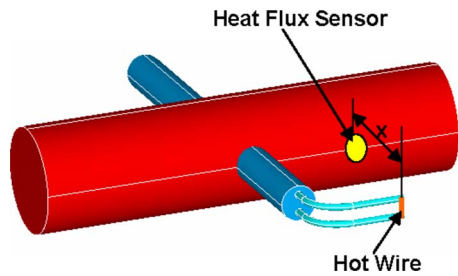


Fig. 2 Instrumented cylinder model

hot-wire anemometer system was estimated to be around 30 kHz with the square wave test. The hot wire was calibrated in an air jet at similar velocity and temperature as the wind tunnel flow. The local turbulence intensity was calculated as the ratio of the rms to the mean linearized voltage. To find the length scale, the autocorrelation of the velocity data was fitted with an exponential function by the least-square method. The resulting equation was integrated with respect to time to determine the time scale and then multiplied by the mean velocity to calculate the length scale [6].

**Instrumented Cylinder Model.** The 6 cm diameter aluminum cylinder model was fitted with a wedge-shaped afterbody to prevent vortex shedding. An electric heater was mounted inside the 1 cm thick walls to maintain the surface temperature at a constant temperature of 44°C. This specifies the Reynolds number for all of the tests as approximately 160,000.

**Instrumentation and Data Acquisition.** As indicated in Fig. 2, a heat flux microsensors (HFM 6) was mounted in a 6.2 mm diameter hole in the cylinder at the stagnation point. This gage consists of two sensors located on the end of a high conductivity aluminum nitride cylinder, which is press fitted into an aluminum housing. The thin-film pattern for the heat flux measurement was about 4.5 mm wide and less than 2 μm thick. The sensor is sputter-deposited onto the substrate, as described by Hager et al. [19]. It consists of several hundred differential thermocouples hooked in series to amplify the signal from the temperature difference across 1 μm thick layers of silicon monoxide. This gives a voltage signal directly proportional to the heat flux and the response time is very fast because the sensor is so thin [20]. The total estimated uncertainty of the experimental heat flux measurement was ±10%.

The surface temperature of the HFM was measured with a resistance temperature sensor (RTS) that is deposited as a thin film surrounding the heat flux sensor. It was calibrated in situ by placing a layer of insulation over the RTS sensor and a reference thermocouple without airflow and allowing steady state to occur. The T-type thermocouple that was used as a reference was connected to the same Doric thermocouple unit that was used for the mainstream air temperature measurement. The resulting gage temperature measurements during all of the tests typically matched the surface temperature of the cylinder within 1% or 2% of the total air to surface temperature difference.

A second hole was located 9.5 mm away from the HFM on the stagnation line to accommodate the hot-wire probe. This was a standard TSI 1212 hot-wire probe with a 90 deg bend mounted in a probe support that was in turn mounted to a stepping motor on the back side of the cylinder. As shown in Fig. 2, the wire was offset from the probe axis by 8 mm, which placed it over the outside edge of the heat flux pattern. As will be demonstrated later, for hot-wire measurements closest to the cylinder surface, the hot-wire probe causes a minimal disruption and will not affect the heat transfer measurements. The hot wire was calibrated in the tunnel at the 7.6 cm position in front of the cylinder using the known mean velocity at that location above the cylinder.

Measurements of time-resolved heat flux, velocity, and surface temperature were recorded with a computer data acquisition sys-

tem at a sampling rate for each channel of 20 kHz for a duration of 5.0 s. The heat flux signal was amplified by a factor of 100,000 using two low-noise amplifiers in series prior to the data acquisition system. A low-pass filter was used for all of the channels set at a frequency of 10 kHz. This gives a sample size for each channel of 100,000 points, which is sufficient to perform the required statistical data analysis.

The dynamic response and spatial resolution of the heat flux sensors and hot-wire anemometer were of importance when analyzing the time-resolved data. The heat flux sensors are sufficiently small compared to the cylinder to provide reasonably good spatial resolution to minimize the effects of spatial averaging. The ratio of the turbulence integral length scale to the heat flux sensor diameter ranged from approximately 1 to 10. This is above the frequency range of interest, since it will be shown that there is no coherence between velocity and heat flux above 1 kHz. The scales of interest discussed later are all on the order of the gage diameter or larger. It has been demonstrated that the gage responds like a first order system with a time constant of 17 μs, or a maximum frequency response of approximately 60 kHz [21].

### Analytical Model

Nix et al. [17] recently presented a simple mechanistic model for the effect of large-scale turbulent eddies on surface heat transfer. The basic tenet of the model is that the eddies penetrate through the boundary layer with little alteration or abatement. Because the boundary layer at the stagnation point is much less than 1 mm thick, the length scale of the turbulence is much larger than the boundary layer thickness. Consequently, the mechanism for the enhanced heat transfer is due to the large-scale motion of fluid with its associated thermal energy transfer from the freestream through the boundary layer to the surface.

By this model, the heat transfer consists of two independent portions—that due to the normal transfer through the boundary layer and that due to the turbulent motions from the freestream to the surface. They are treated independently. The model for the effect of the turbulent motions is surface renewal. The thermal energy is exchanged during the time of the contact of the hot freestream fluid with the surface. It is assumed that the surface itself has a much higher conductivity than the fluid, which in this case is air. The heat transfer into the air can be characterized by the semi-infinite solution, with air as the medium.

$$\Delta q_t = k \frac{(T_\infty - T_w)}{\sqrt{\pi \alpha t}} \quad (2)$$

The characteristic time for this event is the integral length scale of the local turbulence divided by the unsteady turbulent velocity,  $\Lambda_x / u'_{rms}$ . The corresponding heat flux at the end of this time period is

$$\Delta q_t = k \frac{(T_\infty - T_w)}{\left[ \pi \alpha \frac{\Lambda_x}{u'_{rms}} \right]^{1/2}} \quad (3)$$

This is the quantity that is added to the heat flux without freestream turbulence. In terms of the heat transfer coefficient, this equation becomes

$$\Delta h_t = \frac{k}{\left[ \pi \alpha \frac{\Lambda_x}{u'_{rms}} \right]^{1/2}} \quad (4)$$

and the turbulent heat flux is then written as

$$h_{turb} = h_0 + \Delta h_t \quad (5)$$

It should be noted that the model results are only a function of the local conditions of the fluid in the freestream outside of the boundary layer. There are no parameters of the geometry, state of



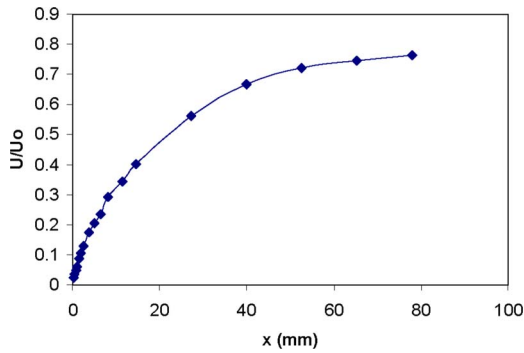


Fig. 3 Velocity profile (no grid)

the boundary layer, or thickness of the boundary layer. There are no empirical coefficients or parameters to fit the results to the experiments.

### Experimental Results

Time-resolved surface heat flux and velocity measurements were performed to investigate how freestream velocity fluctuations affect surface heat transfer to help predict increases in mean heat transfer. The results are organized in sections on velocity and time-averaged and time-resolved heat transfer measurements.

**Velocity.** The mean velocity profile as a function of distance from the cylinder,  $x$ , is shown in Fig. 3 for the case without the turbulence grid in place. The results match well with the potential flow solution and previous measurements in the wind tunnel. Turbulence characteristics are shown in Figs. 4 and 5 for Grid 1 as the hot wire is located at different positions in front of the cylinder. This is given as a typical example for all of the grids. As expected, the local turbulence intensity increases sharply close to the cylinder surface as the mean velocity decreases. As shown in Fig. 5,

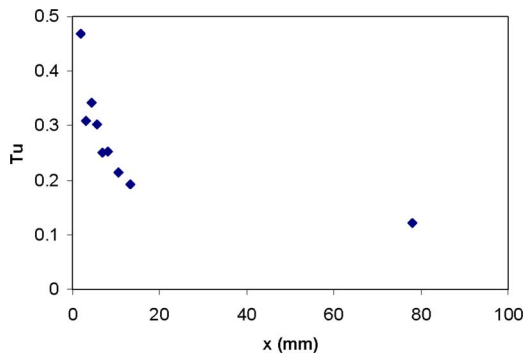


Fig. 4 Turbulence intensity (Grid 1)

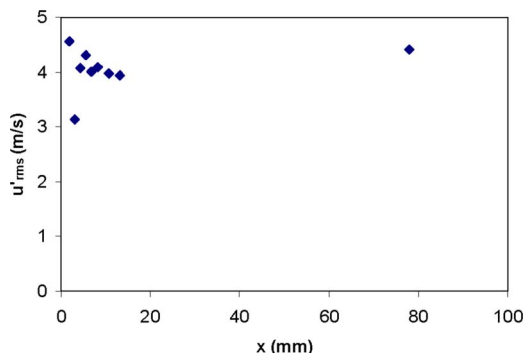


Fig. 5 rms of streamwise velocity (Grid 1)

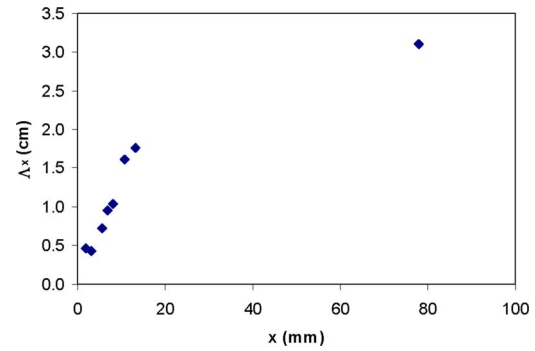


Fig. 6 Turbulent length scale (Grid 1)

the actual rms of the velocity does not change much. The length scale shown in Fig. 6 does decrease substantially close to the cylinder as the presence of the surface influences the turbulence.

The corresponding power spectral density for the velocity is shown in Fig. 7. It is typical for grid-generated turbulence and all of the hot-wire positions are nearly identical. The positions of the hot-wire probe for each run are specified in Table 2.

**Time-Resolved Heat Transfer.** The heat flux data were analyzed the same as the velocity data. A sample of the power spectral density of the heat flux signals for the same grid case as the velocity curves in Fig. 7 is shown in Fig. 8. It can be seen that the velocity and heat flux spectra have very similar shapes until the frequency is out beyond several kilohertz. They both have significant energy at low frequencies.

To further investigate the correlation of the heat flux and velocity signals, the coherence function was applied to the time-resolved velocity and heat flux data in the frequency domain to determine the correlation between the two signals. Coherence is a frequency domain representation of the correlation between two simultaneously sampled signals, defined as the square of the averaged cross spectrum divided by the product of each average power spectrum [22]. A significant coherence magnitude indicates that two independent signals have energy that correlates in time at the indicated frequency.

Figure 9 demonstrates that significant coherence is limited to frequencies below 1 kHz. For isotropic turbulence, the estimated most energetic frequency can be related to the integral length scale [23] by

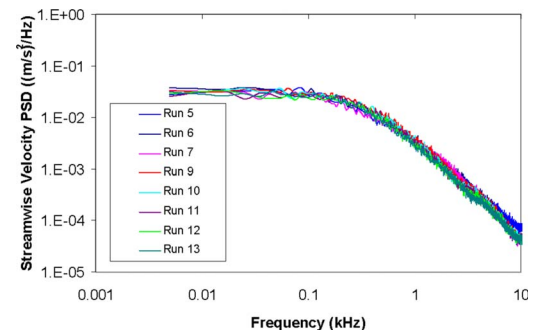


Fig. 7 Velocity power spectral density (Grid 1)

Table 2 Grid 1 hot-wire positions

Run No.	5	6	7	9	10	11	12	13
$x$ (mm)	80	1.8	3.0	5.6	6.9	8.1	10.7	13.2

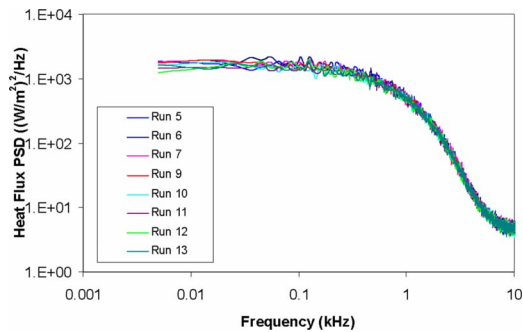


Fig. 8 Heat flux power spectral density (Grid 1)

$$f = \frac{3U}{8\pi\Lambda_x} \quad (6)$$

Shown in the figure is a band of frequencies corresponding to the most energetic frequency range for all of the locations with Grid 1 based on the local values of velocity and length scale. Equation (6) gives values of 290 Hz at the  $x=3.0$  mm position (Run 7) ranging down to the smallest frequency of 140 Hz at the three largest distances from the cylinder (Runs 5, 12, and 13). The largest coherence values generally occur within this range of frequencies for all of the locations. The highest coherence is demonstrated for Run 9, which is the  $x=5.6$  mm position, third closest to the cylinder.

It is also of interest to note the low coherence for test runs 5 and 6. These correspond to the largest distance of 80 mm (Run 5) and the smallest distance of 1.8 mm (Run 6). It might be anticipated that the largest distance would show little coherence because the distance between the velocity and heat flux probes is much larger than the integral length scale. It is a little more surprising that the smallest distance would also show low coherence. The other positions clearly show the ability of lower energy scales to penetrate into the boundary layer to affect surface heat transfer.

The results for all of the other grids were very similar in magnitude and distribution of the coherence for the same locations of the hot-wire probe. There was little coherence very close to the cylinder and far away.

To further substantiate the mechanism for the coherence between the velocity and heat flux, several tests were performed with the hot-wire probe flipped 180 deg away from the HFM. This placed the hot-wire sensor 16 mm away from the heat flux sensor along the cylinder axis. The tests were performed with Grid 6, the largest grid, at  $x$  locations of 5.6 mm and 6.9 mm. These  $x$  locations usually showed the highest coherence. With the probe flipped, however, there was no coherence because the distance between the hot wire and the HFM was now two to three times the local turbulent length scale.

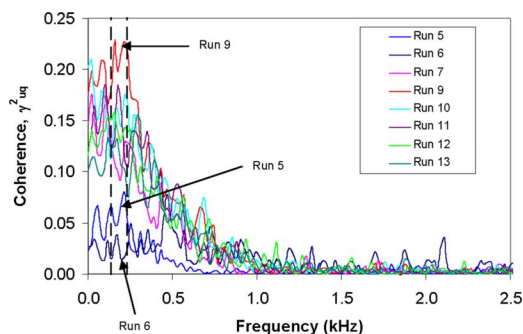


Fig. 9 Heat flux and velocity coherence (Grid 1)

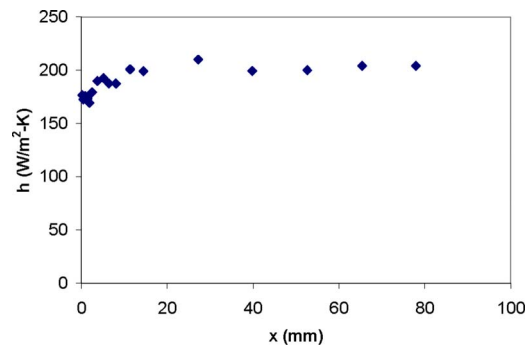


Fig. 10 Hot-wire probe effect on heat transfer (no grid)

**Steady Heat Transfer.** Although the heat transfer gage measures heat flux continuously, the measurements were taken after the cylinder temperature reached steady state to simplify the data reduction. Measurements of steady heat transfer with turbulence were compared with the low turbulence (no grid) measurements. The heat transfer coefficient was calculated directly from the measured heat flux divided by the surface to air temperature difference. Corrections for radiation heat flux and compressibility effects were small and the same for measurements with and without the grids. Therefore, they were neglected.

A sample plot of the resulting values of heat transfer coefficient as a function of the hot-wire position is shown in Fig. 10 for one of the tests with no grid. There is about a 15% increase in measured heat transfer coefficient as the hot wire is moved away from the cylinder. This was attributed to the close proximity of the support for the hot-wire probe to the HFM mounted in the cylinder. As the hot-wire sensor is moved close to the cylinder, only the prongs stick out, which cause minimal fluid disruption. These values in Fig. 10 are approximately 175 W/m<sup>2</sup> K, which corresponds to a Frossling number slightly less than 1, as would be expected for the case without freestream turbulence. This also matches well with the results of Van Fossen et al. [6]. The results for the turbulence grid cases are reported for the same hot-wire locations close to the cylinder.

The mean heat transfer results are reported as the change in heat transfer coefficient with turbulence relative to the no grid turbulence case. This allows a finer discrimination of turbulence effect and makes the comparison of different data simpler. The bias error of the heat flux sensor calibration is the same for all measurements and does not add for separate measurements with the same sensor. Consequently, the uncertainty of the change in heat transfer coefficient can still be maintained at about  $\pm 10\%$  even though the magnitude of the difference is smaller and it is the combination of two different measurements.

The predicted change in heat transfer coefficient was calculated according to Eq. (4) for all of the hot-wire locations using the local turbulence characteristics, as shown in Figs. 5 and 6. An example is shown in Fig. 11 for Grid 1. The values rapidly increase near the cylinder because of the decrease in length scale.

The question from Fig. 11 is which is the proper value to choose to predict the heat transfer increase resulting from the freestream turbulence. Note that all of the positions are outside of the fraction of 1 mm boundary layer thickness. The choice was made to use the closest position that still maintained coherence with the heat flux signal. For Grids 1–4, this is  $x=3$  mm. For Grid 6, the closest measurement made was only 5.6 mm. This is the only case that some of the points were not taken at closer than 3 mm.

The predicted values for the change in heat transfer coefficient due to freestream turbulence are in close agreement with the measured values. The heat transfer coefficient for the no turbulence case of Van Fossen et al. [6] that corresponds to the present data is 165 W/m<sup>2</sup> K. This gives turbulent increases of 45–65% in the

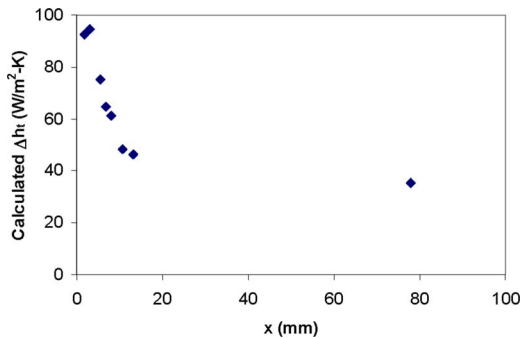


**Fig. 11 Calculated change in heat transfer coefficients with turbulence (Grid 1)**

measured heat transfer. The largest discrepancy between the predicted and presently measured change due to turbulence is for Grid 6. As seen from Fig. 11, the prediction would undoubtedly be larger if the data were available closer to the surface. The measurements of Van Fossen et al. [6] are lower than the prediction for Grids 1 and 2. Otherwise, all of the corresponding heat transfer coefficients are within 5%.

The integral length scales in Table 3 are all slightly larger than the distance to the surface of the cylinder. Additional measurements indicated that there is not much further decrease when the distance to the surface is decreased less than 3 mm. This appears to be the limit on the size of the length scale for this flow situation and range of turbulence.

It must be emphasized that the model used for the prediction included no information on the geometry or constants used to fit the data. The vortex stretching that was seen in the decreases in length scale is included in the model by using the local turbulence characteristics. Although it is more convenient to use the upstream flow conditions for prediction of heat transfer at the stagnation point, the present work demonstrates the fundamental mechanisms at work in augmenting the heat transfer. A simple extension of the method would be to model the change in length scale and unsteady velocity intensity from the upstream condition in the potential flow in front of the cylinder. This would then allow prediction of the freestream turbulence effect on the heat transfer at any stagnation point without the need for local velocity measurements.

## Conclusions

Simultaneous measurements of the local velocity at different distances from the stagnation point and the surface heat flux were used to investigate the effect of freestream turbulence. The decreasing values of integral length scale were indicative of the vortex stretching in this region. The coherence function was used to show the connection between the velocity unsteadiness with the surface heat flux. The coherence disappeared when the velocity sensor was too close or too far away from the surface. This also demonstrated that there is a small band of frequencies for which freestream velocity fluctuations affect surface heat transfer, roughly centered around the frequency of the integral length scale

**Table 3 Comparison of changes in heat transfer coefficient**

Grid	$x$ (mm)	$u'_{rms}$ (m/s)	$\Lambda_x$ (mm)	$\Delta h_{pred}$ (W/m <sup>2</sup> K)	$\Delta h_{meas}$ (W/m <sup>2</sup> K)	$\Delta h_{meas}^a$ (W/m <sup>2</sup> K)
1	3	3.9	4.3	94	94	75
2	3	2.7	3.5	87	77	75
3	3	3.6	3.9	95	101	106
4	3	2.6	4.2	78	78	83
6	5.6	3.2	6.4	70	82	—

<sup>a</sup>Reference 6.

(most energetic eddies) of the freestream turbulence. An analytical model was used with the turbulence characteristics at this location to successfully predict the time-averaged heat flux at the surface. This lends credibility to the model of large-scale turbulent eddies penetrating the boundary layer and superimposing their energy in the form of heat flux increases of the mean heat flux.

## Acknowledgment

The support of an ASEE Summer Faculty Fellowship at NASA Lewis Research Center in the Turbine Heat Transfer Branch is acknowledged by T.E.D. The authors are particularly grateful for the experimental expertise and help of Jim Van Fossen as part of that support at NASA. The analytical portion of this work was sponsored by the Air Force Office of Scientific Research (AFOSR) under Grant/Contract No. F49620-01-1-0177, monitored by Dr. Tom Beutner and by the National Science Foundation, under Grant No. CTS-0423013. This support is gratefully acknowledged.

## Nomenclature

- $b$  = turbulence grid element diameter
- $d$  = cylinder leading edge diameter
- $f$  = frequency
- $h$  = convection heat transfer coefficient
- $h_0$  = heat transfer coefficient without turbulence
- $h_{turb}$  = turbulent heat transfer coefficient
- $k$  = thermal conductivity
- $q'$  = heat flux fluctuations
- $q''$  = heat flux
- Re = Reynold's number,  $\rho U d / \mu$
- $t$  = time
- $T_\infty$  = freestream temperature
- $T_w$  = wall temperature
- Tu = turbulence intensity  $u'_{rms}/U$
- $u'_{rms}$  = rms of streamwise velocity fluctuations
- $U$  = local freestream velocity
- $U_0$  = freestream velocity upstream of cylinder
- $x$  = streamwise distance, distance from cylinder stagnation point
- $w'$  = fluctuating velocity in transverse direction
- $\alpha$  = thermal diffusivity
- $\delta$  = boundary layer thickness
- $\Delta h$  = increase in heat transfer coefficient
- $\Delta h_t$  = modeled increase in heat transfer coefficient
- $\Delta q_t$  = modeled increase in heat flux due to turbulence
- $\Lambda_x$  = turbulent length scale
- $\rho$  = density of freestream air
- $\mu$  = viscosity of freestream air

## References

- [1] Ames, F. E., 1994, "Experimental Study of Vane Heat Transfer and Aerodynamics at Elevated Levels of Turbulence," NASA Report No. CR 4633.
- [2] Lowery, G. W., and Vachon, R. L., 1975, "Effect of Turbulence on Heat Transfer From Heated Cylinders," *Int. J. Heat Mass Transfer*, **18**, pp. 1229–1242.
- [3] Yardi, N. R., and Sukhatme, S. P., 1978, "Effects of Turbulence Intensity and Integral Length Scale of a Turbulent Free Stream on Forced Convection Heat Transfer From a Circular Cylinder in Cross Flow," *Heat Transfer 1978*, Hemisphere Pub. Co., Washington, DC, pp. 347–352.
- [4] Bearman, P. W., 1972, "Some Measurements of the Distortion of Turbulence Approaching a Two-Dimensional Bluff Body," *J. Fluid Mech.*, **53**, pp. 451–467.
- [5] Van Fossen, G. J., and Simoneau, R. J., 1987, "A Study of the Relationship Between Free-Stream Turbulence and Stagnation Region Heat Transfer," *ASME J. Heat Transfer*, **109**, pp. 10–15.
- [6] Van Fossen, G. J., Simoneau, R. J., and Ching, C. Y., 1994, "Influence of Turbulence Parameters, Reynolds Number, and Body Shape on Stagnation Region Heat Transfer," NASA Technical Paper 3487.
- [7] Magari, P. J., and LaGraff, L. E., 1994, "Wake-Induced Unsteady Stagnation-Region Heat Transfer Measurements," *ASME J. Turbomach.*, **116**, pp. 29–38.
- [8] Ching, C. Y., and O'Brien, J. E., 1991, "Unsteady Heat Flux in a Cylinder Stagnation Region With High Freestream Turbulence," *Fundamental Experimental Measurements in Heat Transfer*, D. E. Beasley and J. L. S. Chen, eds.,



- ASME, New York, pp. 57–66.
- [9] Simmons, S. G., Hager, J. M., and Diller, T. E., 1990, “Simultaneous Measurements of Time-Resolved Surface Heat Flux and Freestream Turbulence at a Stagnation Point,” *Heat Transfer 1990*, Vol. 2, G. Hetsroni, ed., Hemisphere, New York, pp. 375–380.
- [10] Dullenkopf, K., and Mayle, R. E., 1995, “An Account of Free-Stream-Turbulence Length Scale on Laminar Heat Transfer,” *ASME J. Turbomach.*, **117**, pp. 401–406.
- [11] Ames, F. E., 1995, “The Influence of Large-Scale High-Intensity Turbulence on Vane Heat Transfer,” *ASME J. Turbomach.*, **119**, pp. 23–30.
- [12] Ames, F. E., 1997, “Aspects of Vane Film Cooling With High Turbulence—Part I: Heat Transfer,” ASME Paper No. 97-GT-239.
- [13] Radomsky, R. W., and Thole, K. A., 2002, “Detailed Boundary Layer Measurements on a Turbine Stator Vane at Elevated Freestream Turbulence Levels,” *ASME J. Turbomach.*, **124**, pp. 107–118.
- [14] Wang, H. P., Goldstein, J., and Olson, R. J., 1999, “Effect of High Freestream Turbulence With Large Scale on Blade Heat/Mass Transfer,” *ASME J. Turbomach.*, **121**, pp. 217–224.
- [15] Holmberg, D. G., Diller, T. E., and Ng, W. F., 1998, “A Frequency Domain Analysis: Turbine Pressure Side Heat Transfer,” ASME Paper No. 98-GT-152.
- [16] Holmberg, D. G., Diller, T. E., and Ng, W. F., 1997, “A Frequency Domain Analysis: Turbine Leading Edge Region Heat Transfer,” ASME Paper No. 97-WA/HT2.
- [17] Nix, A. C., Diller, T. E., and Ng, W. F., “Experimental Measurements and Modeling of the Effects of Large-Scale Freestream Turbulence on Heat Transfer,” ASME Paper No. GT-2004-53460.
- [18] Van Fossen, G. J., and Bunker, R. S., 2002, “Augmentation of Stagnation Region Heat Transfer Due to Turbulence From an Advanced Dual-Annular Combustor,” ASME Paper No. GT-2002-30184.
- [19] Hager, J. M., Onishi, S., Langley, L. W., and Diller, T. E., 1993, “High Temperature Heat Flux Measurements,” *J. Thermophys. Heat Transfer*, **7**, pp. 531–534.
- [20] Holmberg, D. G., and Diller, T. E., 1995, “High-Frequency Heat Flux Sensor Calibration and Modeling,” *ASME J. Fluids Eng.*, **117**, pp. 659–664.
- [21] Popp, O., 1999, “Steady and Unsteady Heat Transfer in a Film Cooled Transonic Turbine Cascade,” Ph.D thesis, Virginia Tech., Blacksburg, VA.
- [22] Newland, D. E., 1975, *An Introduction to Random Vibrations, Spectral and Wavelet Analysis*, 3rd ed., Longman Scientific and Technical, New York.
- [23] Hinze, J., 1975, *Turbulence*, 2nd ed., McGraw-Hill, New York.

# A Conceptual Flutter Analysis of a Packet of Vanes Using a Mass-Spring Model

Roque Corral<sup>1</sup>

e-mail: roque.corral@itp.es

Juan Manuel Gallardo

e-mail: juan.gallardo@itp.es

Technology and Methods Department,  
Industria de TurboPropulsores S.A.,  
28830 Madrid, Spain

Carlos Martel

E.T.S.I. Aeronáuticos,  
Universidad Politécnica de Madrid,  
28040 Madrid, Spain  
e-mail: carlos.martel@upm.es

*The linear aeroelastic stability of a simplified mass-spring model representing the basic dynamics of a packet of  $N_a$  airfoils has been used to uncover a new type of coupled mode flutter. This simple model retains an essential dynamical feature of the vane packet: the presence of a cluster of  $N_a - 1$  nearly identical purely structural natural frequencies due to the much larger stiffness of the lower platform as compared to that of the airfoil. Using this model it may be seen that this degeneracy makes the  $N_a - 1$  associated mode shapes extremely sensible to the addition of small perturbations such as the aerodynamic forces. Since the determination of the aerodynamic vibrational correction (damping and frequency) requires knowing the mode shape, the aerodynamic corrections of the  $N_a - 1$  cluster modes are now unavoidably coupled together. Moreover, the computation of the aerodynamic correction independently for each structural mode shape leads typically to dangerously overpredicting the stabilizing effect of vane packing. It is shown that the expected stabilizing effect due to the packets may be negligible, depending on the relative frequency split associated with the strength of the aerodynamic forces and realistic structural effects such as the finite stiffness of the lower platform. It is also shown that in these cases, the most unstable mode may be, in a first approximation, very similar to that obtained modeling the stator as a continuous ring. [DOI: 10.1115/1.2952364]*

## Introduction

Modern low pressure turbines (LPTs) are made up of very slender and thin airfoils due to the steady trend to design very efficient, low cost, low weight turbomachinery. This is especially true for LPTs since the continuous trend to increase engine's bypass ratio poses extraordinary difficulties to the LPT design. Without a change in the engine architecture, larger fan diameters give rise to a contradictory requirement: the need of extracting the same power of the LPT at a lower shaft speed. Today the LPT may account for up to 20% of the total weight of the engine and 15% of the total cost in large commercial aeroengines.

Cost and weight reductions in LPTs are obtained by reducing the part count, increasing the lift per airfoil, and designing light, high aspect ratio airfoils. The latter lowers the natural frequencies of the assembly and therefore the reduced frequency,  $k$ , up to a point in which the airfoils may become aerodynamically unstable giving rise to the onset of flutter. Nowadays flutter may become a dominant constraint on the design of modern LPTs precluding the use of more efficient aerodynamic and structural configurations.

The problem in rotor blades is more relevant than that of vanes and has been recently addressed in Ref. [1]. However, high aspect ratio vanes may be prone to flutter also. LPT vanes (and some compressor vanes also) are manufactured in packets and this fact adds an extra complexity to the analysis of the problem.

The beneficial effect of grouping the airfoils in packets was first demonstrated by Whitehead and Evans [2]. Kahl [3] studied the stability of a LPT sectored vane of three airfoils and later on Chernysheva et al. [4] extended the stability studies to packets of six vanes. Corral et al. [1] investigated the stabilizing effect of welding the rotor blades in pairs.

It is well known that flutter boundaries are very sensitive to

airfoil mode shapes and that the reduced frequency plays a secondary role [5,6]. Mode shapes of rotor blades and vanes are obtained using three-dimensional finite element computations. These simulations usually include restoring forces just due to the elastic and centrifugal forces (in rotors) but they tend to ignore aerodynamic forces since in general they are much smaller than the others and usually provide just a higher order correction to the purely structural vibration characteristics. This is especially true for modes with well separated frequencies. However, vane packets are constructed casting together between four and ten airfoils (see Fig. 1), and as a consequence of the much higher stiffness of the lower platform, the structure typically exhibits a cluster of  $N_a - 1$  closely spaced frequencies, where  $N_a$  is the number of airfoils of the packet. The frequency distribution of a realistic vane packet for a given nodal diameter is sketched in Fig. 2. It may be noticed that in this case there are five eigenvalues with nearly the same frequency. When several frequencies of the same family are nearly identical, the associated mode shapes become extremely sensible to the addition of small effects, like small aerodynamic forces and geometric perturbations, which in the end discriminate the final resulting mode shapes of the packet. The only robust information about the mode shapes that can be drawn from the purely structural results is the fact that all cluster modes are approximately contained in the same  $(N_a - 1)$  dimensional subspace, and the aerodynamic correction for each of the cluster modes cannot be computed independently because they are inevitably coupled together.

The basic structural dynamics of blade packets have been studied by several researchers [7,8] and a good review may be found in Ref. [9]. However, little attention has been paid to the aeroelastic stability of blade packets, specially using fully coupled simplified methods. In this sense the results and methodology presented in this article are not only new but of practical relevance.

In this article we will first discuss the purely structural dynamics of a mass-spring model representing a simplified model of a vane packet with an infinitely stiff platform in order to elucidate the origin of the  $N_a - 1$  frequency cluster. Then we will introduce the formulation for the aerodynamic forces and we will apply

<sup>1</sup>Also: Associate Professor at the Department of Engine Propulsion and Fluid Dynamics of the School of Aeronautics, Universidad Politécnica de Madrid (UPM).

Contributed by the International Gas Turbine Institute of ASME for publication in the JOURNAL OF TURBOMACHINERY. Manuscript received August 1, 2007; final manuscript received December 5, 2007; published online January 29, 2009. Review conducted by David Wisler. Paper presented at the ASME Turbo Expo 2007: Land, Sea and Air (GT2007), Montreal, Quebec, Canada, May 14-17, 2007.

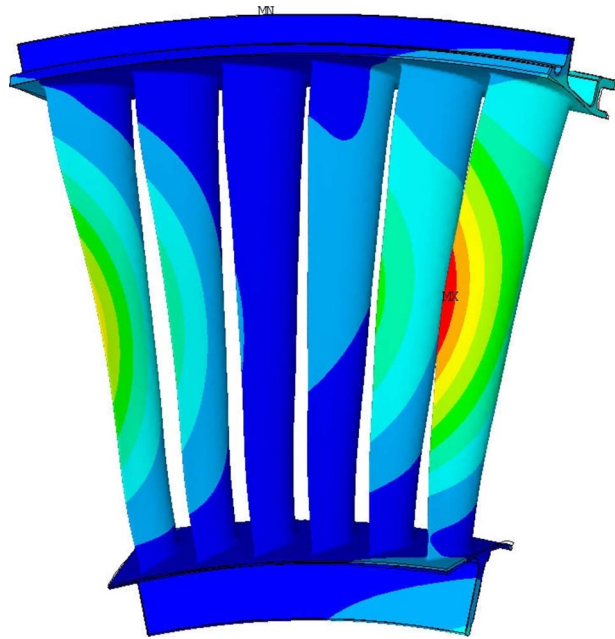


Fig. 1 Typical geometry and mode shape of a LPT vane packet

them to a more complex mass-spring model, which retains the flexibility of the hook and the lower platform of the vane packet. The aeroelastic stability of the system using a fully coupled method will be determined for different aerodynamic conditions, and the large deviation of the results with respect to those obtained from the standard uncoupled aeroelastic approach will also be highlighted.

### Simplified Dynamic Model of Sectored Vanes

The dynamics of a realistic stator made up of  $N_s$  identical packets of vanes is complex and the number of parameters that control its behavior is large. In order to improve the understanding of these configurations we study a simplified mass-spring model that retains their essential characteristics.

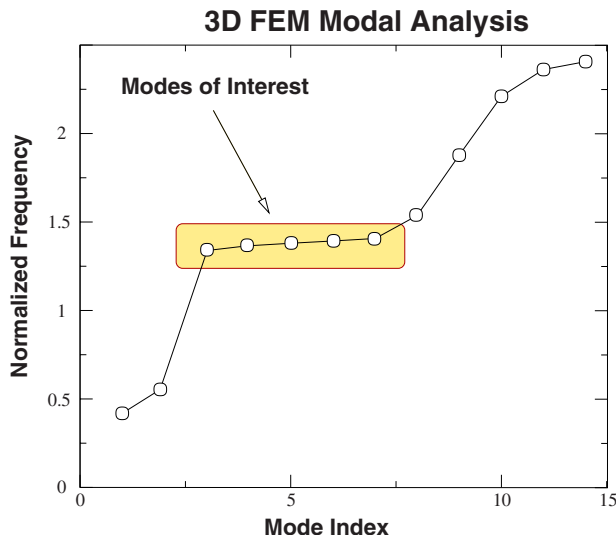


Fig. 2 Mode frequency distribution of a realistic vane packet for a fixed nodal diameter

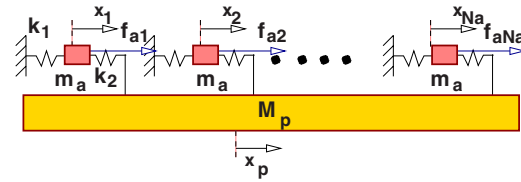


Fig. 3 Mass-spring model of a packet of  $N_a$  vanes with an infinitely stiff platform

The simplest packet model is sketched in Fig. 3: It consists of  $N_a$  identical masses,  $m_a$ , which represent the airfoils, all of them joined to another mass,  $M_p$ , which represents the lower platform of the vane, and clamped to the external casing.

The momentum equation for the  $j$ th airfoil, in the absence of aerodynamic forces, is

$$m_a \ddot{x}_j = -k_1 x_j + k_2 (x_p - x_j) \quad (1)$$

which may be written as

$$\ddot{x}_j + \omega_a^2 x_j = \left( \frac{k_2}{k_1 + k_2} \right) \omega_a^2 x_p \quad (2)$$

where  $\omega_a = \sqrt{(k_1 + k_2)/m_a}$  is the airfoil alone vibration frequency considering that it is clamped at both ends. The momentum equation for the platform reads

$$M_p \ddot{x}_p = -k_2 \sum_{j=1}^{N_a} (x_p - x_j) \quad (3)$$

and may be written as

$$\ddot{x}_p + \omega_p^2 x_p = \omega_p^2 \frac{1}{N_a} \sum_{j=1}^{N_a} x_j \quad (4)$$

with  $\omega_p^2 = N_a k_2 / M_p$ . The eigenvalues and mode shapes of the problem can be obtained in a heuristic way. If we assume that all the airfoils move in such a way that  $\sum_{j=1}^{N_a} x_j = 0$ , then the dynamics of the platform decouples from that of the airfoils and, if we set  $x_p = 0$ , then the resulting frequencies of vibration are equal to  $\omega_a$ . Physically this means that pairs of airfoils moving in antiphase while the platform is at rest define a possible mode shape with frequency  $\omega_a$ , although any other combination satisfying the constraints  $\sum_{j=1}^{N_a} x_j = 0$  and  $x_p = 0$  is also a valid mode shape. In other words, the eigenvalue  $\omega_a$  has multiplicity  $N_a - 1$  and its associated mode shapes are those that verify  $\sum_{j=1}^{N_a} x_j = 0$  and  $x_p = 0$ .

On the other hand, a displacement of the form  $x_1 = x_2 = \dots = x_{N_a}$ , which represents an in-phase movement of all the airfoils, is orthogonal to any of the modes described above, and the governing equations for all-vanes-in-phase modes are given by

$$\ddot{x}_j + \omega_a^2 x_j = \left( \frac{k_2}{k_1 + k_2} \right) \omega_a^2 x_p \quad (5)$$

$$\ddot{x}_p + \omega_p^2 x_p = \omega_p^2 x_j$$

The vibration frequencies of this problem are

$$\omega_N = \sqrt{\frac{1}{2} \left[ (\omega_a^2 + \omega_p^2) \pm \sqrt{\omega_a^4 + \omega_p^4 - 2\omega_a^2 \omega_p^2 \left( \frac{k_1 - k_2}{k_1 + k_2} \right)} \right]}$$

which provide the two remaining frequencies of the problem, and its mode shapes consist in the airfoils and the platform moving in antiphase (positive sign) and in phase (negative sign).

In summary, we have the frequency  $\omega_a$  with multiplicity  $N_a - 1$  plus two more frequencies corresponding to  $\omega_N$  (with both signs) that complete the  $N_a + 1$  degrees of freedom of the system. This frequency  $\omega_a$  with multiplicity  $N_a - 1$  splits when the finite



stiffness of the lower platform or other elastic and geometric effects are taken into account, and it constitutes the germ of the cluster of close frequencies that is found in realistic vane packets (see Fig. 2).

When  $N_s$  independent packets of the type previously described are put together to model a row of vanes, the resulting diagram of natural frequency versus nodal diameter consists of three horizontal lines: one associated with  $\omega_a$  (which corresponds to  $N_a-1$  modes for every nodal diameter!) and two other lines above and below which correspond to the positive and negative signs, respectively, of  $\omega_N$ .

## Aerodynamic Forces

The aeroelastic model is completed with the addition of the airfoil aerodynamic forces,  $F_j^a$ , due to the airfoil motion. The force on the airfoil  $j$  depends on the displacements of the airfoil itself and the rest of the airfoils

$$F_j^a = F_j^a(\mathbf{x}, \dot{\mathbf{x}}) \quad (6)$$

where  $\mathbf{x}$  is a column vector with the displacements of all the airfoils

$$\mathbf{x} = \begin{Bmatrix} x_1 \\ x_2 \\ \vdots \\ x_N \end{Bmatrix} \quad (7)$$

and  $N=N_a \times N_s$  is the total number of airfoils of the wheel. In using the above expression (6) for the aerodynamic forces we are implicitly assuming that, for the modes we are interested in, all the airfoils in the wheel vibrate with essentially the same mode shape, although with different amplitudes and phases, as may be observed in Fig. 1.

Although the model we are describing is quite general, it was originally intended to represent the aeroelastic behavior of LPT sector vanes. Since the steady aerodynamics of LPT airfoils lacks strong nonlinear phenomena, and we are analyzing the onset of flutter, we will assume that the unsteady aerodynamics is linear.

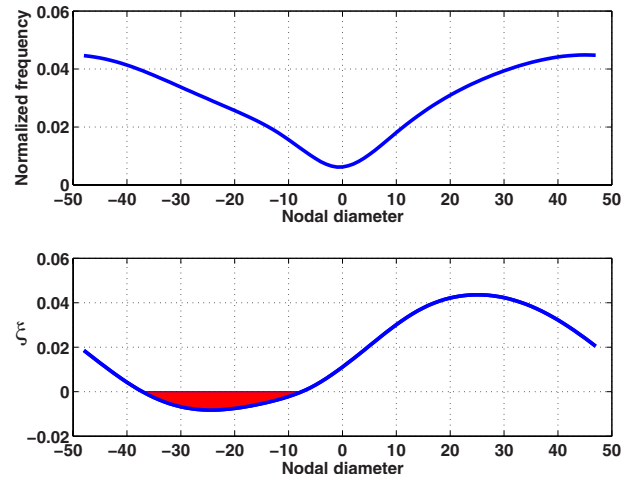
Unfortunately, unsteady aerodynamic forces are not available in the general form expressed in Eq. (6), and are usually computed in a very specific way, i.e., in the traveling-wave basis, with neighboring airfoils vibrating with constant interblade phase angle (IBPA),  $\sigma$ , between them and with a common frequency,  $\omega$ . We have neglected the dependence of the aerodynamic forces with the vibration frequency, and we have actually computed them only for the frequency  $\omega_a$  because we are only interested in the description of the aeroelastic behavior of the mode cluster of the vane packet, and all these modes have frequencies close to  $\omega_a$ . This approach has been successfully used in the fundamental [10] and asymptotic [11] mistuning models to account for the variations in the stability of bladed disks due to manufacturing tolerances. To retain an explicit variation of the aerodynamic forces with the frequency is not difficult from a technical point of view but does not change the problem from a qualitative point of view.

Figure 4 displays the nondimensional aerodynamic force,  $\tilde{f}_\sigma = f_\sigma^a / (m_a \omega_a^2 \delta_a)$ , computed in the frequency domain and in the traveling-wave basis of the individual airfoils with a linearized code for a potentially unstable torsion mode as a function of the number of nodal diameters of the traveling wave (that is basically the IBPA,  $\sigma$ ). The real and imaginary parts of  $\tilde{f}_\sigma$ ,

$$\tilde{f}_\sigma = (\Delta \omega_\sigma + i 2 \xi_\sigma)$$

correspond to the aerodynamic correction of the structural natural frequency and the critical damping ratio, respectively.

If we now go back to the airfoil displacement basis from the traveling-wave basis, then the aerodynamic forces on the airfoils  $\mathbf{F} = \text{Re}(\hat{\mathbf{F}} e^{i\omega t})$  due to a harmonic displacement of the form  $\mathbf{x}$



**Fig. 4 Aerodynamic nondimensional frequency correction (top) and damping, expressed as a fraction of the critical damping (bottom) for traveling wave with the indicated number of nodal diameters and computed at the cluster frequency  $\omega_a$**

$= \text{Re}(\hat{\mathbf{x}} e^{i\omega t})$  are given by  $\hat{\mathbf{F}} = [\mathbf{C}]\hat{\mathbf{x}}$ , and the influence coefficient matrix is computed from the change of basis expression  $[\mathbf{C}] = [\mathbf{E}]\text{diag}(f_\sigma^a)[\mathbf{E}]^{-1}$ , where  $E_{k,j} = e^{ikl2\pi/N}$  is the Fourier matrix and  $f_\sigma^a$  is obtained from the results in Fig. 4. Summing up all the above, the final expression for the aerodynamic forces on the airfoils takes the form

$$\mathbf{F} = \begin{Bmatrix} F_1^a \\ F_2^a \\ \vdots \\ F_N^a \end{Bmatrix} = \alpha \text{Re}([\mathbf{E}]\text{diag}(f_\sigma^a)[\mathbf{E}]^{-1} \hat{\mathbf{x}} e^{i\omega t}) \quad (8)$$

where  $\alpha$  is a factor that has been added in order to account for extra scaling effects, like variations on the operating regime or on the stage number.

The stability of the system is finally computed solving the eigenvalue problem

$$(-\omega^2[\mathbf{M}] + [\mathbf{K}] + [\mathbf{C}])\hat{\mathbf{x}} = 0 \quad (9)$$

where mass  $[\mathbf{M}]$  and stiffness  $[\mathbf{K}]$  matrices come from the structural model problem, while the influence coefficient matrix  $[\mathbf{C}]$  is constructed using the data shown in Fig. 4 and expression (8). Due to the cyclic symmetry of the problem (with basic sector equal to a packet of  $N_a$  airfoils) and the special form of the aerodynamic forces (also cyclic symmetric but with basic sector equal to a single airfoil), the solution of Eq. (9) is packet traveling waves, and the damping does not necessarily have to be equal to that shown in Fig. 4.

## Advanced Aeroelastic Model

The objective of this section is to compute the stability of a realistic packet of vanes following the previous methodology. The eigenvalue structure of a packet of six vanes is outlined in Fig. 2, where the set of eigenvalues we are interested in is highlighted. Its main characteristic is that contains five highly clustered frequencies.

With the aim of reproducing such structure, a more complex mass-spring model has been constructed (see top plot in Fig. 5). In this model, apart from the flexibility of the lower platform,  $k_p$ , we have also included a spring associated with the finite stiffness of the hook,  $k_h$ . In the model, different levels of coupling between neighboring packets through the springs  $k_c$  and  $k_{hc}$  have been included as well. If  $k_c = k_p$  and  $k_{hc} = k_h$ , we recover the continuous platform approach, while if  $k_c = 0$  and  $k_{hc} = 0$  we obtain fully split

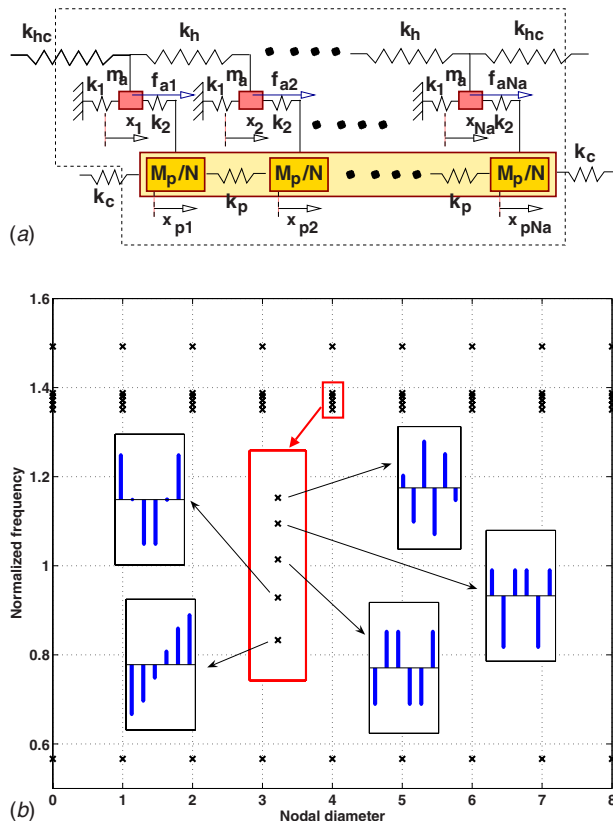


**Fig. 5** Top: Advanced mass-spring model of a packet of  $N_a$  vanes, with flexible platform and hook. Bottom: Vibration frequencies versus nodal diameter for a stator of completely independent vane packets for the parameter values given in the text (insets show the in-sector vane displacements for the modes in the frequency cluster).

upper and lower ring  $s$  (completely independent vane packets). In this study we have considered both limiting cases since any real configuration will be somehow in between these two extreme situations.

All the cases studied consider a stator made up of 16 packets ( $N_s=16$ ) of six airfoils each ( $N_a=6$ ), and the parameters have been chosen to mimic the nondimensional separation in frequency among the different eigenvalues of the realistic case presented in Fig. 2:

$$m_a = 6, \quad M_p/N_a = 7, \quad k_1 = 6, \quad k_2 = 5, \quad k_h = 0.15, \quad k_p = 1000$$

Note that the dimensional values of the constants are irrelevant provided that the results are presented in nondimensional form (all frequencies are normalized using the cantilever vibration frequency of the vane  $\sqrt{k_1/m_a}$ ).

The resulting vibration frequencies and in-sector mode shapes for the case of completely independent vane packets do not depend on the IBPA, as it can be appreciated from the lower plot of Fig. 5. Furthermore the in-sector displacements of the vanes for all modes in the frequency cluster nearly verify the condition  $\sum_{j=1}^{N_a} x_j = 0$  because the stiffness of the lower platform is finite but still much higher than that of the airfoil.

**Realistic Aerodynamics.** In this subsection the stability of the previous model when a realistic aerodynamic model, namely, that shown in Fig. 4, is computed. The resulting nondimensional damping and natural frequencies for the packet ( $k_c=0, k_{hc}=0$ ) and the continuous ring model ( $k_c=k_p, k_{hc}=k_h$ ) are presented at the top and bottom of Fig. 6, respectively. The crosses in the horizontal axis represent the purely structural eigenvalues (without aerody-

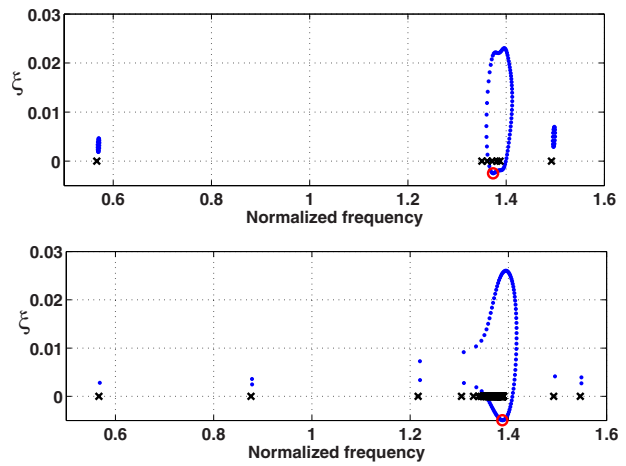


**Fig. 6** Stability of the vane packet using realistic aerodynamics. (Symbols:  $\times$ , structural eigenvalues;  $\bullet$ , aeroelastic eigenvalues;  $\circ$ , most unstable mode. Top: Packet model; bottom: continuous ring).

amic forces) that have no damping. For the packet model it may be observed that the frequency of multiplicity 5, in the infinitely stiff platform, is now split into five eigenvalues when the stiffness of the platform becomes finite and do not depend on the nodal diameter (see also lower plot of Fig. 5). On the other hand, the structural frequencies for the continuous ring model (that can also be regarded as a cyclic structure with  $N$  sectors of one vane) are significantly different from those of the packet model, exhibiting the expected dependence with the nodal diameter associated with the coupling between adjacent sectors. However, highly clustered eigenvalues are also obtained for high nodal diameters.

The aerodynamic damping of the continuous ring just reproduces that shown in Fig. 4, exhibiting a region of unstable traveling-wave modes. The most remarkable result is that, due to the effect of the aerodynamics, the structural modes of the packet model become coupled and the resulting dampings and frequencies (Fig. 6, top) are very similar to those obtained for the continuous ring model (Fig. 6, bottom), although slightly less unstable.

Figure 7 represents the most unstable mode shape of the packet model (for the continuous ring model all modes are pure traveling waves). It can be easily appreciated from the lower plot in Fig. 7

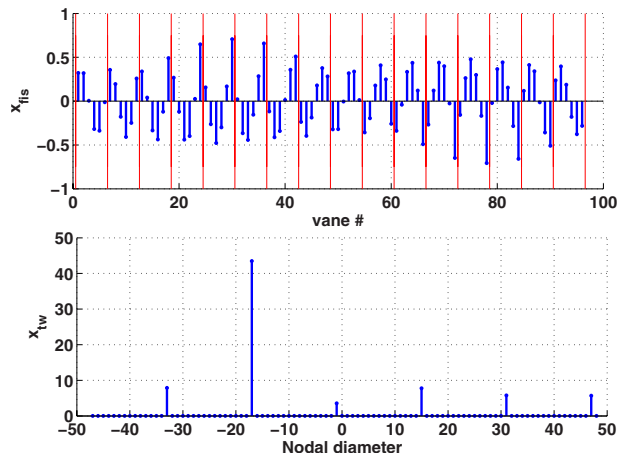


**Fig. 7** Representation of the most unstable mode shape for the tuned and realistic aerodynamics (top: physical space with vertical lines marking each packet; bottom: traveling-wave decomposition)

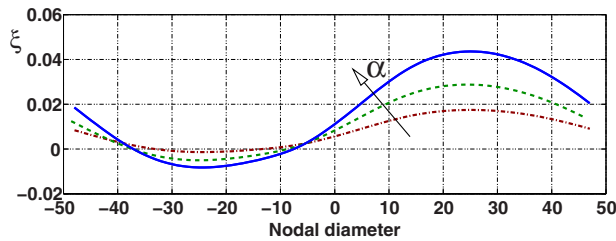


Fig. 8 Effect of the density variation in the damping of the continuous ring model

that, in spite of the lack of coupling in the lower platform, the resulting most unstable mode shape is essentially made of one of the most unstable traveling waves (according to Fig. 4) with five small additional sidebands. It is interesting to notice that the packet model is also a cyclic structure, and its structural and aeroelastic modes are also traveling waves but with  $N_s = 16$  sectors that, when expanded in the traveling-wave basis of the  $N = N_s \times N_a = 16 \times 6 = 96$  individual airfoils, give rise necessarily to only six nonzero components separated by 16 nodal diameters. The independent vane packets assembly is surprisingly unstable, exactly as it would have been predicted by the continuous ring model, which constitutes a conservative approach. Note that the in-sector displacements of the vanes for the most unstable mode (Fig. 7, top) nearly verify the condition  $\sum_{j=1}^{N_a} x_j = 0$ , as it does the purely structural model.

**Mild Aerodynamics.** The nondimensional aerodynamic work per cycle,  $\Theta$ , is rather insensitive to variations in the density and depends essentially on the reduced frequency and the mode shape. This means that the variation of  $\Theta$  in a turbine is relatively small since the mode shape and frequency variations within the operation regime are small and the airfoil exit velocity scales roughly with the square of the temperature. This means that the range of unstable modes of the base line continuous model may be considered constant in a first approximation. However, the dimensional work per cycle,  $W_{\text{work per cycle}}$ , scales with the fluid density undergoing a dramatic variation both with the engine shaft speed and across different turbine stages, since

$$W_{\text{work per cycle}} = \rho_a U_c \delta^2 \omega_N S \Theta(k, \text{mode shape})$$

An equivalent method to retain density variations is to use a scaling factor,  $\alpha$ , for the nondimensional aerodynamic forces, see Eq. (8). The effect of the scaling on the damping may be seen in Fig. 8: The range of the unstable IBPAs is constant but the peak-to-peak variation is substantially modified.

While this variation is irrelevant in an uncoupled approach, where the stability depends solely on the range of unstable IBPAs, the situation is completely different in a fully coupled approach where the ability of the aerodynamics to couple structural modes depends on its strength.

Figure 9 shows a close-up of the dampings and frequencies of the same structural model used in the previous subsection when the strength of the aerodynamics is reduced to a point in which it loses its ability to couple different structural modes. In this particular case the density has been reduced about ten times with respect to the realistic aerodynamic model used in the previous subsection. The aeroelastic eigenvalues of the packet model (top) lie in separated elongated ellipses without any point in common; this means that the aerodynamic forces cannot couple different structural modes and thus the resulting aeroelastic modes do not resemble traveling waves of the individual airfoils, as it happened in the previous case, and there is a clear stabilization effect. The less stable mode is plotted in Fig. 10; it is basically made of the same in-sector distribution (corresponding to the lowest frequency structural mode of the cluster in Fig. 5) but modulated from sector to sector. In this case there is not a dominant TW (the contribution

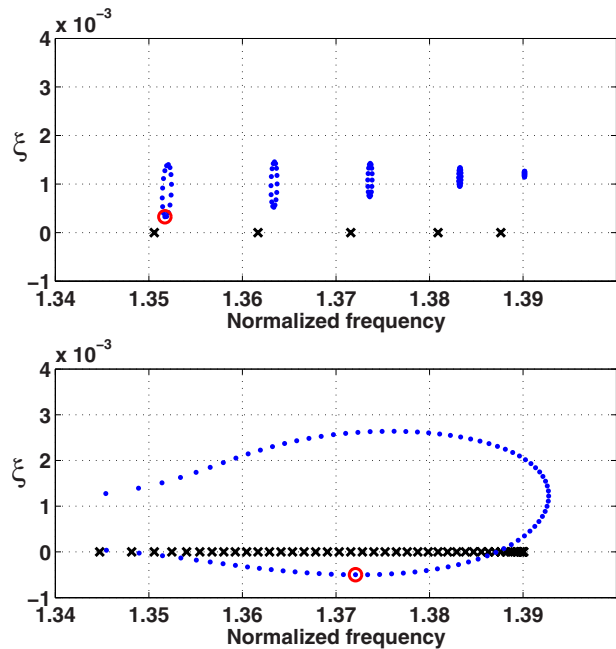


Fig. 9 Stability of the vane packet using mild aerodynamics. (Symbols: x, structural eigenvalues: ●, aeroelastic eigenvalues; ○, most unstable mode. Top: packet model; bottom: continuous ring).

of the sidebands is large) and the mode shape presents a well defined packet structure. The packet model is now stable, the grouping of the vanes has in this case a clear stabilizing effect, and the continuous ring model continues to be unstable; it has the same range of unstable modes but now the instability is weaker because of the scaling of the aerodynamics.

**Uncoupled Approach.** The standard inexpensive approximation for computing the aeroelastic stability of a bladed disk or a packet of vanes is the so-called uncoupled approach. The method essentially consists of obtaining first the structural modes ignoring any aerodynamic effects and then computing the aerodynamic correction (frequency and damping) for each structural mode independently. Roughly speaking the method relies in two basic hypotheses: the “light air” assumption (i.e., the structure is much heavier than the air that surrounds it) and that the natural frequen-

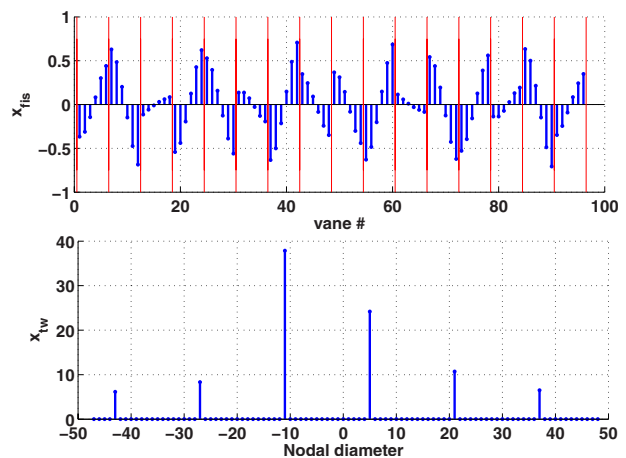
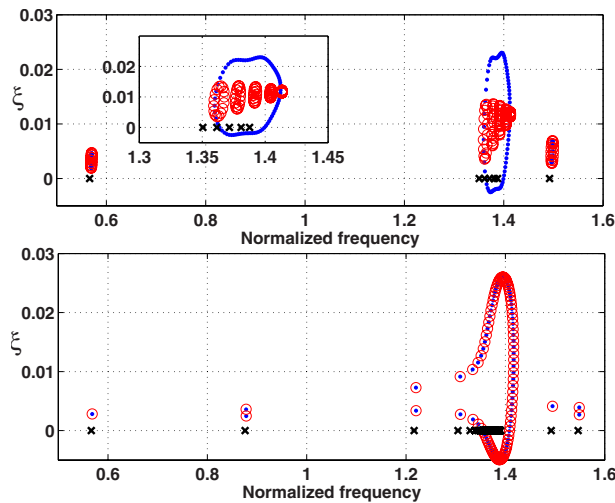


Fig. 10 Fourier representation of the less stable mode for the complex model and mild aerodynamics (Top: physical space with vertical lines marking each packet; bottom: traveling-wave decomposition)





**Fig. 11 Comparison of the fully coupled (dots) and uncoupled (open circles) approaches. Top: Packet model; bottom: continuous ring.**

cies of the modes for a given nodal diameter are separated well apart. It is important to notice that while in blade disks it is very common to find modes within the same family with nearly the same frequency, they have different nodal diameters and therefore they are orthogonal among them. In our case the situation is completely different. Modes of different families, and identical nodal diameters, have very similar eigenvalues and they may potentially interact among them. Under these circumstances the uncoupled approach is not justified and may yield misleading results. This approach was followed by Chernysheva et al. [4]. They assumed that the vane packet mode shapes could be either all-vanes-in-phase modes or any arbitrary combination of airfoils moving in antiphase by pairs. These modes satisfy the constraint  $\sum x_j = 0$ . They computed the stability for all the potential combinations; however, they did not consider the possibility of modes such that the individual vibration amplitude of the airfoils could be different among them. The main hypothesis of the method was that the mode shapes of the problem were known.

It is important to remark that from a numerical point of view the clustered modes we are interested in are well defined. This means that there is not any numerical problem in computing the actual mode shapes. This could be the case if the eigenvalues were so close that the numerical method could not accurately compute them depending on the final result in round-off errors or an arbitrary selection of the basis of the eigenvalue subspace, for instance. Our eigenvalues are not so close and the variations we may appreciate in the mode shapes are not related with numerical but physical considerations.

To illustrate this pathological phenomenon we have analyzed the model of the Realistic Aerodynamics section following an uncoupled approach and then compared the results with the fully coupled approach. This is represented in Fig. 11 (top), where the dampings and natural frequencies obtained using both approaches are displayed. Open circles represent the results obtained by the uncoupled approach. The purely structural modes are first computed and then expanded in TW form. The aerodamping for each structural mode is then computed independently as a linear combination of the aerodampings of its constitutive TWs, obtained from the single passage problem. It may be seen that the five modes corresponding to vibration of the airfoils are perturbed by the aerodynamics but remain separated as five elongated ellipses. The mode shapes retain the packet effect and the problem is stable. The fully coupled approach provides a completely different answer since the original structural modes interact among them to generate a complete different solution, which is unstable, and the

most unstable mode looks like a traveling wave (Fig. 7, bottom). Figure 11 (bottom) shows the same results for the continuous ring model. It may be appreciated that in this case the assumption that the aeroelastic modes are pure traveling wave is correct and the differences between the uncoupled and coupled approaches are negligible.

## Concluding Remarks

A conceptual mass-spring model to study the aeroelastic stability of vane packets has been presented. It has been shown that the much higher stiffness of the lower platform than of the airfoils gives rise to a cluster of  $N_a - 1$  modes with very similar frequencies. It is concluded that the unsteady aerodynamic forces associated with the airfoil motion may significantly couple the structural mode shapes, producing aeroelastic modes that can be very different from the purely structural ones, changing dramatically the flutter margin of the vane packet.

When the aerodynamic forces are small enough the aeroelastic and purely structural modes are very similar. In this regime the system is very stable since the mode shapes exhibit a clear effect of the packet structure.

On the other hand, if the aerodynamic forces are large enough then the stabilizing effect of the packet structure is lost. The aerodynamic effects are now capable of coupling the different structural modes in the frequency cluster and the resulting aeroelastic mode shapes are, in a first approximation, traveling waves of the continuous ring problem and the system is now unstable, as it is the continuous ring model.

Moreover, if the aeroelastic analysis is performed using the standard uncoupled methodology in which the aerodynamic correction (frequency and damping) of each structural mode is computed independently, then the aerodynamic instability of the system can be dangerously underestimated.

It should be recalled that the previous conclusions have been obtained with a simple mass-spring model and therefore there are some three-dimensional effects that may not be accounted for in it. This is especially true for the modification of the airfoil mode shape at the edge of the packets, which induces additional mistuning effects with respect to the continuous ring or the level of coupling among the packets. However, these effects, and any other that could have been missed in the simplified model, only delay the trends described in this paper. The importance of these missing effects depends on the detailed design of the vane packet, which on the other hand depends on the design style of the different companies. The reader should carefully consider how the current results apply to his individual case, keeping in mind that the trends outlined here will be present as well in his aeroelastic model.

## Acknowledgment

The authors want to thank ITP for the permission to publish this paper. This work has been partially supported by the Spanish Minister of Education and Science under Grant No. TRA2006-15015/TAIR, by the Universidad Politécnic de Madrid under Grant No. CCG06-UPM/IME-328, and by ITP under Contract No. DT-ITP-05-039 to the School of Aeronautics of the UPM.

## Nomenclature

$[C]$	= influence coefficient matrix
$k_c$	= stiffness of the coupling between packets
$k_h$	= stiffness of the hook
$k_p$	= stiffness of platform
$N_a$	= number of airfoils of the packet
$N_s$	= number of vane packets
$S$	= airfoil surface
$t$	= time
TW	= traveling wave
$U_{ref}$	= characteristic velocity of the mean flow

$W$  = work per cycle of the airfoil  
 $x_j, x_p$  = airfoil and platform degrees of freedom  
 $\delta_a$  = characteristic vibration amplitude of the airfoil  
 $\rho_a$  = characteristic air density  
 $\sigma$  = interblade phase angle  
 $\omega$  = vibration frequency  
 $\omega_N$  = natural vibration frequency for the all-vanes-in-phase mode  
 $\omega_a$  = vane alone natural vibration frequency

## References

- [1] Corral, R., Gallardo, J., and Vasco, C., 2007, "Aeroelastic Stability of Welded-in-Pair Low Pressure Turbine Rotor Blades: A Comparative Study Using Linear Methods," *ASME J. Turbomach.*, **129**, pp. 72–83.
- [2] Whitehead, D. S., and Evans, D., 1992, "Flutter of Grouped Turbine Blades," ASME Paper No. 92-GT-227.
- [3] Kahl, G., 1995, "Application of the Time Linearized Euler Method to Flutter and Forced Response Calculations," ASME Paper No. 95-GT-123.
- [4] Chernysheva, O. V., Fransson, T. H., Kielb, R. E., and Barter, J., 2003, "Effect of Sector Mode Shape Variation on the Aerodynamic Stability of a Low-Pressure Turbine Sector Vane," ASME Paper No. 2003-GT-38632.
- [5] Panovsky, J., and Kielb, R., 2000, "A Design Method to Prevent Low Pressure Turbine Blade Flutter," *ASME J. Eng. Gas Turbines Power*, **122**, pp. 89–98.
- [6] Nowinski, M., and Panovsky, J., 2000, "Flutter Mechanisms in Low Pressure Turbine Blades," *ASME J. Eng. Gas Turbines Power*, **122**, pp. 89–98.
- [7] Smith, D., 1948, "Vibration of Turbine Blades in Packets," *Proceedings of the Seventh Conference for Applied Mechanics*, Vol. 3, p. 178.
- [8] Prohl, M., 1958, "A Method for Calculating Vibration Frequency and Stress of a Banded Group of Turbine Buckets," *Trans. ASME*, **80**, pp. 169–175.
- [9] Rao, J., 1991, *Turbomachine Blade Vibration*, Wiley New York.
- [10] Feiner, D. M., and Griffin, J. H., 2002, "A Fundamental Model of Mistuning for a Single Family of Modes," *ASME J. Turbomach.*, **124**, pp. 597–605.
- [11] Martel, C., Corral, R., and Llorens, J. M., 2008, "Stability Increase of Aerodynamically Unstable Rotors Using Intentional Mistuning," *ASME J. Turbomach.*, **130**, p. 011006.

# Effect of Upstream Wake With Vortex on Turbine Blade Platform Film Cooling With Simulated Stator-Rotor Purge Flow

**Lesley M. Wright**

Department of Aerospace and Mechanical Engineering,  
The University of Arizona,  
Tucson, AZ 85721-0119

**Sarah A. Blake**

Turbine Heat Transfer Laboratory,  
Department of Mechanical Engineering,  
Texas A&M University,  
College Station, TX 77843-3123

**Dong-Ho Rhee**

Korea Aerospace Research Institute,  
Daejeon, 305-333 Korea

**Je-Chin Han**

Distinguished Professor  
Marcus Easterling Endowed Chair  
Turbine Heat Transfer Laboratory,  
Department of Mechanical Engineering,  
Texas A&M University,  
College Station, TX 77843-3123  
e-mail: jc-han@tamu.edu

*Detailed film cooling effectiveness distributions were experimentally obtained on a turbine blade platform within a linear cascade. The film cooling effectiveness distributions were obtained on the platform with upstream disturbances used to simulate the passing vanes. Cylindrical rods, placed upstream of the blades, simulated the wake created by the trailing edge of the stator vanes. The rods were placed at four locations to show how the film cooling effectiveness was affected relative to the vane location. In addition, delta wings were placed upstream of the blades to model the effect of the passage vortex (generated in the vane passage) on the platform film cooling effectiveness. The delta wings create a vortex similar to the passage vortex as it exits the upstream vane passage. The film cooling effectiveness was measured with the delta wings placed at four locations, to investigate the effect of the passing vanes. Finally, the delta wings were coupled with the cylindrical rods to examine the combined effect of the upstream wake and passage vortex on the platform film cooling effectiveness. The detailed film cooling effectiveness distributions were obtained using pressure sensitive paint in the five blade linear cascade. An advanced labyrinth seal was placed upstream of the blades to simulate purge flow from a stator-rotor seal. The coolant flow rate varied from 0.5% to 2.0% of the mainstream flow, while the Reynolds number of the mainstream flow remained constant at  $3.1 \times 10^5$  (based on the inlet velocity and chord length of the blade). The film cooling effectiveness was not significantly affected with the upstream rod. However, the vortex generated by the delta wings had a profound impact on the film cooling effectiveness. The vortex created more turbulent mixing within the blade passage, and the result is reduced film cooling effectiveness through the entire passage. When the vane induced secondary flow is included, the need for additional platform cooling becomes very obvious.*

[DOI: 10.1115/1.2952365]

## Introduction

As more demand is placed on gas turbines, it is vital that these engines operate as efficiently as possible. Increasing the thermal efficiency of the engine can be achieved by increasing the temperature of the working gas entering the turbine. An array of cooling techniques must be implemented to protect and remove heat from the turbine airfoils. One technique heavily relied on is film cooling. With film cooling, relatively cool air forms a protective film on the outer surface of the airfoil, creating an additional layer of resistance between the hot mainstream gas and the metallic airfoil. With the platform of the blade comprising a large percentage of the area directly exposed to the hot gas, it is vital that this area is adequately protected from the hot gases. Film cooling on the platform must be designed to provide adequate protection with as little coolant as possible. Several reviews have been published by Han et al. [1], Langston [2], Chyu [3], and Simon and Piggush [4], which give an overview of the flow near the end wall and platform regions, as well as heat transfer and film cooling on these regions.

The secondary flows near the platform increase the heat transfer between the mainstream gases and the uncooled platform. The flows also make film cooling on the platform more difficult. Studies by Langston et al. [5,6] revealed some features of these flows.

When a boundary layer flow approaches a blade or vane, a vortex forms at the leading edge and continues along each side of the blade or vane forming a horseshoe vortex. The pressure distribution in each passage causes the suction side leg of the horseshoe vortex to follow the suction side of the blade near the end wall. The pressure side leg of the horseshoe vortex is carried across the passage and gains strength. This large vortex is often called the passage vortex and crosses the passage to meet the suction side leg of the horseshoe vortex on the adjacent blade. Goldstein and Spores [7] and Wang et al. [8] found several "corner" vortices that formed near the intersection of the blade surface and the end wall.

Film cooling is commonly used to protect the platform. Coolant may enter through discrete holes (similar to the midspan of the airfoil). Takeishi et al. [9] studied film cooling through discrete holes in three locations on a vane end wall. They found that the coolant was swept from the pressure side of the passage toward the suction side. Also, the film cooling effectiveness near the leading edge of the blade is very low due to the formation of the horseshoe vortex. Harasgama and Burton [10] placed film cooling holes evenly along an iso-Mach line near the leading edge of a passage. The pressure side of the passage received very little coolant. Similarly, Jabbari et al. [11] found that coolant from discrete holes in the downstream half of the passage did not produce uniform coverage, as the coolant moved away from the pressure side of the passage.

Studies by Friedrichs et al. [12,13] also showed that evenly spaced rows of coolant holes do not provide even coverage for the end wall. Using an ammonia and diazo technique, they measured the amount of coolant coverage at every point on the end wall.

Contributed by the International Gas Turbine Institute of ASME for publication in the JOURNAL OF TURBOMACHINERY. Manuscript received August 5, 2007; final manuscript received August 30, 2007; published online February 3, 2009. Review conducted by David Wisler. Paper presented at the ASME Turbo Expo 2007: Land, Sea, and Air (GT2007), Montreal, Quebec, Canada, May 14–17, 2007.



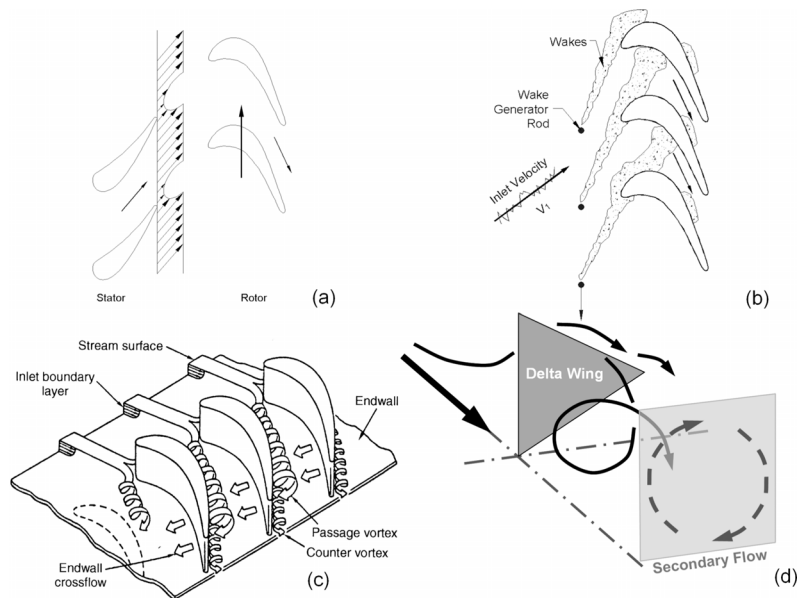


**Fig. 1 Rod and delta wing conceptual flows: (a) unsteady wake, (b) rod generated unsteady wake, (c) passage vortex in vane [6], and (d) vortex generated by delta wing**

The horseshoe vortex prevented the coolant from covering the leading edge of the blade, while the passage vortex lifted the coolant in its path off of the surface. The coolant in the passage is swept from the pressure side toward the suction side by the passage flow. Based on these results, Friedrichs et al. [14] repositioned the film cooling holes to attempt to cover the entire end wall with the same amount of coolant. Coverage in the majority of the passage was significantly improved, but the coverage near the leading edge and close to the suction surface was still poor, due to the horseshoe vortex and the suction side corner vortex. In a recent study, Barizozzi et al. [15] compared film cooling designs with cylindrical holes or fan-shaped holes. With increasing blowing ratios, the passage vortex weakened and cross flow in the passage was reduced.

Upstream of the inlet guide vane, a gap commonly exists between the combustion chamber and the vane end wall. A similar gap exists between the vane end wall and the rotor platform, ensuring that the rotor can move freely. Coolant air is often injected through these gaps, or slots, in order to prevent hot mainstream gases from entering the engine cavity. This coolant air has a secondary effect of protecting the end wall region, and if this air is used effectively, the need for separate film cooling can be reduced. An early study by Blair [16] showed that the film cooling effectiveness for upstream slot injection varied greatly through the passage due to the secondary flows. Granser and Schulenberg [17] showed that coolant from an upstream slot can reduce the secondary flows in the passage by increasing the momentum of the boundary layer. Similarly, coolant slots used by Roy et al. [18] reduced the heat transfer near the leading edge. Burd et al. [19] and Oke et al. [20,21] also studied film cooling through slots upstream of vanes. They found that coolant from the slot could provide coverage for most of the passage.

In order to provide adequate coverage for the entire end wall or platform, an upstream slot can be combined with discrete holes. Nicklas [22] measured the heat transfer coefficients and film cooling effectiveness with an upstream slot and three rows of discrete holes. Liu et al. [23] found that an increased blowing ratio gave more uniform protection to the platform for the densely spaced cooling holes they used to simulate upstream slot cooling.

Zhang and Jaiswal [24] and Zhang and Moon [25] used pressure sensitive paint to measure the film cooling effectiveness for

two rows of discrete holes upstream of the passage or for a single slot. They confirmed that effectiveness is significantly improved with increasing blowing ratio. Knost and Thole [26] found that areas that are typically difficult to cool, including the area near the leading edge, can be cooled effectively with upstream slot injection. Cardwell et al. [27] showed that effectiveness is reduced significantly if two adjacent vanes are not properly aligned. Wright et al. [28–30] considered a variety of stator-rotor seal configurations, discrete film hole combinations, and flow parameters. They concluded that the film cooling effectiveness on the blade platform (within a linear cascade) is significantly affected by the upstream seal configuration. In addition, it is possible to minimize the purge flow, if the purge flow is thoughtfully combined with additional discrete film cooling.

Numerous studies have found that the secondary flows in a vane or rotor passage greatly affect film cooling. However, most of the studies have been performed on linear cascades or turbine vanes, so the effect of the upstream vane on rotor platform cooling has not been examined. Han et al. [31] found that the unsteady wake from the trailing edge of the vane affects the heat transfer coefficients on the rotor blade midspan. They used rotating rods placed upstream of the blades to simulate the relative motion of the blades with respect to the vanes. As shown in Fig. 1, a wake forms downstream of the vane, and this wake will influence flow around the turbine blades. Cylindrical rods can be used to model this interaction and create a wake similar to that created by the trailing edge of the vane. The unsteady wake caused boundary layer transition to occur closer to the leading edge, leading to significantly higher heat transfer coefficients. The effect varied with both Reynolds number and Strouhal number. Ou et al. [32] found this effect to be secondary to the increase in heat transfer coefficients caused by film cooling. Zhang and Han [33,34] extended this study to include the effect of mainstream turbulence. Both increased mainstream turbulence and unsteady wake individually increase the heat transfer coefficients on the midspan of the blade, but with high mainstream turbulence the effect of the unsteady wake is reduced. Similarly, with the unsteady wake present, increasing the mainstream turbulence has a reduced effect. Mhetras and Han [35] used stationary rods to simulate the unsteady wake effect by measuring the film cooling effectiveness on the blade surface with the rods in each of four positions; this

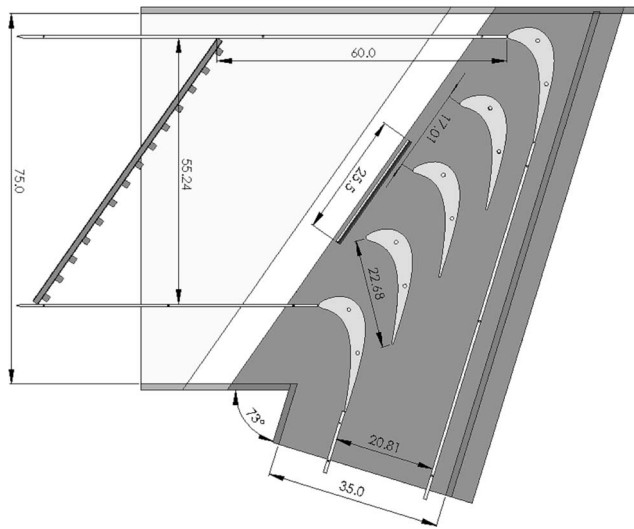


Fig. 2 Low speed wind tunnel with turbine blade details

method showed the instantaneous wake effect rather than the average effect of the wake. Due to the wake created by the rods, the film cooling effectiveness was reduced, especially on the suction side of the blade.

The objective of the current study is to examine the effect of the passing upstream vane on film cooling on the rotor platform. Coolant will be injected through a labyrinthlike seal upstream of a linear cascade of high pressure turbine blades. Stationary cylindrical rods in four positions will be used to simulate the unsteady wake created by the trailing edge of the vanes. Delta wings (which will later be described in detail) will also be placed upstream of the passage to simulate the passage vortex created in the vane. For each upstream condition, detailed film cooling effectiveness distributions will be obtained on the platform using the pressure sensitive paint (PSP) technique. The coolant flow rate will vary between 0.5% and 2.0% of the mainstream flow. The freestream turbulence intensity will be 5.0% upstream of the rods and delta wings. The film cooling effectiveness distributions obtained will demonstrate how the upstream vane can affect the flow near the platform.

## Experimental Facility

**Low Speed Wind Tunnel and Linear Cascade Design.** Figure 2 shows the layout of the existing low speed wind tunnel previously used by Wright et al. [30]. The flow conditions remain unchanged from the previous study with an inlet velocity ( $V_1$ ) of 20 m/s and an exit velocity ( $V_2$ ) of 50 m/s. This gives a mainstream Reynolds number (based on the inlet velocity and blade chord) of  $3.1 \times 10^5$ . For additional details of the open-loop wind tunnel, the reader is referred to recent platform cooling studies [28–30]. To create a background turbulence of 5% at the inlet of the cascade, the turbulence grid is moved to a location 60 cm upstream of the cascade inlet. As determined by Zhang and Han [36], with a grid made of 1.3 cm square bars spaced 4.8 cm apart, the turbulence intensity at the inlet of the cascade is 5% with a dissipation length scale of 1.5 cm.

Figure 2 also shows the advanced, high pressure turbine blade used for this study. The blade, which was scaled up five times, has a 107.49 deg turning angle with an inlet flow angle of 35 deg and an outlet flow angle of  $-72.49$  deg. The chord length of the blade is 22.68 cm and the height of the blade is 25.4 cm. The blade-to-blade spacing at the inlet is 17.01 cm with a throat-to-span ratio of 0.2.

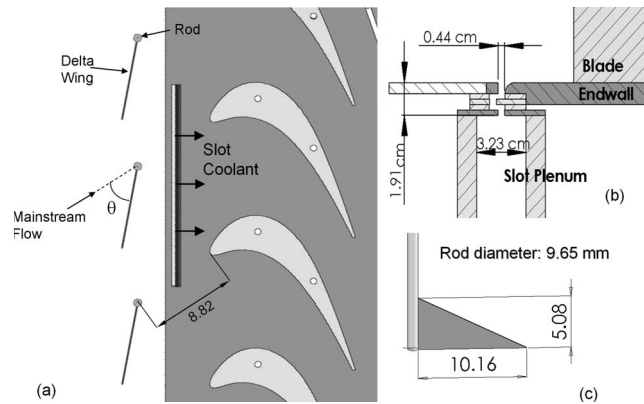
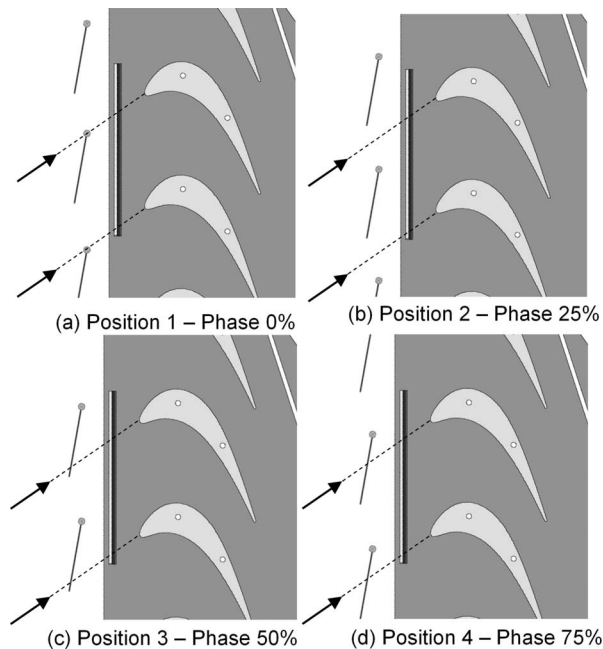


Fig. 3 Platform film cooling configuration (dimensions in centimeters): (a) detail of cooled platform with rod and delta wing, (b) detail of labyrinthlike stator-rotor seal, and (c) detail of rod and delta wing

**Linear Cascade With Stator-Rotor Seal.** The advanced, labyrinthlike stator-rotor seal used previously [30] is used in the current study. As shown in Fig. 3, the seal is located 4.34 cm upstream of the blade leading edge, and the seal covers 1.5 passages of the linear cascade. Figure 3(b) shows that the width of the advanced slot is 0.44 cm, and the coolant travels through the labyrinthlike geometry ( $l_s/w=6.84$ ), turning 180 deg before being expelled onto the passage end wall. An ASME orifice meter is used to measure the coolant flow rate before the coolant fills a plenum and is then expelled onto the platform. The flow rate of the coolant is varied, so the film cooling effectiveness can be measured over a range of flow rates varying from 0.5% to 2.0% of the mainstream flow.

**Upstream Wake and Vortex Generation.** As mentioned previously, this study is aimed at reproducing the interaction of stator vanes with the rotor blades. A number of studies have used either rotating or stationary rods to model the trailing edge of the upstream vane, and subsequently the wake formed downstream of the trailing edge [31–34]. This study will consider how the wake influences the film cooling effectiveness on the blade platform. The upstream wake has been shown to have a profound effect on the film cooling effectiveness on the blade span, so it is necessary to confirm or refute this finding on the blade platform with upstream coolant injection. The wake is generated by placing 9.7 mm rods 8.82 cm upstream of the blades. The rod size and distance have previously been used by Han et al. [31] as an appropriate representation of the trailing edge of the upstream vanes. Unlike this previous study, the rods will remain stationary, and the effectiveness will be measured with the rods placed at four positions within the passage. Rather than obtaining an average effect from rotating rods, the film cooling effectiveness can be measured with the rods at four specific locations. The four locations are selected by dividing the passage into quarters. Figure 4 shows the location of the rods relative to the stagnation line of the mainstream flow. The wake forming downstream of the rods (Fig. 1(b)) will affect the platform differently at each position. Therefore, it is interesting to know the instantaneous film cooling effectiveness as an attempt to identify the potential problems.

The effect of wakes on both the film cooling effectiveness and heat transfer coefficients on the blade surface has been thoroughly considered. However, it is likely that there is a more dominant force influencing the heat transfer coefficients and film cooling effectiveness on the turbine blades. Many studies have shown the profound effect of passage secondary flow on heat transfer coefficients and film cooling effectiveness on vane end walls and blade platforms. Because the effect of the passage induced flow cannot be ignored, groups are proactively attempting to eliminate



**Fig. 4 Rod and delta wing positions in reference to stagnation lines**

the passage vortex [37–41]. However, the effect (if any) of the passage vortex created between two adjacent vanes on flow around the downstream turbine blades should be considered.

Figure 1(d) shows that a delta wing can be used to generate a vortex. Rather than placing a vane cascade upstream of the blade cascade, delta wings are placed upstream of the blades to replicate the passage vortex. The exact flow exiting the vane passage is unknown; therefore, the size and strength of the passage vortex are also unknown. However, previous studies of secondary flow through a vane passage can be referenced to quantify the passage vortex at the trailing edge of the vane passage. From numerical predictions [42], it has been predicted that the passage vortex lifts from the end wall. Along the suction surface of the vane, the circulation of the vortex occupies approximately 15% of the vane span. Therefore, it is desirable to select a delta wing geometry (size and angle), which will generate a similar vortex entering the blade passage.

Armed with this information, preliminary numerical simulations were performed using FLUENT 6.0 to determine how a delta wing would influence flow through the current blade passage. A single passage was modeled, and  $1.5 \times 10^6$  cells defined the domain. Simulations were performed with coolant flow rates of 1.0% of the mainstream flow with and without the delta wing. The predicted pathlines obtained using the Reynolds stress model with a nonequilibrium wall function are shown in Fig. 5. The height of the delta wing was chosen as 20% of the blade span, and the wing is oriented 45 deg from the mainstream flow. The delta wing is shown at Positions 2 and 4.

Through several numerical predictions, the delta wing was sized to have a height of 5.08 cm. This height was selected as it is 20% of the blade height, and from the numerical predictions, the vortex formed by the delta wing is also approximately 20% of the blade height. The size and position of this vortex resulting from the delta wing (placed 8.82 cm upstream of the blades) are comparable to the passage vortex predicted to form in a typical vane passage [42]. It is more difficult to know the strength of the passage vortex exiting the vane passage. By changing the angle of attack of the delta wing, the strength of the vortex approaching the blade passage changes, while the physical size remains relatively unchanged. The angle of the delta wing,  $\theta$  (Fig. 3(a)), will be

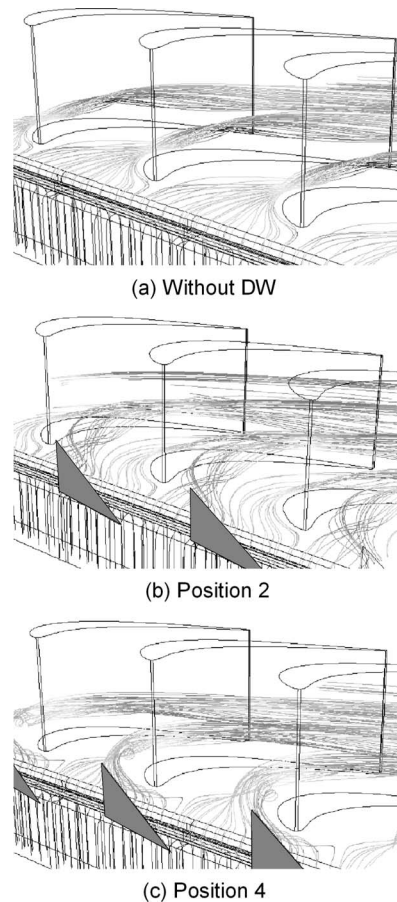


**Fig. 5 Path lines seeded near the platform (colored by velocity magnitude)**

varied (30 deg and 45 deg) to consider how the film cooling effectiveness varies with passage vortices of different strengths. As with the rods, the delta wings will be moved, relative to the blades, so the film cooling effectiveness can be measured at four relative locations (Fig. 4).

In addition to the isolated effects of the trailing edge wake and vane passage induced vortex, the rod and delta wing are combined to consider the combined effect of these two factors. As shown in Figs. 3(a) and 3(c), the delta wing is attached to the rod. Both orientations of the delta wing are considered (30 deg and 45 deg), and the rod-wing combination is moved to all four positions relative to the blades.

**Pressure Sensitive Paint for Film Cooling Effectiveness Measurement.** As in the previous platform film cooling studies [30], PSP is used to measure the film cooling effectiveness on the platform within the linear cascade. Zhang et al. [24,25] first used PSP to measure the film cooling effectiveness on a vane end wall, and since, PSP has been applied to a flat plate [43], cylinder [44], blade tip [45], blade span [35], rotating leading edge [46,47], and rotating platform [48]. All of these studies involve very different flow conditions, but PSP has proven to be a very powerful experimental technique in each of these cases.

The premise behind PSP is an oxygen quenching effect. As the oxygen partial pressure of the gas in direct contact with the surface increases, the intensity of light emitted by the PSP decreases (hence, oxygen quenched). The PSP can be calibrated to determine the relationship between the emission intensity of the paint and the surrounding pressure. A test plate is sprayed with the Uni-FIB PSP (UF470-750) supplied by Innovative Scientific Solutions, Inc. (ISSI) and placed inside a vacuum chamber. At each



measurement point, the PSP sample is excited using a strobe light equipped with a 500 nm broadband pass filter. A charge-coupled device (CCD) camera with a 630 nm filter records the intensity emitted by the PSP.

After the PSP has been properly calibrated, the film cooling effectiveness can be measured on the desired test surface. Due to the size of the end wall passage, two sets of images are required to capture the entire passage. The procedure to measure the effectiveness on both the upstream and downstream halves of the passage is identical, and the results are combined to give a complete picture of the film cooling effectiveness on the platform. The film cooling effectiveness is measured based on a mass transfer technique. Two similar tests are required to calculate the film cooling effectiveness: one with air as the coolant and one with nitrogen as the coolant. The film cooling effectiveness can be calculated based on the concentration of oxygen, which is related to the partial pressure of oxygen. Therefore, the film cooling effectiveness can be calculated using Eq. (1).

$$\eta = \frac{C_\infty - C_{\text{mix}}}{C_\infty} = \frac{(P_{\text{O}_2})_{\text{air}} - (P_{\text{O}_2})_{\text{N}_2}}{(P_{\text{O}_2})_{\text{air}}} \approx 1 - \frac{I_{\text{air}}}{I_{\text{N}_2}} \quad (1)$$

To accurately determine the film cooling effectiveness, a total of four images are required: (1) a black image to remove any background noise from the optical components (no mainstream flow, no coolant flow, no excitation light), (2) a reference image to establish the intensity at the reference atmospheric pressure (no mainstream flow, no coolant flow, PSP is excited with the strobe light), (3) an air image to measure the partial pressure of oxygen with air as the coolant (mainstream flow, air as coolant flow, excitation by strobe light), and (4) a nitrogen image to measure the partial pressure of oxygen with nitrogen as the coolant (mainstream flow, nitrogen as coolant flow, excitation by strobe light). In the presence of oxygen, the emission intensity falls, so the intensity ratio ( $I_{\text{ref}}/I$ ) increases. When nitrogen is injected as the coolant, the emission intensity increases (due to the lack of oxygen), and the intensity ratio decreases. The partial pressure of oxygen with air or nitrogen injection is determined based on the calibration of the emission intensity and pressure. The film cooling effectiveness can be determined at every pixel, giving a detailed film cooling effectiveness distribution on the passage end wall.

Experimental uncertainty was considered using a 95% confidence level as presented by Coleman and Steele [49]. The uncertainty of the film effectiveness measurements varies depending on the intensity level measured by the CCD camera. The experimental uncertainty is less than 2% for film effectiveness measurements greater than 0.5. However, as the effectiveness begins to approach zero (where the measured light intensities are relatively low), the uncertainty rises. For a film cooling effectiveness of 0.07, the uncertainty is approximately 10% and continues to rise as the effectiveness approaches zero. All experimental results were repeated multiple times to confirm the repeatability of the data. The data proved to be repeatable for the entire range of film effectiveness that was measured.

## Results and Discussion

There are many possible combinations of results that are available for consideration. Table 1 summarizes the experimental test cases that have been considered. However, detailed film cooling effectiveness distributions will not be presented for every case. Results have been selected to aid the discussion of how the film cooling effectiveness on the rotor platform is affected by simulated flow through a vane passage. In all cases a grid is placed in the mainstream flow to create a background turbulence intensity of 5% at the cascade inlet.

**Detailed Film Cooling Effectiveness Distributions.** In order to consider how the film cooling effectiveness is affected by the upstream vane passage flow, a set of base line conditions must be

**Table 1 Mainstream and coolant flow conditions for the present study (Tu=5%)**

Vane effect	Cascade model	Upstream location	Seal flow rate
None	—	—	0.5%, 1.0%, 1.5%, 2.0%
Trailing edge wake	Stationary rod	0%, 25%, 50%, 75%	0.5%, 1.0%, 1.5%, 2.0%
Passage secondary flow	30 deg delta wing	0%, 25%, 50%, 75%	0.5%, 1.0%, 1.5%, 2.0%
Passage secondary flow	45 deg delta wing	0%, 25%, 50%, 75%	0.5%, 1.0%, 1.5%, 2.0%
Combined wake and secondary flow	Rod+30 deg delta wing	0%, 25%, 50%, 75%	0.5%, 1.0%, 1.5%, 2.0%
Combined wake and secondary flow	Rod+45 deg delta wing	0%, 25%, 50%, 75%	0.5%, 1.0%, 1.5%, 2.0%

established. Figure 6 shows the detailed film cooling distributions on the rotor platform with no upstream vane influence with Tu = 5%. The film effectiveness distributions are shown for the four coolant flow rates being considered. At the lowest flow rate of  $m_s=0.5\%$  (Fig. 6(a)) a large portion of the passage is left uncovered. Although the coolant exits the labyrinth seal uniformly, at the entrance of the passage, the coolant is quickly carried from the pressure side of the passage to the suction side. With formation of the horseshoe vortex at the leading edge of the passage, and the movement of the pressure side leg across the passage to the suction side, the effectiveness of the coolant quickly diminishes. Doubling the amount of coolant to 1.0% of the mainstream flow yields only marginal improvement over the 0.5% flow rate. The coolant covers a large area of the upstream half of the passage, but a large portion of the downstream half of the passage remains unprotected. Further increasing the coolant through the seal results in a more uniform distribution of the coolant on the upstream half of the passage. Increasing the coolant flow rate weakens the effect of the passage vortex, and thus more uniform film cooling effectiveness distributions are present on the upstream half of the passage. These trends have been observed in other platform cooling studies [28–30].

The effect of the trailing edge wake is considered in Fig. 7. All four plots show the film cooling effectiveness distributions mea-

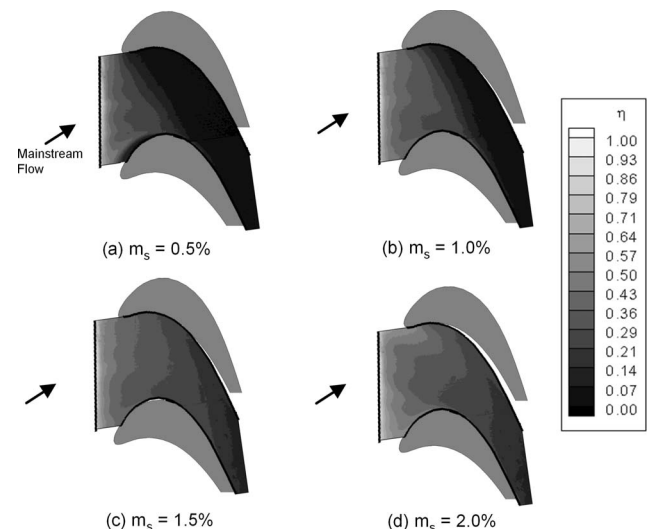


**Fig. 6 Film cooling effectiveness on platform with freestream turbulence of 5% and various seal injection rates**

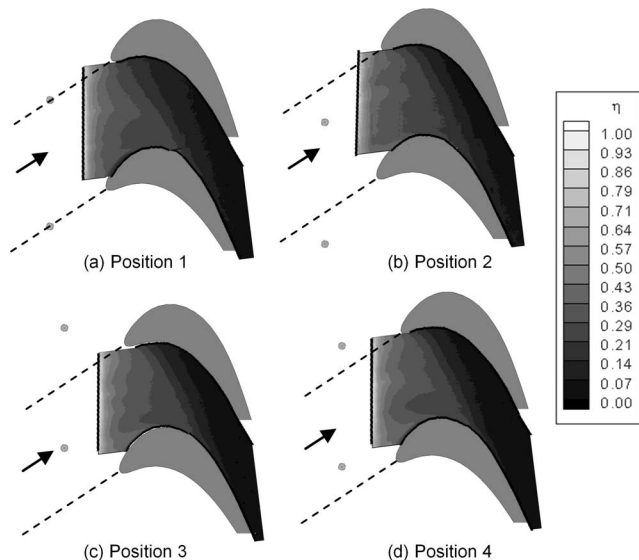


**Fig. 7 Film cooling effectiveness on platform with wake rod in four positions ( $m_s=1.0\%$ )**

sured with a coolant flow rate of 1.0% (a generalization of the following discussion can be applied to the other coolant flow rates considered). The position of the rod changes in each of the figures. Figure 7(a) shows that the rod aligned with the stagnation point of the blades (Position 1 or 0%). Comparing Fig. 7(a) with 6(b) shows no appreciable difference in the film cooling effectiveness. The wake created by the upstream rod is directed to the leading edge of the blades, and thus the wake interacts with the horseshoe vortex at the blade leading edge. When considering the effect of the upstream rod on the platform film cooling effectiveness, more than the downstream wake should be considered. Along the platform, a horseshoe vortex will also form around the rod. However, both of these effects are masked by the coolant from the stator-rotor seal, and the horseshoe vortex formed at the blade leading edge.

As the rod moves to other upstream positions, the changes to the platform film cooling effectiveness are minimal. Even when the downstream wake would extend to the center of the passage (Fig. 7(c)), there is no clear evidence of the wake on the film cooling effectiveness. With the coolant being injected into the mainstream flow, the effects of the wake and horseshoe vortex from the rod are mitigated.

With the rod simulating the trailing edge of the stator vane offering no appreciable difference to the platform film cooling effectiveness, it is necessary to introduce the vortex that models the passage induced vortex from the vane passage. To create the vortex, the delta wing is placed upstream of the stator-rotor seal, and it is oriented 30 deg to the mainstream flow. Figure 8 shows the measured film cooling effectiveness with the delta wing placed at each of the four upstream positions. Subtle differences can be noticed between Figs. 6(b) and 8(a). The area of coolant coverage does not extend as deep into the passage when the delta wing is placed upstream of the blades. As the vortex passes over the seal, the coolant lifts off the platform and is mixed with the mainstream. Therefore, it does not remain attached to the surface as it does in the absence of the delta wing.

Other changes can be noticed with the delta wing at Positions 2 (Fig. 8(b)) and 4 (Fig. 8(d)). When the delta wing is placed at Position 2 (Fig. 8(b)), the vortex forms close to the center of the passage. The vortex generated by the delta wing is directed toward the center of the passage, and into the passage, the coolant is skewed toward the pressure side of the passage. The passage vortex formed in the vane passage competes with the blade passage induced vortex. Although the coolant distribution is altered from

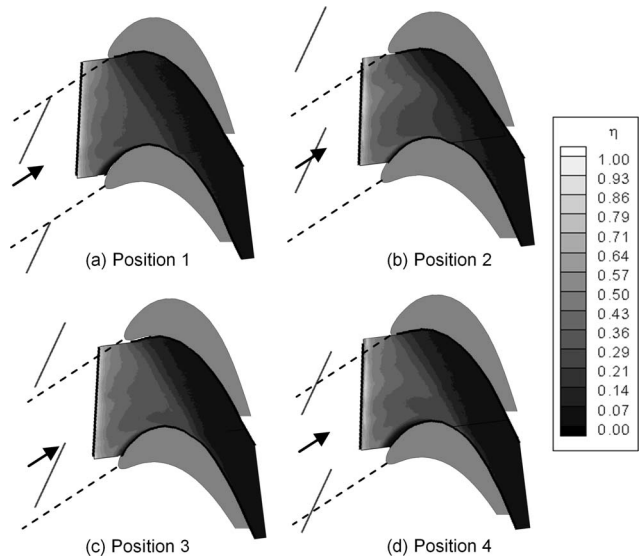


**Fig. 8 Film cooling effectiveness on platform with delta wing in four positions ( $m_s=1.0\%$ ,  $\theta=30$  deg)**

the base line case, the secondary flow induced in the blade passage continues to dictate the platform film cooling effectiveness. Position 4 (Fig. 8(d)) is unique, compared to the other positions with the 30 deg delta wing, because an area along the suction side of the blade, just downstream of the leading edge, is left unprotected. This was also observed at Position 1 (Fig. 8(a)), but the area with no coverage has increased. With the delta wing at these positions (1 and 4), the vortex from the delta wing combines with the suction side leg of the horseshoe vortex to strengthen the horseshoe vortex at the blade leading edge. The stronger vortex lifts the coolant from the platform, and thus less film coverage occurs.

Dramatic consequences of the passage vortex resulting from the upstream vane passage are shown in Fig. 9. In this figure the delta wing is oriented 45 deg to the mainstream flow. Because the exact size and strength of the passage vortex leaving the vane passage, corresponding to the present blade geometry, are not known, it is important to consider a range of possibilities. Although we have confirmed that the delta wing produces a passage vortex that is

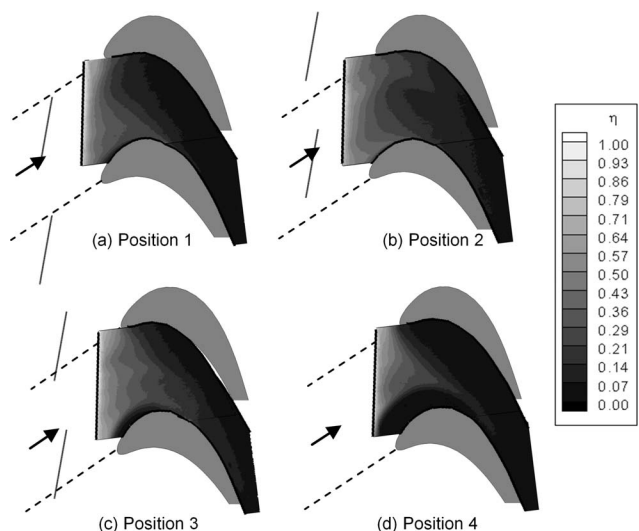


**Fig. 9 Film cooling effectiveness on platform with delta wing in four positions ( $m_s=1.0\%$ ,  $\theta=45$  deg)**

comparable to that predicted from other vane studies, the precise size and strength of the vortex are dependent on many variables and the vortex may vary with these parameters. Therefore, it is necessary to consider a variety of flow conditions. It is clear from Fig. 9 that the impact of the vortex created by the 45 deg delta wing is more severe than that created by the 30 deg wing. The 45 deg delta wing blocks nearly half of the passage and generates a stronger vortex than generated by the wing oriented at 30 deg. At the coolant flow rate of 1.0%, the effect of the upstream vortex is radically different with the delta wing placed at each position. Figure 9(a) shows that when the delta wing is aligned with the leading edge of the blades, the coolant distribution does not follow the expected path of the blade passage vortex (from pressure side to suction side of the passage). The coolant lifts off the surface due to the upstream vortex. In addition, the upstream vortex intersects the passage vortex near the pressure side of the passage. At this intersection, more mixing of the coolant with the mainstream occurs, and the film cooling effectiveness is further reduced.

When the delta wing is shifted 25% of the passage width (Position 2), the interaction of the two vortices results in a very non-uniform film cooling effectiveness distribution. Although it has not been confirmed with flow measurements, it appears that the blade passage vortex crosses from the pressure side to the suction side of the passage. In addition the vortex generated by the delta wing intersects the blade passage vortex, and due to the increased strength of this vortex, it is able to push through the passage vortex to the pressure side of the passage. This is seen by the increased effectiveness along the pressure side of the passage. The coolant extends further along the pressure side of the passage, but the effectiveness diminishes to nearly zero closer to the leading edge of the blades (when compared to the unobstructed flow).

With the delta wing placed at Position 3 (Fig. 9(c)), the film cooling effectiveness distributions are similar to those observed without the upstream delta wing (Fig. 6(b)). The primary difference is the reduction in the film cooling effectiveness downstream of the leading edge along the suction side of the passage. This same trend is seen when the delta wing is moved to Position 4 but is significantly amplified. At both of these positions, the upstream vortex combines with the horseshoe vortex at the leading edge of the blades, and the coolant is lifted off the platform. As shown in Fig. 9(d), the effect is dramatic over the entire passage when the delta wing is placed at Position 4 (75%). The protection offered by the purge flow is limited to a small area in the center of the passage. In addition, the coverage is reduced below that of the original coolant flow rate of 0.5% (Fig. 6(a)).

With knowledge that the effect of an upstream vortex can be significant, it is necessary to consider how the upstream vortex combines with the wake. This is done by coupling the 45 deg delta wing with the circular rod. Figure 10 shows the coupled effect of the rod and delta wing on the platform film cooling effectiveness. At the given coolant flow rate of 1.0%, there is no appreciable difference between the film cooling effectiveness distributions measured with the rod coupled to the delta wing (Fig. 10) and only the delta wing (Fig. 9). The vortex generated by the delta wing is, without question, dominant over the wake and horseshoe vortex created by the rod.

The adverse effect of the delta wing generated vortex is further considered in Fig. 11. This figure shows the film cooling effectiveness measured with the 45 deg delta wing and rod placed at Position 4 (75%) for each of the coolant flow rates. In all the cases, the reduction in the film cooling effectiveness is dramatic. At the lowest flow rate of 0.5% (Fig. 11(a)), only a fraction of the passage is covered by the coolant, and the coverage area only partially extends into the passage between the blades. At increased flow rates, large areas of the passage remain unprotected. Without the delta wing, the coolant extended to the trailing edge of the passage; however, with the delta wing, only the upstream half of

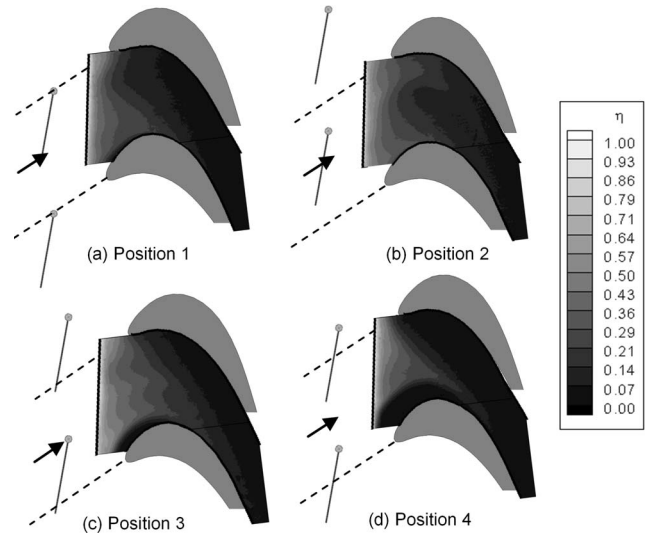


Fig. 10 Film cooling effectiveness on platform with wake rod and delta wing in four positions ( $m_s=1.0\%$ ,  $\theta=45$  deg)

the passage is covered by the coolant. The very intense vortex generated upstream of the blades creates turbulent mixing, and the coolant does not remain attached to the surface.

**Laterally Averaged Film Cooling Effectiveness.** More general comparisons of all the cases studied can be made by comparing the laterally averaged film cooling effectiveness. Figures 12–15 compare the cases by coolant flow rate and rod/delta wing location. Figure 12 shows the average effectiveness with the lowest coolant flow rate of 0.5%. Generally, the film cooling effectiveness decreases sharply immediately downstream of the seal. This was also noticed in the previous study of Wright et al. [30]. The effectiveness approaches zero beyond  $x/C_{ax}=0.5$ . The averages show that the film cooling effectiveness is only significantly affected in the presence of the 45 deg delta wing, and this was clearly illustrated in the previous contour plots. The same trends are observed when the coolant flow rate is increased to 1.0% of the mainstream flow, as shown in Fig. 13. The vortex generated by the 45 deg delta wing is most detrimental to the film cooling effectiveness, when it is located at Position 4 (75%), and it has the

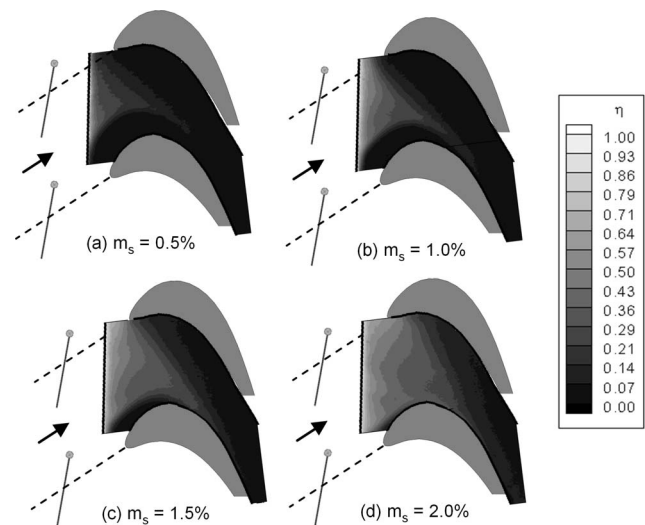


Fig. 11 Film cooling effectiveness on platform with wake rod and delta wing in position 4 ( $\theta=45$  deg)



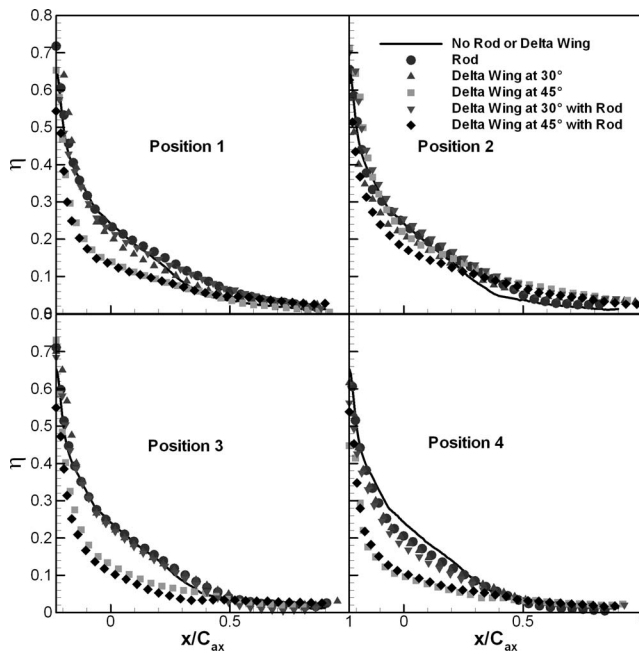


Fig. 12 Comparison of laterally averaged film cooling effectiveness on the platform for various upstream conditions ( $m_s = 0.5\%$ )

least impact at Position 2 (25%).

When the coolant flow rate is further increased to 1.5%, Fig. 14 shows that the film cooling effectiveness is more sensitive to the upstream flow condition. With the rod or delta wing inline with the stagnation line (Position 1, 0%), the film cooling effectiveness is unchanged due to the wake formed downstream of the rod. However, the average film cooling effectiveness decreases due to the vortex created by the 30 delta wing, and the effectiveness is further reduced with the 45 deg delta wing. It has been shown that increasing the seal flow rate reduces the effect of the blade pas-

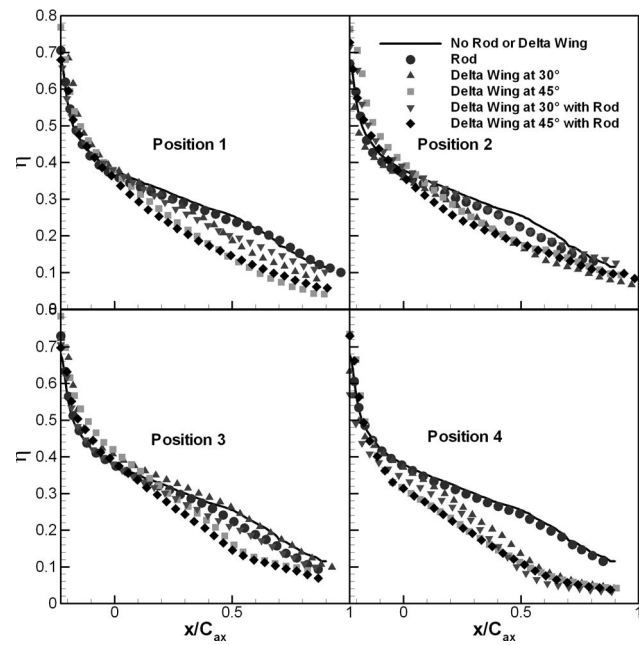


Fig. 14 Comparison of laterally averaged film cooling effectiveness on the platform for various upstream conditions ( $m_s = 1.5\%$ )

sage vortex [30]. With the effect of the passage induced secondary flow weakened, the effect of the upstream vortex becomes more apparent. As the strength of the vortex increases with the insertion of the 45 deg delta wing, the effectiveness is further reduced. Again the greatest decrease in the film cooling effectiveness is shown with the obstruction in Position 4, and the effectiveness is the least affected with the rod or delta wing at Position 2.

Finally, the averaged effectiveness is presented for the greatest coolant flow rate of 2.0% in Fig. 15. The trends are similar to those observed with the flow rate of 1.5%. It is obvious that the

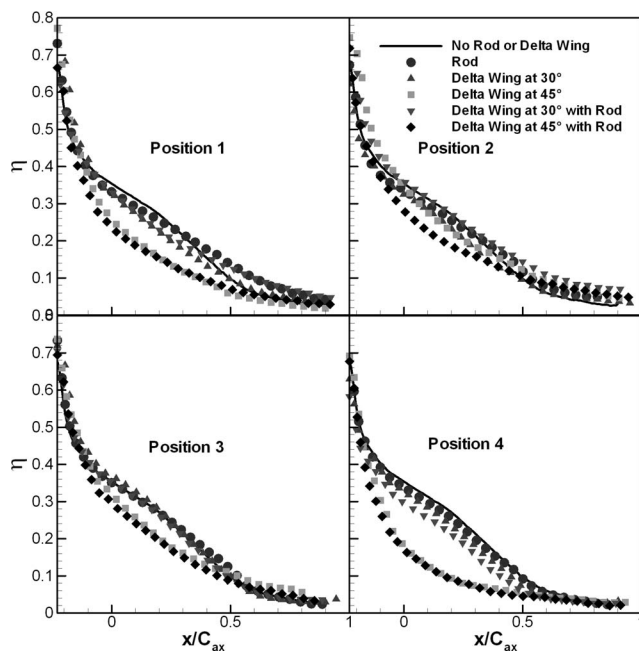


Fig. 13 Comparison of laterally averaged film cooling effectiveness on the platform for various upstream conditions ( $m_s = 1.0\%$ )

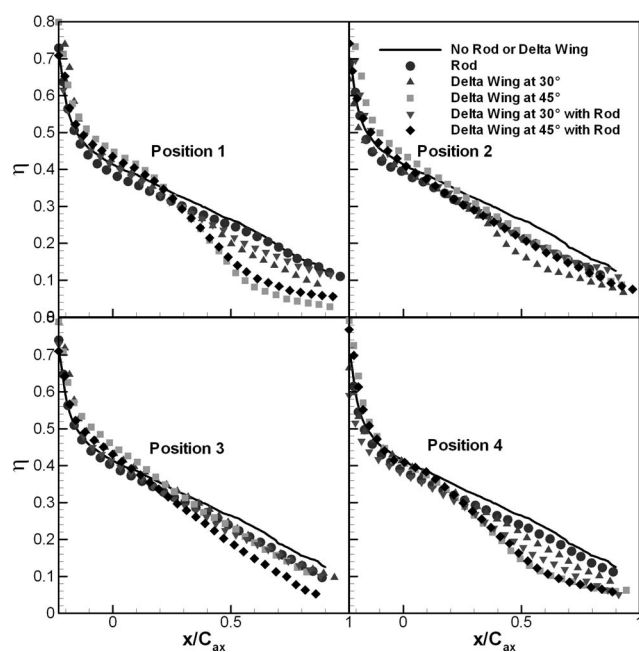


Fig. 15 Comparison of laterally averaged film cooling effectiveness on the platform for various upstream conditions ( $m_s = 2.0\%$ )

film cooling effectiveness is most severely affected by the 45 deg delta wing at Positions 1 and 4. At these two positions coverage does not extend into the latter half of the passage. This is significant because additional cooling is needed to adequately protect the entire platform even at the very large seal flow rate.

## Conclusions

An experimental study was undertaken to measure the film cooling effectiveness on a turbine blade platform (within a linear cascade) subject to purge flow from an advanced stator-rotor seal. The labyrinthlike seal was upstream of the blades, and the amount of purge flow through the seal varied from 0.5% to 2.0% of the mainstream flow. Several obstructions were placed upstream of the blades to create flow patterns likely to result from stator vanes located upstream of the blades. A cylindrical rod was used to model the trailing edge of the vane, so the effect of the downstream wake could be considered. A delta wing was used to generate a vortex upstream of the blade passage; this vortex is similar to the passage vortex that would be created as the mainstream flow travels through the vane passage.

Using pressure sensitive paint to measure the film cooling effectiveness, it was determined that the upstream wake had only a negligible effect on the platform film cooling effectiveness. With the rod placed at four locations upstream of the blades, the film cooling effectiveness was not significantly altered for any seal flow rate or rod position. However, the film cooling effectiveness could be significantly reduced with the generation of a vortex upstream of the blade passage. Because the exact strength and structure of the vortex created in the vane passage are unknown, two variations were considered to show how the effectiveness changes as the upstream vortex structure changes. The vortex created by the 45 deg delta wing was apparently much stronger than that created by the 30 deg delta wing with the film cooling effectiveness on the platform being dramatically reduced. Depending on the location of the blades relative to the upstream vane (delta wing), the film effectiveness distribution is altered as the film cooling effectiveness is dependent on both the upstream vortex and the passage vortex created in the blade passage. The upstream vortex has the dominant effect on the film effectiveness on the blade platform.

Numerous studies have measured and predicted the flow through a vane passage. This information was drawn upon to replicate the passage vortex at the trailing edge of the vane passage. Numerical predictions were used to size a delta wing that was placed upstream of the current blade passage. The effect of the vortex created by the delta wing was considered by measuring the film cooling effectiveness on the blade platform. From this experimental study, it is clear that the secondary flow induced in the upstream vane passage has a profound effect on the rotor platform film cooling effectiveness. The need for additional cooling on the latter half of the passage is obvious from the detailed film cooling distributions. If this behavior is not considered, the results can be detrimental to the life of the engine.

## Acknowledgment

This publication was partially sponsored by the US Department of Energy, Office of Fossil Energy, National Energy Technology Laboratory. In addition, partial funding for this study was also received from the Korean Research Foundation (KRF) KRF-2005-214-D00244 for support of Dong-Ho Rhee, a Visiting Scholar at Texas A&M University—Turbine Heat Transfer Laboratory.

## Nomenclature

- $C$  = true chord length of the blade  
 $C_{ax}$  = axial chord length of the blade  
 $C_{mix}$  = oxygen concentration of mainstream-coolant mixture

- $C_{\infty}$  = oxygen concentration of mainstream  
 $h$  = local heat transfer coefficient ( $W/m^2 K$ )  
 $I$  = emission intensity of PSP  
 $I_{air}$  = emission intensity of PSP recorded with air as the coolant  
 $I_{N_2}$  = emission intensity of PSP recorded with nitrogen as the coolant  
 $I_{ref}$  = emission intensity of PSP at reference (atmospheric) pressure  
 $l_s$  = slot length  
 $m_s$  = slot injection mass flow ratio (percentage of the mainstream flow)  
 $M_s$  = slot injection blowing ratio  
 $(= \rho_s V_s / \rho_m V_{m1} \cong V_s / V_{m1})$   
 $(P_{O_2})_{N_2}$  = partial pressure of oxygen measured with nitrogen as the coolant  
 $(P_{O_2})_{air}$  = partial pressure of oxygen measured with air as the coolant  
 $Tu$  = turbulence intensity  
 $V_{m1}$  = mainstream velocity at the cascade inlet (m/s)  
 $V_{m2}$  = mainstream velocity at the cascade exit (m/s)  
 $V_s$  = slot injection velocity (m/s)  
 $w$  = slot width (m)  
 $x$  = axial distance from the cascade leading edge (m)  
 $\theta$  = delta wing orientation with respect to inlet mainstream flow  
 $\rho_m$  = density of mainstream ( $kg/m^3$ )  
 $\rho_s$  = density of slot coolant ( $kg/m^3$ )  
 $\eta$  = film cooling effectiveness

## References

- Han, J. C., Dutta, S., and Ekkad, S. V., 2000, *Gas Turbine Heat Transfer and Cooling Technology*, Taylor & Francis, New York, p. 646.
- Langston, L. S., 2001, "Secondary Flows in Axial Turbines—A Review," *Ann. N.Y. Acad. Sci.*, **934**, pp. 11–26.
- Chyu, M. K., 2001, "Heat Transfer Near Turbine Nozzle Endwall," *Ann. N.Y. Acad. Sci.*, **934**, pp. 27–36.
- Simon, T. W., and Piggush, J. D., 2006, "Turbine Endwall Aerodynamics and Heat Transfer," *J. Propul. Power*, **22**, pp. 310–312.
- Langston, L. S., Nice, L. M., and Hooper, R. M., 1976, "Three-Dimensional Flow Within a Turbine Cascade Passage," *ASME Paper No. 76-GT-50*.
- Langston, L. S., 1980, "Crossflows in a Turbine Cascade Passage," *ASME J. Eng. Power*, **102**, pp. 866–874.
- Goldstein, R. J., and Spores, R. A., 1988, "Turbulent Transport on the Endwall in the Region Between Adjacent Turbine Blades," *ASME J. Heat Transfer*, **110**, pp. 862–869.
- Wang, H. P., Olson, S. J., and Goldstein, R. J., 1997, "Flow Visualization in a Linear Turbine Cascade of High Performance Turbine Blades," *ASME J. Turbomach.*, **119**, pp. 1–8.
- Takeishi, K., Matsuura, M., Aoki, S., and Sato, T., 1990, "An Experimental Study of Heat Transfer and Film Cooling on Low Aspect Ratio Turbine Nozzles," *ASME J. Turbomach.*, **112**, pp. 488–496.
- Harasgama, S. P., and Burton, C. S., 1992, "Film Cooling Research on the Endwall of a Turbine Nozzle Guide Vane in a Short Duration Annular Cascade: Part 1—Experimental Technique and Results," *ASME J. Turbomach.*, **114**, pp. 734–740.
- Jabbari, M. Y., Marston, K. C., Eckert, E. R. G., and Goldstein, R. J., 1996, "Film Cooling of the Gas Turbine Endwall by Discrete-Hole Injection," *ASME J. Turbomach.*, **118**, pp. 278–284.
- Friedrichs, S., Hodson, H. P., and Dawes, W. N., 1996, "Distribution of Film-Cooling Effectiveness on a Turbine Endwall Measured Using the Ammonia and Diazo Technique," *ASME J. Turbomach.*, **118**, pp. 613–621.
- Friedrichs, S., Hodson, H. P., and Dawes, W. N., 1997, "Aerodynamic Aspects of Endwall Film Cooling," *ASME J. Turbomach.*, **119**, pp. 786–793.
- Friedrichs, S., Hodson, H. P., and Dawes, W. N., 1998, "The Design of an Improved Endwall Film Cooling Configuration," *ASME Paper No. 98-GT-483*.
- Barigozzi, G., Benzoni, G., Franchini, G., and Derdichizzi, A., 2005, "Fan-Shaped Hole Effects on the Aero-Thermal Performance of a Film Cooled Endwall," *ASME Paper No. GT2005-68544*.
- Blair, M. F., 1974, "An Experimental Study of Heat Transfer and Film Cooling on Large-Scale Turbine Endwall," *ASME J. Heat Transfer*, **96**, pp. 524–529.
- Granser, D., and Schulenberg, T., 1990, "Prediction and Measurement of Film Cooling Effectiveness for a First-Stage Turbine Vane Shroud," *ASME Paper No. 90-GT-95*.
- Roy, R. P., Squires, K. D., Gerendas, M., Song, S., Howe, W. J., and Ansari,

- A., 2000, "Flow and Heat Transfer at the Hub Endwall of Inlet Vane Passages—Experiments and Simulations," ASME Paper No. 2000-GT-198.
- [19] Burd, S. W., Satterness, C. J., and Simon, T. J., 2000, "Effects of Slot Bleed Injection Over a Contoured End Wall on Nozzle Guide Vane Cooling Performance: Part II—Thermal Measurements," ASME Paper No. 2000-GT-200.
- [20] Oke, R., Simon, T., Shih, T., Zhu, B., Lin, Y. L., and Chyu, M., 2001, "Measurements Over a Film-Cooled Contoured Endwall With Various Coolant Injection Rates," ASME Paper No. 2001-GT-0140.
- [21] Oke, R. A., and Simon, T. W., 2002, "Film Cooling Experiments With Flow Introduced Upstream of a First Stage Nozzle Guide Vane Through Slots of Various Geometries," ASME Paper No. GT-2002-30169.
- [22] Nicklas, M., 2001, "Film-Cooled Turbine Endwall in a Transonic Flow Field: Part II—Heat Transfer and Film Cooling Effectiveness," ASME J. Turbomach., **123**, pp. 720–729.
- [23] Liu, G., Liu, S., Zhu, H., Lapworth, B. C., and Forest, A. E., 2004, "Endwall Heat Transfer and Film Cooling Measurements in a Turbine Cascade with Injection Upstream of Leading Edge," Heat Transfer Asian Res., **33**, pp. 141–152.
- [24] Zhang, L. J., and Jaiswal, R. S., 2001, "Turbine Nozzle Endwall Film Cooling Study Using Pressure-Sensitive Paint," ASME J. Turbomach., **123**, pp. 730–735.
- [25] Zhang, L. J., and Moon, H. K., 2003, "Turbine Nozzle Endwall Inlet Film Cooling—The Effect of a Backward Facing Step," ASME Paper No. GT2003-38319.
- [26] Knost, D. G., and Thole, K. A., 2004, "Adiabatic Effectiveness Measurements of Endwall Film Cooling for a First Stage Vane," ASME Paper No. GT2004-53326.
- [27] Cardwell, N. D., Sundaram, N., and Thole, K. A., 2005, "Effects of Mid-Passage Gap, Endwall Misalignment and Roughness on Endwall Film-Cooling," ASME Paper No. GT2005-68900.
- [28] Wright, L. M., Gao, Z., Yang, H., and Han, J. C., 2006, "Film Cooling Effectiveness Distribution on a Gas Turbine Blade Platform With Inclined Slot Leakage and Discrete Film Hole Flows," ASME Paper No. GT2006-90375.
- [29] Wright, L. M., Blake, S., and Han, J. C., 2006, "Effectiveness Distributions on Turbine Blade Cascade Platforms Through Simulated Stator-Rotor Seals," AIAA Paper No. AIAA-2006-3402.
- [30] Wright, L. M., Blake, S., and Han, J. C., 2006, "Film Cooling Effectiveness Distributions on a Turbine Blade Cascade Platform With Stator-Rotor Purge and Discrete Film Holes Flows," ASME Paper No. IMECE2006-15092.
- [31] Han, J.-C., Zhang, L., and Ou, S., 1993, "Influence of Unsteady Wake on Heat Transfer Coefficient From a Gas Turbine Blade," ASME J. Heat Transfer, **115**, pp. 904–911.
- [32] Ou, S., Han, J.-C., Mehendale, A. B., and Lee, C. P., 1994, "Unsteady Wake Over a Linear Turbine Blade Cascade With Air and CO<sub>2</sub> Film Injection: Part I—Effect on Heat Transfer Coefficients," ASME J. Turbomach., **116**, pp. 721–729.
- [33] Zhang, L., and Han, J.-C., 1994, "Influence of Mainstream Turbulence on Heat Transfer Coefficients From a Gas Turbine Blade," ASME J. Heat Transfer, **116**, pp. 896–903.
- [34] Zhang, L., and Han, J.-C., 1995, "Combined Effect of Free-Stream Turbulence and Unsteady Wake on Heat Transfer Coefficients From a Gas Turbine Blade," ASME J. Heat Transfer, **117**, pp. 296–302.
- [35] Mhetras, S., and Han, J. C., 2006, "Effect of Unsteady Wake on Full Coverage Film-Cooling Effectiveness for a Gas Turbine Blade," AIAA Paper No. AIAA-2006-3403.
- [36] Zhang, L., and Han, J. C., 1994, "Influence of Mainstream Turbulence on Heat Transfer Coefficients From a Gas Turbine Blade," ASME J. Heat Transfer, **116**, pp. 896–903.
- [37] Sauer, H., Muller, R., and Vogerler, K., 2000, "Reduction of Secondary Flow Losses in Turbine Cascades by Leading Edge Modification at the Endwall," ASME Paper No. 2000-GT-0473.
- [38] Zess, G. A., and Thole, K. A., 2002, "Computational Design and Experimental Evaluation of Using a Leading Edge Fillet on a Gas Turbine Vane," ASME J. Turbomach., **124**, pp. 167–175.
- [39] Becz, S., Majewski, M. S., and Langston, L. S., 2003, "Leading Edge Modification Effects on Turbine Cascade Endwall Loss," ASME Paper No. GT2003-38898.
- [40] Shih, T. I.-P., and Lin, Y.-L., 2002, "Controlling Secondary—Flow Structure by Leading-Edge Airfoil Fillet and Inlet Swirl to Reduce Aerodynamic Loss and Surface Heat Transfer," ASME Paper No. GT-2002-30529.
- [41] Lethander, A. T., Thole, K. A., Zess, G., and Wagner, J., 2004, "Vane-Endwall Junction Optimization to Reduce Turbine Vane Passage Adiabatic Wall Temperatures," J. Propul. Power, **20**, pp. 1105–1116.
- [42] Hermanson, K., Kern, S., Picker, G., and Parneix, S., 2003, "Predictions of External Heat Transfer for Turbine Vanes and Blades With Secondary Flow Fields," ASME J. Turbomach., **125**, pp. 107–113.
- [43] Wright, L. M., Gao, Z., Varvel, T. A., and Han, J. C., 2005, "Assessment of Steady State PSP, TSP, and IR Measurement Techniques for Flat Plate Film Cooling," ASME Paper No. HT2005-72363.
- [44] Gao, Z., Wright, L. M., and Han, J. C., 2005, "Assessment of Steady State PSP and Transient IR Measurement Techniques for Leading Edge Film Cooling," ASME Paper No. IMECE2005-80146.
- [45] Ahn, J., Mhetras, S., and Han, J. C., 2004, "Film-Cooling Effectiveness on a Gas Turbine Blade Tip Using Pressure Sensitive Paint," ASME Paper No. GT2004-53249.
- [46] Ahn, J., Schobeiri, M. T., Han, J. C., and Moon, H. K., 2004, "Film Cooling Effectiveness on the Leading Edge of a Rotating Turbine Blade," ASME Paper No. IMECE2004-59852.
- [47] Ahn, J., Schobeiri, M. T., Han, J. C., and Moon, H. K., 2005, "Film Cooling Effectiveness on the Leading Edge of a Rotating Film-Cooled Blade Using Pressure Sensitive Paint," ASME Paper No. GT2005-68344.
- [48] Suryanarayanan, A., Mhetras, S. P., Schobeiri, M. T., and Han, J. C., 2006, "Film Cooling Effectiveness on a Rotating Blade Platform," ASME Paper No. GT2006-90034.
- [49] Coleman, H. W., and Steele, W. G., 1989, *Experimentation and Uncertainty Analysis for Engineers*, Wiley, New York.



**Jonathan McGlumphy**  
e-mail: jmcglump@vt.edu

**Wing-Fai Ng**  
e-mail: wng@vt.edu

Department of Mechanical Engineering,  
Virginia Polytechnic Institute & State University,  
Blacksburg, VA 24061

**Steven R. Wellborn**  
e-mail: steven.r.wellborn@rolls-royce.com

**Severin Kempf**  
e-mail: severin.g.kempf@rolls-royce.com

Compressor and Fan Aerodynamic Design,  
Rolls-Royce Corp.,  
Indianapolis, IN 46206

# Numerical Investigation of Tandem Airfoils for Subsonic Axial-Flow Compressor Blades

*The tandem airfoil has potential to do more work as a compressor blade than a single airfoil without incurring significantly higher losses. Although tandem blades are sometimes employed as stators, they have not been used in any known commercial rotors. While the long-term goal for this program is development of a commercially viable tandem rotor, this paper discusses tandem airfoils in subsonic, shock-free rectilinear cascade flow. Existing literature data on tandem airfoils in rectilinear cascades have been compiled and presented in a Lieblein loss versus loading correlation. Large scatter in the data gave motivation to conduct an extensive 2D computational fluid dynamics (CFD) study evaluating the overall performance as a function of the relative positions of the forward and aft airfoils. CFD results were consistent with trends in the open literature, both of which indicate that a properly designed tandem airfoil can outperform a comparable single airfoil on and off design. The general agreement of the CFD and literature data serves as a validation for the computational approach.*  
[DOI: 10.1115/1.2952366]

*Keywords:* gas turbine, tandem blade, compressor, cascade, computational

## Introduction

A major limitation on the pressure rise in a subsonic axial-flow compressor stage is boundary layer separation on the blade suction surface and endwalls. One method of controlling the suction surface boundary layer is to employ tandem airfoil blades, shown in Fig. 1 with their main design parameters. The basic concept is that a new boundary layer forms on the second (aft) airfoil, allowing for greater overall loading without large flow separations. Tandem airfoils are used as flaps and slats on aircraft to improve lift during takeoff and landing. In turbomachinery, tandem blades have been employed as stators, examples of which include the GE J-79 compressor [1] and an advanced single-stage low pressure (LP) compressor built by Honeywell [2]. However, they have not been used in commercial rotors.

Brent and Clemmons [3], Bammert et al. [4,5], and Hasegawa et al. [6] have all constructed and tested experimental tandem blade compressor rotors. While the particular machines varied in size and scope, they all shared the shortcoming of narrow stability range from design conditions, which may explain why tandem blades have not yet been employed in commercial rotors.

The end goal of the project is to evaluate the feasibility of a commercially viable tandem blade rotor. This technology could be used to reduce the number of stages in the back of a core compressor while maintaining an acceptable overall efficiency and stability range. It should be noted here that unlike the rotors of Bammert and Hasegawa, this study limits inlet Mach numbers to 0.6 to avoid the complexities of passage shocks.

This paper presents the first portion of our efforts, which is a numerical study of tandem airfoils in the 2D rectilinear cascade frame of reference. This initial focus on the rectilinear cascade stems from the large amount of data available in the open literature to which we can directly compare our results. Future publications will showcase work in the 3D rotating frame of reference.

**Literature Review.** A survey of open literature on 2D tandem airfoils reveals a wide range of methods and flow conditions that have been examined in rectilinear cascade configuration [7–22]. Experimental studies of various airfoil families and geometric configurations have been conducted for inlet Mach numbers ranging from 0.05 to 1.6. Some employed endwall and sidewall boundary layer removal, while others did not. Computational studies have ranged from potential flow with boundary layer codes to fully viscous Reynolds-averaged Navier–Stokes (RANS) solvers. More detailed descriptions are given by McGlumphy [23].

Because the current interest is in core compressor stages, the most pertinent works are those that meet the following criteria:

- subcritical inlet flow (no shocks are present)
- boundary layer removal employed for experimental data (AVDR  $\sim$  1.0)

Railly and El-Sarha [9] performed low-speed wind tunnel tests on a tandem cascade with fixed airfoil shapes. They varied overall camber by changing the stagger angles of each airfoil. They also examined several axial overlap (AO) and percent pitch (PP) combinations. Wu et al. [16] examined the double-circular arc (DCA) tandem airfoils in a series of moderate speed ( $M_{11} \sim 0.30$ ) wind tunnel tests. By varying stagger angles, AO, and PP, they had 24 combinations of the tandem airfoil design parameters. Roy and Saha [18–20] conducted low-speed wind tunnel tests to directly compare a tandem airfoil to a single airfoil using controlled diffusion airfoils (CDAs).

Sanger [14] used an incompressible potential flow model with a boundary layer code to analyze several configurations of DCA tandem airfoils. He examined the effects of several variables, including chord ratio, camber ratio, AO, as well as the convergence ratio of the gap formed between the two airfoils at the overlap region. More recently, Canon-Falla [22] performed an incompressible-flow computational study on tandem airfoils of NACA-65 profiles. His results were obtained using the commercially available code FLUENT.

Several key points about 2D tandem airfoils emerge from the following.

Contributed by the Turbomachinery Division for publication in the JOURNAL OF TURBOMACHINERY. Manuscript received August 8, 2007; final manuscript received September 21, 2007; published online February 3, 2009. Review conducted by David Wisler. Paper presented at the 2007 ASME International Mechanical Engineering Congress (IMECE2007), Seattle, WA, November 10–16, 2007.

- 1.) Airfoil family (e.g. NACA, DCA)
- 2.) Cambers:
  - a. forward airfoil:  $\varphi_{FA} = \kappa_{11} - \kappa_{12}$
  - b. aft airfoil:  $\varphi_{AA} = \kappa_{21} - \kappa_{22}$
  - c. Overall:  $\varphi_{ov} = \kappa_{11} - \kappa_{22}$
- 3.) Effective chord, spacing, and solidity:
  - a. Chord:  $C_{eff} = (C_{FA} + C_{AA}) / (1 + AO)$
  - b. Spacing,  $s_{eff} = (1 - 0.5 * AO) * s$
  - c. Solidity:  $\sigma_{eff} = C_{eff} / s_{eff}$
- 4.) Axial overlap:  $AO = \Delta x_1 / \Delta x_2$
- 5.) Percent pitch:  $PP = t / s$

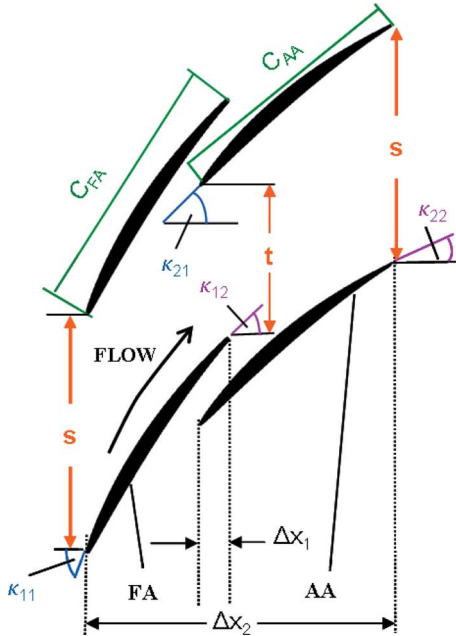


Fig. 1 Tandem airfoil geometrical parameters

- AO and PP have a first-order effect on performance.
- The best performance is achieved with high PP and low AO similar to that shown in Fig. 1.
- At high loading, an optimized tandem airfoil will produce less loss than a comparable single airfoil.
- Airfoil camber ratio ( $\varphi_{FA} / \varphi_{AA}$ ), which is proportional to the loading ratio, also affects tandem performance.
- The interaction of the flow fields between the forward and aft airfoils is important.

From a compressor designer's standpoint, it would be useful to see these data in a graphical format such as a loss versus loading correlation. To accomplish this, we employ the Lieblein diffusion factor (henceforth referred to as the D-factor) as a measure of airfoil loading, defined here for a tandem airfoil as

$$D \equiv \left(1 - \frac{w_{22}}{w_{11}}\right) + \left(\frac{w_{\theta,11} - w_{\theta,22}}{2\sigma_{eff}w_{11}}\right) \quad (1)$$

where the first and second terms represent velocity diffusion and turning, respectively. The associated loss parameter is a representation of the boundary layer momentum thickness at the trailing edge (TE) normalized by the airfoil chord length, defined for a tandem airfoil as

$$\omega_p \equiv \left(\frac{\theta^*}{C_{eff}}\right) \approx \omega_c \frac{\cos \beta_{22}}{2\sigma_{eff}} \left(\frac{\cos \beta_{22}}{\cos \beta_{11}}\right)^2 \quad (2)$$

where  $\omega_c$  is the mass-averaged stagnation pressure loss coefficient

$$\omega_c \equiv \frac{P_{0,11} - P_{0,22}}{P_{0,11} - P_{11}} \quad (3)$$

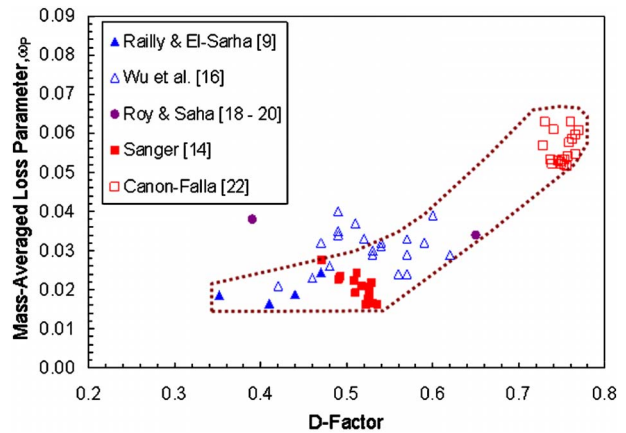


Fig. 2 Lieblein chart of selected literature

These parameters allow for a wide range of cambers and solidities to collapse onto a single performance curve for a given airfoil family, as Lieblein demonstrated with low-speed NACA single airfoil cascade data [24]. The loss parameter versus D-factor has historically proven to be an excellent indicator of 2D performance even for flows that are radically different from Lieblein's original assumptions [25]. Thus, we are comfortable adapting the method for use with tandem airfoils.

Available data from Refs. [9,14,16,18–20,22] have been expressed in terms of D-factor and loss parameter, as shown in Fig. 2. The general trend is outlined by the dashed shape and is similar to a typical single airfoil [24]. Scatter in the data can be partially attributed to the variety of airfoil families and airfoil shapes examined. However, it is noteworthy that scatter exists even among the data of researchers who used only one set of tandem airfoils [9,22]. For example, Canon-Falla [22] changed only AO and PP; yet, there is a noticeable variation in the loss levels of his tandem configurations. This serves as a visual reinforcement of the idea that PP and AO have first-order effects on overall performance.

Several of the points on Fig. 2 lie above the general performance trend. The common characteristic among these outlying points is that each configuration had a camber ratio greater than unity, suggesting that the forward airfoil (FA) was more loaded than the AA. Ihlenfeld [8] recommended that the airfoils be equally loaded for the best loading-to-loss ratio. A CFD study of the effects of loading distribution on 2D tandem performance arrived at the same conclusion: Shifting the loading distribution to either airfoil tends to increase losses for the tandem configuration [23].

Figure 2 serves to show the trend of tandem performance at minimum loss conditions (hereafter referred to as design conditions for convenience). Unfortunately, there is only one data point for each airfoil family/AO/PP combination. From the designer's standpoint, it would be useful to have curves of performance sensitivity to these parameters over a wide range of D-factors, i.e.,  $0.4 < D < 0.7$ . Given the size of the test matrix for an even modest sweep of AO and PP, gathering these data experimentally would be an expensive and time-consuming task. Therefore, a computational approach seems more appropriate; the results of which are the focus of this paper.

## 2D CFD Analysis

The purpose of the CFD analysis was threefold. The first goal was to examine on-design performance sensitivity to the tandem airfoil parameters of AO and PP over a wide range of D-factors for a single airfoil family.

The second goal was to examine off-design performance. By definition, the D-factor is calculated at the minimum loss incidence angle, meaning that it is necessary to generate a loss coef-

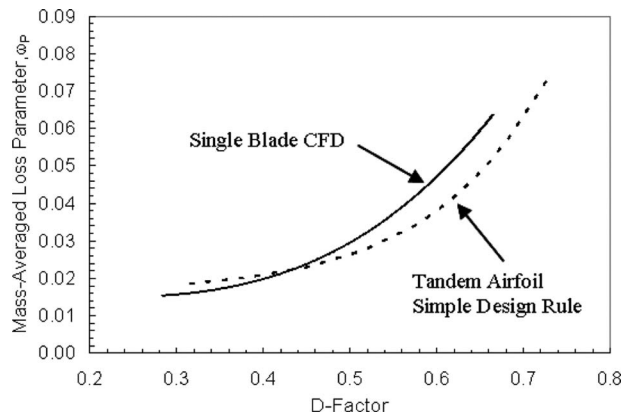


Fig. 3 Single CFD versus tandem design rule

ficient versus incidence plot (i.e., loss bucket) for each tandem configuration. Since these data are requisite for a Lieblein chart, it was also possible to determine the incidence range for each tandem airfoil, giving an indication of off-design performance. Incidence range is defined here as the difference between the two flow angles that produce a loss coefficient twice that of the minimum value.

Finally, the CFD solutions were interrogated to evaluate the governing fluid mechanics behind both the on- and off-design performance trends.

**Simple Design Rule.** In order to perform the tandem airfoil CFD study in an efficient manner, a simple “back-of-envelope” design rule was developed. The purpose of the design rule was to estimate the required camber and stagger angles such that both the forward and aft airfoils were operating at minimum loss at design conditions.

The underlying assumption of the design rule is that the forward and aft airfoils act independently of one another. One can then specify the individual airfoil D-factors and subsequently calculate the overall D-factor for the airfoils in tandem. If a loss versus loading correlation is available for the chosen airfoil family, the individual airfoil losses can be determined based upon the specified D-factors. Individual airfoil losses are then superposed to give the estimated overall loss for the tandem airfoil.

While certainly not the most potent of airfoils, there are a large amount of openly available data on the NACA-65 family [24], making it a convenient choice for use in this simple design rule. The NACA-65 data are presented in a way that allows one to select the required airfoil metal angles ( $\kappa_{11}$ ,  $\kappa_{12}$ ,  $\kappa_{21}$ ,  $\kappa_{22}$ ) for minimum loss operation at a desired D-factor. The procedure is conceptually similar to the one used by Canon-Falla [22], who set his airfoil metal angles based on NACA-65 Mellor diagrams. For a more detailed explanation of the simple design rule, see the Appendix.

As a final preparation, several CFD cases were run on NACA-65 single airfoils at an inlet Mach number of 0.6, consistent with the requirement that no shocks be present in the flow field. This gave a basis for direct comparison between the tandem airfoil and single airfoil. Also, the loss versus loading curve for the single airfoil was used to estimate overall losses in the tandem design rule. Figure 3 shows curves of the CFD-generated single airfoil and the design rule estimate for a tandem airfoil. Comparing the single airfoil to the tandem design rule, there is approximately a 20% drop in loss levels at an overall D-factor of 0.62.

It should again be emphasized that the design rule assumes no interaction between the flow fields of the forward and AAs. Other researchers—Bammert and Staude [4], for example—have demonstrated that the interaction effects of a properly designed tandem configuration can result in overall losses that are less than the

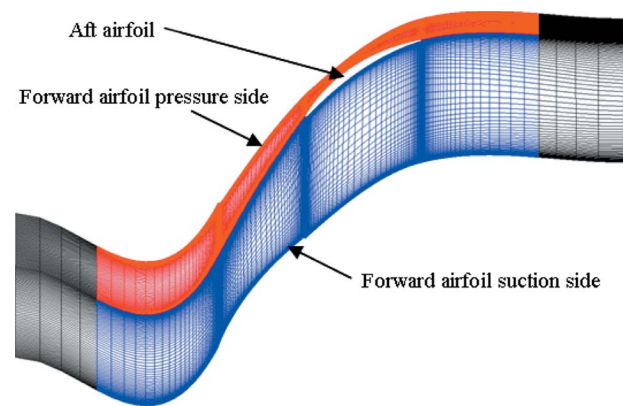


Fig. 4 Typical 2D tandem airfoil mesh

sum of the individual airfoil losses. We can therefore infer that the simple design rule gives a conservative estimate of the loss reductions that can be achieved at high loading.

The design rule was also used in the tandem airfoil CFD study to set the airfoil metal angles for minimum loss operation. This is described the next section.

**Tandem Airfoil CFD Setup.** The aim was to generate data points ranging from an overall D-factor of 0.4–0.7. Once an overall D-factor was specified, the simple design rule was used to determine the individual airfoil D-factors and required metal angles for minimum loss operation. Because the design rule relied on NACA-65 data, those were the airfoil profiles used in the CFD study. As previously mentioned, both the open literature (outlying data points on Fig. 2 and Ref. [8]) and a CFD analysis [23] indicate that losses are greater when the airfoils are unequally loaded. To minimize losses, the forward and aft airfoils were designed to have equal individual D-factors.

Once metal angles had been determined, the tandem airfoil flow fields were simulated with AOs ranging from  $-10$  to  $30$ , and PP values from  $5$  to  $95$ . Negative AO indicates a separation of the forward and aft airfoils. Loss buckets for each AO/PP combination were all simulated at inlet Mach number of  $0.6$ .

Computational meshes were created to be radially thin slices of a blade profile at mid-span in order to simulate 2D cascade flow (AVDR=1.0). The forward and aft airfoil meshes were generated separately, and then combined into a single tandem airfoil mesh consisting of four blocks: inlet, lower passage, upper passage, and exit, and example of which is shown in Fig. 4. Tandem meshes were as large as 181,000 points.

Boundary conditions included inviscid endwalls in order to create a 2D streamtube, and the viscous airfoil surfaces had no rotation since the goal was to model cascade flow. Both the inlet flow angles and exit back pressures were varied to ensure a constant inlet Mach number at each point on the loss buckets.

The CFD solver employed is called Advanced Ducted Propfan Analysis Code (ADPAC), a RANS code that was developed specifically to analyze ducted turbofan engines. Time marching was carried out by the explicit, four-stage Runge–Kutta scheme. ADPAC has three available turbulence models: Baldwin–Lomax algebraic, Spalart–Allmaras one equation, and Goldberg two equation. Detailed descriptions of each are given in Ref. [26]. In order to strike a reasonable balance between solution convergence time and accurate modeling of separated flows, all results were obtained using the Spalart–Allmaras model. The maximum value of  $y^+$  was generally kept below 5.

Grid independency was ensured by taking a typical tandem configuration and incrementally increasing the number of points on the airfoil surfaces in the axial direction to see if pertinent aerodynamic quantities (e.g., incidence, and turning) changed for a given set of boundary conditions. The number of airfoil surface



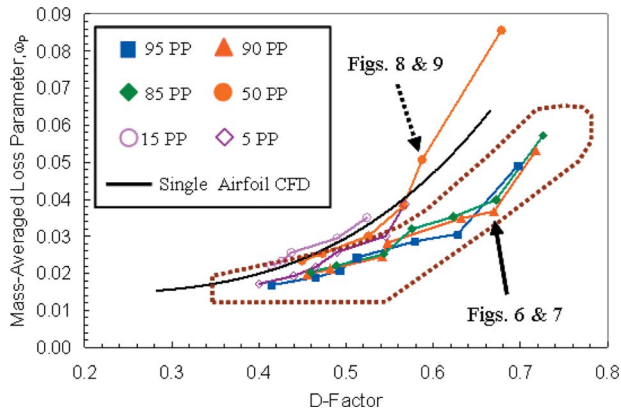


Fig. 5 CFD results of selected PP configurations at zero AO

points was increased until there was no longer a significant variation—2% or less—in aerodynamic quantities. The same procedure was repeated for the number of pitchwise points in the flow passages. In this manner, we established the minimum number of points for grid independency and used at least that many for all results reported below.

**Results: On-Design (Minimum Loss).** The caveat to the CFD data presented in this section is that it is based on a decades-old airfoil family. This is reasonable, since we are primarily interested in sensitivity trends rather than absolute performance levels. It will be shown that the “sweet spot” of AO and PP is in agreement with previous works. Therefore, it is likely that the same general trends would continue to hold for a more modern airfoil family. The difference being that the absolute loss levels would likely be lower for a given overall D-factor.

The general effect of varying AO on tandem performance was similar for all values of PP examined. Likewise, the effects of varying PP were similar for all values of AO. It is not fair to say that AO and PP are completely independent. However, examining each parameter separately provided insight into the basic flow mechanisms of the tandem airfoil. As such, the results are discussed in two sections.

**Percent Pitch.** Figure 5 shows the performance curves for several selected values of PP at zero overlap, as well as the range of literature data, indicated by the dashed shape from Fig. 2. As will be discussed in the next section, zero AO results in the best performance at a given PP.

From Fig. 5, it is evident that best performance is achieved at the high PP (85, 90, and 95) configurations, which is consistent with findings in the literature. This gives some validation to the methodology and boosts our confidence in using the software tools for more advanced tandem blade analysis.

Also shown on Fig. 5 is the CFD curve for a single NACA-65 airfoil that was used in the simple design rule (solid line in Fig. 3). It can be seen that when airfoil interaction effects are included, there is as much as a 40% reduction in loss levels from a single airfoil to a comparable tandem airfoil at an overall D-factor of 0.62. However, while a properly designed tandem is superior to a comparable single airfoil, the benefits can be quickly lost if a designer deviates too far from the optimum PP, as evidenced by the curve of 50 PP. At first, it would seem that the 0 AO, 50 PP configuration would match the simple tandem design rule. However, it will be seen from Figs. 8 and 9 that at 50 PP the AA is operating several degrees away from minimum loss incidence, resulting in a higher overall loss parameter. Losses on low PP configurations (5 and 15) grew so rapidly with overall D-factor that converged solutions were unobtainable above  $D_{ov} \sim 0.55$ .

It is noteworthy that the trend of sensitivity to PP is consistent throughout the range of D-factors examined. While previous in-

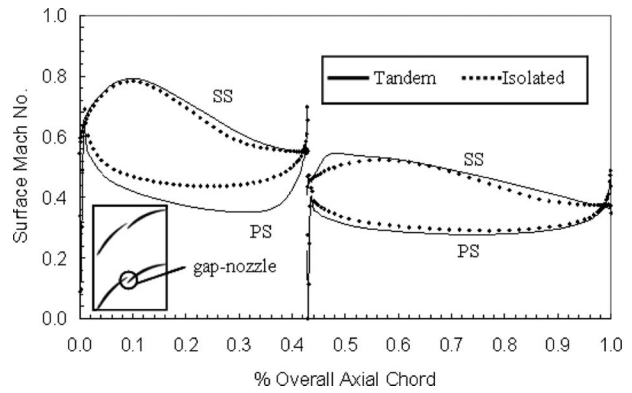


Fig. 6 Surface isentropic Mach number at 0 AO, 90 PP

vestigations certainly hinted at this, here it is presented for the first time in a comprehensive plot that could easily be incorporated into a design system.

As the simple design rule demonstrated in Fig. 3, the tandem airfoil can be superior to a comparable single airfoil even without considering flow field interaction. When such interactions are taken into account, the tandem airfoil appears even more promising.

Figure 6 is a plot of airfoil surface isentropic Mach number versus overall axial chord for the 0 AO, 90 PP configuration indicated by the solid arrow on Fig. 5. Visualization of the flow field is shown in Fig. 7. The solid curves of Fig. 6 represent the forward and aft airfoils when simulated in tandem. The airfoils from this particular configuration were also simulated in isolation using the same inlet flow conditions as they experienced when in tandem (i.e., same inlet Mach numbers and incidence angles). This allows one to study the effects of flow field interaction. These isolated cases are shown by the dashed curves in Fig. 6.

The most noticeable difference between the tandem and isolated cases in Fig. 6 is the loading envelope of the FA, particularly on the pressure side (PS). This is caused by the stagnation region of the AA near the FA TE. In effect, the AA induces additional circulation on the FA, resulting in greater FA loading, i.e., more turning and a higher D-factor. This can be considered a benefit so long as it does not push the FA to the point of flow separation.

On the AA there is a small region of acceleration on the suction side (SS) near the leading edge (LE), resulting from the contracting gap between the two airfoils that acts as a nozzle (see Fig. 6).

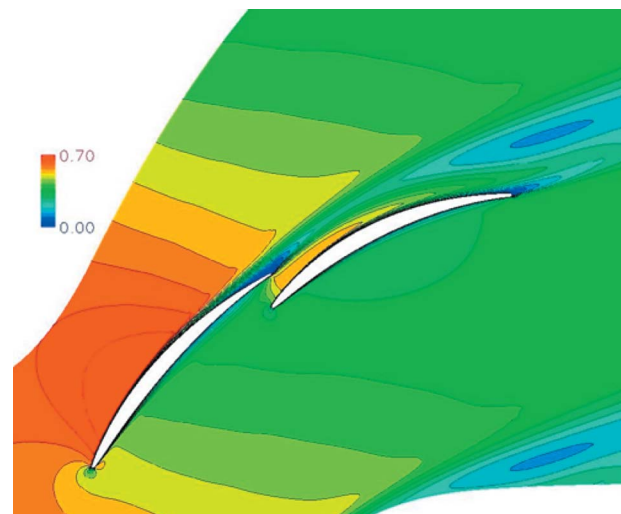


Fig. 7 Mach number contours at 0 AO, 90 PP

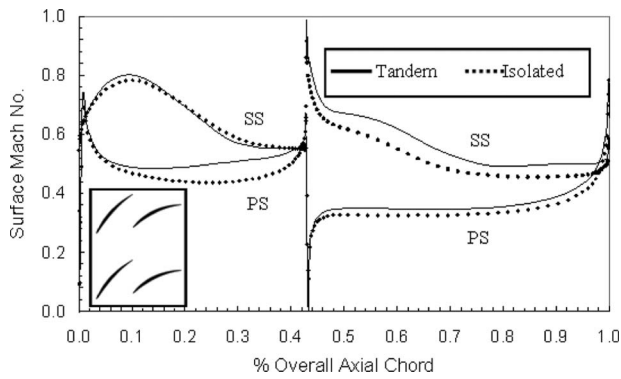


Fig. 8 Surface isentropic Mach number at 0 AO, 50 PP

This local acceleration leads to a favorable dumping velocity, a term used to describe the velocity of the fluid discharging from the FA TE onto the AA LE. Without that region of accelerated flow, there would be a local adverse pressure gradient near the AA LE that could unfavorably affect the newly developing boundary layer.

Both the induced circulation and dumping velocity are phenomena commonly observed in external flows such as with a wing and flap. The reader is referred to Smith's paper [27] on high-lift aerodynamics for a more detailed discussion.

Figure 8 is a surface Mach number plot for the 0 AO, 50 PP data point indicated by the dashed arrow on Fig. 5. Figure 9 is a visualization of the flow. The configurations shown in Figs. 6–9 are geometrically identical in every way except for the pitchwise location of the AA, yet their respective positions on the Lieblein chart differ dramatically. Upon moving the AA away from the FA in the circumferential direction, the induced circulation diminishes resulting in less loading on the FA and a lower overall D-factor. The AA is also subject to a noticeably higher incidence angle, as evidenced by the sharp velocity peak at the SS LE (Fig. 8). The subsequent strong diffusion on the AA SS leads to significantly greater losses than are seen at the higher PP configurations. The indication is that the FA acts to guide the flow onto the AA, and moving the AA too far away in the circumferential direction can result in it operating at off design. One could arguably place the AA in midpassage and orient it such that it operates at minimum loss but that would sacrifice the induced additional loading on the FA, reducing overall work capability. Hence, the 50 PP curve on

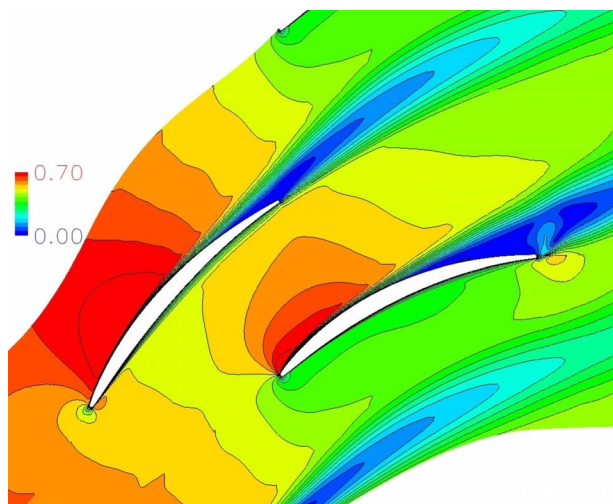


Fig. 9 Mach number contours at 0 AO, 50 PP

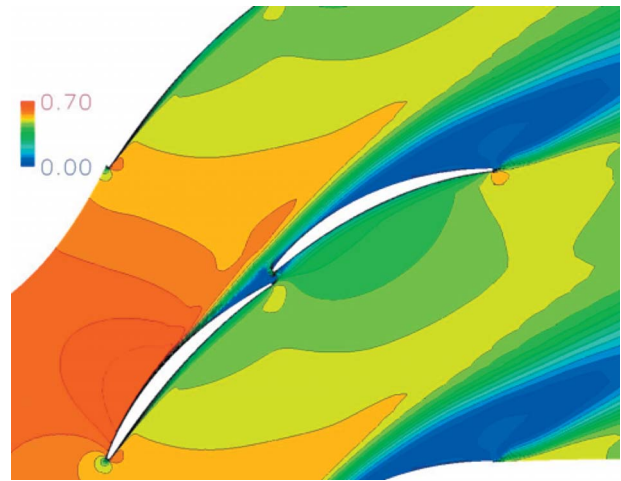


Fig. 10 Mach number contours at 0 AO, 5 PP

Fig. 5 would shift down but not to the right.

At low PP, e.g.,  $PP < 15$ , the stagnation region from the AA has an adverse effect on the already diffusing FA SS. This can easily result in boundary layer separation on the FA, with the AA LE immersed in the ensuing large wake (Fig. 10).

**Axial Overlap.** Figure 11 is a plot of mass-averaged loss parameter versus D-factor for axial overlaps of  $-10$ ,  $0$ , and  $10$  at  $90$  PP. The single airfoil curve from Figs. 3 and 5 is also shown for reference. As evidenced by Fig. 11, holding all other geometric parameters constant, varying the AO from zero tends to diminish performance, particularly at high loading. This trend held true across the range of PP values examined.

To understand the fluid mechanics behind the diminished performance at positive overlap, consider Fig. 12, which is a plot of airfoil isentropic surface Mach number for an AO of  $10\%$  at  $90$  PP. With positive overlap, the gap-nozzle acceleration on the FA PS moves upstream of the TE. This tends to counteract the additional loading from the induced circulation and can be seen by comparing the FA PS Mach numbers in tandem from Figs. 6 and 12. At higher overlaps (i.e.,  $AO > 15$ ), the FA can experience a substantial reduction in loading, even to the point of contributing no work. This phenomenon holds true regardless of where the AA is positioned pitchwise, though it is most pronounced at high PP.

With negative overlap, i.e., axial separation, the increasing distance between the FA TE and the AA stagnation region reduces the induced circulation. Since both airfoils are designed to operate

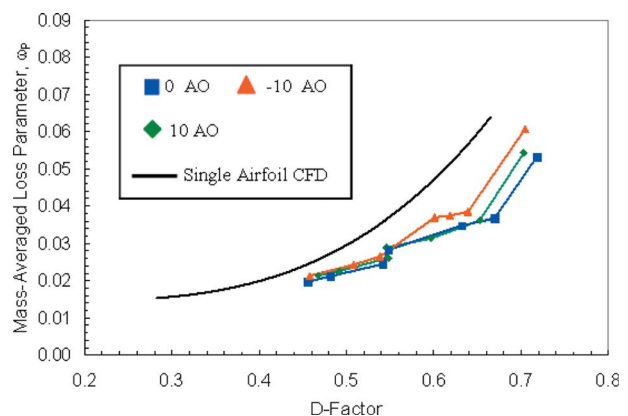


Fig. 11 CFD results of selected AO configurations at 90 PP

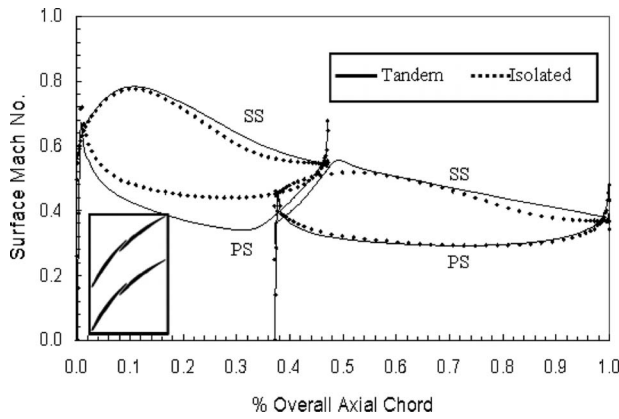


Fig. 12 Surface isentropic Mach number at 10 AO, 90 PP

below the point of separation, reducing the FA loading will not substantially reduce the losses, the result being a mostly leftward shift on the Lieblein chart.

**Results: Off-Design (Incidence Range).** For each point on a Lieblein chart, there is an associated loss bucket, an example of which is shown in Figure 13. The minimum loss incidence angle is denoted by  $\alpha^*$ . This is where the D-factor is calculated for purposes of the Lieblein chart. Having a complete loss bucket also allows one to determine the incidence range of a given single or tandem airfoil. Here, the incidence range is defined as the difference in flow angles that produce a loss coefficient twice that of the minimum. The airfoils would be considered stalled at this point.

One way to evaluate airfoil off-design performance is to plot the incidence range of each loss bucket against its associated minimum loss D-factor. Figure 14 is such a plot that includes the tandem and single airfoil CFD data points from Fig. 5, as well as the band of literature from Fig. 5.

It can easily be seen from Fig. 14 that the incidence range of both tandems and single airfoils decreases with increasing minimum loss D-factor. This is to be expected, since operating range tends to diminish with higher design loading. Second, the CFD indicates a clear trend that the tandem airfoil can offer better incidence range over a single airfoil. The reader should be reminded at this point that both the tandem and single airfoil CFD are for geometrically similar airfoils and the same inlet Mach number, allowing for direct comparison. However, the data from the literature were gathered using different airfoil families, and more importantly, at lower Mach numbers (0.3 or less versus 0.6 for the CFD). Therefore, the literature data should be taken only as an indication of trend from experiments, not as a direct com-

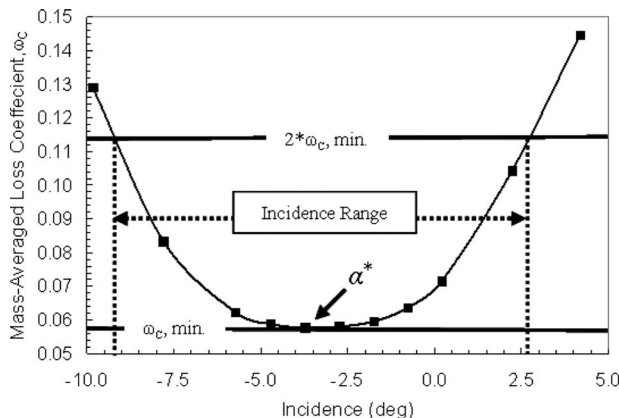


Fig. 13 Example loss bucket with incidence range

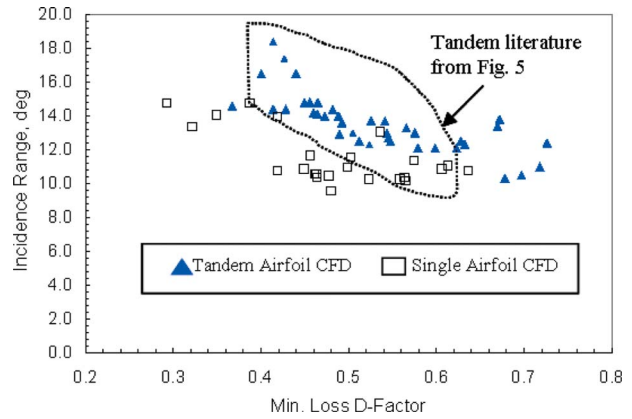


Fig. 14 Incidence range versus minimum loss D-factor

parison to the CFD.

The mechanism behind the superior incidence range of the tandem airfoil can be explained by considering the inlet flow to each airfoil separately. The AA sees a lower inlet Mach number than the FA (0.4 versus 0.6 in the CFD study), so it tends to have a lower and wider loss bucket than the FA. Consequently, the FA can operate several degrees away from minimum loss incidence before the AA experiences a substantial increase in loss. It must be emphasized that the CFD data in Fig. 14 includes a wide range of PP configurations (5–95) at 0 AO. It is rather interesting to note that the AA pitchwise position has little effect on incidence range, despite having a first-order effect on minimum loss performance. The dominating influence of the FA on overall tandem incidence range may explain this insensitivity.

## Conclusion

The tandem airfoil concept has been revisited to determine its potential as a rotor in a subsonic core compressor. Pertinent available 2D data on tandem airfoils from the open literature have been compiled and presented in a format that is particularly useful for compressor designers.

A back-of-envelope simple design rule has demonstrated that a tandem configuration can be highly loaded (i.e.,  $D_{ov} > 0.60$ ) and produce lower loss levels than a comparable single airfoil.

A 2D CFD study of the tandem airfoil was conducted to examine on- and off-design performance sensitivities to AO and PP. The major findings are summarized as follows.

- Tandem on-design performance is highly sensitive to AO and PP, and the trend is shown to be consistent throughout a wide range of overall D-factors.
- The optimum configuration (high PP and low overlap) is consistent with existing literature, giving some validation to the methods and tools used in this study.
- Tandem airfoil off-design performance is superior to that of a comparable single airfoil of the same family.

Given the results shown here, the tandem airfoil as applied to a core compressor is worth further investigation. Future work will involve 3D simulations of realistic tandem blade rotor rows using the same computational tools as in this study. We anticipate that the results from that work will serve to address two main issues. The first being whether or not the tandem bladed rotor offers enough of a performance benefit (i.e., pressure rise, efficiency, and acceptable stability margin) to warrant its use in a core compressor. The second—and more challenging—aspect of the 3D work will be to evaluate the fluid mechanisms of a tandem bladed rotor to possibly determine why previously constructed machines have not been deemed commercially viable.



## Acknowledgment

The authors would like to express thanks to Rolls-Royce Corporation for providing financial support for this project, and for permission to publish the results.

## Nomenclature

AA	=	aft airfoil
AO	=	axial overlap of tandem airfoils
AVDR	=	axial-velocity density ratio
C	=	chord
D	=	Lieblein diffusion factor
FA	=	forward airfoil
LE	=	leading edge
M	=	Mach number
P	=	pressure (static unless denoted otherwise)
PP	=	percent pitch of AA LE relative to FA spacing
PS	=	pressure side
SS	=	suction side
s	=	pitchwise spacing between blade rows
TE	=	trailing edge
t	=	pitchwise spacing between FA TE and AA LE
w	=	velocity in cascade frame of reference
y <sup>+</sup>	=	dimensionless distance from viscous surface

## Greek

$\alpha^*$	=	minimum-loss incidence angle
$\beta$	=	flow angle relative to axial coordinate
$\Delta x_1$	=	axial distance between FA TE and AA LE
$\Delta x_2$	=	axial distance between AA TE and FA LE
$\kappa$	=	airfoil metal angle relative to axial coordinate
$\theta^*$	=	boundary layer momentum thickness at TE
$\varphi$	=	camber
$\sigma$	=	solidity, C/s
$\omega_C$	=	stagnation pressure loss coefficient
$\omega_p$	=	momentum thickness loss parameter

## Subscripts

eff	=	effective
ov	=	overall
0	=	stagnation conditions
11	=	FA inlet station
12	=	FA exit station
21	=	AA inlet station
22	=	AA exit station
$\theta$	=	pitchwise direction

## Appendix: Development of the Simple Design Rule for Tandem Airfoils

A Lieblein performance curve is one of the desired outputs from the design rule. Other outputs are the appropriate airfoil metal angles to achieve minimum loss operation at a desired overall D-factor. Table 1 summarizes the inputs and outputs of the design rule.

Two initial assumptions are made that allow for easy development of the simple design rule. The first is that there is no interaction between the flow fields of the two airfoils. This eliminates the parameters of AO and PP from the design rule. The second assumption is that the flow field is incompressible. While not

**Table 1 Simple design rule inputs and outputs**

	Inputs	Outputs
Flow	$\beta_{11}$	$\beta_{12}, \beta_{21}, \beta_{22}$
Loading	$D_{FA}, D_{AA}$	$D_{ov}$
Geometric	$\sigma_{FA}, \sigma_{AA}$ ( $s_{FA}=s_{AA}$ )	$\kappa_{11}, \kappa_{12}, \kappa_{21}, \kappa_{22}$
Losses		$\omega_{p,FA}, \omega_{p,AA}, \omega_{p,ov}$

completely accurate for most turbomachinery applications—the typical inlet Mach number to a compressor stage is above 0.3—it does allow the D-factor to be expressed in terms of effective solidity and flow angles:

$$D = \left( 1 - \frac{\cos \beta_{11}}{\cos \beta_{22}} \right) + \left( \frac{\cos \beta_{11} (\tan \beta_{11} - \tan \beta_{22})}{2\sigma_{\text{eff}}} \right) \quad (\text{A1})$$

Equation (A1) can be used for the individual airfoils by making the appropriate substitutions for flow angles and individual airfoil solidity. The flow and loading parameters can now be found by the following procedure:

1. Specify the desired FA and AA D-factors,  $D_{FB}$  and  $D_{AB}$ .
2. Specify the desired inlet flow angle,  $\beta_{11}$ .
3. Calculate  $\beta_{12}$  using Eq. (A1) modified for the FA.
4. Set the AA inlet flow angle equal to the FA exit flow angle, i.e.,  $\beta_{21} = \beta_{12}$ .
5. Calculate  $\beta_{22}$  using Eq. (A1) modified for the AA.
6. Calculate overall D-factor,  $D_{ov}$ , using  $\beta_{11}$  and  $\beta_{22}$  in Eq. (A1).

The above procedure for finding overall loading and airfoil flow angles is valid for any family of airfoils. Information on losses and required metal angles are family-specific, and can be found either experimentally or computationally. The decision was made to use the NACA-65 family of airfoils due to the large amount of experimental data on them that is available in the open literature. Since the FA and AA D-factors have already been specified, the loss parameter ( $\omega_p$ ) for the airfoils can be individually determined from the available correlation. The respective stagnation pressure loss coefficients,  $\omega_{C,FA}$  and  $\omega_{C,AA}$ , can then be found by substituting the appropriate flow angles for the FA and AA in Eq. (2) and solving for  $\omega_C$ . The loss in stagnation pressure due to the individual airfoils can be superposed to form the overall loss coefficient of the tandem configuration:

$$\omega_{C,ov} = \omega_{C,FA} + \left( \frac{\cos \beta_{11}}{\cos \beta_{21}} \right)^2 \omega_{C,AA} \quad (\text{A2})$$

The cosine-squared term in Eq. (A2) accounts for the change in dynamic head between the FA inlet and the AA inlet. The overall loss parameter can then be calculated using Eq. (2). The final output from the design rule is the metal angles for each airfoil:  $\kappa_{11}$ ,  $\kappa_{12}$ ,  $\kappa_{21}$ , and  $\kappa_{22}$ . The NACA-65 experimental data are presented in such a way that if the individual airfoil solidity and inlet flow angle are known, one can easily obtain the required metal angles from a chart.

## References

- [1] Gostelow, J. P., 1984, *Cascade Aerodynamics*, Pergamon, Oxford, Chap. 9.
- [2] Barton, M. T., and Gentile, D. P., 2005, "The Use of a Circumferentially Nonuniform Stator to Attenuate Harmful Aerodynamic and Mechanical Interactions in an Advanced Mixed Flow Splintered Rotor/Tandem Variable Stator LP Compressor." ASME Paper No. GT2005-68178.
- [3] Brent, J. A., and Clemmons, D. R., 1974, "Single-Stage Experimental Evaluation of Tandem-Airfoil Rotor and Stator Blading for Compressors," NASA Report No. CR-134713.
- [4] Bammert, K., and Staude, R., 1979, "Optimization for Rotor Blades of Tandem Design for Axial Flow Compressors," ASME Paper No. 79-GT-125.
- [5] Bammert, K., and Beelte, H., 1980, "Investigations of an Axial Flow Compressor With Tandem Cascades," ASME J. Eng. Power, **102**, pp. 971-977.
- [6] Hasegawa, H., Matsuoka, A., and Suga, S., 2003, "Development of Highly Loaded Fan With Tandem Cascade," AIAA Paper 2003-1065.
- [7] Ohashi, H., 1959, "Theoretical and Experimental Investigations on Tandem Pump Cascades With High Deflection," Ing.-Arch., **27**, pp. 202-226.
- [8] Ihlenfeld, H., 1965, "Stromungsvorgange an Stark Verzögernden Spaltflügelgittern," Maschinenbautechnik, Berlin, Verlag Technik **14**(7/8), pp. 361-365.
- [9] Raily, J. W., and El-Sarha, M. E., 1965, "An Investigation of the Flow through Tandem Cascades," Proc. Inst. Mech. Eng., **180**, pp. 66-73.
- [10] Sieverding, C., 1966, "Experimental Data for Tandem Cascade in the High Subsonic Regions," Von Karman Institute for Fluid Dynamics, Internal Note, 15.
- [11] Hopwood, D. J., 1967, "Tandem/Slotted Cascade Tests for High Deflection Stators," Rolls-Royce Ltd., Compressor Department Report No. RCR 90117.

- [12] Dettmering, W., and Becker, B., 1968, "Steps in the Development of a Supersonic Compressor Stage," AGARD CP 34, Paper No. 13.
- [13] Mikolajczak, A., Weingold, H., and Nikkanen, J., 1970, "Flow Through Cascade of Slotted Compressor Blades," ASME J. Eng. Power, **92**, pp. 57–64.
- [14] Sanger, N., 1971, "Analytical Study of the Effects of Geometric Changes on the Flow Characteristics of Tandem-Bladed Compressor Stators," NASA Report No. TN-D-6264.
- [15] Paine, C. J., 1972, "Design and Test of a Small, High-Pressure Ratio, Axial Compressor With Tandem and Swept Stators," SAE Paper No. 720713.
- [16] Wu, G., Zhuang, B., and Guo, B., 1985, "Experimental Investigations of Tandem Blade Cascades With Double Circular Arc Profiles," ASME Paper No. 85-IGT-94.
- [17] Sachmann, J., and Fottner, L., 1993, "Highly Loaded Tandem Compressor Cascade With Variable Camber and Stagger," ASME Paper No. 93-GT-235.
- [18] Roy, B., and Saha, U. K., 1995, "Experimental Analysis of Controlled Diffusion Compressor Cascades With Single and Tandem Airfoils," ASME Paper No. 95-CTP-41.
- [19] Roy, B., and Saha, U. K., 1995, "High Diffusion Cascades for Axial Flow Compressor Applications," *Proceedings of 15th Canadian Congress of Applied Mechanics*.
- [20] Roy, B., and Saha, U. K., 1996, "On the Application of Variable Camber Blading in Axial Flow Fans and Compressors," ASME Paper No. 96-TA-58.
- [21] Weber, A., and Steinert, W., 1997, "Design, Optimization, and Analysis of a High-Turning Transonic Tandem Cascade," ASME Paper No. 97-GT-412.
- [22] Canon-Falla, G. A., 2004, "Numerical Investigation of the Flow in Tandem Compressor Cascades," Diploma thesis, Departamento de Ingenieria Macanica, Universidad Nacional de Colombia, written at Insitute of Thermal Powerplants, Vienna University of Technology.
- [23] McGlumphy, J., 2008, "Numerical Investigation of Subsonic Axial-Flow Tandem Airfoils for a Core Compressor Rotor," Ph.D. dissertation, Virginia Polytechnic Institute & State University.
- [24] Lieblein, S., 1965, "Aerodynamic Design of Axial-Flow Compressors," NASA Report No. SP-36.
- [25] Wennerstrom, A. J., 1990, "Highly Loaded Axial Flow Compressors: History and Current Developments," ASME J. Turbomach., **112**, pp. 567–578.
- [26] Hall, E. J., Heidegger, N. J., Delaney, R. A., 1999, "ADPAC v1.0—User's Manual," NASA Report No. CR-1999-206600.
- [27] Smith, A. M. O., 1975, "High-Lift Aerodynamics," J. Aircr., **12**, pp. 501–530.

# Synchronizing Separation Flow Control With Unsteady Wakes in a Low-Pressure Turbine Cascade

M. Bloxham

D. Reimann

K. Crapo

J. Plum

J. P. Bons

Department of Mechanical Engineering,  
Brigham Young University,  
Provo, UT 84602

*Particle image velocimetry (PIV) measurements were made on a highly loaded low-pressure turbine blade in a linear cascade. The Pack B blade has a design Zweifel coefficient of 1.15 and a peak  $C_p$  at 63% axial chord on the suction surface. Data were taken at  $Re_c = 20 K$  with 3% inlet freestream turbulence and a wake-passing flow coefficient of 0.8. Without unsteady wakes, a nonreattaching separation bubble exists on the suction surface of the blade beginning at 68% axial chord. The time-averaged separation zone is reduced in size by approximately 35% in the presence of unsteady wakes. Phase-locked hot-wire and PIV measurements were used to document the dynamics of this separation zone when subjected to synchronized, unsteady forcing from a spanwise row of vortex generator jets (VGJs) in addition to the unsteady wakes. The phase difference between VGJ actuation and the wake passing was optimized. Both steady state  $C_p$  and phase-locked velocity measurements confirm that the optimal combination of wakes and jets yields the smallest separation. [DOI: 10.1115/1.2952376]*

## Introduction

Low-pressure turbine (LPT) blades have been shown to be susceptible to boundary layer separation at low Reynolds numbers [1–3]. Many techniques have been developed to decrease the extent of the separation in an attempt to reduce the total pressure losses. Of these techniques, vortex generator jets (VGJs) have shown considerable promise in both steady and unsteady applications. As an active system, VGJs offer the benefit of being adaptable to different Reynolds number flows (i.e., flight conditions). Experimental results have revealed that steady VGJs offer substantial separation control due to the streamwise vortical structures, which pull high momentum fluid from the freestream down into the separated region, re-energizing the flow [4,5]. This control has been shown for a wide range of VGJ blowing ratios [1].

Experiments have also shown that pulsed vortex generator jets are effective at controlling boundary layer separation for a wide range of operating parameters. The mechanisms of control for pulsed VGJs are currently not completely understood. Computational studies performed by Postl et al. [6] suggested that the primary mechanism of control for unsteady VGJs was due to the boundary layer transition rather than streamwise vortical structures. These results were obtained at VGJ blowing ratios below unity. Postl et al. [6] did note that vortical structures began to play a more important role as the blowing ratios were increased. They also noted the formation of a 2D (spanwise) disturbance in the separation bubble. This disturbance formed after VGJ actuation and helped to accelerate reattachment. Subsequently, Bloxham et al. [7] performed experiments validating some of these conclusions.

Bons et al. [8] studied the impact of unsteady VGJs on a separation bubble using the Pack B blade profile. They used boundary layer traverses and static pressure taps to monitor the changes in the separation zone with both steady and unsteady VGJ controls. They reported reductions in the wake loss profile of over 50% with unsteady control, which was later substantiated by the results Volino [9] obtained using synthetic jets. The unsteady result ob-

tained by Bons et al. [8] compared favorably to the control achieved with steady VGJs but at a fraction of the mass flow requirements. These results were obtained over a range of forcing frequencies and duty cycles with the conclusion that both variables had little impact on the time-averaged wake losses. The forcing frequency independence was demonstrated over a forcing frequency range of  $0.1 < F^+ < 7.7$ . The dimensionless forcing frequency was defined by Bons et al. [8] as the VGJ forcing frequency normalized by the ratio of average freestream velocity (from the jet location to the trailing edge) to the suction surface length (from the jet location to the trailing edge). Bons et al. [8] further showed that the extent of the control was more profoundly impacted by the starting and ending of the jet pulse rather than the amount of time the jet remained active.

Previous work with LPT flow control has been conducted in steady flow cascades without accounting for the unsteady nature of the flow in an actual engine. In a LP turbine, unsteady disturbances are continually produced by the upstream blade row. Unsteady wakes have been shown to re-energize separation regions as they convect downstream. Stieger et al. [10] attributed this effect to boundary layer embedded vortical structures. They first noted large amplitude pressure fluctuations as a result of these wake-induced vortical structures. Later, these structures were identified using PIV. Stieger et al. [10] hypothesized that these vortical structures were created by a rollup of the separated shear layer induced by the wake disturbance.

Gostelow et al. [11] also observed this effect using wake disturbed flow over a flat plate with an imposed pressure distribution. The pressure distribution was representative of the diffusion distribution seen on a compressor blade and encouraged the development of a laminar separation bubble. An upstream rod, parallel with the leading edge of the flat plate, was fastened to a rotating disk. The disk rotated at a rate of 60 rpm, thereby creating two different wakes (one from the rod at an upstream location and the second from a downstream location) every second. Gostelow et al. [11] collected their data by traversing a single-element hot wire through the separation bubble at discrete locations. They showed that the wake-induced disturbance stabilized the boundary layer. The wake-induced disturbance was followed by a calmed region that delayed transition and stabilized the boundary layer against separation. This result was further substantiated by similar studies recently performed by Funazaki et al. [12] and Cattanei et al. [13].

Given these well documented effects of wakes on separated

Contributed by the International Gas Turbine Institute of ASME for publication in the JOURNAL OF TURBOMACHINERY. Manuscript received August 14, 2007; final manuscript received August 29, 2007; published online February 3, 2009. Review conducted by David Wisler. Paper presented at the ASME Turbo Expo 2007: Land, Sea and Air (GT2007), Montreal, Quebec, Canada, May 14–17, 2007.



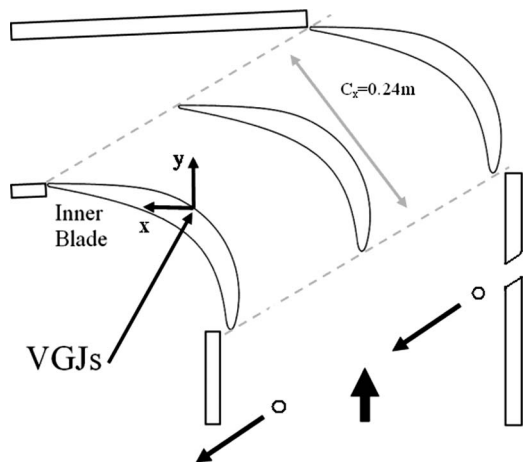


Fig. 1 Three blade linear cascade

flows, it is clear that any active flow control scheme must be compatible with the inherently unsteady flow environment in the LTP. To date, the synchronization of unsteady wakes and unsteady control had not previously been investigated. One of the primary objectives of this study was to identify a blowing ratio, jet duration, and synchronization between the unsteady wake disturbance and the unsteady jet disturbance that caused the greatest time-averaged reduction of the separation bubble. This objective was accomplished using static pressure taps and boundary layer data obtained with a single-element hot film. Upon completion of the optimization study, phase-locked and time-resolved PIV and hot-film data were taken to identify the relative impacts of the two unsteady disturbances and to identify the flow physics that determined the optimal conditions.

### Experimental Configuration

A detailed description of the cascade facility used for this study is found in Eldredge and Bons [14]. The open-loop wind tunnel is powered by a centrifugal blower. After passing through a series of flow conditioners, the air enters an acrylic duct with a velocity uniformity of  $\pm 2\%$ . The duct has a cross-sectional area of  $0.15 \text{ m}^2$ . A square-bar passive grid is placed  $5.2$  axial chords upstream of the test section to produce  $3\%$  freestream turbulence at the cascade inlet.

The test section is a two passage cascade containing the Pratt & Whitney Pack B blade configuration. A depiction of the cascade is found in Fig. 1. The Pack B blade has an axial chord of  $0.238 \text{ m}$ , a span of  $0.38 \text{ m}$ , a design Zweifel coefficient of  $1.15$ , and provides a cascade solidity of  $1.14$ . At Reynolds numbers below  $20,000$  (based on inlet velocity and axial chord), a nonreattaching separation bubble forms on the aft portion of the blade beginning near  $68\% C_x$ . The innermost blade in the cascade contains  $13$  static pressure taps. The taps are located near midspan and are used to provide a  $C_p$  profile of the suction surface of the blade. The  $C_p$  profile is produced by sequentially connecting these pressure taps to a  $0.1 \text{ in. H}_2\text{O}$  Druck differential pressure transducer referenced to a pitot tube located upstream of the cascade inlet. This differential pressure is then divided by the dynamic pressure at the inlet to yield  $C_p$ . The resulting  $C_p$  distribution was compared to the prediction generated by the Air Force Research Laboratory using a 2D viscous solver (VBI, Rao et al. [15]). After the blades were geometrically positioned, adjustments in the location of the tailboards and inlet bleeds were made to most nearly approximate the VBI solution at high (nonseparating) Reynolds numbers.

The inner blade of the cascade houses a pressure cavity, which connects to a spanwise row of VGJs. These jets are  $2.6 \text{ mm}$  in diameter ( $d$ ) and are spaced  $10d$  apart along the full span of the

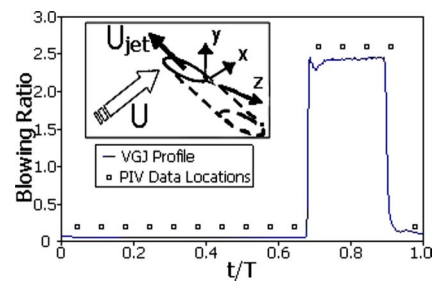


Fig. 2 VGJ exit velocity profile and data acquisition locations (PIV). VGJ orientation and coordinate system.

blade at  $59\% C_x$ . The jets are injected into the flow at a  $30$  deg pitch angle and a  $90$  deg skew angle to the flow as seen in the inset of Fig. 2. The pressure cavity is connected to high pressure air with an inline solenoid valve that regulates the exit velocity of the VGJs. The jet blowing ratio in this study was fixed near  $B_{\max} = 2.5$ , where the blowing ratio is defined as the ratio of the jet exit velocity to the local freestream velocity ( $U_{\text{jet}}/U_e$  at  $59\% C_x$ ). The jet profile was measured as the VGJ exited the blade into a quiescent environment using a single-element hot-film anemometer positioned normal to the jet exit. The resulting jet history plot is presented in Fig. 2. The jet profile is essentially a step function with the initial, high-frequency oscillations attributed to the compressibility of the air in the pressurized cavity. Also featured in Fig. 2 are the times of data acquisition for the PIV data.

A wake generator is placed  $12.7 \text{ cm}$  ( $0.53 C_x$ ) upstream of the cascade inlet. A CAD model of the wake generator and its position in the tunnel can be seen in Fig. 3.

Unsteady wake disturbances are created using  $6 \text{ mm}$  diameter carbon fiber rods. The rods are oriented in the spanwise direction and are drawn through the tunnel on a chain sprocket system driven by a variable frequency motor. Low density foam is used at both the tip and base of the rods to dampen vibrations and seal the tunnel. An optical sensor detects the passage of the rods as they exit the tunnel (see note in Fig. 3) and sends a signal to the Parker-Hannifin pulse driver ( $t=0$  in Fig. 2). This pulse driver controls a solenoid valve used to actuate the VGJs. The pulse driver is used to set the duration of the VGJ pulse and the time of actuation relative to the input signal from the rod sensor ( $t=0$ ). The speed of the rods was adjusted to maintain a normalized velocity near  $U_{\text{rod}}/U_{\text{in}} = 0.95$  (flow coefficient,  $\varphi = 0.85$ ) with a fluctuation of approximately  $\pm 2\%$ . The period between rods was measured to be  $225 \text{ ms}$ . Since the VGJs are synchronized to the rod passing frequency, this wake period yields a dimensionless

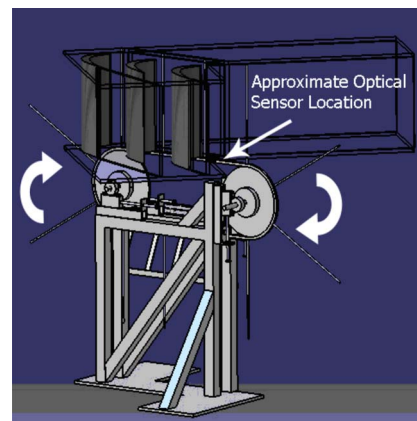
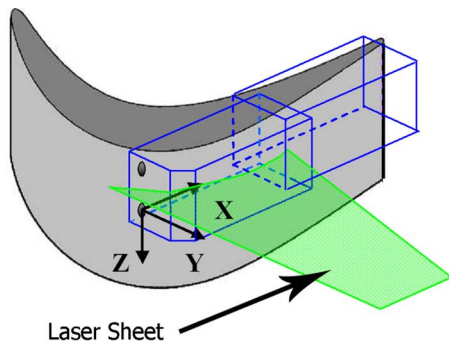
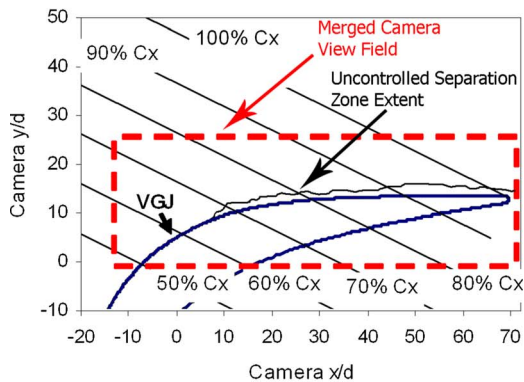


Fig. 3 CAD model of wake generator and test section of tunnel. Curved white arrows indicate direction of rotation. Straight arrow represents location of optical sensor.



a. Primary PIV Configuration



b. Merged Camera View Field

**Fig. 4 (a) The primary PIV configuration depicting both data regions. (b) The coordinate system used to present the data. Also included are the merged camera view fields, the axial chord lines of the Pack B, and a representation of the separation bubble.**

forcing frequency of  $F^+ = 0.27$  for this study. The rods are spaced at  $L/S = 1.64$ , where  $L$  is the distance between the rods and  $S$  is the blade spacing. The larger spacing between rods (compared to the cascade spacing) is intended to simulate vane wakes impinging on a rotor blade row since the vane count is typically 60–75% of the blade count for a given LPT stage.

Data were taken using a LaVision PIV system mounted to a three axis traverse below the test section. A Nd:YAG (yttrium aluminum garnet) laser was used to project two consecutive 1 mm thick laser sheets (with 250  $\mu$ s time separation) in the  $x$ - $y$  plane into the test section (see Fig. 1 for coordinate system). The flow was seeded with olive oil particles having diameters between 1  $\mu$ m and 2  $\mu$ m. A high-speed digital camera was positioned below the test section. The camera has a resolution of  $1376 \times 1040$  pixels. Measurements were taken in 18 spanwise ( $z$ ) locations. The  $z$  locations were 1.5 mm apart and spanned one VGJ hole pitch. The first  $z$  location was taken directly below a midspan VGJ where the flow was shown to be spanwise uniform. Subsequent levels were taken by traversing toward the top of the test section in the negative  $z$  direction according to the right hand rule ( $x$  is the flow direction and  $y$  is normal to the blade surface). This data set required two different test windows to capture flow along the entire blade. These windows covered an upstream ( $\sim 50\%$  to  $\sim 81\%$   $C_x$ ) and a downstream ( $\sim 80\%$  to  $\sim 100\%$   $C_x$ ) portion of the blade with approximately 6 mm of overlap (see Fig. 4(a)). The data windows were later merged together to create a continuous set of data as depicted in Fig. 4(b).

The rod passing period of 225 ms was divided into 15 equal segments. Each segment was phase locked to the passing of the

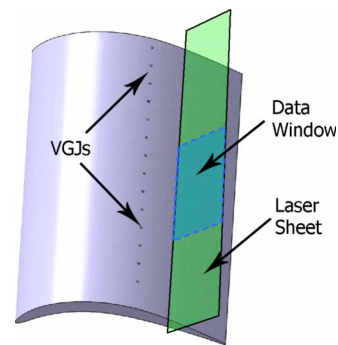


**Fig. 5 The in-plane PIV configuration. The green plane is a representation of the laser sheet.**

rod using the optical sensor. Figure 2 shows the 15 nondimensional time locations of PIV data acquisition. Time “zero” corresponds with the rod passing through the optical sensor located outside of the cascade flow path. The first data set was collected at a nondimensional time  $t/T = 0.044$  (where  $t$  is the time relative to the signal from the optical sensor, and  $T$  is the wake-passing period). The subsequent data sets were taken 15 ms apart. For each time, data were taken in the upstream and downstream windows at all 18  $z$  locations. At each location, window and nondimensional time, 40 images were taken, processed, and averaged. It was previously shown that averaging with more than 40 images made no notable difference in the average velocity field results [16]. Vector processing was initially performed with  $64 \times 64$  pixel interrogation windows. The interrogation windows were then refined to  $32 \times 32$  pixels. A 50% overlap was employed during the vector processing. According to LaVision [17], the uncertainty in the seed particle displacement is approximately 0.2 pixel. This translates to a velocity uncertainty of  $\pm 0.08$  m/s. The resulting 3D blocks of data provide  $u$  and  $v$  velocity data.

It should be noted that this set of PIV data is presented in the camera coordinate system. In the region of interest (59–100% axial chord), the blade is relatively flat. The result is that the  $x$  and  $y$  coordinates of the camera are approximately streamwise and surface normal in this region (though not exactly).

A secondary set of PIV data was used to capture the VGJ-induced streamwise vorticity in the plane of the laser sheet. In this configuration, the laser was placed on a traverse below the test section, introducing the laser sheet in the  $y$ - $z$  plane, as shown in Fig. 5. The laser created 1.5 mm, consecutive laser sheets with a time separation of 150  $\mu$ s. A smaller time separation was required to ensure that a majority of the seed remained in the laser sheet. A single high-speed camera was placed downstream of the cascade outside of the flow path. Data were collected over four VGJ pitches ( $\sim 100$  mm). Measurements were taken at five  $x/d$  locations (10, 15, 20, 35, and 43) in order to track the vortical structure from near inception until it interacts fully with the separation zone. At each  $x/d$  position, eight phase-locked data sets were measured ranging from 20 ms to 100 ms. The data sets were phase locked to the VGJ pulse ( $B = 2$ , 25% duty cycle).

At each location and nondimensional time, 100 images were taken, processed, and averaged. Vector processing was initially performed with  $64 \times 64$  pixel interrogation windows. The interrogation windows were further refined to  $16 \times 16$  pixels. A 50% overlap was employed during the vector processing.

Prior to taking phase-locked PIV data, the jet duration, blowing ratio, and time delay (between the optical sensor signal and VGJ actuation) were optimized to achieve the greatest extent of time-averaged separation bubble reduction.  $C_p$  distributions were used to measure the impact of each of these parameters over a broad range of values (time delay of 50–150 ms, jet duration of 15–50 ms, and blowing ratio 1.7–2.5). The  $C_p$  comparisons led to

**Table 1 Test matrix for synchronization parameter study**

Case	Jet duration (ms)	Time delay (ms)	Blowing ratio
No control (1)	—	—	—
Wakes only (2)	—	—	—
VGJs only (3)	50	N/A	2.5
4	50	50	2.5
5	50	100	2.5
6	50	150	2.5
7	50	150	1.7
8	30	150	2.5

the selection of a smaller range of parameters to be used for qualitative comparisons. The test matrix for the qualitative comparisons is presented in Table 1. Once the test matrix was selected, the integrated boundary layer momentum flux losses were calculated with (from Olson et al. [18])

$$\Gamma = \int_0^\delta \frac{U_e^2 - U(y)^2}{U_{in}^2} dy \quad (1)$$

This calculation provides an estimate of total pressure loss in the suction surface boundary layer and was used to compare the relative momentum flux losses for each of the cases listed in the test matrix. Several boundary layer velocity profiles were collected at the same location in the separation region (~87% axial chord) using a single-element hot-film (uncertainty in velocity of ±0.03 m/s). The profiles were taken near midspan four jet diameters above the bottom edge of a VGJ.

**Results**

**VGJ Optimization With Wakes.** Time-averaged  $C_p$  distributions (uncertainty in  $C_p$  of ±0.12) are presented in Fig. 6 for four of the eight test cases in Table 1 (not shown are Cases 4, 5, 7, and 8). The solid lines representing the VBI and MISES predictions are also included. In this  $C_p$  comparison, the VBI is used as the benchmark of nonseparated flow over the turbine, since it is for a high, nonseparating Reynolds number. The MISES prediction is included because it is a better representation of the expected  $C_p$  distribution at lower Re numbers without control (no jets or wakes).  $C_p$  distributions that closely resemble the VBI are considered to be attached, while deviations from the VBI are indicative of boundary layer separation. The symbols represent the  $C_p$  from each static pressure tap along the suction and pressure surfaces of

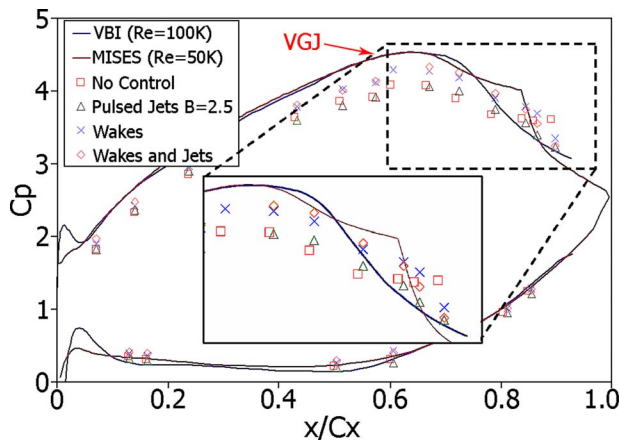


**Fig. 6 Experimental  $C_p$  distributions for the Pack B compared to the VBI. Plot includes no control (no wakes or jets), wake only, VGJ only, and combined wakes/jets data.**

**Table 2 Normalized results from the integrated boundary layer momentum flux loss parameter**

Case	Jet duration (ms)	Time delay (ms)	Blowing ratio	$\Gamma/\Gamma_0$
No control (1)	—	—	—	1
wakes only (2)	—	—	—	0.75
VGJs only (3)	50	N/A	2.5	0.68
4	50	50	2.5	0.65
5	50	100	2.5	0.62
6 (Optimum)	50	150	2.5	<b>0.55</b>
7	50	150	1.7	0.63
8	30	150	2.5	0.59

the Pack B blade for each test case.

The no control  $C_p$  data lie well below the VBI prediction. The separation zone is depicted by the relatively flat region in the  $C_p$  distribution from 70% to 90% axial chord. The introduction of unsteady VGJ control (Case 3) eliminates a portion of this flattened region, suggesting reattachment of the separation bubble near 80% axial chord. For this case, the VGJs had a blowing ratio of  $B_{max}=2.5$ , a jet duration of 50 ms, and a duty cycle of 23% (where duty cycle is the ratio of jet duration to the period). The unsteady wake configuration (Case 2) resembles the VBI more than the unsteady jet results in the region from 70% to 80% axial chord but also has a larger deviation from 80% to 90% axial chord. The addition of VGJs to the unsteady wakes (Case 6) further enhances the control achieved by the unsteady wakes or jets exclusively. This enhancement was seen over the entire range of the measured separation zone from 70% to 90% axial chord. As mentioned earlier, the parameters used for the combined unsteady wake and jet  $C_p$  distribution in Case 6 ( $B=2.5$ , jet duration =50 ms, and time delay=150 ms) were determined following a rigorous optimization study.

The  $C_p$  distribution results suggest that synchronization of unsteady wakes and VGJs is beneficial but does not give any indication as to how sensitive these optimal conditions are to variations in the control variables. The integrated boundary layer momentum flux loss parameter ( $\Gamma$ ) was used to quantify the control effectiveness. The normalized results are tabulated below in Table 2. A comparison of the normalized boundary layer momentum flux loss parameters for wakes only and VGJs only ( $\Gamma/\Gamma_0 = 0.75$  versus 0.68, respectively) shows that unsteady VGJs have a more pronounced impact on the momentum flux losses (separation region). This was an unexpected result given that the unsteady wake disturbance is a spanwise event while the VGJ disturbance is not. However, since the  $z/d$  location where the boundary layer (and thus  $\Gamma$ ) data were taken aligned directly with the VGJ trajectory ( $z/d=6$ ), it is expected that the relative advantage of the VGJ only case would decrease if the same measurements were taken at other  $z/d$  locations less influenced by the jet. This is due to the three-dimensionality of the VGJ disturbance and its effect on the separation bubble dynamics, as will be shown later.

A number of other important synchronization factors can be gleaned from this study. Three time delays were tested while holding the jet duration and blowing ratio constant. It is evident that the largest time delay (150 ms) resulted in the greatest momentum flux loss reduction (Case 6 ( $\Gamma/\Gamma_0=0.55$ ) compared to Case 5 ( $\Gamma/\Gamma_0=0.62$ ) and Case 4 ( $\Gamma/\Gamma_0=0.65$ )). This would suggest that the timing between the passing wake and the VGJ disturbances is an important factor in identifying an optimal synchronization condition. Once the “optimal” time delay was determined, a study was performed to identify the separation bubbles’ dependence on the jet duration. Jet durations of 50 ms and 30 ms were compared and resulted in the flux losses, of 0.55 and 0.59, respectively. Jet durations larger than 50 ms were not studied to maintain low mass



flow requirements. These results suggest that jet duration also has an impact on the flux losses, which corroborates results obtained by Bloxham et al. [7] for a different blade profile. The final parameter that was adjusted was the blowing ratio. A blowing ratio of 2.5 was shown to be significantly more effective at reducing the total pressure losses due to the separation bubble. Higher blowing ratios were not studied because the maximum allowable pressure on the inline solenoid valve was near  $B_{\max}=2.5$ .

**Detailed Phase-Locked Flow Measurements.** Once an optimal synchronizing configuration was obtained, PIV measurements were taken to identify the flow physics responsible for the reduced momentum flux losses. Comparisons of the wake and jet disturbances were also made. Figure 7 contains isosurfaces of the velocity magnitude computed using the PIV data. An isovelocity surface of  $U/U_{\text{in}}=1.0$  was selected because it clearly depicts the distinct influences of the passing wake and jet. Each of the 15 data acquisition times is represented in the figure, depicting the separation bubbles' behavior over the complete period. Figure 7 also includes an isovelocity surface without wakes or VGJs for comparison. These surfaces give an indication of the jet and wake effects on the flow. In order to facilitate identification of the separation bubble, the curvature of the turbine blade was removed from the isovelocity surface height. Thus, the vertical axis ( $y/d$ ) represents the distance from the isovelocity contour to the blade surface. Accordingly, elevated portions of the isovelocity surface are attributed to the separation bubble. The flow moves from right to left as  $x/d$  extends from 0 to 67 (approximately 59–100% axial chord). The VGJ is located near a  $z/d$  of 9 (hole center) but is only active in the range of  $t/T=0.71$ – $0.84$ .

Since  $t/T=0$  is referenced to the passing of the rod through the optical sensor, indication of a passing wake is not immediately evident in the isovelocity surfaces. At  $t/T=0.04$ , the lingering effects of a VGJ/separation bubble interaction are still present. This VGJ pulse started about  $\Delta t/T=0.33$  (75 ms) prior to the passing of the rod through the optical sensor (it is therefore phase locked to the previous rod passing). The VGJ has caused the separation bubble to reattach at the upstream end. The higher momentum fluid in the reattached region meets the slow moving separation bubble and causes an elevated bulge in the isovelocity surface. This bulge convects off the end of the blade in subsequent data sets. The three-dimensional effect of the VGJ on the separation bubble is still very apparent as the separation bubble moves off the blade in  $t/T$  of 0.11, 0.18, and 0.24.

The three-dimensional nature of the jet's unsteady effect on the separation bubble has previously been attributed primarily to a VGJ-induced transition of the boundary layer [19]. In-plane PIV data were used to clarify the role of vortical structures in the VGJ control. In order to isolate the influence of the VGJ, the in-plane data were taken without the wake disturbance. Figure 8 contains streamwise vorticity data ( $y$ - $z$  plane) collected 5 ms before the VGJ deactivated. In this study, the blowing ratio of the VGJ was  $B_{\max}=2$ , the jet duration was 50 ms, and the duty cycle was 25%. The streamwise vorticity for four  $x/d$  locations ( $x/d=10, 20, 25$ , and 35) is provided in the figure to track the vortical development. The VGJ location is represented in the figure by the red arrow near  $z/d=9$  (jet hole center).

The plot of  $x/d=10$  depicts the strong positive and negative VGJ-induced vorticity cores. The cores are positioned near  $z/d=7$  and  $y/d=2$ . These strong vorticity cores dissipate in the subsequent plots. Despite the energy dissipation, the positive vortex maintains its structure up to  $x/d=35$  (well into the separation region). As the vortical structures move downstream, they migrate away from the wall. By  $x/d=35$ , the positive core has migrated out to  $y/d=4$ . Close examination of the isovelocity surfaces presented previously in Fig. 7 ( $t/T=0.84$ ) suggests that the vortex is migrating away from the wall due to the presence of the separation bubble. The in-plane PIV data for subsequent time steps (not presented) show the vortex core migrate back toward the wall as

the separation bubble is re-energized and pushed off the turbine.

The vortex cores also migrate away from the jet location in the spanwise direction. This movement was expected since the VGJ is injected with spanwise momentum. By  $x/d=35$ , the positive vortex core is positioned near  $z/d=5$ . Given that vortical structures promote mixing, it should be expected that the separation bubble would react to the presence of the vortex. Close inspection of the three-dimensional nature of the VGJ's impact on the upstream end of the separation bubbles ( $t/T=0.84, 0.92$ , and  $0.98$  of Fig. 7) shows that reattachment begins near  $z/d=5$  and then propagates outward. The downwash of the vortex causes the depression in the separation bubble as high momentum fluid is carried into the low momentum bubble. Similar VGJ-induced boundary layer modifications have been observed by Hansen and Bons [5] and Khan and Johnston [20]. Although the in-plane PIV data were collected without the addition of passing wakes, similar three-dimensional structures were seen in both sets of data. These data suggest that streamwise vortices also participate in the removal of the separation bubble.

Once the separation bubble is ejected from the blade ( $t/T=0.24$  in Fig. 7), there is a period of time before the bubble begins to recover. The isovelocity surfaces at  $t/T$  of 0.31, 0.38, and 0.44 show very little growth in the separation region. By  $t/T=0.51$ , the boundary layer begins to separate again. To better understand this period of sustained control, single-element hot-film data were taken using a blade follower device. This device keeps the hot film at a predetermined distance from the wall. The follower is fixed to a single axis traverse, which allows the hot film to traverse from 48% axial chord to the trailing edge. Thirteen profiles were taken ranging from 2 mm to 16 mm from the wall. Each profile was taken at a  $z/d=6$  (four jet hole diameters above the bottom edge of a VGJ hole). Phase-locked data were taken for 24 s at 10 kHz (approximately 106 wake-passing cycles). The data analysis technique described in Bons et al. [21] was employed to obtain  $U_{\text{rms}}$  after removing the phase-locked mean velocity from the raw velocity signal.

$U_{\text{rms}}/U_{\text{in}}$  data were presented in Fig. 9 to help identify the wake disturbance. Figure 9 is divided into 24 plots representing 24 phase-locked data windows taken over the wake-passing period ( $T$ ). Similar to the PIV data, the hot-film data were phase locked using the rod optical sensor. The nondimensional time is shown in the upper right corner of each plot. The use of  $U_{\text{rms}}/U_{\text{in}}$  plots assists in the identification of the separated flow region, the pulsed jet trajectory, and (to a lesser extent) the wake trajectory. From  $t/T=0.04$ – $0.25$ , the separation bubble ( $x/C_x>0.8$ ) is decreasing in size due to the influence of the previous VGJ disturbance. The wake disturbance (shown as a red arrow) then enters the measurement domain as evidenced by a slight increase in freestream turbulence upstream of the separation bubble. The separation bubble is further reduced in size due to the passing of the wake ( $t/T=0.54$ – $0.71$ ). Once the wake has passed, there remains a region of low turbulence referred to by Gostelow et al. [11] as a "calmed zone." This region of low turbulence is seen at the trailing edge ( $x/C_x>0.9$ ) from  $t/T=0.75$  until the influence of the jet disturbance arrives (green arrow).

The calmed zone is further evident in the time history plot at  $y/d=0.80$  presented in Fig. 10(a). The two-sided red arrow identifies the calmed zone that results from the wake disturbance. The smaller black arrow identifies the calmed zone that results from the VGJ disturbance. Figure 10(b) is the time history plot for the wakes only case. In the absence of an intermediate jet disturbance, this plot shows bubble regrowth ( $U_{\text{rms}}/U_{\text{in}}>5\%$ ) beginning at  $t/T=1.1$ . It appears that the VGJ disturbance arrives at the separation bubble just prior to the breakdown of the calmed zone caused by the wake. This new disturbance prevents regrowth of the separation bubble and produces another calm zone. A short time later, a new wake disturbance re-establishes the wake-induced calmed zone and the cycle continues. These figures sug-

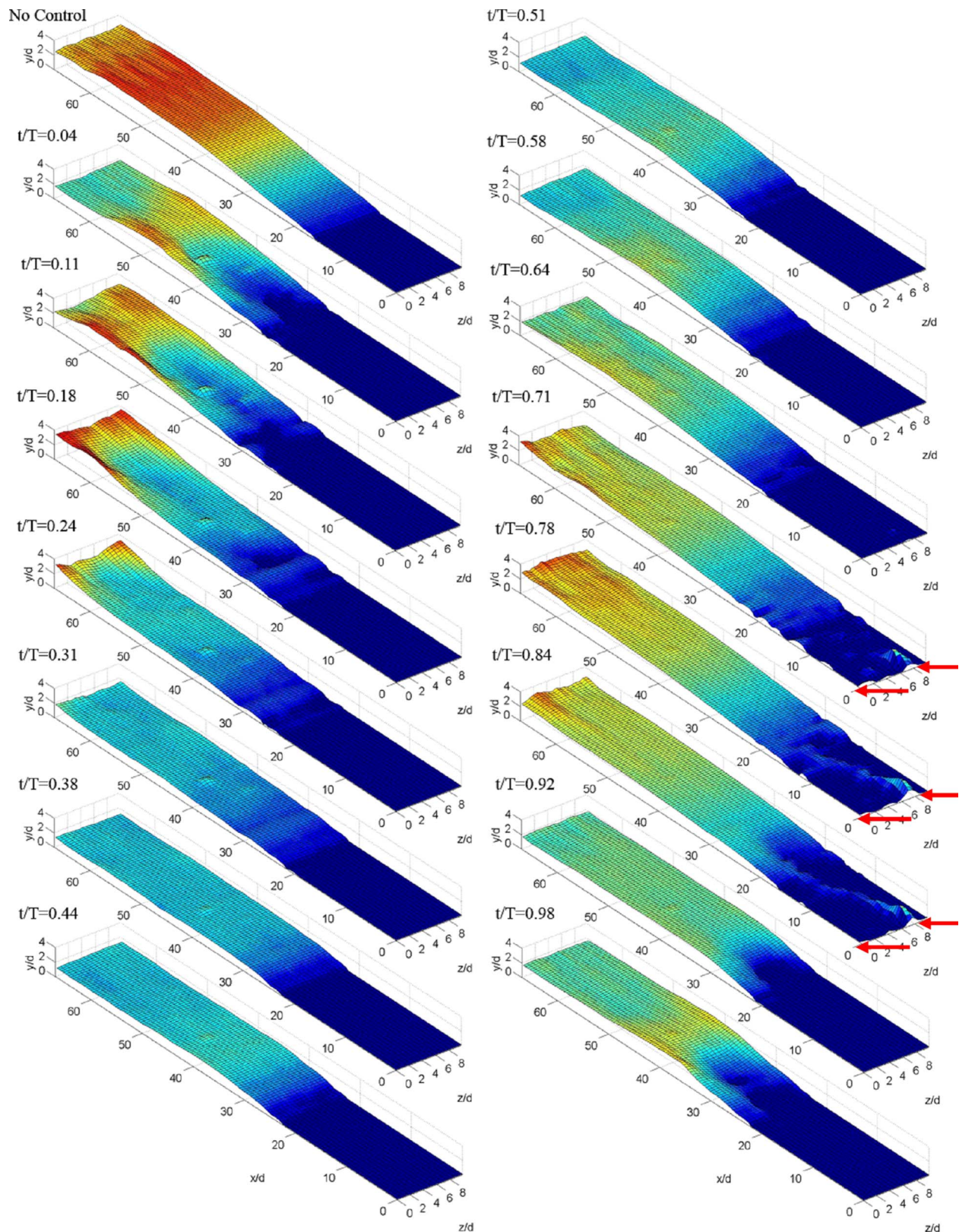


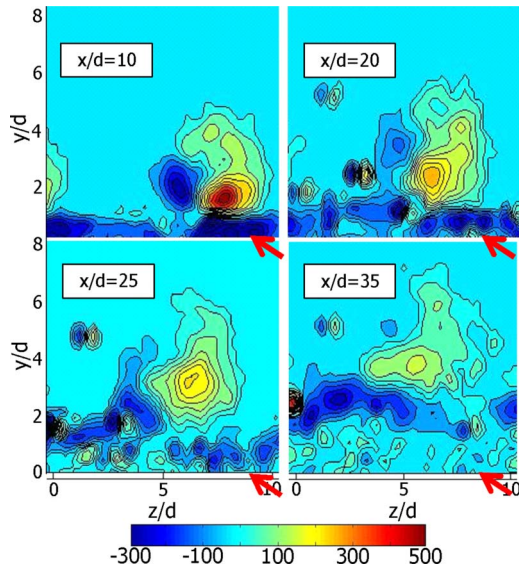
Fig. 7 Phase-locked isovelocity surfaces ( $U/U_{in}=1.0$ ) for wakes/jets (Case 6) configuration. The red arrows indicate approximate jet locations.

gest that the optimal synchronization of jets/wakes prolongs the calm zone and suppresses separation bubble regrowth. In order to optimize the control of wakes/jets, the jet disturbance should interact with the separation zone just prior to the end of the wake-

induced calm zone.

Returning to Fig. 7, the separation bubble begins to recover after the jet-induced calm zone. Then, between  $t/T=0.51$  and  $0.58$ , the separation bubble is impacted by the wake disturbance

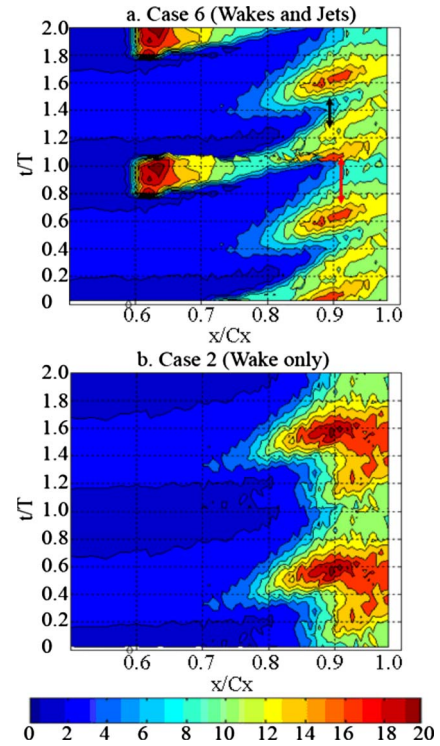




**Fig. 8 Streamwise vorticity comparison for VGJs only (Case 3). VGJ at  $x/d=0$  and  $z/d=9$  (hole center). Blowing ratio,  $B_{max}=2$ .**

(see Fig. 9). The wake interaction with the separated zone results in a spanwise-uniform bulge in the isovelocity surface that is subsequently carried off the blade by  $t/T=0.91$ . The upstream end of the residual separation bubble is then impacted by the next VGJ disturbance.

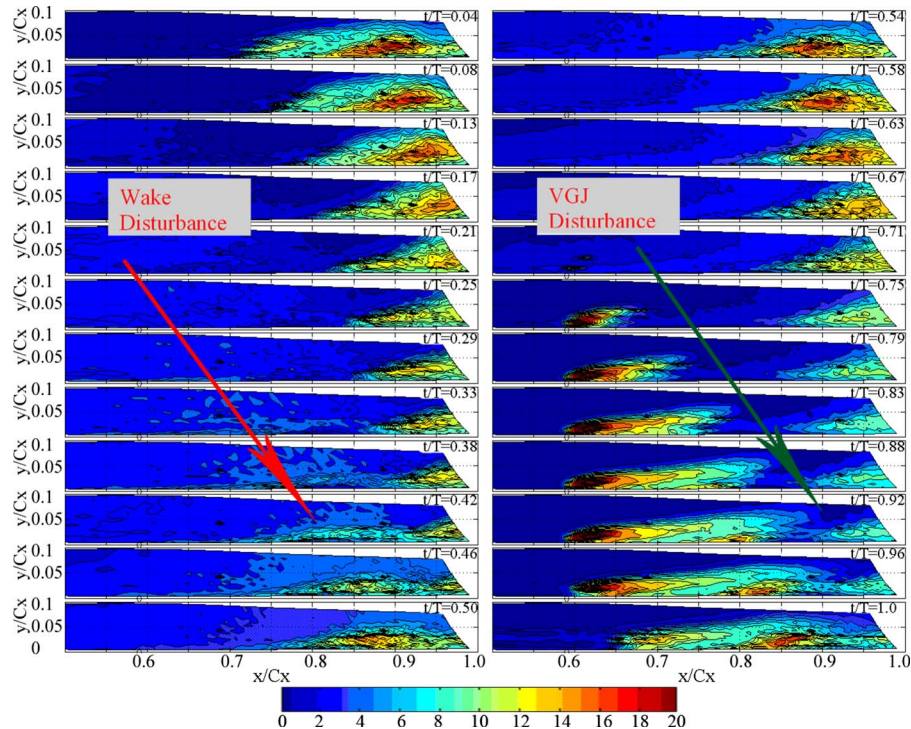
After the wake passes in the plot of  $t/T=0.91$ , there is a significantly larger separation bubble in comparison to the residual bubble after the jet disturbance ( $t/T=0.31-0.51$ ). In order to quantify the size of the separation bubbles at each  $t/T$ , each isovelocity surface from Fig. 7 was averaged in the spanwise direction. The resultant average isovelocity surfaces were then inte-



**Fig. 10 Time history plots ( $U_{rms}/U_{in}$ ) depicting wake/jet and wake only interaction with the separation bubble**

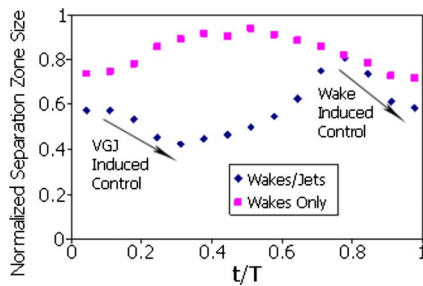
grated and normalized by the no control case. Figure 11 is a plot of this integrated measurement for each of the nondimensional times (wakes/jet and wakes only data).

Figure 11 shows the impact of each of the disturbances and their relative effectiveness in suppressing the separation bubble.



**Fig. 9  $U_{rms}/U_{in}$  plots of the wakes/jets (Case 6) configuration. The nondimensional time is labeled in the upper right corner of each plot.**





**Fig. 11 Integrated isovelocity surfaces (Cases 6 and 2) at each data acquisition time. The data were normalized by the size of the no control separation bubble.**

The configuration with wakes only causes a decrease in the normalized separation zone from 0.94 to 0.72. At  $t/T=0.78$ , the normalized separation bubble grows to nearly 0.81 as the 2D wake disturbance impacts it. The bubble size then decreases to 0.58 as the 2D disturbance is ejected from the blade. The average size of the separation bubble decreases very rapidly as evidenced by the slope of the line during wake-induced control. A similar reduction is noted in the VGJ-induced control. A comparison of the speed and size of these reductions indicates that the spanwise-average wake-induced control might actually have more impact than the jet. After the wake passes, the jet disturbance interacts with a partial separation bubble. The remainder of the low momentum fluid is re-energized, further decreasing the separation bubble to 0.42 (0.3 less than the wakes only configuration). These results suggest that at the optimal synchronizing configuration the wake disturbance prepares the separation bubble for maximum jet effectiveness.

## Conclusions

Surface static pressure and hot-film data were used to identify “optimal” conditions for the synchronization of VGJ and wake disturbances. Results suggest that jet duration, blowing ratio, and the time delay between disturbances all have a significant impact on control effectiveness. Single camera PIV and hot-film data were used to identify the relative impacts of the two unsteady disturbances and the flow physics that resulted in the control effectiveness. In-plane PIV data showed that the three-dimensional shape of the jet-disturbed separation bubble coincided with the location of a streamwise vortical structure. The depression in the separation bubble corresponded with the downwash of the vortical structure. Hot-film and PIV data were used to show that the wake and jet disturbances produced calmed zones. At optimal conditions, the jet disturbance arrived at the separation bubble just prior to the breakdown of the wake-induced calmed zone. Consequently, the jet disturbance interacted with a smaller separation bubble. This resulted in the most substantial removal of the separation zone. The location of the VGJs in this study was based on separation predictions in a wake-free environment. The addition of the unsteady wakes moved the separation bubble further downstream away from the VGJs. The vortex generator jets would likely be more effective, and consequently require less mass flow, if placed closer to the new separation region.

## Acknowledgment

This research could not have been performed without the sponsorship of the Air Force Office of Scientific Research, with Dr. Thomas Beutner and Lt. Col. Rhett Jefferies as program managers.

## Nomenclature

$B$  = blowing ratio ( $U_{jet}/U_e$  at 59%  $C_x$ ) (use  $U_{max}$  if pulsed VGJs)

$C_x$  = axial chord (24 cm)  
 $C_p$  = pressure coefficient ( $(P_{tin}-P)/(P_{tin}-P_{sin})$ )  
 $F^+$  = dimensionless forcing frequency ( $f/(U_{av}/SSLJ)$ )  
 $L$  = distance between rods  
 $P$  = pressure  
 $Re_c$  = Reynolds number based on inlet velocity and axial chord ( $C_x U_{in}/\nu$ )  
 $S$  = blade spacing  
 $SSLJ$  = suction surface length from jet location to the trailing edge  
 $U$  = velocity magnitude  
 $U_{av}$  = average freestream velocity from jet location to the trailing edge  
 $T$  = rod passing period (225 ms)  
 $d$  = jet hole diameter (2.6 mm)  
 $f$  = VGJ forcing frequency  
 $t$  = time (s)  
 $u$  = x-component of velocity (approximately streamwise)  
 $v$  = y-component of velocity (approximately blade normal)  
 $w$  = z-component of velocity (spanwise)  
 $x$  = approximate streamwise coordinate  
 $y$  = approximate blade normal coordinate  
 $z$  = spanwise coordinate ( $z=0$  at bottom of VGJ hole)  
 $\delta$  = boundary layer thickness  
 $\phi$  = flow coefficient ( $U_{in,axial}/U_{rod}$ )  
 $\Gamma$  = integrated boundary layer momentum flux loss  
 $\nu$  = kinematic viscosity

## Subscripts

axial = axial direction  
 $e$  = boundary layer edge  
in = cascade inlet conditions  
jet = VGJ jet  
max = max  
 $o$  = base line case without wakes or VGJ control  
rod = wake generator rod  
rms = root mean square  
 $S$  = static  
 $T$  = total

## References

- [1] Sondergaard, R., Bons, J. P., and Rivir, R. B., 2002, “Control of Low-Pressure Turbine Separation Using Vortex Generator Jets,” *J. Propul. Power*, **18**(4), pp. 889–895.
- [2] Sharma, O., 1998, “Impact of Reynolds Number of LP Turbine Performance,” *Proceedings of 1997 Minnowbrook II Workshop on Boundary Layer Transition I Turbomachines*, NASA/CP-1998-206958, pp. 65–69.
- [3] Matsunuma, T., Abe, H., Tsutsui, Y., and Murata, K., 1998, “Characteristics of an Annular Turbine Cascade at Low Reynolds Numbers,” *ASME Paper No. 98-GT-518*.
- [4] Eldredge, R. G., and Bons, J. P., 2004, “Active Control of a Separating Boundary Layer With Steady Vortex Generating Jets—Detailed Flow Measurements,” presented at the AIAA Aerospace Sciences Meeting, Reno, NV, Jan. 5–8.
- [5] Hansen, L. C., and Bons, J. P., 2006, “Phase-Locked Flow Measurements of Pulsed Vortex-Generator Jets in a Separating Boundary Layer,” *J. Propul. Power*, **22**(3), pp. 558–566.
- [6] Postl, D., Gross, A., and Fasel, H. F., 2003, “Numerical Investigation of Low-Pressure Turbine Blade Separation Control,” *AIAA Paper No. 2003-0614*.
- [7] Bloxham, M., Reimann, D., and Bons, J. P., 2006, “The Effect of VGJ Pulsing Frequency on Separation Bubble Dynamics,” presented at the AIAA 44th Aerospace Sciences Meeting and Exhibit, Reno, NV, Jan. 9–12, Paper No. AIAA 2006-0876.
- [8] Bons, J. P., Sondergaard, R., and Rivir, R. B., 2002, “The Fluid Dynamics of LPT Blade Separation Control Using Pulsed Jets,” *ASME J. Turbomach.*, **124**, pp. 77–85.
- [9] Volino, R. J., 2003, “Separation Control on Low-Pressure Turbine Airfoils Using Synthetic Vortex Generator Jets,” *ASME Paper No. GT2003-38729*.
- [10] Stieger, R., Hollis, D., and Hodson, H., “Unsteady Surface Pressures Due to

- Wake Induced Transition in a Laminar Separation Bubble on a LP Turbine Cascade," ASME Paper No. GT2003-38303.
- [11] Gostelow, J. P., and Thomas, R. L., 2003, "Response of a Laminar Separation Bubble to an Impinging Wake," ASME Paper No. GT2003-38972.
- [12] Funazaki, K., Yamada, K., Ono, K., Segawa, K., Hamazaki, H., Takahashi, A., and Tanimitsu, H., "Experimental and Numerical Investigations of Wake Passing Effects Upon Aerodynamic Performance of a LP Turbine Linear Cascade With Variable Solidity," ASME Paper No. GT2006-90507.
- [13] Cattanei, A., Zunino, P., Schroder, T., Stoffel, B., and Matyschok, B., 2006, "Detailed Analysis of Experimental Investigations on Boundary Layer Transition in Wake Disturbed Flow," ASME Paper No. GT2006-90128.
- [14] Eldredge, R. G., and Bons, J. P., 2004, "Active Control of a Separating Boundary Layer with Steady Vortex Generating Jets—Detailed Flow Measurements," presented at the AIAA Aerospace Sciences Meeting, Reno, NV, Jan. 5–8, Paper No. AIAA-2004-0751.
- [15] Rao, K. V., Delaney, R. A., and Topp, D. A., "Turbine Vane-Blade Interaction: Vol. 1.2-D Euler/Navier-Stokes Aerodynamic and Grid Generation Developments," U.S. Air Force Research Laboratory, Report No. WL-TR-94-2073.
- [16] Bons, J. P., Hansen, L. C., Clark, J. P., Koch, P. J., and Sondergaard, R., 2005, "Designing Low-Pressure Turbine Blades With Integrated Flow Control," ASME Paper No. GT2005-68962.
- [17] LaVision, 2004, DAVIS FLOWMASTER, v. 7.0, Mar., LaVision GmbH, Anna-VandenHoeck-Ring, 19, D-37081 Gottingen.
- [18] Olson, D. H., Reimann, D., Bloxham, M., and Bons, J. P., "The Effect of Elevated Freestream Turbulence on Separation Control With Vortex-Generating Jets," presented at the AIAA 43rd Aerospace Sciences Meeting and Exhibit, Reno, NV, Jan. 10–13, Paper No. AIAA 2005-1114.
- [19] Reimann, D., Bloxham, M., Crapo, K., Pluim, J., and Bons, J. P., "Influence of Vortex Generator Jet-Induced Transition on Separating Low Pressure Turbine Boundary Layers," AIAA Fluid Dynamics Conference, San Francisco, Jun. 5–8, Paper No. AIAA2006-2852.
- [20] Khan, Z. U., and Johnston, J. P., 2000, "On Vortex Generating Jets," *Int. J. Heat Fluid Flow*, **21**, pp. 506–511.
- [21] Bons, J. P., Bloxham, M., and Reimann, D., 2006, "Separated Flow Transition on an LP Turbine Blade With Pulsed Flow Control," ASME Paper No. GT2006-90754.

# Reduced Rough-Surface Parametrization for Use With the Discrete-Element Model

**Stephen T. McClain**

Assistant Professor  
Mechanical Engineering Department,  
Baylor University,  
One Bear Place, No. 97356,  
Baylor, TX 76796-7356  
e-mail: stephen\_mcclain@baylor.edu

**Jason M. Brown**

Graduate Student  
Department of Mechanical Engineering,  
The University of Alabama at Birmingham,  
1530 3rd Avenue South, BEC 257,  
Birmingham, AL 35294-4461  
e-mail: jmbrown@rockwellcollins.com

*The discrete-element model for flows over rough surfaces was recently modified to predict drag and heat transfer for flow over randomly rough surfaces. However, the current form of the discrete-element model requires a blockage fraction and a roughness-element diameter distribution as a function of height to predict the drag and heat transfer of flow over a randomly rough surface. The requirement for a roughness-element diameter distribution at each height from the reference elevation has hindered the usefulness of the discrete-element model and inhibited its incorporation into a computational fluid dynamics (CFD) solver. To incorporate the discrete-element model into a CFD solver and to enable the discrete-element model to become a more useful engineering tool, the randomly rough surface characterization must be simplified. Methods for determining characteristic diameters for drag and heat transfer using complete three-dimensional surface measurements are presented. Drag and heat transfer predictions made using the model simplifications are compared to predictions made using the complete surface characterization and to experimental measurements for two randomly rough surfaces. Methods to use statistical surface information, as opposed to the complete three-dimensional surface measurements, to evaluate the characteristic dimensions of the roughness are also explored. [DOI: 10.1115/1.2952379]*

## Introduction

Many flows of engineering interest are constrained by rough surfaces. Examples of flows over rough surfaces are the flow of combustion products over erosion and fuel deposits on gas turbine blades, the flow of air over aircraft wings with ice accretions, the flow over a reentry body with ablation roughness, the flow of air over wind turbine blades with insect roughness, the flow of water over pump impellers roughened by cavitation, and the flow of water over ship hulls with barnacle roughness. Surface roughness significantly affects skin friction drag and heat transfer. While many engineering flows occur over rough surfaces and the effects of the roughness are significant, predicting the drag and heat transfer for flows over rough surfaces is a major shortcoming of the widely used computational fluid dynamics (CFD) codes [1].

The equivalent sand-grain roughness technique is commonly used in the gas-turbine industry for predicting rough-surface skin friction and heat transfer. To use the equivalent sand-grain roughness technique, empirical correlations or wall-function techniques that include the effects of the roughness in the turbulence model are used to make skin friction and heat transfer predictions after determining a surface's sand-grain roughness height. Many deficiencies in the equivalent sand-grain roughness technique have been noted [2].

- (1) Wind-tunnel measurements of flow over a particular randomly rough surface are required to accurately predict skin friction.
- (2) In general, a surface with sandlike roughness elements does not have an equivalent sand-grain roughness height equal to its physical height.
- (3) An effective wall location, which is needed to measure the effective roughness height based on the intercept offset of the "law of the wall equation," is not apparent.

- (4) A single length scale, effective height, is not sufficient to correlate sand-grain roughness to many other roughness geometries. In general, correlations between the effective roughness height and some "distribution density" parameters exhibit as much as 100% difference between predicted and measured equivalent sand-grain roughness heights [2].
- (5) Attempts to include the sand-grain roughness model in finite-difference boundary layer codes by altering the law of the wall result in ill-defined boundary conditions at the wall.
- (6) There is no theoretical reason that heat transfer data should correlate with effective sand-grain height.

While the Sigal–Danberg parameter [3], introduced after Taylor's discussion [2], provides a better correlation for equivalent roughness height, the density parameter is still limited to Sigal–Danberg parameter values between 20 and 200. Bons [4] has also shown that the Sigal–Danberg parameter is difficult to define for roughness elements with random spacings, shapes, and heights and that measured equivalent sand-grain roughness heights for randomly rough surfaces can vary as much as 40% from predicted heights using logarithmic data curve fits based on the Sigal–Danberg parameter. Once an equivalent sand-grain roughness height is determined for a randomly rough surface, empirical correlations, such as the one provided by Dipprey and Sabersky [5], or CFD codes employing wall function parameters must be used to evaluate the skin friction and heat transfer interaction between the fluid and the rough surface.

Others have investigated flows over roughness using direct numerical simulation by creating grids that resolve the features of individual roughness elements. Matheis et al. [6], Matheis and Rothmayer [7], and Huebsch and Rothmayer [8] have focused their efforts on simulating flows over Gaussian roughness elements similar to hemispheres on flat plates and leading edges of airfoils, representing the beginning stages of ice accretion on aircraft wings. Wang et al. [9], however, resolved the flow over a randomly rough section of a flat plate. While the direct numerical simulations are enlightening, the computational storage and time requirements for simulating flows over real engineering compo-

Contributed by the International Gas Turbine Institute of ASME for publication in the JOURNAL OF TURBOMACHINERY. Manuscript received August 28, 2007; final manuscript received October 22, 2007; published online February 3, 2009. Review conducted by David Wisler. Paper presented at the ASME Turbo Expo 2007: Land, Sea and Air (GT2007), Montreal, QC, Canada, May 14–17, 2007.



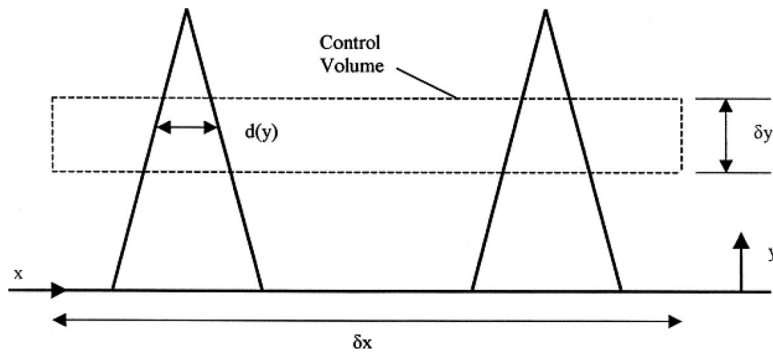


Fig. 1 The discrete-element roughness model control volume schematic

nents that resolve the individual roughness elements are staggering, even with the adaptive grids of Wang et al. [9].

The discrete-element model (DEM) is another alternative for predicting the effects of surface roughness on heat transfer and skin friction. In the DEM, the effects of the roughness elements: decreased flow area, the drag on the roughness elements, and the heat transferred from the roughness elements to the flow stream, are evaluated by solving equations of fluid motion specifically derived to include the effects [2,10]. The DEM is a spatially averaged model, so while the information about the roughness elements must be resolved in the direction normal to the solid wall, the roughness-element shape information is not resolved in the two directions parallel to the solid wall. By incorporating the effect of the roughness elements into the equations of fluid mechanics, the DEM captures the important physics of flow over rough surfaces based on integral quantities of the boundary layer while requiring much less computational storage and time than direct numerical simulations that fully resolve the roughness elements and the flow field. The DEM is semiempirical in that correlations, based on experimental data for flows over banks of cylinders, are used to describe the drag and heat transfer interactions of the roughness elements protruding into the fluid.

McClain et al. [10] recently adapted the DEM for use with randomly rough surfaces. McClain et al. [10] and Bons and McClain [11] demonstrated very encouraging results. By fully characterizing the randomly rough surfaces in terms of the distribution of roughness-element diameters at multiple height levels, predictions made with the DEM agreed within 7% of experimentally measured skin friction coefficients for four randomly rough surfaces. Stanton number predictions for the same randomly rough surfaces agreed within 16% of the experimentally measured values.

While the agreement between the DEM predictions and the experimental measurements is impressive, areas to improve the DEM were identified through discussions with members of the gas-turbine industry. The main limitation of the model is that the randomly rough DEM has not been implemented in a CFD code. The DEM for random roughness is currently implemented in an educational boundary-layer code using a mixing-length turbulence model with van Driest damping. The boundary-layer code currently used does not have the ability to consider important characteristics of flows over rough surfaces, such as the increased turbulence intensity levels.

Variations of the DEM have also been implemented in the boundary layer codes TEXSTAN [12] and TEN [13], which have higher order turbulence models. However, each of these codes uses a cone model of surface roughness. In the cone model, a randomly rough surface is represented by a distribution of cones or truncated cones that matches a set of statistical parameters and the Sigal–Danberg parameter. However, the Sigal–Danberg parameter and correlation is itself an empirical method with considerable variation in experimental data from the best available correlation [14]. Using the Sigal–Danberg parameter to create conical

representations of randomly rough surfaces introduces substantial uncertainty into the already semiempirical DEM. The compounding of empiricism has produced wildly varying levels of agreement when comparing cone-model DEM predictions to experimental measurements of flows over randomly rough surfaces [12,13].

The DEM has most recently been implemented in a boundary-layer code called ALPHA using a two-layer turbulence model and an intermittency transition model [15]. The results presented in Ref. [15] for flows over surfaces with conical roughness elements are a good example of how well the DEM performs, even on highly accelerated transitional boundary layers. Given the promising results of Refs. [10,11,15], the DEM formulation must be explored to determine a better way to represent a randomly rough surface with a reduced number of characteristic dimensions or parameters.

The appropriate method to produce a reduced DEM surface description from a three-dimensional surface measurement or profilometry trace is important. In the design process, however, the full three-dimensional measurement of a surface is not known. In the gas-turbine industry, a large data set exists relating the development of surface roughness, described by statistical parameters, as a function of operating time and conditions [16–18]. The DEM would be far more useful in the gas-turbine design process if the reduced DEM surface description were expressed in terms of the statistical surface parameters correlated to the operating time and conditions in literature.

To make the DEM a more useful tool for industry and research, the DEM must be implemented in a Navier–Stokes CFD code using available statistical descriptions of randomly rough surfaces. The objectives of this effort are as follows:

- (1) to determine what randomly rough surface parameters must be matched to use a reduced (characteristic) representation of the surface for use with the DEM,
- (2) to determine how the reduced parameters must be evaluated for a three-dimensionally measured randomly rough surface for use with the DEM,
- (3) to explore methods using statistical parameters of a randomly rough surface to produce a reduced DEM representation, and
- (4) to use many applications of the DEM with the various options for using the statistical parameters to determine the most sensitive randomly rough characteristics to match using the statistical parameters.

### Discrete-Element Model

The DEM is formulated for roughness elements with three-dimensional shapes for which the element cross section can be defined at every height,  $y$ . The differential, boundary-layer equations including roughness effects are derived by applying the basic conservation statements for mass, momentum, and energy to a control volume such as that shown in Fig. 1. The concept that the

two-dimensional, time-averaged turbulent boundary-layer equations can be applied in the flow region below the crests of the roughness elements is basic to this approach. The flow variables are spatially averaged over the transverse ( $z$ ) direction and the streamwise ( $x$ ) direction. The physical effects of the roughness elements on the fluid in the control volume are modeled by considering the flow blockage, the local element heat transfer, and the local element form drag. The void factors,  $\beta$ , are defined as the fraction of the area open to flow. For nonuniform roughness, the total form drag force on the control volume is due to all of the roughness elements penetrating the control volume and is expressed using a local drag coefficient as

$$F_D = \frac{1}{2} \rho u^2 \delta y \sum_{i=1}^{N_r} C_{D,i} d_i(y) \quad (1)$$

Likewise, the rate of heat transfer between the elements penetrating the control volume and the fluid is expressed using a local Nusselt number as

$$Q = \pi k_f (T_R - T) \delta y \sum_{i=1}^{N_r} K_{\varepsilon,i} \text{Nu}_{d,i} \quad (2)$$

where  $K_{\varepsilon,i}$  is a correction factor that accounts for the increased "wetted" surface area for heat transfer based on an elliptical blockage representation [10].

Using the above ideas, the continuity, momentum, and energy equations for a steady, Reynolds-averaged, two-dimensional turbulent boundary layer with nonuniform roughness become

$$\frac{\partial}{\partial x} (\rho \beta_x u) + \frac{\partial}{\partial y} (\rho \beta_y v) = 0 \quad (3)$$

$$\begin{aligned} \beta_x \rho u \frac{\partial u}{\partial x} + \beta_y \rho v \frac{\partial u}{\partial y} = & - \frac{\partial}{\partial x} (\beta_x P) + \frac{\partial}{\partial y} \left[ \beta_y \left( \mu \frac{\partial u}{\partial y} - \overline{\rho u' v'} \right) \right] \\ & - \frac{1}{2} \rho \frac{u^2}{L_p L_t} \sum_{i=1}^{N_r} C_{D,i} d_i \end{aligned} \quad (4)$$

and

$$\begin{aligned} \beta_x \rho u \frac{\partial H}{\partial x} + \beta_y \rho v \frac{\partial H}{\partial y} = & \frac{\partial}{\partial y} \left[ \beta_y \left( \frac{k_f}{c_p} \frac{\partial H}{\partial y} - \overline{\rho v' h'} \right) \right] + u \frac{\partial}{\partial x} (\beta_x P) \\ & + \beta_y \frac{\partial u}{\partial y} \left( \mu \frac{\partial u}{\partial y} - \overline{\rho u' v'} \right) + \frac{1}{2} \rho \frac{u^3}{L_p L_t} \sum_{i=1}^{N_r} C_{D,i} d_i \\ & + \frac{\pi k_f}{L_p L_t} (T_R - T) \sum_{i=1}^{N_r} K_{\varepsilon,i} \text{Nu}_{d,i} \end{aligned} \quad (5)$$

where

$$K_{\varepsilon} = \left[ \frac{1}{2} \left( 1 + \frac{1}{\varepsilon^2} \right) - \frac{1}{8.8} \left( 1 - \frac{1}{\varepsilon} \right)^2 \right]^{1/2} \quad (6)$$

and where  $\beta$  is the fraction of area open to flow, which is  $(1 - \alpha)$  where  $\alpha$  is the blockage fraction, and  $L_p$  and  $L_t$  are the parallel and transverse spacing parameters for uniform roughness or the parallel length or transverse width of the control volume for nonuniform roughness. The boundary conditions for Eqs. (3)–(5) are

$$\begin{aligned} y = \bar{y}: u = v = 0, \quad H = H_w \\ y \rightarrow \infty: u = U_e, \quad H = H_e \end{aligned} \quad (7)$$

The turbulence model is not presently modified to include roughness effects. In this study, the Prandtl mixing length with van Driest damping is used for turbulence closure. Hence,

$$-\overline{\rho u' v'} = \rho l_m^2 \left( \frac{\partial u}{\partial y} \right) \left| \frac{\partial u}{\partial y} \right| \quad (8)$$

where

$$l_m = \begin{cases} 0.41y[1 - \exp(-y^+/26)] & \text{for } l_m \leq 0.09\delta \\ l_m = 0.09\delta & \text{otherwise} \end{cases} \quad (9)$$

Closure in the energy equation is achieved using a turbulent Prandtl number,  $\text{Pr}_t$ , of 0.9.

In addition to the usual turbulence modeling closure requirements for  $-\overline{\rho u' v'}$ ,  $\overline{u'^2}$ , and  $-\overline{\rho v' h'}$ , the roughness model has closure requirements for  $C_D$  and  $\text{Nu}_d$ .  $C_D$  and  $\text{Nu}_d$  are formulated as functions of the local roughness-element Reynolds number

$$\text{Re}_d = \frac{\rho u d}{\mu} \quad (10)$$

thus directly including information on the roughness-element size and shape. The functional forms for  $C_D$  and  $\text{Nu}_d$  used in this study for elliptical roughness elements are

$$C_D = \begin{cases} \left( \frac{\text{Re}_d}{1000} \right)^{-0.125} \varepsilon^{0.73456}, & \text{Re}_d < 60,000 \\ 0.6 \varepsilon^{0.73456}, & \text{Re}_d > 60,000 \end{cases} \quad (11)$$

and

$$\text{Nu}_d = \begin{cases} 1.7 \text{Re}_d^{0.49} \text{Pr}^{0.4} & \text{for } \text{Re}_d \leq 13,776 \\ 0.0605 \text{Re}_d^{0.84} \text{Pr}^{0.4} & \text{for } \text{Re}_d > 13,776 \end{cases} \quad (12)$$

The values of the constants and exponents for the  $C_D$  correlation were determined by extensive calibrations using a number of deterministic surface roughness data sets [2]. The  $\text{Nu}_d$  correlation constants were determined by Hosni et al. [19]. The functional form for  $\text{Nu}_d$  has produced good agreement compared to heat transfer measurements for surfaces with a wide range of uniform surface roughness shapes and distributions from a number of data sets [18–20].

Once the boundary-layer equations have been solved, the skin friction coefficient is evaluated as

$$C_f = \frac{(1 - \alpha) \mu \left. \frac{du}{dy} \right|_{y=\bar{y}} + \frac{1}{2} \frac{1}{L_t L_p} \int_{\bar{y}}^{\infty} \left( \rho u^2 \sum_{i=1}^{N_r} C_{D,i} d_i \right) dy}{\frac{1}{2} \rho U_e^2} \quad (13)$$

and the Stanton number is determined using the expression

$$\text{St} = \frac{-(1 - \alpha) k_f \left. \frac{dT}{dy} \right|_{y=\bar{y}} + \frac{1}{L_t L_p} \int_{\bar{y}}^{\infty} \pi k_f (T_R - T) \sum_{i=1}^{N_r} K_{\varepsilon,i} \text{Nu}_{d,i} dy}{\rho U_e c_p (T_w - T_e)} \quad (14)$$

Equations (13) and (14) demonstrate that the skin friction on a rough surface is the sum of the shear force on the flat part of the surface and the drag on the individual roughness elements and that the heat transfer between a flow and a rough surface is evaluated as the sum of the convection through the fluid in contact with the flat surface and the heat transferred between the fluid and the individual roughness elements.

## Characteristic Surface Descriptions

In the current application of the DEM for random roughness, the complete surface must be characterized by measuring the roughness-element diameter distribution versus the height of the roughness elements. Since the DEM is a spatially averaged model, a complete surface characterization requires that, at each grid point, the momentum sink and local heat transfer terms be summed over the distribution of roughness-element diameters at

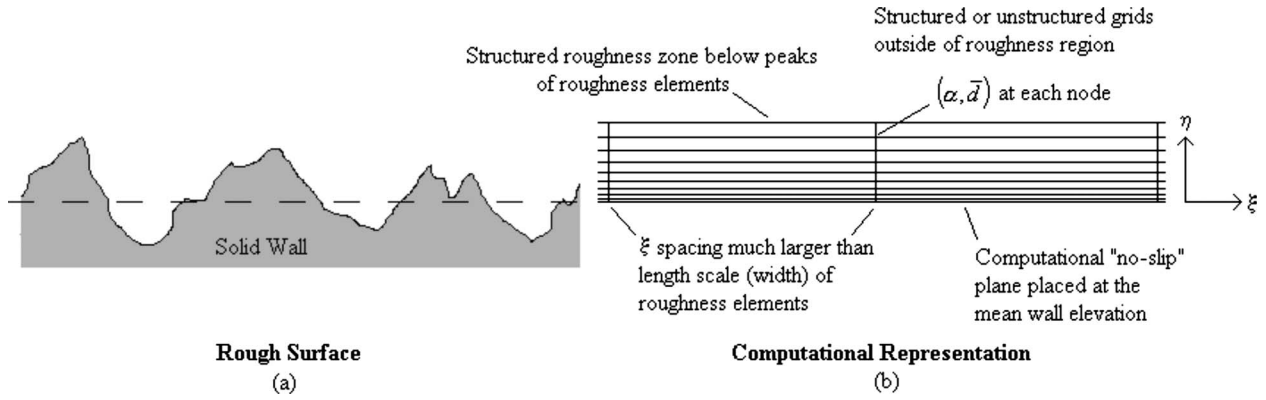


Fig. 2 A rough surface (a) and its computational DEM representation (b)

the prescribed height level. For CFD computations, averaging the momentum sink and local heat transfer over the roughness-element distribution is computationally expensive. A method to determine one or more average or characteristic dimensions at each height from the computational no-slip surface would be much more efficient. More than one characteristic dimension may be required to match both skin friction and heat transfer simultaneously.

Using the reduced surface description, a blockage fraction ( $\alpha$ ) and a set of characteristic dimensions ( $\bar{d}_1, \bar{d}_2, \dots$ ) are assigned to every point or cell in the roughness zone. Outside the roughness zone, structured or unstructured grids would be used to determine the larger scale features of the flow. An example of a randomly rough surface and a computational representation of the rough surface are presented in Fig. 2. In the next sections, the DEM formulation is used to explore the best mechanisms for determining characteristic dimensions for a randomly rough surface.

**Characteristic Friction Diameter.** For each location from the mean elevation, one characteristic dimension is desired that produces the same roughness drag per unit volume of the control volume as the complete roughness distribution. Examining Eq. (4), the roughness drag per unit volume is

$$\frac{F_D}{L_p L_t \Delta y} = \frac{1}{2} \rho \frac{u^2}{L_p L_t} \sum_{i=1}^{N_r} C_{D,i} d_i \quad (15)$$

The drag coefficient is a piecewise function of the local element diameter. For this study, only low speed flows were investigated and the local element Reynolds numbers were rarely above 13,000. Hence, substituting for the local drag coefficient for  $Re_d < 60,000$  yields

$$\frac{F_D}{L_p L_t \Delta y} = \frac{1}{2} \rho \frac{u^2}{L_p L_t} \sum_{i=1}^{N_r} \varepsilon_i^j G_f \left( \frac{\rho u d_i}{\mu} \right)^{-0.125} d_i \quad (16)$$

where  $j=0.73456$  and  $G_f=(1/1000)^{-0.125}$ . Collecting constant terms outside of the summation results in

$$\frac{F_D}{L_p L_t \Delta y} = \frac{1}{2} \rho u^2 G_f \left( \frac{\rho u}{\mu} \right)^{-0.125} \frac{\sum_{i=1}^{N_r} \varepsilon_i^j d_i^{0.875}}{L_p L_t} \quad (17)$$

In the above equation,  $L_p$  and  $L_t$  are the dimensions of the profilometer trace. For the reduced surface description, the profilometer trace area must be represented in terms of the blockage fraction at a given height and in terms of the measured blockage element diameters, eccentricities, and shape factors at the given height.

$$L_p L_t = \frac{\pi \sum_{i=1}^{N_r} d_i^2 S_i}{4 \sum_{i=1}^{N_r} \varepsilon_i} \quad (18)$$

where  $S_i$  is introduced as the shape factor.  $S_i$  accounts for the different plan-form areas of the randomly shaped blockages compared to the elliptical representation based on the maximum transverse width and maximum length. For any individual blockage, the shape factor is

$$S_i = \frac{4 \varepsilon_i A_i}{\pi d_i^2} \quad (19)$$

where  $A_i$  is the plan-form area of an individual roughness blockage at a specific elevation. Substituting in the pressure exhibited on the control volume by the roughness elements,

$$\frac{F_D}{L_p L_t \Delta y} = \frac{2}{\pi} \alpha \rho u^2 G_f \left( \frac{\rho u}{\mu} \right)^{-0.125} \frac{\sum_{i=1}^{N_r} \varepsilon_i^j d_i^{0.875}}{\sum_{i=1}^{N_r} \frac{d_i^2 S_i}{\varepsilon_i}} \quad (20)$$

The intent is to represent the surface with characteristic properties that produce the same distributed force over the control volume area. Equation (20) identifies four parameters that must be represented with characteristic values: the blockage fraction, element eccentricity, element diameter, and element shape factor. Thus, Eq. (20) is rewritten in terms of characteristic values. That is,

$$\frac{F_D}{L_p L_t \Delta y} = \frac{2}{\pi} \alpha \rho u^2 G_f \left( \frac{\rho u}{\mu} \right)^{-0.125} \frac{\bar{\varepsilon}^{j+1} \bar{d}_f^{0.875}}{\bar{d}_f^2 \bar{S}} \quad (21)$$

where the overbar represents average or characteristic dimensions. Equating the expressions for the roughness drag yields

$$\frac{\bar{\varepsilon}^{j+1} \bar{d}_f^{0.875}}{\bar{d}_f^2 \bar{S}} = \frac{\sum_{i=1}^{N_r} \varepsilon_i^j d_i^{0.875}}{\sum_{i=1}^{N_r} \frac{d_i^2 S_i}{\varepsilon_i}} \quad (22)$$

The right hand side of the above equation is not easily separable. However, making the argument that the eccentricity and shape factor of each individual blockage, while important, are secondary to the diameter in determining the drag contribution of the blockage, then average values of the eccentricity and shape factor can be factored from the right hand side.



$$\frac{\bar{\varepsilon}^{j+1} \bar{d}_f^{0.875}}{\bar{d}_f^2 \bar{S}} \approx \frac{\bar{\varepsilon}^{j+1} \sum_{i=1}^{N_r} d_i^{0.875}}{\bar{S} \sum_{i=1}^{N_r} d_i^2} \quad (23)$$

The results of McClain et al. [10] provide some justification for using an average eccentricity. In Ref. [10], experimental measurements of skin friction were compared to DEM predictions made using average eccentricities (for all elevations measured) and using the measured eccentricity for each blockage element at each elevation. Using the average eccentricity produced no more than an 8% difference with the predictions using the measured eccentricity of each individual blockage.

Canceling terms in Eq. (23) and solving for the characteristic friction diameter yield

$$\bar{d}_f \approx \left( \frac{\sum_{i=1}^{N_r} d_i^2}{\sum_{i=1}^{N_r} d_i^{0.875}} \right)^{8/9} \quad (24)$$

In terms of the characteristic friction diameter, average eccentricity, and average shape factor, the momentum equation Eq. (4) becomes

$$\beta_x \rho u \frac{\partial u}{\partial x} + \beta_y \rho v \frac{\partial u}{\partial y} = - \frac{\partial}{\partial x} (\beta_x P) + \frac{\partial}{\partial y} \left[ \beta_y \left( \mu \frac{\partial u}{\partial y} - \overline{\rho u' v'} \right) \right] - \frac{1}{2} \rho u^2 \frac{4\alpha \bar{\varepsilon}}{\pi \bar{d}_f \bar{S}} C_D \quad (25)$$

The skin friction coefficient is then evaluated as

$$C_f = \frac{(1-\alpha) \mu \left. \frac{du}{dy} \right|_{y=\bar{y}} + \frac{1}{2} \int_{\bar{y}}^{\infty} \rho u^2 \frac{4\alpha \bar{\varepsilon} C_D}{\pi \bar{d}_f \bar{S}} dy}{\frac{1}{2} \rho U_e^2} \quad (26)$$

**Characteristic Convection Diameter.** For the control volume identified in Fig. 1, the heat transfer from the roughness elements per unit volume is

$$\frac{Q}{L_p L_t \Delta y} = \frac{\pi k_f (T_R - T)}{L_p L_t} \sum_{i=1}^{N_r} K_{\varepsilon,i} \text{Nu}_{d,i} \quad (27)$$

Eliminating the profilometer trace lengths yields

$$\frac{Q}{L_p L_t \Delta y} = 4\alpha k_f (T_R - T) \frac{\sum_{i=1}^{N_r} K_{\varepsilon,i} \text{Nu}_{d,i}}{\sum_{i=1}^{N_r} \frac{d_i^2 S_i}{\varepsilon_i}} \quad (28)$$

Substituting the local Nusselt expression for local Reynolds numbers less than 13,000 yields

$$\frac{Q}{L_p L_t \Delta y} = 4\alpha k_f (T_R - T) G_h \frac{\sum_{i=1}^{N_r} K_{\varepsilon,i} \left( \frac{\rho u d_i}{\mu} \right)^{0.49}}{\sum_{i=1}^{N_r} \frac{d_i^2 S_i}{\varepsilon_i}} \quad (29)$$

where  $G_h = 1.7 \text{Pr}^{0.4}$ . Collecting constant terms outside of the summation results in

$$\frac{Q}{L_p L_t \Delta y} = 4\alpha k_f (T_R - T) G_h \left( \frac{\rho u}{\mu} \right)^{0.49} \frac{\sum_{i=1}^{N_r} K_{\varepsilon,i} d_i^{0.49}}{\sum_{i=1}^{N_r} \frac{d_i^2 S_i}{\varepsilon_i}} \quad (30)$$

As was the case with the characteristic friction diameter development, the intent is to represent the surface with characteristic properties that produce the same distributed heat transfer to the control volume; thus, the above equation is placed in terms of characteristic values.

$$\frac{Q}{L_p L_t \Delta y} = 4\alpha k_f (T_R - T) G_h \left( \frac{\rho u}{\mu} \right)^{0.49} \frac{\bar{\varepsilon} K_{\varepsilon} \bar{d}_c^{0.49}}{\bar{d}_c^2 \bar{S}} \quad (31)$$

Equating the previous two equations yields

$$\frac{\bar{\varepsilon} K_{\varepsilon} \bar{d}_c^{0.49}}{\bar{d}_c^2 \bar{S}} = \frac{\sum_{i=1}^{N_r} K_{\varepsilon,i} d_i^{0.49}}{\sum_{i=1}^{N_r} \frac{d_i^2 S_i}{\varepsilon_i}} \quad (32)$$

As was the case with Eq. (23), the right hand side of the above equation is not easily separable. However, making the argument that the eccentricity and shape factor of each individual blockage, while important, are secondary to the diameter in determining the heat transfer contribution of the blockage, then average values of the eccentricity and shape factor can be factored from the right hand side.

$$\frac{\bar{\varepsilon} K_{\varepsilon} \bar{d}_c^{0.49}}{\bar{d}_c^2 \bar{S}} \approx \frac{\bar{\varepsilon} K_{\varepsilon} \sum_{i=1}^{N_r} d_i^{0.49}}{\bar{S} \sum_{i=1}^{N_r} d_i^2} \quad (33)$$

Solving for the characteristic heat transfer diameter yields

$$\bar{d}_c \approx \left( \frac{\sum_{i=1}^{N_r} d_i^2}{\sum_{i=1}^{N_r} d_i^{0.49}} \right)^{0.6623} \quad (34)$$

Equation (34) indicates that the characteristic dimension required to produce a roughness heat transfer rate equal to that of the roughness distribution does not equal the characteristic dimension required to match the distribution drag.

Using the characteristic convection diameter, the energy equation (Eq. (5)), then becomes

$$\begin{aligned} \beta_x \rho u \frac{\partial H}{\partial x} + \beta_y \rho v \frac{\partial H}{\partial y} &= \frac{\partial}{\partial y} \left[ \beta_y \left( \frac{k_f}{c_p} \frac{\partial H}{\partial y} - \overline{\rho v' h'} \right) \right] + u \frac{\partial}{\partial x} (\beta_x P) \\ &+ \beta_y \frac{\partial u}{\partial y} \left( \mu \frac{\partial u}{\partial y} - \overline{\rho u' v'} \right) + \frac{1}{2} \rho u^3 \frac{4\alpha \bar{\varepsilon}}{\pi \bar{d}_f \bar{S}} C_D \\ &+ \frac{4\alpha \bar{\varepsilon} k_f}{\bar{d}_c^2 \bar{S}} (T_R - T_f) K_{\varepsilon} \text{Nu}_{\bar{d}_c} \end{aligned} \quad (35)$$

The Stanton number is then evaluated as

$$St = \frac{-(1-\alpha)k_f \left. \frac{dT_f}{dy} \right|_{y=\bar{y}} + \int_{\bar{y}}^{\infty} \frac{4\alpha\bar{e}k_f}{\bar{d}_c^2\bar{S}} (T_R - T_f) K_{\bar{e}} Nu_{\bar{d}_c} dy}{\rho U_e c_p (T_w - T_e)} \quad (36)$$

Thus, using the formulation of the DEM, a method for evaluating the effects of random surface roughness using characteristic surface information has been developed. For a set height above a randomly rough surface in a turbulent flow (for  $Re_d < 13,000$ ), the effects of the random distribution of elements may be determined by specifying the characteristic DEM parameters of

1. blockage fraction,  $\alpha$
2. characteristic friction diameter,  $\bar{d}_f$
3. characteristic convection diameter,  $\bar{d}_c$
4. average element eccentricity,  $\bar{e}$
5. average shape factor,  $\bar{S}$

Each of the characteristic DEM parameters must be evaluated as functions of distance from the mean elevation. For surfaces with three-dimensional profilometry measurements, the characteristic DEM parameters may be readily determined.

### Statistical Surface Descriptions

The previous sections demonstrated how a complete three-dimensional surface measurement could be used to evaluate the characteristic dimensions required for use with the DEM. In predicting the decrease in performance of gas-turbine blades caused by erosion or deposition, correlations for statistical parameters based on operation time and conditions are commonly used [18]. The correlations are based on statistical parameters such as the centerline average height ( $R_a$ ), the root-mean-square height ( $R_q$ ), or the ten-point roughness height ( $R_z$ ). Of the parameters listed above,  $R_q$ , defined as

$$R_q = \left[ \frac{1}{N} \sum_{i=1}^N (y_i - \bar{y})^2 \right]^{1/2} \quad (37)$$

where  $y_i$  is the locally measured height of the surface, is the most convenient for describing surfaces whose randomness is normal or Gaussian.

In the following subsections, methods to use  $R_q$  to match the important characteristic DEM parameters of randomly rough surfaces are explored. Three-dimensional profilometry measurements of two randomly rough surfaces are used to investigate the appropriateness of the methods developed. The two randomly rough surfaces used to investigate the statistical methods were randomly rough surfaces created from scaled profilometer traces taken from real gas turbine surface roughness [10,4]. The two surface measurements used are the erosion surface and the deposit surface described in detail by McClain et al. [10].

**Blockage Fraction.** The blockage fraction variation versus height is relatively simple to describe using Gaussian statistics. For a given profilometry trace, the blockage fraction at a given elevation is the number of measurements with an elevation higher than the prescribed elevation. If a surface has a Gaussian distribution of roughness heights, then the blockage fraction may be represented using the single-tailed Gaussian probability function. Using  $R_q$  as the population standard deviation, the blockage fraction function versus height may be stated as

$$\alpha(\tau) = 0.5 - \frac{1}{\sqrt{2\pi}} \int_0^{\tau} e^{-\tau'^2/2} d\tau' = \frac{1}{2} \operatorname{erfc}\left(\frac{\tau}{\sqrt{2}}\right) \quad (38)$$

where

$$\tau = \frac{y - \bar{y}}{R_q} = \frac{y'}{R_q}$$

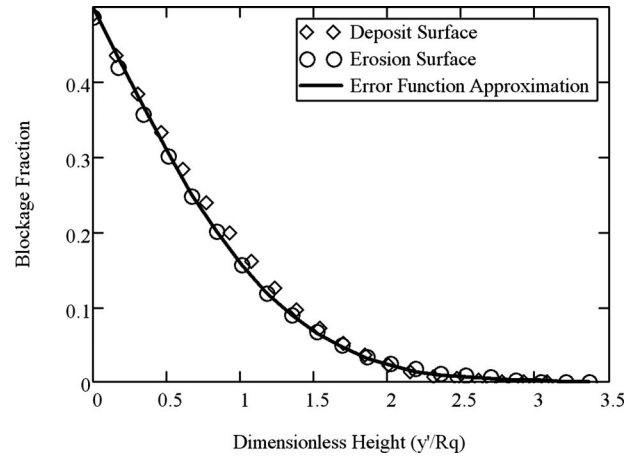


**Fig. 3 Blockage fraction of the deposit and erosion surfaces compared to error function approximation**

Figure 3 shows the blockage fraction of the erosion and deposit surfaces and Eq. (38) for each surface versus the dimensionless height,  $\tau$ . Figure 3 demonstrates that the Gaussian distribution, or complimentary error function approximation of Eq. (38), captures the variation in blockage fraction versus height well for both randomly rough surfaces.

**Characteristic Diameters.** Two main issues complicate the use of standard statistical information to evaluate the characteristic friction and convection diameters. First, the primary statistical parameters such as  $R_a$ ,  $R_q$ , and  $R_z$  describe the deviation of the surface measurements in the direction normal to the mean elevation plane. Spectral densities or primary wavelengths that relate to the widths of the roughness elements are not commonly reported in literature or used to develop roughness history correlations. Second, Eqs. (24) and (34) weight the larger blockage elements more heavily in the calculation of the characteristic diameters. If the spectral densities or primary wavelengths are known, the appropriate means to weight the primary wavelengths and convert the wave forms to produce functions for the characteristic diameters versus height are not currently evident.

If only the primary statistical parameters are available, expressing the characteristic DEM diameters in terms of the product of a constant,  $C$ , some statistical parameter,  $R$ , and either a linear function, Eq. (39), quadratic function, Eq. (40), or a decreasing exponential function, Eq. (42), of height from the mean elevation would be advantageous.

$$\bar{d}_f(y', y_{\max}, R)_{\text{linear}} = C_1 R \left( 1 - \frac{y'}{y_{\max}} \right) \quad (39)$$

$$\bar{d}_f(y', y_{\max}, R)_{\text{quadratic}} = C_2 R \left( 1 - \frac{y'}{y_{\max}} \right)^2 \quad (40)$$

$$\bar{d}_f(y', y_{\max}, R)_{\text{exp}} = C_3 R C_4^{-y'/y_{\max}} \quad (41)$$

Figures 4 and 5 present the average diameter and characteristic diameter variation as a function of height for the deposit surface and the erosion surface, respectively. The extreme difference between the average blockage diameter and either characteristic diameter is immediately obvious from Fig. 4. This difference reflects the fact that Eqs. (24) and (25) weight the larger blockage elements more heavily than the smaller blockage elements.

A commercial analysis software package was used to evaluate the constants for each characteristic friction diameter functions, Eqs. (39)–(41), using  $R_q$  as the statistical parameter. The constants that best fit the data are reported in Table 1. The best-fit functions

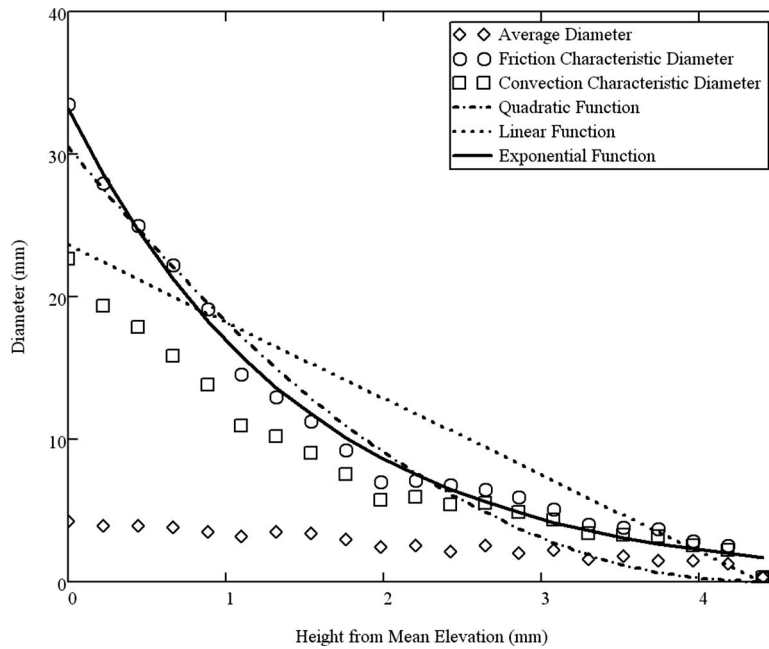


Fig. 4 Characteristic dimensions of the deposit surface

are also shown in Figs. 4 and 5 for each surface.

Figures 4 and 5 show that the linear best-fit function underestimates the characteristic friction diameter near the bases and overestimates the characteristic friction diameter over a wide range near the midheights of both the deposit and erosion surfaces. Figures 4 and 5 demonstrate that equivalent cone models cannot adequately capture the characteristic friction diameter variation versus height for a randomly rough surface.

Figures 4 and 5 show that the quadratic best-fit function follows the characteristic friction diameter variation very closely for both the deposit and erosion surfaces until about two-thirds of the maximum height above the mean elevation. In the top one-third of the heights, the quadratic best-fit function significantly underesti-

mates the characteristic friction diameters.

Figure 4 shows that the exponential best-fit function captures the variation in characteristic friction diameter very well for the deposit surface. Figure 5, however, shows that the exponential best-fit function does not capture an unusual feature of the erosion surface. At about 1.2 mm from the mean elevation of the erosion surface, the characteristic friction diameter, as well as the mean diameter, increases with elevation until about 1.7 mm from the mean elevation.

The constants in each of the best-fit functions were evaluated using the full characterization of the surface. Further work is needed to explore methods for determining the regression con-

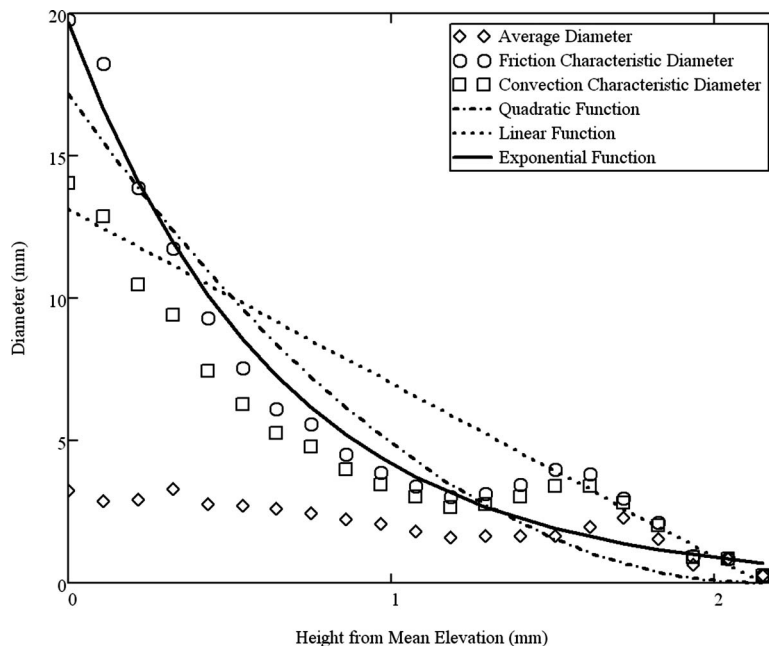


Fig. 5 Characteristic dimensions of the erosion surface



**Table 1 Best-fit constants for each randomly rough surface**

Constant	Deposit surface	Erosion surface
$C_1$	16.549	20.580
$C_2$	21.449	26.898
$C_3$	23.258	30.851
$C_4$	19.266	27.684

stants when only the spectral densities, primary wavelengths, or other transverse and flow direction statistics are known for randomly rough surfaces.

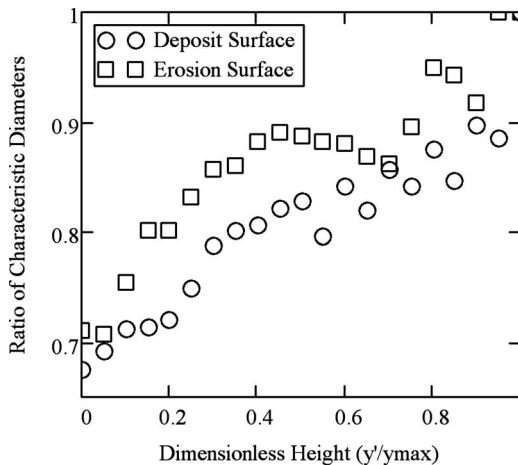
The same curve-fitting procedure may be performed to evaluate a characteristic heat transfer diameter variation versus elevation. However, a more convenient method would be to identify a relationship between the characteristic friction diameter and the characteristic heat transfer diameter.

Figure 6 presents the ratio of the characteristic diameters,  $\bar{d}_c/\bar{d}_f$ , as a function of the dimensionless height for both the deposit and erosion surfaces. Figure 6 demonstrates that the ratio of the characteristic diameters at the mean elevation is approximately 0.7 for both surfaces. The function increases as a function of height reaching unity at the maximum elevation. While significant scatter appears in the data, a linear variation in the characteristic diameter ratio is reasonable for design calculations. Hence, the characteristic heat transfer diameter may be estimated using

$$\bar{d}_c = \bar{d}_f \left( 0.7 + 0.3 \frac{y'}{y_{\max}} \right) \quad (42)$$

**Element Eccentricity.** A method for using common statistical parameters to evaluate an average eccentricity is not evident, especially for statistical parameters that primarily represent height characteristics of a surface. One option may consist of using crossing 2D traces. The dominant roughness wavelengths of the 2D traces from fast fourier transforms (FFTs) or power spectrum analyses should be related to the average element eccentricity. However, the DEM requires measurements of the maximum widths and lengths of individual roughness elements, and single traces rarely cross the maximum width or length of individual elements. An alternate method using 3D Fourier transforms or power spectra also deserves investigation.

For design calculations, roughness geometry is unknown and until other information is available indicating otherwise, the roughness may be treated as isotropic. Hence, for design purposes,



**Fig. 6 Ratio of characteristic diameters versus dimensionless height**

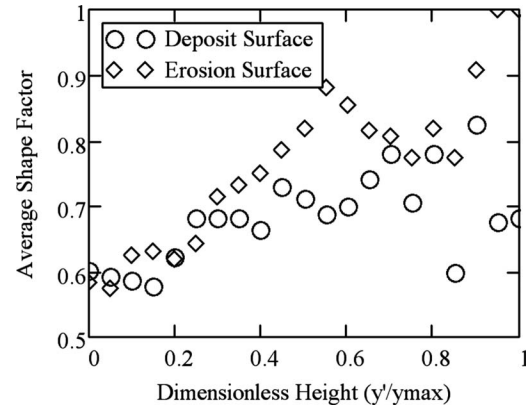


**Fig. 7 The variation in average shape factor versus height**

$\varepsilon=1.0$ . However, if 3D profilometry measurements for a surface are available, the use of an average eccentricity for all levels is suggested.

**Shape Factor.** Similar to the discussion of element eccentricity, a basis for evaluating the average shape factor at a given elevation using height statistics is not evident. Hence, the erosion and deposit surface 3D profilometry measurements are used to explore the variation in element shape factor through the roughness region.

Figure 7 presents the average shape factor as a function of normalized height ( $y'/y_{\max}$ ) for the deposit surface and the erosion surface. Figure 7 demonstrates that the average shape factor of both surfaces starts at approximately 0.6 at the mean elevation and increases as the elevation increases. From Fig. 7, a linear variation in the average shape factor appears to be a reasonable approximation for design calculations.

$$\bar{S} \approx 0.6 + 0.3 \frac{y'}{y_{\max}} \quad (43)$$

A constant value of approximately 0.75 would also be a reasonable design assumption.

**Roughness Maximum Height.** The maximum roughness height above the mean elevation must also be evaluated using statistical information. For the deposit and erosion surfaces, the maximum dimensionless deviations from the mean elevation are:

$$\left( \frac{y_{\max}}{R_q} \right)_{\text{deposit}} = 3.080$$

$$\left( \frac{y_{\max}}{R_q} \right)_{\text{erosion}} = 3.369$$

For a Gaussian distribution, the value of the dimensionless probability variable that corresponds to a single-tailed coverage of 99.9% of the values of the variable  $X$  is 3.09.

$$\tau_{99.9\%} = \frac{X_{99.9\%} - \mu_X}{\sigma} = 3.09$$

Thus, while only sample information may be taken from a real surface, the maximum roughness height may be estimated using the Gaussian estimate of the 99.9%, single-tailed coverage based on  $R_q$ .

$$y_{\max} = 3.09R_q \quad (44)$$

This estimate has a statistical basis and compares well with the maximum measured heights of the two surfaces investigated.

**Summary.** When constructing computational grids for use with solvers including the DEM, the following relationships based on statistical descriptions of randomly rough surfaces are suggested for evaluating the blockage fraction:

$$\alpha(y', R_q) = \frac{1}{2} \operatorname{erfc}\left(\frac{\sqrt{2} y'}{2 R_q}\right) \quad (45)$$

the characteristic friction diameter:

$$\bar{d}_f(y', R_q) = C_3 R_q C_4^{(-y'/3.09R_q)} \quad (46)$$

the characteristic heat transfer diameter:

$$\bar{d}_c(y', R_q) = C_3 R_q \left(0.7 + 0.3 \frac{y'}{3.09 R_q}\right) C_4^{(-y'/3.09R_q)} \quad (47)$$

the average element eccentricity:

$$\varepsilon \approx 1.0 \quad (48)$$

and the average element shape factor:

$$\bar{S} \approx 0.6 + 0.3 \frac{y'}{3.09 R_q} \quad (49)$$

Methods to determine the constants  $C_3$  and  $C_4$  and to determine the average element eccentricity using two-dimensional and three-dimensional FFTs and power spectrum analyses will be explored in the future.

### Computational Exploration Results

The DEM was employed in a finite-difference boundary-layer code and used to compare the experimental measurements of Bons [4] to predictions based on the full-surface discrete-element description and with various options for employing a simplified discrete-element description.

The wind tunnel used by Bons [4] is housed at the Air Force Research Laboratory (AFRL) at Wright-Patterson Air Force Base in Dayton, OH. The wind tunnel is an open-loop tunnel with a nominal cross section of  $0.24 \times 0.38 \text{ m}^2$  in the test section. For the experimental measurements presented here, the wall was adjusted to produce zero freestream acceleration [4]. Flow enters the test section through a main conditioning plenum and an entry section. As the flow exits the entry section and just before the flow enters the test section of the tunnel, the boundary layer is bled from the flow using a knife-edge boundary-layer bleed and a boundary-layer suction blower. This creates the situation where the boundary-layer thickness is zero at the entry of the test section.

For all skin friction measurements, the flow was tripped turbulent using a 1.6 mm diameter cylinder placed 2.54 cm from the knife-edge. Roughness panels, 0.32 m in length, were placed 1.04 m from the knife-edge of the test section. The tunnel then continues 0.62 m beyond the trailing edge of the roughness panels. The freestream turbulence intensity,  $Tu = u_{rms}/U_e$ , was measured using a hot-wire anemometry system and was found to be consistently 0.9% for all of the skin friction measurements.

The skin friction coefficients were determined by suspending the roughness panels in the wind tunnel using wires attached to the wind-tunnel framing and measuring the downstream movement of the panels during a test. Detailed information on the wind tunnel and the average skin friction coefficient determination technique can be found in Ref. [4]. Bons [4] reported a systematic uncertainty (bias) of 0.00022 in the measured skin friction coefficients with a 2.8% random uncertainty (repeatability).

A transient method was used to determine the convective heat transfer coefficient from the rough surfaces. The method used to evaluate the convection coefficient is based on the method of Schultz and Jones [21]. Using the temperature responses of both the fluid and the roughness panel as heated air is blown over the panels, the average convection coefficient was calculated. Bons [4] reported a systematic uncertainty of 0.00008 in the measured Stanton numbers with a 3% random uncertainty. Detailed infor-

**Table 2 Boundary-layer characteristics for the skin friction coefficient measurements for the rough surfaces**

	$Re_{\bar{x}}$	$Re_{\theta}$	$k^+$	$y_{max}/\delta$
Deposit	924,800	2530	228	0.192
Deposit	517,300	1540	126	0.176
Erosion	925,700	2650	117	0.091
Erosion	518,300	1580	64	0.084

mation on the wind tunnel, the average skin friction coefficient determination technique, and the average convection coefficient determination method can be found in Ref. [4].

Skin friction and Stanton number measurements were made for each surface at two Reynolds numbers based on the distance from the leading edge to the center of the roughness panel: around 900,000 and 500,000. Table 2 summarizes the boundary-layer and freestream conditions for the rough-surface skin friction measurements. The momentum thickness and boundary-layer thickness were not measured directly in the experiments for all experimental cases. The values of  $Re_{\theta}$  and  $k/\delta$  presented in Table 2 are based on the full-surface DEM predictions. Detailed information on the full-surface DEM simulations and their comparisons to the experimental data can be found in Ref. [22].

Table 3 presents experimental skin friction measurements for turbulent flow at two Reynolds numbers, based on the distance from the wind-tunnel knife-edge to the center of the roughness section, for the deposit and erosion surfaces. Table 3 also presents skin friction coefficient predictions with various DEM options for turbulent flow at two Reynolds numbers for the deposit and erosion surfaces. Table 4 presents experimental Stanton number measurements and discrete-element predictions with various options for turbulent flow at two Reynolds numbers for the deposit and erosion surfaces. In Tables 3 and 4, the discrete-element  $C_f$  and  $St$  predictions are presented as ratios to the experimental measurements (RCM for  $C_f$  and RSM for  $St$ ) and as ratios to the discrete-element predictions made using the full-surface descriptions (RCF for  $C_f$  and RSF for  $St$ ).

The subscripts used in Tables 3 and 4 for the comparison of experimental measurements and discrete-element predictions are as follows:

smooth = the measured  $C_f$  or  $St$  as reported by Bons [4] for flow over smooth surfaces with  $Re_{\bar{x}}$  values within 3% of the randomly rough surface values

**Table 3 Results of skin friction simulations**

Surface	Deposit	Deposit	Erosion	Erosion
$Re_{\bar{x}}$	924,800	517,300	925,700	518,300
$C_{f,smooth}$	0.00349	0.00377	0.00349	0.00377
$C_{f,meas}$	0.00937	0.00928	0.01030	0.00980
$C_{f,full}$	0.00891	0.00863	0.01053	0.00979
$RCM_{full}$	0.9509	0.9300	1.0223	0.9990
$RCM_{e,S}$	1.0085	0.9935	0.9068	0.8888
$RCF_{e,S}$	1.0606	1.0684	0.8870	0.8897
$RCM_{ea,Sa}$	1.0213	1.0097	0.8932	0.8796
$RCF_{ea,Sa}$	1.0741	1.0857	0.8737	0.8805
$RCM_{erf}$	1.0064	0.9968	0.8806	0.8653
$RCF_{erf}$	1.0584	1.0718	0.8613	0.8662
$RCM_{lin}$	0.8943	0.8804	0.7592	0.7398
$RCF_{lin}$	0.9405	0.9467	0.7426	0.7406
$RCM_{quad}$	1.3767	1.3912	1.0388	1.0541
$RCF_{quad}$	1.4478	1.4959	1.0161	1.0552
$RCM_{exp}$	1.0139	1.0054	0.8903	0.8816
$RCF_{exp}$	1.0662	1.0811	0.8708	0.8825
$RCM_{stat}$	0.9808	0.9698	0.9447	0.9327
$RCF_{stat}$	1.0314	1.0429	0.9240	0.9336

**Table 4 Results of stanton number simulations**

Surface	Deposit	Deposit	Erosion	Erosion
$Re_{\bar{r}}$	905,500	515,000	902,000	520,000
$St_{smooth}$	0.00216	0.00235	0.00216	0.00235
$St_{meas}$	0.00308	0.00341	0.00308	0.00329
$St_{full}$	0.00349	0.00395	0.00334	0.00363
$RSM_{full}$	1.1331	1.1584	1.0844	1.1033
$RSM_{\epsilon,S}$	1.1558	1.1935	1.0292	1.0486
$RSF_{\epsilon,S}$	1.0201	1.0304	0.9491	0.9504
$RSM_{\epsilon a,Sa}$	1.1516	1.1965	1.0162	1.0334
$RSF_{\epsilon a,Sa}$	1.0163	1.0329	0.9371	0.9366
$RSM_{erf}$	1.1396	1.1848	1.0032	1.0182
$RSF_{erf}$	1.0057	1.0228	0.9251	0.9229
$RSM_{lin}$	0.9643	0.9883	0.8864	0.8936
$RSF_{lin}$	0.8510	0.8532	0.8174	0.8099
$RSM_{quad}$	2.3571	2.4340	1.6136	1.5350
$RSF_{quad}$	2.0802	2.1013	1.4880	1.3912
$RSM_{exp}$	1.1071	1.1496	1.0422	1.0669
$RSF_{exp}$	0.9771	0.9924	0.9611	0.9669
$RSM_{stat}$	1.0747	1.1114	1.1201	1.1398
$RSF_{stat}$	0.9484	0.9595	1.0329	1.0331

- meas = the measured  $C_f$  or  $St$  as reported by Bons [4]
- full = the predicted  $C_f$  or  $St$  with the full-surface representation from McClain et al. [10]
- $\epsilon,S$  = the predicted  $C_f$  or  $St$  with an eccentricity and shape factor for each level; the characteristic diameter from Eq. (24) or Eq. (34) is used in the prediction
- $\epsilon a,Sa$  = the predicted  $C_f$  or  $St$  with an average eccentricity and an average shape factor for all levels; the characteristic diameter from Eq. (24) or Eq. (34) is used in the prediction
- erf = the predicted  $C_f$  or  $St$  with an average eccentricity and an average shape factor for all levels and evaluating the blockage fraction using a Gaussian probability density function; the characteristic diameter from Eq. (24) or Eq. (34) is used in the prediction
- lin = the predicted  $C_f$  or  $St$  with an average eccentricity and an average shape factor for all levels, evaluating the blockage fraction using a Gaussian probability density function, and using the linear function, Eq. (39), for the diameter distribution
- quad = the predicted  $C_f$  or  $St$  with an average eccentricity and an average shape factor for all levels, evaluating the blockage fraction using a Gaussian probability density function, and using a quadratic function, Eq. (40), for the diameter distribution
- exp = the predicted  $C_f$  or  $St$  with an average eccentricity and an average shape factor for all levels, evaluating the blockage fraction using a Gaussian probability density function, and using the exponential function, Eq. (41), for the diameter distribution
- stat = the predicted  $C_f$  or  $St$  using the statistical representation described by Eqs. (45)–(47) and (49); the measured average eccentricities are used for each surface (0.803 for the deposit surface and 1.284 for the erosion surface)

Inspecting the values of  $RCM_{full}$ ,  $RCM_{\epsilon,S}$ ,  $RCM_{\epsilon a,Sa}$ , and  $RCM_{erf}$  from Table 3, using the characteristic diameters with an average eccentricity and an average shape factor, does affect the predictions of skin friction coefficient and Stanton number. The average percentage difference to the full-surface characterization

between  $C_{f,\epsilon,S}$ ,  $C_{f,\epsilon a,Sa}$ , and  $C_{f,erf}$ , is 6.5% for the deposit surface and 11.7% for the erosion surface. The average percentage difference to the full-surface characterization between  $St_{\epsilon,S}$ ,  $St_{\epsilon a,Sa}$ , and  $St_{erf}$  is 2.1% for the deposit surface and 6.3% for the erosion surface. This indicates the level of uncertainty incurred by separating Eqs. (22) and (32) using the average eccentricity and shape factor. Tables 3 and 4 show that the differences between  $RCM_{erf}$ ,  $RCM_{full}$ , and  $RCM_{\epsilon a,Sa}$  and between  $RSM_{erf}$ ,  $RSM_{full}$ , and  $RSM_{\epsilon a,Sa}$  are small. This indicates that the error function approximation adequately represents the deterministic blockage fraction variation as a function of height for both surfaces. Tables 3 and 4 also indicate that the linear functions for the characteristic diameters underestimate the  $C_f$  and  $St$  predictions while the quadratic functions significantly overestimate the  $C_f$  and  $St$  predictions. Figures 4 and 5 demonstrate that the linear functions overestimate the characteristic diameters in the midheights of the roughness elements and that the quadratic functions significantly underestimate the roughness-element diameters near the tops of the roughness elements. Examining Eq. (23), the drag per unit control volume is a function of  $\bar{d}_f^{-1.125}$ . Examining Eq. (32), the heat transfer per unit control volume is a function of  $\bar{d}_c^{-1.51}$ . Since the linear characteristic diameter function overestimates the diameters near the midheights, the skin friction and heat transfer predictions with the linear function fall much lower than the predictions with the full-surface representation. Since the quadratic characteristic diameter function underestimates the diameters near the tops of the roughness elements where the fluid velocities are highest, the skin friction and heat transfer predictions with the quadratic function are much higher than the predictions with the full-surface representation.

Tables 3 and 4 indicate that predictions of  $C_f$  and  $St$  based on the exponential functions for the characteristic diameters are in general closer to the predictions based on the full-surface representation for both surfaces studied. Tables 3 and 4 also indicate that the values of  $C_{f,exp}$  and  $St_{exp}$  are very close to the values of  $C_{f,\epsilon a,Sa}$  and  $St_{\epsilon a,Sa}$  for both surfaces, indicating that exponential diameter function adequately captures the variations in characteristic friction diameter and characteristic heat transfer diameter.

Finally, Tables 3 and 4 indicate that the predictions of  $C_f$  and  $St$  based on the statistical surface descriptions are all within 10% of the predictions based on the full surface descriptions. Tables 3 and 4 also indicate that the levels of agreement of  $C_f$  and  $St$  based on the statistical surface descriptions with the measured values are consistent with the level of agreement exhibited by the predictions based on the full-surface descriptions.

## Conclusions

To make the DEM method less computationally expensive for CFD solvers, deterministic and statistical methods for evaluating reduced rough-surface descriptions were explored. The primary findings of the investigation are as follows.

1. For a randomly rough surface, at each height from the mean elevation below the maximum height of the roughness, the DEM indicates that five characteristic dimensions must be matched:
  - (a) blockage fraction
  - (b) characteristic friction diameter
  - (c) characteristic convection diameter
  - (d) average element eccentricity
  - (e) average shape factor
2. The effects of the five characteristic dimensions are intertwined in friction and heat transfer predictions based on the full-surface DEM. Isolating characteristic diameters using average eccentricities and shape factors introduces uncertainties on the order of 10% into the discrete-element predictions.



- Gaussian statistical methods were found to capture the blockage fraction variation and maximum heights of the surfaces studied using the root-mean-square roughness heights.
- Three functions were explored to represent the empirical characteristic diameter variation for the two surfaces studied. The linear function and the quadratic function either overestimated or underestimated the diameters in important height regions causing poor agreement with predictions based on full-surface DEM characterization. A decreasing exponential function was tested that, while introducing another empirical constant, adequately replicated DEM predictions based on the use of average eccentricities and shape factors.
- Predictions based on the Gaussian statistical representation, using the empirical constants for the variations in characteristic diameters, were all within 8% of the predictions based on the full-surface descriptions.

Methods to evaluate the constants for the characteristic diameter distribution are identified as an important future effort to improve the reduced parameter DEM. Since the statistical information reported in the literature is related to height characteristics, methods that represent dominant surface wavelengths, such as FFT or power spectrum methods, will be used in future efforts. The intent of the future efforts will be to express the average eccentricity and the constants in the exponential function for characteristic friction diameter in terms of the dominant wavelengths identified through a FFT or power spectrum analysis.

Future efforts with the reduced parameter DEM will also include investigation of  $Re_d$  higher than 13,000. The empirical correlations used for the local element drag coefficients and local element Nusselt numbers are piecewise functions of the local element Reynolds number. Because of the experimental study used, the reduced parameter methods were only explored for the low  $Re_d$  range where simple continuous functions for drag coefficient and Nusselt number could be used. Methods for evaluating characteristic dimensions of surfaces with higher local  $Re_d$  should be investigated in the future. Evaluating characteristic dimensions for cases where different elements of a randomly rough surface are in different regimes of the local drag coefficient and local Nusselt number functions should also be explored.

Future efforts are also needed to explore reduced characterizations for surfaces that are not Gaussian. Bons [4] presented measurements demonstrating that skewness and kurtosis values of actual turbine roughness can depart remarkably from their Gaussian distribution values. The limitations of the current approach related to non-Gaussian surface roughness or new approaches to describe non-Gaussian surface roughness for use with the DEM should be explored.

Gas-turbine blades and vanes also commonly experience high levels of freestream turbulence. The use of higher order turbulence models that are able to capture the effect of high freestream turbulence and that are able to investigate the influence of roughness on freestream turbulence must be investigated using the randomly rough DEM and the reduced parameter DEM.

Finally and most importantly, more experimental data are required to further validate the DEM for flows over randomly rough surfaces using the complete and reduced surface DEM descriptions. Current experimental data available for flows over fully described random roughness are too limited to fully validate the DEM for randomly rough surfaces. More data are required to fully explore the range of validity of important DEM assumptions.

### Acknowledgment

The authors thank the Department of Mechanical Engineering at the University of Alabama at Birmingham for support of this effort. The advice of Dr. B. Keith Hodge at Mississippi State University is also greatly appreciated. Discussions and collabora-

tions with Dr. Jeffrey P. Bons at Brigham Young University are also greatly appreciated.

### Nomenclature

$A$	= roughness blockage plan-form area
$a$	= maximum width of elliptical element in transverse direction
$b$	= maximum length of elliptical element in streamwise direction
$C_D$	= local element drag coefficient
$C_f$	= skin friction coefficient
$d$	= local roughness-element diameter
$\bar{d}_f$	= characteristic friction diameter
$\bar{d}_c$	= characteristic convection heat transfer diameter
$F_D$	= drag force of roughness blockage distribution
$h$	= convection heat transfer coefficient
$H$	= enthalpy
$h'$	= turbulent fluctuating specific enthalpy
$k^+$	= nondimensional roughness height;
	$y_{\max}/\nu\sqrt{\tau_w/\rho}$
$k_f$	= fluid thermal conductivity
$K_\varepsilon$	= elliptical element area correction factor
$L_p$	= length of profilometry trace in streamwise direction
$L_t$	= length of profilometry trace in transverse direction
$l_m$	= mixing length
$N_r$	= number of roughness elements
$Nu_d$	= local element Nusselt number
$P$	= pressure
$Pr$	= Prandtl number
$Pr_t$	= turbulent Prandtl number
$Q$	= local element heat transfer
$R_a$	= centerline-averaged roughness height
RCF	= ratio of the predicted skin friction coefficient to the DEM prediction based on the full-surface representation of McClain et al. [10], $C_f/C_{f,\text{full}}$
RCM	= ratio of the predicted skin friction coefficient to the experimentally measured values reported by Bons [4], $C_f/C_{f,\text{meas}}$
$Re_d$	= local element Reynolds number
$Re_x$	= Reynolds number based on length from knife-edge to the center of the roughness panel
$Re_\theta$	= Reynolds number based on the momentum thickness
$R_q$	= root-mean-square roughness height
RSF	= ratio of the predicted Stanton number to the DEM prediction based on the full-surface representation of McClain et al. [10], $St/St_{\text{full}}$
RSM	= ratio of the predicted skin friction coefficient to the experimentally measured values reported by Bons [4], $St/St_{\text{meas}}$
$R_z$	= ten-point roughness height
$S$	= roughness blockage shape factor
$St$	= Stanton number
$T$	= temperature
$T_R$	= local roughness-element temperature
$t$	= time
$U_e$	= freestream velocity
$u$	= local streamwise velocity
$u'$	= turbulent fluctuating streamwise velocity
$v$	= local velocity normal to wall
$v'$	= turbulent fluctuating normal velocity
$X$	= general measurement variable
$x$	= streamwise flow direction
$y$	= direction normal to wall

$y^+$  = inner variable nondimensional height;  
 $y / \nu \sqrt{\tau_w / \rho}$   
 $y'$  = height of surface above mean surface elevation;  
 $y - \bar{y}$   
 $\bar{y}$  = mean surface elevation  
 $y_{\max}$  = the maximum height of a surface above the mean elevation  
 $z$  = transverse flow direction

### Greek

$\alpha$  = blockage fraction  
 $\beta$  = openage or void fraction,  $1 - \alpha$   
 $\delta$  = boundary-layer thickness  
 $\varepsilon$  = ellipse eccentricity  
 $\theta$  = momentum thickness  
 $\kappa$  = von Karman constant  
 $\mu$  = dynamic viscosity  
 $\mu_X$  = mean value of repeated measurements of  $X$   
 $\nu$  = kinematic viscosity  
 $\rho$  = density  
 $\sigma$  = standard deviation  
 $\tau_w$  = wall shear

### References

- [1] Patel, V. C., 1998, "Perspective: Flow at High Reynolds Number and Over Rough Surfaces—Achilles Heel of CFD," *ASME J. Fluids Eng.*, **120**(3), pp. 434–444.
- [2] Taylor, R. P., 1983, "A Discrete Element Prediction Approach for Turbulent Flow Over Rough Surfaces," Ph.D. thesis, Department of Mechanical and Nuclear Engineering, Mississippi State University, Mississippi State, MS.
- [3] Sigal, A., and Danberg, J. E., 1990, "New Correlation of Roughness Density Effect on the Turbulent Boundary Layer," *AIAA J.*, **28**(3), pp. 554–556.
- [4] Bons, J. P., 2002, "St and  $C_f$  Augmentation for Real Turbine Roughness With Elevated Freestream Turbulence," *ASME J. Turbomach.*, **124**, pp. 632–644.
- [5] Dipprey, D. F., and Sabersky, R. H., 1962, "Heat and Momentum Transfer in Smooth and Rough Tubes at Various Prandtl Numbers," *Int. J. Heat Mass Transfer*, **6**, pp. 329–353.
- [6] Matheis, B. D., Rothmayer, A. P., and Huebsch, W. W., "Three-Dimensional Steady Navier-Stokes-Calculations of Flow Past Isolated Airfoil Leading Edge Surface Roughness," presented at the 33rd Fluid Dynamics Conference and Exhibit, Orlando, FL, June AIAA Paper No. 2003–3725.
- [7] Matheis, B. D., and Rothmayer, A. P., 2004, "Impact of Surface Roughness on Local Aerodynamics Using a Three-Dimensional Navier–Stokes Solver," presented at the 42nd Aerospace Sciences Meeting and Exhibition, Reno, NV, Jan., AIAA Paper No. 2004–0058.
- [8] Huebsch, W. W., and Rothmayer, A. P., 2004, "Numerical Prediction of Unsteady Vortex Shedding for Large Leading-Edge Roughness," *Comput. Fluids*, **33**(3), pp. 405–434.
- [9] Wang, Z. J., Chi, X., Shih, T. I., and Bons, J., 2004, "Direct Simulation of Surface Roughness Effects With RANS and DES Approaches on Viscous Adaptive Cartesian Grids," Fluid Dynamics Conference, Portland, OR, July, AIAA Paper No. 2004–2420.
- [10] McClain, S. T., Hodge, B. K., and Bons, J. P., 2004, "Predicting Skin Friction and Heat Transfer for Turbulent Flow Over Real Gas-Turbine Surface Roughness Using the Discrete-Element Method," *ASME J. Turbomach.*, **126**, (2), pp. 259–267.
- [11] Bons, J. P., and McClain, S. T., 2004, "The Effect of Real Turbine Roughness With Pressure Gradient on Heat Transfer," *ASME J. Turbomach.*, **126**, (3) pp. 385–394.
- [12] Tolpadi, A. K., and Crawford, M. E., 1998, "Predictions of the Effect of Roughness on Heat Transfer From Turbine Airfoils," *ASME Paper No. 98-GT-087*.
- [13] Tarada, F., and Suzuki, M., 1993, "External Heat Transfer Enhancement to Turbine Blading Due to Surface Roughness," *ASME Paper No. 93-GT-74*.
- [14] McClain, S. T., Collins, S. P., Hodge, B. K., and Bons, J. P., 2006, "The Importance of the Mean Elevation in Predicting Skin Friction for Flow Over Closely Packed Surface Roughness," *ASME J. Fluids Eng.*, **128**, (3), pp. 579–586.
- [15] Stripf, M., Schulz, A., and Bauer, H.-J., 2006, "Modeling of Rough Wall Boundary Layer Transition and Heat Transfer on Turbine Airfoils," *ASME Paper No. GT-2006–90316*.
- [16] Taylor, R. P., 1990, "Surface Roughness Measurements on Gas Turbine Blades," *ASME J. Turbomach.*, **112**, (2), pp. 175–180.
- [17] Bogard, D. G., Schmidt, D. L., and Tabbita, M., 1998, "Characterization and Laboratory Simulation of Turbine Airfoil Surface Roughness and Associated Heat Transfer," *ASME J. Turbomach.*, **120**, pp. 337–342.
- [18] Bons, J. P., Taylor, R. P., McClain, S. T., and Rivir, R., 2001, "The Many Manifestations of Turbine Surface Roughness," *ASME J. Turbomach.*, **123**, (4), pp. 739–748.
- [19] Hosni, M. H., Coleman, H. W., and Taylor, R. P., 1989, "Measurement and Calculation of Surface Roughness Effects on Turbulent Flow and Heat Transfer," Report No. TFD-89–1, Mechanical and Nuclear Engineering, Mississippi State University, Mississippi State, MS.
- [20] Taylor, R. P., and Hodge, B. K., 1993, "A Validated Procedure for the Prediction of Fully-Developed Nusselt Numbers and Friction Factors in Pipes With 3-Dimensional Roughness," *J. Enhanced Heat Transfer*, **1**, (1), pp. 23–35.
- [21] Schultz, D. L., and Jones, T. V., 1973, "Heat-Transfer Measurements in Short-Duration Hypersonic Facilities," Advisory Group for Aerospace Research and Development (165), NATO.
- [22] McClain, S. T., 2002, "A Discrete Element Model for Turbulent Flow Over Randomly Rough Surfaces," Ph.D. thesis, Department of Mechanical Engineering, Mississippi State University, Mississippi State, MS.

# Effects of Large Scale High Freestream Turbulence and Exit Reynolds Number on Turbine Vane Heat Transfer in a Transonic Cascade

Shakeel Nasir

Jeffrey S. Carullo

Wing-Fai Ng

Karen A. Thole

Hong Wu

Department of Mechanical Engineering,  
Virginia Polytechnic Institute and State  
University,  
Blacksburg, VA 24061

Luzeng J. Zhang

Hee Koo Moon

Heat Transfer Department,  
Solar Turbines Inc.,  
San Diego, CA 92186

*This paper experimentally and numerically investigates the effects of large scale high freestream turbulence intensity and exit Reynolds number on the surface heat transfer distribution of a turbine vane in a 2D linear cascade at realistic engine Mach numbers. A passive turbulence grid was used to generate a freestream turbulence level of 16% and integral length scale normalized by the vane pitch of 0.23 at the cascade inlet. The base line turbulence level and integral length scale normalized by the vane pitch at the cascade inlet were measured to be 2% and 0.05, respectively. Surface heat transfer measurements were made at the midspan of the vane using thin film gauges. Experiments were performed at exit Mach numbers of 0.55, 0.75, and 1.01, which represent flow conditions below, near, and above nominal conditions. The exit Mach numbers tested correspond to exit Reynolds numbers of  $9 \times 10^5$ ,  $1.05 \times 10^6$ , and  $1.5 \times 10^6$  based on a vane chord. The experimental results showed that the large scale high freestream turbulence augmented the heat transfer on both the pressure and suction sides of the vane as compared to the low freestream turbulence case and promoted a slightly earlier boundary layer transition on the suction surface for exit Mach 0.55 and 0.75. At nominal conditions, exit Mach 0.75, average heat transfer augmentations of 52% and 25% were observed on the pressure and suction sides of the vane, respectively. An increased Reynolds number was found to induce an earlier boundary layer transition on the vane suction surface and to increase heat transfer levels on the suction and pressure surfaces. On the suction side, the boundary layer transition length was also found to be affected by increase changes in Reynolds number. The experimental results also compared well with analytical correlations and computational fluid dynamics predictions.*

[DOI: 10.1115/1.2952381]

*Keywords:* gas turbine, vane, high turbulence, Reynolds number, heat transfer, thin film gauge

## Introduction

One way to increase the cycle efficiency of a gas turbine engine is to operate at higher turbine inlet temperatures (TITs). In most engines, the TITs have increased to be well above the metallurgical limit of engine components. Cooling of turbine engine components (blades and vanes) is a widely used technique that allows higher TITs by maintaining material temperatures within acceptable limits. Accurate turbine section heat transfer modeling can lead to an optimized cooling design and therefore higher TITs.

Numerical modeling of heat transfer through turbine passages is a challenge as it is complicated by several factors such as Reynolds number, Mach number, combustor-generated high freestream turbulence, turbulence length scale, hot streaks, and secondary flows, just to name a few. The efforts of this work are to experimentally and numerically investigate the effects of large scale high freestream turbulence on first stage turbine vane heat transfer at realistic engine Mach number conditions.

**Summary of Past Literature.** While measuring the turbulence level in a gas turbine is extremely difficult, researchers have found that combustion systems typically produce turbulence levels between 7% and 30% [1,2]. Ames et al. [3] reported that the exit turbulence levels depend on combustor core flow to vane inlet contraction ratio and the residence time of the flow in the combustor.

Several research groups have performed heat transfer experiments on turbine vane geometries in low speed cascade facilities. Ames et al. [3–5] investigated the effects of freestream turbulence and length scale on vane heat transfer at different exit Reynolds number conditions. In all these studies with different turbulence generators, Ames et al. observed that turbulence augmented the heat transfer in the laminar region with the highest augmentation in the stagnation region and on the pressure side. An earlier transition to a turbulent boundary layer was also observed on the suction side of the vane when the turbulence level was increased. The length scale effect was also observed with the augmentation on pressure side heat transfer increased as the length scale was decreased. Radomsky and Thole [6] documented surface heat transfer and the highly turbulent flow field around a scaled-up stator vane. Their observations of the heat transfer augmentation on the vane surface were also consistent with Ames [4].

Several experimental studies have also been performed in transonic cascade facilities to investigate the effect of freestream tur-

Contributed by the Turbomachinery Division of ASME for publication in the JOURNAL OF TURBOMACHINERY. Manuscript received September 18, 2007; final manuscript received October 21, 2007; published online February 3, 2009. Review conducted by David Wisler. Paper presented at the 2007 ASME International Mechanical Engineering Congress (IMECE2007), Seattle, WA, November 10–16, 2007.



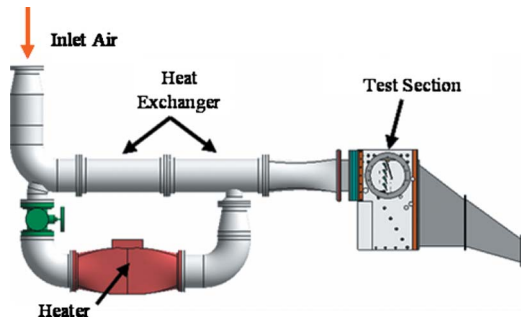


Fig. 1 Virginia Tech transonic cascade wind tunnel

bulence, Mach number, and exit Reynolds number on vane heat transfer. Nealy et al. [7] found that turbulence augmented heat transfer on the vane surface. He also found that an increase in Reynolds number increased heat transfer levels on the vane surface and the exit Mach number controlled the heat transfer distribution on the suction side of the vane. Arts and Lambert de Rouvoit [8] found augmentation levels of up to 100% on the laminar portion of the vane subjected to 6% turbulence levels.

Hoffs et al. [9] investigated the effects of Reynolds number and turbulence on smooth vane heat transfer in a high speed facility and found that the boundary layer on the pressure side started transition with an increase in the heat transfer coefficient near the trailing edge. Bunker [10] also investigated the effects of high freestream turbulence (13%) and Reynolds number on the vane heat transfer in a linear cascade. He found that pressure side heat transfer was less affected by turbulence but showed a consistent increase with turbulence over the whole pressure surface. He found that increased turbulence hastened suction side transition. Bunker also found that heat transfer on the suction side of the vane aft of transition followed a proportionality of  $Re^{1.0}$ .

### Experimental Setup and Instrumentation

**Wind Tunnel Facility.** The two-dimensional Virginia Tech transonic cascade wind tunnel, shown in Fig. 1, is a blowdown facility that is capable of sustaining a constant inlet pressure in the test section for up to 25 s. Prior heat transfer research that has been performed in this facility includes work of Carullo et al. [11], Nix et al. [12], Holmberg and Diller [13], Smith et al. [14], and Popp et al. [15]. Air is supplied from high pressure air tanks that are charged up to 1380 kPa (200 psi (gauge)) prior to testing. A control valve regulates the flow from the air tanks to the test section. Cascade inlet pressures range from 20.7 kPa (3 psi (gauge)) to 69.0 kPa (10 psi (gauge)) depending on the objective test conditions. Between the control valve and the test section, the air passes through a passive heat exchanger, which heats the cascade inlet flow up to 120°C. After the air passes through the heat exchanger, the air goes through a contraction and enters the test section before being exhausted to the atmosphere.

The turbine vane tested in these experiments is similar in geometry to a first stage turbine vane for a small industrial gas turbine. The vane was scaled one and a half times so that the nominal exit Reynolds number would be at the desired value. Table 1 summarizes the geometry of the turbine vane.

Table 1 Vane geometry

Chord	91.2 mm (3.59 in.)
Axial chord	50.0 mm (1.97 in.)
Pitch	83.0 mm (3.27 in.)
Span	152.4 mm (6.00 in.)
Inlet and exit angles	0 deg and 73.5 deg

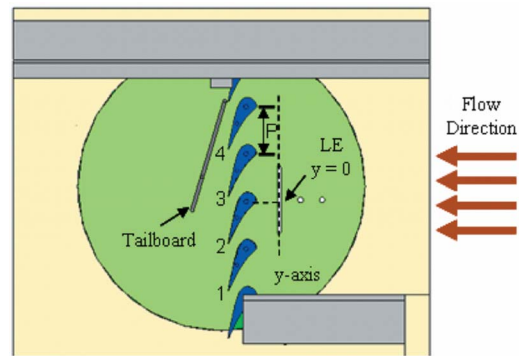


Fig. 2 Cascade diagram showing the vanes and the axis orientation for measurements with the traverse

A diagram of the vane cascade is provided in Fig. 2. From the vane geometry and the test section size, the vane cascade consists of four full vanes and two partial vanes, which result in four full passages and one partial passage. A tailboard placed at the vane exit angle aids in creating periodic flow through the cascade. The full vanes are numbered starting from the lower bottom of the cascade, with Vane 2 being the vane that is fully instrumented to make static pressure and heat transfer measurements. The slot located 0.45C upstream of the cascade is used to measure the turbulence and velocity distributions at the inlet of the cascade.

**Static Pressure Measurements.** To calculate the isentropic Mach number distribution on the vane surface, the turbine vane was instrumented with static pressure taps placed at the midspan of the vane. Vane 2 was instrumented with 7 taps on the pressure side, 18 taps on the suction side, and 1 tap near the leading edge. Static pressure taps were also instrumented on the suction side of Vane 1 and on the pressure side of Vane 3 to check the periodicity of the flow. The static pressure measurements were made through experiments conducted independently of the heat transfer experiments. In addition to calculating the isentropic Mach number distribution, the acceleration parameter distribution on the vane surface was calculated.

Static pressure taps on the end wall of the cascade were used to measure the inlet and exit static pressures and characterize the inlet and exit flows. Fourteen inlet static taps were located 0.45C upstream of the vane passages and 14 exit static taps were located 0.45C downstream of the vane passages. Figure 3 provides typical cascade inlet temperature and inlet and exit Mach number time histories during a blowdown test run.

**Heat Transfer Measurements.** Heat transfer measurements were made with thin film gauges that allow for high spatial resolution measurements on the vane surface with minimal flow dis-

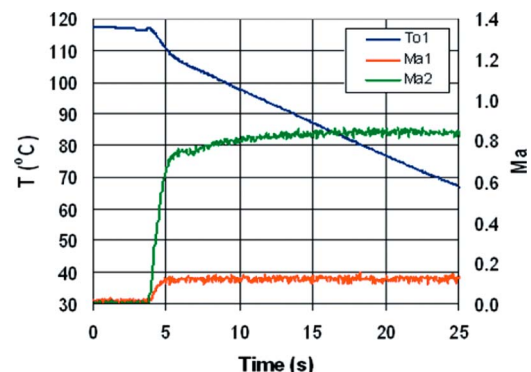


Fig. 3 Cascade inlet temperature and Mach number history

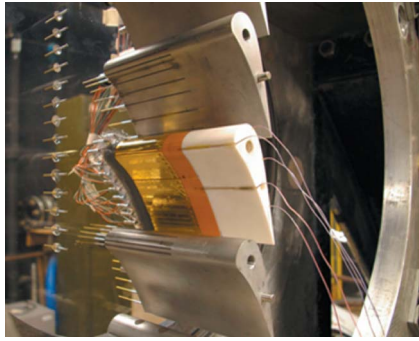


Fig. 4 Photograph of thin film gauges in wind tunnel

ruption. Thin film gauges were originally developed by Schultz and Jones [16], and variations of the original design were used by Doorly and Oldfield [17] and Dunn [18]. The thin film gauges that were used in these experiments are two-layer thin film gauges similar to the gauges developed by Doorly and Oldfield [17]. The gauges were manufactured according to the procedure described by Joe [19].

Each thin film gauge consists of a 3.18 mm (0.125 in.) long platinum sensor attached to copper leads, which are sputtered to a Kapton sheet that is ( $k=0.12$  W/m K)  $50 \mu\text{m}$  thick. The Kapton sheet with the gauges is attached to a vane manufactured from a low thermal conductivity ceramic material, Macor ( $k=1.46$  W/m K). A photograph of the gauges installed on the vane is shown in Fig. 4. Forty-three thin film gauges were instrumented on the vane, with platinum sensors placed at the midspan of the vane.

Thin film gauges are used to measure a change in temperature on the surface of the vane. The platinum sensor of the thin film gauge changes resistance with temperature and is therefore calibrated for temperature coefficients of resistivity prior to testing. Since the gauge changes resistance with temperature, the gauge is used as one arm of a Wheatstone bridge circuit. The Wheatstone bridge used in these experiments is described by Joe [19]. The change in voltage across the bridge during the experiment is sampled at 1 kHz during the experiment using a 16 bit NI SCXI-1600 data acquisition system. The data from up to 31 gauges can be recorded in this facility during a single test.

To reduce the heat transfer data, several steps must be taken. The voltage output from each Wheatstone bridge is converted into a surface temperature using the gauge calibration and basic Wheatstone bridge operating principles. Next, the heat flux for each gauge is calculated by using a finite-difference code developed by Cress [20]. The finite-difference code uses the time history of the surface temperature of the gauge as a boundary condition and solves the one-dimensional transient heat conduction equation. Over the majority of the vane, the conduction is assumed to be semi-infinite since Macor conducts heat very slowly. Near the trailing edge, the heat flux is calculated over a finite material thickness, with the surface temperature measured by the gauges on each side of the vane used as the boundary conditions to calculate heat flux. Once the heat flux is determined, the heat transfer coefficient can then be calculated by using

$$h = \frac{q''}{(T_{aw} - T_{gauge})} \quad (1)$$

where the adiabatic wall temperature is defined as

$$T_{aw} = T_{o1} \left( \frac{1 + r_c \frac{\gamma - 1}{2} \text{Ma}^2}{1 + \frac{\gamma - 1}{2} \text{Ma}^2} \right) \quad (2)$$

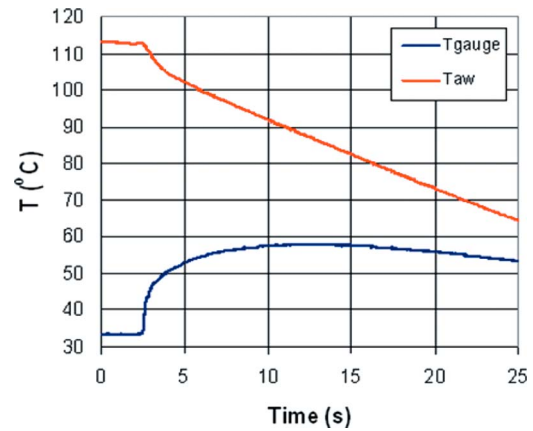


Fig. 5 Typical vane surface and adiabatic wall temperatures history

It was assumed that the boundary layer was turbulent everywhere, so a recovery factor of  $r_c = \text{Pr}^{1/3}$  was applied to all of the gauges. The heat transfer coefficient can then be nondimensionalized by calculating the Nusselt number as

$$\text{Nu} = \frac{hC}{k_a} \quad (3)$$

The heat transfer coefficient can also be nondimensionalized in terms of the Stanton number given by

$$\text{St} = \frac{h}{\rho_L U_L C_p} \quad (4)$$

Figure 5 shows typical vane surface temperature and adiabatic wall temperature time histories, and Fig. 6 shows the calculated heat flux and heat transfer coefficient time histories during a blow-down test run.

**Uncertainty Analysis.** The experimental uncertainty of the heat transfer measurements was calculated by using the perturbation method described by Moffat [21]. The analysis took into account the bias error and precision error. An uncertainty was calculated for each gauge at every test condition. The total uncertainty of the heat transfer coefficient for the gauges ranged between  $\pm 8.5\%$  and  $\pm 11.0\%$  with the bias error contributing to the majority of the total uncertainty. For each test condition, measurements were performed at least three times to establish repeatability.

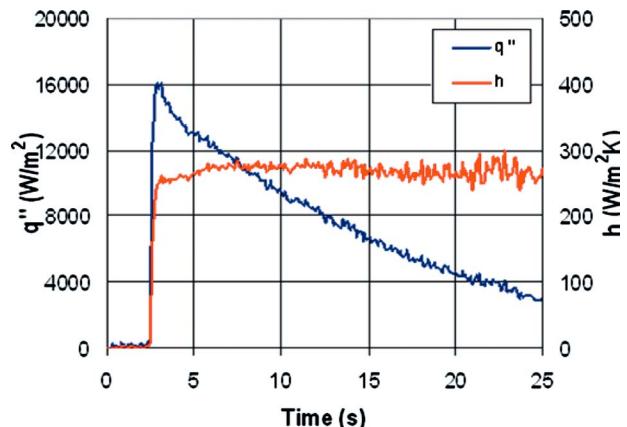


Fig. 6 Typical vane surface heat flux and heat transfer coefficient history

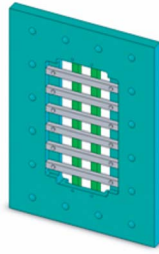


Fig. 7 Square mesh turbulence grid

### Turbulence Generation

To generate freestream turbulence levels of 16%, a passive square mesh turbulence grid was used. A schematic of the turbulence grid is provided in Fig. 7. The grid design was based on the correlations reported by Baines and Peterson [22] and on research performed by Nix et al. [23] on turbulence grids in the cascade wind tunnel. The square mesh grid has bar widths of 1.91 cm (0.75 in.) and is spaced to create  $3.81 \times 3.81 \text{ cm}^2$  ( $1.5 \times 1.5 \text{ in.}^2$ ) square openings. The porosity of the square mesh grid is 52%.

The location of turbulence grid relative to the test section is provided in Fig. 8. The turbulence grid is oriented so that the flow is perpendicular to the grid bars. The mesh grid was placed downstream of the two-dimensional contraction with a spacer (1.25 in. thick) placed between the contraction and test section. The non-dimensional streamwise distance from the turbulence grid to the turbulence measurement slot is given by  $x/B=16$ .

The velocity fluctuations in the streamwise direction were measured using a single hot-film probe with a  $50 \mu\text{m}$  diameter and roughly 1.5 mm long film that was connected to a constant-temperature anemometer. Hot-film data were sampled for approximately 1.3 s at 100 kHz and filtered at 40 kHz. The hot-film probe was discretely traversed over one vane pitch along the vertical slot, as shown in Fig. 2. The turbulence intensity and integral turbulence length scales were calculated at each measurement location. The turbulence length scales were calculated using the methods described by Nix et al. [23] who applied Taylor's hypothesis of frozen turbulence. The turbulence levels and length scales were measured for the square mesh grid and a base line case where no turbulence grid was installed in the tunnel. The turbulence intensity and the normalized integral length scale distributions along the vane inlet pitch are provided in Figs. 9 and 10, respectively. The summary of turbulence measurements is provided in Table 2.

To check the uniformity of the inlet flow to the vane passages downstream of the turbulence grid, a Kiel probe was continuously traversed at low speed along the measurement slot shown in Fig. 2. A velocity ratio was obtained by dividing the velocity measured from the Kiel probe by the velocity measured from a stationary Pitot probe. The velocity ratio for the square mesh grid and a base line configuration tested is provided in Fig. 11.

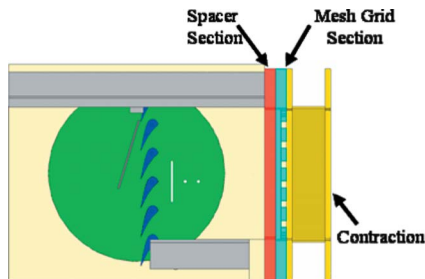


Fig. 8 Square mesh turbulence grid location relative to the test section

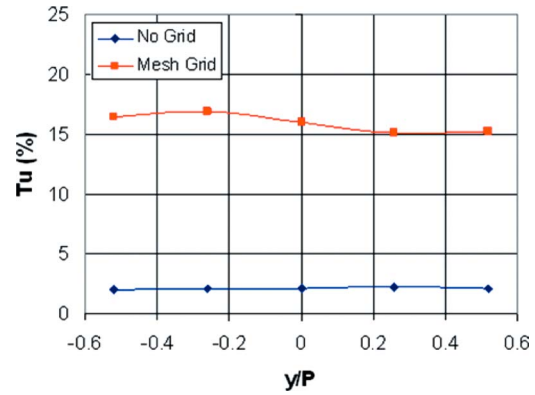


Fig. 9 Turbulence intensity along the inlet pitch

### Vane Static Pressure Distribution

Figure 12 shows the local Mach number distributions on the vane surface for three exit Mach number conditions. The Mach number distribution varies smoothly along the pressure side and does not exhibit any velocity peak downstream of the stagnation region. The flow on the suction side continuously accelerates up to the geometric throat area ( $s/C=0.51$ ). The exit Mach 0.6 and 0.8

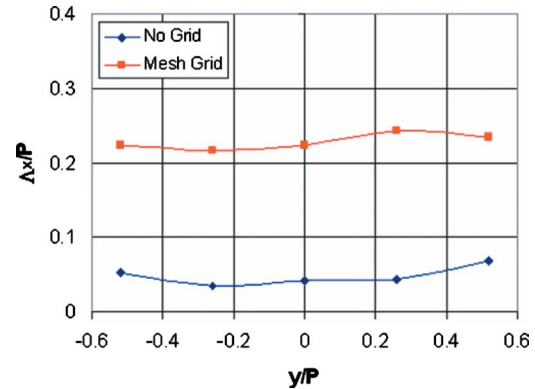


Fig. 10 Integral length scale along the inlet pitch

Table 2 Summary of grid generated turbulence

	Tu intensity	Length scale ( $\Lambda_x/P$ )	Turbulent KE ( $k/U_1^2$ )
Base line	2%	0.05	0.0002
Mesh grid	16%	0.23	0.0128

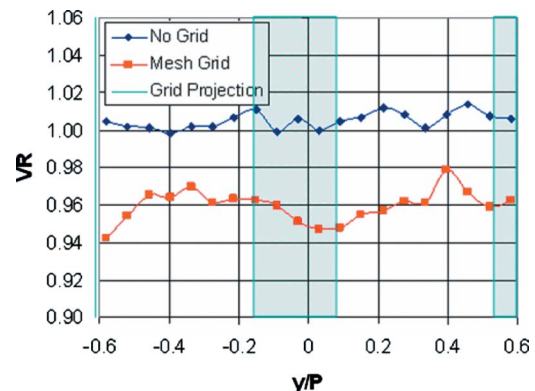


Fig. 11 Velocity ratio distribution along the inlet pitch



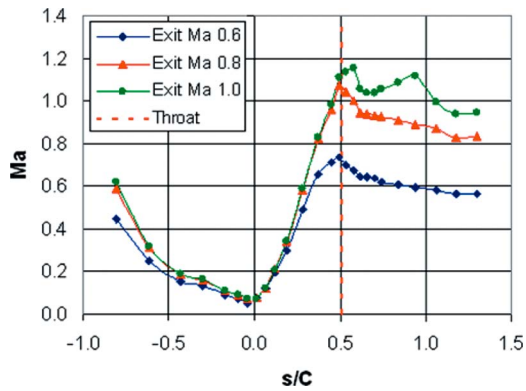


Fig. 12 Local Mach number distribution

cases decelerate immediately after the throat, whereas the exit Mach 1.0 case continues to accelerate and becomes supersonic. A trailing edge shock from the adjacent vane impinging on the suction surface ( $s/C=0.58$ ) causes the multiflow decelerations after the throat for the exit Mach 1.0 case.

The periodicity of the flow at exit Mach 0.8 is provided in Fig. 13. The flow periodicity is shown by comparing the local Mach number distribution over the vane surfaces. The suction sides of Vanes 1 and 2 show the same local Mach number distributions over the majority of the suction surface. There is a slight variation in the local Mach numbers near the geometric throat. The pressure side of Vanes 2 and 3 shows almost identical local Mach number distributions with very small variation downstream of the stagnation region.

The distribution of acceleration parameter,  $k$ , on the vane surface for each exit Mach number is provided in Fig. 14. A positive acceleration parameter indicates that the flow is accelerating and a negative value indicates that the flow is decelerating. On the pressure side of the vane, the acceleration parameter for exit Mach 0.6 case barely reaches the critical value of  $3 \times 10^{-6}$  after  $s/C = -0.43$ . This critical value of  $k$  has been observed by Jones and Launder [24] and Mayle [25] as a criterion for boundary layer relaminarization.

### Vane Heat Transfer Distribution

**Test Conditions.** Heat transfer measurements were performed at exit Mach numbers of 0.55, 0.75, and 1.01. The turbulence levels were varied between 2% and 16% at each exit Mach number. The test matrix produced heat transfer data for six different flow conditions. For each test condition, measurements were performed at least three times to establish repeatability. Table 3 provides

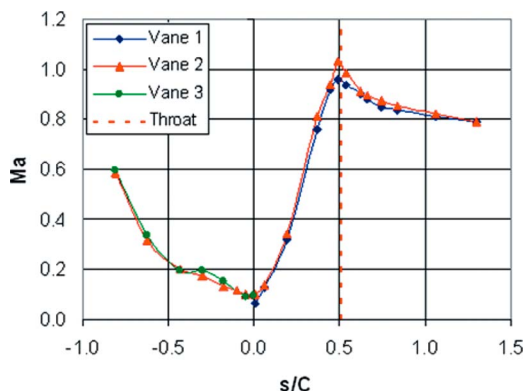


Fig. 13 Flow periodicity through vane passages

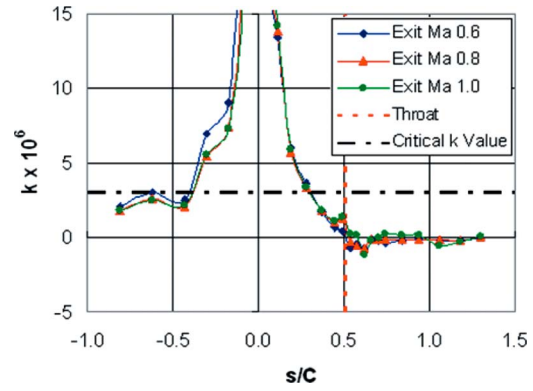


Fig. 14 Acceleration parameter distribution

vides the flow and heat transfer conditions for each test. The exit Reynolds number coupled with the exit Mach number is based on a vane chord and is defined by

$$Re_2 = \frac{\rho_2 U_2 C}{\mu_2} \quad (5)$$

where the average pressure and temperature data during the test run were used to calculate the exit Reynolds number.

**Effect of Freestream Turbulence.** This section discusses the effect that increasing freestream turbulence has on the heat transfer distribution over the turbine vane surface. Plots of the heat transfer distribution over the vane surface are shown in terms of the Nusselt number and the Nusselt number augmentation relative to the low freestream turbulence cases.

Figures 15–17 provide the heat transfer distributions for each freestream turbulence level at exit Mach 0.55, 0.75, and 1.01, respectively. The large scale high freestream turbulence augments the heat transfer at the leading edge, on the pressure side, and on the suction side of the vane where the boundary layer is laminar. The general shape of the heat transfer distribution over the vane surface is the same for all cases. After having achieved a relatively high heat transfer value at the leading edge, the heat transfer decreases

Table 3 Test conditions for each case

	Exit Ma	Tu (%)	Exit Re	$T_{o1}$ (°C)	$T_{init,w}$ (°C)
Case 1	0.55	2	900,000	105	30.4
Case 2	0.55	16	908,000	107	28.2
Case 3	0.74	2	1,050,000	102	33.4
Case 4	0.75	16	1,060,000	107	33.3
Case 5	1.02	2	1,520,000	103	29.0
Case 6	1.01	16	1,500,000	104	32.0

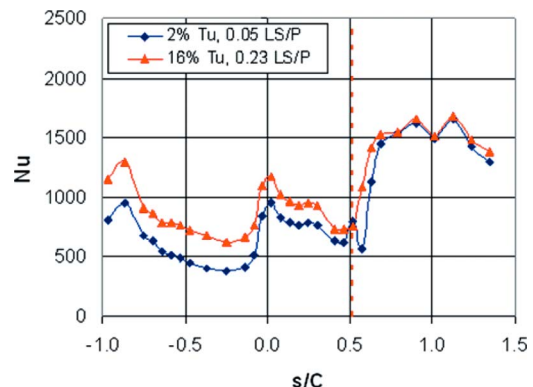


Fig. 15 Heat transfer distribution at exit Ma 0.55

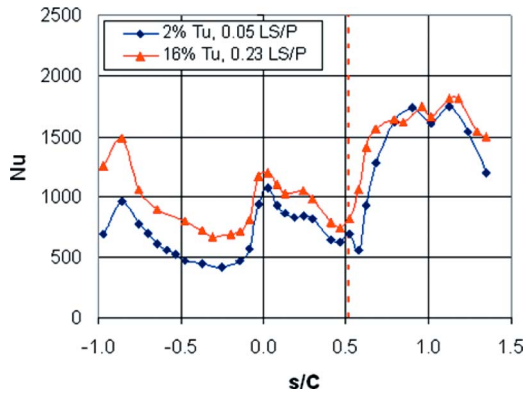


Fig. 16 Heat transfer distribution at exit Ma 0.75

creases as the flow proceeds down the suction and pressure sides due to the development of a laminar boundary layer. The heat transfer on the suction surface also responds to the pressure gradient along the surface and decreases until the boundary layer transitions, where a large increase in heat transfer occurs. The heat transfer on the pressure surface shows a decrease until  $s/C = -0.25$  and then a continuous increase until  $s/C = -0.86$ .

On the suction side, the transition to a turbulent boundary layer occurs downstream of throat at  $s/C = 0.57$  for the low turbulence level at exit Mach 0.55 and 0.75. The boundary layer transition length over the vane surface is short for the exit Mach 0.55 and 0.75 cases because the flow is decelerating downstream of the throat. The boundary layer transition for the low turbulence at exit Ma 1.01 occurs at  $s/C = 0.40$ . Since the flow is still accelerating at this point, the transition length is affected. The effect of acceleration on the transition length was also noted in the study performed by Zhang and Han [26].

The start of the transition for the high turbulence tests at exit Mach 0.55 and 0.75 appears to begin slightly earlier at  $s/C = 0.51$ . Again, the boundary layer transition length over the vane surface is short for the exit Mach 0.55 and 0.75 cases because of flow deceleration downstream of the throat. The boundary layer transition for the high turbulence at exit Ma 1.01 occurs also at  $s/C = 0.40$ . For the exit Mach 1.01 case, the transition location is observed to be not influenced by the large scale high freestream turbulence. The transition length for both turbulence cases at exit Mach 1.01 is interrupted around  $s/C = 0.57$ , which corresponds to the location where trailing edge shock from the adjacent vane impinges on the suction surface. The slow transition could be attributed to the interaction of the shock with the transitioning boundary layer. Once the boundary layer goes turbulent on the suction side, the effect of the large scale high freestream turbulence level on heat transfer diminishes. This observation is con-

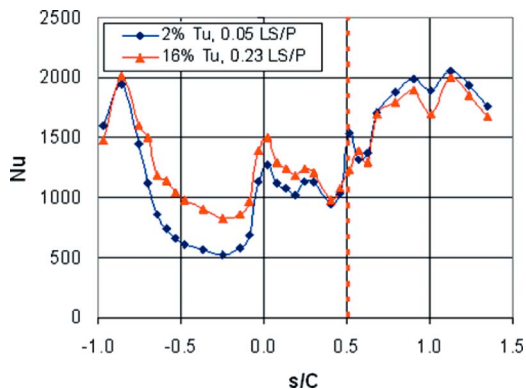


Fig. 17 Heat transfer distribution at exit Ma 1.01

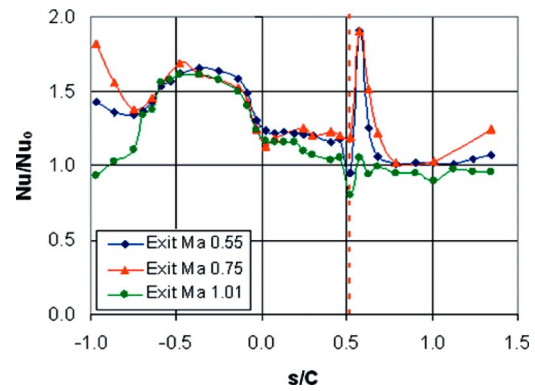


Fig. 18 Heat transfer augmentation at all exit Ma cases

sistent with Ames and Moffat [27] and Thole and Bogard [28] who showed that relatively large scale turbulence has a reduced effect on turbulent boundary layer heat transfer augmentation.

The heat transfer data at high turbulence level were also normalized with the 2% turbulence data to show the augmentation levels due to turbulence. The augmentation plots for exit Mach 0.55, 0.75, and 1.01 are shown in Fig. 18. There is a peak in the augmentation plot on the suction side for the exit Mach 0.55 and 0.75 cases because the transition occurs slightly earlier than low freestream turbulence. Relatively higher augmentation levels can be seen over the majority of the pressure surface as compared to the suction surface. For instance, at exit Mach 0.75, average heat transfer augmentations of 52% and 25% were observed on the pressure and suction sides of the vane, respectively.

The heat transfer augmentation trends are similar over the majority of vane pressure surface for all exit Mach conditions. However, these augmentation plots show a change in shape at the aft end of the pressure surface. The upturn in the augmentation plot at exit Mach 0.55 and 0.75 shows a boundary layer transition behavior on the pressure surface. This upturn in the augmentation plot goes away at exit Mach 1.01, which shows that the low freestream turbulence case achieves a complete boundary layer transition on the pressure surface.

In the stagnation region, relatively lower augmentation levels are observed at exit Mach 0.75 and 1.01 than for the exit Mach 0.55 case. Since the Mach number and the Reynolds number are coupled in our facility, this behavior is consistent with the stagnation region heat transfer study of Radomsky and Thole [6] that indicates very little heat transfer augmentation with increasing Reynolds number at high freestream turbulence. The augmentation levels are similar over the majority of vane suction surface for exit Mach 0.55 and 0.75. However, at exit Mach 1.01, the augmentation level is lower in the laminar region than at exit Mach 0.55 and 0.75. This might be due to the diminishing influence of large scale high freestream turbulence on heat transfer augmentation with increasing Reynolds number.

The heat transfer data were also compared to the flat plate correlations for a laminar and turbulent boundary layer. While the flat plate correlations do not take into account the effect of pressure gradient or curvature on heat transfer, the correlations do provide insight on boundary layer behavior. The flat plate correlations reported by Incropera and DeWitt [29] in terms of the local Nusselt number are

$$\text{Laminar: } Nu_L = 0.332 Re_L^{1/2} Pr^{1/3} \quad (6)$$

$$\text{Turbulent: } Nu_L = 0.0296 Re_L^{4/5} Pr^{1/3} \quad (7)$$

The local Reynolds number given by

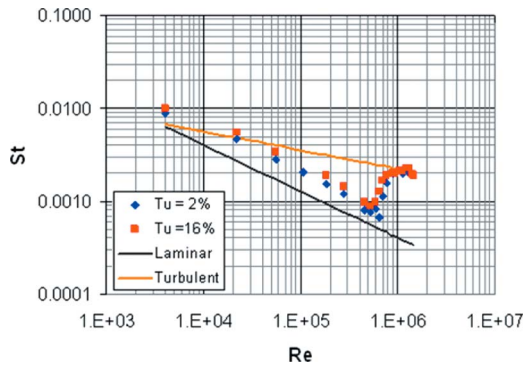


Fig. 19 Suction side data compared to the flat plate correlations at exit Ma 0.75

$$Re_L = \frac{\rho_L U_L s}{\mu} \quad (8)$$

was used to find the Nusselt number distribution of the correlation. Averaged pressure and temperature data taken during the test run were used to calculate the local Reynolds number. The local Nusselt number was converted into a heat transfer coefficient at each measurement location by using

$$h = \frac{Nu_L k_a}{s} \quad (9)$$

and then the Stanton number is calculated by using Eq. (4).

Figure 19 shows how the experimental data compare with the laminar and turbulent flat plate heat transfer correlations on the suction side of the vane at exit Mach 0.75. Before transition occurs, the boundary layer data lie between the laminar and turbulent boundary layer correlations for each case and follow the trend of laminar correlation. The difference between the laminar correlation and the low freestream turbulence data in the laminar region can be attributed to the effect of a favorable pressure gradient. The augmentation due to turbulence can also be seen on the suction side. A good agreement between the turbulent flat plate correlation and the experimental data is shown for all of the data once the flow goes turbulent on the suction surface. Similar trends were also observed for the exit Mach 0.55 and 1.01 cases.

The comparison of the experimental data at exit Mach 0.75 with the laminar and turbulent flat plate correlations on the pressure side is provided in Fig. 20. For low freestream turbulence, the data initially follow the trend of the laminar correlation and then approach the turbulent correlation toward the end of the pressure surface. At high freestream turbulence the data follow the trend of the turbulent correlation. Similar trends were also observed for exit Mach 0.55 and 1.01 cases. From the acceleration parameter in

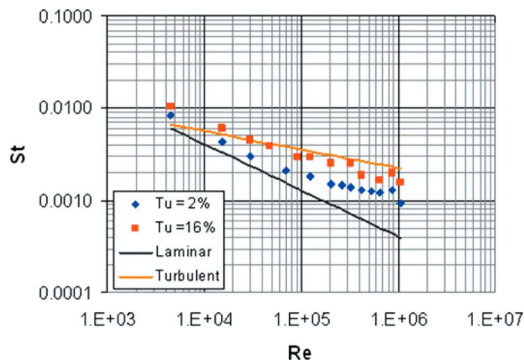


Fig. 20 Pressure side data compared to the flat plate correlations at exit Ma 0.75

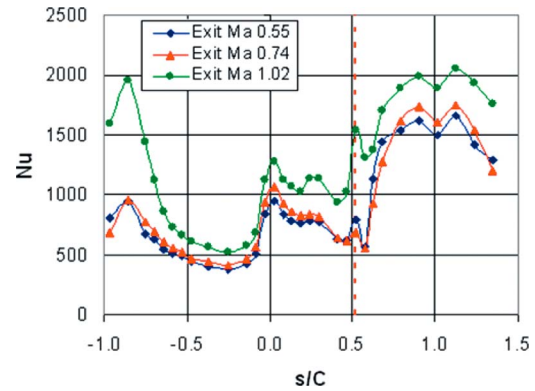


Fig. 21 Heat transfer distribution at Tu=2%

Fig. 14, the acceleration parameter barely reaches the critical value over the pressure side after  $s/C = -0.43$ , so there was no evidence of boundary layer relaminarization at any exit Mach condition.

**Effect of Reynolds Number.** The primary objective of this work was to examine the effect of freestream turbulence on heat transfer at three exit Mach number conditions. Because of this objective, the exit Mach number was not decoupled from the exit Reynolds number. An increase in exit Mach number corresponds to an increase in the exit Reynolds number. To remain consistent with the previous sections, the data will be compared by stating the Mach number. The actual exit Reynolds numbers measured for each test are provided in Table 3.

The Nusselt number distributions showing the effect of increasing the Reynolds number at turbulence levels of 2% and 16% are shown in Figs. 21 and 22, respectively. As expected, there is an overall increase in heat transfer due to the increase in Reynolds number. The increase in heat transfer level is most noticeable at the highest Reynolds number (Mach 1.01). Another effect that the highest Reynolds number has on the heat transfer is to promote an early boundary layer transition ( $s/C = 0.40$ ) on the suction side. An earlier boundary layer transition on the suction side is observed at both turbulence levels.

On the pressure side, steeper streamwise Nusselt number gradients are observed at the highest Reynolds number. These Nusselt number gradients are more noticeable at the low freestream turbulence, indicating a boundary layer transition at the aft end of the pressure side.

**Leading Edge Correlation.** The experimental data at the leading edge were compared to the correlation developed by Dullenkopf and Mayle [30]. The correlation takes into account the effects of freestream turbulence and integral length scale on

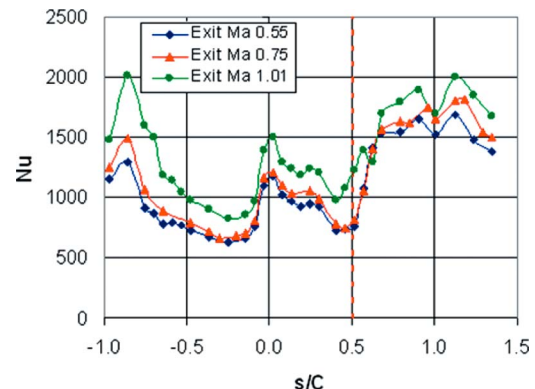


Fig. 22 Heat transfer distribution at Tu=16%



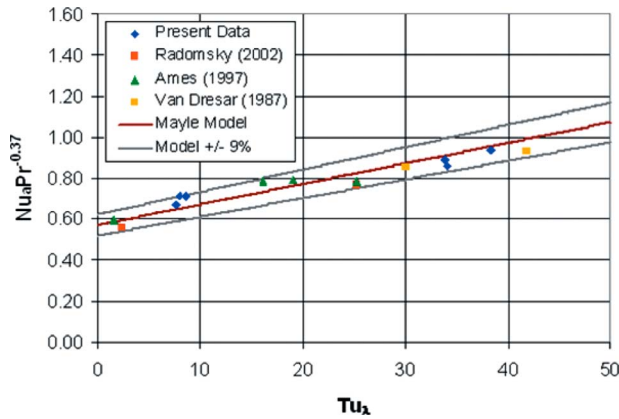


Fig. 23 Stagnation region data compared to Dullenkopf and Mayle's correlation

stagnation region heat transfer. The correlation requires the determination of an "effective" leading edge diameter of the vane. The effective leading edge diameter of the vane is determined by fitting the velocity distribution around the suction side of the vane to a potential flow theory for a cylinder in crossflow. The correlation uses an effective turbulence level and also takes into account the strain rate. The effective Nusselt number is presented as a function of this effective turbulence level  $Tu_\lambda$  by

$$Nu_a Pr^{-0.37} = 0.571 + 0.01 Tu_\lambda \quad (10)$$

where

$$Nu_a = \frac{Nu_D}{\sqrt{a_1 Re_D}} \quad (11)$$

and the value of  $Tu_\lambda$  is determined by

$$Tu_\lambda = \frac{Tu_a \sqrt{L_a}}{(1 + 0.004 L_a^2)^{5/12}} \quad (12)$$

The dimensionless length scale  $L_a$  is given by

$$L_a = (\Lambda_s/D) \sqrt{a_1 Re_D} \quad (13)$$

and

$$Tu_a = Tu \sqrt{a_1 Re_D} \quad (14)$$

It must be mentioned that the dimensionless strain rate  $a_1=4$  was used for the stagnation data. Figure 23 shows the comparison of current heat transfer data and the previous literature investigations [4,6,31] with Dullenkopf and Mayle's correlation for stagnation region heat transfer. The experimental data at the leading edge compare rather well with the correlation. All of the data follow the same trend as the correlation and lies within  $\pm 9\%$  (bias error) of the correlation.

**FLUENT and TEXSTAN Comparison.** Computational fluid dynamics (CFD) heat transfer predictions at low freestream turbulence were performed using a commercially available software package (FLUENT 6.2.6). A 2D computational domain representing one full vane passage with periodic boundary conditions was employed to simulate the cascade test condition. The computational inlet was located at  $0.45C$  upstream of the vane leading edge. For all test cases, total pressure and total temperature were specified at the inlet and static pressure was specified at the outlet. The vane geometry was simulated with constant wall temperature boundary condition. Freestream turbulence level and length scale were also specified at the inlet for all test cases. Fluid specific heat, thermal conductivity, and molecular viscosity were kept constant for all test cases.

For the FLUENT solver, a coupled implicit solution method with the second-order upwind discretization scheme was chosen. The

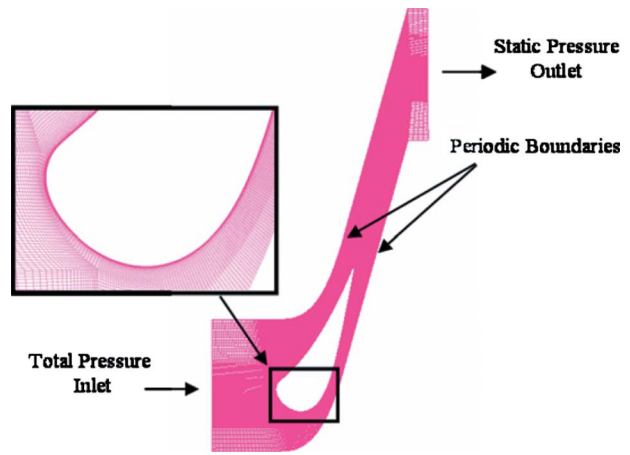


Fig. 24 Computational domain for CFD predictions

Reynolds-averaged Navier-Stokes (RANS) based  $v^2-f$  turbulence model, originally suggested by Durbin [32], was used in all numerical predictions. A 2D hexahedral mesh consisted of 73,300 cells and was refined near the wall to better capture wall heat transfer, as shown in Fig. 24. This was achieved by adjusting the near-wall spacing  $y^+$  to be less than 1. The convergence of calculation was assumed to be reached when all normalized residuals were smaller than  $10^{-5}$ , except energy smaller than  $10^{-7}$ . In general, 3000 iterations were required for full convergence.

Figure 25 shows the comparison of predicted and measured Mach number distributions around the vane surface for three exit Mach number conditions. Overall, the FLUENT results compare very well with the experimental data on the pressure side at all exit Mach conditions. On the suction side, the FLUENT predictions also compare well with the experimental data at exit Mach 0.6 and 0.8. For the exit Mach 1.0 case, the FLUENT prediction matches the experimental data up to  $s/C=0.58$ , but then the FLUENT model is unable to reasonably predict multiflow decelerations caused by the shock wave on suction side Mach number distribution.

Figures 26–28 provide the comparison of measured and predicted Nusselt number distributions for low freestream turbulence levels at exit Mach 0.55, 0.75, and 1.01, respectively. The  $v^2-f$  model compares generally well over the majority of the vane pressure surface at all exit Mach conditions, as observed by other authors [33,34]. The model overpredicts the heat transfer at the leading edge and in the laminar region on the suction side for the exit Mach 0.55 and 0.75 cases. The  $v^2-f$  model also predicts an early boundary layer transition on the suction side and overpredicts the heat transfer at the end of transition for the exit Mach 0.55 and 0.75 cases. An early boundary layer prediction and over-

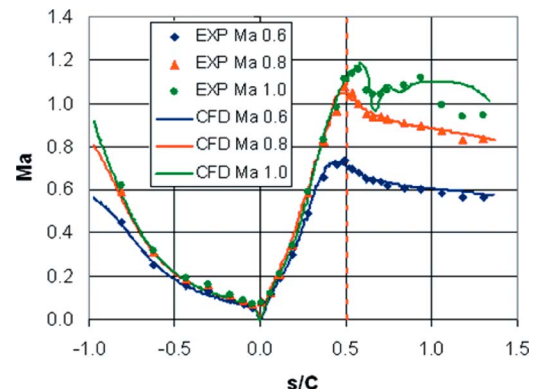


Fig. 25 Local Mach number distribution comparison

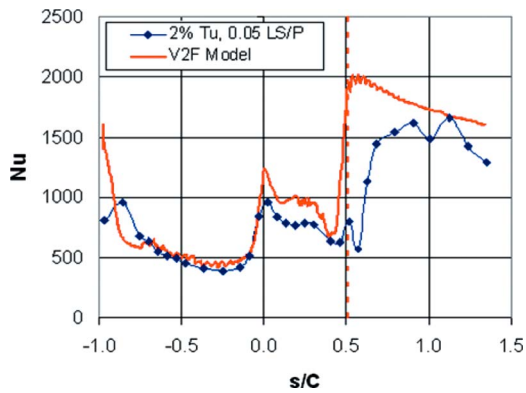


Fig. 26 FLUENT prediction at exit Ma 0.55, 2% Tu

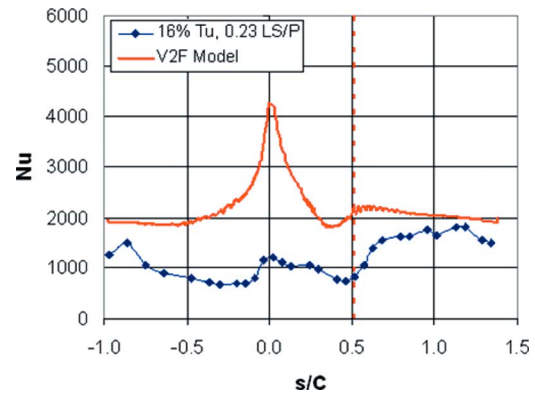


Fig. 29 FLUENT prediction at exit Ma 0.75, 16% Tu

prediction of the heat transfer at the end of transition has also been observed by Luo and Razinsky [34]. At exit Mach 1.01, the  $v^2-f$  model overpredicts heat transfer at the leading edge but then underpredicts it in the region from  $s/C=0.25$  to  $s/C=0.5$ . Also the  $v^2-f$  model underpredicts turbulent boundary layer heat transfer on the suction and pressure sides of the vane at exit Mach 1.01.

An attempt was also made to perform FLUENT  $v^2-f$  heat transfer predictions at high freestream turbulence level but the  $v^2-f$  model profoundly overpredicted heat transfer at high freestream turbulence on the entire surface of the vane at all exit Mach conditions. Figure 29 provides a comparison of measured and predicted Nusselt number distributions for a high freestream turbulence level at exit Mach 0.75. The leading edge heat transfer is profoundly overpredicted and seems to affect the heat transfer levels on the entire surface of the vane. Modeling freestream turbulence eddy viscos-

ity as a function of large length scale, proper scaling of high freestream turbulence near the wall, and developing correct models to account for the heat transfer augmentation in the leading edge region and both surfaces of the vane at high freestream turbulence are challenging and require more work.

The experimental data were also compared with the numerical predictions of an academic version of TEXSTAN developed by Crawford [35]. To model the flow through the vane passages, the two-equation Lam–Bremhorst turbulence model was used with the Schmidt–Patankar transition model. A constant surface temperature boundary condition was applied to the vane, and the constant freestream turbulence kinetic energy was set throughout the computational domain by freezing the turbulence dissipation rate.

At low freestream turbulence, the TEXSTAN predictions match well with the experimental data at all exit Mach conditions on the pressure side until  $s/C=-0.53$  but then start to deviate from the measurements, as shown in Figs. 30–32. On the suction side, the predictions match well with the data in the laminar region downstream of the leading edge, but the above mentioned turbulence and transition models did not predict boundary layer transition. For the low freestream turbulence case at all exit Mach conditions only, the TEXSTAN was forced to transition at the location where the experimental data indicated transition by using an abrupt transition model.

At high freestream turbulence, TEXSTAN overpredicted the heat transfer on both the pressure and suction sides of the vane at all exit Mach conditions, as shown in Figs. 33–35. The leading edge heat transfer is also overpredicted at all exit Mach conditions. However, the suction side predictions show a similar trend in the laminar region, with the data only coming close to the prediction after the transition. The pressure side predictions at all exit Mach conditions also show a similar trend, with the data coming close to prediction at the aft end of the pressure surface.

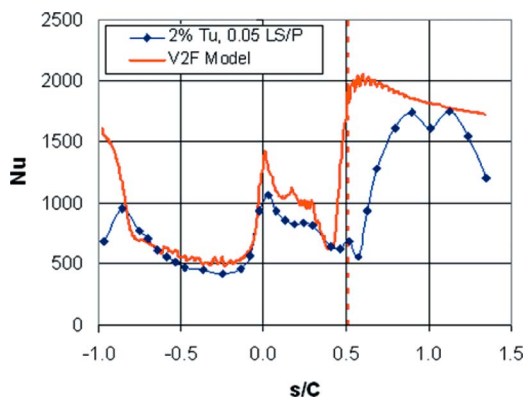


Fig. 27 FLUENT prediction at exit Ma 0.75, 2% Tu

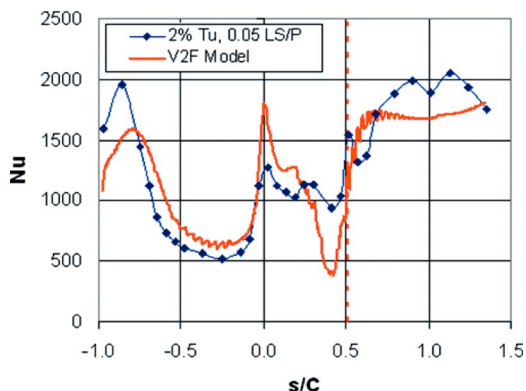


Fig. 28 FLUENT prediction at exit Ma 1.01, 2% Tu

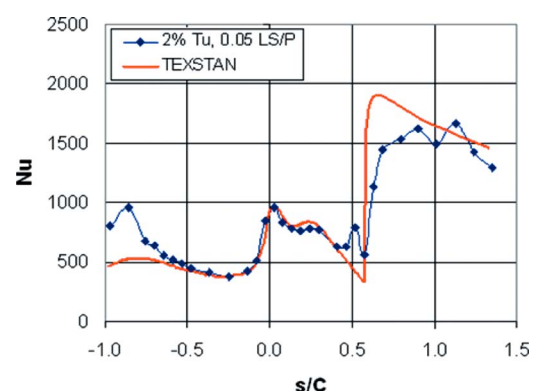


Fig. 30 TEXSTAN prediction at exit Ma 0.55, 2% Tu

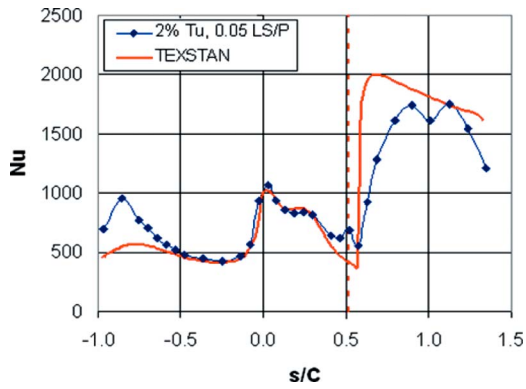


Fig. 31 TEXSTAN prediction at exit Ma 0.75, 2% Tu

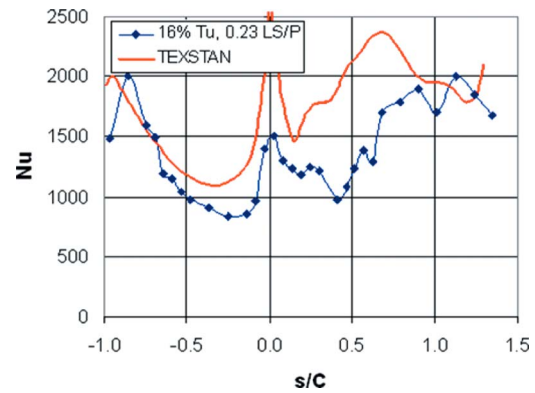


Fig. 35 TEXSTAN prediction at exit Ma 1.01, 16% Tu

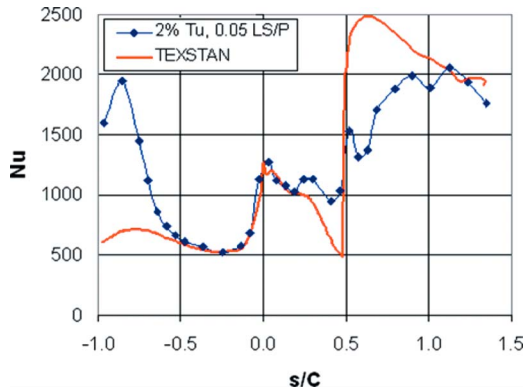


Fig. 32 TEXSTAN prediction at exit Ma 1.01, 2% Tu

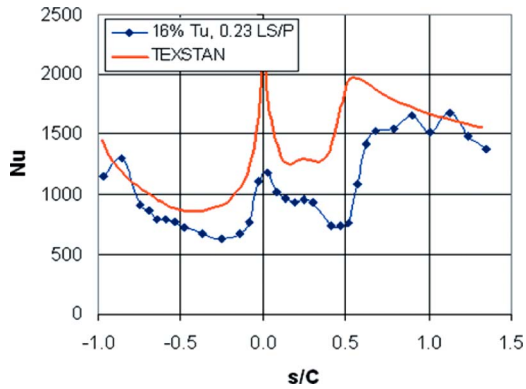


Fig. 33 TEXSTAN prediction at exit Ma 0.55, 16% Tu

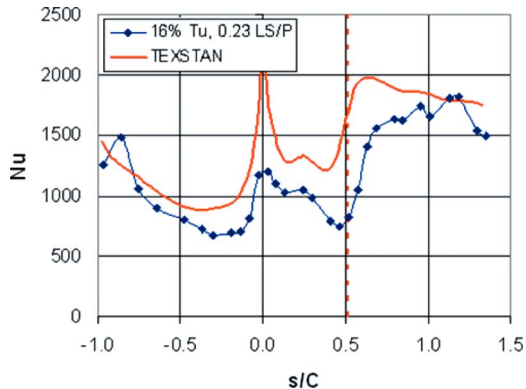


Fig. 34 TEXSTAN prediction at exit Ma 0.75, 16% Tu

## Conclusions

Aerodynamic and heat transfer measurements were made on a turbine vane at flow conditions representative of engine operating conditions. Large scale high freestream turbulence was generated by using a passive turbulence grid. Increasing the turbulence level was observed to augment the heat transfer over the vane surface.

Relatively higher augmentation levels were seen over the majority of the pressure surface as compared to the suction surface for all exit Mach conditions. High freestream turbulence hastened the boundary layer transition on the suction side for the exit Mach 0.55 and 0.75 cases. For the exit Mach 1.01 case, the turbulence augmentation was small on the suction surface as compared to the exit Mach 0.55 and 0.75 cases. Also for the exit Mach 1.01 case, increasing the freestream turbulence was observed to not influence the location of boundary layer transition on the suction surface.

As expected, increasing the exit Reynolds number was shown to increase the heat transfer levels and cause earlier boundary layer transition on the suction side for the highest Reynolds number ( $1.5 \times 10^6$ ). On the pressure side, steeper streamwise Nusselt number gradients were observed at the highest Reynolds number. These Nusselt number gradients were more noticeable at the low freestream turbulence, indicating a boundary layer transition to turbulent flow at the aft end of the pressure side.

Several comparisons were made between the data using the analytical flat plate correlations, leading edge correlation developed by Dullenkopf and Mayle [30], FLUENT  $v^2-f$  model, and TEXSTAN predictions. The heat transfer data showed a good agreement with flat plate and leading edge correlations. The  $v^2-f$  model, and TEXSTAN resulted in an overall reasonable prediction of the heat transfer at low freestream turbulence levels. At high freestream turbulence, FLUENT  $v^2-f$  model and TEXSTAN was found to significantly overpredict the heat transfer levels on the vane surface.

## Acknowledgment

This work was sponsored by Solar Turbines Inc. We would also like to express our gratitude to Dr. Richard Anthony and Dr. Marcus Polanka of the Air Force Research Laboratory, Wright-Patterson AFB for their help with manufacturing and implementation of the thin film gauges. Laboratory, Wright-Patterson AFB for their help with the manufacturing and implementation of the thin film gauges.

## Nomenclature

- $a_1$  = dimensionless strain rate
- $B$  = bar width of turbulence grid
- $C$  = vane chord
- $C_p$  = constant pressure specific heat
- $D$  = effective leading edge diameter of vane
- $f$  = elliptic operator in the V2F model



$h$  = heat transfer coefficient  
 $k_a$  = thermal conductivity of air  
 $k$  = acceleration parameter/thermal conductivity/  
 turbulent kinetic energy  
 $L_a$  = dimensionless length scale  
 $LS$  = integral turbulence length scale  
 $Ma$  = Mach number  
 $Nu$  = Nusselt number  
 $Nu_a$  = effective Nusselt number  
 $Nu_0$  = Nusselt number at  $Tu=2\%$   
 $Nu_D$  = Nusselt number based on  $D$   
 $P$  = vane pitch  
 $Pr$  = Prandtl number  
 $q''$  = heat flux  
 $r_c$  = recovery factor  
 $Re$  = Reynolds number  
 $Re_D$  = Reynolds number based on  $D$ , evaluated at  
 inlet conditions  
 $s$  = vane surface distance from stagnation point  
 $St$  = Stanton number  
 $T$  = temperature  
 $Tu$  = streamwise freestream turbulence intensity  
 $Tu_a$  = modified turbulence intensity  
 $Tu_\lambda$  = effective turbulence intensity  
 $U$  = local velocity  
 $v^2$  = wall normal Reynolds stress component  
 $x$  = streamwise distance from turbulence grid  
 $y^+$  = equivalent normal distance

#### Greek

$\gamma$  = specific heat ratio of air  
 $\Lambda_x$  = integral turbulence length scale  
 $\rho$  = local density of air  
 $\mu$  = dynamic viscosity of air

#### Subscripts

$1, 2$  = inlet conditions, exit conditions  
 $aw, w$  = adiabatic wall, wall  
 $gauge$  = thin film gauge (surface) measurement  
 $init$  = initial  
 $L$  = local conditions  
 $o$  = stagnation

#### References

- Zimmermann, D. R., 1979, "Laser Anemometer Measurements at the Exit of a T63-C20 Combustor," NASA Report No. CR-159623.
- Van Fossen, G. J., and Bunker, R. S., 2001, "Augmentation of Stagnation Heat Transfer Due to Turbulence From a DLN Can Combustor," ASME J. Turbomach., **123**, pp. 140–146.
- Ames, F. E., Wang, C., and Barbot, P. A., 2003, "Measurement and Prediction of the Influence of Catalytic and Dry Low  $NO_x$  Combustor Turbulence on Vane Surface Heat Transfer," ASME J. Turbomach., **125**, pp. 221–231.
- Ames, F. E., 1997, "The Influence of Large-Scale High Intensity Turbulence on Vane Heat Transfer," ASME J. Turbomach., **119**, pp. 23–30.
- Ames, F. E., Argenziano, M., and Wang, C., 2004, "Measurement and Prediction of Heat Transfer Distributions on an Aft Loaded Vane Subjected to the Influence of Catalytic and Dry Low  $NO_x$  Combustor Turbulence," ASME J. Turbomach., **126**, pp. 139–149.
- Radomsky, R., and Thole, K. A., 2002, "Detailed Boundary Layer Measurements on a Turbine Stator Vane at Elevated Freestream Turbulence Levels," ASME J. Turbomach., **124**, pp. 107–118.
- Nealy, D. A., Mihelc, M. S., Hylton, L. D., and Gladden, H. J., 1990, "Measurements of Heat Transfer Distribution Over the Surfaces of Highly Loaded Turbine Nozzle Guide Vanes," ASME J. Eng. Gas Turbines Power, **106**, pp. 149–158.
- Arts, T., and Lambert de Rouvoit, M., 1992, "Aero-Thermal Performance of a Two-Dimensional Highly Loaded Transonic Turbine Nozzle Guide Vane: A Test Case for Inviscid and Viscous Flow Computations," ASME J. Turbomach., **114**, pp. 147–154.
- Hoffs, A., Drost, U., and Bolcs, A., 1996, "Heat Transfer Measurements on a Turbine Airfoil at Various Reynolds Numbers and Turbulence Intensities Including Effects of Surface Roughness," ASME Paper No. GT-1996-169.
- Bunker, R. S., 1997, "Separate and Combined Effects of Surface Roughness and Turbulence Intensity on Vane Heat Transfer," ASME Paper No. GT-1997-135.
- Carullo, J. S., Nasir, S., Cress, R. D., Ng, W. F., Thole, K. A., Zhang, L. J., and Moon, H. K., 2007, "The Effects of Freestream Turbulence, Turbulence Length Scale, and Exit Reynolds Number on Turbine Blade Heat Transfer in a Transonic Cascade," ASME Paper No. GT-2007-27859.
- Nix, A. C., Diller, T. E., and Ng, W. F., 2007, "Experimental Measurements and Modeling of the Effects of Large-Scale Freestream Turbulence on Heat Transfer," ASME J. Turbomach., **129**, pp. 542–550.
- Holmberg, D. G., and Diller, T. E., 2005, "Simultaneous Heat Flux and Velocity Measurements in a Transonic Turbine Cascade," ASME J. Turbomach., **127**, pp. 502–506.
- Smith, D. E., Bubb, J. V., Popp, O., Grabowski, H. C., Diller, T. E., Schetz, J. A., and Ng, W. F., 2000, "An Investigation of Heat Transfer in a Film Cooled Transonic Turbine Cascade—Part I: Steady Heat Transfer," ASME Paper No. 2000-GT-202.
- Popp, O., Smith, D. E., Bubb, J. V., Grabowski, H. C., Diller, T. E., Schetz, J. A., and Ng, W. F., 2000, "An Investigation of Heat Transfer in a Film Cooled Transonic Turbine Cascade—Part II: Unsteady Heat Transfer," ASME Paper No. 2000-GT-203.
- Schultz, D. L., and Jones, T. V., 1973, "Heat Transfer Measurements in Short Duration Hypersonic Facilities," AGARD Paper No. AG-165.
- Doorly, J. E., and Oldfield, M. L. G., 1987, "The Theory of Advanced Multi-Layer Thin Film Heat Transfer Gages," Int. J. Heat Mass Transfer, **30**, pp. 1159–1168.
- Dunn, M. G., 1995, "The Thin-Film Gage," *Von Karman Institute for Fluid Dynamics Lecture Series 1995*.
- Joe, C. R., 1997, "Unsteady Heat Transfer on the Turbine Research Facility at Wright Laboratory," Ph.D. thesis, Syracuse University.
- Cress, R. D., 2006, "Turbine Blade Heat Transfer Measurements in a Transonic Flow Using Thin Film Gages," MS thesis, Virginia Polytechnic Institute and State University.
- Moffat, R. J., 1988, "Describing Uncertainties in Experimental Results," Exp. Therm. Fluid Sci., **1**, pp. 3–17.
- Baines, W. D., and Peterson, E. G., 1951, "An Investigation of Flow Through Screens," Trans. ASME, **73**, pp. 467–480.
- Nix, A. C., Smith, A. C., Diller, T. E., Ng, W. F., and Thole, K. A., 2002, "High Intensity, Large Length-Scale Freestream Turbulence Generation in a Transonic Turbine Cascade," ASME Paper No. GT-2002-30523.
- Jones, W. P., and Launder, B. E., 1972, "The Prediction of Laminarization With a Two-Equation Model of Turbulence," Int. J. Heat Mass Transfer, **15**, pp. 301–314.
- Mayle, R. E., 1991, "The Role of Laminar-Turbulent Transition in Gas Turbine Engines," ASME J. Turbomach., **113**, pp. 509–537.
- Zhang, J., and Han, J.-C., 1994, "Influence of Mainstream Turbulence on Heat Transfer Coefficient From a Gas Turbine Blade," ASME J. Heat Transfer, **116**, pp. 896–903.
- Ames, F. E., and Moffat, R. J., 1990, "Heat Transfer With High Intensity, Large Scale Turbulence: The Flat Plate Turbulent Boundary Layer and the Cylindrical Stagnation Point," Thermosciences Division of Mechanical Engineering, Stanford University, Report No. HMT-44.
- Thole, K. A., and Bogard, D. G., 1995, "Enhanced Heat Transfer and Skin Friction Due to High Freestream Turbulence," ASME J. Turbomach., **117**, pp. 418–424.
- Incropera, F. P., and DeWitt, D. P., 2002, *Fundamentals of Heat and Mass Transfer*, 5th ed., Wiley, New York.
- Dullenkopf, K., and Mayle, R. E., 1995, "An Account of Free-Stream-Turbulence Length Scale on Laminar Heat Transfer," ASME J. Turbomach., **117**, pp. 401–406.
- Van Dresar, N. T., and Mayle, R. E., 1989, "A Quasi-Steady Approach to Leading Edge Heat Transfer Rates," ASME J. Turbomach., **111**, pp. 483–490.
- Durbin, P., 1991, "Near-Wall Turbulence Closure Modeling Without 'Damping Functions'," Theor. Comput. Fluid Dyn., **3**, pp. 1–13.
- Pecnik, R., Pieringer, P., and Sanz, W., 2005, "Numerical Investigation of the Secondary Flow of a Transonic Turbine Stage Using Various Turbulence Closures," ASME Paper No. GT-2005-68754.
- Luo, J., and Razinsky, E. H., 2007, "Conjugate Heat Transfer Analysis of a Cooled Turbine Vane Using the  $v^2-f$  Turbulence Model," ASME J. Turbomach., **129**, pp. 773–781.
- Crawford, M. E., 1986, "Simulation Codes for Calculation of Heat Transfer to Convectively-Cooled Turbine Blades," *A Set of Four Lectures in Convective Heat Transfer and Film Cooling in Turbomachinery VKI Lecture Series 1986*.